LONG-TERM PERFORMANCE OF RECYCLED STEEL FIBRE REINFORCED CONCRETE FOR PAVEMENT APPLICATIONS

(Volume 1)

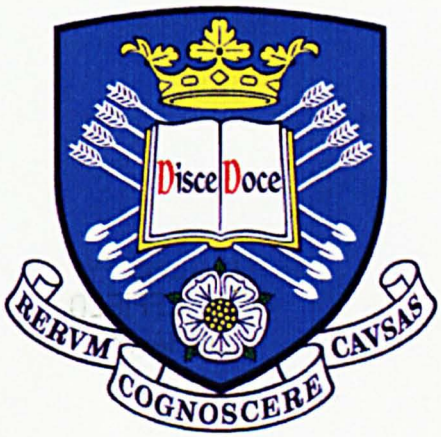

A thesis submitted for the degree of Doctor of Philosophy in the Faculty of Engineering of the University of Sheffield

By

Ângela Gaio Graeff

(BSc, MSc)

Centre for Cement and Concrete
Department of Civil and Structural Engineering
The University of Sheffield

Sheffield

April 2011

"A minha vida, Eu preciso mudar todo dia...
...Os meus sonhos, Eu procuro acordar
E perseguir meus sonhos... Eu quero sempre mais"

"My life, I need to change it every day...
... My dreams, I try to wake up
and follow them... I always want more."

*Edgard Scandurra (**Eu quero sempre mais**/*I always want more*)*

To my parents João Valter and Adelina,
the strong foundation of my life.
To my husband Lélio,
the durable columns of my heart.
Amo vocês.

ACKNOWLEDGEMENTS

Here I am, trying to use some lines to express my deepest gratitude for the persons who passed through my life in the past 3 ½ years. Some of them, hopefully, are not just passing...

I don't have problems in thanking people for their help, but I do have concerns on the best way to do it. It is obvious that just few lines are definitely not enough to show how grateful I am to a large number of people. For sure I could write another thesis-like just to express part of my feelings, but for the moment, I will try to use this space to demonstrate how important and how unforgettable these 3 ½ years are in my life.

First, I would like to express my gratitude to Prof. Kypros Pilakoutas for accepting me as his tutee and to "fully open" the doors of the University of Sheffield for me. I thank him for proposing the topic of the thesis and for accepting me as part of a major European Union Project. However, my main acknowledgement is for his always valuable and accurate advices. For sure this thesis would not be reality if not by his support.

I also would like to thank Dr. Cyril Lynsdale for his supervision throughout the durability topics of the research, especially by instigating discussions and raising important questions.

My gratitude also goes to Dr. Kyriacos Neocleous for his restless and endless supervision during the whole thesis (and always for chasing me on the deadlines!). Thanks also for his valuable advices during the decision-making periods and for the detailed corrections of the thesis.

I would like to acknowledge the financial support of Capes Foundation, an agent of the Brazilian Ministry of Education, which allowed my full-time dedication to this thesis.

To the University of Sheffield, for the opportunity to be a student of one of best UK Universities and also a worldwide well ranked and recognised University.

To the Ecolanes Project, for adopting me as a research member and for allowing me to work in a group of important multicultural academic and industrial partners. Also for the financial support that allowed the development of the experimental programme.

I would like to thank the technicians of the Structures Laboratory, for their continuous and excellent quality help (which sometimes sounded like an endless work, sorry!) during the experimental phase. Especially, I would like to thank Kieran Nash and Paul Blackbourn.

To the Federal University of Rio Grande do Sul, especially to the Laboratory of Physics Metallurgic (LAMEF), for spending time and technical support and for providing the physical structure and equipments for the fatigue tests. A special gratitude is for the laboratory manager Fabiano Mattei.

To the academic colleagues of Federal University of Rio Grande do Sul, Laboratory of Testing and Structural Models (LEME), for spending their time helping to perform the fatigue tests, which without their support would have not been accomplished. Especially, I would like to thank the coordination of Vânia Peres and the contributions of Josué Chies and Édina Quissini.

To my MSc supervisor and friend Prof. Luiz Carlos P. Silva Filho for his support prior and during the PhD course, always encouraging a possible academic link between Porto Alegre and Sheffield.

I also would like to thank the amazing team of PhD students of the Construction Innovation Group (which also includes the Earthquake Engineering Group!!!) not only for their help when needed, but mainly for the enjoyable and happy moments. My Brazilian heart allows me to remove the 'PhD student' tag from their description and add a 'friend' tag instead. Especially, I would like to thank my colleague-flatmate-friend Andreea for her support and sweet words when they were more than welcomed and for her patience in living with me.

To my friends-for-life, I would like to thank them for missing me so much (I believed when they said that!!!) while I was away (drinking several cups of tea per day). Especially, I would like to thank Adri, Aline, Bizu, Camila, Ivone, Letis, Lulu and Paulete (in alphabetical order to avoid competition). Thanks for the encouragement, for the laughs, for being my friends.

Special thanks are for my parents João Valter and Adelina for giving me unconditional love, care and for always stimulating my studies. I also thank them for accepting my distance during these 3 ½ years of absence. To my brother Daniel for giving me inspiration that one day I could become half as intelligent as he is. To my 'heart's mom' Didi (in memoriam) for her love and endless support, and for being the first one to know that: "I got the scholarship, I am going to the UK."

And finally, I would like to express not only my gratitude, but my true love to my husband Lélio. He was the one who first introduced me the beauty of Europe and who shared with me his love for the UK (never forgetting our 'gaucho' soul). I want to thank him for encouraging my studies, for being my fortress in the bad moments, and for accepting my absence in the last two years. This thesis has my name on it, but has his heart in every page!

ABSTRACT

Due to environmental concerns and increasing asphalt prices concrete pavements are seen as a sustainable alternative for road construction. Steel fibres are used as reinforcement for concrete pavements due to ease of construction, as well as improvement in the post-cracking, tensile/flexural and fatigue behaviour of the concrete. However, cost and method of construction are two major barriers for their use. Recycled fibres obtained from post-consumer tyres are a new alternative due to their lower cost and potential environmental benefits. The roller compacted concrete technique is also an alternative that enables road construction with the use of conventional asphalt equipment. These were the two main innovations being investigated by the FP6 EU Project Ecolanes. Understanding the durability of recycled steel fibre reinforced concrete (SFRC) is very important before these technologies can be used in real structures.

This thesis addresses the issue of long-term behaviour of recycled SFRC, based on an experimental programme divided in two main studies: 1) the mechanical properties (compressive and flexural behaviour), pore structure (porosity, density and free-shrinkage) and transport mechanisms (permeability, sorptivity and diffusivity) and 2) the main deterioration processes affecting the performance of concrete pavements, corrosion (accelerated by means of wet-dry cycles in chloride solution), freeze-thaw (accelerated by continuous submerged freezing and thawing cycles) and fatigue (accelerated by flexural cyclic loads). A probabilistic analysis in terms of service life design has also been developed.

Recycled fibres can increase the flexural strength of the concrete by up to 70% compared to plain concrete and they can significantly enhance the post-cracking behaviour. Recycled fibres, when added 2-6% by mass, do not affect the pore structure and the transport mechanisms of the concrete. Exceptions apply when contents around 6% by mass lead to compaction problems or affect the rheological properties of the concrete.

Recycled fibres improve the fatigue resistance by allowing approximately 30% higher stresses than plain concrete for an endurance life of 2 million cycles. Fibres also contribute to slowing down the advanced stage of freeze-thaw degradation of concrete. Both fatigue and freeze-thaw are enhanced since these fibres control different stages of crack propagation. When subjected to wet-dry cycles, the fibres appear to be well protected inside the concrete and the main consequences are only in terms of superficial rust.

The coupled benefits of mechanical and long-term performance of recycled SFRC make it a promising alternative for concrete pavements, especially in blends with industrially produced fibres. If these advantages are taken into account in the design of concrete pavements, a 20% reduction in the thickness of the concrete pavements should be expected, leading to less use of natural resources and to a further 10% reduction in costs.

TABLE OF CONTENTS

LIST OF FIGURES xv

LIST OF TABLES xxiii

LIST OF SYMBOLS AND ABBREVIATIONS xxv

1. INTRODUCTION 1

1.1 BACKGROUND OF THE PROBLEM AND CONTEXT 1

1.2 AIMS AND OBJECTIVES 6

1.3 STRATEGY 7

1.4 PRESENTATION OF THE THESIS 8

2. ENVIRONMENTAL ISSUES, SFRC AND RIGID PAVEMENTS 10

2.1 ENVIRONMENTAL ASPECTS OF END OF LIFE TYRE DISPOSAL 10

2.1.1 Landfill or Incineration Disposal 10

2.1.2 Recycling of Post-consumer Tyres 11

2.1.2.1 Use of rubber extracted from tyres 12

2.1.2.2 Polymer and steel reinforcement 13

2.1.3 Legislation on Post-consumer Tyres 14

2.1.3.1 European Union 14

2.1.3.2 United States 14

2.1.3.4 Discussion 15

2.2 FIBRE REINFORCED CONCRETE AND FIBRE TYPES 15

2.2.1 Types of Fibres for Concrete Reinforcement 16

2.2.2 Industrially Produced Steel Fibres 18

2.2.3 Recycled Steel Fibres from Post-consumer Tyres 20

2.2.3.1 Recycled SFRC 20

2.2.3.2 Processes to obtain recycled fibres from post-consumer tyres 21

2.2.3.3 Physical and mechanical properties of recycled fibres 23

2.3 PROPERTIES OF SFRC 25

2.3.1 Properties of Fresh SFRC 25

2.3.1.1 Workability 25

2.3.1.2 *Balling* of fibres 26

2.3.1.3 Distribution of fibres 27

2.3.2 Properties of Hardened SFRC 30

2.3.2.1 Compressive behaviour 31

2.3.2.2 Tensile behaviour 33

2.3.2.3 Flexural behaviour 36

2.3.2.4 Shear 40
2.3.2.5 Impact resistance 40
2.3.2.6 Other properties 41
2.4 CONCRETE PAVEMENTS – TYPES AND DESIGN METHODS 41
2.4.1 Conventional Concrete Pavements 44
2.4.2 RCC Pavements 46
2.4.2.1 RCC reinforced with steel fibres 47
2.4.2.2 Durability of RCC 48
2.4.3 Other Types of Concrete Pavements 49
2.4.4 Design methods for concrete pavements 49
2.4.4.1 Pioneer Method of Westergaard (1926) 50
2.4.4.2 Influence Charts of Picket and Ray (1951) 51
2.4.4.3 PCA Method (1966) 51
2.4.4.4 PCA Method (1984) 51
2.4.4.5 American Association of State Highway and Transportation Officials (AASHTO) Guide (1993) and Supplement (AASHTO, 1998) 52
2.4.4.6 NCHRP Guide (2002) 53
2.4.4.7 DNIT Rigid Pavement Manual (2005) 53
2.4.4.8 Highways Agency Method (2006a) 54
2.4.4.9 Technical Report TR34 (2003) on Industrial Floors 54
2.4.4.10 Design of SFRC pavements based on existing methods 55
2.5 SUMMARY AND CONCLUSIONS 58

3. DURABILITY ISSUES AND PORE STRUCTURE OF SFRC 61
3.1 DURABILITY ISSUES OF SFRC FOR PAVEMENTS 61
3.1.1 Flexural fatigue 62
3.1.2 Corrosion of fibres 65
3.1.3 Freeze-thaw 68
3.2 PORE STRUCTURE OF SFRC – TRANSPORT MECHANISMS AND PROPERTIES AFFECTING DURABILITY 72
3.2.1 Transport Mechanisms 74
3.2.1.1 Permeability 76
3.2.1.2 Capillary absorption 79
3.2.1.3 Diffusivity 81
3.2.2 Other Properties Affecting the Durability of Concrete 84
3.2.2.1 Porosity 84
3.2.2.2 Density 86
3.2.2.3 Shrinkage 87
3.3 SUMMARY AND CONCLUSIONS 90

4. DETAILS OF THE EXPERIMENTAL PROGRAMME 92
4.1 DESCRIPTION OF MATERIALS 94
4.1.1 Cementitious Materials 94
4.1.2 Aggregates 95
4.1.2.1 Wet consistency mixes 95
4.1.2.2 Dry consistency mixes 96
4.1.3 Fibres 97
4.1.3.1 Recycled steel tyre-cord fibres 97
4.1.3.2 Industrially produced steel fibres 98
4.1.4 Admixtures 99
4.2 MIX PROPORTIONS 99
4.2.1 Wet consistency mix 99
4.2.2 Dry consistency mix 101
4.3 VARIABLES OF THE RESEARCH 104
4.3.1 Pore Structure-related Properties of Concrete and Transport Mechanisms 104
4.3.2 Durability Issues 105
4.3.2.1 Flexural fatigue 105
4.3.2.2 Corrosion 106
4.3.2.3 Freeze-thaw 108
4.4 TESTING – METHODOLOGY 109
4.4.1 Casting of Specimens 109
4.4.1.1 Batching, mixing and placing of wet consistency mix 109
4.4.1.2 Batching, mixing and placing of dry consistency mix 110
4.4.2 Mechanical Properties 112
4.4.2.1 Compressive strength 112
4.4.2.2 Flexural behaviour 113
4.4.2.3 Modulus of elasticity 115
4.4.3 Density 116
4.4.3.1 Preconditioning of specimens 116
4.4.3.2 Dry and saturated density test 118
4.4.4 Porosity 119
4.4.5 Free Shrinkage 120
4.4.6 Transport Mechanisms 121
4.4.6.1 Permeability 121
4.4.6.2 Sorptivity 122
4.4.6.3 Diffusivity and chloride content test 124
4.4.7 Corrosion 125
4.4.8 Freeze-thaw 127

4.4.9 Fatigue 131
4.5 SUMMARY AND CONCLUSIONS 133

5. MECHANICAL PROPERTIES, DENSITY, POROSITY AND FREE SHRINKAGE RESULTS 135

5.1 COMPRESSIVE STRENGTH 135
5.2 FLEXURAL BEHAVIOUR 137
5.2.1 Wet Mixes 138
5.2.1.1 Flexural strength at the limit of proportionality f_{LOP} and ultimate flexural strength f_{ult} 138
5.2.1.2 Residual flexural strengths $f_{R,i}$ 141
5.2.1.3 Equivalent flexural strength f_{eq3} and equivalent flexural ratio $R_{e,3}$ 142
5.2.2 RCC Mixes 142
5.2.2.1 Flexural strength at the limit of proportionality f_{LOP} and ultimate flexural strength f_{ult} 143
5.2.2.2 Residual flexural strengths $f_{R,i}$ 145
5.2.2.3 Equivalent flexural strength f_{eq3} and equivalent flexural ratio $R_{e,3}$ 145
5.2.3 Comparison of f_{LOP} with f_{cm} 146
5.3 MODULUS OF ELASTICITY 147
5.3.1 Results 147
5.3.2 Comparison of E with f_{cm} 148
5.3.3 Comparison of Experimental E with Predicted Results 149
5.3.4 Load-Spreading Effect 151
5.4 DENSITY 152
5.4.1 Use of Different Temperatures and Methods to Precondition Specimens 152
5.4.1.1 Discussion on w_e and w_{e80} 154
5.4.1.2 Discussion on w_{e50} 155
5.4.2 Density Results 156
5.4.3 Law of Mixtures to Calculate Dry Density of SFRC 158
5.4.4 Influence of Preconditioning Temperature on the Density of Concrete 159
5.4.5 Comparison of Dry Density with f_{cm}, f_{LOP} and E 162
5.5 POROSITY 164
5.5.1 Porosity results 164
5.5.2 Influence of Preconditioning Temperature on the Porosity of Concrete 166
5.5.3 Air Content Results 167
5.5.4 Discussion on Porosity and Air Content Results 168
5.6 FREE SHRINKAGE 168
5.6.1 Shrinkage Results 168
5.6.2 Discussion on Free Shrinkage Results 170
5.7 SUMMARY AND CONCLUSIONS 171

6. TRANSPORT MECHANISMS RESULTS 173
6.1 PERMEABILITY 173
6.1.1 Permeability Results 173
6.1.2 Influence of Preconditioning Temperature on the Permeability of Concrete 175
6.1.3 Discussion on Permeability Tests 177
6.2 SORPTIVITY 177
6.2.1 Sorptivity Results 177
6.2.2 Resistance Coefficient 179
6.2.3 Influence of Preconditioning Temperature on the Sorptivity of Concrete 180
6.2.4 Discussion on Sorptivity Test 181
6.3 DIFFUSIVITY 182
6.3.1 Chloride Content Results 182
6.3.2 Diffusion Coefficient 185
6.4 SUMMARY AND CONCLUSIONS 186

7. CORROSION RESISTANCE OF SFRC 188
7.1 VISUAL ANALYSIS 188
7.1.1 Scale for External Level of Corrosion Deterioration 188
7.1.2 Prior to Corrosion Simulation 190
7.1.3 After 5 Months of Corrosion Simulation 191
7.1.4 After 10 Months of Corrosion Simulation 194
7.1.5 Wet-dry cycles at 20 °C and 40 °C 197
7.1.6 Discussion 198
7.2 MECHANICAL PROPERTIES 199
7.2.1 Compressive strength 199
7.2.2 Flexural Behaviour 201
7.2.2.1 Un-cracked specimens subjected to wet-dry cycles at 20 °C 202
7.2.2.2 Cracked and un-cracked specimens subjected to wet-dry cycles at 20°C and 40°C 207
7.3 INFLUENCE OF TRANSPORT MECHANISMS, DENSITY AND POROSITY ON THE CORROSION RESISTANCE 211
7.3.1 Compressive Strength 212
7.3.1.1 Permeability, sorptivity and porosity 212
7.3.1.2 Diffusivity 214
7.3.1.3 Density 214
7.3.2 Flexural Strength at the Limit of Proportionality 215
7.4 SUMMARY AND CONCLUSIONS 217

8. FREEZE-THAW RESISTANCE OF SFRC 219
8.1 VISUAL ANALYSIS 219

8.1.1 Wet mixes 219
8.1.2 RCC Mixes 222
8.1.3 Discussion on the Visual Analysis 224
8.2 LOSS OF MASS 226
8.3 MECHANICAL PROPERTIES 228
8.3.1 Compressive Strength 229
8.3.2 Flexural Behaviour 231
8.3.2.1 Modulus of elasticity 231
8.3.2.2 Flexural strength at the limit of proportionality 232
8.3.2.3 Ultimate flexural strength 233
8.3.2.4 Residual flexural strength 234
8.3.2.5 Equivalent flexural strength and equivalent flexural ratio 235
8.4 INFLUENCE OF TRANSPORT MECHANISMS, POROSITY AND DENSITY ON THE FREEZE-THAW RESISTANCE 237
8.4.1 Density 237
8.4.2 Porosity 238
8.4.3 Permeability 239
8.4.4 Sorptivity 239
8.4.5 Diffusivity 240
8.5 SUMMARY AND CONCLUSIONS 241

9. FATIGUE RESISTANCE OF SFRC 243
9.1 CONTROL TESTS – STATIC FLEXURAL AND COMPRESSIVE STRENGTH 243
9.2 *s – log(N)* CURVES 245
9.2.1 Wet Mixes 246
9.2.2 RCC Mixes 248
9.2.3 Discussion on the RCC and Wet Mixes Results 251
9.3 VERTICAL DISPLACEMENT ANALYSIS 253
9.3.1 Amplitude and Pattern of Displacements 254
9.3.2 Fracture Toughness 263
9.3.3 Discussion on the Vertical Displacements Analysis 266
9.4 DESIGN RECOMMENDATIONS FOR FATIGUE OF SFRC PAVEMENTS 267
9.5 SUMMARY AND CONCLUSIONS 270

10. PROBABILISTIC ANALYSIS 272
10.1 SLD METHODS 272
10.1.1 Probabilistic Methods for SLD 273
10.1.2 Reliability of Structures or Structural Elements 274
10.2 SLD METHOD FOR CHLORIDE CORROSION 275

10.2.1 Serviceability Limit State for Corrosion 276
10.2.2 Ultimate Limit State for Corrosion 277
10.2.3 Results of Chloride Corrosion Probabilistic SLD 277
10.2.3.1 Proposed Method for the Comparison of Accelerated Tests to Real (Less Severe) Conditions 278
10.2.3.2 Parametric study 284
10.3 SLD METHOD FOR FREEZE-THAW 291
10.3.1 Serviceability Limit State for Freeze-Thaw 292
10.3.1.1 Frost induced internal damage 292
10.3.1.2 Salt-frost induced surface scaling 293
10.3.2 Ultimate Limit State for Freeze-Thaw 296
10.3.3 Results of Freeze-thaw Probabilistic SLD 297
10.3.3.1 Proposed Probabilistic Method to predict SLD of Concrete Exposed to Freeze-Thaw 297
10.3.3.2 Sensitivity Analysis 303
10.3.3.3 Characteristics and limitations of the method 307
10.4 FATIGUE PROBABILISTIC ANALYSIS 308
10.4.1 Graphical Method – Procedures 308
10.4.2 Mathematical Method – Procedures 309
10.4.3 Results – Graphical and Mathematical Methods 310
10.4.3.1 Wet mixes 310
10.4.3.2 RCC mixes 314
10.4.4 Discussion on the Probabilistic Analysis 318
10.5 SUMMARY AND DISCUSSION 321

11. CLOSURE 323
11.1 DISCUSSION AND CONCLUDING REMARKS 323
11.2 ANSWER TO QUESTIONS 330
11.3 RECOMMENDATIONS FOR FUTURE WORK 332

REFERENCES 335

APPENDIX A. ECOLANES PROJECT A.1

APPENDIX B. EQUATIONS AND CHARTS OF RIGID PAVEMENT DESIGN METHODS B.1

APPENDIX C. FLEXURAL BEHAVIOUR C.1

APPENDIX D. FEA ANALYSIS D.1

APPENDIX E. TABLE OF RESULTS – DENSITY, POROSITY AND FREE-SHRINKAGE E.1

APPENDIX F. RESULTS – PERMEABILITY, SORPTIVITY AND CHLORIDE CONTENT F.1

APPENDIX G. COMPRESSIVE STRENGTH G.1

APPENDIX H. FUNDAMENTAL OF CHLORIDE INGRESS H.1

APPENDIX I. MATLAB SCRIPTS I.1

APPENDIX J. FATIGUE RESULTS J.1

LIST OF FIGURES

Figure 1 – Concrete pavement road. 1
Figure 2 – Dumping of tyres. 4
Figure 3 – Cracked concrete pavement. 5
Figure 4 – Diagram of the research outline and main expected output results. 7
Figure 5 – Typical tyre section and components [Bridgegate Tyres, 2009]. 11
Figure 6 – Products made by recycled rubber from tyres. 12
Figure 7 – Small and large cracks in FRC. 16
Figure 8 – Categories of fibres used in concrete and examples. 17
Figure 9 – Most common steel fibre geometries. 20
Figure 10 – Recycled fibres obtained from a) shredding and b) pyrolysis process. 21
Figure 11 – a) Tyre shredder blades and b) before and after the shredding process. 22
Figure 12 – Range of tyre shredding sizes. 22
Figure 13 – a) Loose steel fibres collected by an electromagnetic conveyor belt b) appearance of the fibres. 23
Figure 14 – Appearance of recycled steel fibres. 24
Figure 15 – Statistical analysis of recycled fibres. 24
Figure 16 – Influence of fibre reinforcement index on slump [after Bayasi and Soroushian, 1992] 26
Figure 17 – Fibre balling. 27
Figure 18 – Fibre arrangements in one, two or three dimensions. 28
Figure 19 – Orientation of steel fibres into concrete due to a) two parallel and b) four boundaries conditions closely spaced [after Soroushian and Lee, 1990b] 28
Figure 20 – Orientation of fibres disturbed by the boundary conditions [after Boulekbache *et al.*, 2010] 29
Figure 21 – 2D and 3D orientation factors for various specimen geometries [after Soroushian and Lee, 1990b]. 29
Figure 22 – Influence of fibre addition in the compressive behaviour of SFRC [after Fanella and Naaman, 1985]. 31
Figure 23 – Qualitative analysis of the effect of adding fibre to concrete: a – ideal; b – accounting for fibre distribution and other mixing issues. 32
Figure 24 – Influence of fibre addition in the tensile behaviour of SFRC [after Soroushian and Bayasi, 1987] 34
Figure 25 – Variation of shear bond strength with embedded length of fibre [after Gray, 1984]. 35
Figure 26 – Typical pull-out curve obtained from smooth fibres [after Naaman *et al.*, 1991]. .. 36
Figure 27 – Influence of bond strength on the flexural strength σ_{MR} [after Hannant, 1978]. 37
Figure 28 – Strain and stress distribution in flexure for SFRC. 37
Figure 29 – Toughness indices for flexural load-deflection curve [after ASTM, 1997] 39

Figure 30 – Load-deflection or load-CMOD curve to calculate residual flexural strength [after RILEM, 2002]. 39
Figure 31 – Load-deflection curve to calculate residual strength classes [after BS, 2005b]. 40
Figure 32 – Comparison of long-term cost between asphalt and concrete road [Sullivan, 2009]. 42
Figure 33 – Comparison of initial cost between asphalt and concrete road [Sullivan, 2009]..... 42
Figure 34 – Load transfer to subgrade in a) concrete and b) asphalt pavements [ACPA, 2010b]. 43
Figure 35 – JPCP [ACPA, 2011]. 45
Figure 36 – CRCP before concrete placement. 46
Figure 37 – Trial of RCC in London in 2008. 47
Figure 38 – Model to represent the subgrade reaction of concrete slabs [Pavement Interactive, 2007]. 50
Figure 39 – Depth of JPCP for various design guidelines. 57
Figure 40 – Comparison of JSFRCP and JPCP based on the various codes. 58
Figure 41 – Possible long-term behaviour of FRC in terms of strength *S* and toughness *T* over time [Bentur, 2003]. 61
Figure 42 – Fatigue crack growth stages [Rossi and Parant, 2008]. 64
Figure 43 – Typical flexural versus load deflection curves for specimens cured in air and exposed to marine cycles (MC cured) [Mangat *et al.*, 1989]. 66
Figure 44 – Types of freeze-thaw damages. 69
Figure 45 – a) air entrained pores free from water and b) excess water from expansion due to freezing reaches the air entrained bubbles. 70
Figure 46 – Pore size distribution [Setzer, 1977 cited in CEB, 1992]. 73
Figure 47 – Idealised model for various transport mechanisms according to the moisture condition of the concrete [The Concrete Society, 2008]. 75
Figure 48 – Schematic arrangement for water or gas permeability test [after The Concrete Society, 2008]. 77
Figure 49 – Relationship between the pore radius and the depth of water uptake due to sorptivity test [The Concrete Society, 2008]. 80
Figure 50 – Stages of water absorption by soaking and boiling. 85
Figure 51 – Bending load versus vertical displacement curve for W-CIP-2I and W-CIP-6R. ... 93
Figure 52 – a) Coarse and b) fine aggregate used for wet consistency mixes. 95
Figure 53 – Aggregate sieve analysis for wet consistency mixes. 95
Figure 54 – Aggregate used for dry consistency mixes. 96
Figure 55 – Aggregate sieve analysis for dry consistency mixes. 97
Figure 56 – Sorted steel tyre-cord fibres. 97
Figure 57 – Length distributions of recycled fibres. 98
Figure 58 – Industrially produced steel fibres. 98
Figure 59 – Apparatus used for RCC compaction (frame developed at USFD) [Angelakopoulos, 2011]. 102
Figure 60 – Bulk (wet) and dry densities of RCC for water contents ranging from 4% to 9%. 103

Figure 61 – Slump test and equipment used to measure air content of fresh wet concrete..... 110
Figure 62 – Compaction of RCC. 111
Figure 63 – Testing machine used for compressive strength test..... 112
Figure 64 – Load configuration used for flexural strength test. 113
Figure 65 – Calculation of flexural modulus of elasticity according to the two approaches (mix W-CIP-2R). 115
Figure 66 – Specimens in controlled temperature and humidity chamber..... 118
Figure 67 – Apparatus to vacuum saturate concrete specimens..... 118
Figure 68 – Measuring device used for shrinkage measurement. 121
Figure 69 – a) Permeability cell and b) volumetric pipette connected to the permeability cell to measure the flow rate. 122
Figure 70 – Specimens tested for sorptivity..... 123
Figure 71 – Typical result for sorptivity test (mix R-CIP-0 preconditioned at 80 °C)..... 123
Figure 72 – Typical dx/dy curve with the peak corresponding to the amount of chlorides..... 125
Figure 73 – a) wet and b) dry cycles of corrosion simulation. 126
Figure 74 – Overhead crane used to immerse and remove specimens out of solution. 126
Figure 75 – Container with chloride solution at a 40 °C. 127
Figure 76 – Containers with cubes and prisms. 128
Figure 77 – Freeze-thaw chamber with containers and specimens. 129
Figure 78 – Thermocouple placed in the centre of a randomly chosen cube..... 129
Figure 79 – Predicted and real temperature profile measured during the freeze-thaw cycles... 130
Figure 80 – Setup to test fatigue specimens. 132
Figure 81 – Steps to mount three prisms for fatigue tests. 133
Figure 82 – Effect of fibre content on compressive strength. 136
Figure 83 – Typical plain (mix W-LEC-0) and SFRC (mix W-LEC-6R) bending load *versus* mid-span deflection. 137
Figure 84 – Bending load *versus* vertical displacement for wet mixes..... 138
Figure 85 – f_{LOP} and f_{ult} for wet mixes. 139
Figure 86 – Typical elastic behaviour of SFRC (mix W-CIP-6R)..... 139
Figure 87 – Influence of recycled fibre content on the f_{LOP} and f_{ult} of wet mixes..... 140
Figure 88 – $f_{R,i}$ for wet mixes. 141
Figure 89 – a) f_{eq3} and b) $R_{e,3}$ for wet mixes..... 142
Figure 90 – Bending load *versus* vertical displacement for RCC mixes..... 143
Figure 91 – f_{LOP} and f_{ult} for RCC mixes..... 144
Figure 92 – $f_{R,i}$ for RCC mixes. 145
Figure 93 – a) f_{eq3} and b) $R_{e,3}$ for RCC mixes..... 145
Figure 94 – Comparison of f_{LOP} to f_{cm}. 146
Figure 95 – E for wet and RCC mixes. 147
Figure 96 – Comparison of E with f_{cm}. 148

Figure 97 – Comparison of experimental results of E to predicted values according to Eurocode, CEB-FIP and LOM. 149
Figure 98 – $E_{LOM}/E_{experimental}$ *versus* fibre content. 150
Figure 99 – Load-spreading effect. 151
Figure 100 – Evaporable moisture concentration w_e at 105 °C. 153
Figure 101 – Evaporable moisture concentration w_{e80} at 80 °C. 153
Figure 102 – Evaporable moisture concentration w_{e50} at 50 °C. 153
Figure 103 – Equilibrium moisture concentration $w_{e,75}$ at 50 °C. 155
Figure 104 – Comparison between w_e and $w_{e,75}$ 156
Figure 105 – Density at 105 °C. 157
Figure 106 – Density at 80 °C. 157
Figure 107 – Density at 50 °C. 157
Figure 108 – Experimental and predicted LOM dry density 159
Figure 109 – Experimental and predicted LOM dry density for RCC mixes, accounting for the porosity of the mixes. 159
Figure 110 – Comparison of dry and saturated density results to different preconditioning temperatures. 160
Figure 111 – Comparison between saturated density and a) evaporable moisture concentration and b) degree of saturation. 161
Figure 112 – Comparison between dry density and a) evaporable moisture concentration and b) degree of saturation. 161
Figure 113 – Comparison of dry density to f_{cm} for a) wet mixes and b) RCC mixes 162
Figure 114 – Comparison of dry density to f_{LOP} for a) wet mixes and b) RCC mixes. 163
Figure 115 – Comparison of dry density to E for a) wet mixes and b) RCC mixes 163
Figure 116 – Porosity at 105 °C. 164
Figure 117 – Porosity at 80 °C. 164
Figure 118 – Porosity at 50 °C. 165
Figure 119 – Comparison of porosity results to different preconditioning temperatures. 166
Figure 120 – Comparison between porosity and a) evaporable moisture concentration and b) degree of saturation. 167
Figure 121 – Free shrinkage for a) wet and b) RCC mixes 169
Figure 122 – RCC free shrinkage results compared to Pittman and Ragan (1998) results. 169
Figure 123 – a) Wet and b) RCC permeability for specimens preconditioned at 105 °C. 173
Figure 124 – a) Wet and b) RCC permeability for specimens preconditioned at 80 °C. 174
Figure 125 – a) Wet and b) RCC permeability for specimens preconditioned at 50 °C. 174
Figure 126 – Comparison of permeability results to different preconditioning temperatures. . 176
Figure 127 – Comparison between permeability and a) evaporable moisture concentration and b) degree of saturation. 176
Figure 128 – Sorptivity at 80 °C 178
Figure 129 – Sorptivity at 50 °C 178
Figure 130 – Resistance coefficient of RCC mixes. 179

Figure 131 – Comparison of sorptivity results to different preconditioning temperatures. 180
Figure 132 – Comparison between sorptivity and a) evaporable moisture concentration and b) degree of saturation. 181
Figure 133 – Chloride content of RCC mixes after 28 days in chloride solution immersion. .. 183
Figure 134 – Chloride content of wet mixes after 28 days in chloride solution immersion. 183
Figure 135 – Diffusion coefficient for wet and RCC mixes. 185
Figure 136 – External appearance of RCC specimens before commencing the wet-dry cycles. 190
Figure 137 – External appearance of wet mix specimens before wet-dry cycles. 191
Figure 138 – External appearance of specimens after 5 months of wet-dry cycles. 192
Figure 139 – Corroded fibres exposed to the concrete surface after 5 months of wet-dry cycles. 192
Figure 140 – Internal appearance of specimens after 5 months of wet-dry cycles. 193
Figure 141 – External appearance of specimens after 10 months of wet-dry cycles. 194
Figure 142 – Corroded fibres exposed to the concrete surface after 10 months of wet-dry cycles. 195
Figure 143 – Internal appearance of specimens after 10 months of wet-dry cycles. 196
Figure 144 – Specimens exposed to 5 months of wet-dry cycles at 20 °C and 40 °C. 197
Figure 145 – Specimens exposed to 10 months of wet-dry cycles at 20 °C and 40 °C. 197
Figure 146 – Micro spalling of concrete after 10 months of wet-dry cycles at 40 °C 198
Figure 147 – Compressive strength after corrosion for a) wet and b) RCC mixes. 199
Figure 148 – Comparison between predicted and real compressive strength after exposure to wet-dry cycles 200
Figure 149 – f_{LOP} and f_{ult} at 5 and 10 months of corrosion simulation. 202
Figure 150 – $f_{R,i}$ of wet mixes at 5 and 10 months of corrosion simulation. 203
Figure 151 – $f_{R,i}$ of RCC mixes at 5 and 10 months of corrosion simulation. 204
Figure 152 – Averaged normalised $f_{R,i}$ for a) wet and b) RCC mixes. 204
Figure 153 – f_{eq3} and $R_{e,3}$ at 5 and 10 months of corrosion simulation. 206
Figure 154 – E at 5 and 10 months of corrosion simulation. 206
Figure 155 – Averaged normalised E for wet and RCC mixes. 207
Figure 156 – a) f_{LOP} and b) f_{ult} for cracked and un-cracked specimens at 20 °C and 40 °C. 208
Figure 157 – Behaviour of control and cracked specimens at 20 °C 209
Figure 158 – Behaviour of control and cracked specimens at 40 °C 209
Figure 159 – $f_{R,i}$ for a) cracked and b) un-cracked specimens; at 20 °C and 40 °C. 210
Figure 160 – a) f_{eq3} and b) $R_{e,3}$ for cracked and un-cracked specimens at 20 °C and 40 °C. 210
Figure 161 – E for cracked and un-cracked specimens at 20 °C and 40 °C. 211
Figure 162 – Correlation of normalised corrosion f_{cm} to permeability. 212
Figure 163 – Correlation of normalised corrosion f_{cm} to sorptivity. 213
Figure 164 – Correlation of normalised corrosion f_{cm} to porosity. 213
Figure 165 – Correlation of normalised corrosion f_{cm} to diffusivity. 214

Figure 166 – Correlation of normalised corrosion f_{cm} to dry density..... 215
Figure 167 – Correlation of normalised corrosion f_{LOP} to permeability..... 215
Figure 168 – Correlation of normalised corrosion f_{LOP} to sorptivity..... 216
Figure 169 - Correlation of normalised corrosion f_{LOP} to diffusivity..... 216
Figure 170 – Correlation of normalised corrosion f_{LOP} to porosity..... 216
Figure 171 – Correlation of normalised corrosion f_{LOP} to dry density..... 217
Figure 172 – Wet mixes after 7 freeze-thaw cycles..... 219
Figure 173 – Wet mixes after 14 freeze-thaw cycles..... 220
Figure 174 – Wet mixes after 28 freeze-thaw cycles..... 220
Figure 175 – Pop-outs and exposed aggregates after 28 cycles..... 221
Figure 176 – Wet mixes after 42 freeze-thaw cycles..... 221
Figure 177 – Fibres exposed to surface after 42 cycles..... 221
Figure 178 – Wet mixes after 56 freeze-thaw cycles..... 222
Figure 179 – RCC mixes after 7 freeze-thaw cycles..... 223
Figure 180 – RCC mixes after 14 freeze-thaw cycles..... 223
Figure 181 – RCC mixes after 28 freeze-thaw cycles..... 224
Figure 182 – RCC mixes after 42 freeze-thaw cycles..... 224
Figure 183 – Pore characteristic of a) wet and b) RCC mix..... 225
Figure 184 – Comparison among porosity, air content and dry and saturated density results of W-LEC-0, W-LEC-2I and W-LEC-6R mixes..... 226
Figure 185 – Cube and prism loss of mass for wet mixes..... 227
Figure 186 – Cube and prism loss of mass for RCC mixes..... 228
Figure 187 – Compressive strength after 56 freeze-thaw cycles..... 229
Figure 188 – Comparison between predicted and real compressive strength after freeze-thaw cycles..... 230
Figure 189 – R-LEC-6R after compression (specimen was capped with cement paste due to the high irregularity of the surface)..... 231
Figure 190 – E after 56 freeze-thaw cycles..... 231
Figure 191 – Initial flexural behaviour for mix W-LEC-6R..... 232
Figure 192 – f_{LOP} after 56 freeze-thaw cycles..... 233
Figure 193 – f_{ult} after 56 freeze-thaw cycles..... 234
Figure 194 – $f_{R,i}$ after 56 freeze-thaw cycles for wet mixes..... 234
Figure 195 – $f_{R,i}$ after 56 freeze-thaw cycles for RCC mixes..... 235
Figure 196 – f_{eq3} after 56 freeze-thaw cycles..... 236
Figure 197 – $R_{e,3}$ after 56 freeze-thaw cycles..... 236
Figure 198 – $R_{e,3} = f_{eq3}/f_{ult}$ for RCC mixes after 56 freeze-thaw cycles..... 236
Figure 199 – Influence of density on the residual normalised freeze-thaw strength of concrete..... 237
Figure 200 – Influence of porosity on the residual normalised freeze-thaw strength of concrete..... 238

Figure 201 – Influence of permeability on the residual normalised freeze-thaw strength of concrete. 239

Figure 202 – Influence of sorptivity on the residual normalised freeze-thaw strength of concrete. 240

Figure 203 – Influence of diffusivity on the residual normalised freeze-thaw strength of concrete. 241

Figure 204 – s *versus* log(N) for a) mix W-CIP-0 and b) mix W-CIP-2R. 246

Figure 205 – s *versus* log(N) for a) mix W-CIP-6R and b) comparison of all wet mixes. 246

Figure 206 – Effect of fibre content on the s *versus* N relationship [after Johnston and Zemp, 1991] 247

Figure 207 – s *versus* log(N) for a) mix R-CIP-0 and b) mix R-CIP-2I. 248

Figure 208 – s *versus* log(N) for a) mix R-CIP-2R and b) mix R-CIP-6R. 249

Figure 209 – s *versus* log(N) for comparison of all RCC mixes. 249

Figure 210 – R-CIP-6R after fatigue failure (stress level of 0.7). 251

Figure 211 – R-CIP-2I after fatigue failure (stress level of 0.7). 251

Figure 212 – Comparison between the fatigue life of wet and RCC mixes. 252

Figure 213 – Endurance limit expressed in terms of stress level. 253

Figure 214 – Typical sinusoidal displacements (mix R-CIP-6R, s = 0.5) 253

Figure 215 – Amplitude of displacements *versus* number of cycles of mix W-CIP-0, s=0.5... 254

Figure 216 – Amplitude of displacements *versus* number of cycles of mix W-CIP-2R, s=0.5. 255

Figure 217 – Amplitude of displacements *versus* number of cycles of mix W-CIP-2R, s=0.7. 255

Figure 218 – Amplitude of displacements *versus* number of cycles of mix W-CIP-6R, s=0.5. 255

Figure 219 – Amplitude of displacements *versus* number of cycles of mix W-CIP-6R, s=0.7. 256

Figure 220 – Amplitude of displacements *versus* number of cycles of mix R-CIP-0, s=0.5.... 256

Figure 221 – Amplitude of displacements *versus* number of cycles of mix R-CIP-0, s=0.7.... 256

Figure 222 – Amplitude of displacements *versus* number of cycles of mix R-CIP-2I, s=0.5... 257

Figure 223 – Amplitude of displacements *versus* number of cycles of mix R-CIP-2I, s=0.7... 257

Figure 224 – Amplitude of displacements *versus* number of cycles of mix R-CIP-2R, s=0.5. 257

Figure 225 – Amplitude of displacements *versus* number of cycles of mix R-CIP-2R, s=0.7. 258

Figure 226 – Amplitude of displacements *versus* number of cycles of mix R-CIP-6R, s=0.5. 258

Figure 227 – Amplitude of displacements versus number of cycles of mix R-CIP-6R, s=0.6. 258

Figure 228 – Amplitude of displacements *versus* number of cycles of mix R-CIP-6R, s=0.8. 259

Figure 229 – Sketch of displacements in concrete reinforced with recycled fibres subjected to fatigue 259

Figure 230 – Last ten cycles before failure (mix R-CIP-6R subjected to the stress level of 0.8). 260

Figure 231 – Comparison between 2R and 6R RCC mixes. 261

Figure 232 – Sketch of displacements in concrete reinforced with industrially produced fibres subjected to fatigue 262

Figure 233 – Industrially produced fibres without their cone ends after failure. 263

Figure 234 – Increase of fracture toughness as the number of cycles increases (Perdikaris *et al.*, 1986) 264

Figure 235 – a) Synchronisation of load and displacement curves and b) fracture toughness calculation (mix R-CIP-6R). 265

Figure 236 – Comparison of depths calculated by design codes and considering a higher stress level. 269

Figure 237 – Limit states of corrosion process in RC structures. 275

Figure 238 – Example of probabilistic fully-saturated chloride ingress considering various depths of chloride ingress. 282

Figure 239 – Probabilistic fully-saturated chloride ingress for wet mixes – different depths. a) W-CIP-2I, b)W-CIP-6R, c)W-LEC-2I and d) W-LEC-6R. 282

Figure 240 – Probabilistic fully-saturated chloride ingress for RCC mixes – different depths. a) R-CIP-2I, b) R-CIP-6R, c)R-LEC-2I and d) R-LEC-6R. 283

Figure 241 – p_f *versus* depth of chloride penetration for the SLD of 50 years (grouped according to same mix and cementitious material). 285

Figure 242 – Influence of fibre content on the depth of chloride ingress. 287

Figure 243 – p_f *versus* depth of chloride penetration for the SLD of 50 years (grouped according to same fibre content and type and cementitious material). 288

Figure 244 – Influence of type of mix on the depth of chloride ingress. 289

Figure 245 – p_f *versus* depth of chloride penetration for the SLD of 50 years (grouped according to same fibre content and type and type of mix). 290

Figure 246 - Influence of cementitious material on the depth of chloride ingress. 291

Figure 247 – Proposed limit states of freeze-thaw process in concrete structures. 292

Figure 248 – T_{air} for Shefield, UK. 300

Figure 249 – Correlation of N_c to scaling S. 301

Figure 250 – Probabilistic SLD for concrete structures subjected to freeze-thaw. 303

Figure 251 – Influence of resistance temperature on SLD of frost exposed concrete. 304

Figure 252 – Influence of critical scaling on SLD of frost exposed concrete. 305

Figure 253 – Influence of model uncertainty on SLD of frost exposed concrete. 306

Figure 254 – Probabilistic analysis for mix W-CIP-0. 311

Figure 255 – Probabilistic analysis for mix W-CIP-2R. 312

Figure 256 – Probabilistic analysis for mix W-CIP-6R. 313

Figure 257 – Probabilistic analysis for mix R-CIP-0. 314

Figure 258 – Probabilistic analysis for mix R-CIP-2I 315

Figure 259 – Probabilistic analysis for mix R-CIP-2R. 316

Figure 260 – Probabilistic analysis for mix R-CIP-6R. 318

Figure 261 – Reliability for the least-cost design [after Basma and Al-Balbissi, 1989] 319

Figure 262 – Number of cycles *versus* stress level (p_f = 25% for fibre reinforced mixes and p_f = 20% for plain concrete). 320

LIST OF TABLES

Table 1 – Properties of the main fibres used for FRC 17
Table 2 – Classification of steel fibres according to BS, ASTM, JCSE and ABNT. 19
Table 3 – Comparison among the procedures for various flexural strength tests of SFRC. 38
Table 4 – AADT of a major highway road in the south of Brazil and near Sheffield, UK. 56
Table 5 – Properties of plain and SFRC 57
Table 6 – Comparison among main sorptivity test methods. 81
Table 7 – Variables of the research. 92
Table 8 – Chemical composition of PFA. 94
Table 9 – Mix proportions used for wet and dry consistency mixtures (nearest 5 kg/m^3). 99
Table 10 – Exposure classes and durability recommendations adopted for the wet mix design. 100
Table 11 – Description of the mixes. 104
Table 12 – Variables used to investigate fatigue 106
Table 13 – Variables used to investigate corrosion 107
Table 14 – Variables used to investigate freeze-thaw. 108
Table 15 – f_{cm} (MPa) and COV results. 135
Table 16 – f_{cm} ANOVA two-factor with replication – wet mixes 136
Table 17 – f_{cm} ANOVA two-factor with replication – RCC mixes 136
Table 18 – Correlation between f_{LOP} and f_{ult} with recycled fibre content (v) 140
Table 19 – f_{LOP} ANOVA two-factor with replication – wet mixes. 141
Table 20 – f_{ult} ANOVA two-factor with replication – wet mixes. 141
Table 21 – f_{LOP} ANOVA two-factor with replication – RCC mixes 144
Table 22 – f_{ult} ANOVA two-factor with replication – RCC mixes. 144
Table 23 – Air content of fresh wet mixes. 167
Table 24 – Chloride content of control plain concrete specimens. 182
Table 25 – Scale of superficial deterioration due to rust 189
Table 26 – Peak load obtained from static flexural tests carried out at UFRGS and USFD. 244
Table 27 – Compressive strength obtained from tests carried out at UFRGS 244
Table 28 – Fatigue loads for each stress level and mix 245
Table 29 – Stresses and stress ratio caused by a 80 kN standard axle in pavement sections. 267
Table 30 – Relation between β and p_f. 274
Table 31 – Target reliability index β for class RC2 structures and structural elements (BS EN 1990, 2002c). 275
Table 32 – Probabilistic parameters used for wet mixes (mean and coefficient of variation). . 280
Table 33 – Probabilistic parameters used for RCC mixes (mean and coefficient of variation). 280
Table 34 – Probabilistic parameters used for wet mixes (mean and coefficient of variation). . 284

Table 35 – Probabilistic parameters used for RCC mixes (mean and coefficient of variation).285
Table 36 – Ranking of specimens for probabilistic analysis (mix R-CIP-0 at stress level of 0.5). 308
Table 37 – Number of cycles and probability of failure (mix R-CIP-0). 309
Table 38 – Experimental constants based on the fatigue life data. 310

LIST OF SYMBOLS AND ABBREVIATIONS

1D: one dimensional

2D: two dimensional

3D: three dimensional

A: usually area

AADT: average annual daily traffic

A_f: cross sectional area of the steel fibres

ANOVA: analysis of variance

AASHTO: American Association of State Highway and Transportation Officials

AASHO: American Association of State Highway Officials

ABNT: Associação Brasileira de Normas Técnicas

ALT: Accelerated Load Traffic

β: reliability

$\beta cc(t)$: ageing coefficient of concrete

b: usually width

BRE: Building Research Establishment

ASTM: American Society for Testing and Materials

BS: Bristish Standard

ACI: American Concrete Institution

c/a: cement to aggregate ratio

C(x,t): chloride content at a depth x, after a time t

C_{crit}: critical chloride content

C_i: initial chloride content

C_s: surface chloride content

C-S-H: Calcium Silicate Hydrate

CEB: Comire Euro-International du Beton

CIP: binary cement composition of 80% CEM I and 20% PFA

CMOD: Crack mouth opening displacement

CONAMA: Conselho Nacional do Meio Ambiente

COV: coefficient of variance

CRCB: Continuously reinforced concrete base

CRCP: Continuously reinforced concrete pavement

D: usually diffusion coefficient

δ: vertical displacement at the centre of the spam

ΔL: difference in length

dF: degree of freedom

DNER: Departamento Nacional de Estradas de Rodagem

DNIT: Departamento Nacional de Infraestrutura de Transportes

D_d: dry density

D_{ref}: reference diffusion coefficient

D_s: saturated density

η: dynamic viscosity of a fluid

E: modulus of elasticity

E_{cm}: predicted modulus of elasticity

E_f: modulus of elasticity of the steel fibres

E_m: modulus of elasticity of the matrix

EPA: US Environmental Protection Agency

erf: Gaussian error function

ESAL: Equivalent Single Axle Load

ETRA: European Tyre Recycling Association

ETRMA: European Tyre and Rubber Manufacturers Association

f_{cm}: cube compressive strength (may also indicate cylinder compressive strength when specified)

$f_{cm(t)}$: mean compressive strength at t days

FEA: Finite Element Analysis

f_{eq3}: equivalent flexural strength

f_{LOP}: flexural strength at the limit of proportionality

FRC: Fibre reinforced concrete

$f_{R,i}$: residual flexural strength

f_{ult}: ultimate flexural strength

γ_{xx}: specific gravity, where xx is: *c* for cement, *fa* for fine aggregate, *ca* for coarse aggregate and *w* for water

GGBFS: ground granulated blast furnace slag

GFRC: Glass fibre reinforced concrete

h_{sp} and h: height

IBAMA: Instituto Brasileiro do Meio Ambiente e dos Recursos Naturais Renováveis

IRI: International Roughness Index

JCI: Japan Concrete Institution

JPCP: Jointed plain concrete pavement

JRCP: Jointed reinforced concrete pavement

JSCE: Japan Society of Civil Engineers

L: usually thickness or the spam

LEC: low energy cement

L_g: gauge length

LOM: Law of mixtures

LOP: Limit of proportionality

LTPP: Long Term Pavement Performance

LVDT: Linear variable displacement tranducer

m: uncertainty factor

m_{xx}: mass, where xx is: *c* for cement, *fa* for fine aggregate, *ca* for coarse aggregate, *w* for water, *2* for mould and concrete, *1* for mould, *o* for specimen at the end of curing, *d* for specimen after over drying, *e,75* for concrete at equilibrium with 75 ± 2% RH, *s* for saturated specimen, *ss* for saturated submerged specimen, *d,n* for oven dried scaled material from cycle n, *s,n* for cumulative loss of mass

MS: mean square

msa: million standard axles

MTS: Material Testing System

ν: Coefficient of Poisson

N: number of cycles (for both fatigue and freeze-thaw)

NBR: Norma Brasileira

N_c: equivalent number of accelerated cycles

NCHRP: National Cooperative Highway Research Program

NMSA: Nominal maximum size of aggregate

N_{wd}: number of wet days during the period where freezing cycles occurs

N_{wfc}: effective number of wet cycles

P: usually porosity or load

P-value: probability

P_a: atmospheric pressure

PCA: Portland Cement Association

PCP: Plain concrete pavement

P_i: total applied pressure

p_f: probability of failure

Q_i: flow rate of oxygen

ρ: density (usually related to dry density)

ρ_b: bulk density

ρ_d: dry density

ρ_w: density of water

R: usually resistance coefficient

RC: reinforced concrete

RCC: Roller compacted concrete

Rebar: conventional reinforcement steel bar

$R_{e,3}$: equivalent flexural ratio

RH: relative humidity

RILEM: Reunion Internationale des Laboratoires et Experts des Materiaux

RMA: Rubber Manufacturers Association

s: stress ratio or ageing coefficient depending on the cementitious material

$S(t_{SL})$: scaled material at a time t_{SL}

S_{cr}: critical limit for scaling

SFRSCC: Steel fibre reinforced self compacting concrete

SS: sum of squares

St_{crit}: critical degree of saturation at which frost damage starts to occur

$St(t_{SL})$: saturation at a time t_{SL}

t: usually time

T_{air}: temperature of the air

T_{sky}: corresponding sky temperature

$T(t_{SL})$: concrete temperature at a time t_{SL}

t_c: time to measure level of water water

T_R: resistance scaling temperature

t_{ref}: time of curing

TRL: Transport Research Laboratory

t_{SL}: service life

USFD: The University of Sheffield

UFRGS: Federal University of Rio Grande do Sul

V: usually volume

V_f: volume content of fibres

x: concrete cover

X: usually level of water uptake after t_c

w/c: water to cement ratio

w_e: evaporable moisture concentration (usually related to the temperature of 105 °C)

w_{e80}: evaporable moisture concentration at 80 °C

w_{e50}: evaporable moisture concentration at 50 °C

W_e: total evaporable water content

$w_{e,75}$: equilibrium moisture concentration

$W_{e,75}$: equilibrium water content at 75 ± 2% RH

CHAPTER 1

1. INTRODUCTION

1.1 BACKGROUND OF THE PROBLEM AND CONTEXT

Concrete is the most widely used structural material in civil engineering primarily due to its low cost and excellent resistance to compressive stresses. Concrete can also be used in non-structural applications, as a filler, to resist impact, or in plate form to resist flexural loads. Concrete is a durable material when well designed and constructed.

However, concrete is weak in resisting tensile stresses and, as a result, it is a brittle material. To overcome these weak properties, concrete is usually used in combination with tensile reinforcement such as the conventional steel rebar or steel fibres. The addition of fibres in concrete may be also useful in controlling shrinkage cracks, improving flexural toughness as well as enhancing impact and fatigue resistance, which is especially important for pavements, as shown in Figure 1.

Figure 1 – Concrete pavement road.

Roads (paved and unpaved) are an important part of the infra-structure that allows people to move as well as the transport of goods. They may also be seen as a measure of the development

of a nation. Unfortunately, most roads in a large number of countries are still unpaved, especially in developing countries. A survey developed by the World Bank in 2006 shows that only around 36% of the roads in the world are paved[1] or sealed. According to the same source, in the UK it is considered that 100% of the road network system is paved, while in the European Union and Central Asia this value drops to 74%. In the United States, according to U. S. Department of Transportation (2008), 65.2% of the roads were paved by 2006. In Brazil, according to ANTT (2006), only 13.9% of the roads were paved by 2005. Besides the large number of totally unpaved roads, it is important to add that among the roads considered as *paved*, there are many roads with urgent need of maintenance.

Asphalt is still the most commonly used pavement material, mostly due to cost, tradition and availability of equipment. Usually the construction cost of an asphalt road is less than that of a concrete road (Thomas, 2006). However, the increase in oil prices is having an impact on asphalt prices reducing the price difference between the flexible/asphalt pavements and rigid/concrete pavements. The development of concrete technologies is also helping to reduce the construction costs of concrete roads. Such technologies include the use of high strength concrete and/or fibres to reduce the pavement thickness or the use of low cement content concrete, such as roller compacted concrete (RCC).

As life-cycle and durability are taken more into account in recent years, the use of concrete pavements is increasing (Perlman, 2010 and Sullivan, 2009). Concrete pavements, when well designed and constructed, require less maintenance when compared to asphalt pavements and also achieve a longer service life (ACPA, 2008 and 2010a; Sullivan, 2009).

The main types of concrete pavements are the continuously reinforced concrete pavements (CRCP) and the jointed plain concrete pavements (JPCP). For the former, reinforcement is used to resist the flexural tensile stresses, while for the latter, the flexural tensile stresses are resisted by thicker concrete slabs and higher strength concrete. Both the reinforcement and the higher strength concrete lead to high initial costs. For the CRCP, extra time and effort is required for the preparation and placement of the reinforcement, which is viewed as a trip hazard for workers.

RCC can also be used in pavements. RCC is a dry concrete with zero slump, and the cement content is usually lower than for conventional concrete (typically 200-350 kg/m^3). According to Tilles *et al.* (1990), RCC has high initial strength which means that traffic of equipment is allowed at early ages or even just after the placement of concrete. To achieve this good

[1] A paved road, according to the World Bank, are roads surfaced with crushed stone and hydrocarbon binder or bituminized agents, with concrete, or with cobblestones.

performance, RCC normally requires the use of high quality materials (Ribeiro and Almeida, 1999), which may add to the cost.

Steel fibres may be a good alternative to overcome the economic barrier associated with concrete pavements. They can be used as an alternative to steel reinforcement in CRCP, as reinforcement for JPCP to reduce the slab thickness, or as an alternative to high quality materials in RCC.

Fibres are randomly distributed inside the concrete and usually a larger volume of fibres is required to achieve the same performance as conventional reinforcement, and this turns to be again a cost-associated problem. However, recycled steel fibres obtained from post-consumer tyres may be used as an alternative to industrially produced steel fibres.

Some studies have already been undertaken on the inclusion of recycled steel fibres (Wang *et al.*, 2000; Pilakoutas and Strube, 2001; Pilakoutas *et al.*, 2004; Tlemat, 2004; Tlemat *et al.*, 2006, 2004a and 2004b; Neocleous *et al.*, 2006; Angelakopoulos *et al.*, 2008a and 2008b; Graeff *et al.*, 2009 and 2010; Aiello *et al.*, 2009). The results, mostly in terms of mechanical properties, show that recycled steel fibres may be a good alternative to the manufactured fibres. The use of recycled steel fibres for use in concrete has been patented by the University of Sheffield (USFD, 2001). Recycled steel fibres in concrete pavements may reduce the initial costs and the environmental impact of road construction and provide long-term performance.

Sustainability has been the focus of an increasing number of studies in the concrete area aiming to reduce the emission of CO_2 and to provide means for the better use of natural resources. The use of recycled materials in concrete, especially for pavements, is in line with this idea.

The disposal of post-consumer tyres is still a major concern worldwide (Figure 2). Even though some efforts have been focused at lowering the number of tyres disposed in landfills and illegal dumping places (i.e. new regulations that forbid landfills to accept whole or partial tyres – European Union: Council Directive 1999/31/EC, 1999; U. S.: no Federal Laws but 48 states have their own regulation for scrap tyres; Brazil: Conama Resolution 301, 2009a), the figures are still shocking. In the UK alone, almost 50 million tyres are generated each year for disposal or recovery (UTWG, 2009). The European Tyre Recycling Association (ETRA, 2010) says that 300 million of post-consumer tyres are discarded each year in the European Community. According to the U. S. Environmental Protection Agency (2009), it is estimated that in the United States approximately 290 million post-consumer tyres are generated every year (according to 2003 statistics provided by Rubber Manufacturers Association). In Brazil, it is estimated that there are more than 100 million post-consumer tyres already dumped in the environment and that approximately 65 million tyres are discarded each year (IBAMA, 2008).

Figure 2 – Dumping of tyres.

Most of the efforts concerning the recycling of tyres are focused on the extraction and the use of rubber. Even though approximately 15 to 25% by weight of a tyre is composed of steel wire (ETRA, 2010), there are only very few studies on reusing this material. A certain amount of steel from tyres is remelted for steel production, but the contamination of steel with other tyre residues is preventing its extensive use as scrap steel. In addition, remelting steel may not be the most environmentally friendly solution if uses can be found that utilise the steel fibres substantially as they are. Regarding the use of recycled steel fibres for concrete, WRAP (2007) reports that the University of Sheffield (USFD) is leading the studies in Europe.

This thesis aims to address the issue of the use of recycled steel fibres obtained from post-consumer tyres in concrete. This work was undertaken alongside the European Research Project *Ecolanes* – Economical and Sustainable Pavement Infrastructure for Surface Transport, as described in Appendix A. The project was developed to provide a complete feedback on the use of recycled steel fibres in concrete for pavement applications, including the characterisation of the fibres, the mechanical properties of concrete, the cost and environmental analysis and the construction of road trials (Neocleous *et al.*, 2011).

Mechanical properties of recycled steel fibre reinforced concrete (SFRC) have been studied in previous works, however, the durability and the long-term performance of this concrete has not yet been studied (except some limited work on shrinkage behaviour by Wang *et al.*, 2000). In addition, there are limited studies on durability behaviour of SFRC with industrially produced fibres and they mainly focus on corrosion.

Billions of dollars are spent every year, worldwide, to solve unexpected problems related to the durability of concrete. In the UK, alone, it is estimated that around 2 billion dollars are spent every year to solve deterioration problems in concrete, which according to Broomfield (2005),

corresponds to approximately 3% of the total amount spent by the UK construction industry. In the United States, it is estimated that around 3% of the Gross Domestic Product (GDP) is spent every year to remediate corrosion deterioration, which corresponds to about 276 billion dollars in 1998 (NACE, 2001). In Brazil, it is estimated that 20 billion dollars were spent in 2002 to solve problems caused by corrosion in the construction industry (IPEN, 2002), which corresponds to more than 5 times the total amount spent on research and development in all disciplines in the same year.

Pavements alone are susceptible to various deteriorative processes including cyclic traffic loads, which can cause deterioration due to fatigue. Chemical attack by chlorides and carbonation can lead to the corrosion of reinforcement or fibres. Due to the large amount of concrete used, heat of hydration and shrinkage may also influence the performance of pavements. Freeze-thaw deterioration is another issue, since the concrete slabs are continuously exposed to weather action and, in many cases, in direct contact with soil which can often be saturated. Figure 3 shows a severely cracked concrete pavement slab.

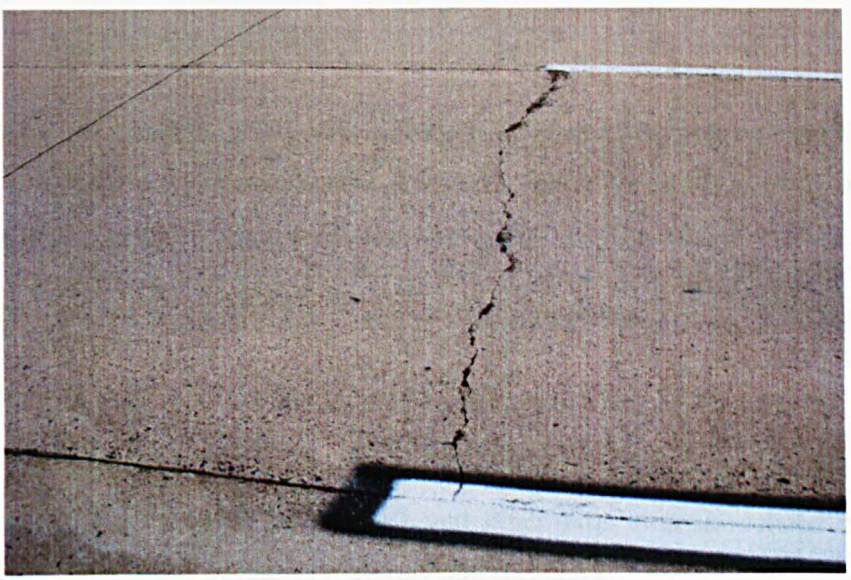

Figure 3 – Cracked concrete pavement.

To address the issue of long-term behaviour of SFRC and to provide means for the understanding of the durability performance of recycled SFRC before applying it to real structures (especially concrete pavements), there is a need to investigate the pore-structure properties of conventional concrete and RCC, such as permeability, porosity, sorptivity, diffusivity and shrinkage. Deteriorative processes such as corrosion, fatigue and freeze-thaw resistance also need to be examined.

Particular research questions that will be addressed in this work comprise the following:

- Are the recycled fibres a good alternative for concrete pavement reinforcement?
- What are the main benefits (regarding structural and durability performance) of using recycled SFRC compared to asphalt or any other commonly used pavement technique?
- How is the pore structure of the concrete affected when steel fibres (recycled or industrial) are added as reinforcement?
- How does recycled SFRC respond against the main durability challenges for pavements (i.e. corrosion, freeze-thaw and fatigue)?
- Is there a model that can be applied to predict the life-cycle of recycled SFRC, used for pavement applications?
- How can the knowledge on the durability resistance of recycled SFRC contribute to the design and maintenance of pavements constructed with this material?

1.2 AIMS AND OBJECTIVES

The main aim of this work is to determine whether recycled SFRC can be used for pavement applications considering its durability and long-term performance. This study also aims to provide some tools for the life-cycle prediction of recycled SFRC pavements.

Several specific objectives are proposed to achieve the above aim:

a) Understand how recycled SFRC (both conventional and RCC) performs in terms of mechanical properties;

b) Investigate the transport mechanisms and other pore structure-related properties of recycled SFRC, such as porosity, density and shrinkage;

c) Evaluate the resistance of recycled SFRC specimens against corrosion by exposing them to wet-dry cycles;

d) Measure the effects of accelerated freezing and thawing cycles in recycled SFRC;

e) Examine the fatigue behaviour of recycled SFRC by accelerating cyclic loads;

f) Make comparisons with plain concrete and SFRC using both recycled and industrial fibres;

g) Compare the behaviour of RCC and conventional concrete, in terms of mechanical properties and long-term performance;

h) Correlate the procedures used to accelerate corrosion and freeze-thaw with real environmental conditions, based on a probabilistic analysis.

1.3 STRATEGY

To assess the durability resistance of recycled SFRC, an extensive experimental plan was developed followed by a probabilistic analysis. The experimental programme is divided into two distinct phases. One phase is related to the understanding of the transport mechanisms (permeability, sorptivity and diffusivity) and other pore structure-related properties (porosity, density and shrinkage). The second phase deals with the main deterioration processes that may affect the long-term performance of recycled SFRC pavements, such as corrosion of fibres, freeze-thaw and fatigue.

The probabilistic analysis is based on the development of models to predict the service life behaviour of recycled SFRC pavements, due to corrosion, freeze-thaw and fatigue.

Figure 4 illustrates the main stages of this study.

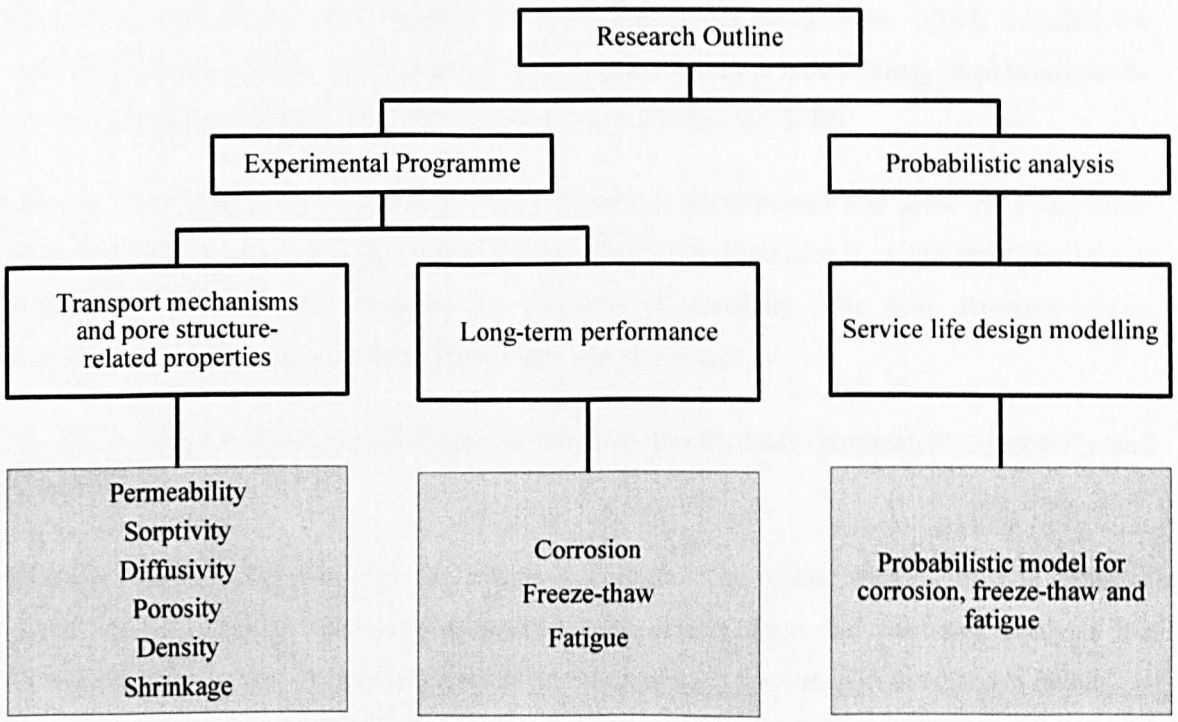

Figure 4 – Diagram of the research outline and main expected output results.

Some of the limitations of this study are associated with the limited time available for a PhD programme, especially when durability issues are examined. Deterioration in structures,

subjected to real environmental conditions, occurs over a long period of time. Hence, for the purpose of this work, the deterioration processes need to be accelerated.

1.4 PRESENTATION OF THE THESIS

This thesis is composed of 11 chapters. The first chapter introduced the background of the research, posed some research questions and presented the objectives and the strategy used to pursue them.

Chapter 2 comprises a literature review on the main issues related to post-consumer tyres, the main types of FRC (fibre reinforced concrete), the mechanical properties of SFRC and finally, an explanation on the main types of concrete pavements and concrete pavement design methods.

Chapter 3 describes the main types of deterioration processes that may affect the performance of concrete pavements, such as fatigue, corrosion and freeze-thaw. It also explains the transport mechanisms that influence the ingress of aggressive agents into concrete and other pore structure-related properties.

Chapter 4 explains the main aspects of the experimental programme, which includes the description of the materials, the variables of the research and the methodology used to assess the various properties and long-term performance issues of recycled SFRC.

Chapter 5 deals with the results from the mechanical performance and some pore structure-related properties of control specimens. The mechanical performance is investigated in terms of compressive and flexural strength and modulus of elasticity. The pore structure-related properties studied are the porosity, density and free shrinkage.

Chapter 6 is based on the results from the transport mechanisms (permeability, sorptivity and diffusivity).

Chapter 7 presents the results of the corrosion analysis. The results are presented in terms of visual analysis and mechanical performance. The results from the corrosion analysis are correlated with the pore structure-related properties and with the transport mechanism results.

Chapter 8 explains the results obtained from the accelerated freeze-thaw study. The outputs are shown in terms of visual analysis, loss of mass and mechanical performance. A comparison is made to correlate the freeze-thaw results with the pore-structure related properties and transport mechanisms.

Chapter 9 describes the fatigue results, which are presented in terms of stress level *versus* number of cycles curves and includes an analysis in terms of vertical displacements.

Chapter 10 focuses on the probabilistic analysis for corrosion, freeze-thaw and fatigue.

Finally, Chapter 11 presents the main conclusions of the thesis. It also proposes answers to the research questions posed in Chapter 1 as well as some suggestions for future activities aiming to complement the work in this thesis.

CHAPTER 2

2. ENVIRONMENTAL ISSUES, SFRC AND RIGID PAVEMENTS

This chapter initially introduces the environmental aspects of post-consumer tyre disposal and recycling. The subsequent sections deal with the characteristics and properties of SFRC and provide information on steel fibres. Finally, the main types and design methods of concrete pavements are explained.

2.1 ENVIRONMENTAL ASPECTS OF END OF LIFE TYRE DISPOSAL

2.1.1 Landfill or Incineration Disposal

The disposal of post-consumer tyres in the environment is still a major concern especially in developing countries. According to Batayneh *et al.* (2008), post-consumer tyres are considered as non-decay materials and for this reason are classified as hazardous materials. Scrap tyres are prone to water accumulation where mosquitoes and other insects may find it fertile for breeding, including the ones responsible for fatal diseases such as for Dengue Fever and Encephalitis (Fiksel *et al.*, 2010; Meyer, 2009; Motta, 2008). Rodents and other pests are also found in scrap tyre piles increasing further the risk of spreading human and animal diseases.

Special characteristics of tyres, such as their dark colour that absorbs heat and their volatile nature at elevated temperatures, make scrap piles fire hazards. Smoke generated from burning tyres, due to the low combustion temperatures, contains hazardous components, such as benzene derivatives, dioxins, oxides of nitrogen and sulphur, carbon monoxide, heavy metals, aromatic hydrocarbons and particulate matter (Amgai, 2004). These components may contaminate soils, air and water and also burden authorities with costs to extinguish the hazardous fires and to decontaminate land (Fiksel *et al.*, 2010).

Whole tyres were commonly discarded in landfills in the past. However, they tend to float to the surface breaking the landfill cover leading to groundwater contamination due to leachate (Reddy

et al., 2010 and Fiksel *et al.*, 2010). In many countries, landfilling of tyres or tyre components is prohibited by law.

One of the most common alternatives to landfill discard is to use shredded tyres as a source of fuel for cement kilns, furnaces, power plants and other industrial boilers and kilns. This usually represents one of the highest percentage of post-consumer tyre usage – 37% in European Union (ETRMA, 2010 – ref data 2008), 54% in United States (RMA, 2009 – ref data 2007) and 32% in Brazil (IBAMA, 2008 – ref data 2004). The burning process associated with the use of post-consumer tyres in cement kilns is still controversial. Some believe that the smoke generated by tyre fire is hazardous due to the release of toxins, responsible for pollution, environmental attack and human health problems (notoxinburning.org, 2006; Shakya *et al.*, 2008). Others believe that burning of tyres in cement kilns releases reduced amount of toxic pollutants due to the high combustion temperature (Fiksel *et al.*, 2010). However, the fundamental objection to burning tyres is that a lot of energy had already been used to produce the rubber, polymer reinforcement and steel, and if the constituent materials could be reused, that would be the preferred environmental solution.

2.1.2 Recycling of Post-consumer Tyres

There are several ways of recycling post-consumer tyres. Most of these focus on reusing the rubber constituents and very few deal with the other tyre components, such as textile and steel. A typical section of a tyre is shown in Figure 5.

1. Airtight synthetic rubber inner liner
2. Textile fibre cords for casing ply
3. Lower bead area
4. Bead wire
5. Rubber sidewalls
6. Very fine steel cords
7. Nylon cords for the safety ply
8. Thread rubber layer

Figure 5 – Typical tyre section and components [Bridgegate Tyres, 2009].

When used in combination with gravel, shredded post-consumer tyres can be used in landfill as a layer for leachate and methane collection. Use of tyres in these applications is beneficial due

to the good drainage capability and to the protection of the underneath liner system (Edil *et al.*, 2004; Bhalla *et al.*, 2010; Reddy *et al.*, 2010).

Tyre steel mesh and rubberised tyre wire can be used for post-tensioning masonry walls to avoid out-of-plane bending failure (Turer and Gölalmis, 2007).

Naturally, the best use of post-consumer tyres is to reuse or retread them when possible.

2.1.2.1 Use of rubber extracted from tyres

Rubber from post-consumer tyres can be used in the manufacture of various products such as carpets, floor laminates, highway barriers, shoe soles, base for artificial grass, playground surfaces, insulation layers, vases, etc. Some applications for rubber from tyres are shown in Figure 6.

Figure 6 – Products made by recycled rubber from tyres.

Civil engineering also makes a large contribution to the recycling of rubber from post-consumer tyres. In the European Union, it represents 39% of the total amount of recycled tyres (ETRMA, 2010 – ref data 2008). The United States recycle about 12% of tyres in civil engineering applications (RMA, 2009 – ref data 2007) and Brazil is responsible for less than 7.5% (IBAMA, 2008 – ref data 2004). Examples described below represent only few possibilities to reuse rubber from tyres in civil engineering but several more are supposed to appear as research evolves.

- Tyre crumb rubber can be used in asphalt pavements as a modifier binder (Specht, 2004; Zheng *et al.*, 2008), helping to minimize the road noise and the maintenance costs by improving its durability (Fiksel *et al.*, 2010). It improves the resistance to permanent deformation and fatigue loads and it is also attractive from an economical point of view (Xiao *et al.*, 2009). However, only a small amount of rubber can be incorporated in asphalt (Specht, 2004; Ayerra, 2010).

- A mixture of soil and rubber from tyres can be used in highway embankment constructions helping to solve stability problems associated with soft soils (Rao and Dutta, 2006; Yoon *et al.*, 2006; Edinçlider *et al.*, 2010). However, rubber crumb is much more expensive than normal sand and soil and, hence, unlikely to be used in large quantities.

- Different sizes of rubber particles can be used as aggregate for concrete elements (Siddique and Naik, 2004; Turatsinze *et al.*, 2005; Yilmaz and Degirmenci, 2009). According to Meyer (2009), even if the strength and stiffness of concrete are reduced, rubber particles seem to control crack propagation, which improves ductility. Other properties such as permeability and insulation are also improved (Batayneh *et al.*, 2008; Albuquerque 2009). Rubber aggregates can be used to produce lightweight concretes. Rubber concrete can be used to absorb vibration and impact, for facades and other architectural elements (Fattuhi and Clark, 1996). The loss of strength due to the inclusion of rubber is very significant and the cost of rubber aggregates is high, so the benefits need to compensate the disadvantages, hence, only few large scale applications are feasible.

2.1.2.2 Polymer and steel reinforcement

The polymer reinforcement comes out in the form of 'fluff' and at the moment is a serious problem for the tyre recyclers since it does not have any uses. It is sometimes used as fuel in incinerators but it is more often discarded in landfills.

The steel reinforcement is also currently a problem since it is often contaminated with organic material and as a result it is difficult to get the steel furnaces to accept it for remelting. However, the steel cord is a high quality high strength wire which, if appropriately treated, can be used as reinforcement for concrete (Pilakoutas *et al.*, 2004).

2.1.3 Legislation on Post-consumer Tyres

2.1.3.1 European Union

According to ETRMA (2010), the European Union will apply a new directive on the impact of the management of post-consumer tyres in approximately ten years from the date of this thesis. Up to the present, the following directives apply to tyre recycling in the European Union.

- The Council Directive 1999/31/EC (European Union, 1999) says that no whole tyres should be discarded in landfills after July 2003. Shredded tyres were also banned from landfills from July 2006. Bicycle tyres and tyres measuring more than 1.4 m in diameter were exempted from the regulation, hence are still allowed to land disposal;

- The Council Directive 2008/98/EC (European Union, 2008) explains the definitions of waste and how to deal with it in the European Community. Four 'Rs' are proposed for the waste management to avoid disposal: reduce, reuse, recycle and recover;

- According to ETRMA (2010) and ETRA (2010), other regulations are somehow related to the post-consumer tyre recycling such as Council Directives 2000/53/EC (2000a) – related to the best way to recover end of life vehicles, including their tyres – and 2000/76/EC (2000b) – associated to emission limits for cement kilns and other incinerator plants.

2.1.3.2 United States

Each state is responsible for its own regulation regarding the disposal and recovery of post-consumer tyres. According to U. S. Environmental Protection Agency (2008), the vast majority of states – 48 – have regulations regarding the management of end of life tyres. States that have no regulation on post-consumer tyres are Alaska and Delaware. The same agency shows that the majority of states do not allow the disposal of whole tyres to landfills and 11 states banned all forms of discarding tyres in land. However, the disposal of shredded tyres is still allowed in 35 states. Even though the discarding of tyres is not 100% banished in the United States, continuous work is being done to clean tyre stockpiles and on methods to reuse scrap tyres. This also applies to the couple of states that do not have any legislation on the management of post-consumer tyres.

Common topics among the regulations include: 1) the programme funding of the post-consumer tyre management through taxes or fees on cars and tyres; 2) alternatives for reusing post-

consumer tyres; 3) cleaning of tyre stockpiles; 4) norms for post-consumer tyre manufacturer and users among others.

2.1.3.3 Brazil

Brazilian regulation on the management of the disposal of post-consumer tyres to landfills was first established in 1999 by the Conama Resolution 258 (CONAMA, 1999). The legislation supported the gradual removal of tyres from the environment by the tyre manufacturers which were made responsible for their collection and recycling.

In 2009, the Conama Resolution 258 (CONAMA, 1999) was substituted by Resolution 416 (CONAMA, 2009b). This resolution says that tyre manufacturers are responsible for the environmentally correct recycling of every new tyre produced. The resolution also obliges manufacturers to create a plan for tyre collection and recycling. It also bans the disposal of tyres in the environment, including landfills and open burning. Shredding alone is not considered as a recycling technique, hence, disposal of shreds in landfills is also not permitted. Tyres can be used as fuel if supported by specific regulation regarding emission limits.

Imports of post-consumer tyres were prohibited by Conama Resolutions 23 (CONAMA, 1996) and 235 (CONAMA, 1998). In 2009, the import of used tyres was banned by the Brazilian Superior Tribune – STF (Reciclanip, 2009).

2.1.3.4 Discussion

It is clear that legislation worldwide is trying to make the manufacturers responsible for the end of life tyres and/or to prohibit the disposal of tyres and their derivatives. Since the tyre derivatives are high quality materials, there is an urgent need for the development of new applications for these materials. Clearly construction, being one of the biggest users of materials, could find uses for the tyre derivatives if a proper understanding of their properties is developed.

Steel wire is currently used as concrete reinforcement and using steel extracted from tyres can be an alternative, as it will be discussed in the next section.

2.2 FIBRE REINFORCED CONCRETE AND FIBRE TYPES

Fibre reinforced concrete (FRC) is no longer considered as a new material in civil engineering. Asbestos fibres were used in concrete since the 1900s (Wikipedia, 2008) while extensive studies undertaken on the addition of various types of fibres into concrete started since the 1960s, and

new achievements have continuously been obtained (Barr and Swamy, 1989). FRC was adopted massively in civil engineering industry in the last three decades, such as for industrial floors, shotcrete, precast thin elements, pipes, roofs, etc.

Concrete has micro-cracks in the transition zone between the matrix and the coarse aggregate. When these micro-cracks suddenly propagate into macro-cracks, this leads to a brittle behaviour of concrete (Metha and Monteiro, 2006). Fibres act on this weak property in an attempt to sew the cracks, as shown in Figure 7.

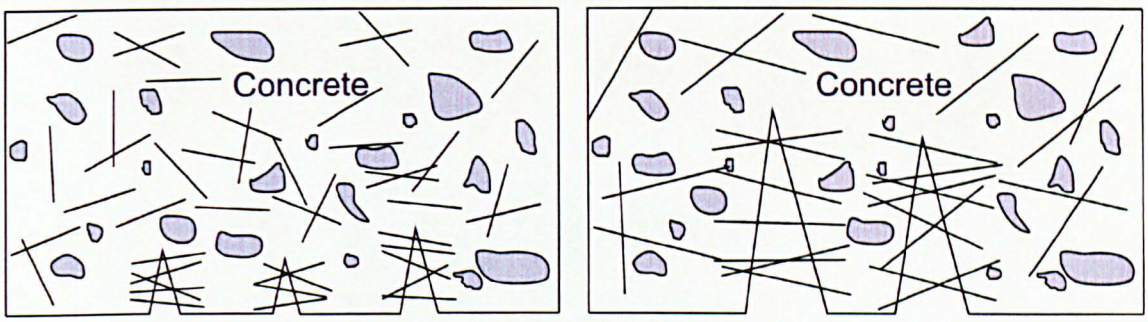

Figure 7 – Small and large cracks in FRC.

Smaller and thinner fibres are used to bridge small cracks (Rossi and Parant, 2008), and are mostly used to improve shrinkage behaviour. Larger fibres are used to limit or prevent the propagation of wider cracks and can thus enhance the structural properties of FRC.

2.2.1 Types of Fibres for Concrete Reinforcement

There are various types of fibres that may be added into concrete. Besides their origin, they vary in shape, geometry, mechanical properties and density. These can be divided into two main groups, natural and synthetic, as shown in Figure 8. Natural fibres are those collected from nature and used as they are, without major industrial treatment. Synthetic fibres are human-made fibres and they can be either organic or inorganic.

ACI (1982) gives the typical properties in terms of tensile strength, young modulus, elongation and specific gravity for some of the most used fibres in concrete, as shown in Table 1. The original table has been updated with the inclusion of other fibres and sub-categories.

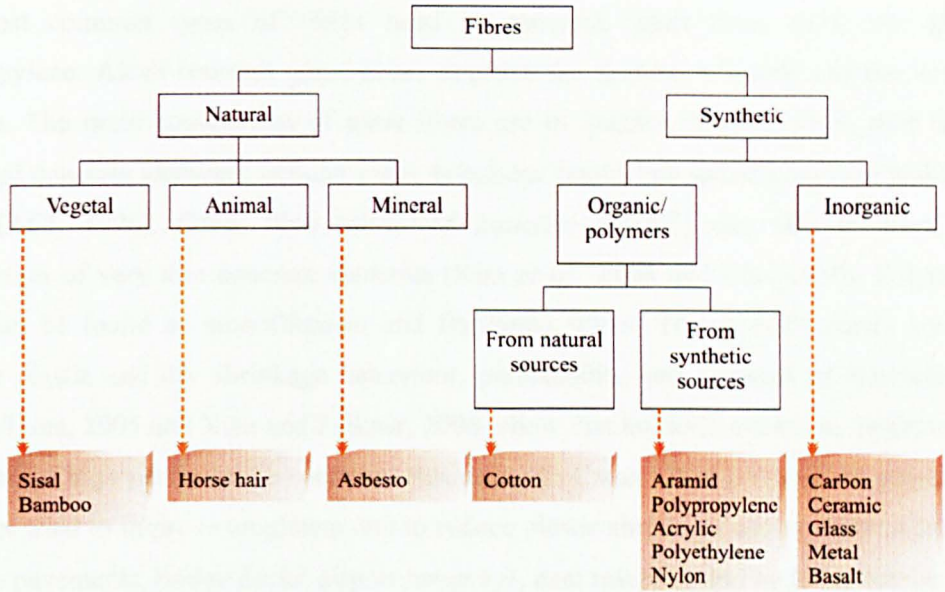

Figure 8 – Categories of fibres used in concrete and examples.

Table 1 – Properties of the main fibres used for FRC.

Fibre type	Tensile strength [MPa]	Young Modulus [GPa]	Elongation [%]	Specific gravity
Acrylic[1]	210 - 410	2	25 - 45	1.1
Aramid[2]	2300 - 3100	55 - 145	1.5 - 4.4	1.5
Asbestos[1]	550 - 970	82 - 138	12 - 20	3.2
Carbon high modulus[3]	1500 - 4700	345 - 590	0.6 - 1.4	1.9
Carbon high strength[3]	3300 - 5000	230 - 300	1.5 - 2.2	1.8
Cotton[1]	410 - 690	5	3 - 10	1.5
Alcali resistant glass[4]	1800 - 3500	70-76	2 - 3	2.3
Nylon[1]	760 - 830	4	16 - 20	1.1
Polyethylene[1]	690	0.1 - 0.4	10	0.95
Polypropylene[1]	550 - 690	3	25	0.90
Monofilament polypropylene[5]	>500	>3.9	>8%	0.91 - 0.93
Fibrillated polypropylene[5]	>400	>3.5	10 - 50	0.91
Steel	280 - 2760	200	0.5 - 35	7.8

[1] according to ACI Committee 544.1R-82 (1982)
[2] according to Yang (1993) cited in Bernardi (2003)
[3] according to Kendall (1999) cited in Beber (2003)
[4] according to fib bulletin 40 (2007)
[5] according to Cmax supplier (2009)

The most common types of fibres used in concrete, apart from steel, are glass and polypropylene. Alcali-resistant glass fibres improve the flexural strength and the ductility of concrete. The main applications of glass fibres are in facades, interior walls, roof tiles, pre-fabricated concrete elements, cellular slabs, telephone boots, bus shelters, storage tanks, among others (ACI, 1996). Glass fibre reinforced concrete (GFRC) can also be used for the construction of very thin concrete elements (Kim *et al.*, 2008 and Che, 2010). Polypropylene fibres can be found as monofilament and fibrillated fibres. The monofilaments are used to improve plastic and dry shrinkage behaviour, permeability and abrasion of concrete. Recent studies (Lima, 2005 and Xiao and Falkner, 2006) show that monofilaments can improve the fire resistance of high performance concrete. According to Cmax (2009), fibrillated polypropylene fibres are used to improve toughness and to reduce plastic shrinkage and settlement cracking in concrete pavements, bridge decks, airport runaways, dam reservoir and highway barrier walls.

Natural fibres can also be used as reinforcement in concrete, however, they have poor durability when in contact with the alkalinity of concrete. Another problem is the mineralisation of the fibres caused by the deposition of hydration products of cement[2] in the fibre pores, which turns the fibres into a brittle material. Despite the durability problem, natural fibres can improve toughness and impact resistance (Savastano Jr. *et al.*, 2009 and Al-Oraimi and Seibi, 1995).

Fibres with relatively low stiffness do not generally enhance the flexural properties of concrete, since they are not effective in arresting crack propagation.

Steel fibres are most commonly used for structural properties, and for this reason specific sections have been designated for them, as explained below.

2.2.2 Industrially Produced Steel Fibres

Steel fibres are the most commonly used structural fibres in the construction industry. They vary in shape, geometry and performance level. The flexural toughness, impact resistance and good fatigue behaviour are the main properties enhanced by the inclusion of fibres (ACI, 1996).

There are several applications for steel fibres in civil engineering. They are used as reinforcement for industrial floors usually subjected to high and concentrated loads and impacts, for bridge rehabilitation, for airport runaways and for airfield pavements. Dams and hydraulic structures can incorporate steel fibres due to their capacity of resisting erosion and cavitation. Steel fibres are commonly used in shotcrete for tunnelling, rock slope stabilization, and precast

[2] Hydration products of cement can also be called gel, and represent the crystallised hydrates of the various compounds such as C-S-H (calcium-silicate-hydrate) (Neville, 2003).

elements such as concrete pipes, culverts and lids for urban downtake pipe systems. SFRC is also used for military purposes by the use of SIFCON[3] to construct hardened missile silos. Stainless steel fibres may also be used as reinforcement to monolithic refractories to be used in petroleum refining applications, rotary kills in cement production, incinerators, among others (ACI, 1996).

Considering the variety of steel fibres that can be found in the industry, different standards propose different classifications for the fibres. British Standard BS EN 14889-1 (2006a) classifies the fibres according to their manufacturing process and they are divided in five types. The same criterion is adopted by ASTM A820 (2006a) but the number of steel types is restricted to four. Japanese Standard JSCE SF-4 (1984) classifies the steel fibres according to the shape of their cross section, and three types are proposed. Brazilian Standard NBR 15530 (ABNT, 2007a) divides the steel fibres into 7 categories according to the geometric shape and manufacturing process. Table 2 shows the classification used for these standards.

Table 2 – Classification of steel fibres according to BS, ASTM, JCSE and ABNT.

Standard	Type I	Type II	Type III	Type IV	Type V	Type VI	Type VII
BS EN 14889-1	Cold-drawn wire	Cut sheet	Melt extracted	Shaved cold drawn wire	Milled from blocks	-	-
ASTM A820	Cold-drawn wire	Cut sheet	Melt extracted	Other types	-	-	-
JSCE SF-4	Square section	Circular section	Crescent section	-	-	-	-
NBR 15530	Anchored cold-drawn wire	Anchored cold-cut sheet	Corrugated cold-drawn wire	Corrugated cold-cut sheet	Corrugated shaved cold-drawn wire	Straight cold-drawn wire	Straight cold-cut sheet

Apart from fibre type, according to the BS EN 14889-1 (2006a), steel fibres need to be characterised by their shape, length, diameter (or equivalent for non cylindrical cross section fibres), tensile strength, ductility, consistence and effect on strength of concrete. The standard also requires that the addition of fibres in concrete should achieve a residual flexural strength of 1.5 MPa at 0.5 mm crack mouth opening displacement (CMOD) and 1.0 MPa at 3.5 mm CMOD.

[3] Slurry Infiltrated Fibre Concrete (SIFCON) is a type of concrete in which fibres are first placed in moulds in order to occupy the entire volume. Concrete paste is added to the moulds to fill the gaps. The result is a concrete with very high strength and toughness capacity that may be used for blast and impact applications.

The average aspect ratio of steel fibres varies from 20 to 100 and length from 6.4 to 76 mm (ACI, 1996). The most common types of steel fibre geometry are the straight, deformed (also called crimped), crimped-end wire (also called hooked) and coned-end, as shown in Figure 9a, b, c and d, respectively. These fibres are derived from the cold-drawn process of production. Fibres that are not straight have been flattened or bent at the ends to increase bond, except the crimped fibre which has been produced already in its final shape.

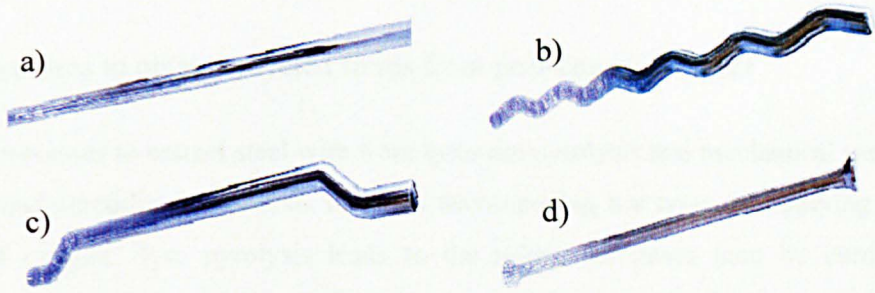

Figure 9 – Most common steel fibre geometries.

Due to the vast use and benefits of steel fibres associated with the subject of this study, the properties of SFRC are explained in Section 2.3.

2.2.3 Recycled Steel Fibres from Post-consumer Tyres

2.2.3.1 Recycled SFRC

Wang *et al.* (2000) made a comparative study on the inclusion of various industrial and post-consumer waste materials in concrete to restrain shrinkage, including the use of steel fibres from post-consumer tyres. According to the authors, the recycled steel fibres used were too small (< 6 mm) to effectively restrain the propagation of cracks.

After a series of initial investigations, in 2001 the use of recycled steel fibres from post-consumer tyres in concrete was patented by the USFD (2001).

Several studies have been undertaken since then at the USFD on the use of recycled steel fibres from post-consumer tyres (Pilakoutas and Strube, 2001; Pilakoutas *et al.*, 2004; Tlemat, 2004; Tlemat *et al.*, 2004a, 2004b, 2006; Neocleous *et al.*, 2006; Angelakopoulos *et al.*, 2008a and 2008b). These studies mostly focused on the mechanical properties, such as compressive and flexural strength, toughness and pull-out behaviour of fibres from concrete. The results showed that the behaviour of recycled SFRC could be comparable with industrially produced SFRC.

Several other studies were performed alongside the *Ecolanes* Project, for which more details are given in Appendix A.

Other studies show good performance of recycled SFRC in terms of compressive and flexural strength, toughness, pull-out behaviour (Aiello *et al.*, 2009) and splitting tension strength (Papakonstantinou and Tobolski, 2006). However, the amount of tyre residues bonded to the fibres for both studies was higher compared to the fibres currently in use at the USFD.

2.2.3.2 Processes to obtain recycled fibres from post-consumer tyres

The main processes to extract steel wire from tyres are pyrolysis and mechanical treatment (e.g. cryogenic and shredding). Pyrolysis involves decomposing the tyres by applying heat in the absence of oxygen. Tyre pyrolysis leads to the release of gases (can be used for power generation), oils (can be used as fuel or for the manufacture of oil products), solid carbon residue (generates low grade carbon black or solid fuel) and steel (Pyreco, 2010; Williams *et al.*, 2001). The mechanical treatment by cryogenic process is used to break post-consumer tyres by cooling them at temperatures of – 80 °C. The material becomes brittle and the components can be separated by a hammer mill. The cryogenic process is an efficient alternative to produce rubber granules, however, the method requires high energy input to cool the tyres and may also lead to steel embrittlement.

The mechanical treatment by shredding process seems to be the most economical and environmentally friendly alternative due to the low energy spent for breaking down the tyres. The figure below shows tyre wire obtained by shredding (Figure 10a) and pyrolysis (Figure 10b). The recycled fibres used in this study are obtained by the shredding process, and more detailed information is shown below.

a)  b) 

Figure 10 – Recycled fibres obtained from a) shredding and b) pyrolysis process.

The first step of the shredding process is normally dedicated to removing the bead wires from truck tyres due to the high strength and size of the steel wire, which could damage the shredding

equipment. The bead wire is usually removed mechanically and individually by pulling the wire and detaching it from the rubber by a hydraulic pulling system.

Tyres (both from cars and trucks without bead wire) first pass through various rotating discs on parallel axes that resemble a gear-shaped cutter with teeth, as shown in Figure 11a. Tyres are cut in small pieces (shreds) of approximately 50-300 mm, depending on the efficiency of the shredder and on the distance between the cutters. Figure 11b shows tyres before and after initial shredding.

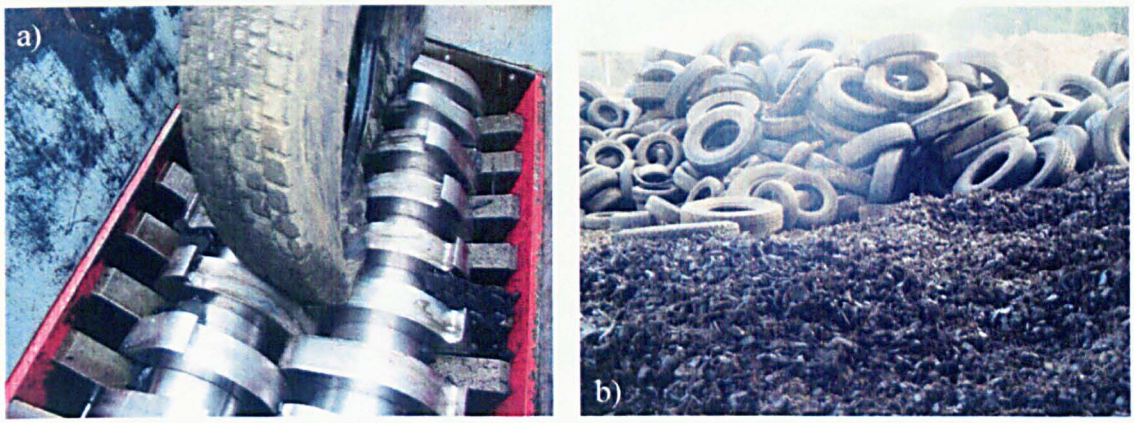

Figure 11 – a) Tyre shredder blades and b) before and after the shredding process.

The subsequent stage normally involves passing the shredded tyres through the rotating discs for a second time. The distance between discs is now reduced to provide smaller tyre chips of about 10 to 50 mm. Both first and second shredding processes are enough for cement kilns and other incinerators when the rubber chips or shreds are used as fuel. Rubber chips are further granulated to produce various sizes of rubber particles which can be used in several applications (see Section 2.1.2.1). Figure 12 illustrates the range of tyre shredding sizes. During this stage the steel fibres are detached from rubber and collected using magnets. Textile residues are removed from the steel fibres by blowing the residues away or by a vacuum system.

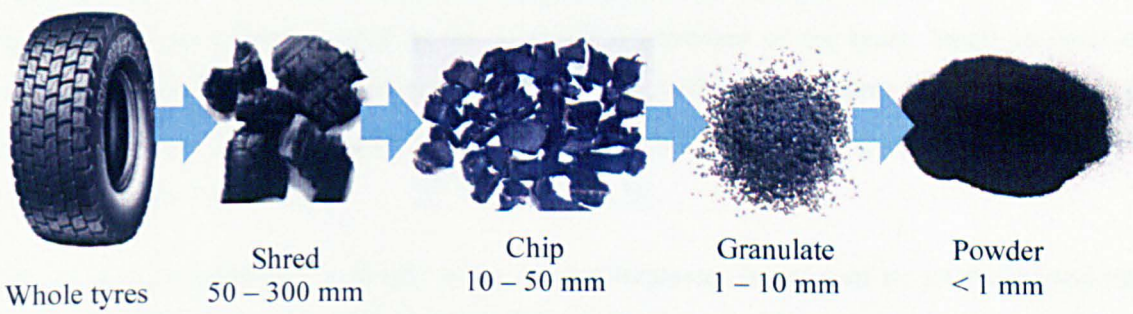

Figure 12 – Range of tyre shredding sizes.

Steel fibres which are not bonded to large rubber pieces can be separated by a magnetic conveyor that collects the loose fibres, as shown in Figure 13a. These fibres have pieces of rubber, textile and other residues attached to them and different geometric shapes, as shown in Figure 13b.

Figure 13 – a) Loose steel fibres collected by an electromagnetic conveyor belt b) appearance of the fibres.

The fibres used in this study need to pass through a post mechanical treatment to clean and sort the fibres by specific geometric features, such as the range of length and diameter, which make them suitable to reinforce concrete.

Sieving is normally required to get the range of length required for fibres to improve the mechanical behaviour and also to avoid balling during mixing of concrete. Information on the mechanical and physical properties of recycled steel fibres suitable for concrete is given below.

2.2.3.3 Physical and mechanical properties of recycled fibres

Recycled steel fibres, obtained from post-consumer tyres, have irregular shape and a diameter ranging from 0.1 to 0.3 mm. Fibres with larger diameter (1 to 2 mm) can also be found if the bead wire is not extracted prior to the mechanical treatment of the tyres. Small amounts of rubber particles and textile residues can also be found with the steel fibres. The tensile strength of recycled steel fibres is usually around 2000 MPa (Tlemat, 2004). Figure 14 shows the fibre appearance after processing.

Fibres vary considerably in length and a sieving treatment is required to get the appropriate range of length for use in concrete. Short fibres cannot be properly anchored to concrete and for this reason are not as efficient. Long fibres, however, get interlocked among themselves due to the irregular shape of the fibres and are prone to balling. Previous studies at the Univesity of

Sheffield have shown that the most appropriate size of fibres is in the range of 15 to 25 mm and with an average diameter of around 0.2 mm (USFD, 2001).

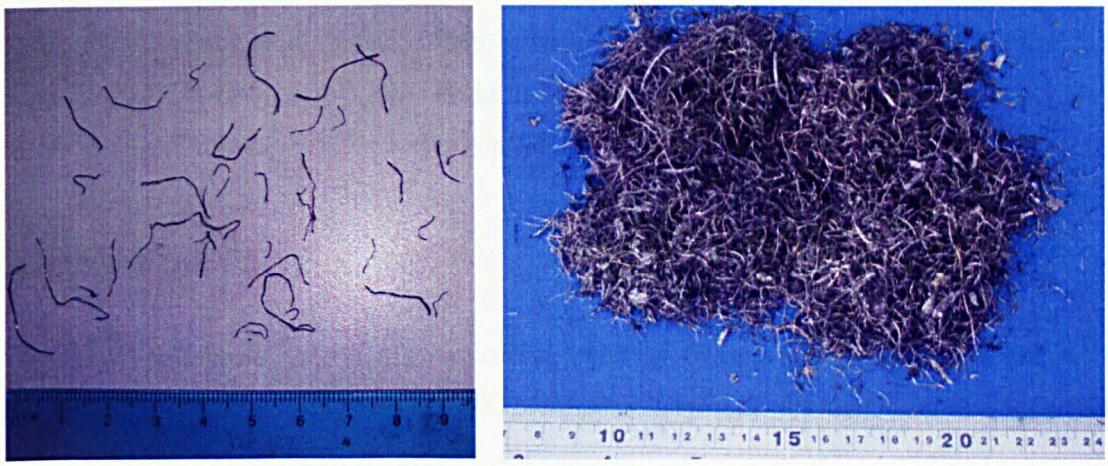

Figure 14 – Appearance of recycled steel fibres.

An optical analysis is needed to determine the fibre range of lengths. Analysis must be performed on a representative sample of fibres. A considerable amount of fibres needs to be collected from a bag of fibres and this is divided into small pieces by dividing the total amount by two, and then the two halves again in two, etc. After dividing the total amount in small fractions, one of them is chosen randomly and the statistical analysis is carried out.

Fibres are scanned in sets of 100 fibres per page and the images are further analysed by Digimizer®, which determines the area of the fibre shapes. Knowing the average diameter of the fibres, the length is determined. The procedure is repeated to as many scanned images as necessary to finish the randomly chosen fibre sample. The results are plotted in a histogram of cumulative percentage of fibres. The amount of fibres in between a certain length interval can now be assessed. Figure 15, for instance, shows that 80% of the fibres have length between 3 and 18 mm.

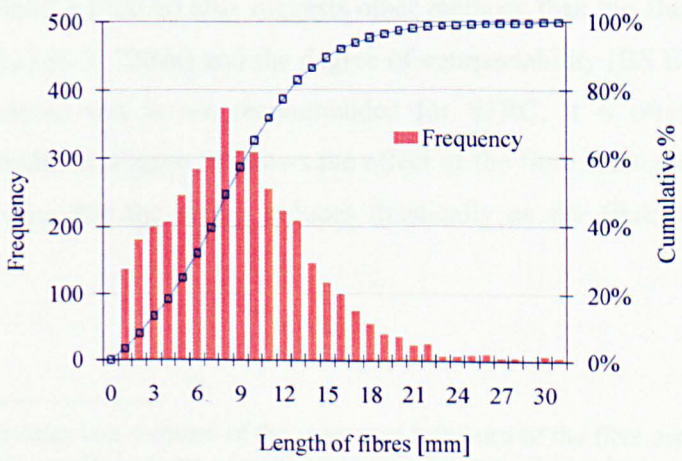

Figure 15 – Statistical analysis of recycled fibres.

The next section deals with the main properties of fresh and hardened SFRC, and mainly focuses on industrially produced SFRC since more works have been undertaken on this type of fibre. However, since various studies (Pilakoutas and Strube, 2001; Pilakoutas *et al.*, 2004; Tlemat, 2004; Tlemat *et al.*, 2004a, 2004b, 2006; Neocleous *et al.*, 2006; Angelakopoulos *et al.*, 2008a and 2008b) have shown that similar performance can be obtained when recycled fibres are used, this information will be useful when dealing with recycled SFRC.

2.3 PROPERTIES OF SFRC

SFRC properties described in this section are referred to conventionally placed *wet mixed* SFRC. The properties of *dry mixed* RCC with steel fibres are further described in Section 2.4.2.1.

2.3.1 Properties of Fresh SFRC

2.3.1.1 Workability

The workability of SFRC is influenced by the aspect ratio of the fibre, the volume content and the aggregate size and volume (Swamy, 1974; Swamy and Mangat, 1974; Hannant, 1978). Long and thin fibres, high fibre content and large aggregate size (responsible for increasing shear in the constituents of concrete during mixing – Swamy and Stravides, 1975) and volume tend to interlock the fibres and form *balls*, as described in the next section.

Workability tends to reduce when typical volumes of fibre content (0.3 – 1% by volume) are added to the concrete mix. Because mechanical vibration procedure is necessary for SFRC compaction, ACI 544.1R Report (ACI, 1996) suggests the use of other methods (e.g. Vebe test by BS 12350-3, 2009a) rather than the typical slump test to characterise fresh SFRC. British Standard BS EN 14845-1 (2007a) also suggests other methods than the slump test, such as the Vebe test (BS EN 12350-3, 2009a) and the degree of compactability (BS EN 12350-4, 2009b). Even though the slump test is not recommended for SFRC, it is often used in practical procedures due to tradition. Figure 16 shows the effect of the fibre reinforcement index[4] on the slump. It can be seen that the slump reduces drastically as the fibre reinforcement index increases.

[4] Fibre reinforcement index is a measure of the combined influence of the fibre aspect ratio (l/d) and the fibre content, the latter usually in terms of percentage by mass but can also be in terms of percentage by volume.

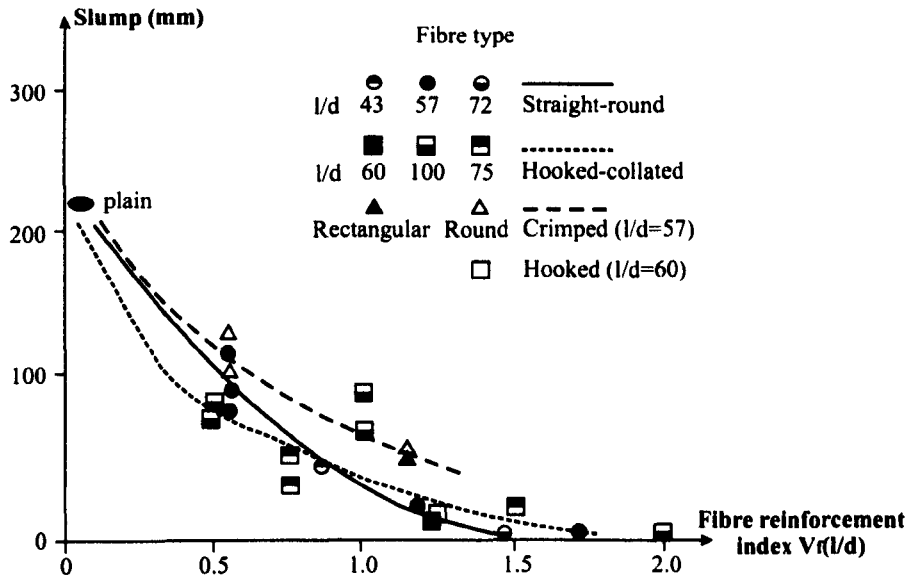

Figure 16 – Influence of fibre reinforcement index on slump [after Bayasi and Soroushian, 1992].

SFRC, as any conventional concrete, must be workable enough to allow it to be placed by mechanical vibrating methods and in general should be free from bleeding and segregation.

Steel fibre reinforced self compacting concrete (SFRSCC) is also used for construction purposes, especially for thin precast elements (Corinaldesi and Moriconi, 2004). In this case, no vibration is required during casting and the concrete is compacted by its own weight. The workability for SFSCC is usually measured by the slump flow test, which can be done using British Standard BS prEN 12350-8 (2007b). According to Torrijos *et al.* (2010), the fibres in SFSCC are prone to be aligned parallel to the flow direction of concrete. This may alter the mechanical properties of concrete depending on the direction of the applied stresses.

2.3.1.2 *Balling* of fibres

Fibres can interlock among themselves creating *balling* in the concrete which cannot be separated by conventional vibration (Figure 17). Among the factors related in the previous section responsible for balling in concrete (fibre content, aspect ratio, aggregate size and volume), the overall gradation of the aggregate, the fibre shape and the procedure of adding the fibres into the mix can also contribute to balling (ACI, 1996). The ACI Report 544.3R (2008) states that fibre balling is mainly caused by the fast way that they are added to the mix, which does not allow the fibres to get mixed well with the matrix. This has been found not to be true since for a certain mix there is always going to be a volume of fibres higher than a certain limit that will cause *balling* (Tlemat *et al.*, 2004a), even if the fibres are slowly added to the mix.

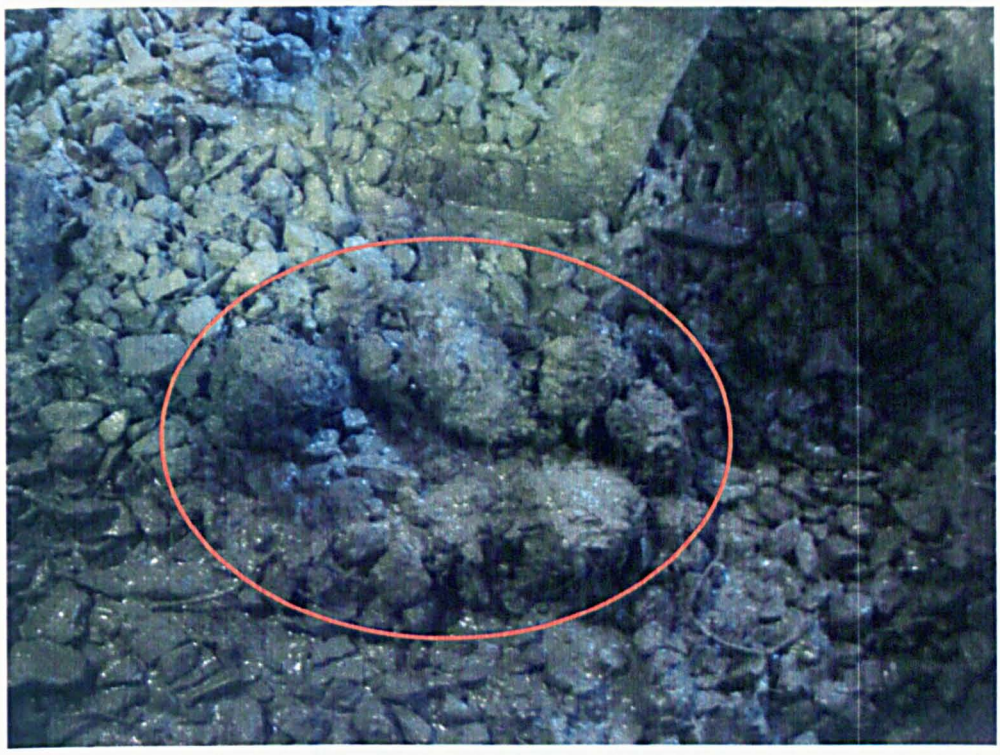

Figure 17 – Fibre balling.

When recycled fibres are added to concrete, the shape of the fibres seems to be another factor influencing the formation of *balling*. Because they are irregular in shape, they tend to interlock more easily, even before added to the mix. As a result, the length of recycled fibres needs to be limited to avoid/reduce the formation of *balls* (see Section 2.2.3.3). During packaging and transportation the fibres are compressed to occupy smaller volume, which also contributes for the fibres to interlock. Because of the shape, packaging and transportation, the method of dispersion of the fibres into concrete is important to avoid the formation of *balling*, especially by pre-separating the fibres before adding them to the mix.

2.3.1.3 Distribution of fibres

Two main factors must be taken into account when considering the fibre distribution inside concrete: 1) the shape and type of the fibres and 2) the orientation in the cementitious matrix (Bentur and Mindess, 2007). The orientation of fibres into the cementitious matrix can be in one (1D), two (2D) or three (3D) dimensions, as shown in Figure 18. Steel fibres are usually oriented in 2D or 3D.

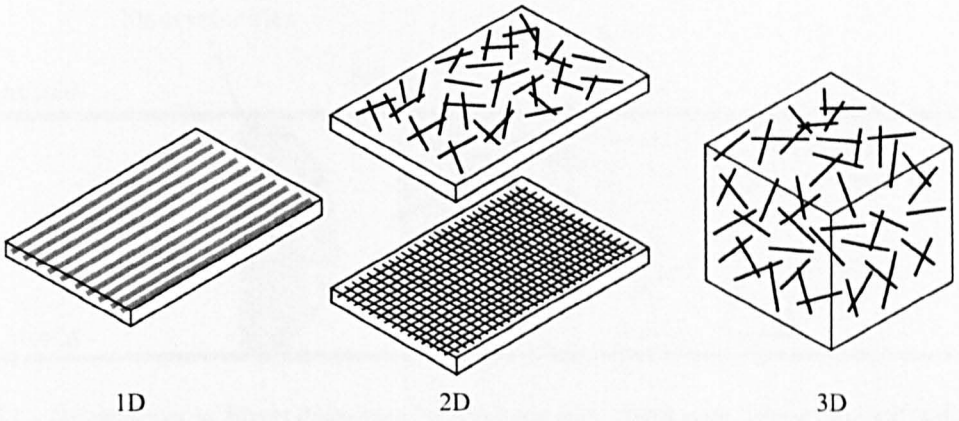

Figure 18 – Fibre arrangements in one, two or three dimensions.

The orientation of fibres depends on the pouring and vibration procedures, the specimen geometry and the mixing conditions. As a result, fibres are not usually randomly and ideally distributed in 3D. According to Bentur and Mindess (2007), when the length of fibres is considerably high compared to the thickness of the element (e.g. thin panels or thin cast overlays), the fibres tend to assume a 2D orientation. Soroushian and Lee (1990a) say that for the same reason the fibres located near two boundaries closely spaced are oriented in-between a 3D and 2D situation (Figure 19a). Soroushian and Lee (1990b) say that a 2D orientation can also be achieved due to excessive vibration of concrete during compaction, which tends to orientate fibres in horizontal planes. In situations when four boundaries are closely spaced (e.g. cubes), the 3D configuration is also restricted and the fibres near the boundaries tend to assume a configuration in-between 3D and 1D (Figure 19b).

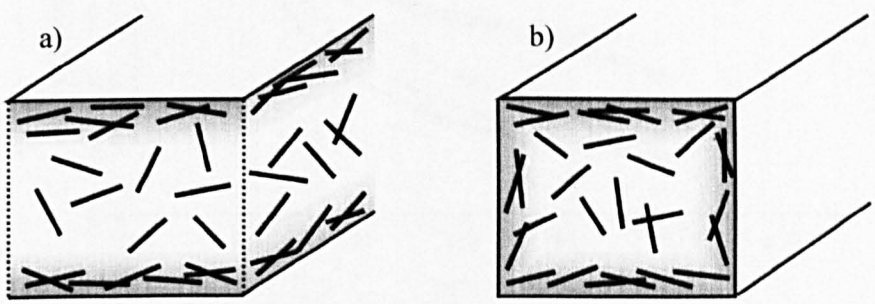

Figure 19 – Orientation of steel fibres into concrete due to a) two parallel and b) four boundaries conditions closely spaced [after Soroushian and Lee, 1990b].

Boulekbache *et al.* (2010) explain that, in the cases where boundary conditions (e.g. mould walls) exist, the fibres tend to align parallel to the walls because the velocity of the flow close to them is almost null and increases as the distance from the boundary condition increases (Figure 20).

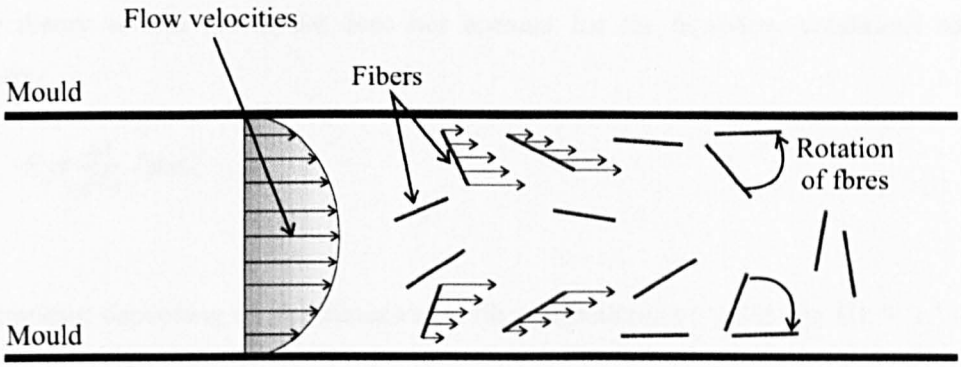

Figure 20 – Orientation of fibres disturbed by the boundary conditions [after Boulekbache *et al.*, 2010].

The orientation of fibres due to various boundaries conditions was calculated by Soroushian and Lee (1990b) as a function of the ratio of the specimen width to the fibre length, as shown in Figure 21. When the orientation factor is close to *one*, it means than the fibres are randomly and ideally distributed in 3D inside concrete, whereas an orientation factor close to *zero* means that the fibres tend to be aligned in one single direction.

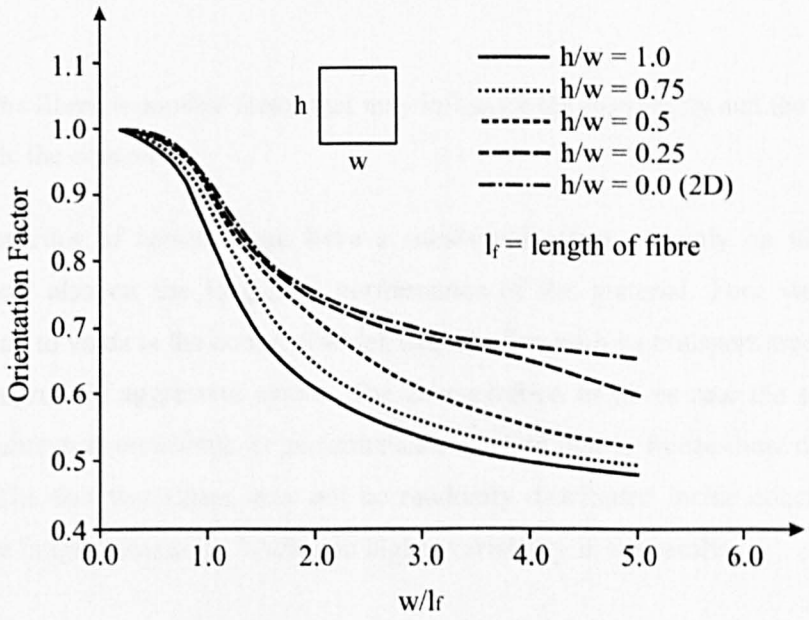

Figure 21 – 2D and 3D orientation factors for various specimen geometries [after Soroushian and Lee, 1990b].

According to Krenchel (1975), the distance between the fibres, called *fibre spacing*, can influence the mechanical properties of the composite material. An expression to calculate the fibre spacing was first proposed by Romualdi and Mandel (1968), and later improved by Krenchel (1975), as shown in Equation 1. The calculations were based on statistical analysis considering the sum of the cross-sectional areas and the volume concentration. The equation is valid for fibres in cylindrical cross sectional areas. However, the main limitation of the *fibre*

spacing theory is that the model does not account for the boundary conditions explained previously.

$$S = \frac{kd}{\sqrt{V_f}} \text{ [mm]} \quad (1)$$

Where:

k = constant depending on the dimensional fibre orientation (= 0.885 for 1D, = 1.11 for 2D and = 1.25 for 3D)

d = fibre diameter [mm]

V_f = volume content of fibres [%]

According to Boulekbache *et al.* (2010), the boundary conditions and the flowability of concrete (related to rheology of concrete – yield stress[5]) are the factors that mostly affect the orientation of fibres inside concrete. The lower the yield stress, the higher mobility and better dispersion of the fibres. The same authors verified through experiments that, in a free surface flow (not affected by boundary conditions), the fibres tend to orient perpendicular to the direction of the flow.

The shape of the fibres is another factor that may influence the flowability and the orientation of the fibres inside the concrete.

The fresh properties of concrete can have a substantial effect not only on the mechanical performance but also on the long-term performance of the material. Poor workability and balling may lead to voids in the concrete which can interfere with its transport mechanisms, thus allowing the ingress of aggressive agents. The concentration of fibres near the surfaces of the concrete elements may contribute to performance reduction due to freeze-thaw or corrosion of those fibres. The fact that fibres may not be randomly distributed inside concrete may also interfere on the fatigue resistance, leading to higher variability in the results.

2.3.2 Properties of Hardened SFRC

The properties of the hardened SFRC of interest to structural engineering relate to the mechanical behaviour of the material. According to Bentur and Mindess (2007), the mechanical properties of SFRC are influenced by various factors, such as the fibre characteristics (type,

[5] Yield stress is the minimum stress that needs to be overcome for the concrete to move. It is usually obtained through a quantitative fundamental test (Tattersall's two point test at which the concrete is sheared at different rates) which also allows the determination of the viscosity of concrete (Lynsdale, 2008).

geometry, aspect ratio, content and distribution), the concrete (strength and nominal maximum size of aggregate – NMSA[6]) and specimen characteristics (size, geometry, loading rate and casting method). The influence of fibres on the compressive, tensile, flexural, shear and impact resistance is presented below.

2.3.2.1 Compressive behaviour

ACI (1988) and Neves and Almeida (2005) stated that the compressive strength due to fibre addition is variable and can go up and down. Hannant (1978) says that the inclusion of steel fibres in concrete can improve compressive strength by up to 25%. Other authors found that the compressive strength of SFRC decreased compared to plain concrete (Boulekbache *et al.*, 2010; Altun *et al.*, 2007; Lee and Barr, 2003). However, it is accepted that fibres keep the integrity of concrete, by controlling crack propagation, even after failure and improve the ductility after first crack (see Figure 22).

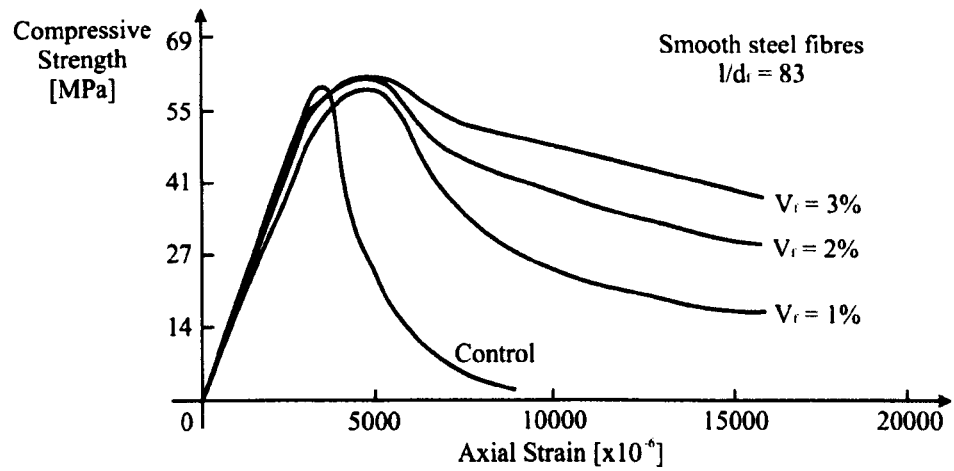

Figure 22 – Influence of fibre addition in the compressive behaviour of SFRC [after Fanella and Naaman, 1985].

When fibres are added to concrete, the two main factors affecting the compressive strength of concrete are the matrix and the fibre characteristics (Neves and Almeida, 2005 and Yazici *et al.*, 2007).

Plain concrete has usually small flaws (micro-cracks due to shrinkage and settlement of fresh concrete) that increase in size when load is applied to the material (Williamson, 1974; Rossi *et al.* 1987). The small flaws propagate through macro-cracks, which tend to connect to other growing flaws perpendicular to the principal tensile stresses, and reduce the compressive

[6] The NMSA is the sieve used for gradation at which the accumulated retained percentage of material is ≤ 5%.

strength and eventually lead to failure of the concrete. Fibres distributed inside concrete tend to block the flaw growth due to the interfacial bond between the fibres and the matrix, thus delaying or preventing the propagation towards macrocracks and enhancing the compressive strength. When macrocracks are formed, the fibres tend to bridge the gaps and increase the material ductility.

Shah and Rangan (1971) say that the aspect ratio, the bond strength and the orientation of fibres are the most significant factors restricting crack propagation. Banthia and Sappakittipakorn (2007) say that the use of fibres with different geometry (or different constitutive response) may improve the performance of SFRC because micro-fibres (or stiffer fibres) are more efficient in restricting the propagation of micro-cracks thus improving strength, whereas the macro-fibres (or more flexible fibres) are more efficient in bridging and limiting the propagation of macro-cracks thus improving toughness.

Adding fibres in concrete to improve the compressive strength is beneficial up to a certain amount. Balling causes strength reduction because the fibre balls are not impregnated well with cementitious materials, thus acting as large voids in the concrete. During mixing, the fibre balls can also restrict the dispersion of fibres (Boulekbache *et al.*, 2010). The boundary conditions in concrete specimens and the casting direction may also affect the SFRC strength (Mansur *et al.*, 1999). The boundary conditions prevent the fibres from being randomly distributed inside concrete, especially when large volumes of fibres are used (Soroushian and Lee, 1990b). Finally, the reduced workability caused by higher fibre contents may entrap more air during compaction than in good workable mixes (Bayasi and Soroushian, 1992). The compressive behaviour of SFRC would be expected to increase as the amount of fibres increases, as shown qualitatively in curve a in Figure 23. However, due to the factors just mentioned, the compressive strength of concrete can go down as shown qualitatively in curve b in Figure 23.

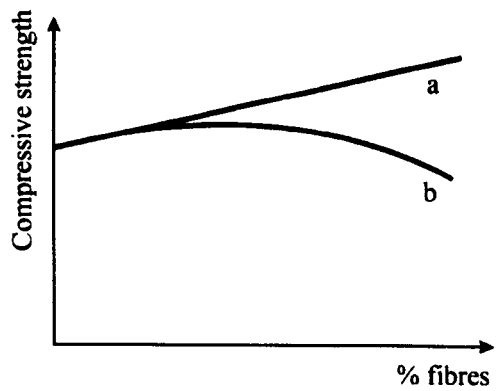

Figure 23 – Qualitative analysis of the effect of adding fibre to concrete: a – ideal; b – accounting for fibre distribution and other mixing issues.

Even though the addition of fibres into concrete can significantly alter the compressive behaviour of SFRC (especially in terms of ductility), the modulus of elasticity of SFRC is not considerably affected (Neves and Almeida, 2005; Mansur *et al.*, 1999; Rossi and Harrouche, 1990; Chern and Young, 1989; Williamson, 1974; Fanella and Naaman, 1983). According to Hannant (1978), the modulus of elasticity E_c of an ideal composite material can be calculated from Equation 2.

$$E_c = E_f V_f + E_m(1 - V_f) \text{ [MPa]} \quad (2)$$

Where:

E_f = modulus of elasticity of the fibre [MPa]

V_f = volume content of fibres [%]

E_m = modulus of elasticity of the concrete [MPa]

The equation above is based on the *rule of mixtures*, which states that the properties of a composite are based on the weighted average of the properties of its individual components (Bentur and Mindess, 2007). The equation is only valid if the behaviour of both components is linear, elastic and they are fully bonded. For this reason, the rule of mixtures is only valid in the pre-cracked and elastic zone of SFRC.

The modulus of elasticity of SFRC is usually experimentally obtained by compressive or flexural strength tests. The equation used to calculate the flexural modulus of elasticity is further shown in Section 4.4.2.3.

2.3.2.2 Tensile behaviour

The increase of the tensile strength of SFRC for fibre volumes up to 3% can be as high as 30%, while the strain increase is normally around 50% (Hannant, 1978). Soroushian and Bayasi (1987) say that the tensile strength of SFRC is dependent on the fibre type and aspect ratio. The tensile strength is also influenced by the volume of fibres (see Figure 24) and the concrete strength (Mangat, 1976 and Soroushian and Bayasi, 1987).

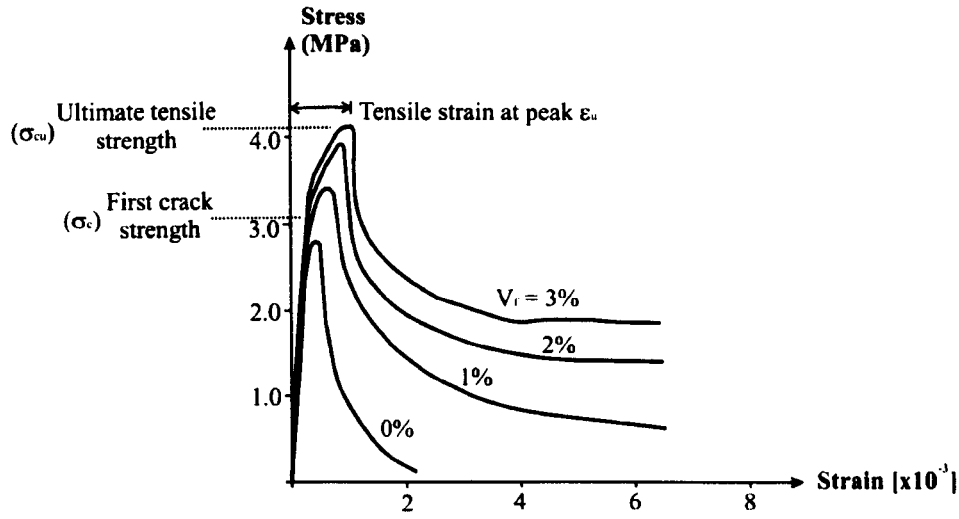

Figure 24 – Influence of fibre addition in the tensile behaviour of SFRC [after Soroushian and Bayasi, 1987].

The tensile behaviour of concrete is directly dependent on the number of fibres crossing the cracking zone (Pilakoutas, 2008 and Shah and Rangan, 1971). A commonly used expression to calculate the number of fibres per unit area N_l of the cracked section is given by the following equation (Sorushian and Lee, 1990a and 1990b; Naaman *et al.*, 1973; Swamy and Al-Ta'an, 1981):

$$N_1 = \alpha \frac{V_f}{A_f} \tag{3}$$

Where:

V_f = volume content of steel fibres in concrete [%]

A_f = cross sectional area of fibres (considering circular section)

α = orientation factor[7] (usually ranging from 0.41 to 0.82 – Soroushian and Lee, 1990b – see Section 2.3.1.3)

Direct tension tests are not commonly used due to problems observed in practice, which are usually associated with misalignment of the specimen and stress concentration on the grips, thus giving unstable response. Tensile splitting and flexural tests are used as an alternative to measure the indirect tensile strength of concrete.

The cracking behaviour in plain concrete was already mentioned in the previous Section 2.3.2.1. However, some aspects of the cracking behaviour relate particularly to SFRC in tension and,

[7] The orientation factor is the average ratio for all possible fibre orientations of the projected fibre length acting to resist the direct tensile strength (Soroushian and Lee, 1990b) – see Section 2.3.1.3.

according to Soroushian and Bayasi (1987), there are some assumptions that may explain this behaviour: 1) failure occurs by pull-out of fibers rather than fibre fracture; 2) the ultimate tensile strength of SFRC is obtained when fibres reach the peak pull-out strength (with no contribution from the matrix) and 3) both pull-out strength and matrix properties contribute to the tensile strength of SFRC. However, ACI (1988) considers that the tensile strength of SFRC is generally of the same order as that for plain concrete, meaning that fibres only contribute to ductility. Because the addition of fibres generally contributes to an increase of the tensile strength, it is reasonable to assume that both fibres and matrix interact together when load is applied. Mangat (1976) presented laboratory tests that demonstrated that failure usually occurs by fibre pull-out and matrix failure simultaneously.

Pull-out behaviour

Since pull-out of fibres appears to govern the tensile behaviour of SFRC, some aspects of pull-out behaviour of steel fibres are discussed further. According to Alwan *et al.* (1991), the ductility of SFRC is based on two mechanisms: material deformation and cracking. The material will deform only if the energy supplied is large enough to overcome the strength of the material. If this occurs, cracking is then initiated and the propagation of cracks depends on the amount of energy supplied and the material capacity to restrict their growth. Fibres contribute to these mechanisms and can improve energy absorption by either deforming or pulling-out, depending on their bond characteristics (Alwan *et al.*, 1991 and Mangat and Azari, 1984).

The resistance to pull-out is caused mainly by the interfacial bond shear strength and the anchored area of the fibre (Gray, 1984). However, the non-linear behaviour of the bond shear strength throughout the fibre length (Figure 25) suggests that more factors may affect the pull-out behaviour of fibres in concrete. According to Naaman *et al.* (1991), these factors could be the physical and chemical adhesion between the fibre and matrix, the mechanical component due to the shape (e.g. crimped, hooked, twincone) and the fact that fibres can interlock among themselves.

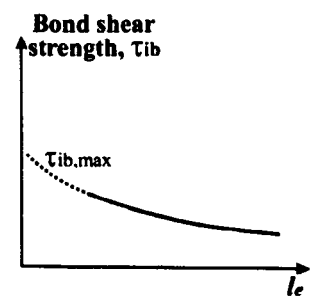

Figure 25 – Variation of shear bond strength with embedded length of fibre [after Gray, 1984].

A typical pull-out curve obtained from experiments with smooth fibres is shown in Figure 26. Bond and friction govern the pull-out behaviour. The first phase (I) is controlled only by the bond interaction between the fibre and the matrix, and both fibre and matrix deforms elastically together. The second phase (II) represents the fracture of concrete through the formation of cracks and the curve starts to descend when friction becomes more significant than bond. The third phase (III) is governed only by friction strength and continues until the fibre length embedded in concrete is pulled-out from the matrix.

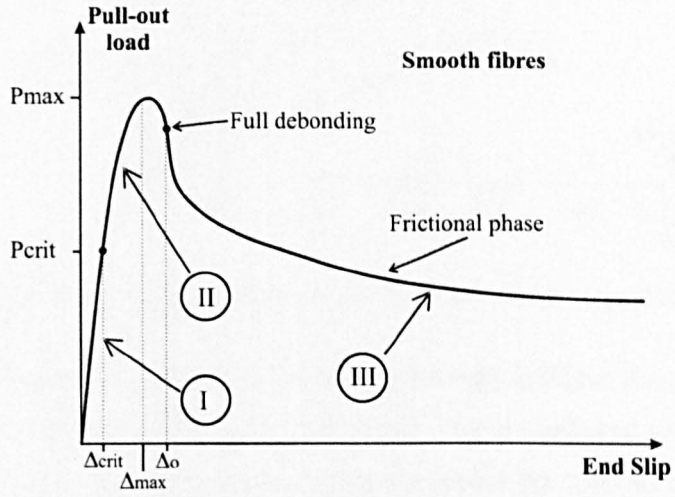

Figure 26 – Typical pull-out curve obtained from smooth fibres [after Naaman *et al.*, 1991].

2.3.2.3 Flexural behaviour

The flexural strength of SFRC is influenced by the fibre content, aspect ratio, bond strength and fibre orientation (Hannant, 1978). Bentur and Mendess (2007) add that the flexural behaviour of fibre reinforced cementitious materials is governed by the tensile strength of concrete (which relates to the fibre characteristics and content) and the post-cracking ductility.

The influence of bond on the flexural strength of SFRC, considering a certain fibre index, is shown in Figure 27. It can be seen that the flexural strength increases as the bond strength increases.

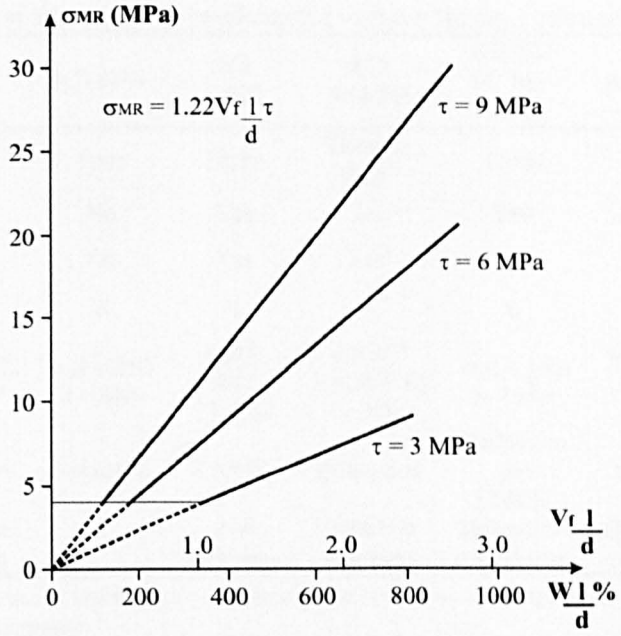

Figure 27 – Influence of bond strength on the flexural strength σ_{MR} [after Hannant, 1978].

ACI (1996) reports that the increase in the flexural strength is higher than the increase observed for compressive and direct tensile strength of SFRC. This is attributed to the ductility added by the fibres, which alters the stress-strain distribution along the specimen depth after cracking. After cracking, the neutral axis in SFRC moves towards the compressive zone, as shown in Figure 28. According to Hannant (1975), the neutral axis can be located from 0.2d to 0.25d from the compression surface, the latter being the most conservative assumption.

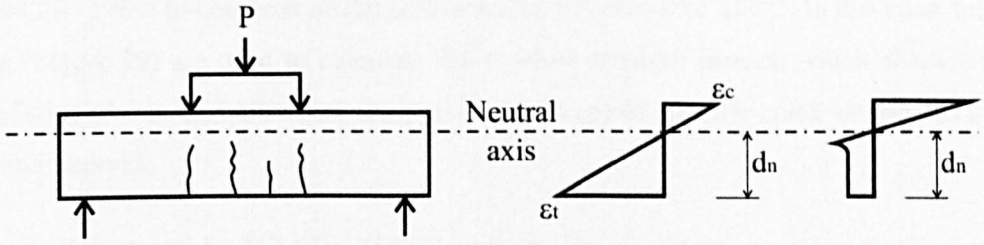

Figure 28 – Strain and stress distribution in flexure for SFRC.

Test methods for flexural strength in SFRC

Typical measurements for flexural behaviour include the load *versus* deflection or crack mouth opening displacement *CMOD* curves, which enable the quantification of the post-cracking behaviour of concrete, in terms of strain capacity and toughness. Several standards have different recommendations to perform flexural tests (ASTM C 1018, 1997; JCI SF-4, 1984; JCI S-002, 2003; ACI 544.2R, 1989; RILEM TC-162-TDF, 2002; BS EN 14651, 2005a and BS 14488-3, 2006b), and some of the specifications are summarised in Table 3.

Table 3 – Comparison among the procedures for various flexural strength tests of SFRC.

	ASTM C1018	JCI SF-4	JCI S-002	ACI 544.2R	RILEM TC 162-TDF	BS 14651	BS 14488-3
Three or four point test	Four	Four	Three	Three or four[d]	Three	Three	Four
Notch	No	No	Yes	No	Yes	Yes	No
Yoke	Yes[a]	Yes	Yes	Yes[a]	Yes	Yes	Yes
Number of specimens	3	6	4	3	6	6	No reference
Geometry of specimens [mm]	w,d = 100 l = 350[b]	w,d = 150 l = 600	w,d ≥ $4d_a$[c] l ≥ 3.5d	d ≥ $3f_l$[b] l ≥ 3d + 50 ≥ 350	w,d = 150 b = 550	w,d = 150 550 ≤ l ≤ 700	d = 75 w = 125 l ≥ 500[e]
Deflection or CMOD	Deflection	Deflection	CMOD	Deflection	Deflection and CMOD	CMOD[d]	Deflection
Limit of Proportionality	Based on equation		No reference	Based on equation	Deflection = 0.05 mm	Deflection = 0.05 mm	Deflection = 0.1 mm

[a] The method also allows the use of transducers positioned in the centreline of the specimen top surface (one at mid-span and another two on the supports)

[b] Preferred size. Also proposed: $d \geq 3f_l$; $l \geq 3d + 50 \geq 350$ where f_l is the fibre length

[c] d_a – aggregate diameter

[d] Preferred

[e] The method does not explain clearly the appropriate specimen size. Another size is also proposed: d = 150 mm; l ≥ 3.5d

All methods agree that toughness should be calculated considering the area under the load versus deflection or CMOD curve, however, the calculation to characterise the post-peak behaviour of SFRC varies. Toughness indices[8] are proposed by the ASTM C1018 (1997) and ACI 544.2R (1989) to characterise the post-cracking behaviour of SFRC. In this case, toughness indices (Figure 29) are used to calculate the residual strength factors, which characterise the level of strength retained after first crack as a percentage of the first-crack strength at a certain deflection interval.

The method proposed by JCI SF-4 (1984) explains the procedures to calculate the equivalent flexural strength up to a certain deflection interval (= 3 mm), as well as the equivalent flexural ratio based on the relation between the equivalent flexural strength and the flexural strength at the limit of proportionality. The Concrete Society method (2003) for industrial floors is based on the JCI-SF4 (1984) method to calculate the equivalent flexural ratio. The JCI S-002 method (2003) shows how to calculate the fracture energy of specimens by considering the area under the CMOD curve up to the rupture of specimen.

[8] According to ASTM (1997), toughness index is the number obtained by dividing the area up to a certain deflection by the area up the first crack.

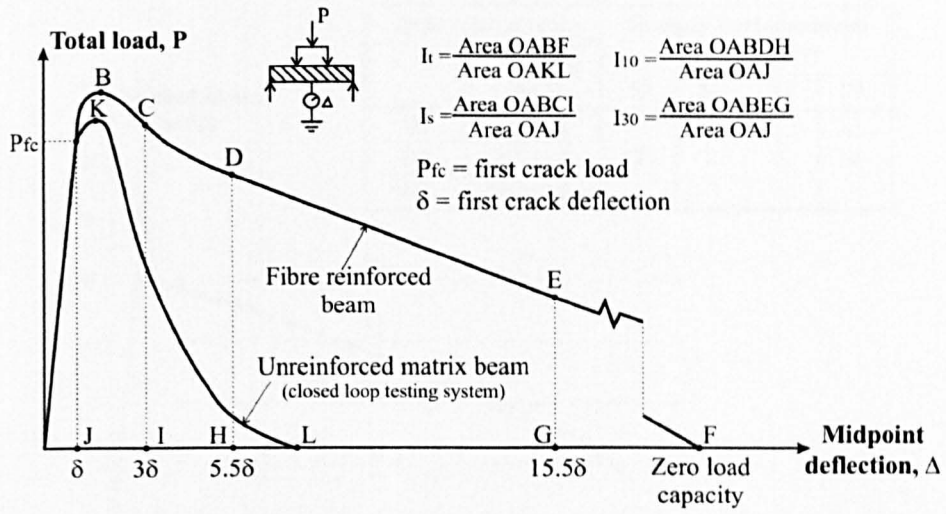

Figure 29 – Toughness indices for flexural load-deflection curve [after ASTM, 1997].

The RILEM method (2002) recommends the calculation of the equivalent flexural strength up to certain deflection intervals. Residual flexural strength can also be calculated assuming an elastic stress distribution for certain deflections or CMODs, as shown in Figure 30. BS EN 14651 (2005a) is based on the RILEM method (2002), however, there is no reference to the calculation of equivalent flexural strengths.

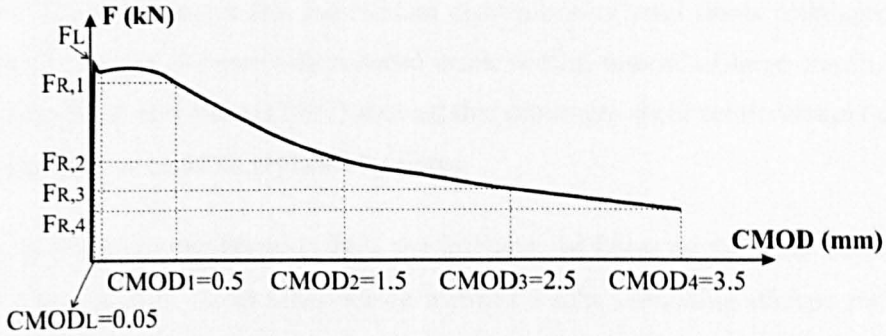

Figure 30 – Load-deflection or load-CMOD curve to calculate residual flexural strength [after RILEM, 2002].

BS 14488-3 method (2006b), recommended for sprayed concrete, shows how to calculate the residual flexural strengths based on the minimum load for a certain deflection interval. The residual strength classes (Figure 31) can be obtained following the procedures of BS 14487-1 (2005b), which refers to a certain strength level considering a certain deflection interval.

Information on flexural fatigue behaviour of SFRC can be found in Section 3.1.1.

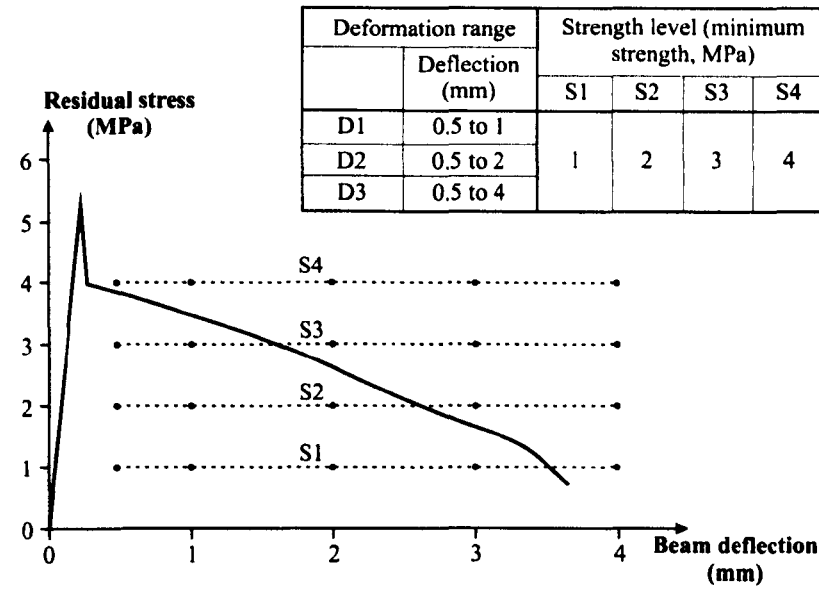

Deformation range		Strength level (minimum strength, MPa)			
	Deflection (mm)	S1	S2	S3	S4
D1	0.5 to 1	1	2	3	4
D2	0.5 to 2				
D3	0.5 to 4				

Figure 31 – Load-deflection curve to calculate residual strength classes [after BS, 2005b].

2.3.2.4 Shear

Steel fibres increase the shear and torsion capacity of SFRC. According to ACI (1996), the increase in pure shear capacity could be as high as 30% when 1% by volume of fibres is added to concrete. The report states that the random distribution of steel fibres collaborates to create small cracks along the element with reduced crack widths, instead of large cracks. Meda *et al.* (2005) and Furlan Jr and Hanai (1997) showed that minimum shear reinforcement of reinforced concrete (RC) beams could be replaced by fibres.

According to Furlan Jr and Hanai (1997), the influence of fibres on the shear behaviour can be attributed to two factors: direct influence on inclined cracks simulating stirrups and the indirect contribution on bridging cracks, which increase concrete strength and maintain its integrity.

Steel fibres can also be used in beam-column joints as an alternative to reduce the lateral reinforcement thus avoiding the large amount of steel bars in the joints. Due to the confining effect (caused by the restriction to crack propagation – due to the resistance against pull-out and anchorage to concrete), the fibres have sufficient strength and ductility to replace part of the conventional steel bars and also maintain the integrity of the concrete even when subjected to seismic loads (Bayasi and Gebman, 2002).

2.3.2.5 Impact resistance

Toughness is the most important property that regulates the impact resistance (Naaman and Gopalaratnam, 1983). According to ACI (1989), the impact resistance of SFRC can be

measured according to the test method used considering: 1) the energy consumed to crack a notched beam[9]; 2) the number of impact loads to achieve a certain level of deterioration[10]; 3) the size of the damage or the size and velocity of the spall after the specimen is struck with a projectile or after being subjected to surface blast loading.

Nataraja *et al.* (2005) reported that the post-cracking impact resistance of SFRC can increase by approximately 50% compared to plain concrete. SFRC also showed high resistance to the formation of the first crack. Ramakrishnan *et al.* (1981) says that SFRC is six times more resistant to impact than plain concrete. High strength FRC has also been reported to have four times more impact resistance than plain high strength concrete (Song *et al.*, 2005).

2.3.2.6 Other properties

Other properties of hardened concrete include abrasion, erosion and friction resistance, thermal conductivity, among others. Durability issues related to SFRC (especially regarding SFRC pavements) and the pore structure properties of SFRC are also important to characterise the behaviour of hardened SFRC, however, due to the relevance of the topics for this study, a specific chapter has been designated for them (Chapter 3).

Because SFRC is a good alternative for concrete pavement, which is the structure under analysis in this study, the next section explains the main types of concrete pavements and the most common design methods.

2.4 CONCRETE PAVEMENTS – TYPES AND DESIGN METHODS

Despite the high initial costs traditionally attributed to concrete pavements, in recent years their construction has become competitive compared to asphalt pavements. Life-cycle cost analysis has shown that concrete pavements are more economically attractive than asphalt due to less maintenance activities and longer service life (Thomas, 2006). Perlman (2010), however, states that the short-term analysis is also pointing to an advantage in concrete pavement prices, which is mainly attributed to the increasing price of asphalt in the past five years. In the United States, for instance, shortages of asphalt are expected to occur due to the focus on producing petrol instead of asphalt, which will keep asphalt prices increasing in the future. In addition, the volatile political environment in the Middle East is expected to increase further the cost of asphalt.

[9] Usually measured from the residual energy stored in the pendulum after impact – valid for the weighted pendulum Charpy-type impact test method.
[10] Valid for test methods that use repeated impact loads to cause damage.

Figures 32 and 33 show the paving costs for a standard one mile, two lanes road according to Portland Cement Association (PCA) estimation (Sullivan, 2009). Figure 32 shows that by 2015 savings could be around 44% for concrete pavements compared to asphalt pavements based on a life-cycle analysis (usually around 30 years). Figure 33 shows that from 2009 the economic benefits of concrete pavements are extended to the initial costs of construction, and by 2015 the savings of using concrete instead of asphalt could be as high as 41%.

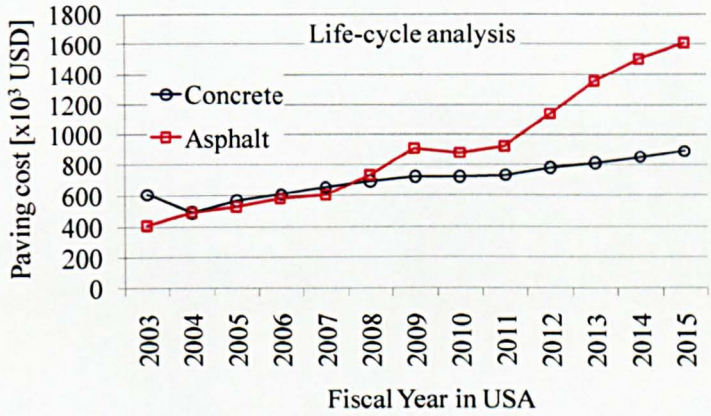

Figure 32 – Comparison of long-term cost between asphalt and concrete road [Sullivan, 2009].

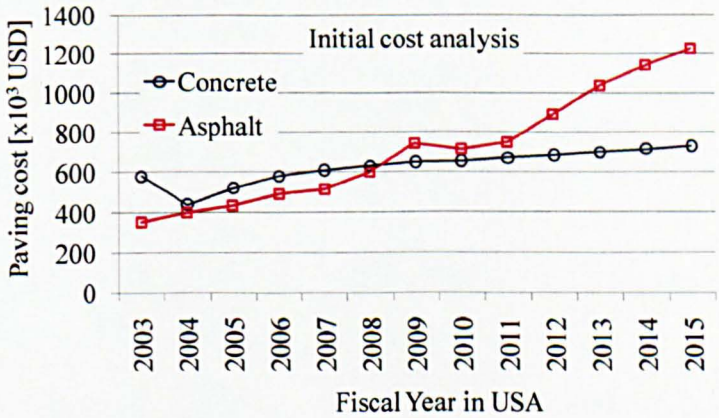

Figure 33 – Comparison of initial cost between asphalt and concrete road [Sullivan, 2009].

The economic advantages of concrete pavements come from their high durability. If well designed and constructed, major rehabilitation in concrete pavements should only be necessary in double the time usually required for asphalt pavement (Sullivan, 2009).

Concrete is less susceptible to changes in temperature thus avoiding common problems associated with asphalt pavements in heavy and concentrated traffic lanes such as cracks and rutting. Possible curling and warping of concrete slabs caused by temperature variations can be reduced/avoided if the pavement and the concrete is properly designed and constructed. Because they are rigid and stiff, concrete pavement slabs can also be placed over deformed subgrade areas. This is possible due to a more uniform distribution of stresses to the foundation. The

traffic loads are usually resisted by the concrete slab itself and the loads transferred to the base structure (when necessary) or subgrade are usually minimal (ACPA, 2010b). Figure 34 compares the load transfer system in asphalt and rigid pavement. Because of this, the overall performance of the pavement is not affected by small variations and irregularities in the sub-base.

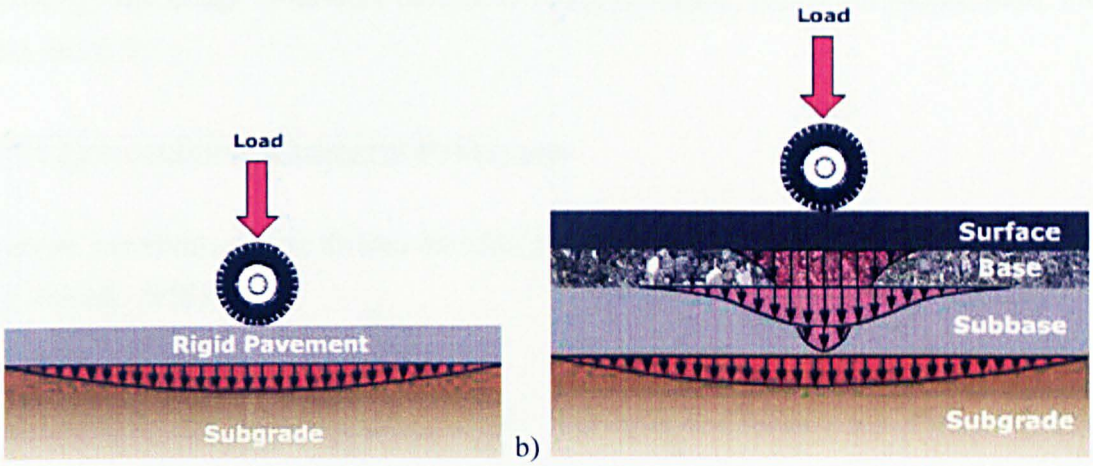

Figure 34 – Load transfer to subgrade in a) concrete and b) asphalt pavements [ACPA, 2010b].

According to Delatte (2008), besides the fact that concrete pavements are durable, the main environmental benefits of this technique are:

- Reduction in energy consumption for road construction;
- Base layers are not required thus the use of aggregates and other materials is reduced compared to asphalt pavement;
- Green house emission by vehicles in concrete pavements is lower because concrete slabs have less rolling resistance than asphalt;
- Concrete can be made with cement blended with pozzolanic materials and other industrial by-products;
- Less energy is required for lightning roads during night because concrete is more reflective than asphalt;
- Reduction in the *heat island* effect because concrete reflects light and is colder than asphalt. This may contribute to reducing the amount of ozone and smog in urban regions.

Some of the disadvantages of concrete compared to asphalt pavements are related to the speed of construction, especially for wet mixes, which require a certain time for curing thus delaying the opening of the road to traffic. The noise and the riding comfort due to roughness is worse

than in asphalt layers. In addition, repairs, when necessary, seem to be more laborious than in flexible pavements.

There are various types of concrete pavements, and they vary according to the design specification, construction technique and concrete technology. Improvements in concrete technology and design codes have brought in new possibilities such as prestressed slabs, FRC slabs and RCC.

2.4.1 Conventional Concrete Pavements

Concrete pavements can be divided into four groups, as explained below (PCA, 1984; Yoder and Witczak, 1975).

Plain Concrete Pavement (PCP)

This type of pavement does not have any type of reinforcement neither dowel or tie bars to connect the concrete plates. Load transfer between plates is made by the aggregate interlock below a saw joint, which is usually required to minimize the effects of shrinkage. Joints act by creating a weak region that concentrate the cracks derived from shrinkage, which allows the structure to resist thermal strains (Pitmann and Ragan, 1998).

Plain concrete pavements are only efficient for small concrete slabs usually not longer than 5 m. They are no longer used and recent works usually do not refer to them anymore (Delatte, 2008; Mallick; El-Korchi, 2009). The Highways Agency (2006) method for design of pavements allows the use of PCP subject to approval of the regulation authority.

Jointed Plain Concrete Pavement (JPCP)

JPCP have regular joints spaced approximately 4 m to 6 m between them. The contraction joints with dowel and tie bars are required to connect plates for load transfer and to avoid cracking due to shrinkage.

Because the flexural stresses are resisted by the concrete itself, slabs must be thick enough to resist to traffic loads. Figure 35 shows a schematic drawing of JPCP.

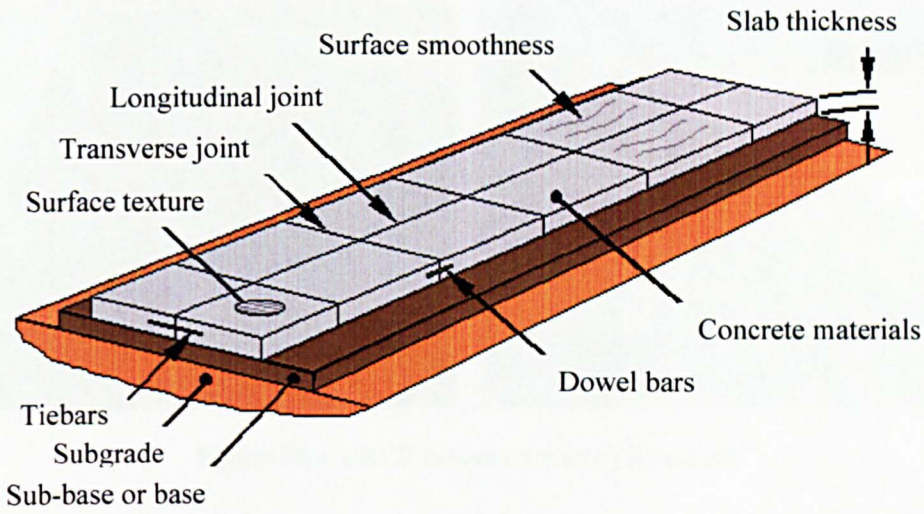

Figure 35 – JPCP [ACPA, 2011].

Jointed Reinforced Concrete Pavement (JRCP)

They are similar to JPCP. However, reinforcement is added near the joints to avoid transversal crack propagation. The main benefit is that joint spacing can be increased to approximately 12-15 m. As for PCP and JPCP, joints are necessary to minimise the effects of shrinkage.

Due to the combined need for joints and reinforcement, this technique becomes usually more laborious than other methods and for this reason is not commonly used. The Highways Agency method (2006) allows the use of this type of pavement only if approved by the regulatory member.

Continuously Reinforced Concrete Pavements (CRCP)

Construction joints are not required and shrinkage cracks are restrained by reinforcement. Concrete thickness is lower compared to the other techniques because the traffic loads are resisted by the steel reinforcement. CRCP is usually more expensive than other techniques and requires extra time and labour to place the reinforcement. However, it seems to be a good alternative for high and heavy traffic roadways because the reduced number of joints leads to less maintenance activities. Figure 36 shows a CRCP before concrete placement.

Figure 36 – CRCP before concrete placement.

2.4.2 RCC Pavements

Even though RCC has been used in different engineering structures as early as 1930s (ACI, 1995), it was still almost unknown in the 1970s and 1980s and only in the 1990s started gaining the confidence of engineers due to its long-term performance, especially for dams and pavement applications (Luhr, 2005). The higher production rate and the lower material cost, especially because of the low cement content, are among the main reasons for the large scale use of RCC. RCC differs from conventional concrete because of its dry consistency and the compaction method, which is performed by pavers with vibrating rollers.

RCC was initially considered as a low performance concrete due to problems reported in the first applications, which were mainly caused by the lack of knowledge about the material. However, after successful studies and practical reports, RCC has proved to have as good performance, or even better, than conventional concrete. The high compaction energy and the high quality component materials used to produce RCC may explain its good performance (Ribeiro and Almeida, 1999).

When RCC is used for pavements, it is layered by an asphalt paver equipped with a heavy duty dual tamping screed and compacted with rollers (see Figure 37 obtained from a RCC pavement trial of Aggregates Industries in London during the EcoLanes Project – Appendix A).

RCC pavements need to be overlaid by an asphalt layer due to the low friction coefficient between the pavement and the vehicle tyres, especially for high speed traffic.

Figure 37 – Trial of RCC in London in 2008.

According to Griffiths and Thom (2007), the typical ultimate compressive strength for in-situ cored specimens is around 40 MPa. PCA (2010a) reports that the compressive strength of RCC may vary from approximately 30 MPa to 70 MPa, while the flexural peak strength values range from 3.5 MPa to 7.0 MPa.

RCC pavements have no dowels or reinforcement, and no formwork is required for casting, contributing to the reduction in costs. Control joints are sawed and aggregate interlock is responsible for the load transfer. RCC can be used as base and sub-base for asphalt and concrete pavements.

2.4.2.1 RCC reinforced with steel fibres

Very few studies can be found in the literature focusing on RCC reinforced with steel fibres. According to Nanni and Johari (1989) and Nanni (1989), the addition of steel fibres in RCC is attractive due to the following:

- Due to practical problems, devices to transfer loads, such as dowels and ties, are usually not convenient for RCC. Fibres can improve the load transfer in sawed or natural joints and help with crack control. Steel fibres can also act as reinforcement, since conventional reinforcement is not viable in RCC.

- The dry consistency of RCC usually reduces the probability of *balling* due to lack of viscosity.
- Pavement thickness can be reduced. The low cement content of RCC avoids/limits curling and warping due to the low heat of hydration, which usually occurs in thin slabs.
- Fibres improve flexural strength and toughness.
- Fibres do not alter the placement and compaction of RCC.

Thom *et al.* (2000) developed an experimental programme to verify the benefits of steel fibres in RCC for road base applications, also called *lean* concrete. They found that fibres can improve the fatigue behaviour and the resistance to reflective cracking when an asphalt layer is required. They also confirm the previous hypothesis that load transfer capacity across cracks is improved by fibres.

Usually, the mechanical properties of conventional SFRC are comparable to steel fibre reinforced RCC.

The use of recycled steel fibres in RCC has only been tried for the first time during the Ecolanes Project (Appendix A).

2.4.2.2 Durability of RCC

RCC is known as a durable material. However, durability of RCC is usually attested by practice and only few studies can be found on the durability resistance of RCC. Sun *et al.* (1998) say that the fatigue performance of RCC can be 40% higher than that of conventional concrete.

Osipov *et al.* (1992) state that, when well designed, RCC can achieve high strength, low permeability and good frost resistance. On the contrary, Gao *et al.* (2006) and Kokubu *et al.* (1996) say that the concrete paste in RCC is less homogeneous and the low cement content produces voids in the concrete, which may reduce the durability and frost resistance of RCC. Gao *et al.* (2006) suggest the use of fly ash, superplasticiser and expansive agents to solve this problem. Fly ash usually refines the pore structure of concrete, making it denser and less permeable. Superplasticisers may contribute to a more uniform compaction of RCC thus reducing the formation of voids. Finally, expansive agents can compensate for shrinkage, thus avoiding/reducing the formation of drying cracks. According to Kokubu *et al.* (1996), a durable RCC should have less than 3% of porosity.

It is expected that the dry consistency of RCC, responsible for eliminating the bleeding of concrete, and the high energy used for compaction should drastically reduce the plastic shrinkage of this type of concrete. According to Pittman and Ragan (1998), drying shrinkage is also reduced because of the low water content and the high amount of aggregates in RCC.

2.4.3 Other Types of Concrete Pavements

Other types of concrete pavements include concrete overlays, SFRC, prestressed, precast and porous concrete.

Overlays are layers of concrete pavement cast above existing asphalt or concrete pavements. They can be used as a rehabilitation method for damaged structures. Concrete overlays are usually not bonded to the existing structure to prevent reflective cracking from the underneath pavement. The new structure acts independently and the damaged structure is normally used as a base.

SFRC can be used as an alternative to CRCP. However, to achieve the same performance as CRCP, a large amount of fibres is required, thus making it not cost-effective. Fibres are usually added in a limited amount as reinforcement to JPCP to increase the joint spacing in industrial floors applications (Griffiths and Thom, 2007).

Prestressed and precast concrete pavements are not commonly used (Yoder and Witczak, 1975; Delatte, 2008). Pavement thickness can be reduced due to compressive stresses caused by tendons. However, prestressed pavements require specific construction techniques to prestress the plates to avoid buckling, and the joints need to be accurately constructed. According to Yoder and Witczak (1975), this technique may be suitable for situations where there is lack of materials, since the reduced thickness of the pavement requires less use of natural resources.

Porous concrete allows water to percolate through the structure thus collaborating to reducing stormwater storage demand and to reduce runoff into urban waterway systems (Tyner *et al.*, 2009). Because porous concrete has low strength, it is mainly used for parking pavements and low traffic areas (Delatte, 2008).

2.4.4 Design methods for concrete pavements

Most design codes currently in use mainly focus on the design of conventional concrete pavements. This section presents some of the methods used for concrete pavement design, from the first analytical-empirical equations to modern computational methods.

2.4.4.1 Pioneer Method of Westergaard (1926)

The first empirical-theoretical model to calculate stresses in a pavement slab was proposed by Westergaard in 1926. Equations were based on the Plate Linear Theory of Kirchoff-Love (Love, 1888). This model introduced the concept of *modulus of subgrade reaction* which was represented by identical springs simulating the subgrade as a continuous and dense liquid (Figure 38). The deflections of the subgrade are considered to be proportional to the deflections of the slab. The theory assumed that no shear stresses existed between the plate and the subgrade. Only a single plate is considered, hence, load transfer between plates is not dealt with in the model. Westergaard equations are shown in Appendix B.

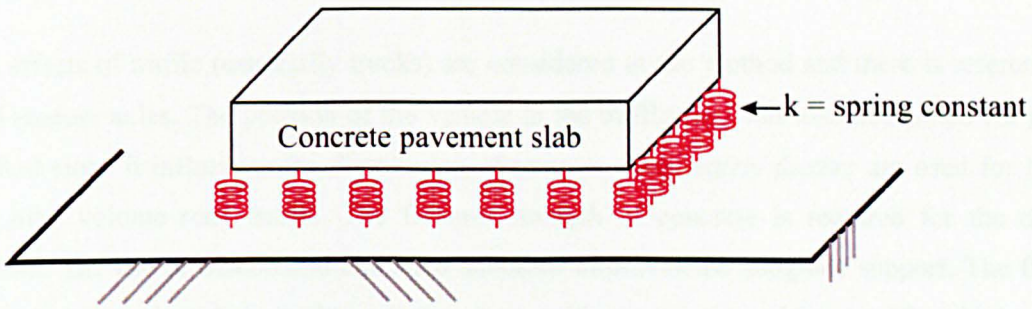

Figure 38 – Model to represent the subgrade reaction of concrete slabs [Pavement Interactive, 2007].

This early work has several limitations as summarised by Balbo (2003):

- The initial equations by Westergaard (1926) did not consider the temperature effect on the slabs. It should be noted that Westergaard (1927) improved the equations to include the warping and curling effect due to temperature change.
- A uniform slab thickness is assumed.
- The theory is valid only for uniform subgrade with a given stiffness.
- Does not account for dynamic loads.
- Only one point of load with a circular contact area can be considered.
- The model applies to large plates.

According to Wiggenraad (2007), even though the model applies to large plates and the majority of concrete pavements do not fit this criterion, many design guidelines are still based on Westergaard equations.

2.4.4.2 Influence Charts of Picket and Ray (1951)

The influence charts proposed by Picket and Ray (1951) follow the same principles of Westergaard (1926), however, any shape of contact area between the wheel and the plate and more than one load point are allowed.

2.4.4.3 PCA Method (1966)

PCA method (1966) is a standardisation of the previous methods of Westergaard (1926) and Picket and Ray (1951). It is based on model and full-scale tests, experimental pavements subjected to controlled test traffic and real pavements subjected to mixed traffic.

The effects of traffic (especially trucks) are considered in the method and there is reference to dual tandem axles. The position of the vehicle in the traffic lane was also accounted for in the method since it influences the distribution of stresses. *Load safety factors* are used for heavy and high volume road traffic. The flexural strength of concrete is required for the design method. The use of treated and untreated subbases improves the subgrade support. The failure criterion is based on fatigue, through the concept of *consumption of fatigue life,* which means the relation between the predicted number of cycles and the allowed number of cycles for a specific load. The design is based on a life-cycle of 40 years.

Some of the limitations of the method are: 1) it is only valid for unreinforced concrete pavements; 2) the load transfer devices and joint spacing are not accounted for; 3) the failure criterion is only based on fatigue; 4) truck traffic is considered up to dual tandem axle and 5) the environmental variables are not reported.

2.4.4.4 PCA Method (1984)

PCA method (1984) is considered as an empirical-mechanistic method, which is based on Westergaard (1926), Picket and Ray (1951) and full-scale experimental accelerated traffic data. The theoretical calculation of stresses is based on Finite Element Analysis.

Two design criteria are adopted: fatigue and erosion. Fatigue criterion follows the same principles as in the previous method (PCA, 1966). The erosion criterion limits the pavement deflections on the edges, joints and corners to control erosion of the foundation and shoulder materials.

The method considers the use of dowel bars to transfer loads between plates, the design of reinforced pavements and provides the tools to decide whether a lean concrete base is necessary.

Shoulders are also proposed to improve the road performance. Traffic is only accounted in terms of truck traffic and triple axles are used in the design. *Load safety factors* are adopted for high volume and heavy traffic roads. Some design charts and tables are shown in Appendix B.

The method normally assumes the pavement life-cycle to be around 20 years. However, it is stated that this may reduce if low quality materials are used, the construction is not properly executed or the traffic is higher than the one initially assumed. Life-cycle can be extended to more than 40 years if well designed and constructed.

Some of the main limitations of the method are: 1) the flexural strength of concrete may vary but it is limited to a maximum of 4.5 MPa; 2) truck traffic is considered up to a triple axle and 3) the environmental variables are not accounted.

2.4.4.5 American Association of State Highway and Transportation Officials (AASHTO) Guide (1993) and Supplement (AASHTO, 1998)

The AASHTO Guide (1993) is considered as one of the main and most complete pavement design for both rigid and flexible pavements, and is the basis for many modern methods of design (Griffiths and Thom, 2007). However, the method is essentially based on empirical design theories, obtained from experiments carried out in a two-year period by Accelerated Load Traffic (ALT) equipment performed by the now extinct American Association of State Highway Officials (AASHO). Twenty years of traffic were accelerated into two years by the ALT facilities.

The factors influencing the design of concrete pavements are: 1) the traffic calculated in ESALs[11]; 2) the reliability of the construction considering the type of road urban or rural; 3) the flexural strength and modulus of elasticity of concrete; 4) the drainage system of the road; 5) the load transfer system and 6) the modulus of subgrade reaction (or modulus of resilience of the soil). The life-cycle of the pavement is dependent on an initial and final serviceability index, related to smoothness and deterioration level of the road.

The main equation used for design of concrete pavements, according to AASHTO (1993) is shown in Appendix B.

The Supplement Guide (AASHTO, 1998) was based on the data from LTPP (Long Term Pavement Performance) programme and National Cooperative Highway Research Program (NCHRP) Project 1-30 (1995). The method uses the same input values as the previous method

[11] Equivalent Single Axle Load - converts the various vehicle axles (single, tandem and triple) to a standard axle of 80 kN.

(AASHTO, 1993) with the addition of joint spacing and some environmental effects. The latter is accounted by the mean annual wind speed, air temperature and precipitation.

2.4.4.6 NCHRP Guide (2002)

This method is based on an empirical-mechanistic analysis for the design of concrete pavements and comes as a replacement for the previous AASHTO Guide (1993) and Supplement (AASHTO, 1998). The guide was elaborated by the NCHRP Project 1-37A (2002).

The method uses Finite Element Analysis combined with Neural Networks to calculate the pavement strain and stresses subjected to traffic and environmental loads.

The failure criteria that govern the life-cycle of the pavement are: joints failure; transversal cracking and IRI (International Roughness Index) for the JPCP; and concrete spalling and IRI for the CRCP.

A cost life-cycle analysis is proposed by the guide. Several environmental conditions are necessary as input data for the design of concrete pavements, such as: air temperature, precipitation, wind speed, percentage of sunshine, relative humidity (RH) and depth of groundwater.

Due to the complexity of the guide, a software was released in September 2009 (MEPDG® version 1.1) for general use by engineers.

2.4.4.7 DNIT Rigid Pavement Manual (2005)

The National Department for Roads in Brazil (DNER from the Portuguese *Departamento Nacional de Estradas de Rodagem*) bases the JPCP design on the PCA methods (both 1966 and 1984 versions are accepted). The CRCP design is based on the Westergaard (1926) equations and Picket and Ray (1951) influence charts to calculate the stresses in the concrete plate. The structural design for CRCP is based on the Brazilian Standard NBR 6118 (ABNT, 2007b) for the design of concrete structures. CRCP is not widely used in Brazil.

The method includes the design of specific types of rigid pavements such as the ones used for asphalt pavement rehabilitation (called *whitetopping*), bridge decks and precast pavements.

The method also deals with the design of the drainage system.

2.4.4.8 Highways Agency Method (2006a)

The method proposed by the Highways Agency is an empirical method supported by TRRL (Transport and Road Research Laboratory) Report RR87 (1987) and the TRL (Transport Research Laboratory) Report 630 (2005).

The method prefers the use of CRCP or CRCB (continuously reinforced concrete base) with an asphalt overlay. JPCP and JRCP are also allowed subject to approval by the regulation authority.

Life-cycle is estimated to be 40 years for high and heavy traffic roads. Roads subjected to light traffic can be designed for a life-cycle of 20 years if allowed by the regulation authority.

Traffic is calculated based on ESALs. The existence of concrete shoulders is considered in the method. The compressive strength is the only concrete property influencing the design method (although the flexural strength should always be higher than 5.5 MPa). Four classes of foundation stiffness are considered.

The main chart and equations used to calculate the design thickness of concrete pavements are shown in Appendix B.

2.4.4.9 Technical Report TR34 (2003) on Industrial Floors

The Technical Report TR 34 (The Concrete Society, 2003) aiming at the design of slabs on grade. Even though it is not recommended for the design of highway concrete pavements, it is important to be mentioned here due to the fact that it includes the post-cracking behaviour of SFRC on the calculations, in terms of $R_{e,3}$. The method combines some of Westergaard (1926) principles with other works carried out from 1962 to 1986 on the yield line theory (refer to TR 34 for a full list of studies).

However, the main disadvantages of this method are that the effects of fatigue, environmental loads and other failure criteria usually applied for highway concrete pavements are not included in the design procedures. The method accounts for multiple point loads, however, it does not account for all truck categories as usually accounted in the design guidelines of concrete pavements. Hence, traffic data are not required for the design of concrete slabs.

The main equations used to calculate the concrete slab depth of industrial floors are presented in Appendix B.

2.4.4.10 Design of SFRC pavements based on existing methods

The large scale use of steel fibres as reinforcement for concrete pavements appears to have started in the 1970s (Nanni, 1989). Even though concrete pavements were amongst the first applications of SFRC, the existing design guidelines for rigid pavements are not appropriate for SFRC. Most of the existing design codes are based on empirical investigations and do not account for the post-cracking behaviour of SFRC.

Because there are no specific guidelines for the design of SFRC pavements, a comparison is made to analyse the compatibility of various methods when SFRC is used as a pavement material. The methods used in the comparison are the PCA method (1984), AASHTO Guide (1993), NCHRP Guide (2002), Highways Agency method (2006a) and TR 34 (The Concrete Society, 2003). The following input values are used for the calculation:

- Modulus of subgrade reaction = 80 MPa/m
- With concrete shoulder
- Design life-cycle = 50 years
- Jointed concrete pavement

Two typical road sections are used based on the traffic and environmental conditions of a major highway pavement located a) near Porto Alegre, Brazil (BR 290 Free-way) and b) near Sheffield, UK (M1). The traffic details in AADT (annual average daily traffic), refering to measurements taken in 2009, are shown in Table 4. The values of AADT shown below are for one direction only.

Some methods, such as the AASHTO (1993) and Highways Agency (2006a), requires the calculation of the number of million standard axles (msa) that will pass the road throughout the entire service life. The standard axle is equal to 80 kN for both methods. The various axle configurations are converted to the number of standard axles by using equivalent factors, which are proportional to the 4^{th} power of the ratio of the load of each axle by the standard axle load.

The total number of msa is calculated following the procedures of the Highways Agency (2006b) and the results are used for both AASHTO (1993) and Highways Agency (2006a). This is because the AASHTO (1993) procedure to calculate the number of msa requires information on the actual load of the axles, which are not provided. The Highways Agency (2006b) assumes equivalent factors (also called wear factor) depending on the vehicle class. The growth rate was assumed according to the Highways Agency (2006b) recommendation for the UK road and was assumed as 2% per year according to Concepa (2009). The total number of msa was equal to 176 for the Brazilian road and 314 msa for the UK road.

Table 4 – AADT of a major highway road in the south of Brazil and near Sheffield, UK.

Brazil (Concepa, 2009)			UK (Department for Transport, 2009)		
Type of vehicle[1]	Number of axles	Number of vehicles	Type of vehicle[2]	Number of axles	Number of vehicles
C4	3	631	PSV	2	346
C5	2	0	HGVR2	2	2165
C6	3	717	HGVR3	3	293
C7	4	67	HGVR4	4	268
C8	3	67	HGVA3	3	213
C9	5	216	HGVA5	5	1602
C10	6	150	HGVA6	6	874
C11	5	216			
C12	6	150			
C13	7	106			
Total		2320	Total		5761

[1] Classification according to NCHRP Guide (2002)
[2] Classification according to Highways Agency (2006b)

Other assumed input parameters for the AASHTO (1993) Guide were: 1) for the UK section – overall standard deviation, S_o= 0.34; normal standard deviation, Z_R = -1.037 (reliability of 85%); initial serviceability index, p_o = 4.5; final serviceability index, p_t = 3.0; drainage coefficient, C_d = 1.0; load transfer coefficient, J = 3.2 and 2) for the Brazilian section – S_o= 0.38, Z_R = -1.037, p_o = 4.5, p_t = 2.5, C_d = 1.0 and J = 3.2.

Since no information on the actual axle loads is provided, the simplified procedure of the PCA (1984) method was used.

The NCHRP Guide (2002) requires climatic information of where the road is located. Since the database of the MEPDG® software only includes regions in the U. S., a region with similar climate as Porto Alegre and Sheffield were chosen, such as Orlando, FL for Porto Alegre and Seattle, WA for Sheffield. The default limits of performance were used (IRI = 2.72 mm/m, transversal cracking = 15% and mean joint faulting = 3 mm).

The $R_{e,3}$ value assumed for the TR 34 (The Concrete Society, 2003) was 0.4 and the contact area of tyres was assumed as a rectangule of 200 mm by 200 mm.

The design thickness of JSFRCP (jointed steel fibre reinforced concrete pavement) calculated for the various methods is compared with the thickness of the JPCP. The assumed mechanical properties of both plain and SFRC used in the analysis are shown in Table 5.

Table 5 – Properties of plain and SFRC.

Material	Flexural strength [MPa]	Compressive strength [MPa]	Modulus of elasticity [GPa]
Plain concrete	4.5	55	30
SFRC	6.5	55	30

The calculated thickness of the JPCP, for both roads, is shown in Figure 39. It appears that the PCA (1984) method no longer meets the requirements for JPCP, since the thickness was much lower compared to the newer methods. The AASHTO (1993) gives the highest values of thickness, which are far higher than the thickness proposed by its updated version, the NCHRP Guide (2002). This is an indication that the safety factors used in AASHTO (1993) are considerably high. The Highways Agency (2006a) method, even though it is an empirical method, gives similar results as for the NCHRP (2002).

It can be seen in the graph below that the environmental loads influence the results of the NCHRP (2002) method since the thickness of the Brazilian road is higher than the UK road, which has much more traffic. This is because the high temperatures of the Brazilian region influence the formation of thermal stresses, such as shrinkage, which may lead to failure due to excessive cracking.

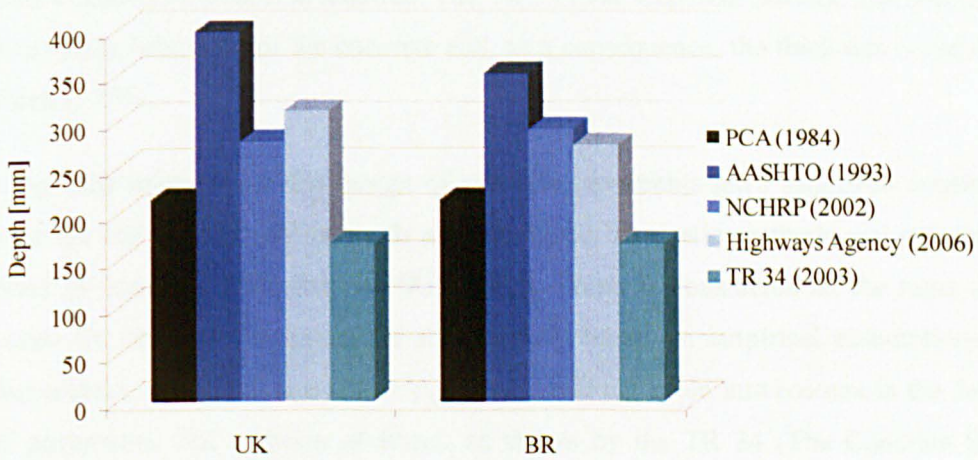

Figure 39 – Depth of JPCP for various design guidelines.

It can be also seen in the above graph that the TR 34 (2003) gives the lowest depth, possibly because it does not take into account fatigue and other failure criteria for concrete pavements.

The thickness of the JPCP obtained from the above graph was compared with the thickness of the JSFRCP, as shown in Figure 40.

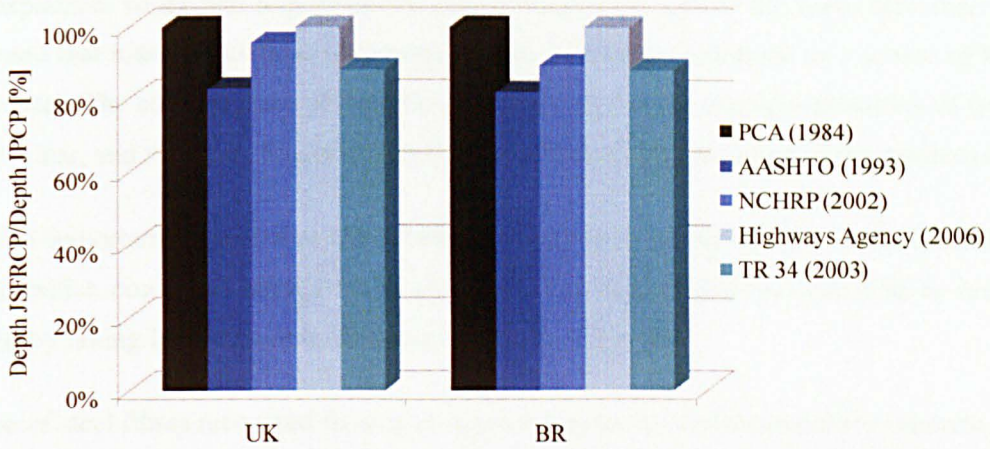

Figure 40 – Comparison of JSFRCP and JPCP based on the various codes.

PCA (1984) and Highways Agency (2006a) show exactly the same thickness when SFRC is used instead of plain concrete. This is because the PCA (1984) does not account for concrete with flexural strength higher than 4.5 MPa and also because the Highways Agency (2006a) only takes into account the compressive strength of the concrete for the design, which is not clearly influenced by the addition of fibres.

The AASHTO (1993) and the NCHRP (2002) consider any value of flexural strength, and they also take into account the modulus of elasticity of the material. However, no input information on the post-cracking behaviour is required. The TR 34 (The Concrete Society, 2003) consideres the post-cracking behaviour of the concrete and, as a consequence, the thickness is reduced by approximately 15%.

Even though the methods for the design of concrete pavements have improved considerably throughout the last century, the methods are still based on elastic methods and standard mix proportions of concrete. Even the NCHRP (2002), which is considered as the most modern design code for concrete pavements, is still partially based on empirical assumptions. As a result, the advance in the concrete technology area is still not taken into account in the design of concrete pavements. The addition of fibres, as shown by the TR 34 (The Concrete Society, 2003), could reduce the total depth of the concrete pavement and contribute, together with the use of recycled materials, to a more sustainable solution for concrete pavements.

2.5 SUMMARY AND CONCLUSIONS

This chapter dealt with a literature review of the main topics related with the subject of this research. Initially, the main issues on the disposal of post-consumer tyres were explained, focusing on the environmental benefits of recycling. Some regulations on the disposal of tyres

were explained, which aim to prevent the landfill disposal of end of life tyres. However, it was also noted that many regulations encourage the use of rubber from tyres as a source of heating for furnaces. The consequences of the release of toxic substances during combustion of tyres are still not clear, and they may be associated to health-diseases and pollution of the environment.

It is also important to note that the rubber from the post-consumer tyres is a manufactured product which consumed energy to be produced. The best alternative would be to reuse the material by taking into account its characteristics and properties.

The use of steel fibres recovered from post-consumer tyres as reinforcement for concrete agrees with the fact that, as for the rubber, the steel from tyres is a high quality manufactured product. Therefore, it should be reused by considering its original properties. This way, the energy consumed during manufacturing of the original product is not completely wasted.

The various types of fibre reinforced concrete and fibre types were discussed, focusing on the properties and geometric characteristics of the most commonly used steel fibres. The properties of the recycled fibres were also introduced, as well as the procedures to obtain the fibres from the post-consumer tyres. The recycled fibres are most commonly obtained from a shredding process, which requires lower amount of energy and is the most cost-effective compared to the other techniques.

The mechanical properties of SFRC were also discussed in terms of compressive, tensile and flexural strength. The main benefit of adding fibres in the concrete is the enhancement of the post-cracking behaviour of the material, by allowing a more ductile behaviour. The concrete is able to sustain loads even after reaching the peak load. The flexural behaviour gives the most important indication on the performance of the concrete, especially when dealing with concrete pavements.

Finally, the types of concrete pavements and their design codes were discussed. JPCP and CRCP are the most commonly used concrete pavements. However, other alternatives, such as the use of SFRC and RCC should also be considered due to their good performance.

The design guidelines for concrete pavements improved considerably during the last century, but even the most recent updated code is still partially based on empirical methods. The empirical methods are usually necessary due to the high variability of traffic and loads. An important limitation of the various design codes is that they do not account for the post-cracking behaviour of the material. As previously concluded, the enhanced post-cracking behaviour is the main benefit from adding fibres to the concrete, which is still not accounted in the concrete pavement design guidelines. The Technical Report TR 34 (The Concret Society, 2003) accounts

for the post-cracking behaviour of SFRC for slabs on grade, however, it does not account for fatigue and other failure criteria that are typical of highway concrete pavements.

Besides the issues examined in this chapter, it is also important to understand the durability aspects of SFRC, especially in terms of the most common deterioration processes usually found in pavement applications and the pore structure of the material. Some of these aspects are explained in more detail in the following chapter.

CHAPTER 3

3. DURABILITY ISSUES AND PORE STRUCTURE OF SFRC

This chapter first deals with the main durability issues that may influence the long-term performance of recycled SFRC used for pavements. The pore structure of SFRC is also described in terms of transport mechanisms and other pore-related properties.

3.1 DURABILITY ISSUES OF SFRC FOR PAVEMENTS

Durability of conventional RC has been widely studied and, as a consequence, it has already been incorporated in most design codes for RC structures. However, only few studies have been carried out to understand the durability of SFRC, especially for pavement applications.

According to Bentur (2003), several different aspects of behaviour of fibrous cementitious materials can affect their long-term performance. The main behavioural trends are shown in Figure 41. The long-term behaviour of each composite material depends mainly on the nature and geometry of the fibres, the properties of the concrete and the interfacial zone between the fibre and concrete.

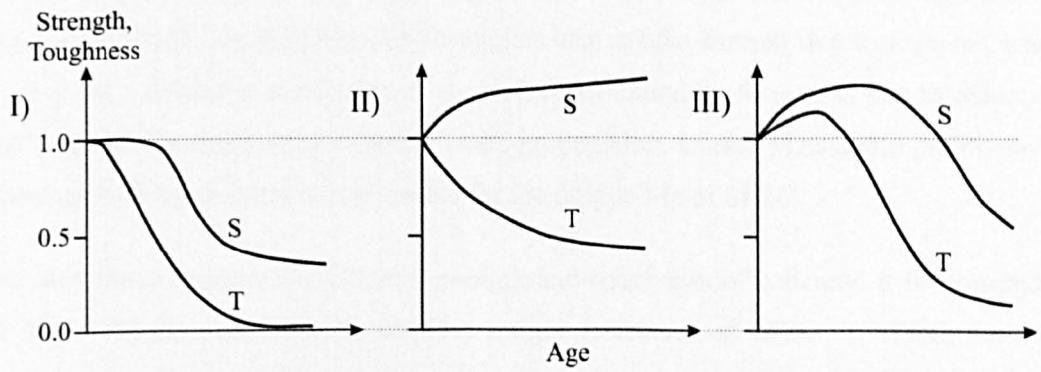

Figure 41 – Possible long-term behaviour of FRC in terms of strength *S* and toughness *T* over time [Bentur, 2003].

Several processes influence the long-term performance of FRC: fibre degradation, fibre-concrete interfacial (physical and chemical) interaction, volume instability and cracking

(Bentur, 2003). In SFRC, fibre degradation is caused by external aggressive agents that penetrate into concrete, such as chlorides and carbon dioxide, to cause corrosion. The fibre-concrete interaction in SFRC can be affected by fatigue and corrosion. Volume changes (which can be caused by temperature and humidity – e.g. freeze-thaw) can cause cracking of SFRC, which may alter the mechanical performance and allow the easy ingress of aggressive agents.

Each deteriorative process may result in different behaviour of the material. It is expected, however, that the combined effects of corrosion, freeze-thaw and fatigue damage, as well as the effect of ageing and continued hydration of cement, would present a long-term behaviour closer to type III, shown in Figure 41.

In order to understand the long-term behaviour of SFRC, this section deals with the main durability issues that may be responsible for the deterioration of SFRC pavements, such as fatigue, corrosion and freeze-thaw.

Because there are only few studies on the use of recycled fibres in concrete, the information presented in this section is based on industrially produced fibres. Information regarding the durability of RCC can be found in Section 2.4.2.2.

3.1.1 Flexural fatigue

Fatigue occurs on elements or structures subjected to repetitive cyclic loads, such as the traffic loads in pavements. The increase in the traffic of heavy vehicles has increased the necessity to study fatigue effects in pavements. According to Lee and Barr (2004), fatigue '*is defined as a process responsible for producing permanent and progressive internal structural changes in a material subjected to repeated loading*'. In concrete, this effect is associated with the growth of micro-cracks. Singh and Kaushik (2003) explain that cracks formed due to repeated loading, even if small, can lead to a decrease of the overall structural performance, due to reduction in the stiffness of the structure and further crack propagation. Li and Matsumoto (1998) say that the crack growth mechanism is responsible for the fatigue life of SFRC.

Since steel fibres enhance the flexural strength and toughness of concrete, it is expected that steel fibres will also contribute to improve fatigue resistance of SFRC. In SFRC, the fatigue behaviour depends on the fibre content, fibre type and geometry (Ramakrishnan *et al.*, 1987; Johnston and Zemp, 1991; Chang and Chai, 1995; Mailhot *et al.*, 2001; Singh and Kaushik, 2003; Lee and Barr, 2004). It is important to add that, as for any other mechanical property, the characteristics of the concrete constituent materials also affect the fatigue behaviour.

Fatigue performance of SFRC is usually obtained by examining the number of cycles until failure and the stress ratio[12] applied to the specimens. However, this type of fatigue data present high deviations because of the random orientation of fibres (Singh *et al.*, 2005a and 2008) and because the specimens tested against fatigue are not the same tested to determine the maximum static flexural load – and consequent stress ratio (Rossi and Parant, 2008).

According to Li and Matsumoto (1998), three mechanisms are responsible for the crack growth in SFRC specimens subjected to fatigue loads: 1) Crack growth law specific for the matrix (not influenced by fibre addition); 2) Crack bridging by fibres and aggregates, and 3) Fatigue damage in the fibre-matrix interface. The authors explain that the interfacial bond strength loss between the fibre and the matrix is more prone to occur in shorter fibres while longer fibres are more susceptible to fatigue fracture of the fibres, which should occur during the second mechanism.

Fatigue experiments in conventional concrete and SFRC show that there are three stages of matrix crack growth due to cyclic loads (Chang and Chai, 1995; Li and Matsumoto, 1998; Rossi and Parant, 2008), as it can be seen in Figure 42. The first stage indicates the formation of micro-cracks usually due to the matrix properties. In SFRC, initial damage is due to the fibre/matrix interface due to the first few loads. The second stage comprises the propagation of cracks to a critical length. A continuous degradation of the fibre-matrix interface is observed in SFRC in this stage. The third stage indicates that various unstable cracks merge to form a continuous crack. For SFRC, when cracks reach certain critical values, it is impossible for fibres to bridge them due to loss of bond or failure of the fibres, thus leading to failure. The curve for specimens resisting more than 2 million cycles is also shown in Figure 42. In this case, the deterioration stabilises after the formation of the initial micro-cracks.

Chang and Chai (1995) and Lee and Barr (2004) say that fibres act in the second stage of the crack growth curve by preventing or delaying the propagation and opening of the cracks thus improving the load carrying capacity.

[12] Stress ratio is the relation between the load applied during dynamic test and the maximum static flexural load

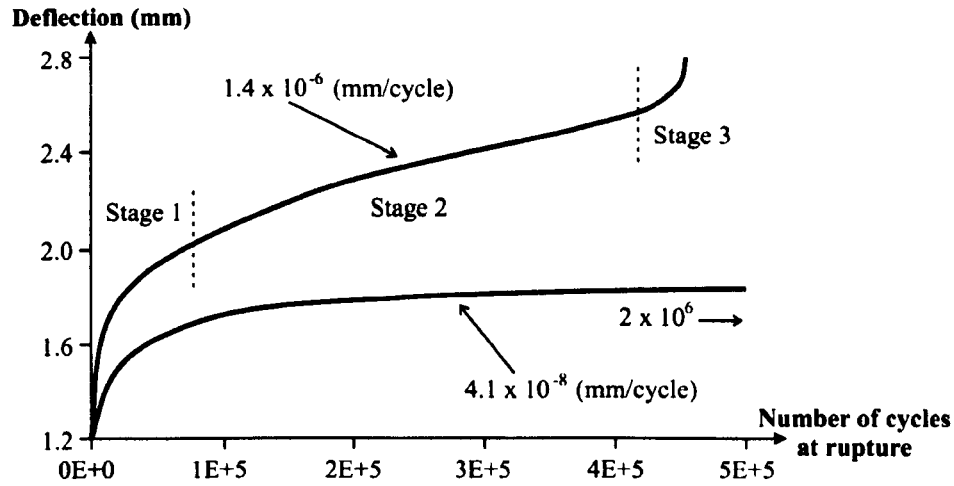

Figure 42 – Fatigue crack growth stages [Rossi and Parant, 2008].

Ramakrishnan et al. (1989) suggest three properties to characterise the fatigue life of SFRC: 1) fatigue strength which is the maximum flexural fatigue stress applied to sustain 2 million cycles of non-reverse load; 2) endurance limit is the maximum flexural fatigue stress applied to sustain 2 million cycles of non-reverse load, expressed as a percentage of the static flexural strength of plain concrete and 3) same as previous, however, it is expressed as percentage of its own static flexural strength. According to Johnston and Zemp (1991), the fatigue endurance limit may have two distinct meanings: the maximum stress at which 2 million cycles can be applied or the maximum load that can be applied to sustain an infinite fatigue life. Both criteria are similar, since it is expected that concrete resisting 2 million cycles should have an infinite fatigue life.

Test methods for fatigue in SFRC

The load system and specimen geometry used to test specimens against fatigue is the same as for static flexural tests (Section 2.3.2.3). Depending on the purpose of the test, slabs and beams with different geometries and load configurations are used. Loads are applied based on a certain stress ratio and frequency, which influences the selection of the actuator and its pumping capacity and specimen geometry and stiffness.

Common frequency rates used for prisms range from 12 to 20Hz, and usually no amplification or resonance problems were reported in the literature. A minimum stress of 10% of the maximum static flexural strength is normally applied to the specimens. The stress ratios vary from 0.50 to 0.98 and the maximum number of cycles applied to the specimens is normally around 2 million (Ramakrishnan *et al.*, 1987 and 1989; Johnston and Zemp, 1991; Mailhot *et al.*, 2000; Singh and Kaushik, 2000, 2001 and 2003; Singh *et al.*, 2005a, 2005b and 2006).

3.1.2 Corrosion of fibres

SFRC pavements may be subjected to de-icing salts in cold climate regions. They may also be exposed to aggressive environments where chlorides and carbonation may corrode the steel fibres. Considering that steel fibres are randomly distributed inside concrete, the ones situated near the concrete surface are not protected by the alkalinity of concrete (Mangat and Gurusamy, 1988; Bentur, 2003; Balouch *et al.*, 2010). As previously explained in Section 2.3.1.3, in specific situations due to casting procedures and specimen size, the fibres tend to align to the mould surfaces, which may accelerate corrosion and pop-out of these fibres.

The corrosion process

The corrosion process initiates when electrolyte (usually water), oxygen and difference in potential are provided, as shown in the reactions below. Steel fibres are protected by the alkalinity of concrete due to the formation of an oxide *passivity film* around the fibres that defends them from reactions with water and oxygen. However, this film can be broken down due to carbonation or chloride attack.

$$Fe \rightarrow Fe^{++} + 2e^{-} \quad (4)$$

$$4e^{-} + O_2 + 2H_2O \rightarrow 4(OH)^{-} \quad (5)$$

$$Fe^{++} + 2(OH)^{-} \rightarrow Fe(OH)_2 \quad (6)$$

$$4Fe(OH)^{-} + 2H_2O + O_2 \rightarrow 4Fe(OH)_3 \quad (7)$$

Carbonation is a process at which hydrated products of cement react with carbon dioxide CO_2 from the atmospheric air. In this process, calcium hydroxide crystals $Ca(OH)_2$ and calcium silicate hydrates *C-S-H* of the hardened cement paste combine with CO_2 to form calcium carbonates $CaCO_3$, which reduces the alkalinity of the concrete. The reactions start from the surface and gradually extend to the interior of the element, depending on the quality of concrete[13] and environmental conditions. Once the carbonation front reaches the fibres, it *depassivates* them and corrosion may take place. Carbonation can also occur through the cracks.

[13] The quality of the concrete refers to the ability of concrete to allow the penetration of CO_2 into concrete, especially in terms of gas diffusion (see Section 3.2 about the pore structure and transport mechanisms of concrete). In good quality concretes, the deposition of calcium carbonates in the pores of concrete may contribute to clogging of the pores, restricting the carbonation reactions only to the surface of the concrete.

When corrosion is caused by chlorides, they participate not only by breaking the passivity film, but also by accelerating the process. Chlorides can reach the steel fibres either through open cracks or by transport mechanisms. In this process, chlorides react with the positively charged ferrous ions to produce rust, as shown below.

$$Fe^{++} + 2Cl^{-} \rightarrow FeCl_2 \quad (8)$$

$$FeCl_2 + 2H_2O + O_2 \rightarrow Fe(OH)_2 + 2HCl \quad (9)$$

The electrolyte and the oxygen necessary for corrosion to take place, for both carbonation and chlorides attack, are provided by the water in the concrete pores and by gas diffusion (if not directly from the environment when cracks exist). The difference in potential can be caused by differences in humidity, salt concentration gradients, non-uniform oxygen flow, among others (Neville, 2003).

Corrosion in SFRC

Mangat and Gurusamy (1987a) explain that steel fibres do not affect the ingress of chlorides by diffusion in concrete. In this case, the diffusion coefficient in SFRC is governed mainly by the hydration and permeability of the concrete, and no influence is caused by fibre addition.

Mangat *et al.* (1989) compared the flexural performance of un-cracked specimens subjected to 2000 marine cycles with the corresponding specimens cured in air, as shown in Figure 43. It can be seen that specimens subjected to corrosion presented considerably higher flexural strength than the ones cured in air. The post-peak behaviour was also not affected by corrosion, which means that the interfacial bond between the concrete and the fibre was not reduced.

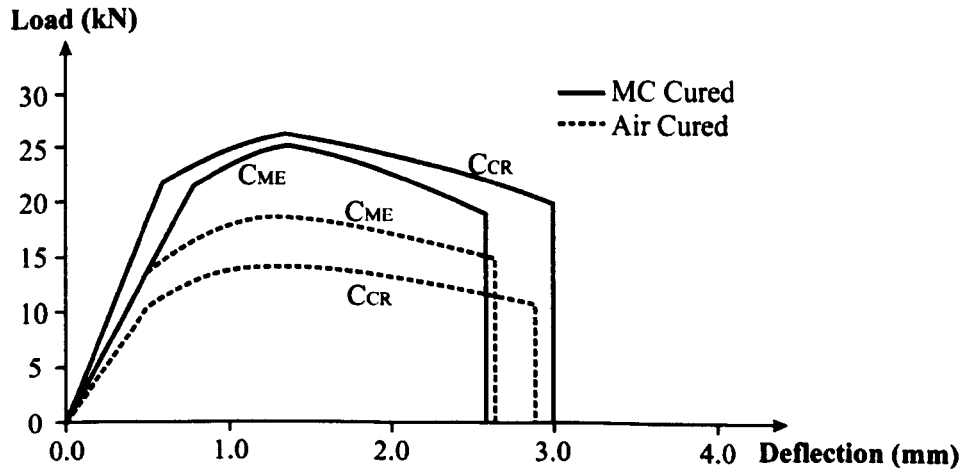

Figure 43 – Typical flexural versus load deflection curves for specimens cured in air and exposed to marine cycles (MC cured) [Mangat *et al.*, 1989].

Kosa and Naaman (1990) initially assumed that two main deterioration processes may occur due to corrosion in steel fibres. One is related to the reduction in the cross section of fibres due to corrosion, which, according to the authors, can cause serious damage to SFRC elements. Another is due to crack formation in the fibre/matrix interface due to rust (which has larger volume than steel) accumulated around the fibres.

Balouch *et al.* (2010) say that the structural deterioration caused by corrosion in SFRC occurs mainly through the cracks in the concrete, which allow chlorides to penetrate the concrete. Mangat and Gurusamy (1987b) say that only cracks larger than 0.2 mm can cause damage to SFRC.

Various other studies on the corrosion of SFRC have reported that corrosion did not penetrate into the concrete fibres and that most signs of corrosion were aesthetic (Mangat and Gurusamy, 1988; The Concrete Society, 2004; Balouch *et al.*, 2010), and not in terms of reduction in performance. Balouch *et al.* (2010) say that the porosity of concrete is the main factor dominating the corrosion of SFRC. According to the authors, the skin of concrete (up to 2 mm cover) is more porous than the centre of concrete elements, thus explaining the corrosion spots near the surface.

Mangat and Gurusamy (1988) explain that the interfacial zone between the fibre and the matrix is composed mainly of segregated lime, and as such it is more effective in protecting thin fibres than conventional reinforcement bars. This rich lime layer acts as a high alkalinity barrier which prevents the ingress of chlorides to the steel fibres. Other theories were also developed to explain the lack of corrosion in SFRC. The Concrete Society (2004) says that the area of fibres (which act as cathode) is small compared to the anodic zones, which leads to low rates of corrosion. Following the same idea, Bentur (2003) says that corrosion may be restricted due to the lack of electrical conductivity between the fibres, possibly caused by their discrete nature, improved matrix microstructure and denser interfacial transition zone compared to conventional rebar. The theories do not contradict each other, hence, the lack of corrosion in steel fibres is probably due to a combination of the theories rather than by a single explanation.

It is expected that only fibres located very near the concrete surface may have their section reduced by corrosion, hence, the performance of concrete is not expected to change, which is in accordance with the majority of the works in the area. The formation of corrosion cracks is unlikely to take place because the amount of rust generated by fibres is so small (compared to conventional rebars) that it can probably be accommodated in the concrete pores.

It is also important to add that the specimens subjected to marine cycles are expected to develop more strength because of their curing condition (wet cycles of marine exposition), which contributes for the continued hydration of cement.

Test methods to simulate corrosion in SFRC

The effects of corrosion in real structures are dependent on the aggressivity level of the environment, the quality of the concrete and maintenance procedures. Since corrosion is a long-term process (based on experience for conventional RC), it needs to be accelerated in the laboratory to allow experiments to be undertaken in a reasonable period of time.

The common ways to simulate chloride corrosion in SFRC is by the salt-spray chamber (Mangat and Gurusamy, 1987a, 1987b and 1988; Granju and Balouch, 2005; Balouch *et al.*, 2010) or through wet-dry cycles (Kosa and Naaman, 1990). For both techniques, a sodium chloride solution (around 3% concentration) is normally used to accelerate corrosion in the wet phase, in an attempt to simulate exposure to sea or de-icing salts. Since no standards are available for accelerated corrosion tests for concrete, the periods of salt spray or immersion in solution and dryness usually vary.

Kosa and Naaman (1990) exposed specimens to 3 days of immersion in sodium chloride solution and three days of dryness. Three different temperatures were used for the sodium chloride solution (20 °C, 50 °C and 80 °C) to verify the influence of the temperature on the penetration of chlorides into concrete. Mangat and Gurusamy (1987a, 1987b and 1988) applied two wet and two dry cycles within 24 hours up to 2000 cycles, aiming to simulate the tidal cycles of the sea. Granju and Balouch (2005) and Balouch *et al.* (2010) simulated corrosion by applying one week of salt spray and one week of dryness.

Kosa and Naaman (1990) also used a carbonation chamber to simulate corrosion. In this case, specimens were exposed to ten daily shots of carbon dioxide during three weeks.

Some studies are also based on exposing specimens to a real marine environment (Mangat and Gurusamy, 1987a and 1988), up to 2000 effective wet-dry cycles.

3.1.3 Freeze-thaw

The severest cases of freeze-thaw damage occur in horizontal structures near the ground level (which is often saturated) subjected to very low temperatures and de-icing salts, and as such concrete pavements are extremely vulnerable. Very few studies are found in the literature

regarding the freeze-thaw durability of SFRC (Ramakrishnan, 1984; Cantin and Pigeon, 1996; Pigeon *et al.*, 1996; Miao *et al.*, 2002; Mu *et al.*, 2002).

The freeze-thaw process

As shown in Figure 44, there are four types of freeze-thaw damage in concrete: 1) surface scaling is a result of the delamination of the concrete surface and is the most common case of freeze-thaw damage; 2) pop-outs are conical depressions caused by localised spalling of concrete, usually due to freezing of the underneath aggregate; 3) D-cracking is formed by parallel cracks near the edges and corners of pavement slabs; and 4) internal damage due to cracks formed essentially in the matrix and have no effect on the coarse aggregate (Harrison *et al.*, 2001).

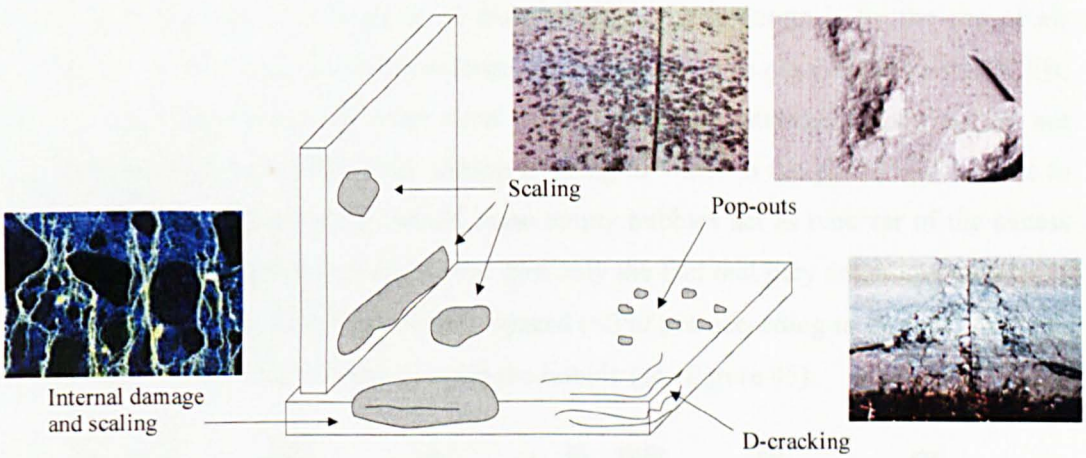

Figure 44 – Types of freeze-thaw damages.

Damage caused by freeze-thaw occurs due to the freezing of the water in the concrete pores, which expands up to 9% compared to the thaw phase. The expansion expels the excess of water from the pores, which moves through the pore system by diffusion causing the growth of small bodies of ice (Neville, 2003).

Continuous cycles of freezing and thawing lead to cumulative damage to concrete because the expansion caused by the water tends to create tensile stresses in the pores, contributing to pore enlargement. During the thawing phase the larger pore can be completely filled with water (considering that water is provided e.g. due to the high RH of the environment, rain, melting of snow, etc.) which may cause larger stresses when frozen.

The main factors that affect freeze-thaw in concrete are the degree of saturation and the pore system of concrete (Jansen and Snyder, 1994; Neville, 2003). The higher the amount of water in the pores, the higher will be the damage caused by freeze-thaw. High degree of saturation in

concrete can be caused by several factors, such as the RH of the environment and other environmental conditions, the age of the concrete (more saturated at early ages), the types of exposure (e.g. immersed in water), among others. The pore structure governs the rate and the level of the damage caused by freeze-thaw. The more interconnected the pores are and the higher the number of large pores is, the more damage is expected to occur. The large and connected bubbles differ from the air entrained bubbles, which are beneficial for freeze-thaw resistance, as explained below.

According to Ramakrishnan (1984), SFRC presents higher freeze-thaw resistance than plain concrete. However, the author suggests a minimum of 6% air content to provide good freeze-thaw durability for SFRC. It is important to add that not only the air content is important, but also the type, size and spacing of the air bubbles.

The most appropriate way to provide good frost resistance of concrete is by the use of air entraining agents. In this case, the bubbles formed are considered as quasi-closed pores (CEB, 1992). They do not get filled with water even when concrete is saturated since they are not connected with adjacent pores. However, during freezing of water in the pores, which leads to expansion and diffusion of the excess water, these empty bubbles act as receiver of the excess water thus relieving the stresses in the concrete. Not only the fact that they are empty bubbles is important, but also that they should be closely spaced (<250 μm according to Powers, 1954) to allow an easy path for the excess water to reach the bubble (see Figure 45).

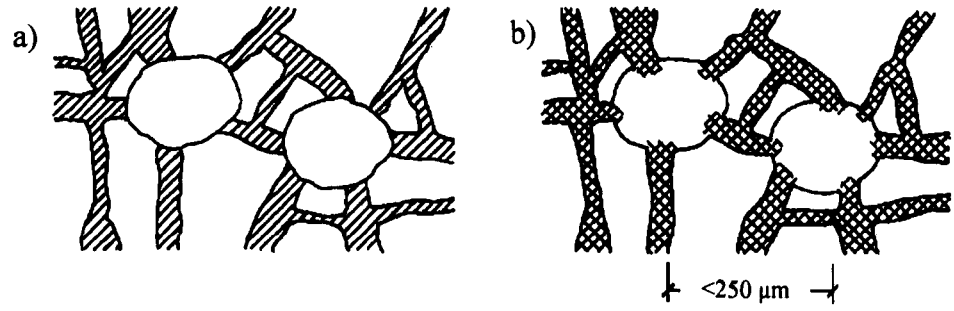

Figure 45 – a) air entrained pores free from water and b) excess water from expansion due to freezing reaches the air entrained bubbles.

The use of air entraining admixtures as the only way to provide frost resistance is not sufficient. A high porous (not considering the air entrained bubbles) and permeable concrete in saturated condition will always have low resistance against freeze-thaw even if air entrained bubbles are provided. This is because the volume of air entrained bubbles is not sufficient to accommodate the large amount of excess water from the non air entrained bubbles during freezing.

Freeze-thaw in SFRC

Cantin and Pigeon (1996) and Cai and Liu (1998) say that the freeze-thaw durability of concrete is related to its pore structure, which means that in SFRC the matrix, and not the fibres, is responsible for the freeze-thaw resistance of the concrete.

Other authors, however, report that the freeze-thaw resistance of SFRC is improved compared to plain concrete (Ramakrishnan, 1984; Pigeon *et al.*, 1996; Mu *et al.*, 2002; The Concrete Society, 2004). This is attributed to the effect of steel fibres in retarding the formation and propagation of cracks due to freeze-thaw cycles. Miao *et al.* (2002) also agree that improvement caused by fibres is due to the ability of fibres to bridge cracks and not by changes in the porosity.

According to ACI (1989), the pore structure of concrete changes when fibres are added to the mixture, especially because voids are trapped in the concrete during vibration (as already mentioned in Section 2.3.2.1, voids trapped due to high volumes of fibres also reduce the compressive strength). According to the same source, these voids cannot be used as a substitute for proper air entrainment in order to prevent freeze-thaw damage. This is probably because the trapped bubbles are not closely and randomly spaced and their amount is variable and usually not sufficient to provide good frost resistance.

Test methods to simulate freeze-thaw in SFRC

Even though there are no specific methods to determine the freeze-thaw resistance of SFRC, some of the test methods used for plain concrete can also be applied to SFRC. The most common methodology used to determine the freeze-thaw behaviour of concrete is by measuring the loss of mass after continuous freezing and thawing cycles. However, this method seems to be inappropriate to SFRC because pieces of concrete detached from the specimen may still be bonded to the fibres thus invalidating the results (ACI, 1989). Hence, tests based on internal damage rather than on loss of mass are recommended for SFRC by ACI (1989).

The ASTM C666 method (2003a) can be used for SFRC and the measurement of freeze-thaw resistance is obtained by determining the fundamental transverse frequency of a specimen, usually a prism. This is obtained according to the procedures of ASTM C215 (2008a). The fundamental frequency allows the calculation of the relative dynamic modulus of elasticity, which is based on the internal damage of concrete. The main advantage is that the method is not as empirical as the tests based on scaling results. The test applies freezing and thawing cycles in

specimens immersed in water with temperatures ranging from 4 °C to -18 °C and each cycle lasting more than 4h but less than 10h.

The draft standard DD CEN/TS 12390-9 (BS, 2006c) is based on the scaling resistance of concrete. For the cube test[14], specimens are fully immersed in water or chloride solution and subjected to cycles with temperatures ranging from 20 °C to -15 °C in a period of 24h. The loss of mass is calculated as a percentage of detached mass considering the total amount of concrete, for a certain number of cycles. The same organisation published a document (PD CEN/TR 15177, 2006b) based on the internal damage of concrete due to freeze-thaw attack. The document follows similar procedures as the ones described by ASTM C666 (2003a), however, the relative modulus of elasticity can be measured by either fundamental transverse frequency or ultrasonic pulse velocity transit time. For slab specimens[14], the temperatures range from 20 °C to -20 °C in 24h. The BS methods are based on the RILEM methods TC 117-FDC (1996) and TC 176-IDC (2004a and 2004b) for the loss of mass and internal damage, respectively.

The ASTM C666 (2003a) method is expected to be more aggressive than the DD CEN/TS 12390-9 (BS, 2006c) and PD CEN/TR 15177 (BS, 2006d) methods due to the shorter period of time of each cycle. The BS methods (2006c and 2006d) are more realistic considering that concrete can freeze and thaw in 24h due to variations of night and day temperatures.

Due to the fact that some durability issues of SFRC (i.e. corrosion and freeze-thaw resistance) seem to be related to the pore structure of concrete, the next section explains the main properties associated to the pore structure of SFRC and the transport mechanisms of concrete.

3.2 PORE STRUCTURE OF SFRC – TRANSPORT MECHANISMS AND PROPERTIES AFFECTING DURABILITY

Two parameters characterise the pore structure of concrete: the open porosity and the pore size distribution (CEB, 1992). Open porosity refers to the connected pores of concrete that allow the transport of aggressive agents into and within the pores. Pore size distribution influences the rate of transport.

According to their size, the pores in concrete can be classified as macro-pores, capillary pores and micro-pores, as shown in Figure 46. Pores affecting the transport of aggressive agents are the capillaries and the macro-pores (CEB, 1992; Neville, 2003; Mehta and Monteiro, 2006).

[14] Three different methods are allowed by the method. The range of temperatures, the specimen geometry, the period of each cycle and the number of saturated surfaces of specimens vary among them.

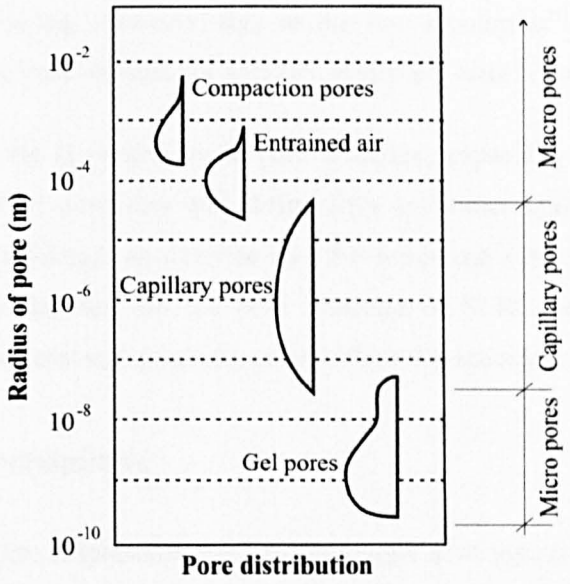

Figure 46 – Pore size distribution [Setzer, 1977 cited in CEB, 1992].

Besides the connectivity and the size of the pores, other factors may also influence the pore structure such as the narrow entrance of some pores and the adsorbed[15] water, which may prevent aggressive agents from penetrating freely into concrete (Neville, 2003).

Apart from their size, concrete pores can also be classified according to their origin as gel, capillary and air (CEB, 1992; Neville, 2003; Mehta and Monteiro, 2006), as also shown in Figure 46. Air can be trapped during compaction and mixing or entrained due to admixtures. Gel pores are the ones formed in-between gel particles of cement and are influenced by the amount of cement and bound water[16]. Usually the gel pores occupy a volume of 28% of the gel cement (Neville, 2003). Capillary pores are the voids formed due to evaporation of the non-bound water of concrete, occurring after placement of the concrete (during hydration and curing).

The Concrete Society (2004) and Vassou *et al.* (2008) say that the addition of fibres may improve the durability of concrete because they reduce bleeding and control cracking (either by limiting or avoiding the crack propagation or formation). El-Dieb (2009) reports, based on experimental data, that the addition of fibres in high strength concrete does not alter the pore structure of concrete compared to the corresponding plain concrete. A microstructural analysis carried out by the author showed that there is a strong bond between the fibres and the cement paste, and that the cement paste around the steel fibres (transition zone between fibres and

[15] Adsorption is a process at which water vapour molecules bind to the surface of the pores due to an excess of energy. It is dependent on the size of pores and the ambient RH (CEB, 1992).
[16] Bound (or combined) water is also called as non-evaporable water and represents the amount of water necessary to hydrate the particles of cement (usually around 23% of the volume of cement) (Neville, 2003 and Mehta and Monteiro, 2006).

cement paste) is very dense. However, due to the low amount of studies in the area, the influence of fibres on the pore structure of concrete is still not clearly understood.

The durability of concrete is related to its pore structure, especially regarding the transport mechanisms (permeability, sorptivity and diffusivity) and other specific properties such as porosity, density and shrinkage, as described in the following sub-sections. Since very few studies were developed focusing on the pore structure of SFRC, most of the information provided is related to conventional concrete, unless otherwise specified.

3.2.1 Transport Mechanisms

Transport mechanisms are responsible for carrying aggressive agents[17] from the outside into concrete or from the inside of the concrete out (Samaha and Hover, 1992; Claisse, 2005) and for this reason they are strongly associated with the durability of concrete (Boel *et al.*, 2007; Torrijos *et al.*, 2010). Transport mechanisms of concrete are also used to refer to the *penetrability* of concrete (Hearn, 1998; Neville, 2003) and are responsible for the deterioration rate of the material (Hearn, 1998).

According to Martys (1995), transport mechanisms are influenced by the pore structure of the concrete paste, which is comprised of hydrated products of cement (C-S-H), non hydrated particles of cement (depending on the age of the concrete) and pores.

The interfacial zone between the cement paste and the aggregates is also part of the pore structure of concrete. This zone (which occupies from one third to one half of the volume of cement paste) is more porous than the remaining concrete due to the difficulty of the hydrated products to pack well near the aggregate boundary. The porous interfacial zone between aggregate and cement paste may lead to paths for water, chloride ions and other aggressive agents (Martys, 1995; Neville, 2003). According to Neville (2003), the interfacial zone is also a focus of early microcracking, probably originated during hydration. Following the same idea, one can say that the addition of fibres in concrete may also create interfacial zones between the fibres and the cement paste thus altering the pore structure of concrete and influencing its durability.

The influence of the interfacial zone on durability is still controversial because no clear correlation could be found on how the interfacial porous zone affects the transport mechanisms of concrete (Larbi, 1993).

[17] Examples of aggressive agents are: water (pure or diluted with aggressive ions – e.g. chlorides, sulphates), carbon dioxide and oxygen (Neville, 2003).

Cracking also influences the transport mechanisms of concrete. Microcracks formed from different processes (e.g. restrained shrinkage, thermal deformations, loads, hydration, etc.) can interconnect and create paths for the ingress of aggressive agents (CEB, 1992; Samaha and Hover, 1992; Aldea *et al.*, 1999a and 1999b; Torrijos *et al.*, 2010).

Finally, the microclimate or environmental conditions at the concrete surface is another factor influencing the transport in concrete. Examples of microclimate include the availability and concentration of water and aggressive agents, the temperature, pressure and the RH of the air that may fill the concrete pores with water due to adsorption[15] (CEB, 1992).

The moisture condition of the concrete pores greatly influences the transport of fluids, gases and aggressive agents on concrete (The Concrete Society, 2008), as shown in Figure 47. A non-saturated pore allows the transport of gases and fluid by air diffusivity and adsorption while a saturated concrete pore can allow fluid flow and ion diffusivity.

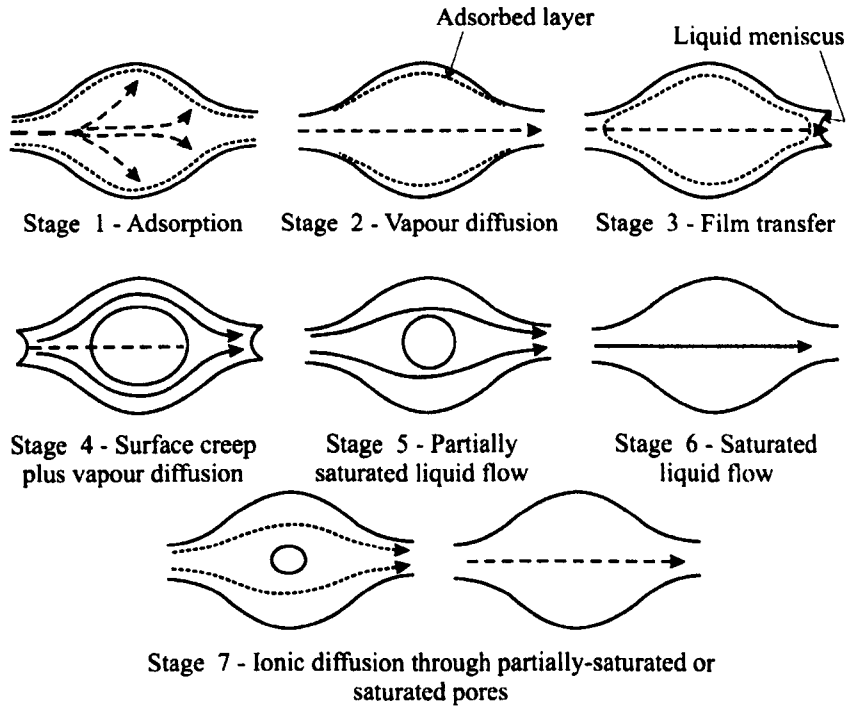

Figure 47 – Idealised model for various transport mechanisms according to the moisture condition of the concrete [The Concrete Society, 2008].

Despite the fact that the transport mechanisms are responsible for carrying aggressive agents into the concrete, it is also important to mention that these mechanisms may also be responsible for continuous hydration of concrete, autogeneous healing and self-sealing of cracks, which may reduce the *penetrability* of concrete. Continuous hydration of cement due to the presence of water contributes to the refinement of the pore structure of the concrete, reducing porosity and permeability. The autogeneous healing is the capacity of cement to heal cracks in concrete

(Hearn, 1998) due to the formation of calcium carbonate crystals in the cracks subjected to continuous water ingress. Self-sealing, according to Charron *et al.* (2008) and Hearn (1998), is a combination of several factors, such as the swelling of concrete when saturated, osmotic pressures, physical blockage and chemical interaction of water and concrete.

For the purpose of this thesis, the three main transport mechanisms are explained: permeability, capillary absorption and diffusivity. Other examples of transport mechanisms consist of electromigration[18], thermal gradient[19], adsorption[15] and osmosis[20] (Claisse, 2005).

3.2.1.1 Permeability

Permeability of concrete is the property associated with the flow rate of a fluid through its pores, when pressure is applied. It is an important property for structures under water (Sahmaran *et al.*, 2007) or dams and tunnel linings (Claisse, 2005).

Darcy's law for laminar flow in a porous system is used to describe the flow of non-compressible fluids (e.g. water) through the pores of concrete, as shown in Equation 10.

$$\frac{dq}{dt}\frac{1}{A} = \frac{K'\Delta p}{\eta L} \qquad (10)$$

Where:

$\frac{dq}{dt}$ = rate of flow of water [m^3/s]

A = cross sectional area of the specimen [m^2]

K' = intrinsic permeability of the material [m^2]

Δp = pressure drop (applied minus the outlet) across the depth of the specimen [N/m^2]

η = dynamic viscosity of the fluid [$N.s/m^2$]

L = specimen thickness [m]

The intrinsic permeability of the material K' does not depend on the fluid involved. The determination of the intrinsic permeability is deterministically viable when a steady flow of the fluid is achieved. For simplicity reasons, the intrinsic permeability is also called as *permeability*.

[18] Occurs when an electric field is applied, forcing ions to migrate from a negative to a positive electrode. This can be derived from an external source or also from the corrosion process in rebars (Claisse, 2005).
[19] The mechanism is based on the migration of water from hot to cold regions of the concrete. This transport mechanism is also associated with the permeability of the concrete (Claisse, 2005)
[20] The mechanism is responsible for the flow of water from the less concentrated to the more concentrated solution. Solid particles in the water are retained by a semi-permeable membrane (Claisse, 2005).

As for conventional concrete, various factors affect the permeability of SFRC, such as water/cement (w/c) ratio, age of concrete, the cracking behaviour, among others. Because of the good post-cracking behaviour of SFRC, many SFRC structures will funcion in the cracked condition. According to Torrijos *et al.* (2010), a crack width ranging from 0.1 to 0.4 mm, which is usually in-between the acceptance values of concrete design structures, can increase the permeability up to four times compared to non cracked concrete.

Test methods for permeability

Permeability of concrete is usually experimentally measured as a flow of water or gas through the concrete pores due to pressure. Water and gas flow permeability tests are usually performed in cylinders or cubes, sealed in all surfaces except two parallel surfaces where a fluid or gas is applied under pressure (see Figure 48). High variability is commonly noticed in permeability results and there is a lack of standard methods to perform the test (El-Dieb and Hooton, 1995; Li and Chau, 2000).

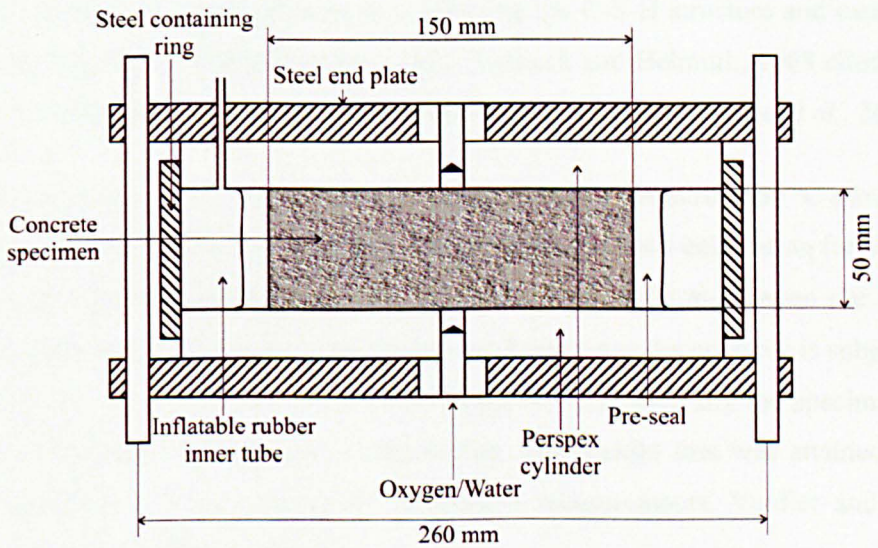

Figure 48 – Schematic arrangement for water or gas permeability test [after The Concrete Society, 2008].

Water flow permeability tests are usually time-consuming since a long time (days or even weeks according to El-Dieb and Hooton, 1995) is required for the water flow to stabilise, especially for good quality concretes. There are also some issues regarding further hydration of cement and other interactions between cement and water (e.g. autogeneous healing of cracks) due to the water flow through the concrete pores, which may reduce the permeability of specimens, thus influencing the results (El-Dieb and Hooton, 1995; Edvardsen, 1999; The Concrete Society, 2008; Lynsdale, 2008; Picandet *et al.*, 2009).

An alternative to water flow is a test that measures the depth of water penetration in concrete under water pressure, which can be performed according to the BS 12390-8 (2009c). The advantage of the method is that there is no need for the flow to stabilise. A water pressure of 500 kPa is applied to the specimen for a period of 72h and the depth of water through the sample is then measured by splitting the specimen parallel to the flow of water.

Another alternative to water flow permeability is the gas flow test (e.g. oxygen and nitrogen). In this case, since a compressible fluid is used, the flow rate needs to be considered at the average pressure across the specimen (Lynsdale, 2008 and Cabrera and Lynsdale, 1988). The main advantage of the method is that gas flow stabilises faster than water flow. Nevertheless, specimens need to be oven dried before testing, to remove the water in the concrete pores, which may cause microcracks in the concrete matrix depending on the temperature (Sanjuán and Muñoz-Martialay, 1996; Abbas *et al.*, 1999; RILEM, 1999; Carcassès *et al.*, 2002).

The temperature of 80 °C causes evaporation of the capillary and adsorbed water with minimum effect on the C-S-H structure. On the other hand, temperature of 105 °C causes the interlayer water and the bound water to evaporate, thus affecting the C-S-H structure and causing initial micro-cracks (Feldman and Ramachandran, 1971; Verbeck and Helmuth, 1968 cited in Farage *et al.*, 2008; Verbeck and Copeland, 1972 cited in Farage *et al.*, 2008; Farage *et al.*, 2008).

The RILEM test method TC 116-PCD-A (1999) says that a temperature of 50 °C should be used to precondition the specimens before testing. The method suggests a calculation for determining the necessary weight loss based on an intermediate drying stage in-between the total dried condition obtained at 105 °C and the semi-drying condition when the concrete is subjected to 20 °C ± 1 °C and 75 ± 2% RH. Abbas *et al.* (1999) used 50 °C to oven dry the specimens and no cracks were observed in the specimens after drying. The weight loss was attained when the specimens reached a constant mass after subsequent measurements. Verdier and Carcassès (2004) also dried the specimens at 50 °C.

Sanjuàn and Muñoz-Martialay (1996) tested four different temperatures to precondition the specimens (20 °C, 40 °C, 60 °C and 80 °C). It was found that the permeability increases with temperature, which can be associated to the degree of saturation of the specimens, since lower temperatures are not efficient in removing the total evaporable water from concrete.

Carcassès *et al.* (2002) suggests a new method to precondition the specimens by using 80 °C to dry the specimens. They say that it is faster than drying at 50 °C and that no cracks are formed using 80 °C.

However, Gardner *et al.* (2005) tested specimens subjected to 85 °C and 105 °C, the latter being the most appropriate because no differences were found on the results and because it is faster than lower temperatures.

The temperature of 80 °C seems to be the most appropriate for the preconditioning of specimens for the gas permeability test. This is mainly because 80 °C seems to be efficient and reasonably fast in terms of eliminating the evaporable water for the specimens and also because it seems not to interfere with the formation of cracks.

3.2.1.2 Capillary absorption

Capillary absorption or sorptivity is the capacity of the concrete to absorb water through its capillaries, which, according to Claisse (2005) and Neville (2003), occurs due to the surface tension of the concrete pores. It occurs when a concrete element is partially submerged. In this case, water penetrates through the surface in contact with water and evaporates at the concrete surfaces exposed to the environment. Sorptivity may also carry ions dissolved in water through the concrete pores, which may lead to crystallisation of the ions (e.g. efflorescence) and further cracking or spalling of concrete.

The smaller the pore size is, the higher are the capillary forces over the water (Assiè *et al.*, 2007), hence sorptivity tests also provide a useful indication of the pore structure of concrete (The Concrete Society, 2008), if the depth of water uptake is recorded. Figure 49 shows the relationship between the pore radius, the depth of water penetration and the time of exposure to water absorption.

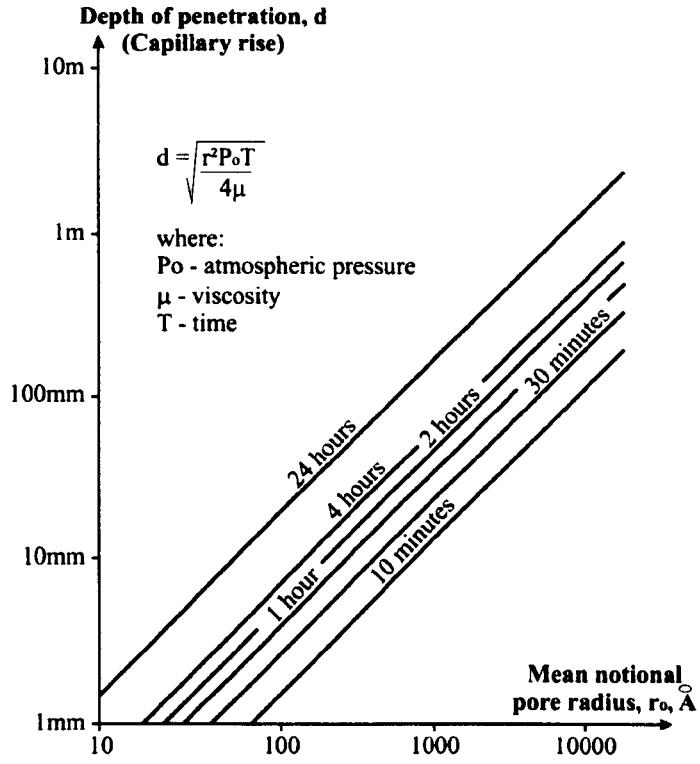

Figure 49 – Relationship between the pore radius and the depth of water uptake due to sorptivity test [The Concrete Society, 2008].

Test methods for sorptivity

Test procedures to measure sorptivity comprise of exposing one surface of concrete specimens to water. The water absorbed and/or the depth of uptake of water is then measured after specific periods of time. The coefficient of absorption is calculated as the slope of the curve of the water uptake per unit area *versus* the square root of time, obtained by linear regression analysis.

The main standards used to measure the coefficient of absorption are the ASTM C1585 (2004), BS EN 13057 (2002a) and RILEM TC 116-PCD-C (1999). The main differences among the standards are shown in Table 6.

The preconditioning of the specimens for all methods is based on using low temperatures (≤ 50 °C) to remove the water from the pores, thus avoiding the formation of cracks. Even though the specimen geometry varies among the methods, the most important difference among them is based on the intervals at which the measurements are taken, such as the frequency and the total period of time. Higher frequencies of measurements give more accurate results on the behaviour of the sorption coefficient and longer periods of test provide more parameters for the characterisation of the sorptivity, such as the secondary sorption coefficient.

Table 6 – Comparison among main sorptivity test methods.

	ASTM C1585	RILEM TC 116-PCD-C	BS 13057
Number of specimens	2	3	3
Geometry of specimens	Cylinder – d = 100 mm; l = 50 mm	Cylinder – d = 150 mm; l = 50 mm [a]	Cylinder – d = 100 mm; $l \geq 20$ mm and $l > 3 \times D_{max}$ [b]
Preconditioning	3 days at 50 °C and RH 80%; 15 days inside sealed containers at 23 °C	According to TC 116-PCD-A (1999) method	Oven dried at 40 °C, minimum of 7 days until reach constant mass
Time for measurements	60s; 5, 10, 20, 30 and 60 min, 2, 3, 4, 5 and 6h; 1, 2 and 3 days; 3 measurements in 4 days; 1 measurement in 2 days	10min, 1h, 4h and 24h	12min, 30min, 1h, 2h, 4h, 24h [c]
Expression of results	1. Absorption[d]; 2. Initial coefficient of absorption[e]; 3. Secondary coefficient of absorption[f]	Amount of water absorbed – no equation for coefficient of absorption is given	1. Absorption[d]; 2. Coefficient of absorption; 3. Resistance coefficient[g]

[a] rectangular specimens with minimum test area of 17500mm^2 is also acceptable.
[b] MNSA
[c] not mandatory. Other reading periods may be used since six readings are taken in a period of 24h.
[d] water uptake per unit area according to specific formula.
[e] before saturation of specimen, also called *coefficient of absorption* or *sorptivity*
[f] after saturation of specimen – change in the slope of the absorption *versus* time curve after a certain period of time
[g] related to the depth at which water will penetrate into the specimen after a certain period of time

For the purpose of this study, because the same specimens tested for permeability can be used to measure sorptivity, and also because the specimen geometry for permeability follows the RILEM TC 116-PCD-A (1999), this method was initially adopted for the sorptivity test. However, because the RILEM method does not explain the calculation of the coefficient of absorption, the time of measurements and the output results followed the procedures of the BS EN 13057 (2002a).

3.2.1.3 Diffusivity

Diffusion in concrete is a process during which ions can circulate into saturated pores of concrete without flow of water as a result of a concentration gradient[21]. It may also take place in air-filled pores of concrete during the circulation of gases such as oxygen and carbon dioxide (Neville, 2003; Mehta and Monteiro, 2006; The Concrete Society, 2008). Examples of cases

[21] From the more concentrated solution to the less concentrated colution.

where diffusion of ions occurs are structures subjected to very humid environments (that saturate the pores of concrete due to adsorption) and structures immersed in water (CEB, 1992).

Diffusion is the main mechanism responsible for the transport of chlorides into concrete, even though chlorides can also be driven into concrete by permeability and absorption (Sahmaran *et al.*, 2007; Odriozola and Gutiérrez, 2008). In tidal zones, for instance, the wetting and drying processes are responsible for allowing ions through concrete by diffusivity and sorptivity.

Diffusion of chlorides directly influences the alkalinity of concrete and the initiation of corrosion. Diffusion, surface chloride content and initial chloride content are responsible for affecting the rate of chlorides ingress into concrete (see Section 3.1.2). Fick's second law is used to characterise the chloride transport in porous materials as shown in Equation 11.

$$\frac{\partial C}{\partial t} = D\frac{\partial^2 C}{\partial x^2} \tag{11}$$

Where:

C = concentration [amount of chlorides/length^3]

t = time [time]

D = diffusion coefficient [length^2/time]

x = depth [length]

If D is constant and the chloride transport occurs in one-dimensional configuration, a general solution for the above equation is given below (Crank, 1979):

$$C(x,t) = C_i - (C_s - C_i)\left[1 - erf\left(\frac{x}{\sqrt{4tD}}\right)\right] \tag{12}$$

Where:

C(x,t) = chloride content at a depth x (cm) [% by concrete mass]

C_i = initial chloride content [% by concrete mass]

C_s = chloride concentration at the concrete surface [% by concrete mass]

t = exposure time [seconds]

D = diffusion coefficient [cm^2/s]

erf = error function

Because sometimes other mechanisms may also be responsible for chloride transport into concrete, Odriozola and Gutiérrez (2008) say that Fick's second law should be used to calculate the 'apparent' diffusion coefficient, which means that it may also account for other types of

transport (e.g. sorptivity) other than pure diffusion. The apparent diffusion coefficient does not account for the chloride binding capacity[22] of the concrete (Ababneh *et al.*, 2003).

Few studies have been developed to evaluate the chloride diffusion of concrete reinforced with steel fibres (Mangat and Gurusamy, 1987a and 1987c). According to the authors, the addition of fibres does not influence the diffusion coefficient of concrete.

Test methods for diffusivity

The methods used to measure the diffusion coefficient of concrete are normally based on the chloride content of concrete. There are two main methods that are commonly used: 1) the titration and 2) the colorimetric method. Both methods expose the concrete specimens[23] to a chloride solution for a certain period of time.

The titration method consists of collecting pulverised concrete samples from several depths of concrete and analysing them by using the potentiometric titration method to obtain the chloride content at each depth. In this test, silver nitrate $AgNO_3$ is gradually added to the sample until the total amount of chloride precipitates, which then causes a change in the potentiostatic signal. The amount of silver nitrate responsible for changing the signal is used to calculate the amount of chlorides. The test to determine the chloride content can be performed according to the procedures of BS EN 14629 (2007c) and C114 (2010a). The diffusion coefficient can be calculated following Fick's second law. The draft standard DD CEN/TS 12390-11 (2010) and the ASTM C1556 (2003b) are based on this method.

The colorimetric method consists of spraying a solution of silver nitrate on to a split fractured concrete surface. The silver nitrate reacts with the chlorides ions showing the maximum depth of chloride penetration. A variation of the Fick's second law can be used to calculate the diffusion coefficient based on the maximum depth of chloride penetration (Poulsen, 1990 cited in Caré, 2008). In this case, the chloride content is not necessary, but the concentration limit of chlorides that can be observed by a solution of silver nitrate must be known.

The rapid chloride permeability test (ASTM C1202, 2010b) can also be used to determine the diffusion coefficient of specimens. During the test, chlorides are forced to pass through the specimens for a certain period of time by an electrical input. The total electrical charge that passes through the specimen provides an estimation of the chloride resistance of the material. Several works were developed to correlate empirically these results to the *diffusion coefficient*

[22] Refer to Section 6.3 for more information on the binding capacity.
[23] Either by immersion, ponding or inversion following the draft standard DD CEN/TS 12390-11 (2010) or by immersion only following the BS EN 13396 (2004) or the ASTM C1556 (2003).

(Yang, 2005; Yang and Wang, 2004; Andrade and Whiting, 1996; Andrade *et al.*, 1994) based on a modified version of Fick's second law, proposed by Andrade (1993). It is important to add that this test is not recommended for SFRC since fibres may create easy paths for the electrical charge to pass through the specimen thus influencing the results.

For the purpose of this study, the method used for the determination of the chloride content and coefficient of diffusion is the one based on the potentiometric titration (according to BS EN 14629, 2007c) due to the precision of the test.

3.2.2 Other Properties Affecting the Durability of Concrete

3.2.2.1 Porosity

Porosity is commonly expressed as a percentage of the volume of voids in the total volume of concrete. Common values are usually around 1% to 10% (Neville, 2003). Porosity alone is not responsible for the durability of concrete. It also depends on the interconnectivity of the pores and how effective they are in restraining the transport of aggressive agents (related to the tortuosity and hydraulic characteristics of the channels). A high porosity concrete with no connected pores can be a durable material. The large volume of voids, however, may considerably reduce the strength of concrete.

The voids in concrete, as already discussed previously, can be classified as gel, capillary or air pores. The porosity of concrete, however, is attributed to the amount of capillary, air entrained and trapped air pores (Neville, 2003). Air entrainer admixtures may be used to entrap non connected air bubbles inside concrete. This type of admixture is beneficial for situations where concrete is exposed to freeze-thaw attack (Powers, 1949; Snyder, 1998 and Chatterji, 2003 – see Section 3.1.3).

The influence of fibres in the porosity of concrete is still not clearly understood. As discussed in Section 2.3.2.1, the addition of high fibre contents may trap air due to reduced workability, which may increase the porosity of concrete. On the other hand, according to The Concrete Society (2004), fibres may reduce the porosity of concrete because they contribute to reducing bleeding of fresh concrete. Therefore, it is expected that no major changes in the porosity should occur when normal volumes of fibre content are added to the mix.

Test methods for porosity

Porosity of concrete is usually measured in terms of the total amount of water that a concrete specimen is able to absorb. The total volume of water absorbed is then considered to be the total volume of air voids of the concrete. Concrete specimens need to be preconditioned prior to the test to remove the evaporable water from the specimen. Two methods are commonly used to absorb water into the concrete pores: 1) vacuum saturation; 2) boiling and soaking.

In the vacuum saturation technique, specimens are first placed into a chamber to evacuate the air from the sample pores by using a vacuum pump. The samples are then submerged in water and the vacuum is released, and atmospheric pressure forces the water into the evacuated concrete pores. Usually a period of soaking is necessary, or sometimes vacuum is again applied while the specimens are fully immersed so as to force the water into the deeper capillaries. Some of the methods used to determine the porosity of concrete by vacuum saturation are described in ASTM C1202 (2010b), RILEM CPC 11.3 (1984) and the draft European standard DD CEN/TS 12390-11 (2010).

In the water absorption test by boiling and soaking, preconditioned specimens are immersed in water for a certain period of time until the specimens reach a constant mass (Figure 50a). The water is then heated and left to boil for another period of time. The boiling period, according to Wilson *et al.* (1999), is responsible for transforming the water in the pores into vapour which, due to pressure, expels the air from the concrete (Figure 50b). During the cooling period, the vapour will recover the water phase, thus reducing its volume and pressure (Figure 50c). The external water will then be forced into the concrete by atmospheric pressure, which fills the pores of concrete (Figure 50d). The test can be performed according to the ASTM C642 (2006b).

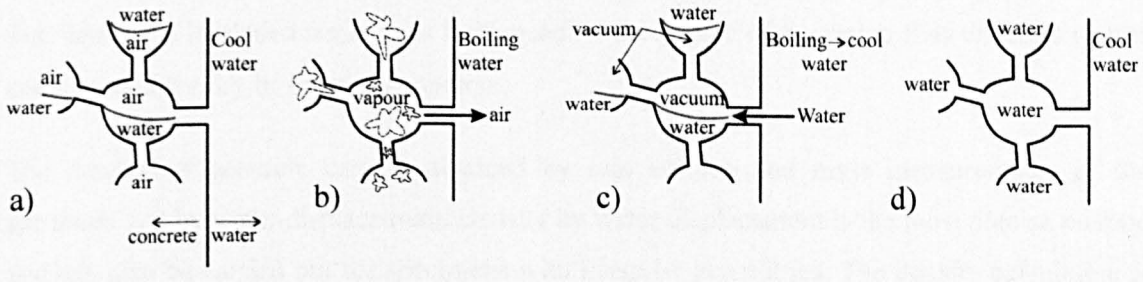

Figure 50 – Stages of water absorption by soaking and boiling.

The British Standards BS EN 12390-7 (2009d) and BS 1881-122 (1983) show procedures for determining the water absorption of concrete by soaking only. Because these standards are not specifically designed for the determination of porosity of concrete, and also because the method described is not very efficient in terms of filling the total amount of concrete permeable pores in

comparison with the previous methods, their results may be misleading and these tests will not be used in this thesis.

Both vacuum saturation and soaking and boiling seem to be efficient in terms of saturating the concrete pores. For practical reasons (availability of the vacuum equipment and reduced period of time to perform the test), the method used in this study to saturate the specimens is the one based on the vacuum technique.

3.2.2.2 Density

Density is another property that may provide an indication of the durability of concrete. The higher the density, the better is the expected concrete performance in terms of durability. For the same mix, a higher density concrete is an indication of a reduced amount of pores. According to Hover (2006), the density of concrete is related to the density of the materials used for the mix, the mix proportion, the compaction procedures and the degree of hydration, among others. At the macro level, concrete is expected to have a uniform density throughout its mass. Changes in density for a specific mix may represent segregation, lack of uniformity of the components and a different degree of consolidation.

Steel fibres are expected to increase the density of concrete due to the higher specific density of the steel compared to the other components of the mix. The change in density also depends on the influence that fibres might have on the pore structure of SFRC. For example, if the addition of fibres also traps air into the concrete, the amount of voids may compensate the extra weight added by the fibres.

Test methods for density

The density of hardened concrete is influenced by the degree of hydration thus different results can be found for dry or saturated concrete.

The density of concrete can be obtained by real volume and mass measurements of the specimen and by water displacement. Density by water displacement is the most precise method and can also be carried out for specimens with irregular geometries. The density calculation is based on the difference in values of the mass in air of the concrete specimen (at the desired saturation level) and the mass in water of the saturated concrete specimen. To saturate the specimens, the same procedures are used as for porosity (Section 3.2.2.1). Examples of standards used to calculate density of concrete are the BS 12390-7 (2009e), ASTM C642 (2006b) and the RILEM CPC 10.2 (1975).

3.2.2.3 Shrinkage

Shrinkage is the volume change in concrete normally associated with the movement of water out of the pores of concrete. However, it is also caused by carbonation and hydration of cement. The different processes that cause shrinkage are classified as: 1) plastic, 2) autogenous, 3) drying, 4) differential and 5) carbonation shrinkage (Neville, 2003).

Plastic shrinkage is caused by the rapid evaporation of water from the concrete surface when concrete is still in the plastic state (before it gains strength). It usually occurs in hot climates, low RH and windy regions (Neville, 2003). Cracks appear when the amount of evaporated water on the concrete surface is higher than the amount of water that comes to the surface due to bleeding. It can also be caused by suction from a dry base, such as soil. This type of shrinkage can cause deep cracks when concrete is restrained and is commonly noticed in concrete pavements.

Autogeneous shrinkage is caused by the consumption of the water in the concrete pores due to hydration of cement. This type of shrinkage is not related to the moisture movement inside concrete and is more accentuated in the very early ages of concrete, soon after concrete sets.

Drying shrinkage is a long-term process caused by the evaporation of capillary and adsorbed water in concrete pores, the latter being responsible for volume changes in concrete, part of them irreversible. Drying shrinkage is more accentuated at the early ages of concrete, due to the high amount of free water available at casting and from the lower amount of hydrated products. Drying shrinkage depends mainly on the size of the specimen, the water to cement ratio and the size and amount of aggregates (Neville, 2003). Large areas of exposed surfaces in relation to the volume of concrete increase the probability of water to evaporate. A higher amount of water in relation to the amount of cement means that a higher amount of free and adsorbed water is available for evaporation. A higher amount and larger size of aggregates can help limit drying shrinkage by physically restraining shrinkage. It should be noted that the term *drying shrinkage* is sometimes erroneously used by various authors to represent all the various types of shrinkage when concrete is exposed to a dry environment.

Differential shrinkage is a type of drying shrinkage caused due to moisture gradient in concrete surfaces, which may cause warping or curling of the element. In this case, the water in the pores, near the surfaces of the element exposed to environment, is more prone to evaporation than the water in pores located on the interior of the concrete, which tends to create tensile strain on the surface. The rest of the slab resists these tensile strains resulting in tensile stresses at the top and compressive stresses at the bottom. This type of shrinkage is commonly noticed in

concrete pavement slabs, due to the large surface area to volume of concrete compared to other structures (Zhang and Li, 2001).

Carbonation shrinkage, as already mentioned in Section 3.1.2 for the corrosion of fibres, occurs due to the combination of $Ca(OH)_2$ and C-S-H from the hydrated cement with CO_2 from the air forming, apart from water and other compounds, $CaCO_3$ which has larger volume than the original compounds of hydrated cement. This increases the weight and volume and reduces the porosity of the surface concrete, which leads to differential shrinkage between the exposed surfaces and the interior of the concrete.

Effects of fibres on shrinkage

Chern and Young (1989) and Tan *et al.*, (1994) report a decrease of free shrinkage strains due to the addition of steel fibres. Mangat and Azari (1984) attribute this fact to the interfacial bond strength between the fibres and the concrete matrix, which contributes to physically restraining shrinkage, as in the case of high amount of aggregates, for example.

Swamy and Stavrides (1979) say that the most significant effect of fibres in shrinkage is due to cracking control. According to ACI (1996), steel fibres act in three different stages to reduce shrinkage: 1) multiple cracks are formed instead of a single crack; 2) tensile stresses are transferred across cracks; 3) because they avoid macro-crack propagation, healing/sealing of the initial cracks may occur in the long-term.

Because plastic shrinkage can cause deep cracks in concrete pavements, it is important to understand the influence of fibres for this specific type of shrinkage. Wang *et al.* (2001) found out that plastic shrinkage can also be affected by changes in the pore structure of concrete caused by fibre addition, other than by limiting crack propagation. According to the authors, the addition of fibres increases the amount of larger pores compared to plain concrete, which reduces the capillary pressure and contributes to the reduction of bleeding and plastic shrinkage. The amount of coarser pores is most probably found on the interfacial zone between the fibres and the cement paste. Nevertheless, the same authors report that there must be a critical amount of larger voids that collaborate to reduce bleeding, otherwise, a large amount of coarser pores may increase plastic shrinkage. Thin and small fibres (e.g. polypropylene) tend to present a higher volume of interfacial zones compared to larger fibres such as steel. It is expected, in this case, that concrete with small fibres will present better performance in terms of plastic shrinkage than a plain concrete. However, better performance is expected from the larger fibres compared to the small ones. This is possibly because the concrete with small fibres seems to exceed the critical amount of large voids.

It is important to add that an increase in concrete pore diameter due to the addition of fibres, even though seems to be beneficial in reducing plastic shrinkage, may be responsible for higher drying shrinkage (as reported by Aly *et al.*, 2008 for polypropylene fibres) and may affect the durability by increasing the porosity and permeability of concrete.

Test methods for shrinkage of concrete

There are basically two different methods to determine the shrinkage resistance of concrete: free and restrained shrinkage tests. The free shrinkage test method allows the specimen to shrink without any external restraint. In this case, specimens do not crack. The restrained method is based on restraining the shrinkage movement of specimens so that tensile stresses can lead to cracking. The first measures the intrinsic shrinkage of concrete, and is influenced by several factors such as the mix proportion and environmental conditions. The second method, besides the mix proportion and the environmental conditions, is based also on the tensile strength and the capacity of concrete to avoid crack propagation. Due to the fact that fibres control cracking, the restrained method seems to be the most appropriate method to determine the influence of fibre addition on shrinkage.

Free shrinkage methods can be performed according to various standards, such as the BS EN 12617-4 (2002b), BS ISO 1920-8 (2009f), ASTM C490 (2009a) and ASTM C341 (2006c). The methods measure the length change of specimens subjected to drying after certain periods of time. The free shrinkage is then expressed in micro-strains.

Only few standards use restrained shrinkage tests and, as a result, different non-standard methods to perform the test can be found in the literature. The most known method is the ring test, which can be performed according to the ASTM C1581 (2009b). The method was first developed in 1965 (Malhotra, 1970) and relies on casting concrete around rigid steel rings. When concrete shrinks, it applies compression stresses on the ring that can be measured by recording the strains. In the literature, the dimensions of the steel ring and the concrete specimen vary (Malhotra, 1970; Swamy and Stravides, 1979; Grzybowski and Shah, 1990).

Another common method to measure restrained shrinkage uses a thin plate specimen restrained in two orthogonal directions (or in one single direction) and exposed to severe drying conditions. The main output of the method is the area of cracks or the average crack width formed due to the restrained condition. The method was initially proposed by Kraai (1985) and then slightly modified by Barluenga and Hernandez-Olivares (2007). The ASTM C1579 (2006d) can be used to perform this test. Plastic shrinkage effects can be clearly seen in this method by the large amount and size of cracks (depending on the characteristics of the mix).

Because the main output is in terms of crack width and area, and because no strains and stresses are measured, it is not considered as a very accurate method.

Another type of restrained shrinkage test utilises linear specimens. One of the manifestations uses linear specimens with anchored ends. In this test the output result is in terms of strains caused by shrinkage (Tongaroonsri and Tangtermsirikul, 2009). Linear specimens can also be allowed to shrink and then forced to their original position. In this case the stresses necessary to return the specimen after certain displacements are measured (Bloom and Bentur, 1995; Aly *et al.*, 2008). This type of test requires very precise load devices and displacement transducers. It also requires continuous monitoring to avoid the development of large strains which can cause the tensile strength to be exceeded at an early stage.

For the purpose of this research, only free shrinkage tests were performed due to the limited period of time for the research, and also to comply with the objectives of Ecolanes Project. The tests were performed according to the BS EN 12617-4 (2002b).

3.3 SUMMARY AND CONCLUSIONS

The main deterioration processes affecting the performance of concrete pavements were addressed in this chapter, followed by the main pore-structure related properties influencing the durability of the concrete.

Some of the main deterioration processes that affect the long-term performance of concrete pavements are caused by fatigue, corrosion and freeze-thaw.

Pavements are subjected to dynamic loads throughout their entire service life, which may lead to problems caused by fatigue. Besides the reduction in performance, fatigue may lead to cracks in the concrete, which are easy paths for the penetration of aggressive agents. The inclusion of fibres contributes to holding the cracks together, thus limiting/preventing their propagation. As a result, the fatigue life of concrete increases. However, it is important to note that, as concluded in the previous chapter, concrete pavements are not designed considering the post-cracking behaviour of the material and more work should be carried out in order to include the benefits of SFRC in the design guidelines. The provisions of TR 34 (The Concrete Society, 2003) for industrial floors account for the post-cracking behaviour of SFRC, however, it does not account for the fatigue behaviour of SFRC.

Corrosion in SFRC, according to many authors, is a chemical process that leads mainly to aesthetic issues, such as a rusty surface. Many authors agree that the ingress of chlorides into

concrete does not influence its performance since fibres do not get corroded at the same extend as for conventional rebars in RC. Nevertheless, the ingress of chlorides through the cracks may lead to corrosion of the fibres exposed to the fractured concrete, which could affect the performance of the material. This appears to be an important issue when dealing with recycled fibres due to the small diameter of the fibres.

Freeze-thaw process in SFRC is still largely to be studied. It is assumed that the main advantage of using fibres in concrete is due to cracking control. Since the stresses caused when water freezes lead to cracking of the concrete. The steel fibres may collaborate on holding the cracks together and decreasing the level of deterioration.

No studies have been carried out to understand the fatigue behaviour, the corrosion and the freeze-thaw process of concrete reinforced with recycled steel fibres, which encourages the studies performed in this thesis.

The pore structure of the concrete influences the durability of the material: large and connected pores lead to the easy access of aggressive agents into concrete, which speeds up various degradation processes.

The penetration of aggressive agents into concrete is governed by the transport mechanisms and the porosity of the material: 1) Corrosion is mainly influenced by diffusion of chloride ions or carbon dioxide into concrete, and also by sorptivity when the structure is subjected to non-saturated condition; 2) Freeze-thaw is influenced by the size of connected pores, permeability and sorptivity. Non-connected entrained pores contribute to reducing freeze-thaw damage and 3) Fatigue is influenced by the amount and size of pores. Large pores lead to potential initial micro-cracks in the concrete. These micro-cracks may easily propagate into meso and macro-cracks as the cycles are applied.

Aiming to understand the long-term performance of recycled SFRC, and also the effects of its pore-structure in the main deterioration processes of concrete pavements, an extensive experimental programme was carried out. The main motivation for the experimental programme was the lack of studies on the durability of recycled SFRC. The following chapter explains the main aspects of the experimental programme.

CHAPTER 4

4. DETAILS OF THE EXPERIMENTAL PROGRAMME

The full experimental programme was developed based on the variables shown in Table 7. An abbreviation is designated to each of the variables, which will later be used to compound the labels for the mixes used in the research.

Table 7 – Variables of the research.

Variable	Values	Abbreviation
Type of mix	Wet	W
	RCC	R
Cementitious material	80% CEM I[a] + 20% PFA[b]	CIP
	Low energy cement	LEC
Fibre content[d] and type	0% (plain)	0
	2% industrially produced	2I
	2% recycled	2R
	6% recycled	6R

[a] CEMI 42.5N – Portland Cement type I according to the BS 197-1 (2000a)
[b] Pulverised fly ash
[d] by mass of concrete

Conventional (wet) and RCC concrete were investigated in this thesis. The vast practical and academic knowledge on conventionally placed concrete for pavements motivated its use as a variable for this research, and also to fill-in the knowledge gaps, especially when recycled fibres are used. The use of RCC was encouraged due to the environmental benefits of this type of concrete (e.g. low amount of cement) and because of the high speed of construction when used for pavement applications.

The cementitious materials used in the study were chosen in an attempt to combine the use of recycled fibres with replacement cementitious materials, such as GGBFS (ground granulated blast furnace slag, commonly called *slag* only), which is the main constituent of LEC (low energy cement), and PFA.

Even though this research is focused on the use of recycled fibres as an alternative to plain and continuous reinforced pavements, industrially produced fibres were used to allow the comparison of the results, obtained with the recycled fibres, to a known type of reinforcement. The amount of 2%[24] (by mass) of industrially produced fibres was chosen since this is the content of fibres normally used in practical applications, and it is also a typical fibre content proposed by ACI (1996). The same amount of 2% (by mass) was used for recycled fibres to allow comparison between the two fibre types. The content of 6% was chosen because this is the maximum content of recycled fibres that can be added to the mix without reducing its performance (Angelakopoulos, 2007). It is also the amount that provides the most similar mechanical performance, in terms of post-cracking behaviour, as for 2% of industrially produced fibres, as it can be seen in Figure 51, which shows the bending load *versus* vertical displacement curve for mixes W-CIP-2I and W-CIP-6R. According to trial mixes developed for the EcoLanes project (Appendix A) at the USFD (Angelakopoulos, 2007), contents higher than 6% seem to cause balling and to trap excessive amounts of air, thus affecting the behaviour of the concrete. Plain concrete (no fibre addition) was used for comparison purposes.

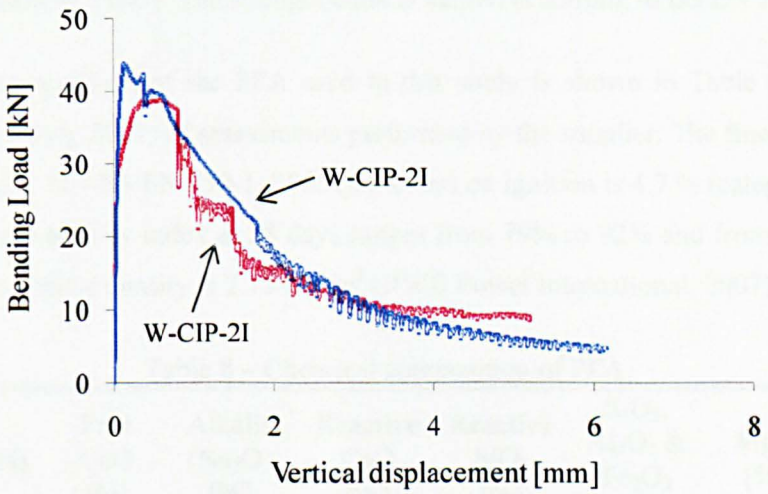

Figure 51 – Bending load versus vertical displacement curve for W-CIP-2I and W-CIP-6R.

This chapter deals with the details of the experimental programme carried out to investigate the long-term performance of concrete reinforced with recycled fibres. The chapter describes the materials, the mix proportions, the main variables and the methodology adopted for the experiments.

[24] 1% by mass of concrete is equivalent to approximately 0.3% by volume for a concrete with 2400 kg/m^3 of density. This varies according to the mix proportion and density of concrete.

4.1 DESCRIPTION OF MATERIALS

4.1.1 Cementitious Materials

Two cementitious materials were used: 1) combination of 80% of CEM I and 20% of PFA and 2) LEC. The CEM I, LEC and the PFA were supplied by Aggregate Industries (2010).

Although a full chemical analysis of both cement types is being performed, a complete set of data was not yet available at the time this thesis was submitted. Whilst more detailed information will be included in future publications, the typical constituents of the cements used in this study are summarised in the following.

CEM I basically consists of calcium silicates, aluminates, ferro-aluminates and sulphates. Other compounds are found in small amount, such as alkalis, lime, magnesia, chlorides and chromium. Secondary constituents may also be present in the chemical composition, such as PFA, limestone, clay and slag. The pH of this type of cement, when wet, can range from 11 to 14 (Paragon Materials, 2005). The strength class is 42.5N, according to BS EN 197-1 (2000a).

The chemical composition of the PFA used in this study is shown in Table 8, based on the monthly average (July 2007) of assessments performed by the supplier. The fineness of the PFA is 25.5% (category N – BS EN 450-1, 2005c), the loss on ignition is 4.7 % (category B – BS EN 450-1, 2005c), the activity index at 28 days ranges from 79% to 92% and from 85% to 97% at 90 days and the particle density is 2.15 Mg/m^3 (RWE Power international, 2007).

Table 8 – Chemical composition of PFA.

SO_2 [%]	Cl^- [%]	Free CaO [%]	Alkalis (Na_2O) [%]	Reactive CaO [%]	Reactive SiO_2 [%]	SiO_2, Al_2O_3 & Fe_2O_3 [%]	MgO [%]	Soluble phosphate [mg/kg]
0.85	0.007	0.24	2.7	3.3	30	83.6	1.8	9

LEC or cemroc® consists of slag, calcium sulphate, additives and secondary constituents. It has low heat of hydration, high resistance against acids and sulphates and also presents reduced risk for alkali-reactive aggregates. Corrosion protection is provided by a pH of around 12 (European Technical Approval, 2008).

4.1.2 Aggregates

4.1.2.1 Wet consistency mixes

The fine and coarse aggregates used for wet consistency mixes were fluvial dragged. The coarse aggregates have a NMSA of 10 mm, are rounded, fully water-worn or completely shaped by attrition (Figure 52a). The sand (Figure 52b) has a NMSA of 5 mm. The gradation curves for both coarse and fine aggregates are shown in Figure 53.

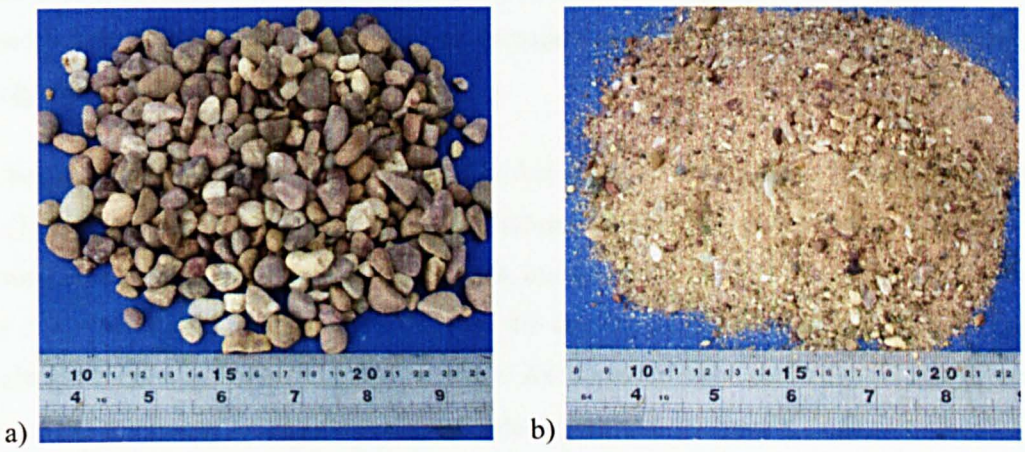

a) b)

Figure 52 – a) Coarse and b) fine aggregate used for wet consistency mixes.

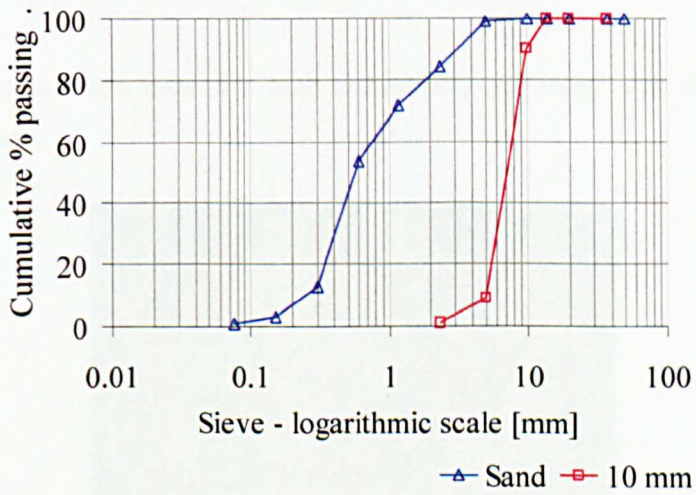

Figure 53 – Aggregate sieve analysis for wet consistency mixes.

Based on the recommendations of BS 12390-1 (2000b), the NMSA of the coarse aggregate should be at least 3.5 times smaller than the minimum size of the moulds. This is complied by all specimen geometries used. The recommendations of the JCI SF-4 (1984), however, say that the NMSA should not be larger than 2/3 of the fibre length. Even though the recommendations

of the JCI SF-4 (1984) are not complied by the recycled fibres, the same aggregates were used for both industrially produced and recycled fibres for comparison purposes.

4.1.2.2 Dry consistency mixes

The aggregate skeleton of RCC is comprised of fine and coarse aggregate, with a NMSA of 14 mm (Figure 54). The NMSA was limited to 14 mm to reduce the potential for segregation during production and placement, as well as to facilitate placing operations and improve surface texture (PCA, 2010b; ACI, 1995, 1999 and 2002). The RCC aggregate used was obtained from crushed basalt. The use of crushed aggregates improves the quality of bond between the paste and aggregate (Koutselas, 2007).

Two bounds for gradation curves were used in this study, one following the limits proposed by ACI (1995) and one as used by Aggregates Industry in the UK, as shown in Figure 55. The gradation *curve 1* was used for most of the tests, except for the fatigue test. The aggregates from *curve 1* were provided in bags of 500 kg and the amount of material required for the castings was always randomly collected from the bags. As it can be seen in the figure below, *curve 1* followed the minimum ACI (1995) recommended gradation. A specific gradation (*curve 2*) that lies in the middle of the UK bounds was adopted for the specimens tested for fatigue. Due to the high variability expected in these results, the aggregates were classified appropriately for each batch.

The same aggregates were used for both industrially produced and recycled fibres for comparison purposes.

Figure 54 – Aggregate used for dry consistency mixes.

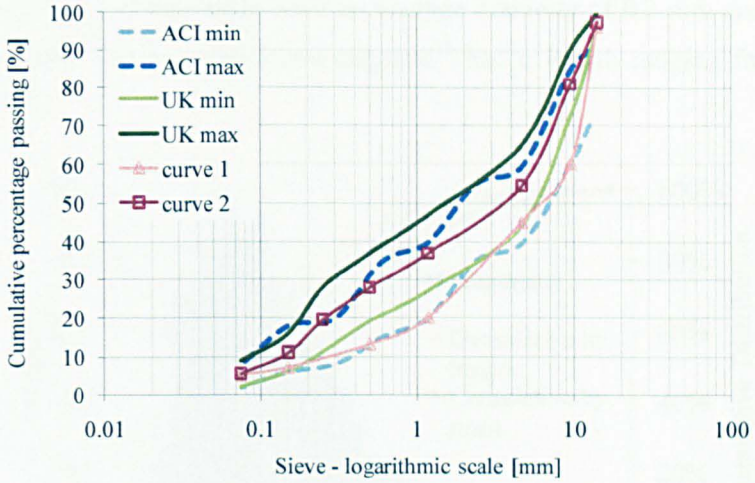

Figure 55 – Aggregate sieve analysis for dry consistency mixes.

4.1.3 Fibres

Two types of steel fibres were examined: one type of recycled and one type of industrially produced steel fibre, and their characteristics are described below.

4.1.3.1 Recycled steel tyre-cord fibres

Steel tyre-cord fibres, produced from the mechanical treatment (e.g. shredding and granulation) of post-consumer tyres, have high variability in length and diameter. In order to use the steel from post–consumer tyres as concrete reinforcement, steel tyre-cord fibres need to pass through a post treatment to remove rubber particles and other residues and to minimize irregularities in geometry (Figure 56). Sieving is required to give the specific length range that contributes to the good performance of concrete (usually around 15-25 mm – USFD, 2001). Section 2.2.3.2 provides more information on the process used to obtain recycled fibres.

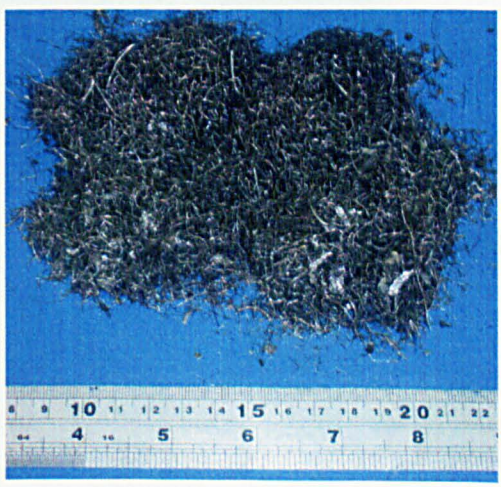

Figure 56 – Sorted steel tyre-cord fibres.

The recycled fibres used in this study have an average diameter of 0.2 mm and tensile strength of around 2000 MPa. The recycled fibres supplied[25] had a length ranging from 4-22 mm, as shown in Figure 57.

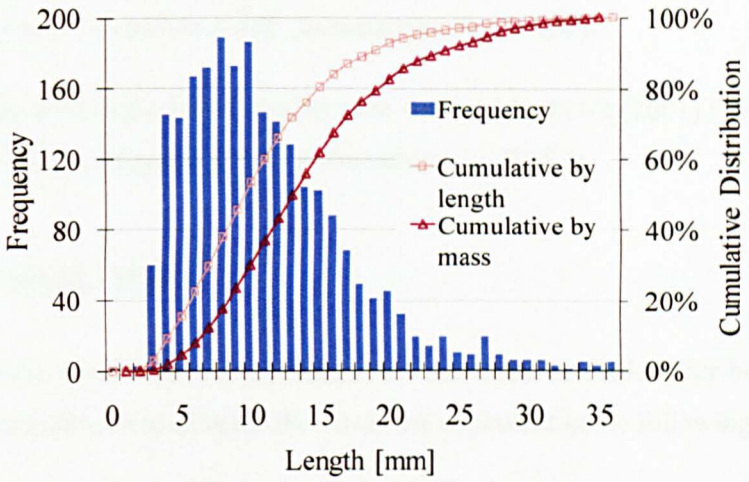

Figure 57 – Length distributions of recycled fibres.

4.1.3.2 Industrially produced steel fibres

The industrially produced fibre used in the experiment is a loose cold-drawn wire fibre (type I according to BS EN 14889-1, 2006a; ASTM A820, 2006a and ABNT NBR 15530, 2007a and type II according to JCI SF-4, 1984 – see Table 2) with a conical head at each end (head diameter ≥ 1.8 mm and cone angle of 60°, as shown in Figure 58). The fibre length is 54 mm and the diameter is 1.0 mm, with tensile strength of around 1100MPa. The fibres were supplied by Arcelor Mittal with the commercial name TwinCone® (ArcelorMittal, 2008).

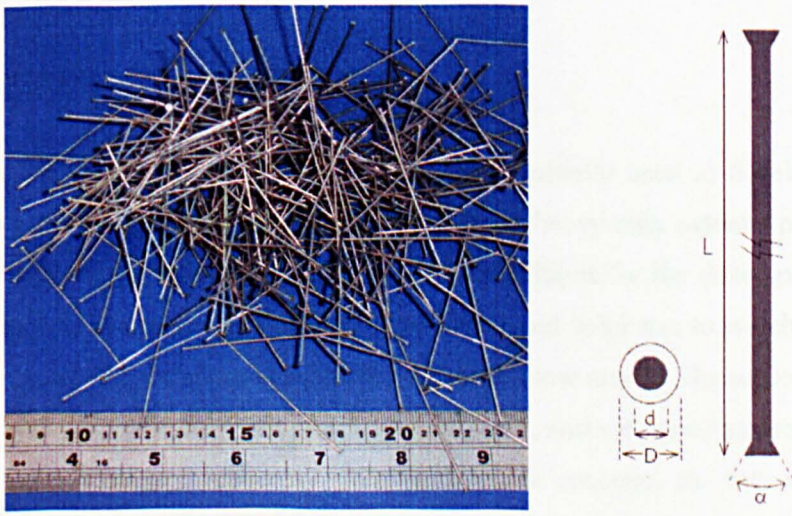

Figure 58 – Industrially produced steel fibres.

[25] The recycled fibres were supplied by ADRIA (Adriatica Riciclaggio e Ambiente) Abruzzo SRL for the EcoLanes Project (Appendix A).

4.1.4 Admixtures

The superplasticiser used was an aqueous solution based on polycarboxylic ether polymers complying with the BS EN 934-2 (2001) (BASF, 2008). The commercial name of the superplasticiser was Glenium Sky 546® (manufactured by BASF).

The air-entraining admixture used complies with the BS EN 934-2 (2001) (BASF, 2008), with the commercial name of Microair 103® (manufactured by BASF).

4.2 MIX PROPORTIONS

The mix proportions used to cast the specimens are presented in Table 9, for both wet and RCC mixes. The procedures used to develop the mixes are explained in the following subsections.

Table 9 – Mix proportions used for wet and dry consistency mixtures (nearest 5 kg/m^3).

Mix type	Cementitious material	Fibre content and type	Cement [kg/m^3]	PFA [kg/m^3]	Aggregate [kg/m^3]	Water [kg/m^3]	w/c	c/a[b]
Wet[a]	CIP	0, 2I, 2R, 6R	305	75	830 (fine); 1000 (coarse)	135	0.35	0.21
Wet[a]	LEC	0, 2I, 2R, 6R	380	-		135	0.35	0.21
RCC	CIP	0, 2I, 2R	240	60	2125	150	0.50	0.14
RCC	CIP	6R	240	60	2100	155	0.52	0.14
RCC	LEC	0, 2I, 2R	300	-	2090	160	0.53	0.14
RCC	LEC	6R	300	-	2070	170	0.57	0.15

[a] admixtures were also used - 0.135% of air-entrainment agent and 0.7–1.6% of superplasticiser, both by mass of cementitious material

[b] ratio of cementitious material/aggregate

4.2.1 Wet consistency mix

The recommendations of the BS 8500-1 (2006e) were initially used to develop a designated *PAV2* mix which is an accredited mix that can be used for heavy-duty external paving for rubber tyre vehicles. The standard considers environmental conditions for the development of the mix proportions, such as the level of chlorides, carbonation and sulphates to which the structure is subjected and also if the structure is subjected to freeze-thaw attack. The recommendations are valid for conventional reinforced and prestressed concrete, and are therefore specific for a given cover. Since steel fibres are randomly distributed inside concrete, the mix was designed to comply with the minimum cover requirement (15 mm) of the standard.

The levels of aggressivity adopted were based on a region located near Sheffield, UK, and are shown in Table 10. The table also presents the durability recommendations[26] proposed by BS 8500-1 (2006e) according to each aggressivity level. Chemical attack due to sulphates was not considered since it may vary considerably according to the exact area designated for the structure. The recommendations can be applied to Portland cement with up to 20% PFA (II-A according to BS 8500-1, 2006e) and to sulphate-resisting Portland cement (SRPC). Since BS 8500-1 (2006e) does not account specifically for LEC, the SRPC recommendations were considered to be the most appropriate to represent the LEC.

Table 10 – Exposure classes and durability recommendations adopted for the wet mix design.

Environmental action	Exposure class (according to Table A.1 of BS 8500-1, 2006e)	Maximum w/c ratio	Minimum cement content [kg/m^3]	Minimum concrete class
Corrosion induced by carbonation	XC3 or XC4 – moderate humidity or cyclic wet and dry	0.45	340	C40/50[a]
Corrosion induced by chlorides other than from sea water	XD3 – Cyclic wet and dry	0.35	380	C45/55[a]
Corrosion induced by chlorides from sea water	XS1 – Exposed to airborne salt but not in direct contact with sea water	0.35	380	C45/55[a]
Freeze-thaw attack[b]	XF4 – High water saturation with de-icing agent or sea water	0.55	340	C28/35[a]

[a] Means the compressive strength (MPa) for cylinders (first value) and cubes (second value).
[b] For the freeze-thaw attack, a minimum of 5.5% of air content is also recommended for mixes with NMSA equal to 10 mm.

Based on Table 10, the cement content and the w/c ratio were established as 380 kg/m^3 and 0.35, respectively, with a minimum air content of 5.5%. The target characteristic compressive strength was C45/55 (the corresponding mean compressive strength is 53 MPa and 63 MPa[27], for cylinders and cubes, respectively – see also Table 15 for experimental results).

The total amount of aggregates (fine and coarse aggregate) was obtained based on a volumetric calculation. This was because the BS 8500-1 (2006e) does not provide information for the design of mix proportions other than the cement content, w/c ratio and strength. The proportion of fine and coarse aggregate was then calculated considering the methodology proposed by the

[26] In terms of w/c ratio and minimum cement content. The expected class of the concrete, in terms of compressive strength, is also given. The durability recommendations shown in Table 10 are valid for an intended working life of 50 years.
[27] According to Eurocode BS EN 1992-1-1 (2004).

Building Research Establishment (BRE, 1997). The method requires information on the NMSA, the gradation curve of the fine aggregate, the w/c ratio and the intended slump of the mix (according to BS 8500-1, 2006e, the slump for the designated PAV2 mix should range from 50 to 90 mm).

An air-entrainment agent was used to achieve the minimum of 5.5% air content. The amount of air-entrainment was determined experimentally by the pressure gauge method (BS EN 12350-7, 2009e). Superplasticiser was added to obtain a slump ranging from 50-90 mm. The amount of superplasticiser varies according to the amount and type of fibres and to the type of cement used.

4.2.2 Dry consistency mix

The RCC mix proportion was initially based on typical mixes used by the UK industry and on trials developed for the EcoLanes Project (Angelakopoulos, 2007). Since the RCC mix has lower cement content and reduced amount of water compared to the wet mix (total amount of materials), the durability recommendations of the BS 8500-1 (2006e), for minimum cement content and w/c ratio cannot be applied for RCC. Nevertheless, the target strength class assumed for wet mixes (C45/55) was followed.

The mix proportion for RCC was developed as follows: 1) the cement content was fixed to 300 kg to provide the target strength of C45/55; 2) six percentages (by mass) of water content were selected for trial mixes – ranging from 4 to 9% –, based on typical values normally used by the industry; and 3) the amount of aggregates for each water content was then obtained by volumetric calculation.

Volumetric calculation is based on the expression shown in Equation 13.

$$\frac{m_c}{\gamma_c} + \frac{m_{fa}}{\gamma_{fa}} + \frac{m_{ca}}{\gamma_{ca}} + \frac{m_w}{\gamma_w} = 1 \qquad (13)$$

Where:

m_c, m_{fa}, m_{ca}, m_w = mass of cement, fine aggregate, coarse aggregate, water, respectively [kg]

γ_c, γ_{fa}, γ_{ca}, γ_w = specific gravity of cement, fine aggregate, coarse aggregate, water, respectively [kg/m^3]

Equation 13 can be adjusted when other materials are added to concrete, by adding an extra term to the left side of the equation. For example, $\frac{m_x}{\gamma_x}$, where m_x is the mass and γ_x is density of the extra material added to the mix.

It is important to note that the RCC aggregate comprised of both fine and coarse aggregate in a single gradation curve (see Section 4.1.2.2). All six trial mixes with water content ranging from 4 to 9% were batched and their bulk and dry densities measured according to the procedures of BS 1377-4 (1990). This standard applies for tests on compacted soils and was used due to the lack of European standards to measure the density of fresh RCC (in the U.S. some standards exist for the measurement of RCC density – PCA, 2004; ASTM C1435, 2008b) .

The already mixed RCC constituents are compacted into a standard cylindrical mould measuring 150 mm in diameter and 180 mm in height. The compaction is done in three layers using an electric hydraulic hammer[28] (Figure 59). The height of the concrete is measured and the mould and the compacted concrete are weighted. The weight of the empty mould is also recorded.

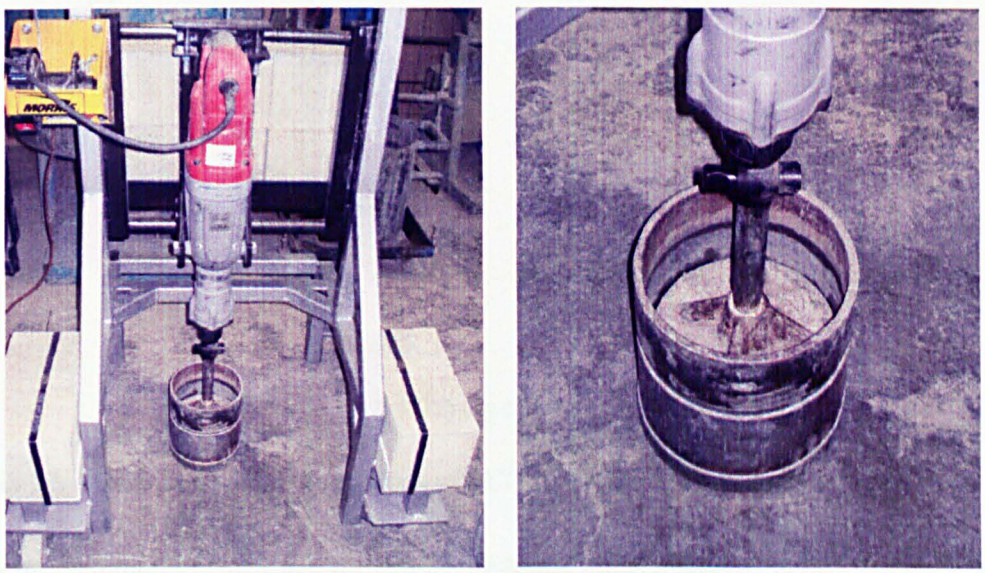

Figure 59 – Apparatus used for RCC compaction (frame developed at USFD) [Angelakopoulos, 2011].

The bulk ρ_b and the dry ρ_d densities [kg/m^3] are calculated according to Equations 14 and 15, respectively.

$$\rho_b = \frac{(m_2 - m_1)}{Ah} \times 1000 \quad (14)$$

Where:

m_2 = mass of the mould and concrete [g]

m_1 = mass of the mould [g]

[28] The Kango 900K hammer used for the experiments weighs 11 kg and has 27 J blow energy. The load rate applied by the hammer varies from 975 to 1950 bpm. The hammer is equipped with anti-vibrating system in all handles (Milwaukee, 2010).

A = circular area of the mould [mm^2]

h = height of the compacted sample [m]

$$\rho_d = \frac{100\rho_b}{100+w} \quad (15)$$

Where:

w = moisture content of the concrete [%]

This procedure was carried out for both types of cement and the results for bulk and dry densities are shown in Figure 60a, for the CEM I + PFA, and in Figure 60b, for the LEC. The figure shows that 6% of water content gives the highest dry density for the CEM I + PFA mix, while the 7% of water content gives the highest density for the LEC mix.

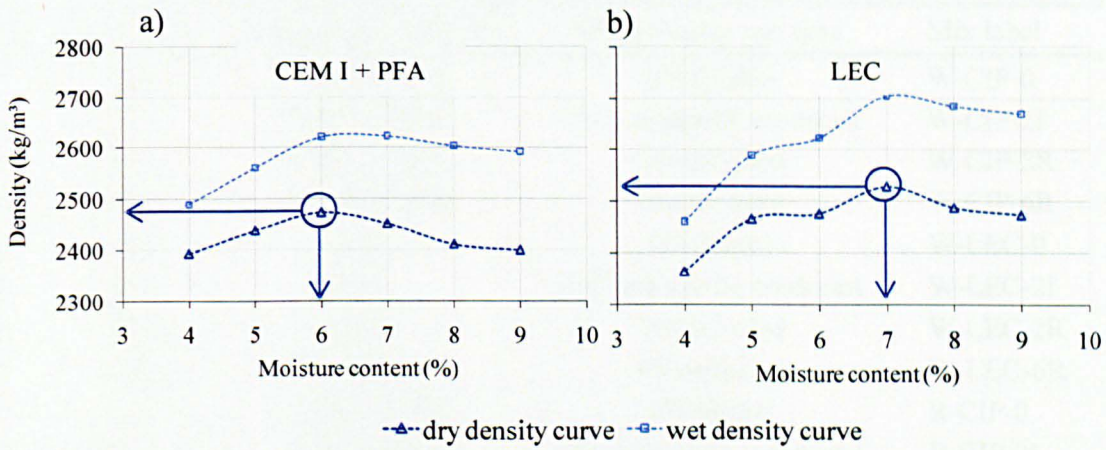

Figure 60 – Bulk (wet) and dry densities of RCC for water contents ranging from 4% to 9%.

The reduced amount of water in the CEM I + PFA mix may be due to the fact that PFA particles are spherical in shape and also have lower specific gravity than CEM I and ground granulated blast furnace slag – GGBFS – (main component of LEC), which gives better workability of the mix, resulting in a reduction in the amount of water.

However, practical problems were noticed when 6% of water content was used for the casting of cubes and prisms for the CEM I + PFA plain mix, such as difficulty in compaction and irregularities on the surface after casting. Based on laboratory practical experience, the amount of water content for the CEM I + PFA mix was altered to 6.4%.

The addition of 2% (both industrially produced and recycled) of fibres did not affect the compaction and the surface appearance of the specimens. The amount of 6% recycled fibres affects slightly the appearance and compaction of the specimens, therefore an extra 0.4% of water was added to the mixes with such fibre content.

4.3 VARIABLES OF THE RESEARCH

The experimental programme can be divided into three main parts: 1) properties of control specimens (e.g. mechanical, density, porosity and free shrinkage); 2) transport mechanisms and 3) durability issues that may affect the long-term performance of SFRC pavements (e.g. corrosion, freeze-thaw and fatigue). Each part of the experimental programme has its own variables, and they were therefore split into the subsequent subsections.

The variables used are based on the main variables previously shown in Table 7. In total, sixteen mixes were studied. Table 11 shows the description of the mixes, including the labels adopted following the abbreviations given in Table 7.

Table 11 – Description of the mixes.

Mix	Type of mix	Cementitious material	Fibre content and type	Mix label
1	Wet	CEM I + PFA	0% (plain)	W-CIP-0
2	Wet	CEM I + PFA	2% industrially produced	W-CIP-2I
3	Wet	CEM I + PFA	2% recycled	W-CIP-2R
4	Wet	CEM I + PFA	6% recycled	W-CIP-6R
5	Wet	LEC	0% (plain)	W-LEC-0
6	Wet	LEC	2% industrially produced	W-LEC-2I
7	Wet	LEC	2% recycled	W-LEC-2R
8	Wet	LEC	6% recycled	W-LEC-6R
9	RCC	CEM I + PFA	0% (plain)	R-CIP-0
10	RCC	CEM I + PFA	2% industrially produced	R-CIP-2I
11	RCC	CEM I + PFA	2% recycled	R-CIP-2R
12	RCC	CEM I + PFA	6% recycled	R-CIP-6R
13	RCC	LEC	0% (plain)	R-LEC-0
14	RCC	LEC	2% industrially produced	R-LEC-2I
15	RCC	LEC	2% recycled	R-LEC-2R
16	RCC	LEC	6% recycled	R-LEC-6R

4.3.1 Pore Structure-related Properties of Concrete and Transport Mechanisms

The properties of the concrete investigated in this study include the mechanical properties (compressive and flexural behaviour), density, porosity and free shrinkage. The transport mechanisms studied are the permeability, sorptivity and diffusivity.

All the 16 mixes described in Table 11 were used to investigate the properties and the transport mechanisms, except for the free shrinkage test. Only one type of cementitious material (LEC)

was used for shrinkage, which means that only mixes 5-8 and 13-16 were analysed. The initial plan was to analyse both types of cementitious materials, however, this was not possible due to the limited time of this research.

It is important to add that the effect of the preconditioning temperature was also examined for the properties and transport mechanisms that require preconditioning prior to the test, such as porosity, density, permeability and sorptivity (see Section 3.2). Permeability, porosity and density were measured in specimens preconditioned at 105 °C, 80 °C and 50 °C, while sorptivity tests were performed in specimens dried at 80 °C and 50 °C only. More details about the preconditioning procedures and the temperatures used can be found in Section 4.4.3.1.

4.3.2 Durability Issues

The durability issues studied in this research are fatigue, corrosion and freeze-thaw. These issues seem to be the most important and frequent causes of damage in SFRC pavements. Other causes of deterioration, such as the sulphate attack (e.g. thaumasite), erosion, abrasion, corrosion by carbonation and alkali-silica reaction, were not investigated in this thesis due to limitation of time. The fact that this research was undertaken during Ecolanes Project also contributed to restrict the issues investigated in order to fulfil the main objectives of the project.

Fatigue in SFRC is a type of deterioration caused by cyclic loads and, contrary to corrosion and freeze-thaw, it is not directly related to the pore structure of concrete. It is, however, associated to the ability of fibres to limit/avoid crack propagation. Nonetheless, cracks formed due to fatigue, apart from reducing the performance of concrete, may contribute to the easy access of aggressive agents through the concrete (e.g. water and chlorides) which may lead to other types of pore structure-related deterioration, such as corrosion and freeze-thaw.

The same variables used for the pore structure properties were used to examine the influence of the durability issues in the long-term performance of SFRC. However, due to the limited period of time of the research, not all 16 mixes were investigated. The variables were defined individually for each durability issue tested, as described in the following sections.

4.3.2.1 Flexural fatigue

The fatigue effects were evaluated according to the variables described in Table 12. Due to the variability usually encountered in fatigue tests (Singh *et al.*, 2005a and 2008), a high number of specimens is required for each stress ratio analysed. Based on that, it was decided that only one type of cementitious material is used in the experiments. It is expected that the cement type

influences the bond strength between fibres and concrete (thus affecting fatigue), however, for the purposes of this research, this effect was considered not to be as important as the type of mix and the addition of different recycled fibre contents.

Table 12 – Variables used to investigate fatigue.

Variable	Values
Type of mix	Wet
	RCC
Cementitious material	80% CEM I + 20% PFA
Fibre content[a] and type	0% (plain)
	2% industrially produced[b]
	2% recycled
	6% recycled
Stress ratio	0.5
	0.7
	0.9

[a] by mass of concrete
[b] only used for RCC mixes

Still aiming to reduce the number of specimens, the industrially produced fibres were used only for the RCC mixes, which still allows a comparison between recycled and industrially produced fibres.

In summary, the mixes used to investigate fatigue were 1-4, 9 and 11-12.

The stress ratio of 0.5 was chosen because it is usually the maximum stress at which concrete pavements are subjected to in reality (based on the fact that the endurance life of concrete pavements tends to infinite when values lower than 0.5 are considered). The stress ratios of 0.7 and 0.9 were chosen based on the common stress ratios normally used to evaluate the effects of fatigue in SFRC (Chang and Chai, 1995; Mailhot *et al.*, 2001; Singh and Kaushik, 2001 and 2003; Lee and Barr, 2004; Singh *et al.*, 2005a and 2008).

4.3.2.2 Corrosion

Corrosion was investigated using the variables presented in Table 13. Corrosion was simulated in SFRC specimens through wet-dry cycles (described in Section 4.4.7). Corrosion, even if accelerated, is a long-term process and utilises a lot of space resource and for this reason the number of mixes was reduced compared to the pore structure-related properties. Since plain concrete is not likely to suffer from corrosion, it was not used as a variable for corrosion. Only

one content of recycled fibres was used. The amount of 6% recycled fibres was chosen because this is the amount that provides similar mechanical performance in terms of ductility as for 2% industrially produced fibres (Angelakopoulos, 2007).

Table 13 – Variables used to investigate corrosion.

Variable	Values
Type of mix	Wet
	RCC
Cementitious material	LEC
	80% CEM I + 20% PFA
Fibre content[a] and type	2% industrially produced
	6% recycled
Months of corrosion simulation	5
	10
Temperature of solution for corrosion simulation	20 °C
	40 °C[b]
Cracked or not cracked	Cracked[b]
	Not cracked
Output result	Residual compressive strength
	Residual flexural strength

[a] by mass of concrete
[b] only used for specimens cast with RCC, CEM I + PFA and 6% recycled fibres

It is expected that the type of mix and the type of cementitious material influence the pore structure of the concrete, and for this reason, were kept as variables for corrosion.

The mixes analysed for corrosion were 2, 4, 6, 8, 10, 12, 14 and 16 (see Table 11).

Tests to understand the effects of corrosion in SFRC are not commonly used and, as a consequence, no standards were so far developed to perform the tests. This makes it difficult to choose the most appropriate technique to perform the tests, up to a certain deterioration level. For the purpose of this research, the specimens were subjected to 5 and 10 months of wet-dry cycles, following the procedures adopted by Kosa and Naaman (1990).

The temperatures of 20 °C and 40 °C were used as variables for corrosion. In addition, the effect of corrosion through cracks is examined. To evaluate the influence of these variables, only one mix was chosen (RCC with 6% recycled fibres and CEM I + PFA). The temperature was applied to the chloride solution in which the specimens were immersed during the wet phase of the cycles. Notched cracked specimens were subjected to static flexural strength (pre-cracking)

test (see Section 4.4.7) prior to the beginning of the corrosion cycles. The flexural test was carried out to induce a crack width of approximately 0.2 mm.

Two types of outputs are required: residual[29] compressive and flexural strength after corrosion simulation. As a result, both cubes and prisms were cast.

4.3.2.3 Freeze-thaw

The variables used to study the effects of freeze-thaw are shown in Table 14. Both wet and RCC mixes were investigated, since the type of mix is expected to affect the pore structure of the material, thus affecting freeze-thaw. The initial plan was to investigate both types of cementitious materials; however, due to the technical problems encountered with the freeze-thaw facility (cooling system was not working properly), just one type of cementitious material was able to be studied. In addition, the mix with 2% recycled fibres was not analysed due to the same reason as for corrosion.

Table 14 – Variables used to investigate freeze-thaw.

Variable	Values
Type of mix	Wet
	RCC
Cementitious material	LEC
Fibre content[a] and type	0% (plain)
	2% industrially produced
	6% recycled
Output result	Loss of mass
	Visual analysis
	Residual compressive strength
	Residual flexural strength

[a] by mass of concrete

The mixes analysed for freeze-thaw were 5, 6, 8, 13, 14 and 16.

The residual[29] compressive and flexural strengths were obtained after freezing and thawing cycles and, for this reason, both cubes and prisms were cast. More information about the methodology used can be found in Section 4.4.8.

[29] For the purpose of this study, *residual* strength is defined as strength obtained after exposure to accelerated deterioration tests (both corrosion and freeze-thaw).

4.4 TESTING – METHODOLOGY

This section first explains the casting procedures used to make the concrete specimens and the procedures to investigate the mechanical performance of concrete. It also describes the methodology used for each test to assess the long-term performance of SFRC, the geometry of the specimens and the main calculations involved for the tests.

4.4.1 Casting of Specimens

The casting of the specimens was undertaken at the Structures Laboratory of the USFD. The casting procedure involved three main stages: 1) batching of materials; 2) mixing and placing of concrete and 3) curing.

The curing procedures were the same for both wet and dry mixes. Specimens were demoulded 24h after casting and cured in a mist room with controlled temperature and humidity (20 °C ± 2 °C and RH ≥ 95%) for a period of 28 days (according to BS EN 12390-2, 2000c), unless otherwise specified.

Different procedures were used for batching the materials, mixing and placing of wet and dry consistency mixes, as described below.

4.4.1.1 Batching, mixing and placing of wet consistency mix

The materials used for wet mixes were weighted and left in the mixing room with ambient temperature (20 ± 5 °C) usually at least 24h before casting to allow all the materials to reach room temperature.

The dry materials (aggregates and cementitious) were mixed in a pan mixer for a period of 60 seconds and 80% of the water and superplasticiser was then added to the mix in 30 seconds. The materials were mixed for 60 seconds, after which the fibres were manually dispersed with the mixer in operation. The mixer was stopped to clean off all the adhered materials on the mixer blades into the pan. The remaining water was then added to mix together with the air entrainment agent for over a period of 30 seconds. Mixing of concrete continued for 30 more seconds. The total mixing time was at least 3 minutes and 30 seconds.

The workability of the fresh concrete was measured by the slump test (BS EN 12350-2, 2000d). Even though the method is not the most appropriate for SFRC, the method was used due to its simplicity and popularity. The air content was measured following the BS EN 12350-7 (2009e)

by the pressure gauge method. Figure 61 shows the slump test and the equipment used to measure the air content of wet mixes.

Figure 61 – Slump test and equipment used to measure air content of fresh wet concrete.

After performing the workability test, the concrete used for the slump test was remixed with the remaining concrete for 15 seconds, while the concrete used for the air content test was disposed of.

Before placing the concrete into the moulds, the inner surfaces of the moulds were covered with a thin layer of demoulding material to prevent the concrete from adhering to the surfaces. The concrete was then placed into the moulds and compacted according to the following methods:

- Cubes and cylinders: vibrating table.
- Prisms: internal vibrator.

Both methods follow the recommendations of the BS EN 12390-2 (2000c). Prisms and cubes were compacted in two layers while cylinders were compacted in three layers. After compaction, the surface of the specimens was levelled by trowels and the specimens were covered with hessian and plastic sheets to protect them from dehydration. Specimens were kept in the moulds for 24h until demoulding.

4.4.1.2 Batching, mixing and placing of dry consistency mix

Because there is no specific standard for casting RCC, the procedures adopted for batching, mixing and placing of dry concrete are based on experimental trials and on the wet mix specifications, when applicable.

The materials for the RCC mixes were weighted 24h before mixing to allow the materials to reach room temperature. The water was added to the aggregates 24h before mixing to allow good lubrification of the aggregates, and the mixture of water and aggregates was put in air tight containers to prevent evaporation.

The cementitious material was added to the mixture of aggregates and water and all the materials were mixed for 3 minutes in a pan mixer. For FRC, fibres were dispersed manually after 1.5 minutes of mixing, with the mixer in operation. After dispersing the fibres, all the materials were mixed for an extra half minute.

The inner surfaces of the moulds were covered with demoulding material to prevent the concrete from adhering to the mould surfaces. The compaction was made by a hydraulic hammer as already mentioned in Section 4.2.2. The hammer was connected to a device developed to minimise user exposure to vibration. Prisms, cubes and cylinders were compacted in three layers. Figure 62a shows the compaction of RCC prisms with the hydraulic hammer and Figure 62b shows the compaction stages of RCC.

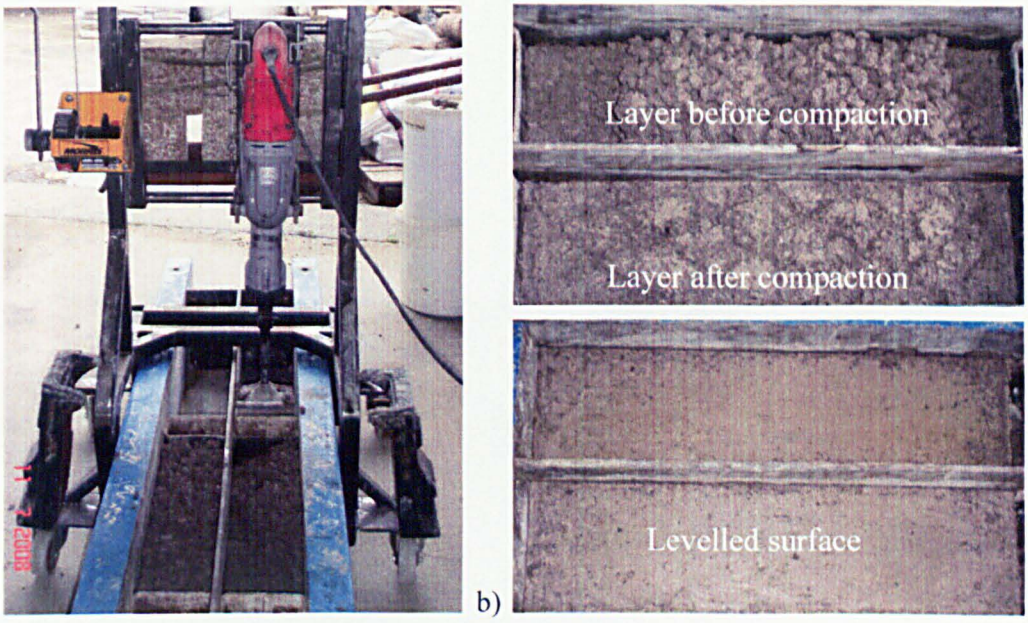

Figure 62 – Compaction of RCC.

After the compaction of the third layer, an extra thin layer of concrete was added to level the surface. A flat steel plate was put over the mould and compacted against the specimen by the hydraulic hammer. After compaction and surface levelling, the specimens were covered with hessian and plastic sheets to protect them from dehydration. Specimens were kept in the moulds for 24h until demoulding.

4.4.2 Mechanical Properties

It is not uncommon to find durability specifications for concrete in terms of mechanical performance, especially regarding its compressive strength. Based on that, the mechanical performance of concrete was used as an output parameter for some of the durability issues investigated in this study (corrosion and freeze-thaw). Some of the output results for these durability issues are the residual compressive and flexural strengths after exposure to accelerated damage. The mechanical performance of non-damaged[30] concrete was tested at the age of 28 days for comparison purposes. The procedures to determine the compressive and flexural strength are described below.

4.4.2.1 Compressive strength

The compressive strength was determined following the recommendations of BS EN 12390-3 (2009g). An automatic compression testing machine with maximum capacity of 3000kN was used to perform the tests (Figure 63).

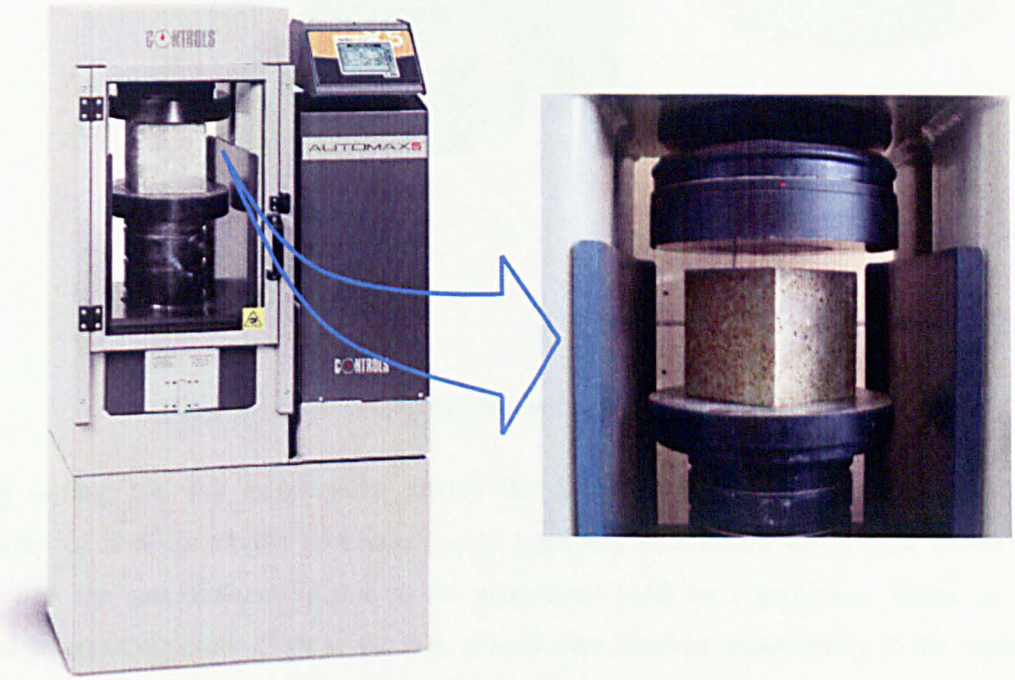

Figure 63 – Testing machine used for compressive strength test.

Cubes measuring 150 mm were used for all the tests. The specimens were centred to the lower platen of the testing machine always keeping the trowelled face of the specimens parallel to the direction of the load. This prevents results to be influenced by possible irregularities on the

[30] Non-damaged specimens were cast and cured for 28 days, and were not subjected to any deteriorative process, such as fatigue, corrosion and freeze-thaw.

trowelled surface. The load was applied at a constant rate of 0.4 MPa/s, in accordance to BS EN 12390-3 (2009g).

4.4.2.2 Flexural behaviour

The flexural strength test of concrete was performed in a third-point configuration, otherwise following the recommendations of RILEM TC-162 TDF (2002). Prisms measuring 150 x 150 x 550 mm were subjected to the loads shown in Figure 64. Three linear variable displacement transducers (LVDTs), held by a yoke[31], were used to measure the vertical displacement (one on each side) and the CMOD. The load applied was controlled by CMOD displacement, as suggested by RILEM (2002). The load rate was 50 μm/min for CMOD ranging from 0 to 0.1 mm and 200 μm/min for CMOD higher than 0.1 mm. The displacements and the load were recorded by a Orion data logger.

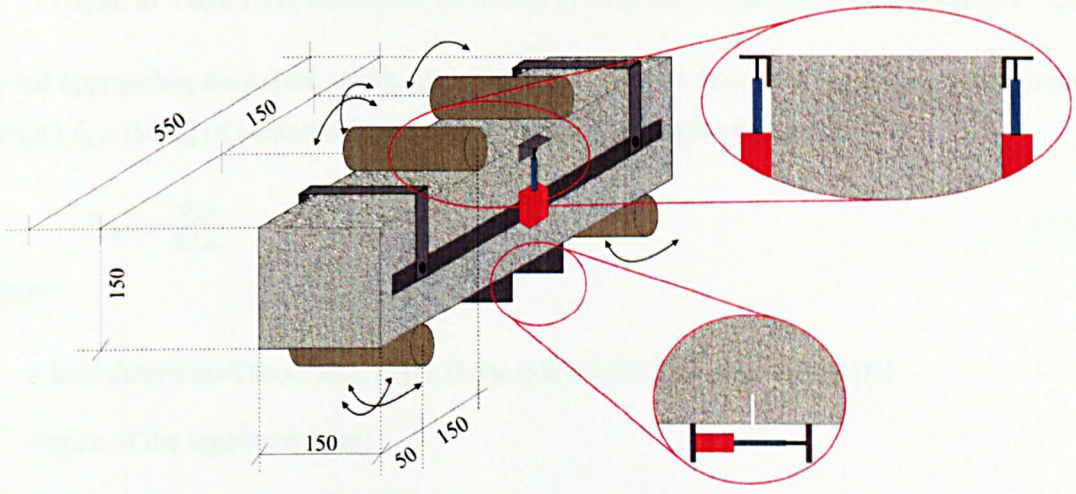

Figure 64 – Load configuration used for flexural strength test.

During testing, the wet mixes were rotated 90° from the casting position, to reduce the possibility of fibre dispersion problems due to boundary conditions, while RCC mixes were tested with the cast surface top due to the procedures used for compaction, based on three parallel layers of concrete. Prior to the test, prisms were notched transversally in the middle of the bottom surface, as shown in the figure above. The notch was 25 ± 1 mm deep and approximately 3 mm wide. Specimens were notched to force the formation of cracks in the centre of the prism.

[31] The *yoke* used in the tests is based on the JCI SF-4 (1984). It is fixed to the specimen in such a way that the rotation and/or the displacement of the specimen during the test do not cause any displacement and/or rotation in the LVDTs in reference to the specimen (only the net deflection of the neutral axis is measured).

Each test lasted approximately one hour. Usually the test was stopped when the CMOD reached 8 mm. However, the test was sometimes interrupted earlier if the load dropped to less than 10% of the peak load.

The flexural strength at the limit of proportionality f_{LOP} was calculated following three approaches:

1) visual approach: f_{LOP} is determined considering the maximum load F_L at which the graph of the bending load *versus* mid-span displacement curve deviates from linear elasticity (as shown in Figure 65a);
2) RILEM (2002): f_{LOP} is calculated based on the maximum load F_L obtained from the CMOD interval ranging from 0 to 0.05 mm (Section 2.3.2.3);
3) Che (2010) method: f_{LOP} is obtained from the F_L load that gives a modulus of elasticity equal to 0.85E (E is calculated according to Che, 2010 approach – next Section 4.4.2.3).

For all approaches described above, the following equation was used to calculate the flexural strength f_{LOP} [MPa] of concrete, based on the elastic distribution of stresses.

$$f_{LOP} = \frac{F_L L}{b h_{sp}^2} \quad (16)$$

Where:

F_L = load determined according to the three approaches described above [N]

L = span of the specimen [mm]

b = width of the specimen [mm]

h_{sp} = height of specimen *minus* depth of notch [mm]

The ultimate strength f_{ult} [MPa] was also calculated using Equation 16. However, in this case, F_L means the maximum load supported by the specimen during the testing period.

The residual flexural strengths[32] $f_{R,i}$ [MPa] were calculated at specific CMOD$_i$s of 0.5 mm, 1.5 mm, 2.5 mm and 3.5 mm (RILEM, 2002). Equation 16 also applies for the calculation of $f_{R,i}$, however, the load F_L is changed by the load taken at the specific CMOD$_i$, called $F_{R,i}$.

The equivalent flexural strength at a deflection of 3 mm, f_{eq3} [MPa], was calculated based on JCI SF-4 (1984), as shown in Equation 17.

[32] In this case the residual flexural strength is not based on the strength after exposure to deterioration processes, but with the capacity of carrying load after cracking (also cited in Section 2.3.2.3)

$$f_{eq3} = \frac{T_{eq3}L}{\delta_{eq3}bh_{sp}^2} \quad (17)$$

Where:

T_{eq3} = area under the load displacement diagram up to a deflection of 3 mm [Nmm]

δ_{eq3} = deflection at midspan = 3 mm

The equivalent flexural ratio $R_{e,3}$ up to a deflection of 3 mm was calculated following Equation 18 (JCI SF-4, 1984). The f_{LOP} used was based on the RILEM (2002) approach.

$$R_{e,3} = \frac{f_{eq3}}{f_{LOP}} \quad (18)$$

4.4.2.3 Modulus of elasticity

Two approaches were used to calculate the flexural modulus of elasticity E of concrete:

1) visual approach: E is calculated considering the point when the bending load *versus* mid-span curve deviates from linear elasticity;
2) Che (2010) method: E is the maximum elastic modulus value obtained from the graph of secant flexural modulus of elasticity *versus* bending load in the range of 30% to 60% of the ultimate load P_{ult}. Figure 65 shows schematically how the modulus is determined according to the two approaches.

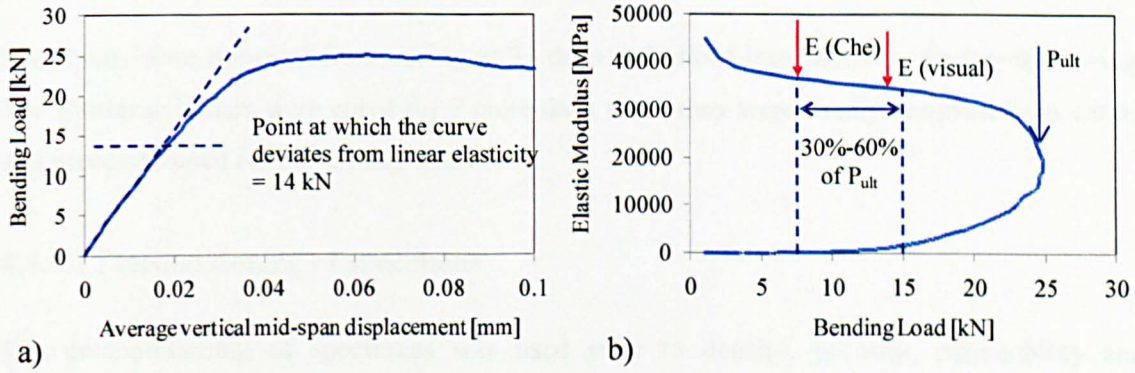

Figure 65 – Calculation of flexural modulus of elasticity according to the two approaches (mix W-CIP-2R).

For both approaches, the flexural modulus of elasticity E [MPa], for a four-point bend test, was calculated following Equation 19, which is derived from the elastic theory. The second term in the right side of the equation accounts for shear effects during flexural tests.

$$E = \left(\frac{23PL^3}{648I\delta} + \frac{2PL(1+\nu)}{3kA\delta}\right) \quad (19)$$

Where:

P = 0.5 × total load applied to the system [N]

ν = coefficient of Poisson

I = moment of inertia of the cross sectional area [mm^4]

δ = vertical displacement at the centre of the span [mm]

A = shear area [mm^2]

k = shear correction factor

4.4.3 Density

The density of dry and saturated concrete was calculated following the BS 12390-7 (2009d) by using the water displacement method.

Cylinders measuring 150 mm in diameter and 50 mm in height were used in the test. This was because the same specimens used for permeability were also used for the density test, avoiding casting of extra samples. Because of the difficulty of compacting RCC samples with these dimensions, the specimens were obtained by slicing a corresponding 300 mm in height cylinder. The same procedure was carried out for the wet mixes to avoid boundary conditions that may affect the distribution of fibres in small cylinders (50 mm height).

Specimens were removed from curing at 21 days and sliced into shorter cylinders by sawing. The shorter cylinders were cured for 7 more days when they were finally removed from curing and preconditioned for the density test.

4.4.3.1 Preconditioning of specimens

The preconditioning of specimens was used prior to density, porosity, permeability and sorptivity test[33]. Specimens were dried before the tests to remove the water from the concrete pores. The drying method is not standardised and various temperatures for preconditioning are published in the literature. Based on recommendations by other researchers (Sanjuan and Martialay, 1996; Carcasses *et al.*, 2002), three different temperatures were used in this study: 50 °C, 80 °C and 105 °C.

The 105 °C and the 80 °C temperatures were applied to the specimens until they reached constant mass. A constant mass was assumed when the difference between two subsequent

[33] Only for the preconditioning temperatures of 50 °C and 80 °C, as shown in Section 4.3.1.

measurements, taken in an interval of 24 h, was less than 0.5 g per specimen (RILEM, 1999). Each specimen weighted approximately 2.2 kg and the scale used had an accuracy of 0.01g.

The temperature of 50 °C was used based on the procedures of RILEM (1999). The necessary mass loss during drying at 50 °C was calculated by considering an intermediate stage in-between the total evaporable water and the evaporable water at 20 °C ± 1 °C and 75 ± 2% RH, as described in Section 3.2.1.1, and shown in Equation 20. The total evaporable water was determined by drying the specimens at 105 °C as described in the above paragraph. The same specimens used to measure the total evaporable water were used to perform the permeability, porosity and density tests at 105 °C.

$$\Delta_m = \left(\frac{w_e - w_{e,75}}{1+w_e}\right) m_o \quad (20)$$

Where:

w_e = evaporable moisture concentration $w_e = W_e/m_d$

W_e = total evaporable water content $W_e = m_o - m_d$ [g]

m_o = mass of specimen at the end of curing [g]

m_d = mass of specimen after oven drying at 105 °C [g]

$w_{e,75}$ = equilibrium moisture concentration $w_{e,75} = W_{e,75}/m_d$

$W_{e,75}$ = equilibrium water content at 75 ± 2% RH $W_{e,75} = m_{e,75} - m_d$ [g]

$m_{e,75}$ = mass of concrete at equilibrium with 75 ± 2% RH [g]

To allow the evaporation of water of concrete exposed to 20 °C and 75% RH, the specimens were sliced into cylinders of 5 mm in height and 150 mm in diameter. Two cylinders were sawed per mix to allow at least 500 g of sample. The specimens were kept in a chamber with controlled temperature and RH (shown in Figure 66) until they reach constant mass (difference between two subsequent readings in 24 h less than 0.1 g).

Specimens were sealed in the circumferential surface to prevent formation of radial moisture gradients. They were placed into a ventilated oven until they reached the mass loss calculated from Equation 20. The specimens were then fully sealed with polyethylene plastic sheet to allow homogeneous moisture redistribution throughout the specimens. The fully sealed specimens were kept in the oven at 50 °C for a period of 14 days, when they were tested for permeability.

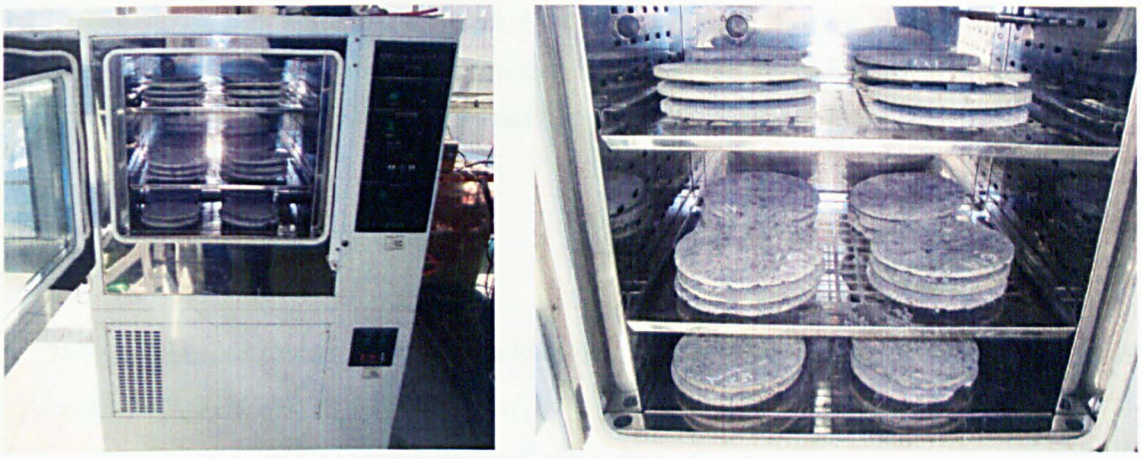

Figure 66 – Specimens in controlled temperature and humidity chamber.

Two specimens were used per mix to measure the permeability at 105 °C and five specimens per mix were used for the 50 °C and 80 °C temperatures, each. The reduced amount of specimens for the 105 °C temperature is because these specimens were initially conceived to calculate the total evaporable water of specimens following the 50 °C preconditioning by the RILEM (1999) method, which requires only 2 specimens.

4.4.3.2 Dry and saturated density test

Two specimens were used per mix per preconditioning temperature. The dry mass of the specimens after preconditioning was initially recorded. The specimens were then subjected to vacuum for a total period of 4 h (Figure 67) and they remained immersed in the deionised water without vacuum for an extra 20 h.

Figure 67 – Apparatus to vacuum saturate concrete specimens.

The specimens were weighted in dried (prior to vacuum) and saturated condition (after vacuum), the latter both in air and submerged in water. The following equation was used to calculate both the dry density D_d [kg/m^3] and the saturated density D_s [kg/m^3] of specimens.

$$D_d \text{ or } D_s = \frac{m}{V} \tag{21}$$

Where:

m = oven preconditioned mass of specimen m_d [kg] for dry density or saturated mass of specimen m_s [kg] for saturated density

V = volume of specimen $V = \frac{m_s - m_{ss}}{\rho_w}$ [m^3]

m_{ss} = saturated mass of water submerged specimen [kg]

ρ_w = density of water at 20 °C = 998 kg/m^3

4.4.4 Porosity

The methodology to obtain the porosity of concrete is based on the procedures of the ASTM C1202 (1997), following the vacuum saturation method. The same specimens tested for density were used, so the preconditioning and casting procedures used for density apply to porosity. From the five specimens cast per mix (for each preconditioning temperature of 80 °C and 105 °C), two specimens were tested for porosity and density. The remaining three specimens per mix (per preconditioning temperature) were tested for sorptivity, as explained in Section 4.4.6.2. The two specimens preconditioned at 105 °C, were also used to determine porosity. The procedures for saturating the specimens are the same as for density.

The saturated specimens were weighted in air and in water. The porosity P [%] was calculated according to the equation below.

$$P = \frac{m_s - m_d}{m_s - m_{ss}} \times 100 \tag{22}$$

Where:

m_s = saturated mass of specimen [kg]

m_d = oven preconditioned mass of specimen [kg]

4.4.5 Free Shrinkage

The free shrinkage test was performed according to the BS EN 12617-4 (2002b). Due to compaction limitations of RCC and to avoid problems with the fibre distribution due to boundary conditions of the moulds, the size of the specimens was changed from 40 x 40 x 160 mm to 150 x 150 x 550 mm.

Stainless steel measurement studs were fixed on the end concrete surfaces after demoulding (24 h after casting) by high performance hot glue. The procedures used for the compaction of RCC specimens prevented the studs from being fixed to the specimens during casting. The adhesion of the studs was inspected after 30 min of fixing and (if ok) the first longitudinal measurement L_o was taken. Specimens were then transported to a room with controlled temperature and humidity (21 °C ± 2 °C and 60 ± 10% RH).

Longitudinal measurements were taken 1, 3, 7, 14, 28, 56 and 112 days after demoulding. The measurement at 112 days did not follow the BS EN 12617-4 (2002b) and were carried out to verify if there was a tendency for the drying shrinkage to stabilise after a prolonged period of time. The strains [mm/m] due to free shrinkage were calculated according to the following equation:

$$Strain = \frac{\Delta L}{L_g} \times 1000 \quad (23)$$

Where:

ΔL = difference in length after n days after demoulding compared with L_o [mm]

L_g = gauge length = specimen length = 550 mm

A measurement device with precision of 0.001 mm was developed to obtain the length of the specimens (Figure 68). A calibration rod of 550 mm was also produced. The measuring device and the calibration rod were maintained in the same room as the specimens until the last measurement was obtained. The measurements were taken following the steps: 1) zero the measuring device with the calibration rod; 2) measure the length of the specimen and record the value; 3) check the measuring device with the calibration rod; 4) if the measurement of the calibration rod ≤ 0.001 mm, the length measured is valid; 5) if the measurement of the calibration rod > 0.001 mm, discard the measurement; 6) repeat steps 1 to 5 until at least 3 measurements are valid.

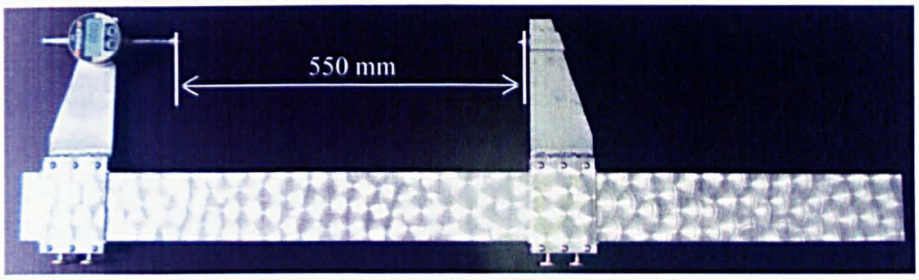

Figure 68 – Measuring device used for shrinkage measurement.

4.4.6 Transport Mechanisms

4.4.6.1 Permeability

The permeability test was performed by the oxygen flow test following the procedures recommended by the RILEM TC 116-PCD-C (1999), also called *Cembureau* method. Five specimens were tested per mix, for each preconditioning temperature of 50 °C and 80 °C, and two specimens were cast per mix for the preconditioning temperature of 105 °C (same specimens used for density and porosity). From the five specimens per mix per preconditioning temperatures of 50 °C and 80 °C, two were used to carry out porosity and density measurements (as previously explained in Sections 4.4.3 and 4.4.4), and three were used to carry out sorptivity tests.

After preconditioning the specimens, permeability was the first test carried out in the specimens, followed by density, porosity or sorptivity. The same casting and preconditioning procedures used for the density tests apply for this test.

Oxygen flow test

The test involves placing the oven-dried sample in the permeability cell as shown in Figure 69a. When the top lid is in place, inflating the inner tube ensures a seal around the sample allowing oxygen to flow only through the specimen. Oxygen is applied at 1 Bar above atmospheric pressure and the flow rate of oxygen through the sample is determined using a volumetric flow meter (Figure 69b).

A certain period of time is required for the oxygen flow to stabilise (i.e. for the oxygen flow to find the interconnected paths of pores across the specimen). The flow of oxygen in low permeability concrete tends to take longer to stabilise. Usually a period of 30 minutes is found to be adequate for normal strength concrete.

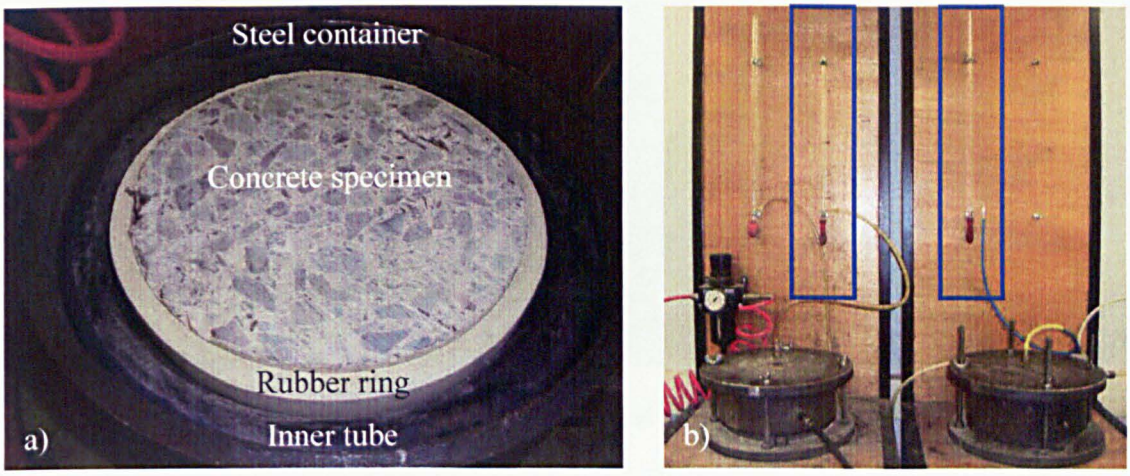

Figure 69 – a) Permeability cell and b) volumetric pipette connected to the permeability cell to measure the flow rate.

The flow rate of oxygen through the sample is measured considering the average pressure across the specimen. The intrinsic permeability, K_i [m^2], for oxygen flow (considering the viscosity of oxygen at 20 °C = 2.02E-5 Ns/m^2) can be calculated from Equation 24 (Cabrera and Lynsdale, 1988; RILEM, 1999), derived from Darcy's law (Equation 10):

$$K_i = \frac{4.04 P_a Q_i L}{A(P_i^2 - P_a^2)} \times 10^{-16} \quad (24)$$

Where:

P_a = atmospheric pressure [Bar]

Q_i = flow rate [cm^3/s]

L = thickness of the specimen [m]

A = cross-sectional area of the specimen [m^2]

P_i = total applied pressure [Bar].

4.4.6.2 Sorptivity

Only the preconditioning temperatures of 50 °C and 80 °C were used. Three specimens per mix for each preconditioning temperatures of 50 °C and 80 °C were used to perform the sorptivity tests, which were previously used to perform the permeability tests.

The test was performed following the BS EN 13057 (2002a). Specimens were marked with eight equi-spaced axial lines around the perimeter of the sample. The cut face of the specimens was positioned over supports in a tray with water. The specimens were immersed in water up to a depth of 2 ± 1 mm, as shown in Figure 70.

Figure 70 – Specimens tested for sorptivity.

The amount of water absorbed by the specimens was recorded 6 times in a period of 24 h, by weighing the specimens. The intervals were usually of 12 min, 30 min, 1 h, 2 h, 4 h and 24 h, but these varied (see Section 3.2.1.2). The height of the wet front from the bottom surface of the specimens was also recorded after 2 h of testing in each of the equi-spaced lines around the specimen.

A graph of the amount of water uptake per unit area *versus* the square root of time was plotted for each specimen and the coefficient of absorption was obtained through the slope of the best fit lines obtained through linear regression analysis. Figure 71 shows a typical sorptivity curve obtained from mix R-CIP-0, preconditioned at 80 °C.

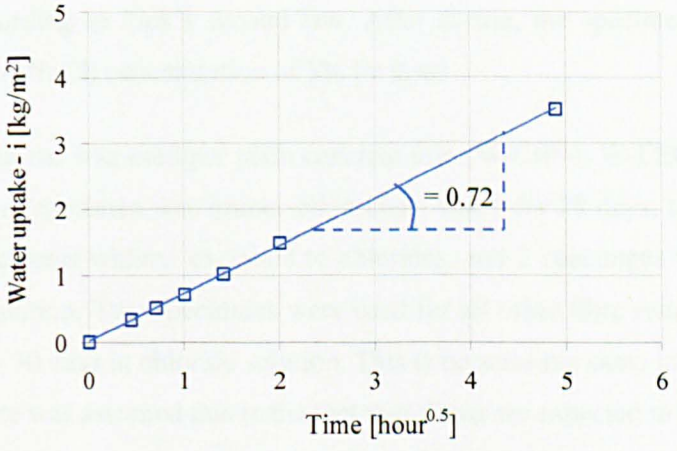

Figure 71 – Typical result for sorptivity test (mix R-CIP-0 preconditioned at 80 °C).

The resistance coefficient R [h/m^2] was calculated according to Equation 25.

$$R = \frac{t_c}{X^2} \tag{25}$$

Where:

t_c = time when the water uptake level was measured = 2 h for all specimens.

X = level of water uptake after 2 h (average of the height of the wet front obtained from the 8 equi-spaced lines) [m]

4.4.6.3 Diffusivity and chloride content test

The diffusion coefficient of concrete, which is based on the chloride content in different depths of concrete, was performed according to the procedures of BS EN 13396 (2004a) and BS EN 14629 (2007c). The draft standard DD CEN/TS 12390-11 was released only in 2010 and for this reason was not used in the tests. The procedures for the draft standard are similar to the procedures of the ASTM C1556 (2003b), cited in Section 3.2.1.3, and they are specific for the calculation of diffusion, whilst the BS EN 14629 (2007c) is more appropriate to obtain the chloride content of the concrete only.

Cylinders measuring 150 mm in diameter and 100 mm in height were used for the tests. The specimens were cut from 300 mm height cylinders for both wet and dry mixes. The 300 mm cylinders were cured for 21 days, fully immersed in a water tank at 20 °C ± 2 °C. They were then cut into shorter cylinders of 100 mm height at 21 days of curing and sealed along the circumferential surface with silicon. The cylinders were returned to the water tank for 7 more days to complete 28 days of curing.

The sealing with silicon was necessary to allow the penetration of chlorides in one dimensional configuration, according to Fick's second law. After curing, the specimens were placed into containers with salt (NaCl) concentration of 3% by mass.

A group of 3 specimens was used per plain concrete mix (W-CIP-0, W-LEC-0, R-CIP-0 and R-LEC-0): one control specimen was immersed in clean water for 28 days, to verify the chloride content of the specimens without exposure to chlorides, and 2 specimens were exposed for 30 days in chloride solution. Two specimens were used for all other fibre reinforced mixes, which were immersed for 30 days in chloride solution. This is because the same initial chloride content as for plain concrete was assumed due to the fact that fibres are expected to be chloride-free.

After 30 days of chloride exposure, pulverised concrete samples were collected from 3 different depths of the specimen: 0-2 mm, 4-6 mm and 8-10 mm. The chloride content of the samples was analysed by potentiometric titration (BS EN 14629, 2007c).

To perform the test, a certain amount of powder sample (around 2-4 g) is diluted and boiled with hot deionised water (100 ml) and nitric acid HNO_3 (10 ml). Silver nitrate $AgNO_3$ (0.1M[34])

[34] Refers to the concentration of $AgNO_3$ (0.1 mol per litre of solution).

is gradually added to the solution (around 0.2 ml each time) and the conductivity is measured for each fraction of $AgNO_3$ added.

The volume of $AgNO_3$ in to the solution (called *dx*) is plotted against the change in conductivity (called *dy*) divided by the gradual volume of silver nitrate (*dx/dy*). The chloride content of the sample is calculated based on the amount of $AgNO_3$ necessary to cause the peak on the *dx/dy* curve, as shown in Figure 72. This peak corresponds to the amount of silver nitrate required to precipitate the chlorides of the solution (3.8 ml for the *dx/dy* curve in Figure 72).

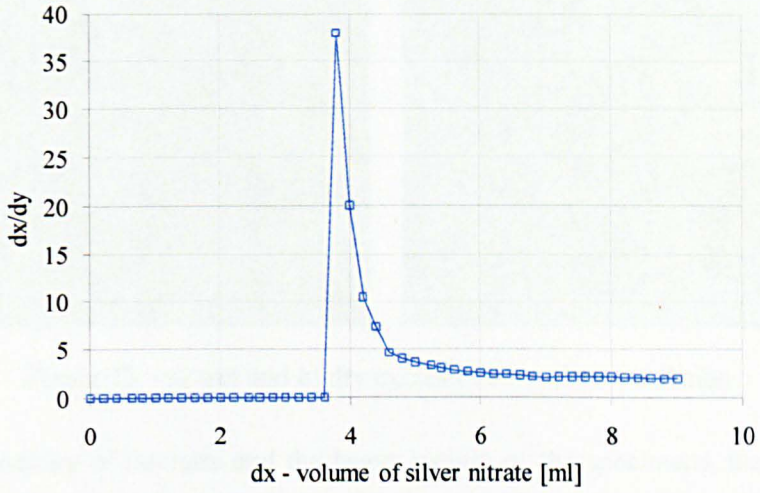

Figure 72 – Typical dx/dy curve with the peak corresponding to the amount of chlorides.

The diffusion coefficient is then calculated following Equation 12 given in Section 3.2.1.3. For that, the surface content is assumed as the chloride content at the 0-2 mm depth and the diffusion coefficient was calculated for both depths of 4-6 mm and 8-10 mm, which were finally averaged. A computational tool such as *goal seek* in Microsoft Excel® was used for the calculations since diffusion coefficient cannot be straight forwardly obtained by Equation 12.

4.4.7 Corrosion

The corrosion effects in SFRC were evaluated mainly in terms of loss of mechanical performance after exposure to accelerated corrosion. Cubes and prisms were used to measure the influence of corrosion in terms of compressive and flexural strength, respectively. A visual analysis was also undertaken in the specimens after corrosion simulation.

Corrosion simulation

Corrosion was accelerated in SFRC specimens by intermittent wet and dry cycles. The cycles were carried out using immersion of specimens in salt solution for 4 days (Figure 73a) followed

by a dry period in a standard laboratory environment for 3 days (Figure 73b). The concentration of salt solution used for the wet cycles was 3% NaCl. Prisms and cubes were placed into a frame inside containers in such a way that the specimens were at least 20 mm apart from each other, thus allowing the contact of the solution with all surfaces of the specimens. Each container has the capacity to accommodate twelve prisms and twelve cubes. The corrosion simulation method used is based on the methodology proposed by Kosa and Naaman (1990).

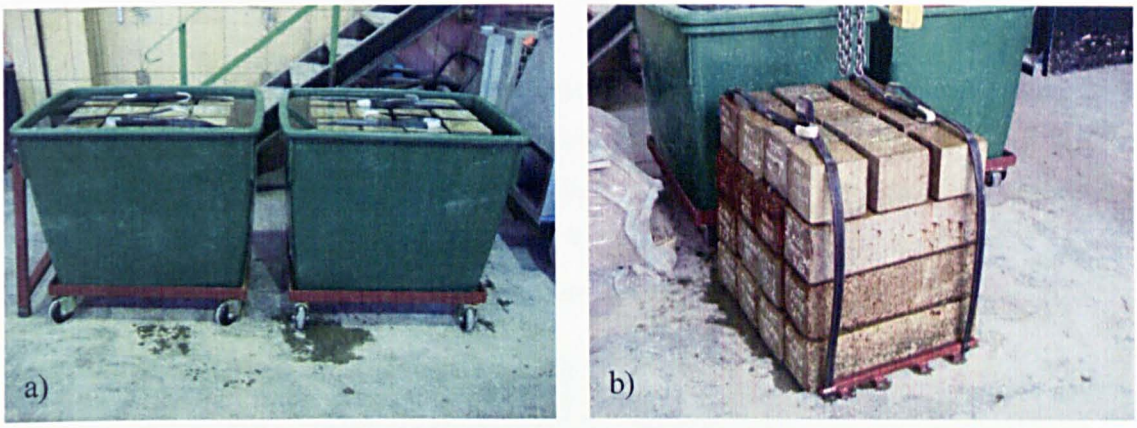

Figure 73 – a) wet and b) dry cycles of corrosion simulation.

Due to the periodicity of the tests and the heavy weight of the specimens, the immersion and removal of specimens in and out of solution was undertaken by using an overhead crane. Figure 74 shows specimens being removed from the containers.

Figure 74 – Overhead crane used to immerse and remove specimens out of solution.

As already mentioned in Section 4.3.2.2, specimens were subjected to 5 and 10 months of wet-dry cycles. Residual strengths were determined after each period of corrosion simulation.

Pre-cracking of specimens

The majority of the tests were performed on non-cracked specimens. However, some specimens (R-CIP-6R) were also pre-cracked before testing to verify the influence of chloride ingress through cracks. For that, prisms measuring 150 x 150 x 550 mm were notched and subjected to

the same procedures as for the flexural strength test. The load was applied until the CMOD reached approximately 0.2 mm (all the pre-cracked specimens exceeded the limit of proportionality). This value is in the range of permissible crack width according to the BS 1992-1-1 (2004b), in terms of durability. The cracked prisms were subjected to corrosion simulation, and the residual flexural strength was obtained after 5 and 10 months.

40 °C chloride solution temperature

Some specimens (R-CIP-6R) were also immersed in a chloride solution at a temperature of 40 °C. To maintain the constant 40 °C temperature of the solution, the containers with chloride solution were placed in a water tank with the desired temperature. The tank was covered up to keep the temperature of the water and air at 40 °C (see Figure 75). The same periods of 5 and 10 month exposure were used to accelerate corrosion.

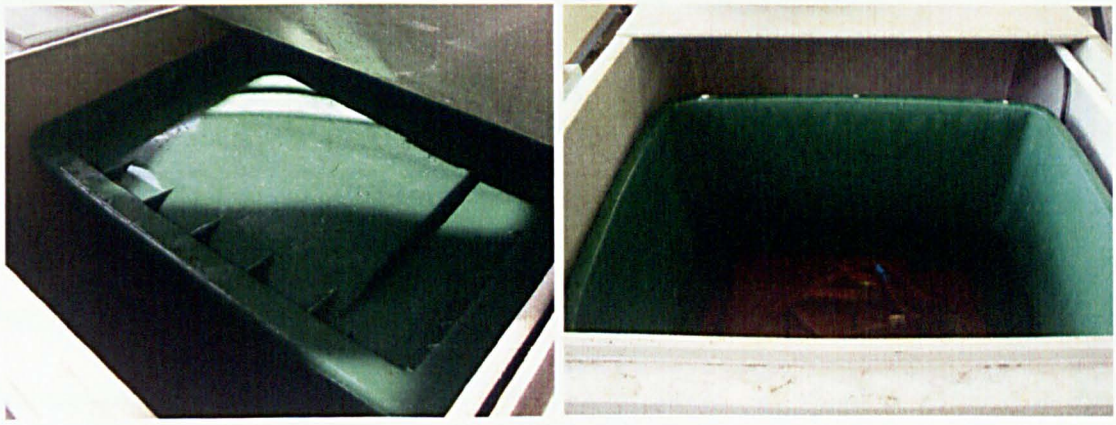

Figure 75 – Container with chloride solution at a 40 °C.

The combined effect of immersing in 40 °C solution and the use of pre-cracked specimens was also investigated for mix R-CIP-6R.

4.4.8 Freeze-thaw

The freeze-thaw tests were performed following the recommendations of the European draft standard DD CEN/TS 12390-9 (2006) for the cube test method. The freeze-thaw test used is based on the loss of mass method due to scaling for 100 mm cubes. The original size of the cubes proposed by the standard was increased to 150 mm to allow better compaction for RCC samples and also to reduce fibre distribution problems.

The influence of freeze-thaw was also investigated by visual analysis and residual mechanical performance after freeze-thaw simulation. The residual compressive strength was also measured

for the cubes used for the measurement of loss of mass. In order to measure the residual flexural strength, prisms measuring 150 x 150 x 550 mm were also cast and exposed to freezing and thawing cycles. The loss of mass of the prisms was also recorded.

To simulate the effect of de-icing salts, specimens (cubes and prisms) were fully immersed in containers with 3% NaCl solution. The containers were designed to fit three cubes measuring 150 mm in height each (Figure 76a). This was also the number of specimens cast per mix. Two prisms were cast per mix and these were placed in separate containers (Figure 76b).

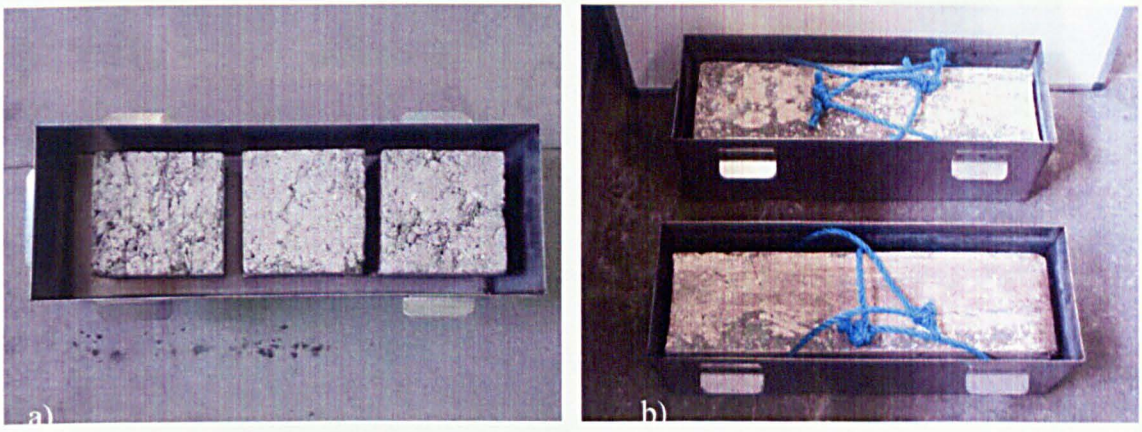

Figure 76 – Containers with cubes and prisms.

Freeze-thaw cabinet

The containers with the specimens and solution were placed into a cabinet designed to apply continuous cycles of freezing and thawing (Figure 77), with temperatures in the centre of the cubes ranging from -15 °C to 20 °C.

A thermocouple was placed in the centre of one of the three cubes in each batch (Figure 78) to control the temperatures of the chamber. Figure 79 shows the desired temperature profile according to DD CEN/TS 12390-9 (2006) and the real temperature profile measured. It can be seen that there is an increase of the overall time per cycle due to limitations of the cooling capacity of the cabinet. A large period of time is required in steps 1 (i=1) and 3 (i=3) to decrease the temperature from 20 to 0 °C and from 0 to -15 °C, respectively.

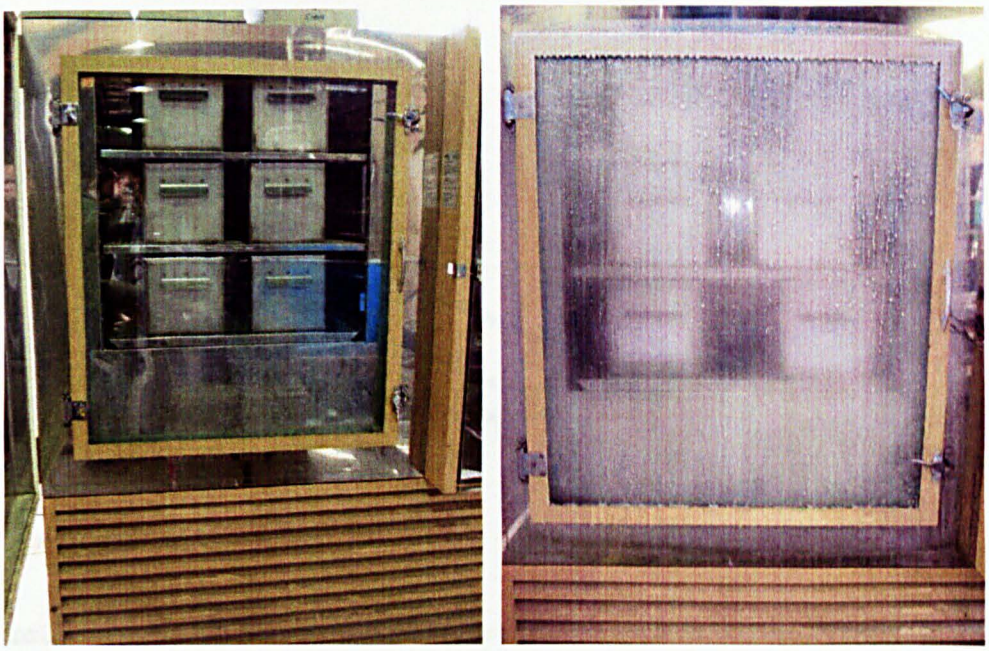

Figure 77 – Freeze-thaw chamber with containers and specimens.

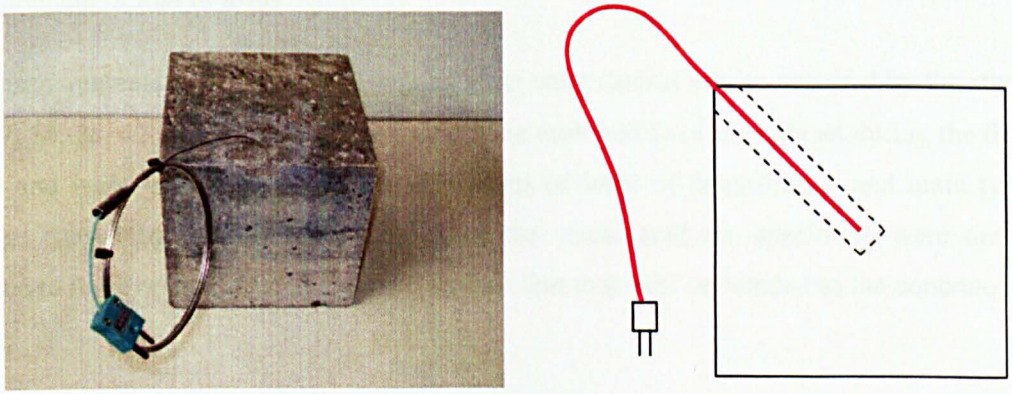

Figure 78 – Thermocouple placed in the centre of a randomly chosen cube.

The cabinet used for the freeze-thaw chamber was automated and controlled by software based on LabVIEW® (National Instruments Corporation, 2008) developed for the purpose of this research (Petkovski, 2008). The temperature time-history was monitored throughout the test.

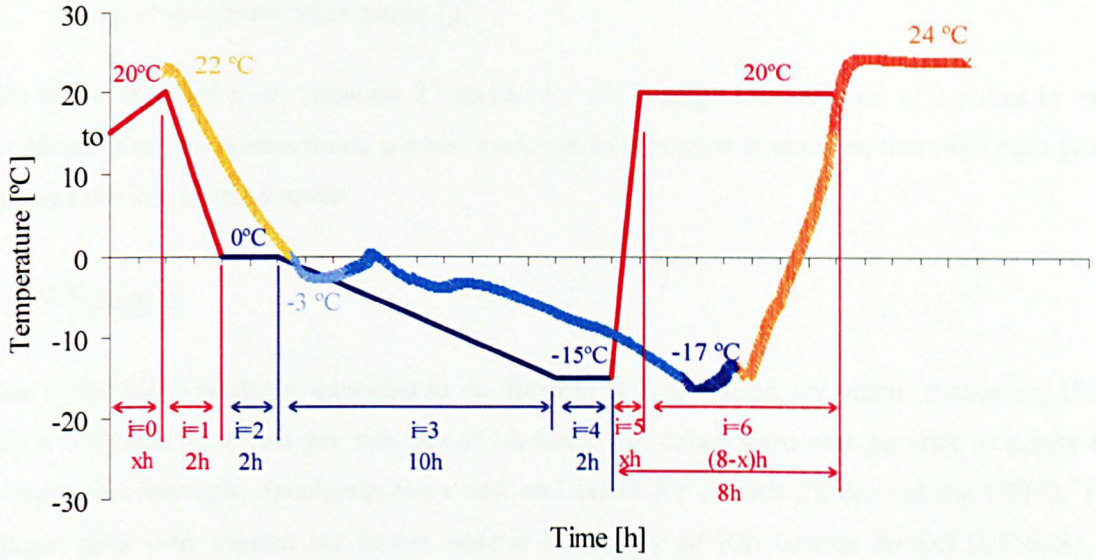

Figure 79 – Predicted and real temperature profile measured during the freeze-thaw cycles.

Measurement of loss of mass

The measurements to determine the loss of mass were carried out, as required by the standard, after 7, 14, 28, 42 and 56 cycles. Specimens were removed from the cabinet during the thawing phase and were first visually examined in terms of level of deterioration and main types of damage caused by freeze-thaw attack. After the visual analysis, specimens were throughly brushed to remove any loose part on the surface that may still be bonded to the concrete and/or fibres.

All detached material was collected, oven dried for 24 h at 105 °C and weighted to the nearest 0.1 g. The specimens were returned to the containers with fresh chloride solution after collecting the scaled material.

The cumulative loss of mass $m_{s,n}$ [g] after n cycles is calculated using the equation below.

$$m_{s,n} = \sum_{i=1}^{n} m_{d,n} \quad (26)$$

Where:

$m_{d,n}$ = oven dried scaled material collected from cycle n [g]

The loss of mass P [%] after n cycles is calculated according to Equation 27.

$$P = \frac{m_{s,n}}{m_o} \times 100 \quad (27)$$

Where:

m_o = mass of specimens after curing [g]

The value obtained from Equation 27 represents the average loss of mass of 3 cubes in each container. The two prisms tested per mix were put in separated containers, therefore each prism had its own loss of mass result.

4.4.9 Fatigue

Due to the high variability expected in the flexural fatigue results, six prisms measuring 150 x 150 x 550 mm were cast per mix per stress ratio. Six cubes were cast per mix to assess the compressive strength. Specimens were cast and cured for at least 28 days at the USFD. The fatigue tests were carried out at the Federal University of Rio Grande do Sul (UFRGS), in Brazil, due to a cooperation agreement between the two Universities. Specimens were shipped from the UK to Brazil (during the EcoLanes Project) in four pallets protected from moving and contact to the environment.

Static flexural tests were carried out prior to dynamic tests. For each mix, the loads obtained from the static tests were multiplied by the stress ratios assumed (0.5, 0.7 and 0.9) to calculate the loads for the fatigue test. At least two samples per mix were tested after 28 days of curing at USFD. Two samples were also tested at UFRGS after arrival of shipment. The static test was undertaken at both Universities to account for ageing of specimens (and probable gain in strength), since they were in transit for nearly two months before arriving at UFRGS. The measurement of the static flexural strength in Brazil was also important to avoid any possible difference between test methods at the two Universities.

The fatigue testing setup initially comprised of three specimens tested at the same time (Figure 80) aiming to optimize the time for testing due to the high number of specimens. Yokes were placed on all beams to hold the LVDTs used to measure the vertical displacement during the fatigue testing. Two transducers were used per prism (one on each side). The specimens tested against fatigue were not notched.

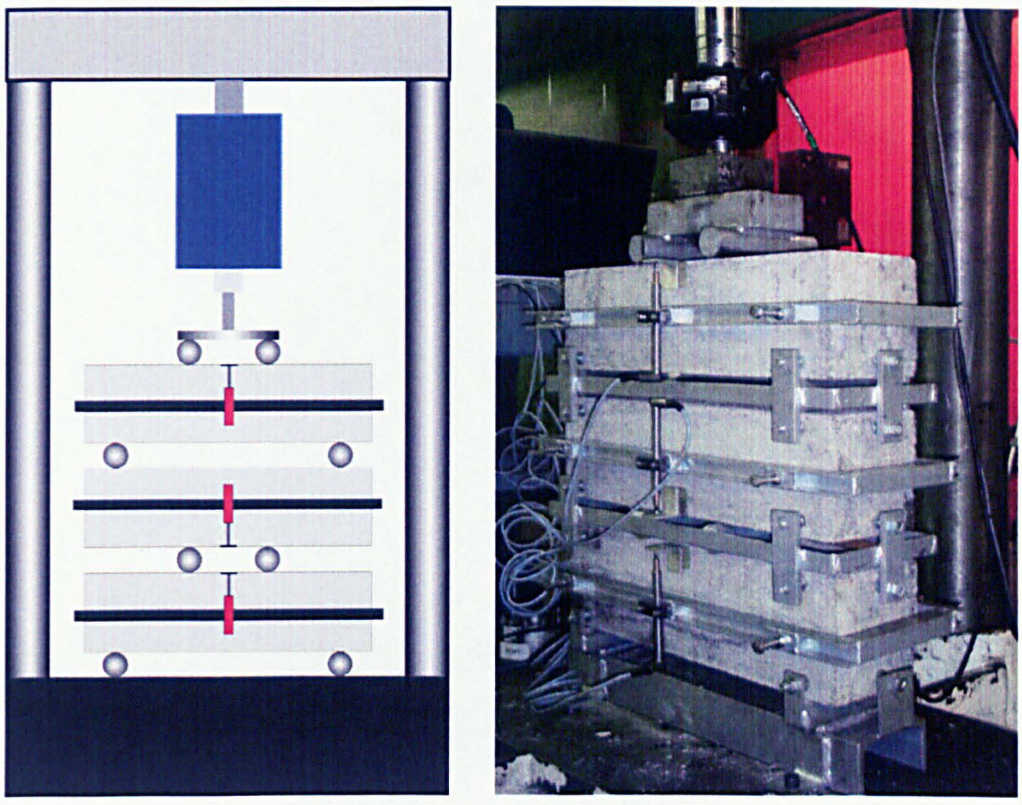

Figure 80 – Setup to test fatigue specimens.

To obtain the fatigue setup shown in Figure 80, the prisms were placed one by one in a self-supporting frame (Figure 81). Special care was taken to fit the prisms exactly in the centre of all loading supports in-between the prisms. The third prism was put in position and the LVDTs were finally connected to the yokes.

The fatigue tests were performed in a MTS® (Material Testing System) machine suitable for fatigue tests. Specimens were placed in a self-supporting frame equipped with a servo-hydraulic actuator (maximum capacity of 100 kN) connected to the MTS controller. Loads were applied following a sinusoidal wave pattern. The main output was the number of cycles until failure. Other information provided are the machine displacements and the minimum and maximum load effectively applied in each cycle. The vertical displacements were also recorded throughout the tests.

The loads applied were calculated based on the stress ratios with respect to the ultimate static flexural strength. During dynamic tests, a minimum of 10% of the load was continuously applied to the specimens. The cyclic loads were applied at a frequency of 15 Hz until any of the three specimens failed or until they reached the maximum number of 2 million cycles.

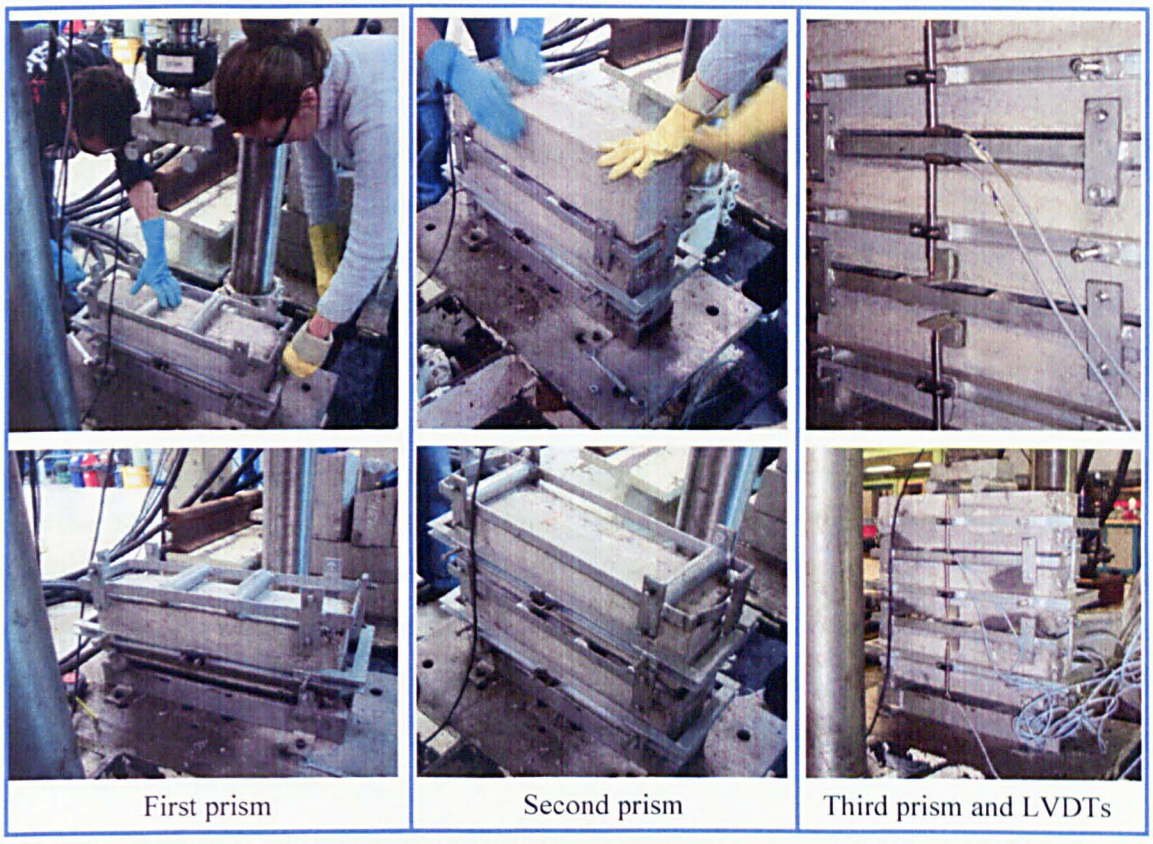

Figure 81 – Steps to mount three prisms for fatigue tests.

The fatigue equipment was set to stop every time the system reached displacements higher than 10 mm, which is an indication that at least one of the prisms had failed due to physical damage. The failed prism was removed and another one was placed in the original position. Cyclic loads continued until another prism failed. For each set of 6 prisms, two specimens remain intact at the end (no failure). The fatigue rig was not suitable to test two specimens only at the same time, and for this reason the two remaining specimens were tested individually.

It is important to add that the fatigue rig to test three specimens at the same time was only suitable for specimens resisting a high number of cycles (specimens subjected to a stress ratio of 0.5). For specimens resisting a low number of cyclic loads, the substitution of failed prisms was not practical, especially if the failed prism was located in the bottom or in the middle of the scheme. For this reason, the majority of prisms subjected to stress ratios of 0.7 and 0.9 were tested individually.

4.5 SUMMARY AND CONCLUSIONS

This chapter dealt with the main aspects of the experimental programme carried out during this PhD course. Since no previous studies were performed on the long-term and durability

performance of recycled SFRC, the experimental programme includes an extensive part of this research.

The experimental programme was developed aiming to encompass various parameters that contribute for the durability characterisation of recycled SFRC. The choice of the parameters and the main variables of the study were made aiming to achieve the objectives and to answer the research questions of the thesis (Chapter 1).

The experimental programme includes a study on the transport mechanisms and some pore-structure related properties and also some of the main deterioration processes that may affect the performance of SFRC. However, this research being a first study on the durability properties of recycled SFRC, and mainly due to time limitation, some topics could not be included in the programme. Examples of the topics that could not be investigated are related to other deterioration processes in concrete pavements (sulphate attack, roughness degradation and damage caused by thermal stresses); and also a more precise evaluation on the pore structure of the concrete, including the use of electronic microscopy and tests related to the pore size distribution of the concrete.

The use of both RCC and wet mixes was to allow a comparison between both types of mix, and also to evaluate the benefits of using RCC for concrete pavements since RCC is not widely utilised for concrete pavements. The use of both recycled and industrially produced fibres was to allow a comparison between both types of fibres. Finally, the fibre contents were selected based on the range of contents commonly used in industry.

The development of the mix proportions and the choice of materials used throughout the thesis were key factors for the experimental programme. The results are all based on specific mixes that appear to be appropriate for use in concrete pavements.

The results obtained from the experiments carried out during this thesis are shown in Chapters 5 to 8 and 10.

CHAPTER 5

5. MECHANICAL PROPERTIES, DENSITY, POROSITY AND FREE SHRINKAGE RESULTS

This chapter presents the results obtained from the experimental programme in terms of mechanical and other pore structure-related properties, such as density, porosity and shrinkage, for control specimens (non-damaged specimens). The mechanical performance is characterised in terms of compressive strength, flexural behaviour and modulus of elasticity. A comparison of the mechanical properties with density and porosity results is also presented in this chapter.

5.1 COMPRESSIVE STRENGTH

The cube compressive strength f_{cm} results obtained from the mixes investigated in this research, at the age of 28 days, are shown in Table 15. The results represent an average of three samples per mix. The coefficient of variance *COV* is also shown in the table.

Table 15 – f_{cm} (MPa) and COV results.

Mix	f_{cm}	COV	Mix	f_{cm}	COV
W-CIP-0	64.7	0.04	R-CIP-0	56.1	0.02
W-CIP-2I	69.1	0.04	R-CIP-2I	58.4	0.03
W-CIP-2R	54.7	0.06	R-CIP-2R	59.8	0.04
W-CIP-6R	68.6	0.06	R-CIP-6R	59.9	0.02
W-LEC-0	58.7	0.06	R-LEC-0	48.2	0.02
W-LEC-2I	62.4	0.01	R-LEC-2I	46.3	0.02
W-LEC-2R	61.1	0.02	R-LEC-2R	49.4	0.03
W-LEC-6R	71.4	0.02	R-LEC-6R	45.0	0.05

The majority of the mixes exceed the target cube strength of 55 MPa, except for mixes R-LEC. This is probably because the LEC, which is mostly composed of slag, has a lower rate of hydration compared to the CIP mixes. Therefore, the target strength for R-LEC mixes is most probably to be reached later due to further hydration of the cementitious material. A higher

strength at 28 days for slag cement (which may also be applied for LEC) can be achieved by higher curing temperature (Soutsos *et al.*, 2009; Barnett *et al.*, 2004).

The influence of the fibre content on the compressive strength is shown in Figure 82. The amount of 6% recycled fibres shows the best performance for wet mixes and also for the R-LEC mix. For CIP mixes (both RCC and wet mixes), 2% of industrially produced fibres show similar performance when compared to 6% recycled fibres.

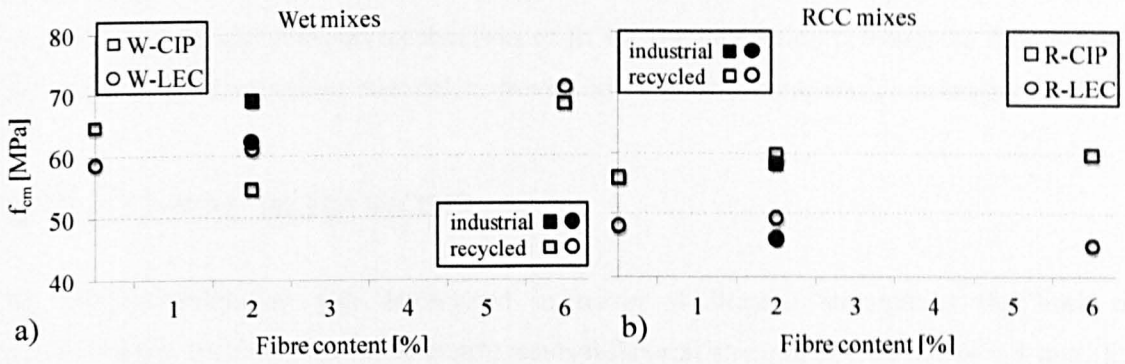

Figure 82 – Effect of fibre content on compressive strength.

The fact that the results are close to each other makes it difficult to draw any further conclusion from the results. An analysis of variance (ANOVA) was performed to verify the effect of the fibre content and type and the cementitious material on the compressive strength results. For that, a two-factor ANOVA with replication analysis was carried out in Microsoft Excel® for both wet and RCC mixes, as shown in Table 16 and Table 17, respectively. The analysis was carried out with a confidence of 95%.

Table 16 – f_{cm} ANOVA two-factor with replication – wet mixes.

Source of variance	SS	dF	MS	F	P-value	F crit
Fibre content and type	489.88	3	163.30	21.81	6.74E-06	3.24
Cementitious material	4.52	1	4.52	0.60	0.448	4.49
Interaction	190.19	3	63.40	8.47	0.001	3.24

SS: sum of squares, dF: degree of freedom, MS: mean square, P-value: probability

Table 17 – f_{cm} ANOVA two-factor with replication – RCC mixes.

Source of variance	SS	dF	MS	F	P-value	F crit
Fibre content and type	23.58	3	7.86	2.46	0.099	3.24
Cementitious material	764.12	1	764.11	239.46	4.79E-11	4.49
Interaction	39.55	3	13.18	4.13	0.024	3.24

The results for wet mixes show that the fibre content and type affects the compressive strength (null hypothesis[35] is rejected since F > Fcrit). The cementitious material, however, does not seem to affect the compressive strength of wet mixes. The interaction between the cementitious material and the fibre type and content affects the results.

The table of results for the RCC mixes shows that the fibre content and type does not influence the compressive strength, whilst the cementitious material affects the results. This is later on explained, from Sections 5.4 to 5.6 and Chapter 6, when compressive strength is compared with the pore structure and transport mechanisms of RCC. The interaction between the fibre content and type and the cementitious material, however, influences the compressive strength of RCC.

5.2 FLEXURAL BEHAVIOUR

The flexural behaviour was determined in terms of flexural strength at the limit of proportionality, ultimate flexural strength, residual flexural strength at CMODs of 0.5 mm, 1.5 mm, 2.5 mm and 3.5 mm and equivalent flexural strength and ratio at a deflection of 3 mm.

The results were calculated based on the bending load *versus* mid-span or CMOD curves obtained from the flexural tests. The graphs obtained from the tests and the properties calculated from the graphs are shown in Appendix C.

Properties referring to the post-cracking behaviour (e.g. residual and equivalent flexural strengths) were only evaluated for fibre reinforced mixes, since no significant post-cracking behaviour is noticed for plain concrete, as shown in Figure 83.

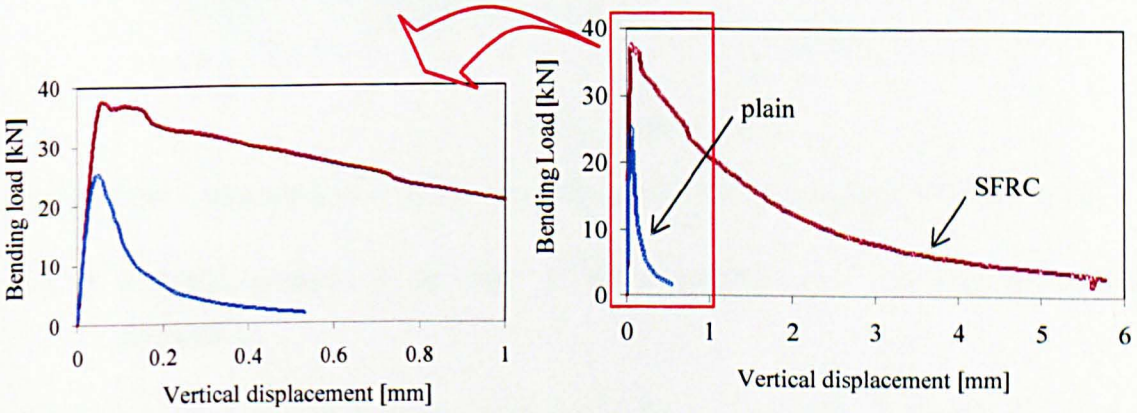

Figure 83 – Typical plain (mix W-LEC-0) and SFRC (mix W-LEC-6R) bending load *versus* mid-span deflection.

[35] Null hypothesis is based on the fact that the samples have similar means, that is, are not affected by the analysed factor. The null hypotheses for this specific situation are: fibre content and type does not affect the compressive strength; cementitious material does not affect the compressive strength; the interaction of both fibre type and content and cementitious material does not affect the compressive strength.

Wet mixes present different behaviour than RCC mixes and for this reason they were analysed separately.

5.2.1 Wet Mixes

The bending load *versus* vertical displacement curves for wet mixes (average of two specimens) are shown in Figure 84. The individual curves for each specimen can be found in Appendix C.

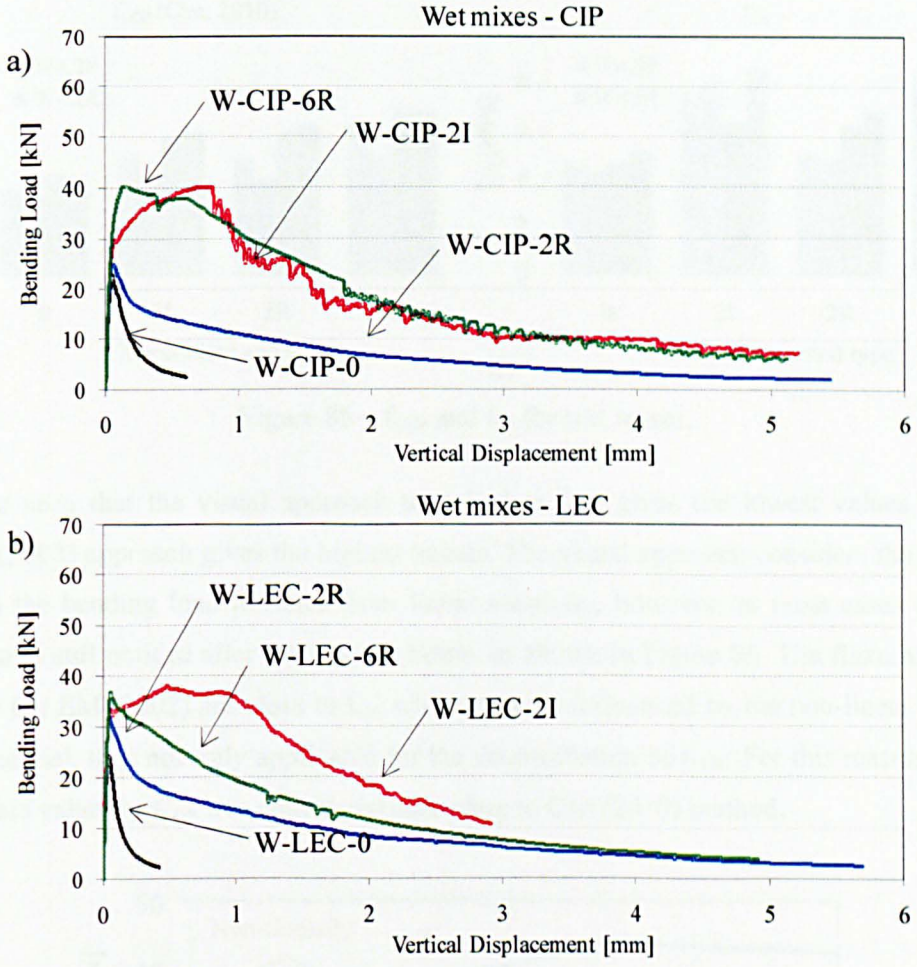

Figure 84 – Bending load *versus* vertical displacement for wet mixes a) CIP and b) LEC.

5.2.1.1 Flexural strength at the limit of proportionality f_{LOP} and ultimate flexural strength f_{ult}

Three approaches were used for the calculation of the f_{LOP} (see Section 4.4.2.2): 1) visual; 2) RILEM (2002) and 3) Che (2010). The f_{ult} was calculated based on the peak load.

Figure 85 shows the influence of fibre content and type as well as cementitious material type on f_{LOP} and f_{ult}. The columns in the graphs represent the results obtained per specimen (two specimens per mix).

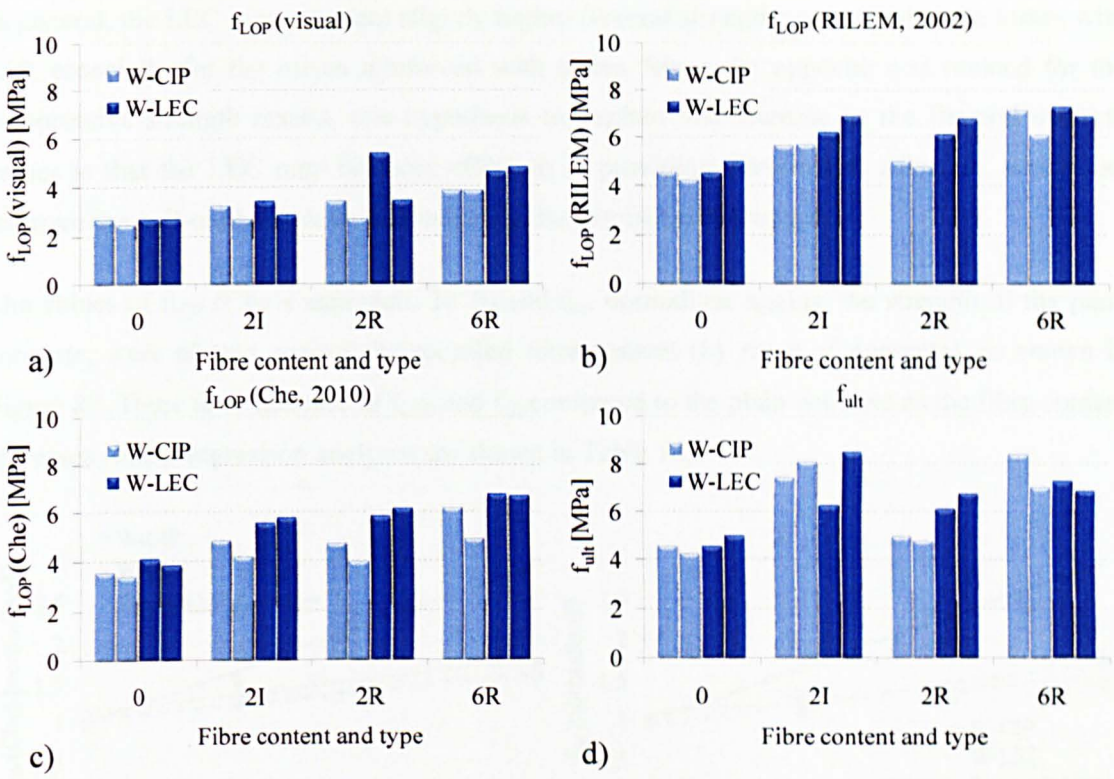

Figure 85 – f_{LOP} and f_{ult} for wet mixes.

It can be seen that the visual approach to calculate f_{LOP} gives the lowest values while the RILEM (2002) approach gives the highest values. The visual approach considers the first point at which the bending load deviates from linear elasticity, however, in most cases the elastic behaviour is still noticed after the first deviation, as shown in Figure 86. The flexural strengths given by RILEM (2002) are close to f_{ult}, which may be influenced by the non-linear behaviour of the material, thus not truly applicable for the determination of f_{LOP}. For this reason, the most appropriate value for f_{LOP} was considered according to Che (2010) method.

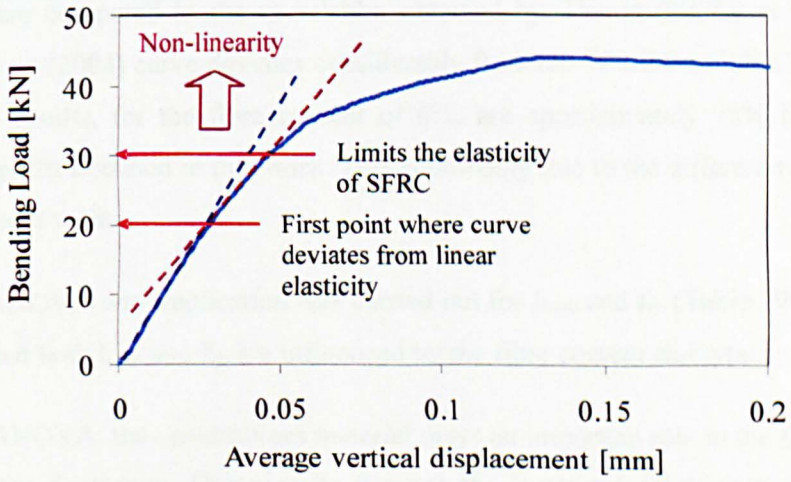

Figure 86 – Typical elastic behaviour of SFRC (mix W-CIP-6R).

In general, the LEC mixes present slightly higher flexural strengths compared to the mixes with CIP, especially for the mixes reinforced with fibres. Since the opposite was noticed for the compressive strength results, one hypothesis to explain this increase in the flexural strength values is that the LEC may be more effective in providing fibre/matrix adhesion, which can improve the pull-out behaviour thus affecting the flexural performance.

The values of f_{LOP} (Che's approach, 2010) and f_{ult}, normalised against the strength of the plain concrete, were plotted against the recycled fibre content (by mass of concrete), as shown in Figure 87. There is an increase of f_{LOP} and f_{ult} compared to the plain concrete as the fibre content increases (linear regression analyses are shown in Table 18).

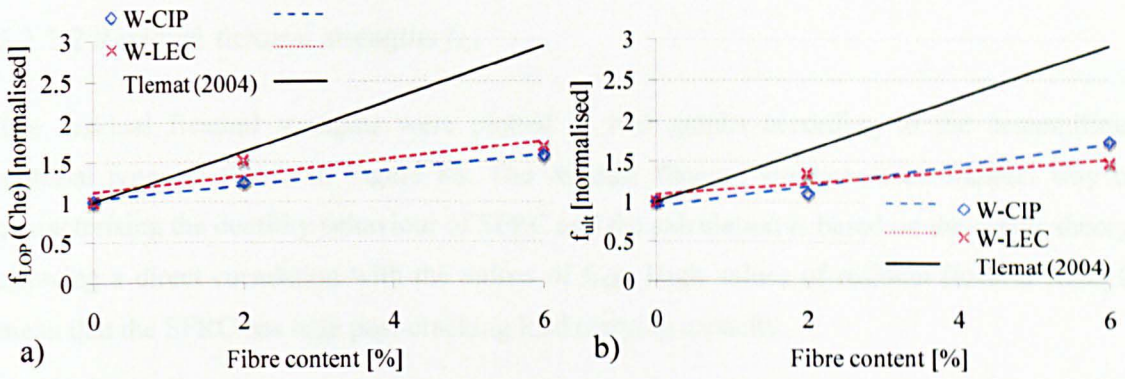

Figure 87 – Influence of recycled fibre content on the f_{LOP} and f_{ult} of wet mixes.

Table 18 – Correlation between f_{LOP} and f_{ult} with recycled fibre content (v).

	W-CIP	W-LEC
f_{LOP}	$f_{LOP} = f_{LOP,plain}(1.02 + 0.10v)$ $R^2 = 0.99$	$f_{LOP} = f_{LOP,plain}(1.12 + 0.11v)$ $R^2 = 0.80$
f_{ult}	$f_{ult} = f_{ult,plain}(0.94 + 0.13v)$ $R^2 = 0.96$	$f_{ult} = f_{ult,plain}(1.08 + 0.07v)$ $R^2 = 0.81$

The results were compared to the correlation obtained by Tlemat (2004), as also shown in Figure 87. Tlemat (2004) curve deviates considerably from the W-LEC and W-CIP regressions. Tlemat (2004) results, for the fibre content of 6%, are approximately 70% higher than the experimental results obtained in this work. This is probably due to the different type of recycled fibres used in both works.

A two-factor ANOVA with replication was carried out for f_{LOP} and f_{ult} (Table 19 and Table 20), which shows that both f_{LOP} and f_{ult} are influenced by the fibre content and type.

According to ANOVA, the cementitious material plays an important role in the f_{LOP}, and it does not influence the f_{ult} results. This may be because the improved adhesion between the LEC matrix and the fibres may be reduced after reaching the limit of proportionality, by the moment fibres start being pulled-out from the concrete.

Table 19 – f_{LOP} ANOVA two-factor with replication – wet mixes.

Source of variance	SS	dF	MS	F	P-value	F crit
Fibre content and type	11.81	3	3.94	22.15	3.14E-04	4.07
Cementitious material	4.82	1	4.82	27.10	8.17E-04	5.32
Interaction	0.71	3	0.24	1.33	0.332	4.07

Table 20 – f_{ult} ANOVA two-factor with replication – wet mixes.

Source of variance	SS	dF	MS	F	P-value	F crit
Fibre content and type	24.69	3	8.23	16.20	9.24E-04	4.07
Cementitious material	0.16	1	0.16	0.32	0.590	5.32
Interaction	2.97	3	0.99	1.95	0.200	4.07

5.2.1.2 Residual flexural strengths $f_{R,i}$

The residual flexural strengths were plotted in two graphs according to the cementitious material type, as shown in Figure 88. The residual flexural strength is an indirect way of characterising the ductility behaviour of SFRC and the calculation is based on the elastic theory, allowing a direct correlation with the values of f_{LOP}. High values of residual flexural strength mean that the SFRC has high post-cracking load carrying capacity.

The 2R mixes present the smallest values of residual flexural strength. However, even though the values are smaller compared to the 2I and 6R mixes, the 2R mixes present continuous ductile behaviour throughout the test (see Appendix C), and they fulfil the requirements of BS 14889-1 (2006a) – 1.5 MPa at 0.5 mm CMOD and 1.0 MPa at 3.5 mm CMOD. The performance of W-CIP-6R mix is better compared to W-CIP-2I. However, the opposite was observed for the LEC. Both fibre content and type seem to have similar effect in terms of $f_{R,i}$.

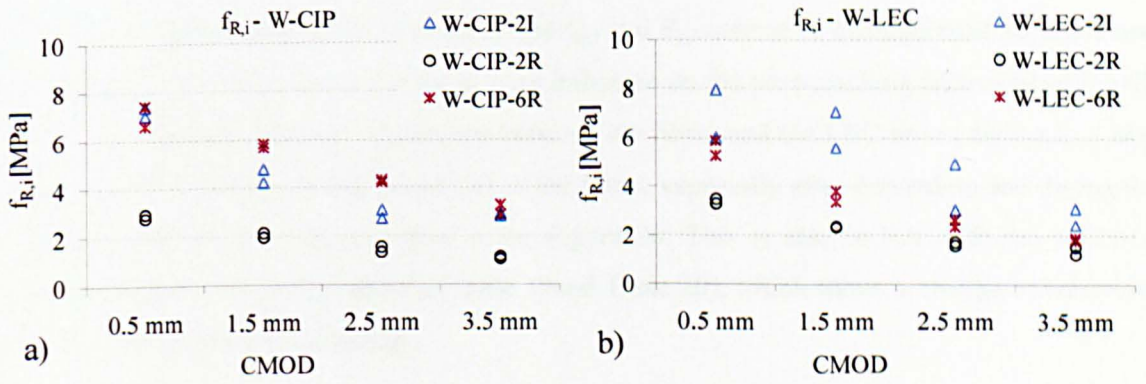

Figure 88 – $f_{R,i}$ for wet mixes.

There is no difference in the overall influence of the cementitious material type on the $f_{R,i}$, since similar results were observed.

5.2.1.3 Equivalent flexural strength f_{eq3} and equivalent flexural ratio $R_{e,3}$

Similar to $f_{R,i}$, the f_{eq3} and $R_{e,3}$ also provide an indication of the post-cracking behaviour of SFRC. To calculate f_{eq3}, the area under the bending load versus mid-span displacement curve, up to a displacement of 3 mm, is considered. Hence, the f_{eq3} can be defined as the post-cracking average stress based on the toughness capacity of the material (Neocleous *et al.*, 2006). The $R_{e,3}$ value indicates the drop in the load capacity up to a mid-span deflection of 3 mm compared to f_{LOP}. When $R_{e,3}$ is lower than 1.0, it indicates softening behaviour after cracking; when $R_{e,3}$ is equal to 1.0, it indicates elastoplastic behaviour and when $R_{e,3}$ is higher than 1.0, it indicates post-cracking hardening. The values obtained for the wet mixes are shown in Figure 89a and Figure 89b, for f_{eq3} and $R_{e,3}$, respectively.

The 2R mixes have the lowest values of f_{eq3} and $R_{e,3}$, which is in line with the results obtained for $f_{R,i}$. The 2I and 6R mixes present similar results, especially for the CIP cementitious material.

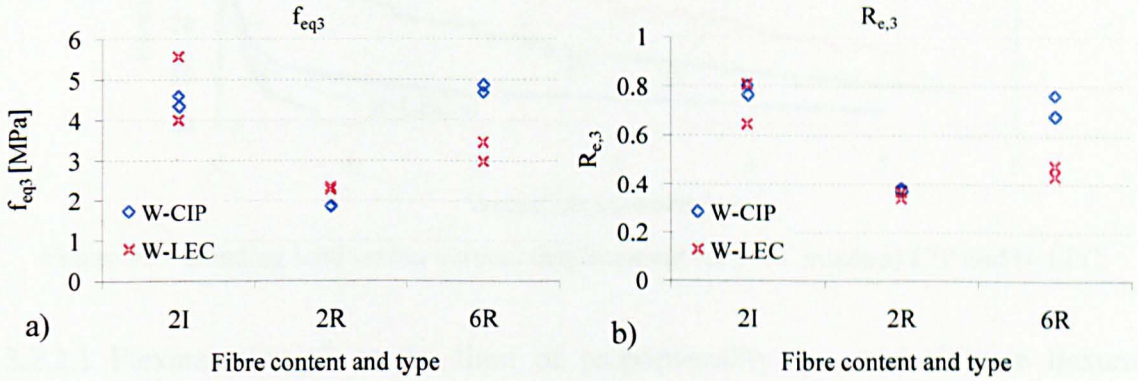

Figure 89 – a) f_{eq3} and b) $R_{e,3}$ for wet mixes.

The effect of the cementitious material on the f_{eq3} and $R_{e,3}$ cannot be distinguished for the 2I and 2R mixes, however, it seems that there is an influence on the post-cracking behaviour of the 6R mixes. The assumed improved adhesion between the fibres and the LEC mixes during f_{LOP} may lead to a more brittle pull-out behaviour of the fibres, especially after debonding and during the friction phase of the pull-out curve – see Figure 26. This is also in line with the ANOVA analysis carried out for f_{LOP} and f_{ult} (Table 19and Table 20), which shows a change in behaviour for the LEC mixes after cracking.

5.2.2 RCC Mixes

The bending load *versus* vertical displacement curves for RCC mixes (average of 2 specimens) are shown in Figure 90. The individual curves for each specimen can be found in Appendix C.

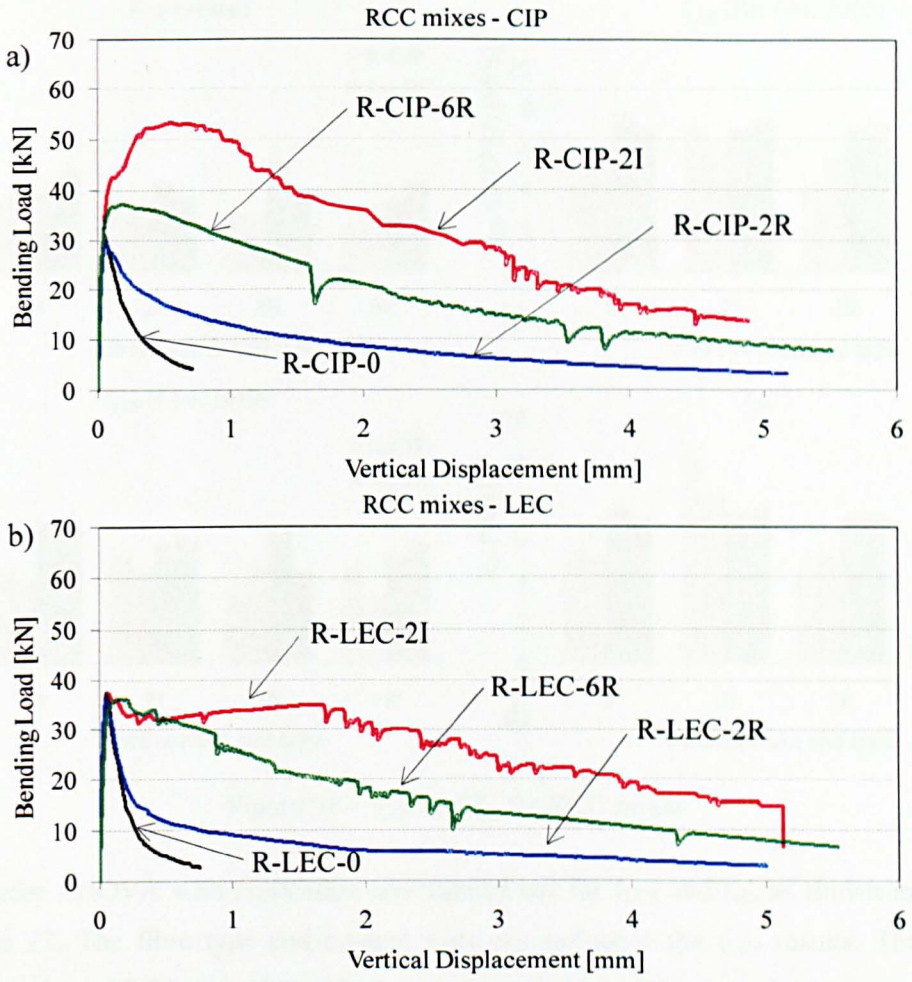

Figure 90 – Bending load *versus* vertical displacement for RCC mixes a) CIP and b) LEC.

5.2.2.1 Flexural strength at the limit of proportionality f_{LOP} and ultimate flexural strength f_{ult}

The results of f_{LOP} and f_{ult} for RCC mixes are shown in Figure 91.

Similar to the wet mixes, there seems to be a slight increase in the flexural strengths of LEC compared to CIP, which is especially true for f_{LOP} results.

The same comments as for wet mixes apply regarding the best method to calculate f_{LOP}.

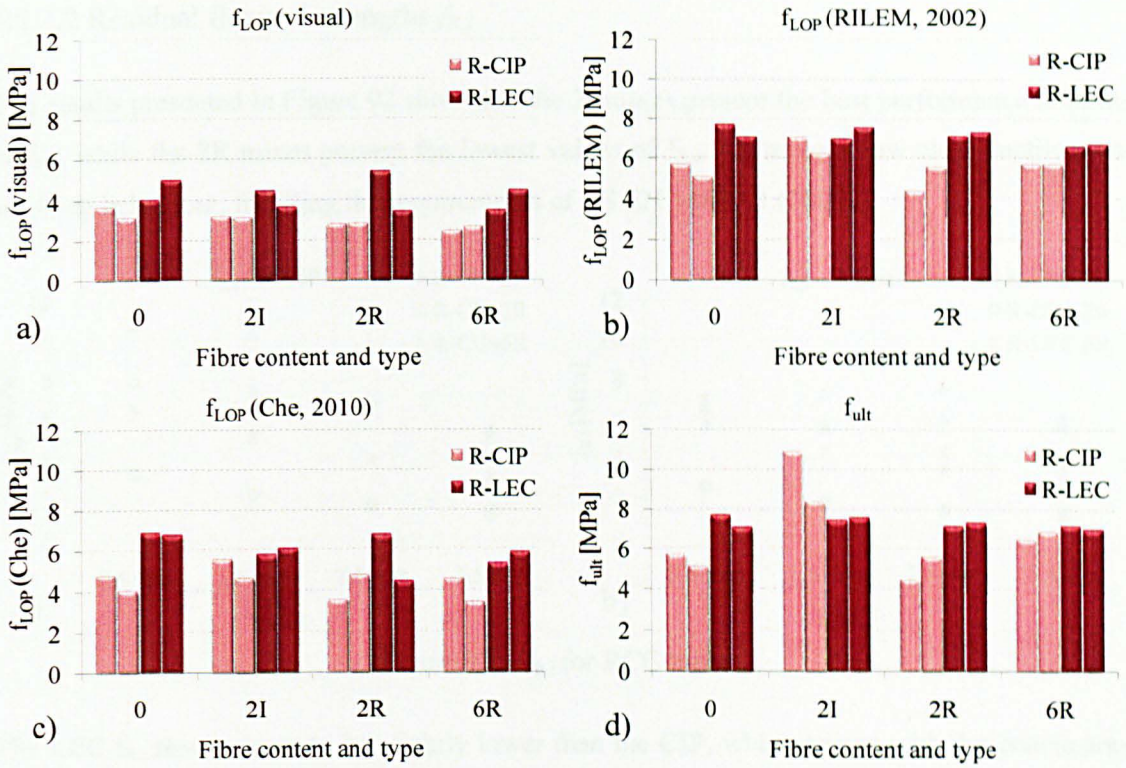

Figure 91 – f_{LOP} and f_{ult} for RCC mixes.

A two-factor ANOVA with replication was carried out for f_{LOP} and f_{ult}, as shown in Table 21 and Table 22. The fibre type and content does not influence the f_{LOP} results. This may be because reinforced RCC are affected by compaction problems (Sections 5.4 to 5.6 and Chapter 6), which lead to voids that are weak regions for propagation of micro-cracks, thus reducing f_{LOP}.

The cementitious material plays an important role in the f_{LOP} and it does not influence the f_{ult} results, leading to same conclusions as observed in the wet mixes ANOVA results.

Table 21 – f_{LOP} ANOVA two-factor with replication – RCC mixes.

Source of variance	SS	dF	MS	F	P-value	F crit
Fibre content and type	2.22	3	0.74	1.21	0.366	4.07
Cementitious material	9.55	1	9.55	15.67	0.004	5.32
Interaction	1.23	3	0.41	0.67	0.594	4.07

Table 22 – f_{ult} ANOVA two-factor with replication – RCC mixes.

Source of variance	SS	dF	MS	F	P-value	F crit
Fibre content and type	14.36	3	4.79	8.61	0.007	4.07
Cementitious material	1.40	1	1.40	2.53	0.151	5.32
Interaction	11.95	3	3.98	7.16	0.012	4.07

5.2.2.2 Residual flexural strengths $f_{R,i}$

The results presented in Figure 92 show that the 2I mixes present the best performance in terms of $f_{R,i}$, while the 2R mixes present the lowest values of $f_{R,i}$. All mixes show clear ductile post-cracking behaviour, fulfilling the requirements of BS EN 14889-1 (2006a).

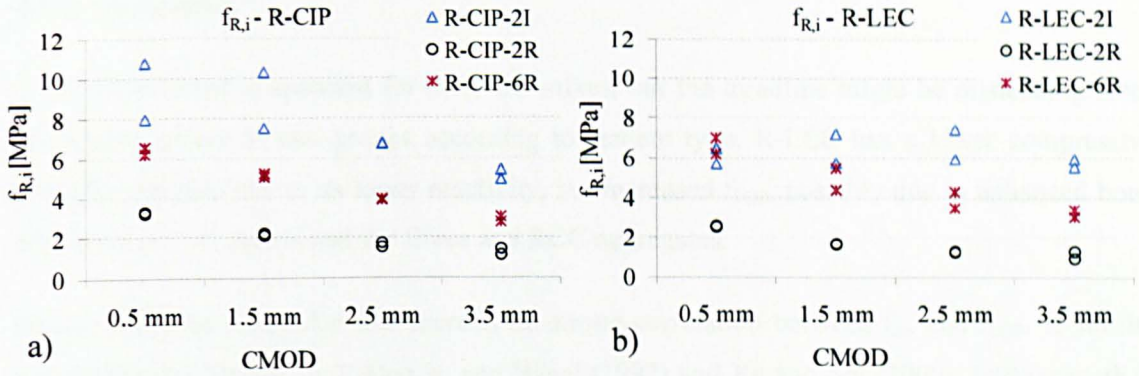

Figure 92 – $f_{R,i}$ for RCC mixes.

The LEC $f_{R,i}$ results seem to be slightly lower than the CIP, which agrees with the conclusions on the brittle pull-out behaviour of LEC mixes shown in Section 5.2.1.2.

5.2.2.3 Equivalent flexural strength f_{eq3} and equivalent flexural ratio $R_{e,3}$

Figure 93a and b show the results for f_{eq3} and $R_{e,3}$, respectively. The 2R mixes show the lowest values of f_{eq3} and $R_{e,3}$, which means the lowest energy absorption capacity when compared to the 2I and 6R mixes. The 2I mixes present the better performance in terms of toughness. The R-CIP-2I mix presents $R_{e,3}$ higher than *1*, which means that the average stresses due to energy absorption in the interval of 0 to 3 mm, are larger than f_{LOP}.

The influence of the cementitious material on the f_{eq3} is negligible. However, the CIP mixes seem to improve the $R_{e,3}$ results. This is probably because the pull-out behaviour of CIP mixes is more ductile than for LEC.

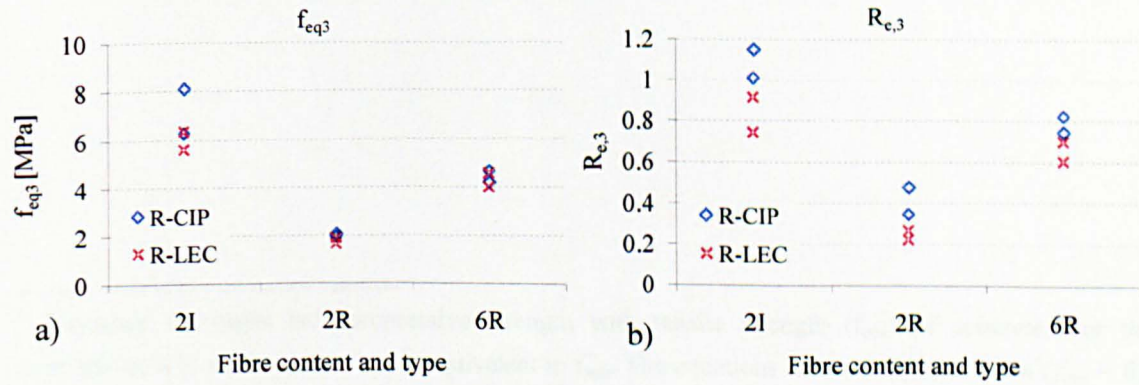

Figure 93 – a) f_{eq3} and b) $R_{e,3}$ for RCC mixes.

5.2.3 Comparison of f_{LOP} with f_{cm}

The values of f_{LOP} (Che, 2010) are compared with the results of f_{cm} in Figure 94 and with the prediction of Eurocode 2 (BS EN 1992-1-1, 2004b) for normal concrete. Overall, there is no clear trend, but for the wet mixes an increase in the f_{cm} increases f_{LOP}, as expected by the Eurocode equation[36].

An opposite trend is apparent for the RCC mixes, but the trendline might be misleading since the results appear in two groups according to cement type. R-LEC has a lower compressive strength, possibly due to its lower reactivity, but increased f_{LOP}, possibly due to enhanced bond between the LEC matrix and the fibres and RCC aggregates.

Hence, it can be concluded that there is no strong correlation between f_{cm} and f_{LOP}. A similar conclusion was arrived by Furlan Jr. and Hanai (1997) and Xu and Shi (2009). Further work is needed to understand why f_{LOP} does not increase in line with f_{cm}.

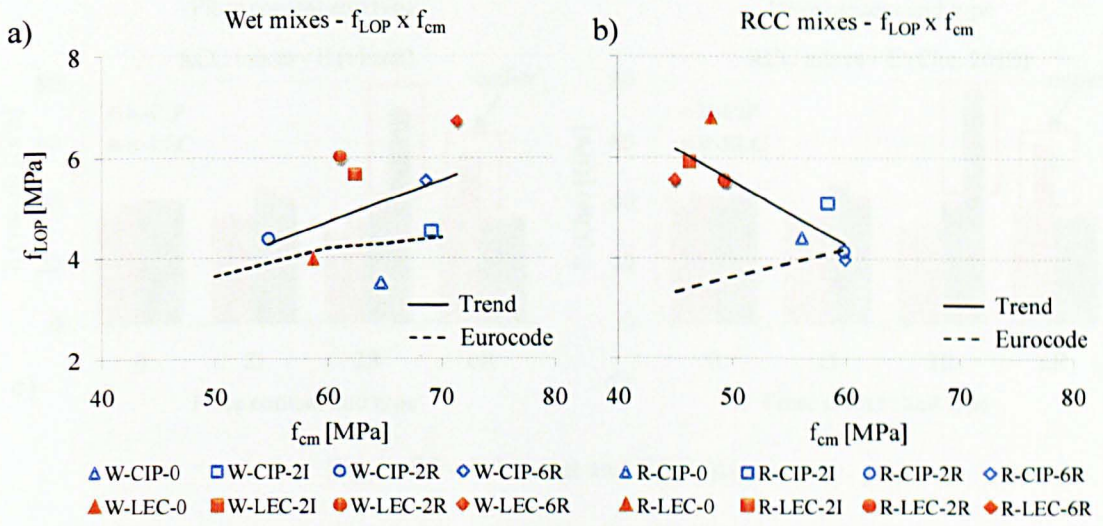

Figure 94 – Comparison of f_{LOP} to f_{cm}.

[36] Eurocode correlates the compressive strength with tensile strength (f_{ctm}) of concrete. For this comparison, it is assumed that f_{LOP} is equivalent to f_{ctm}. The equations used are: $f_{ctm} = 0.3 \times (f_{cm} - 8)^{\frac{2}{3}}$ for $f_{cm} \leq 50/60$ MPa and $f_{ctm} = 2.12 \ln\left(1 + \left(\frac{f_{cm}}{10}\right)\right)$ for $f_{cm} > 50/60$ MPa.

5.3 MODULUS OF ELASTICITY

5.3.1 Results

The modulus of elasticity was calculated by using two approaches (Section 4.4.2.3): 1) visual and 2) Che (2010). The results obtained from both approaches, for wet and RCC mixes, are shown in Figure 95.

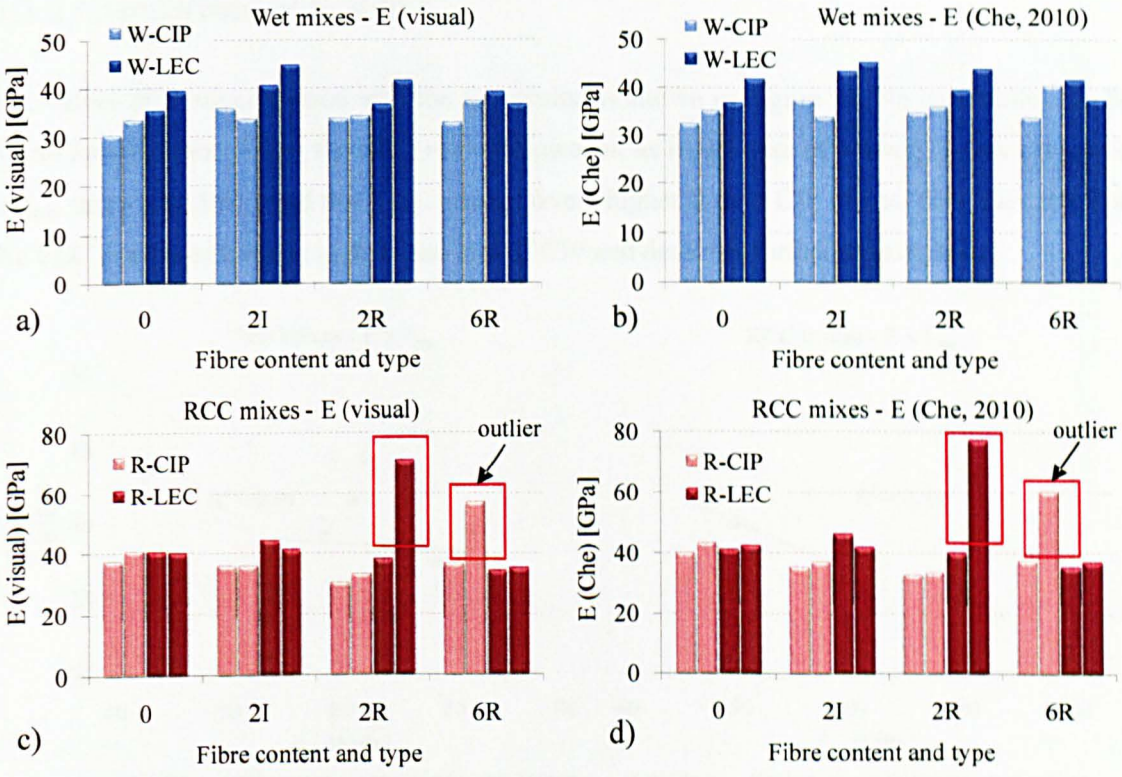

Figure 95 – E for wet and RCC mixes.

Mixes cast with LEC show in general higher E than the mixes cast with CIP. No clear influence of the fibre content and type can be found on the results for both wet and RCC mixes.

The results for the second specimen of both mixes R-LEC-2R and R-CIP-6R (highlighted in Figure 95c and d) deviate considerably from the remaining results. The load *versus* vertical displacement curves from both specimens were analysed to verify possible causes for the high modulus of elasticity. For mix R-LEC-2R, if E is calculated following increments of load and displacement (difference between two consecutive measurements of load and displacement), the value of E drops to similar result (36.7 GPa, visual approach and 40.3 GPa, Che's method) as for the other specimen from the same mix (E curve is shown in Appendix C). This indicates that the initial high stiffness is not valid to represent the elastic behaviour of the material. Mix R-CIP-6R, however, did not show any reduction in the modulus of elasticity and, for this reason,

the value obtained was considered as an outlier. This can be attributed to a mistake on the calibration factors used for the LVDTs during the flexural test of that specimen.

RCC results are usually higher than for wet mixes. Apart from the differences in the mix proportion, the aggregate interlock effect and the high energy used for compaction of RCC may also influence the results, leading to a more stiff material. This also agrees with the density results shown later in Section 5.4.

5.3.2 Comparison of E with f_{cm}

The values of E are compared with the f_{cm} results, as shown in Figure 96. No correlation can be found for either the wet or the RCC mixes. However, as in the case of when f_{LOP} was compared to f_{cm}, there is a clear trend that LEC results have a higher E than CIP mixes. This indicates that the LEC matrix stiffness is higher than that of CIP and deserves further investigation.

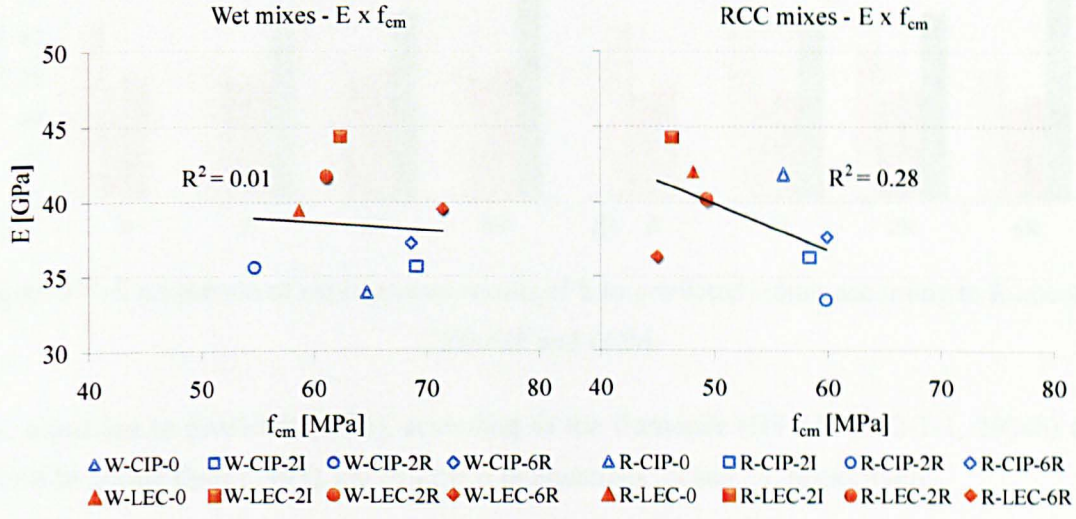

Figure 96 – Comparison of E with f_{cm}.

The lack of correlation between f_{cm} and E conflicts with the codes of practice, since they commonly use f_{cm} to estimate the modulus of elasticity. However, a better correlation between f_{cm} and E is expected when using the same specimens, or at least the same procedure and specimen geometry to perform the tests. As explained in Chapter 4, the modulus of elasticity was obtained from prisms subjected to flexural loads whilst the compressive strength was obtained from cubes. The better approach would be to test cylinders under compression and measure both the compressive and the modulus of elasticity.

Nevertheless, it is also important to note that the behaviour of SFRC is expected to be different than that for normal strength concrete, usually assumed in the E – f_{cm} correlations proposed by the codes of practice.

5.3.3 Comparison of Experimental E with Predicted Results

The experimental results were compared to the predicted values of E according to the *Eurocode* (BS EN 1992-1-1, 2004b), CEB-FIP Model Code (1993) and the rule of mixtures (*LOM* – described previously in Section 2.3.2.1, Equation 2), as shown in Figure 97.

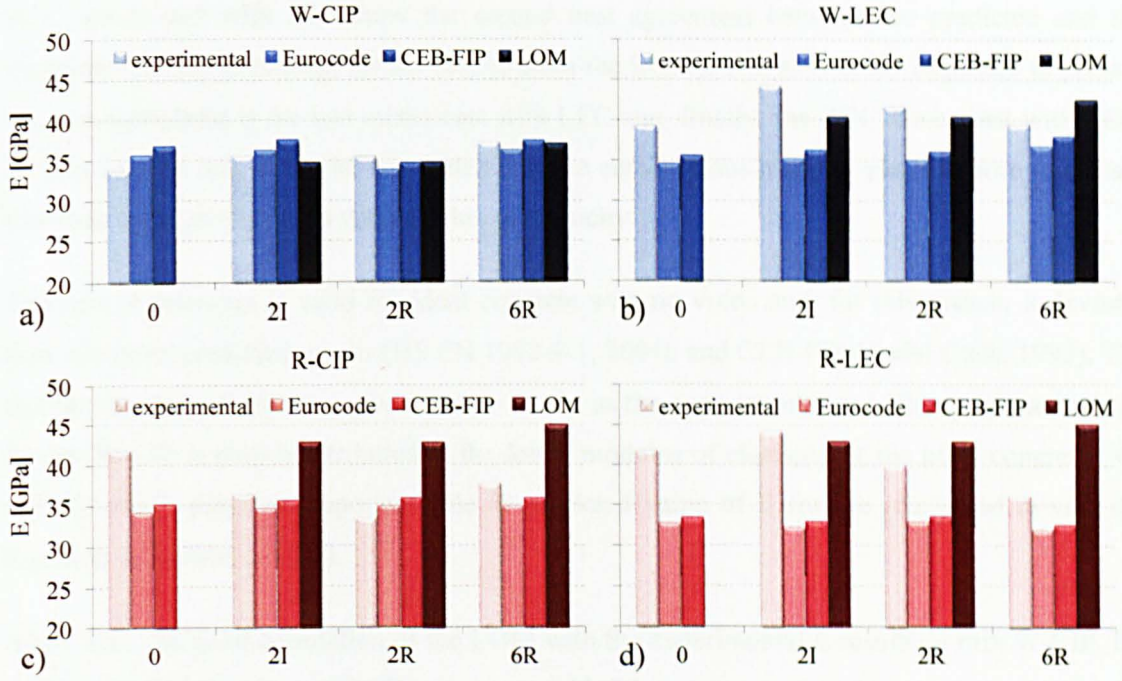

Figure 97 – Comparison of experimental results of E to predicted values according to Eurocode, CEB-FIP and LOM.

The equations to predict E [MPa], according to the Eurocode (BS EN 1992-1-1, 2004b) and CEB-FIP Model Code (1993), are described in Equations 28 and 29, respectively.

$$E_{cm} = 22\left[\frac{(f_{cm})}{10}\right]^{0.3} \quad (28)$$

Where:

f_{cm} = mean value of concrete cylinder compressive strength [MPa][37]

$$E_{cm} = E_{co}\left[\frac{f_{cm}}{f_{cmo}}\right]^{\frac{1}{3}} \quad (29)$$

Where:

E_{co} = 2.15×10^4 MPa

f_{cmo} = 10 MPa

[37] since the experimental compressive strength tests were carried in cubes, the cylinder compressive strength was calculated considering that the strength of the cube is 28.5% higher than the cylinder test (BS EN 1992-1-1, 2004), based on an average of various strength classes shown in the standard.

The graphs above show that the predicted values agree with the results obtained from the wet mixes cast with CIP only (Figure 97a). This is mainly because the Eurocode and CEB-FIP predictions are valid mainly for conventional concrete cast with conventional cement types. RCC and mixes cast with LEC do not fulfil these requirements. Currently, it seems that no models are available in the literature for the prediction of the modulus of elasticity of RCC.

RCC mixes cast with CIP show the second best agreement between the predicted and the experimental results (except for the results from the LOM). The next in the sequence to present the best agreement is the wet mixes cast with LEC and, finally, the RCC mixes cast with LEC. By considering this, it can be concluded that the cementitious material plays a more important role than the type of mix on the modulus of elasticity.

The rule of mixtures is valid for ideal concrete with no voids and, for this reason, it deviates from the other predicted results (BS EN 1992-1-1, 2004b and CEB-FIP Model Code, 1993). The fact that the law of mixtures gives similar results as the experimental and other predicted results for the W-CIP is mainly attributed to the lower modulus of elasticity of the plain concrete (W-CIP-0), which plays an important role in predicted value of E for the reinforced mixes (see Equation 2, Section 2.3.2.1).

Apart from the good correlation of the LOM with the experimental E results of mix W-CIP, the predicted LOM E values of LEC mixes cast with 2R and 2I are also close to the experimental results. This is shown in Figure 98, based on the influence of the fibre content on the predicted values of E calculated by the LOM. CIP mixes have a constant ratio of $E_{LOM}/E_{experimental}$ when the fibre content increases from 2% to 6%. The opposite behaviour is observed for LEC mixes, since the $E_{LOM}/E_{experimental}$ ratio increases considerably when the fibre content increases from 2% to 6%.

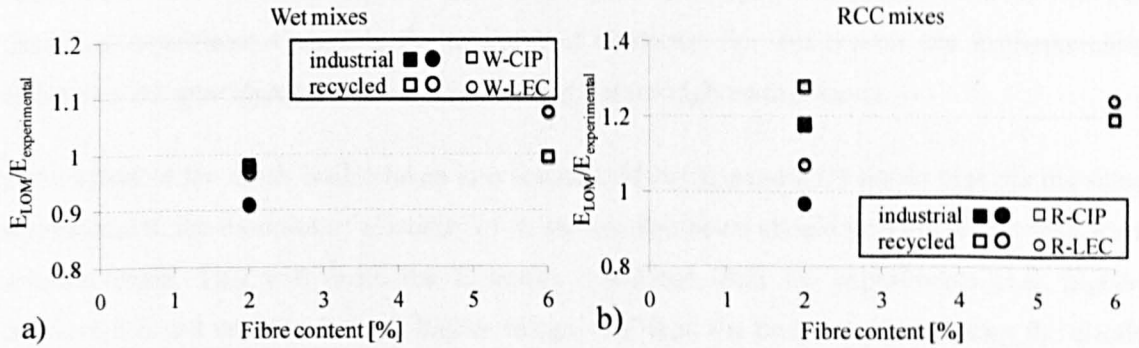

Figure 98 – $E_{LOM}/E_{experimental}$ *versus* fibre content.

5.3.4 Load-Spreading Effect

The results of E obtained for the W-LEC and R-LEC mixes are in general much higher than those predicted values by the BS EN 1992-1-1 (2004b) and CEB-FIP Model (1993). To verify the accuracy of E results obtained from the experiments, a Finite Element Analysis (FEA) was carried out to assess the effect of load distribution throughout the depth of the specimen, also called *load-spreading* effect (Timoshenko and Goodier, 1970). Basically, the load-spreading effect considers that, for deep elements, the concentrated forces applied to the specimen may change to a distributed pressure as shown in Figure 99.

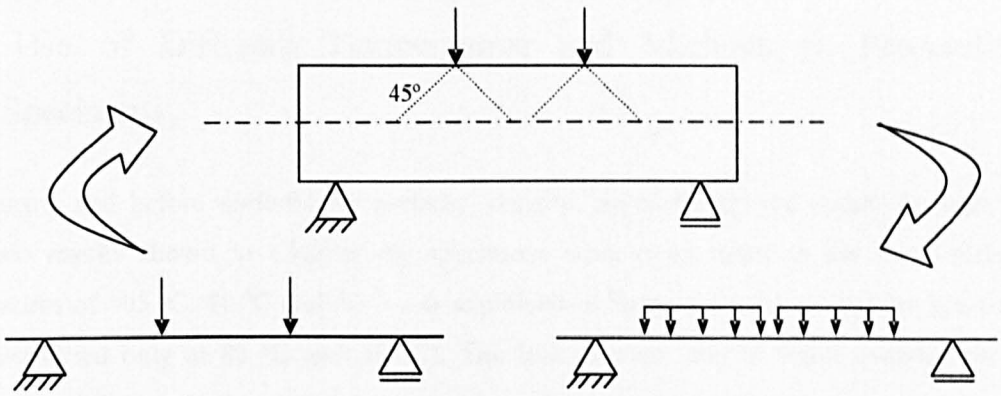

Figure 99 – Load-spreading effect.

The load-spreading effect could be responsible for lower displacements measured during the experiments, and for the consequent high modulus of elasticity. The results of E (shown in Figure 95) were calculated based on the elastic beam theory, which does not account for the effects of the load-spreading effect.

The results of the FEA (detailed in Appendix D) show that the load-spreading effect is responsible for a reduction in the vertical displacements of approximately 2%, which does not cause any significant change in the modulus of elasticity. For this reason, the load-spreading effect was not considered in the analyses carried out throughout this thesis.

If the effect of the notch is also taken into account, FEA (Appendix D) shows that, for the same displacement, the modulus of elasticity of an un-notched beam should be 17% higher than for a notched beam. This will make the E results calculated from the experiments even higher. Because it is not realistic to have higher values of E than the ones calculated using the elastic beam theory, it seems reasonable to assume that the elastic beam theory is valid for the purposes of this study.

The fact that LEC mixes show higher E than the mixes cast with CIP may be attributed to a better bond between the fibres and the matrix due to the chemical constituents and physical characteristics of the cementitious material.

Other parameters (e.g. Poisson ratio) may be responsible for the high values of E, and they should be taken into account in future investigations. It is also important to verify the correlation of the modulus of elasticity obtained from both flexural and compressive tests.

5.4 DENSITY

5.4.1 Use of Different Temperatures and Methods to Precondition Specimens

After curing and before undertaking porosity, density, permeability and sorptivity tests (the latter two results shown in Chapter 6), specimens were oven dried at the three different temperatures of 105 °C, 80 °C and 50 °C, as explained in Section 4.4.3.1 (sorptivity specimens were oven-dried only at 80 °C and 50 °C). The loss of mass due to water evaporation was measured, and the results in terms of evaporable moisture concentrations w_e, w_{e80} and w_{e50}, for the temperatures of 105 °C, 80 °C and 50 °C, are shown in Figures 100, 101 and 102, respectively.

The evaporable moisture concentrations w_e and w_{e80} represent the ratio between the total amount of evaporated water and the dry mass of the specimen after reaching constant mass, when oven dried at 105 °C and 80 °C, respectively. Mixes with higher values of w_e and w_{e80} have a higher amount of free water available in the mix. The amount of free water is an indication of the material porosity: higher values of free water should lead to higher porosity. It is important to add that the total amount of evaporated water at 105 °C can also be called the total evaporable water of the concrete, since it is considered that 105 °C causes total evaporation of the free and adsorbed water and may also influence the interlayer and bound water (Section 3.2.1.1).

Each point in Figure 100 represents the result for one specimen (two specimens per mix) while the columns of Figures 101 and 102 represent an average of 5 specimens per mix. The standard deviation is shown as error bars on the top of the columns (length of error bars is equal to two standard deviations).

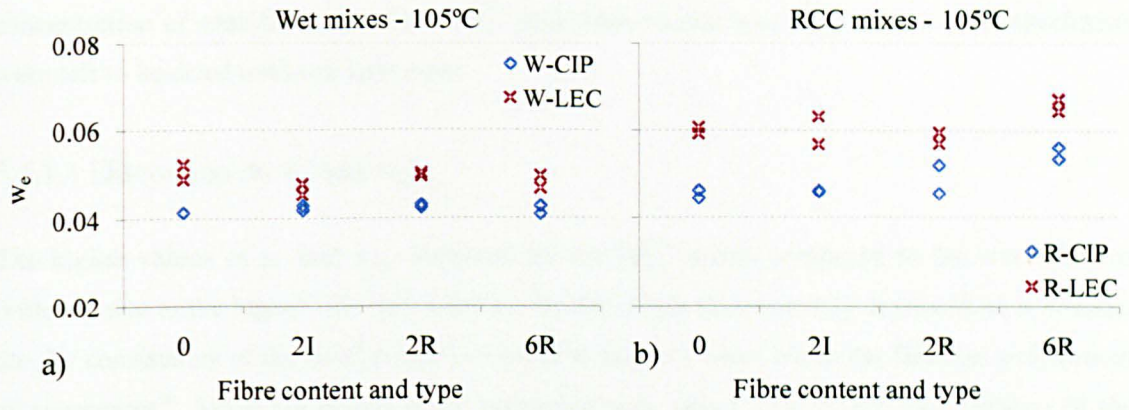

Figure 100 – Evaporable moisture concentration w_e at 105 °C.

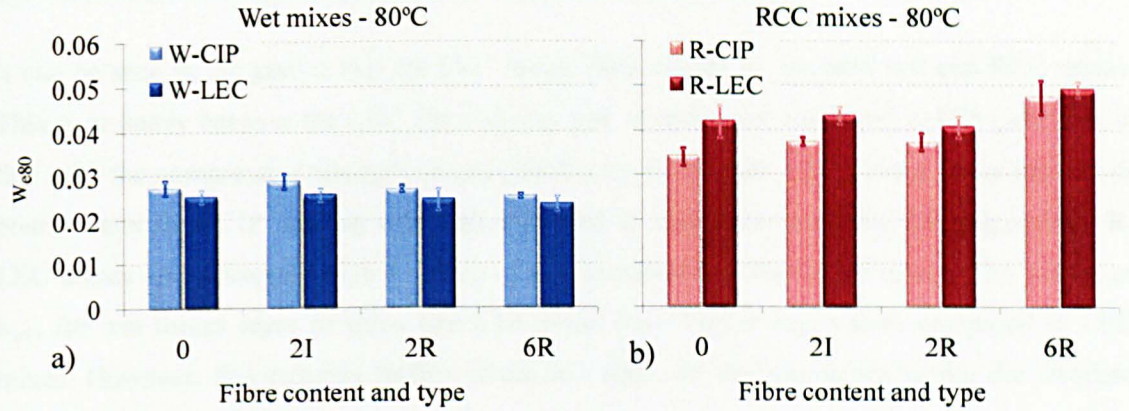

Figure 101 – Evaporable moisture concentration w_{e80} at 80 °C.

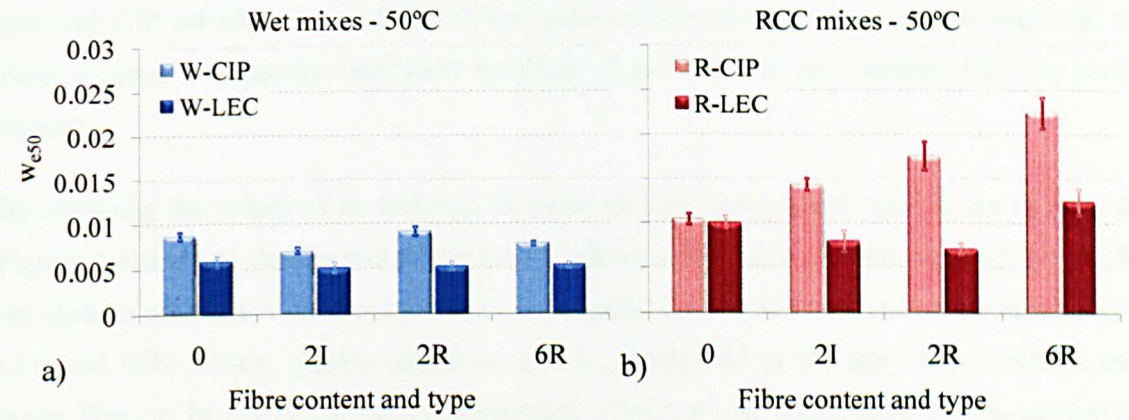

Figure 102 – Evaporable moisture concentration w_{e50} at 50 °C.

For the preconditioning temperature of 50 °C, the amount of evaporable water was predicted according to the procedure given in Section 4.4.3.1. It was not obtained by successive measurements until constant mass, as for the temperatures of 105 °C and 80 °C. It is important to note that the w_{e50} shown in Figure 102 does not refer to the *true* evaporable moisture

concentration of specimens dried at 50 °C, since their values would be higher if the specimens were left to be dried until constant mass.

5.4.1.1 Discussion on w_e and w_{e80}

The higher values of w_e and w_{e80} obtained for the RCC mixes compared to the wet mixes is probably due to the higher w/c ratio used for the dry mixes (Section 4.2). It should be noted that the dry consistency of the RCC mixes is not due to low w/c ratio, but to the fineness and amount of aggregates[38]. Since the bound water represents only about 23% of the total volume of the cement (Section 3.2), the remaining free water is available for evaporation. For this reason, w_e and w_{e80} can give an indirect indication of the porosity of the material.

It can be seen in the graphs that the LEC mixes show higher w_e for both wet and RCC mixes. This is probably because the LEC has a slower rate of hydration compared to CIP (which is in line with the compressive strength results), therefore, mixes with LEC have a lower amount of bound water than CIP, leading to a higher amount of free water available for evaporation. R-LEC mixes also presented higher values of w_{e80} compared to the R-CIP mixes. The values of w_{e80} for wet mixes seem to show that CIP mixes have higher w_{e80} values compared to LEC mixes. However, this requires further discussion since all the results are within the standard deviation errors.

The fact that the RCC mixes cast with LEC present higher w_e and w_{e80} compared to the mixes cast with CIP can also be due to the higher water content used to cast the mixes with LEC to allow a proper compaction and good finishing of the surfaces (see Section 4.2.2 for more details).

By analysing the values of w_e and w_{e80} in terms of fibre content and type, it can be seen in Figures 100 and 101 that the wet mixes are not influenced by fibre addition, since all the results are close to each other. On the other hand, by considering the RCC mixes, the 6R mixes (both LEC and CIP) present slightly higher w_e and w_{e80} compared to the other fibre contents and types. This can be due to compaction limitations of such mixes, which increases the amount of voids and collaborates for the easier evaporation of free water from the specimens. For well compacted mixes, the evaporation of water from the pores located in the centre of the specimens is more difficult (depending on the dimensions of the specimen), hence, even if high temperatures such as 105 °C are applied, part of the water in the middle of the specimen may not evaporate.

[38] Section 4.2 shows that the w/c ratio of RCC mixes is higher than for wet mixes. However, the amount of aggregates in RCC is higher than wet mixes. Also, RCC aggregates are finer than wet aggregates, leading to a drier consistency for RCC mixes.

5.4.1.2 Discussion on w_{e50}

The RCC mixes show higher w_{e50} values than the wet mixes. As already previously explained for the temperatures of 105 °C and 80 °C, the main cause is the higher amount of free water (higher w/c ratio) in the RCC mixes compared to the wet mixes.

It can be clearly noticed that CIP presented higher w_{e50} than the LEC mixes. However, since it is expected that LEC have higher amount of free water than CIP mixes, which should lead to higher amount of evaporable water and w_{e50} for LEC (which is not observed), it is important to understand how the w_{e50} was calculated.

The amount of evaporable water at 50 °C was calculated according to Equation 20 (Section 4.4.3.1). An important factor that governs the equation is the difference between the evaporable moisture concentration w_e and the equilibrium moisture concentration $w_{e,75}$. $w_{e,75}$ is the difference of the mass of specimens conditioned at 20 °C and 75% RH and the dry mass of specimens, divided by the dry mass of specimens. The results for $w_{e,75}$ are shown in Figure 103. If the results of Figure 103 are compared to the results of Figure 100 (shown in Figure 104), it can be seen that the LEC results of w_e and $w_{e,75}$ are similar (for both wet and RCC mixes), while a higher difference is noticed between the results of w_e and $w_{e,75}$ for the CIP mixes. This indicates that the CIP mixes allow higher evaporation of water at 20 °C and 75% RH than the LEC mix.

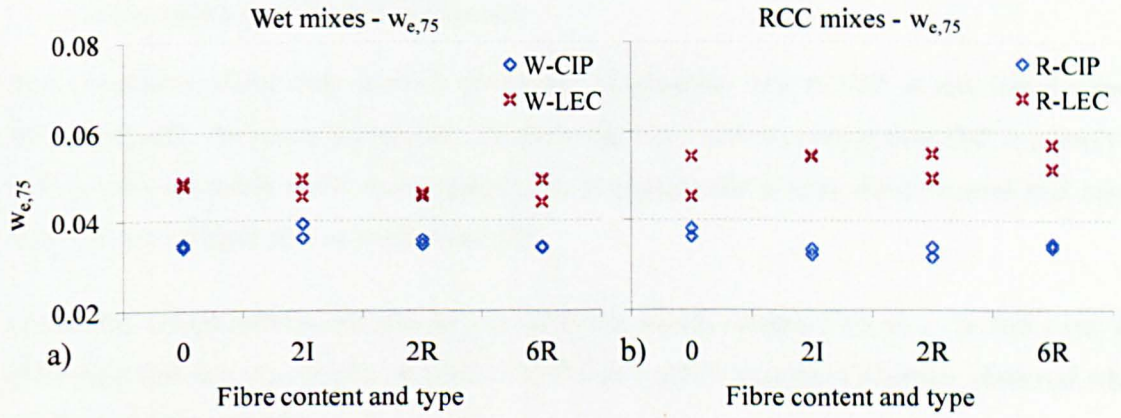

Figure 103 – Equilibrium moisture concentration $w_{e,75}$ at 50 °C.

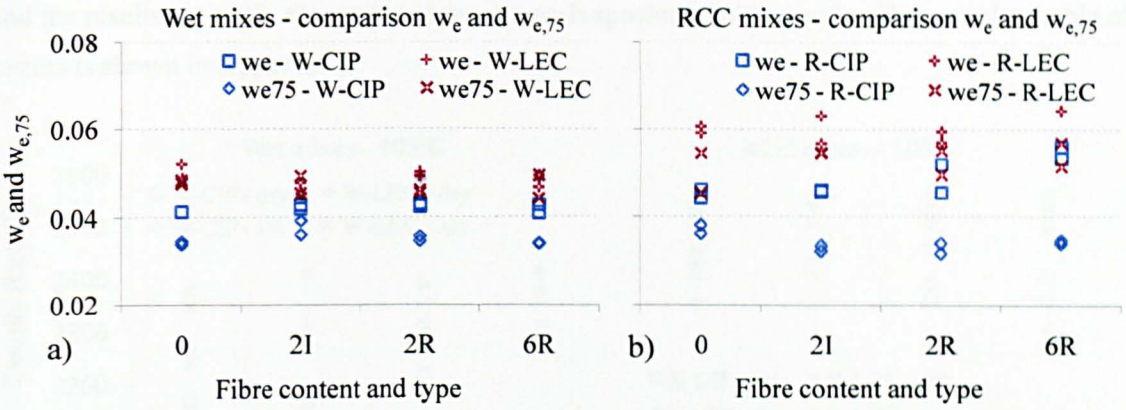

Figure 104 – Comparison between w_e and $w_{e,75}$.

When low temperatures are used, the total evaporable (free) water is not completely removed from the pores, as it is usually assumed when a temperature of 105 °C is applied. Therefore, even though the LEC should present higher amount of free water than CIP, the characteristics of the pore structure of the material also seems to play an important role on the rate of water evaporation from the concrete. Hence, the higher values of w_{e50} and $w_{e,75}$ for the LEC compared to CIP, which is the opposite of what was observed for the 105 °C, can be attributed to one of the two:

1) higher porosity of the CIP compared to LEC

2) larger pores of CIP compared to LEC (according to Abbas *et al.*, 1999, water evaporates faster from larger pores)

The hypotheses above may explain the higher evaporation rate of CIP at low temperatures. Since the results for porosity (Section 5.5) show that LEC is more porous than CIP, it seems that the second hypothesis is the more appropriate to explain the results, which means that mixes with CIP have bigger size of pores than LEC.

The above considerations are also in line with the results obtained for w_{e80}. In that case, the difference between w_{e80} results of LEC to CIP was smaller than the difference observed when considering the w_e results.

5.4.2 Density Results

Density measurements were taken on the same specimens used to determine porosity and permeability of concrete (Sections 5.5 and 6.1). The results obtained for the dry and saturated density of RCC and wet mixes dried at 105 °C, 80 °C and 50 °C are shown in Figures 105, 106 and 107, respectively. Two specimens were analysed per mix, per preconditioning temperature,

and the results shown in the graphs represent each specimen individually. The complete table of results is shown in Appendix E.

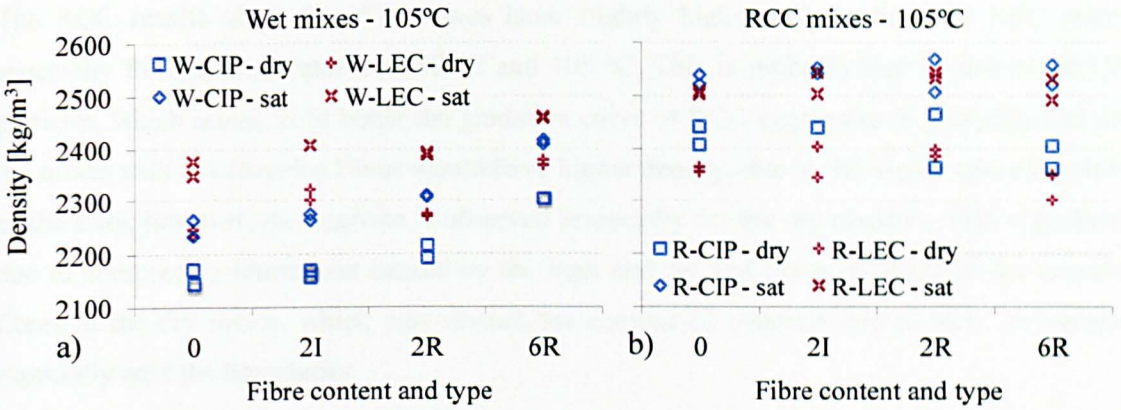

Figure 105 – Density at 105 °C.

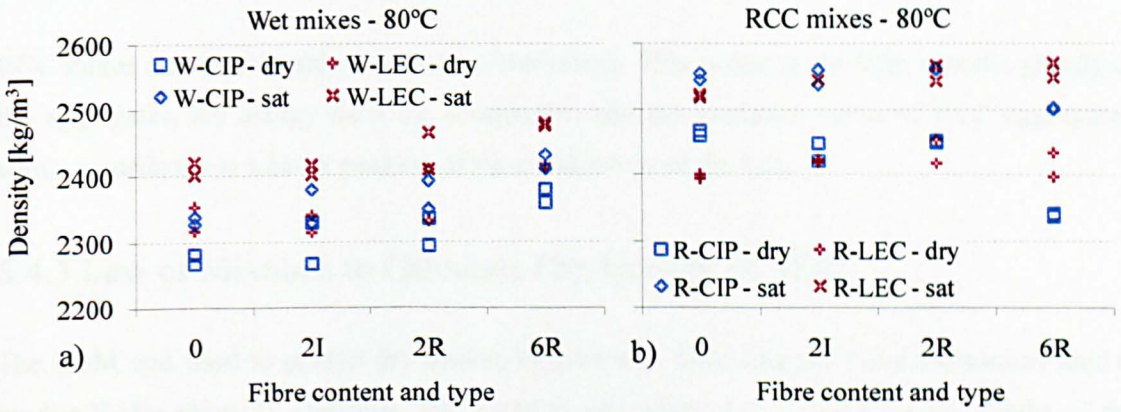

Figure 106 – Density at 80 °C.

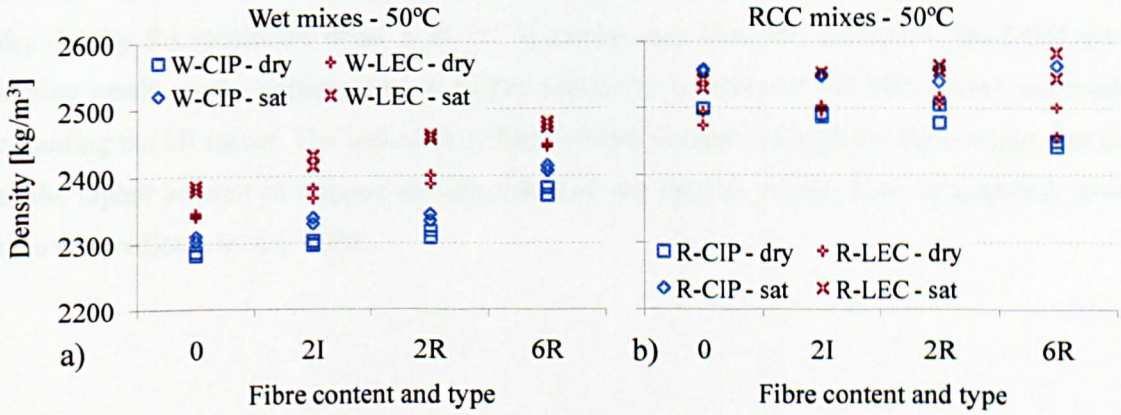

Figure 107 – Density at 50 °C.

By analysing the results for wet mixes, it is observed that the LEC mixes are denser than the CIP mixes. As previously explained, this is probably because the LEC mixes have smaller pore sizes than the CIP mix, which refines the structure of the concrete, thus increasing density.

The higher values of density observed for the 6R wet mixes are probably due to the higher amount of fibres, which have higher specific gravity than the other concrete components[39].

The RCC results show that CIP mixes have slightly higher density than the LEC mixes, especially for the temperatures of 80 °C and 105 °C. This is probably due to size of the CIP particles, which seems to fit better the gradation curve of RCC aggregates. It was expected that the mixes with 6% recycled fibres would have higher density, due to the higher specific gravity of the steel, however, the opposite is observed (especially for the dry density). This is probably due to compaction limitations caused by the high amount and irregular shape of the recycled fibres in the dry mixes, which may disturb the compacted concrete due to their *springiness*, especially next the boundaries.

Fibre content and type appear to influence density, especially for the mixes reinforced with 6% recycled fibres.

RCC mixes are considerably denser than wet mixes. This is due to the high specific gravity of the aggregates, the energy used for compaction and the gradation curve of RCC aggregates, which contributes to a better packing of the constituents of the mix.

5.4.3 Law of Mixtures to Calculate Dry Density of SFRC

The LOM was used to predict dry density of concrete, following the same expression used to predict E (Equation 2). However, the equation was adapted to account for the results of dry density instead of E. Values of plain concrete dry density was used for the calculation of LOM density. Figure 108 shows the comparison of the LOM values with the experimental results of dry density for specimens dried at 80 °C. It can be seen that, for wet mixes, the LOM gives similar results as the experiments. A higher variability is observed for RCC mixes, especially regarding the 6R mixes. The inclusion of fibres should increase density for these mixes, but due to the higher amount of trapped air, experimental dry density values were considerably lower than the predicted by the LOM.

[39] For a plain wet concrete (same mix proportion as W-CIP-0) with density of 2350 kg/m^3, the addition of 1% by mass of fibres increases approximately 0.7% the density of the concrete (based on the volumetric calculation). This varies according to the mix proportion of the concrete.

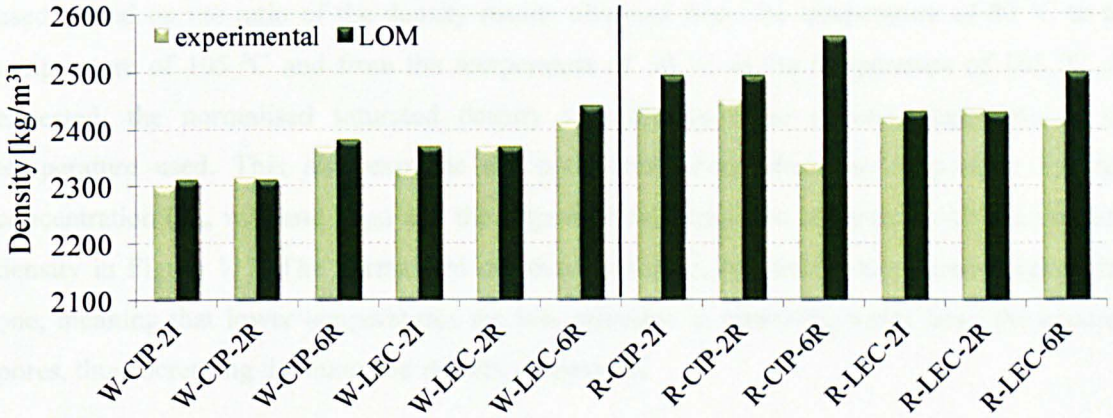

Figure 108 – Experimental and predicted LOM dry density.

If the porosity (Section 5.5) is taken into account for the RCC mixes, the revised predictions are shown in Figure 109. The experimental results agree with the prediction of the LOM, indicating that the compaction method used for RCC mixes increases the amount of trapped air for mixes reinforced with fibres, and that it affects the density results of the material.

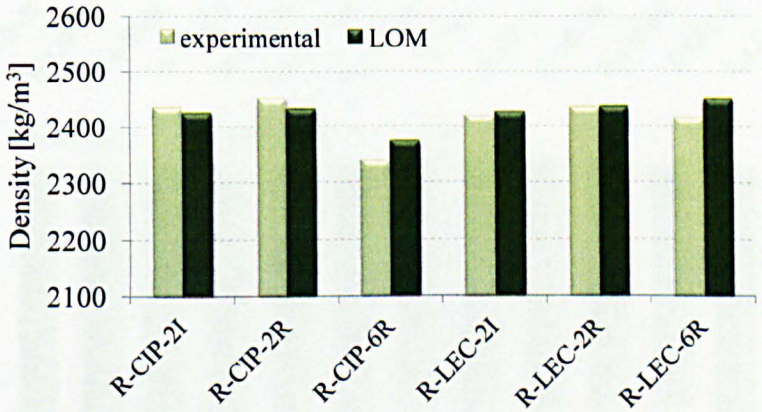

Figure 109 – Experimental and predicted LOM dry density for RCC mixes, accounting for the porosity of the mixes.

5.4.4 Influence of Preconditioning Temperature on the Density of Concrete

The lower the temperature used to oven-dry the specimens, the higher should be the dry density of the specimens, because of the higher amount of water in the pores. The values of saturated density, however, should all be similar when comparing the same mix at different oven-drying temperatures, since the preconditioning temperature affects the degree of saturation of the specimens only, and not the behaviour of the concrete while in fully saturated condition.

Density (saturated and dry) results obtained from the three temperatures used for oven-drying the specimens are compared among them in Figure 110. Normalised values of density were

used, based on the ratio of the density results obtained from the temperature of 80 °C to the temperature of 105 °C and from the temperature of 50 °C to the temperature of 105 °C. As expected, the normalised saturated density was always close to one, regardless of the temperature used. This also explains the poor correlation when the evaporable moisture concentration (w_e, w_{e80} and w_{e50}) and the degree of saturation are compared with the saturated density in Figure 111. The normalised dry density results, however, were mostly higher than one, meaning that lower temperatures are less effective in removing water from the concrete pores, thus increasing the mass and density of samples.

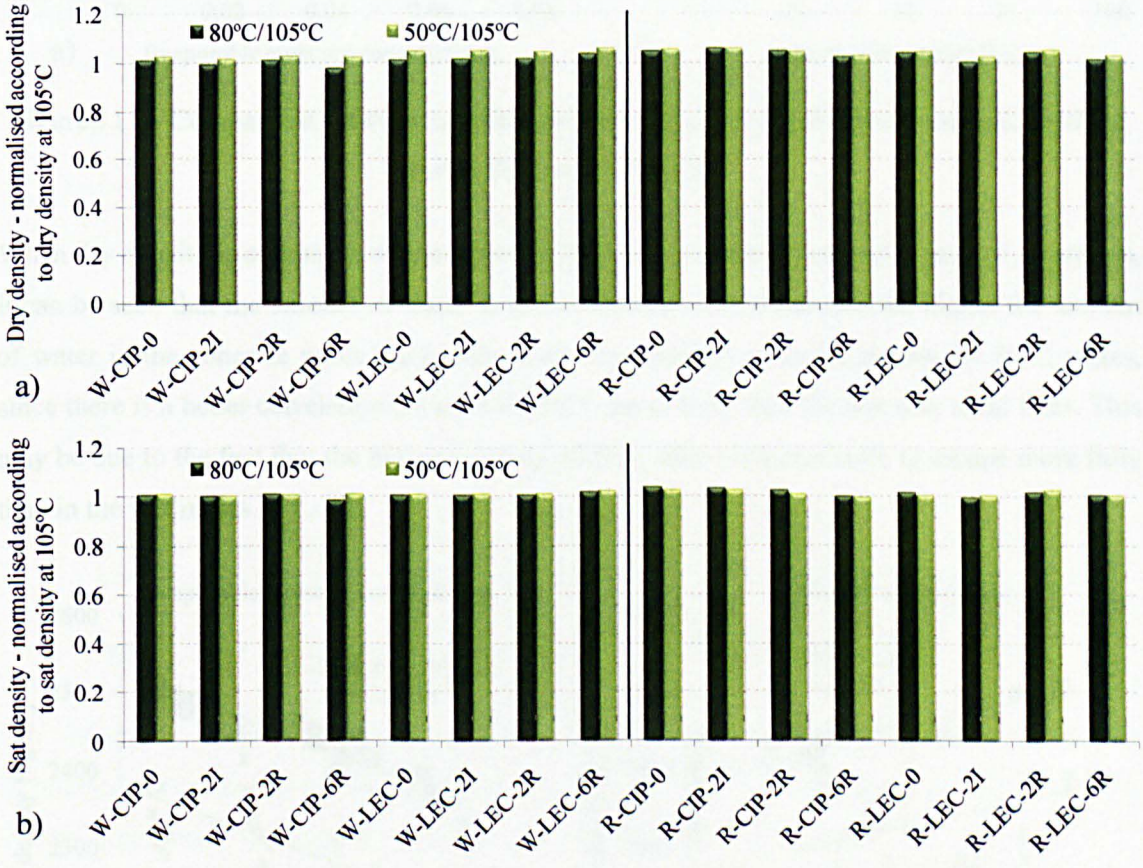

Figure 110 – Comparison of dry and saturated density results to different preconditioning temperatures.

The degree of saturation was calculated considering that the temperature of 105 °C removes 100% of the evaporable water of the specimens (even though not entirely true), giving a degree of saturation of 0%. For the temperatures of 80 °C and 50 °C, the degree of saturation was obtained by comparing the values of the amount of evaporable water from those temperatures to the total evaporable water obtained at 105 °C.

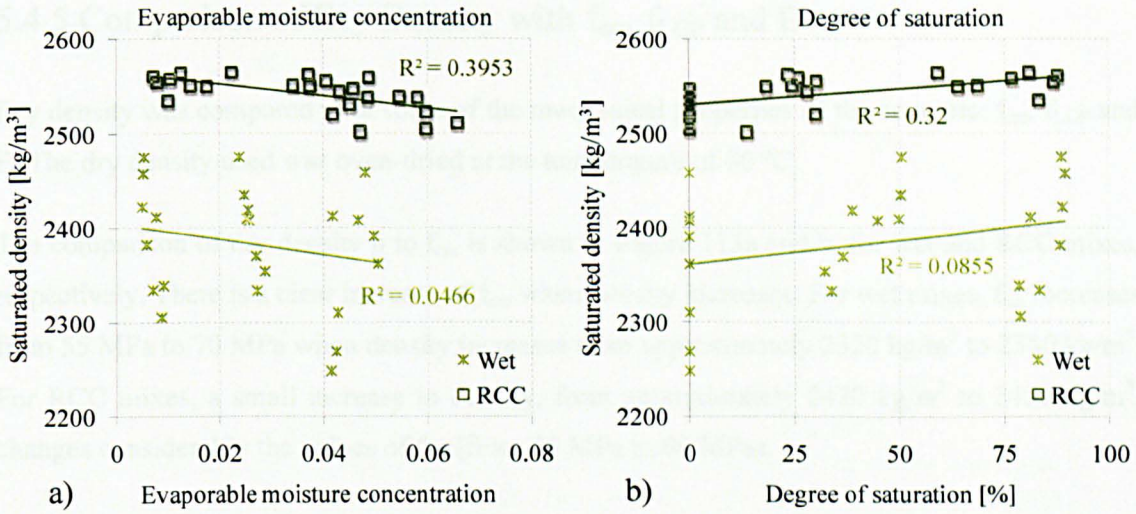

Figure 111 – Comparison between saturated density and a) evaporable moisture concentration and b) degree of saturation.

When dry density is compared with evaporable moisture concentration and degree of saturation, it can be seen that the amount of water in the concrete pores influences (the higher the amount of water in the concrete pores the higher is the dry density) more the results for RCC mixes, since there is a better correlation between the RCC trend lines than the wet mix trend lines. This may be due to the fact that the higher porosity of RCC allows the moisture to escape more fully than in the wet mixes.

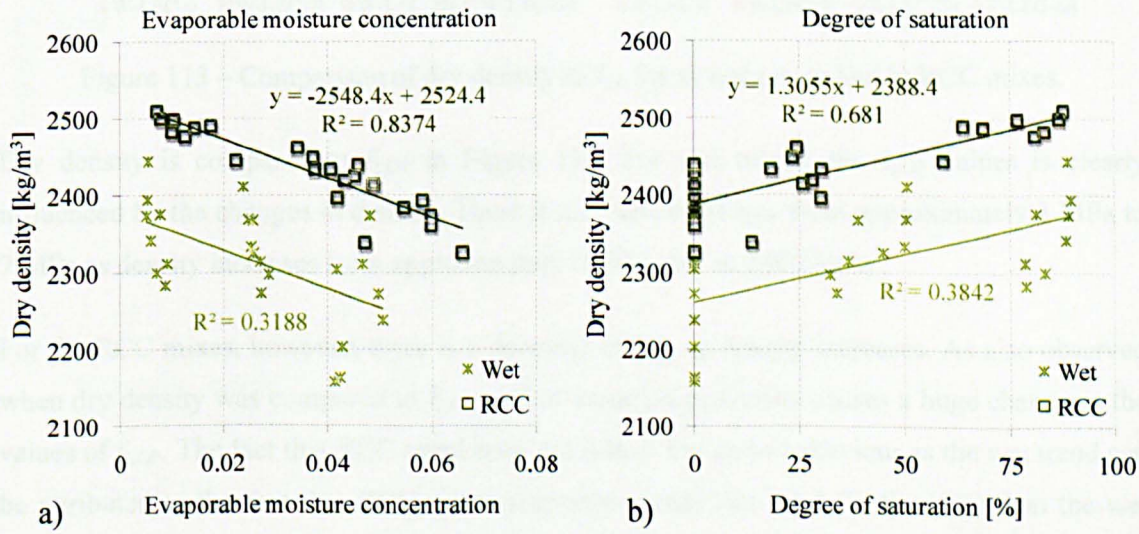

Figure 112 – Comparison between dry density and a) evaporable moisture concentration and b) degree of saturation.

5.4.5 Comparison of Dry Density with f_{cm}, f_{LOP} and E

Dry density was compared with some of the mechanical properties of the concrete: f_{cm}, f_{LOP} and E. The dry density used was oven-dried at the temperature of 80 °C.

The comparison of dry density ρ to f_{cm} is shown in Figure 113a and b, for wet and RCC mixes, respectively. There is a clear increase of f_{cm} when density increases. For wet mixes, f_{cm} increases from 55 MPa to 70 MPa when density increases from approximately 2320 kg/m^3 to 2380 kg/m^3. For RCC mixes, a small increase in density, from approximately 2420 kg/m^3 to 2450 kg/m^3, changes considerably the values of f_{cm} (from 45 MPa to 60 MPa).

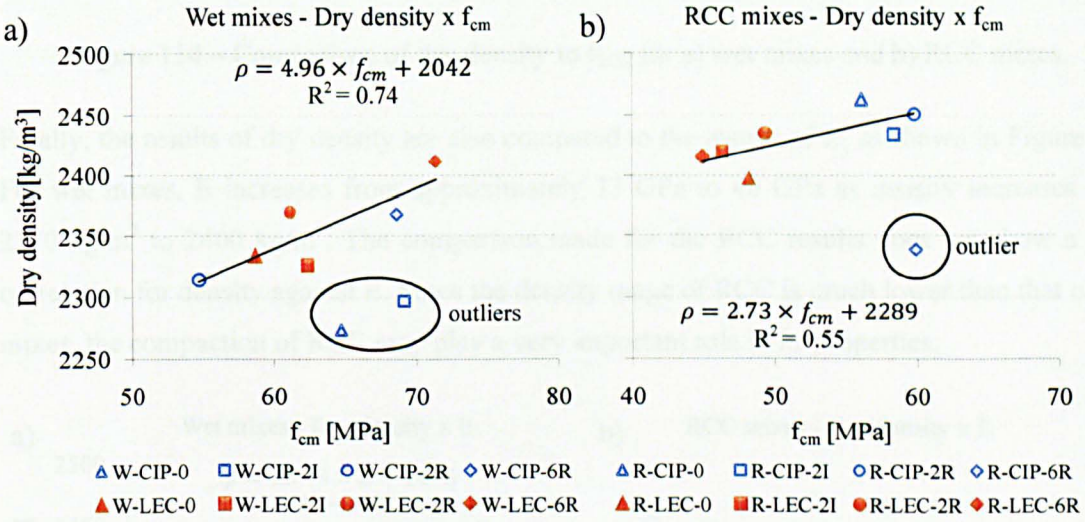

Figure 113 – Comparison of dry density to f_{cm} for a) wet mixes and b) RCC mixes.

Dry density is compared to f_{LOP} in Figure 114. For wet mixes, the f_{LOP} values is clearly influenced by the changes in density. There is an increase of f_{LOP} from approximately 3 MPa to 7 MPa as density increases from approximately 2270 kg/m^3 to 2400 kg/m^3.

For the RCC mixes, however, there is a decrease in f_{LOP} as density increases. As also observed when dry density was compared to f_{cm}, a small variation in density causes a huge change in the values of f_{LOP}. The fact that RCC trend does not follow the same behaviour as the wet trend can be attributed to the fact that RCC mixes trap more voids (see next Section 5.5) than the wet mixes, which leads to the formation of a higher number of initial micro-cracks. Therefore, f_{LOP} in RCC mixes seems to be more influenced by cracking control caused by fibre action than by density of concrete. Another explanation comes from the lower reactivity of LEC, which reduces f_{cm}, and the probable enhanced bond between LEC matrix and fibres, which improves cracking control and increases f_{LOP}.

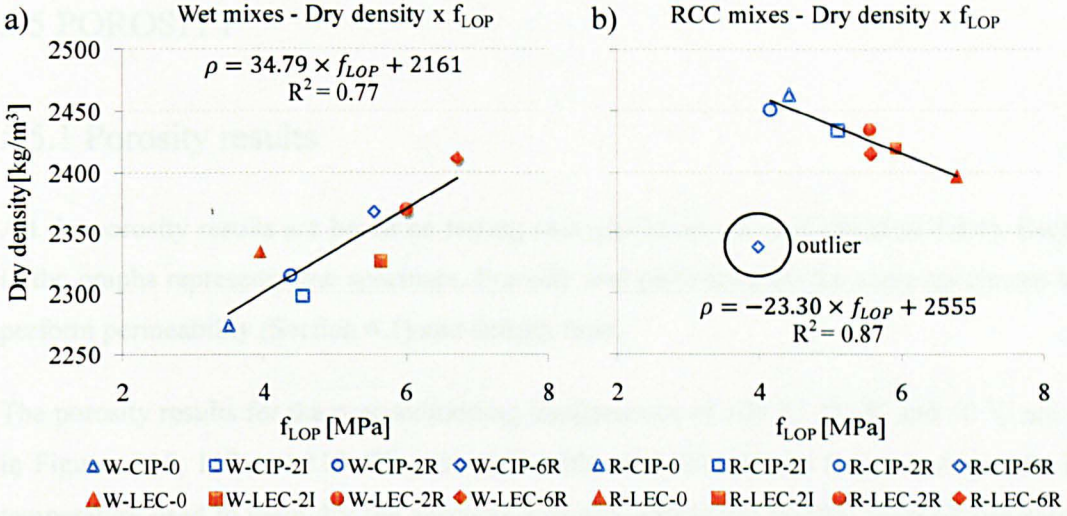

Figure 114 – Comparison of dry density to f_{LOP} for a) wet mixes and b) RCC mixes.

Finally, the results of dry density are also compared to the results of E, as shown in Figure 115. For wet mixes, E increases from approximately 33 GPa to 40 GPa as density increases from 2270 kg/m^3 to 2400 kg/m^3. The comparison made for the RCC results does not show a clear correlation for density against E. Since the density range of RCC is much lower than that of wet mixes, the compaction of RCC may play a very important role in its properties.

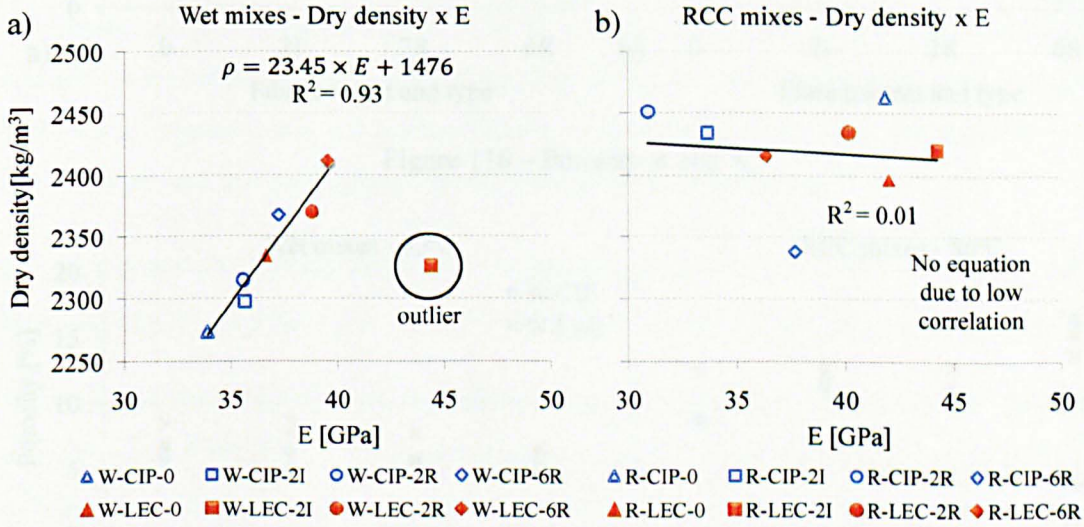

Figure 115 – Comparison of dry density to E for a) wet mixes and b) RCC mixes.

5.5 POROSITY

5.5.1 Porosity results

All the porosity results are based on testing two specimens per mix (Section 4.4.4). Each point in the graphs represents one specimen. Porosity was performed on the same specimens used to perform permeability (Section 6.1) and density tests.

The porosity results for the preconditioning temperatures of 105 °C, 80 °C and 50 °C are shown in Figures 116, 117 and 118. The complete table of results can be found in Appendix E. The temperature used to oven dry the specimens clearly affects the results, since higher porosity is observed in specimens dried at higher temperatures.

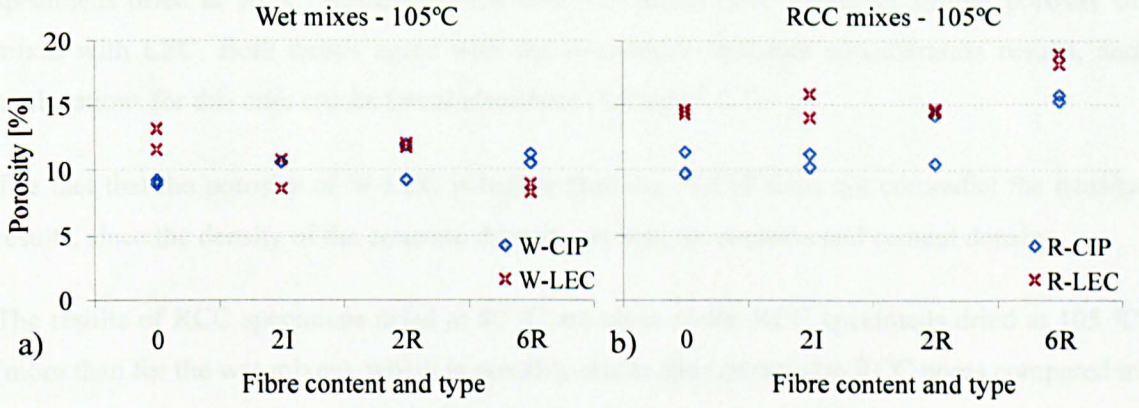

Figure 116 – Porosity at 105 °C.

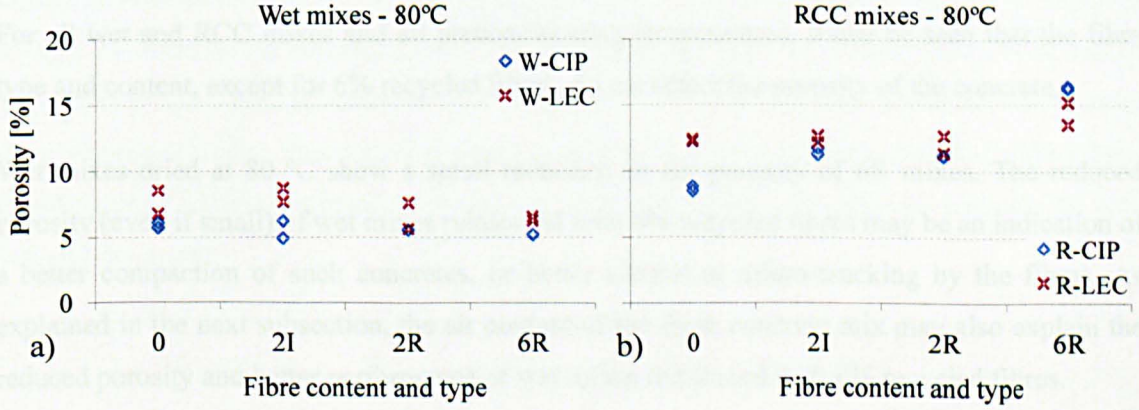

Figure 117 – Porosity at 80 °C.

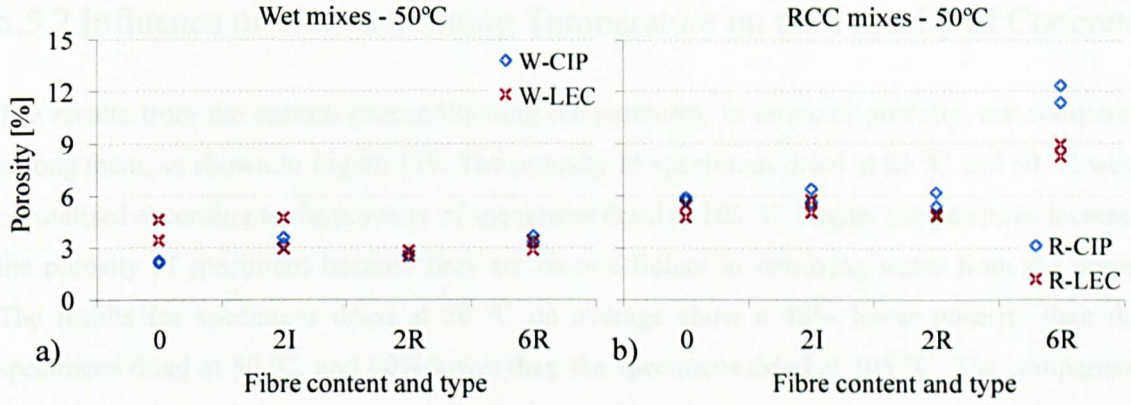

Figure 118 – Porosity at 50 °C.

It can be seen in the porosity of specimens dried at 80 °C and 105 °C that the LEC mixes present, for most of cases, higher porosity than the mixes with CIP. The porosity results of specimens dried at 50 °C, however, show that CIP mixes have higher or similar porosity of mixes with LEC. Both trends agree with the evaporable moisture concentration results, and explanations for this case can be found elsewhere (Section 5.4.1).

The fact that the porosity of W-LEC is higher than the W-CIP does not contradict the density results, since the density of the concrete depends on both air contents and cement density.

The results of RCC specimens dried at 80 °C are close to the RCC specimens dried at 105 °C (more than for the wet mixes), which is possibly due to the coarser size RCC pores compared to wet mixes. Coarser pores are more effective in eliminating water from the concrete at lower temperatures, and this also agrees with the conclusions of Section 5.4.1.

For all wet and RCC mixes and all preconditioning temperatures, it can be seen that the fibre type and content, except for 6% recycled fibres, do not affect the porosity of the concrete.

Wet mixes dried at 80 °C show a small reduction in the porosity of 6R mixes. The reduced porosity (even if small) of wet mixes reinforced with 6% recycled fibres may be an indication of a better compaction of such concretes, or better control at micro-cracking by the fibres. As explained in the next subsection, the air content of the fresh concrete mix may also explain the reduced porosity and better performance of wet mixes reinforced with 6% recycled fibres.

A considerable increase in the porosity, for all temperatures, is reported when 6% recycled fibres are added to RCC mixes. The higher porosity values for the 6R mixes confirm the fact that 6R RCC mixes present compaction problems due to the high amount of recycled fibres in the mix.

5.5.2 Influence of Preconditioning Temperature on the Porosity of Concrete

The results from the various preconditioning temperatures, in terms of porosity, are compared among them, as shown in Figure 119. The porosity of specimens dried at 80 °C and 50 °C were normalised according to the porosity of specimens dried at 105 °C. Higher temperatures increase the porosity of specimens because they are more efficient in removing water from the pores. The results for specimens dried at 50 °C on average show a 48% lower porosity than the specimens dried at 80 °C, and 60% lower than the specimens dried at 105 °C. The comparison among the preconditioning temperatures agrees with the results of density (and further results for permeability and sorptivity in Sections 6.1 and 6.2).

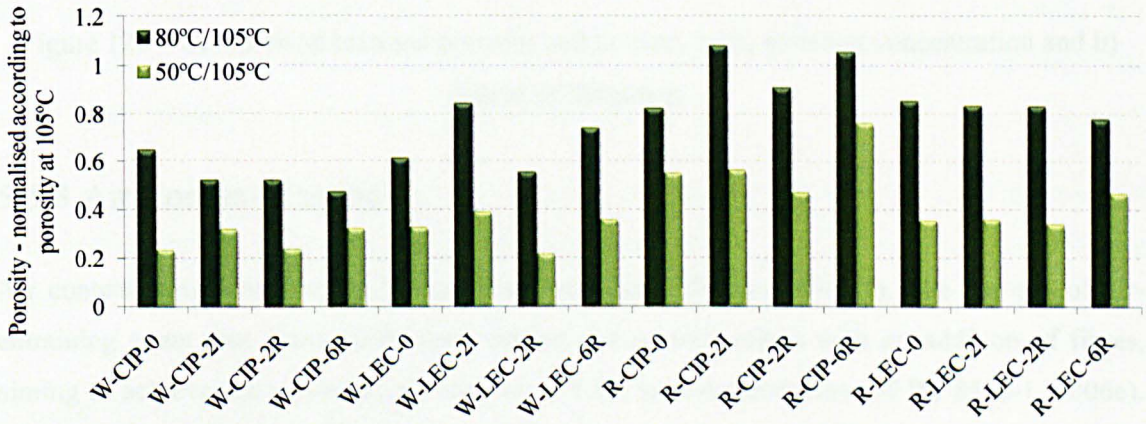

Figure 119 – Comparison of porosity results to different preconditioning temperatures.

Porosity values are compared to evaporable moisture concentration (w_e, w_{e80} and w_{e50}) and degree of saturation, as shown in Figure 120. Porosity is considerably affected by the remaining amount of water in the concrete pores after oven-drying. Pores filled with water, even though they are part of the pore structure of the material, are not accounted when lower preconditioning temperatures are used, thus reducing porosity of the mixes. It is clearly noticed in the graphs that the rate of increase in porosity due to evaporable moisture concentration is similar for both wet and dry mixes.

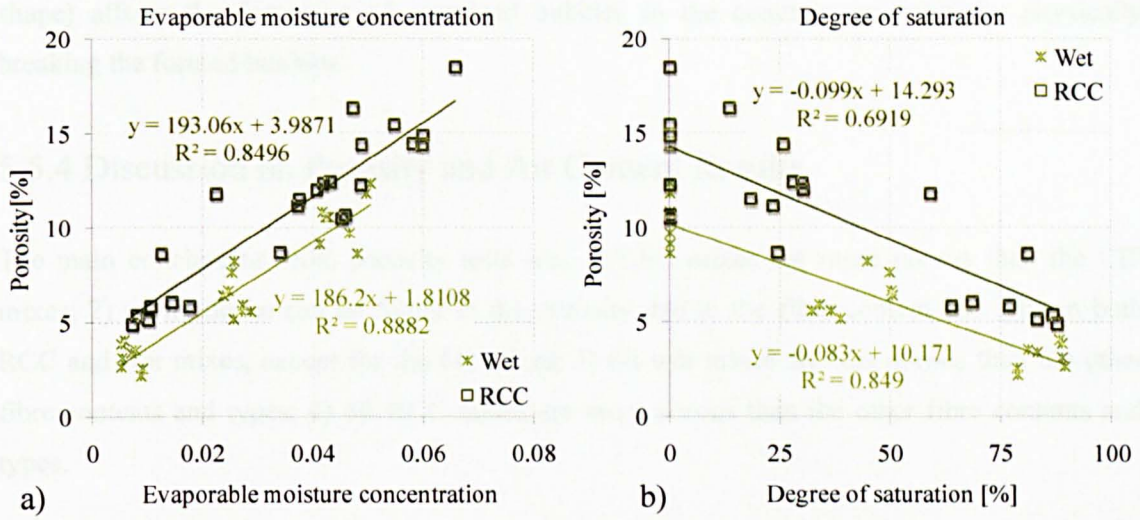

Figure 120 – Comparison between porosity and a) evaporable moisture concentration and b) degree of saturation.

5.5.3 Air Content Results

Air content tests were carried out on fresh wet mixes (Section 4.4.1.1). The amount of air-entraining agent was obtained by tests carried out on trial mixes with no addition of fibres, aiming to achieve the minimum air content of 5.5% (recommendations of BS 8500-1, 2006e). The same amount of air-entrainment agent was used in the mixes containing fibres, for comparison purposes. The results are shown in Table 23.

Table 23 – Air content of fresh wet mixes.

Mix	Air content [%]	Mix	Air content [%]
W-CIP-0	8	W-LEC-0	5.5
W-CIP-2I	8.5	W-LEC-2I	5.0
W-CIP-2R	10.5	W-LEC-2R	5.4
W-CIP-6R	5.2	W-LEC-6R	2.6

The results show that the cementitious material type clearly influences the results. CIP presents the highest values while the LEC mixes have the lowest air content results. This is the opposite of what was observed from the porosity results, and may contribute to explain the higher density of LEC mixes. It seems that the higher porosity of hardened LEC mixes is mainly due to the level of hydration of the cement paste, and not to the amount of air content while fresh.

It can be verified that the mixes with 6% recycled fibres present the lowest results of air content compared to the other fibre contents and types. This agrees with the previous results on porosity and density. It seems that the high amount of recycled fibres (combined with their irregular

shape) affects the formation of entrained bubbles in the concrete, probably by physically breaking the formed bubbles.

5.5.4 Discussion on Porosity and Air Content Results

The main conclusions from porosity tests are: 1) LEC mixes are more porous than the CIP mixes; 2) no influence can be found in the porosity due to the fibre content and type in both RCC and wet mixes, except for the 6R mixes; 3) 6R wet mixes are less porous than the other fibre contents and types; 4) 6R RCC mixes are more porous than the other fibre contents and types.

The temperature and method used to precondition the specimens affects considerably the porosity results. This is due to the amount of water that remains in the concrete pores when lower temperatures are used for oven-drying the specimens.

The air content results show that, while fresh, wet mixes cast with LEC present lower air content that CIP. The higher porosity of the hardened W-LEC mixes may be explained by the lower reactivity of the cementitious material compared to the W-CIP mixes.

5.6 FREE SHRINKAGE

5.6.1 Shrinkage Results

Free shrinkage strain measurements of wet and RCC mixes are shown in Figure 121. The results are presented for the average of three samples per mix. The length of each sample was measured at least 3 times to verify the accuracy of the measurement. The complete table of results can be found in Appendix E. Results were obtained up to 112 days, when free shrinkage seems to stabilise.

The strains obtained from the wet mixes (Figure 121a) are all within the same range of values, and no clear influence of the fibre type and content can be verified. The slightly lower shrinkage strains (similar to plain concrete) of 6R wet mixes compared to the 2I and 2R mixes is probably due to the lower air content and porosity of such mixes.

The RCC mixes (Figure 121b) with recycled fibres present considerably higher free shrinkage strains than the 2I and plain concrete mixes. The shrinkage strains of the R-LEC-2R and R-LEC-6R mixes are 29% and 36%, respectively, higher than the strains measured for R-LEC-0 and R-LEC-2I mixes.

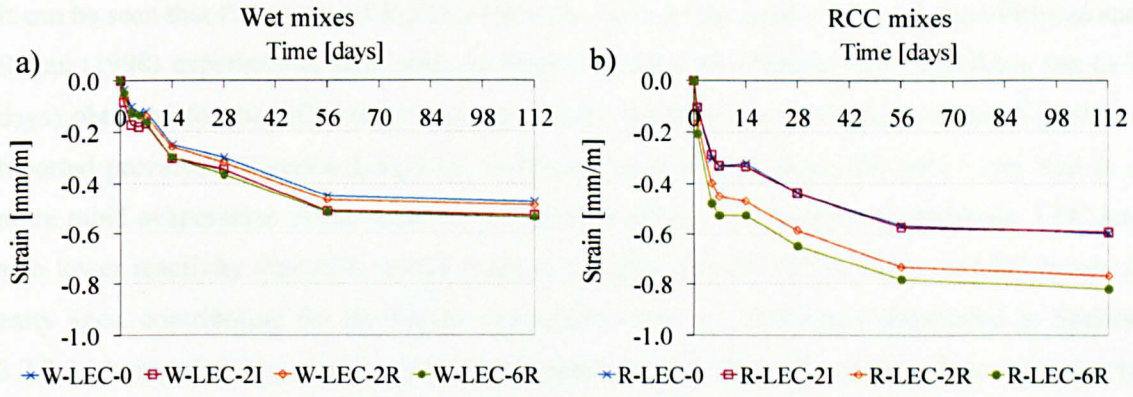

Figure 121 – Free shrinkage for a) wet and b) RCC mixes.

RCC mixes seem to have much higher shrinkage at the early days compared to the wet mixes. Up to 7 days, shrinkage of RCC mixes is, depending on the fibre type and content, more than two times higher than the shrinkage of the wet mixes. The higher shrinkage of RCC mixes is maintained as age increases, however with smaller difference between RCC and wet mixes.

From the literature, it is expected that RCC shows a good shrinkage resistance (Section 2.4.2.2). To verify whether the higher shrinkage of the RCC mixes compared with wet mixes is due to the poor quality of the material itself or to the good quality of the wet mixes, the results were compared with the study by Pittman and Ragan (1998), as shown in Figure 122. Pittman and Ragan (1998) results are based on an RCC mix with very similar aggregate gradation curve as the one used in this study and slightly lower water content (6.4% compared to 7% used in this study). The cementitious material used by Pittman and Ragan (1998) is a combination of 25% PFA and 75% CEM I. Since Pittman and Ragan (1998) experiments are based on plain concrete, their results were compared to R-LEC-0 only.

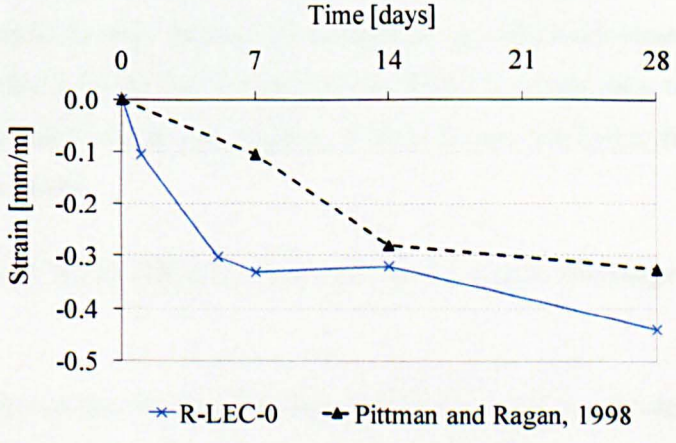

Figure 122 – RCC free shrinkage results compared to Pittman and Ragan (1998) results.

It can be seen that the results of R-LEC-0 mix are close to the results obtained from Pittman and Ragan (1998) experiments, only after 14 days of testing. The higher initial shrinkage (up to 7 days) obtained for the RCC mixes may be due to the type of cementitious material used. As reported previously (Section 5.5), LEC mixes are more porous than CIP, which can lead to a more rapid evaporation of the water in the concrete pores, thus increasing shrinkage. LEC has also lower reactivity than CIP, which leads to a higher amount of free water in LEC mixes at early ages, contributing for the higher evaporation rate. As previously mentioned in Section 3.2.2.3, drying shrinkage can be more accentuated at early ages of concrete, especially due to factors such as the amount of free and adsorbed water and the amount and size of pores.

5.6.2 Discussion on Free Shrinkage Results

It is accepted in the literature that steel fibres improve shrinkage resistance of concrete (Swamy and Stavrides, 1978; Mangat and Azari, 1984; Chern and Young, 1989; Tan *et al.*, 1994; ACI, 1996; Voigt *et al.*, 2004). Shrinkage strain results presented in the previous section, however, show the opposite. The addition of recycled steel fibres in RCC seems to increase strains caused due to free shrinkage. Fibre addition in wet mixes does not affect the shrinkage resistance.

As referenced in Section 3.2.2.3, the addition of fibres seems to alter the pore structure of the concrete, especially in terms of increasing the size of the pores (Wang *et al.*, 2001; Aly *et al.* 2008). The increase in the size of pores, according to these authors, leads to higher drying shrinkage of concrete.

If the resistance coefficient[40] results are taken into account, it can also be observed that the R-LEC-2R mix presents slightly coarser size of pores compared to R-LEC-0 and R-LEC-2I mixes. It was already discussed that the 6R RCC mixes have compaction problems and, as a consequence, they seem to have trapped air during casting, which are larger compared to other types of pores (Section 3.2).The fact that the 2R and 6R RCC mixes seem to have larger size of pores than the plain and 2I mixes may explain, at least in part, the higher free shrinkage strains obtained from those mixes.

The higher porosity of R-LEC-6R also contributes to the highest shrinkage strains obtained for this mix.

It is important to add that the benefits of using steel fibres to improve the shrinkage resistance of the concrete are mainly observed in a restrained situation, by controlling/avoiding cracks

[40] Resistance coefficient results are shown in Section 6.2.2. Higher resistance coefficient is an indication of larger size of pores.

formed due to tensile stresses caused by the restrained shrinkage of concrete (Swamy and Stavrides, 1978; ACI, 1996). However, for the purposes of this study, only the free shrinkage was investigated, and no conclusions on the real performance of recycled and industrially produced steel fibres on the shrinkage behaviour of concrete can be made.

5.7 SUMMARY AND CONCLUSIONS

This chapter explained the experimental results obtained in terms of mechanical properties, density, porosity and free shrinkage of control specimens after 28 days of curing.

CIP mixes have higher compressive strength and are less porous than LEC mixes, which is due to the lower reactivity of LEC compared to CIP, which leads to less C-S-H products / reduced hydration of the matrix. Further hydration of the LEC should increase the strength of the concrete at older ages. On the other hand, LEC mixes have higher f_{LOP}, f_{ult} and E than CIP mixes, and this is attributed to the enhanced chemical bond between the LEC matrix and the fibres. Pull-out tests may be used in further investigations to understand the adhesion of LEC and steel fibres.

6R mixes have, in general, similar flexural behaviour (limit of proportionality and post-cracking behaviour) as for 2I mixes, indicating that recycled fibres, when added at higher amount, give similar flexural behaviour as industrially produced fibres. 2R mixes have lower performance than 6R and 2I, but with a well defined post-cracking behaviour.

RCC mixes have similar flexural behaviour as wet mixes. The lower amount of cement of RCC mixes seems to be compensated by the aggregate interlock effect.

The mechanical properties of wet mixes can be correlated with density results. In this case, f_{cm}, f_{LOP} and E increase as density increases. In RCC mixes, however, there is a tendency for the f_{LOP} to increase as density decreases. This is because RCC mixes have higher amount of trapped air due to the compaction procedures, which leads to various initial micro-cracks. Hence, f_{LOP} of RCC mixes appears to be more affected by cracking control than by density of concrete.

6R RCC mixes are more porous and less dense than other mixes, which is due to compaction limitations when a high content of recycled fibres is added to the mix. On the other hand, 6R wet mixes are less porous and denser than other mixes. This is due to lower air content and due to the inclusion of a high amount of fibres, which are denser than concrete, thus increasing density of the composite concrete.

The use of different preconditioning temperatures to oven-dry the specimens influences the results of porosity and dry density. Higher temperatures are more effective in removing the water from the concrete pores thus increasing porosity and reducing density. The temperature of 80 °C seems to be the most appropriate to oven dry the specimens since it removes most of the evaporable water from the concrete, it is almost as quick as the 105 °C and does not affect the C-S-H structure of the concrete.

The results for free-shrinkage shows that recycled fibres increase the strains caused by free shrinkage tests, especially in RCC mixes. This is attributed to the higher porosity of the mixes, especially for the 6R mixes. It is important to note that the benefits of adding fibres in concrete is mainly observed in terms of restrained shrinkage, where fibres control cracking caused by thermal stresses. This was not investigated in this thesis, and further studies should be carried out.

Aiming to complement the study on the pore structure properties of the concrete, the following chapter explains the main transport mechanisms which are responsible for the transport of aggressive agents into concrete.

CHAPTER 6

6. TRANSPORT MECHANISMS RESULTS

This chapter deals with the results of the transport mechanisms in terms of permeability, sorptivity and diffusivity. The properties were obtained from control (non-damaged) specimens.

6.1 PERMEABILITY

6.1.1 Permeability Results

The permeability results *k* obtained from the specimens preconditioned at 105 °C, 80 °C and 50 °C are shown in Figures 123, 124 and 125, respectively. The full table of results can be found in Appendix F.

For the wet mixes oven dried at 105 °C and 80 °C, it can be noticed that the 6R mixes present the lowest values of permeability compared to the other fibre content and types. This may be attributed to the lower air content of the fresh mix (Section 5.5.3), caused by the fact that the high amount of fibres seem to physically break the air-entrained bubbles.

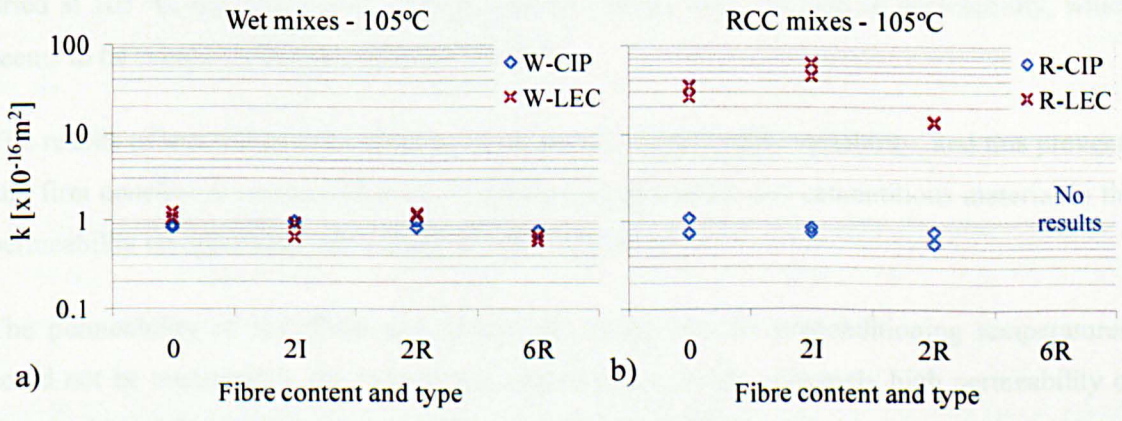

Figure 123 – a) Wet and b) RCC permeability for specimens preconditioned at 105 °C.

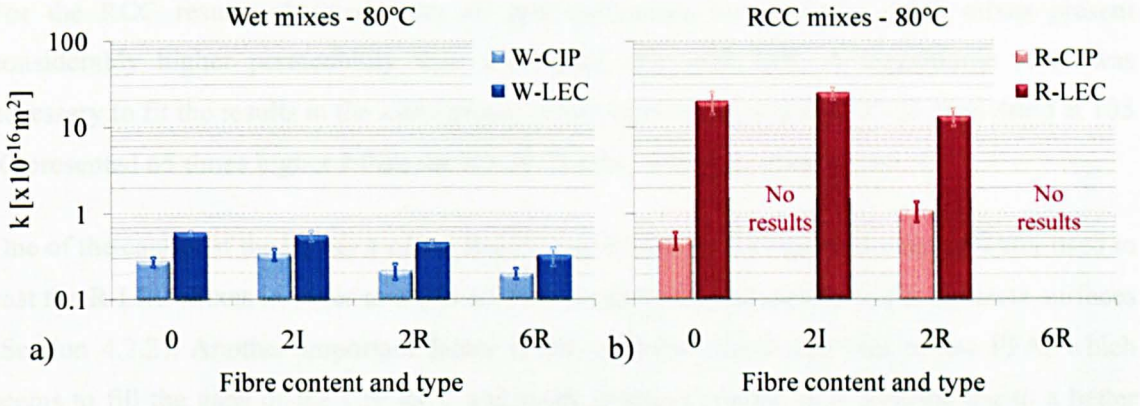

Figure 124 – a) Wet and b) RCC permeability for specimens preconditioned at 80 °C.

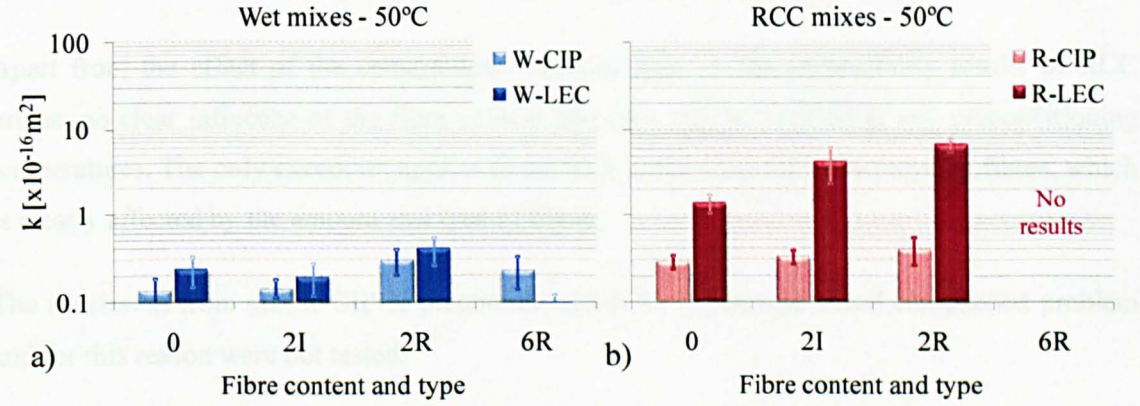

Figure 125 – a) Wet and b) RCC permeability for specimens preconditioned at 50 °C.

The influence of other fibre contents and types cannot be established. The W-LEC mixes oven dried at 80 °C present permeability results approximately two times higher than the corresponding W-CIP mixes. This can again be attributed to the lower reactivity of the LEC mixes, which reduces the amount of hydration products of the concrete. For the wet mixes oven dried at 105 °C, the mixes cast with LEC do not always have the highest permeability, which seems to be caused by the variability of the tests.

The results of wet mixes oven dried at 50 °C present considerable variability, and this prevents any firm conclusion on the influence of fibre type and content and cementitious material in the permeability on specimens oven dried at that temperature.

The permeability of R-CIP-6R and R-LEC-6R mixes, for all preconditioning temperatures, could not be measured in the oxygen test apparatus due to the extremely high permeability of the specimens. It seems that the amount of 6% recycled fibres leads to compaction problems, caused by the large amount of fibres and their irregular shape and the dry consistency of the mix.

For the RCC results obtained from all preconditioning temperatures, LEC mixes present considerably higher permeability than the mixes cast with CIP. A logarithmic scale was necessary to fit the results in the same graph. In the worst case, mix R-LEC-2I oven dried at 105 °C presented 65 times higher *k* than the R-CIP-2I mix, also oven dried at 105 °C.

One of the causes of the higher *k* of the R-LEC can be due to the higher amount of water used to cast the R-LEC mixes in order to allow a better compaction and quality of the concrete surfaces (Section 4.2.2). Another important factor is the spherical shape and size of the PFA, which seems to fill the gaps of the CIP RCC aggregate gradation curve, thus contributing to a better packing of the particles in the mix. Finally, another reason may be due to the lower reactivity of the LEC compared to CIP, which leads to less hydration products at 28 days.

Apart from the effect of the cementitious material type on the permeability results of RCC mixes, no clear influence of the fibre content and type can be verified at any preconditioning temperatures. The only exception applies to the RCC mixes cast with 6% recycled fibres, which is clearly affected by the amount and type of fibres.

The specimens from mix R-CIP-2I preconditioned at 80 °C showed visual compaction problem and for this reason were not tested.

6.1.2 Influence of Preconditioning Temperature on the Permeability of Concrete

The permeability results obtained from the three preconditioning methods were compared for all the mixes, as shown in Figure 126. The permeability results of specimens oven dried at 80 °C and 50 °C were normalised with the permeability results at 105 °C. It can be seen that the preconditioning temperature influences the results. The higher the temperature used, the higher are the values of permeability. This is mainly because higher temperatures are more effective in removing the water from the concrete pores compared to lower temperatures.

The 80 °C results are closer to the results of 105 °C (closer to 1) than when the results for 50 °C are compared to the results of 105 °C which, again, means that the temperature of 80 °C is more efficient in removing water from the concrete pores compared with 50 °C.

Due to the high variability of the 50 °C results, and considering that 105 °C may cause micro-cracks in the concrete due to possible evaporation of part of the interlayer and bound water (Section 3.2.1.1), it is believed that the temperature of 80 °C gives the most reliable results when

permeability is measured by the oxygen apparatus. This was also observed in the study of Carcassez *et al.* (2001).

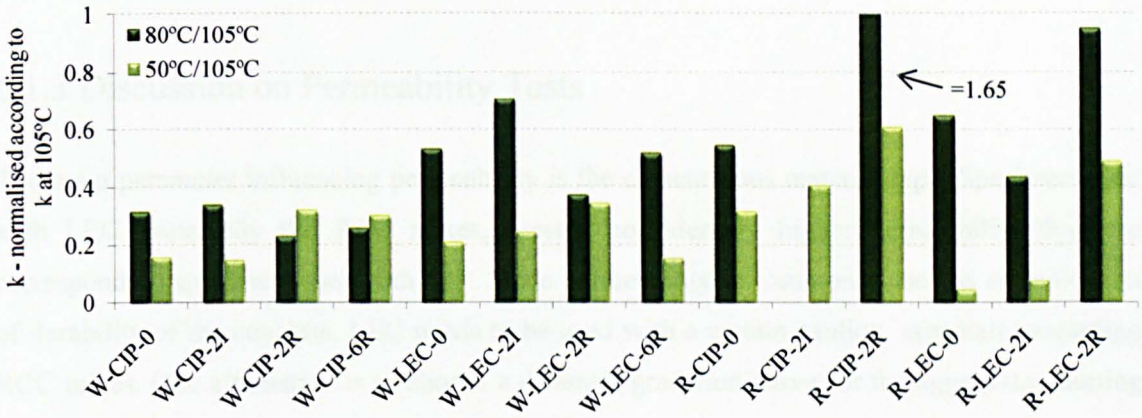

Figure 126 – Comparison of permeability results to different preconditioning temperatures.

The values of permeability were also correlated to the evaporable moisture concentration (w_e, w_{e80} and w_{e50}) and to the degree of saturation, as shown in Figure 127a and b, respectively. This analysis was only performed for wet mixes due to the high variability among the RCC results, which prevented the comparison.

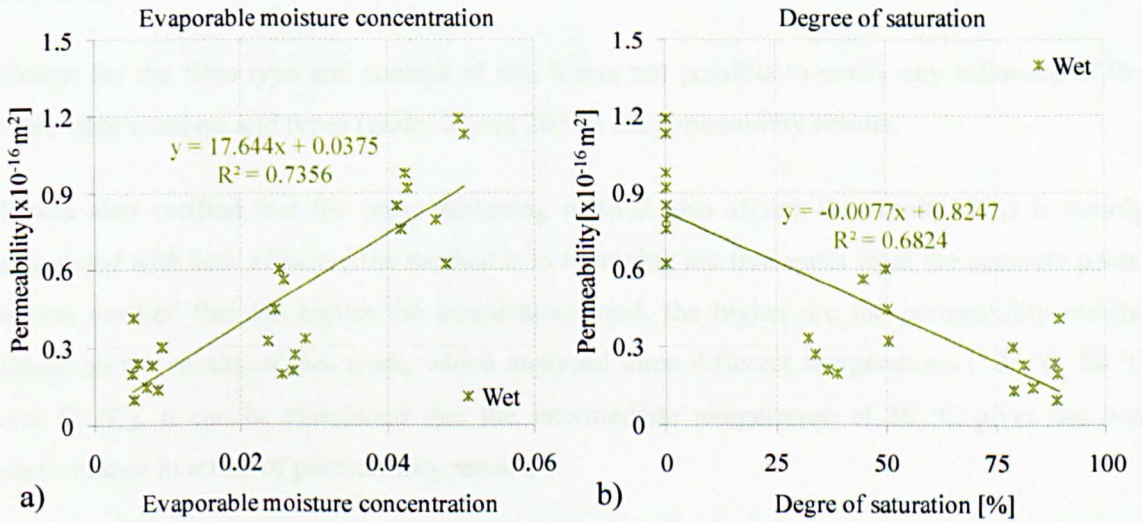

Figure 127 – Comparison between permeability and a) evaporable moisture concentration and b) degree of saturation.

It can be seen that permeability increases with the evaporable moisture concentration. This is because higher values of evaporable moisture concentration lead to higher amount of free water evaporated from the concrete pores, which reduces the blockage of the pores.

It can be clearly observed that the higher the degree of saturation, the lower is the permeability. The water in the concrete pores blocks the oxygen flow during testing, which reduces the permeability results.

6.1.3 Discussion on Permeability Tests

The main parameter influencing permeability is the cementitious material type. Specimens cast with LEC, especially the RCC mixes, present considerably higher permeability than the corresponding specimens cast with CIP. Since permeability is commonly used as an indication of durability of the concrete, LEC needs to be used with a certain caution, especially regarding RCC mixes. One alternative is to choose a different gradation curve for the aggregates, aiming to fit the size of the cementitious material particles to the new gradation curve.

The amount of 6% recycled fibres, which showed good performance in terms of mechanical properties, presented also good permeability performance when added to wet mixes. 6R wet mixes showed the lowest permeability results compared to other types and contents of fibres. Nevertheless, RCC specimens with 6% recycled fibres showed the worst performance. Their permeability was so high that the oxygen apparatus could not be used, and no results could be obtained.

Except for the fibre type and content of 6R, it was not possible to verify any influence of the other fibre contents and types (plain, 2I and 2R) on the permeability results.

It was also verified that the preconditioning method also affects the results. This is mainly associated with how effective the method is in removing the free water from the concrete pores. It was verified that the higher the temperature used, the higher are the permeability results. Based on the results of this work, which analysed three different temperatures (105 °C, 80 °C and 50 °C), it can be concluded that the intermediate temperature of 80 °C gives the best performance in terms of permeability results.

6.2 SORPTIVITY

6.2.1 Sorptivity Results

The sorptivity results are shown in Figures 128 and 129, for specimens oven dried at 80 °C and 50 °C, respectively. The graphs of water uptake *versus* square root of time, used for the calculation of the sorption coefficient, can be found in Appendix F. All sorptivity results are represented by the average of three samples per mix. Standard deviation is shown as error bars

on the top of the columns (each error bar equals to two standard deviations). The sorptivity tests were carried out after undertaking the oxygen permeability tests (on the same specimens), as detailed in Section 4.4.6.2.

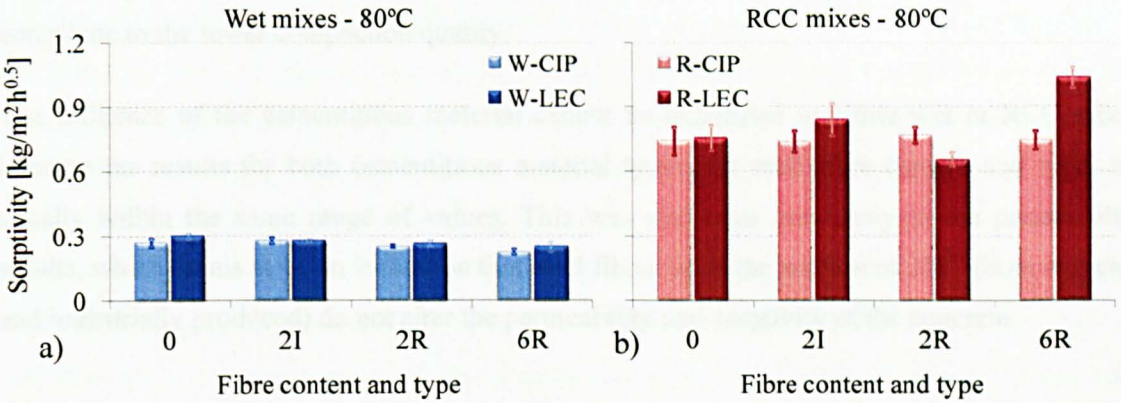

Figure 128 – Sorptivity at 80 °C.

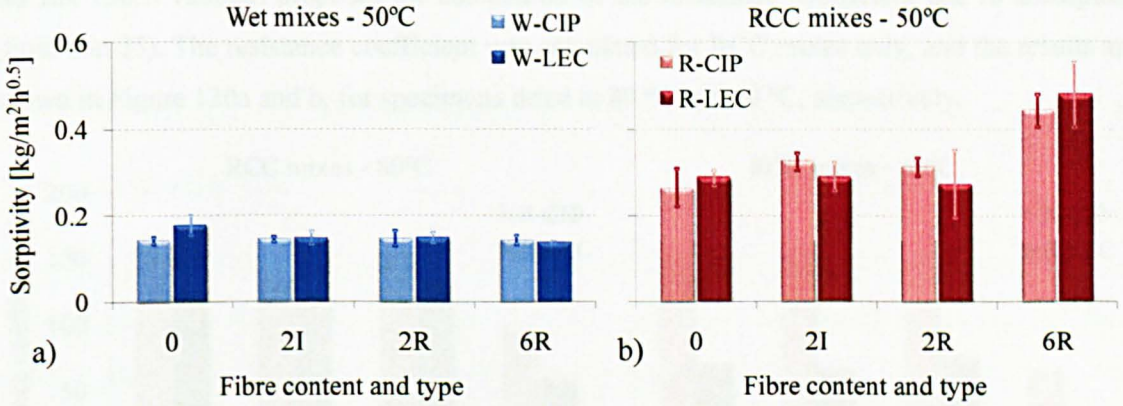

Figure 129 – Sorptivity at 50 °C.

RCC specimens oven dried at 80 °C give sorptivity results which are approximately 3 times higher than for the wet mixes. The difference drops to two times for the specimens preconditioned at 50 °C.

It can be noticed that there is a considerable drop of sorptivity if the preconditioning temperature changes from 80 °C to 50 °C. As explained previously (for density, porosity and permeability results), this is because the temperature of 50 °C is not efficient at removing the evaporable water from the concrete pores, which reduces the amount of water absorbed during the test.

There seems to be a slightly reduction in the sorptivity of wet mixes reinforced with 6% recycled fibres and oven dried at 80 °C, as also observed in the permeability test results.

For the RCC mixes, however, specimens cast with 6% recycled fibres present higher values of sorptivity, especially if considering the mixes cast with LEC. This is in line with the results obtained from the permeability test, and is mainly to compaction limitations observed when 6% recycled fibres are added to dry mixes. The irregular shape and the high amount of fibres contribute to the lower compaction quality.

The influence of the cementitious material cannot be quantified in either wet or RCC mixes because the results for both cementitious material types, for each fibre content and type, are usually within the same range of values. This was also seen previously in the permeability results, which seems to be an indication that steel fibres up to the amount of 2%[41] (both recycled and industrially produced) do not alter the permeability and sorptivity of the concrete.

6.2.2 Resistance Coefficient

BS EN 13057 (2002a) proposes the calculation of the resistance coefficient due to absorption (Equation 25). The resistance coefficient was calculated for RCC mixes only, and the results are shown in Figure 130a and b, for specimens dried at 80 °C and 50 °C, respectively.

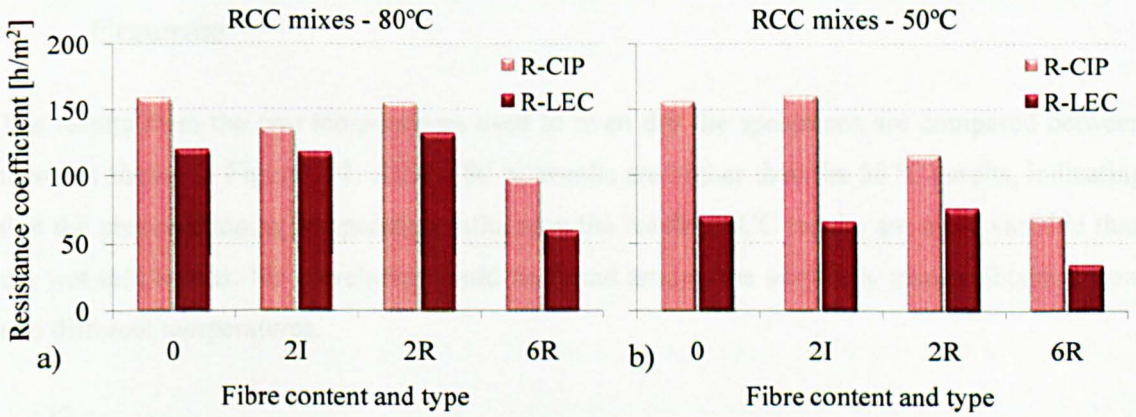

Figure 130 – Resistance coefficient of RCC mixes.

According to the standard, the resistance coefficient gives an indication of the fineness of the material. The higher the resistance coefficient, the lower is the level of water uptake during the test. As mentioned in Section 3.2.1.2, the finer the capillary pores are, the higher are the capillary forces over the water (Assiè *et al.*, 2007), and the lower is the resistance coefficient. The figure above shows that mixes with CIP presented the highest values of resistance coefficient, indicating that the level of water uptake was lower for such mixes. Hence, this seems to be an indication that the pore size of CIP is coarser than the pores size of the LEC

[41] Higher contents of fibres between 2 and 6% may also not influence the transport mechanisms, but further investigations should be carried out.

mixes. This information is in line with the conclusion arrived at in Section 5.4.1, regarding evaporable moisture concentration.

It must be added that the conclusions made in this section are only based on an indirect calculation that only gave an indication of the fineness of the concrete, therefore, they cannot be considered as firm. In addition, one could say that mixes with 6% recycled fibres may also have finer pore structure than the mixes with other fibre contents, due to the lower resistance coefficient observed in the figure below. However, by considering the permeability, density anbd porosity results, it is clear that the RCC mixes with 6% recycled fibres have compaction problems, which traps air, increases porosity, thus reducing the resistance coefficient of absorption. The low resistance coefficient in this case is probably due the poor quality of the concrete rather than the fineness of the capillary pores. Finally, it seems to be reasonable to use the fineness concept when comparing mixes with exactly the same mix proportions but different cementitious material type, but this is not valid for mixes with different types and contents of fibres.

6.2.3 Influence of Preconditioning Temperature on the Sorptivity of Concrete

The results from the two temperatures used to oven dry the specimens are compared between them, as shown in Figure 131. All the 80 °C results are higher than the 50 °C results, indicating that the preconditioning temperature influences the results. RCC results are more variable than the wet mix results. No correlation could be found among the sorptivity results obtained from two different temperatures.

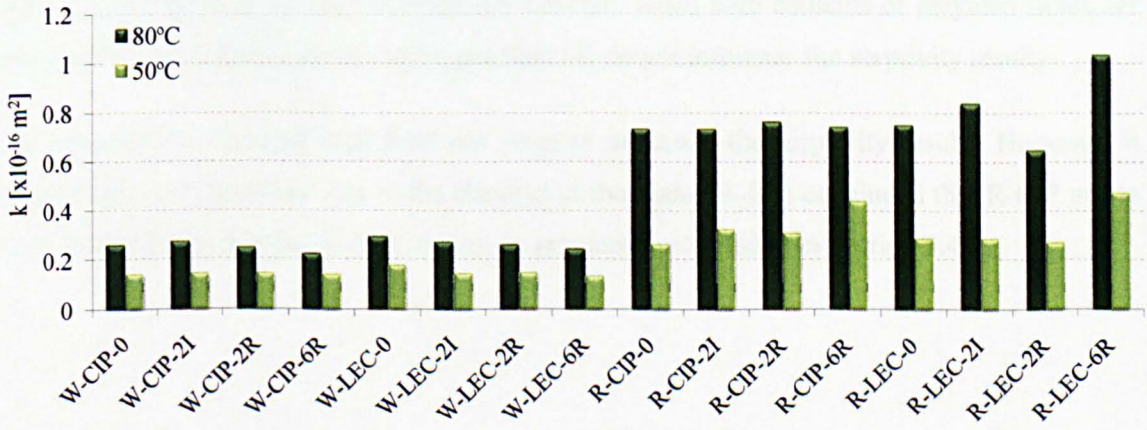

Figure 131 – Comparison of sorptivity results to different preconditioning temperatures.

The sorptivity results for both preconditioning temperatures were compared to their corresponding evaporable moisture concentration w_{e50} and w_{e80} (Figure 132a) and degree of

saturation (Figure 132b). It is observed that the amount of evaporable moisture concentration (and degree of saturation) increases sorptivity for both wet and RCC mixes. The higher the amount of water left in the concrete pores, the lower are the sorptivity values. The sorptivity of RCC mixes are considerably more affected by changes in the degree of saturation than for wet mixes.

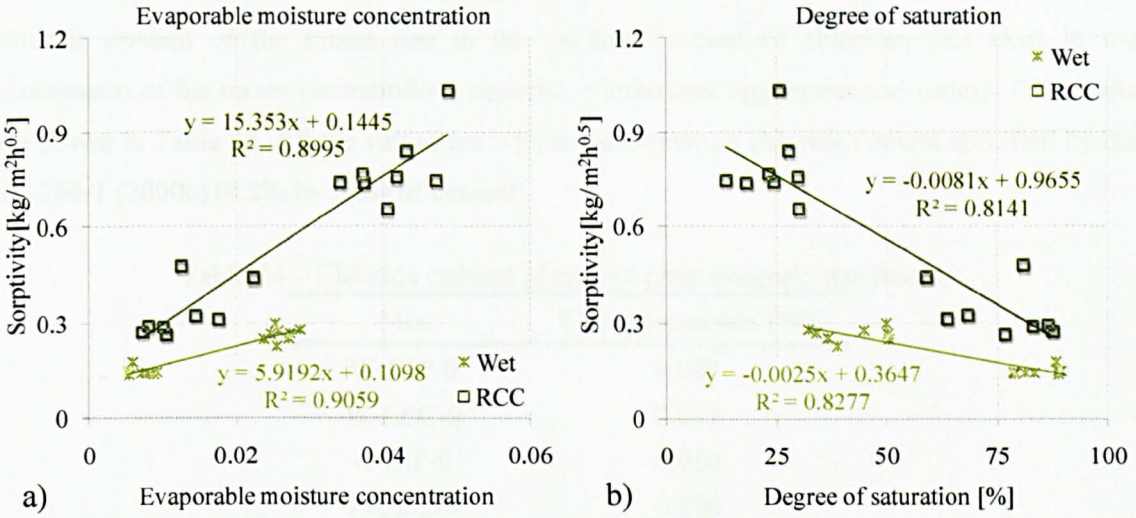

Figure 132 – Comparison between sorptivity and a) evaporable moisture concentration and b) degree of saturation.

6.2.4 Discussion on Sorptivity Tests

Similar outputs as for the permeability test can be observed, such as: 1) 6R wet mixes presented slightly lower sorptivity than the other fibre contents and types; 2) 6R RCC mixes presented the highest values of sorptivity compared to the other fibre contents and types, which is probably caused by compaction limitation of the dry concrete when high contents of recycled fibres are used; and 3) other fibre contents and types than 6R do not influence the sorptivity results.

The cementitious material type does not seem to influence the sorptivity results. However, it seems to play an important role in the fineness of the material. It is concluded that R-CIP mixes have coarser pores than the R-LEC mixes, as previously concluded in Section 5.4.1.

6.3 DIFFUSIVITY

6.3.1 Chloride Content Results

Control samples were collected from the plain mixes (W-CIP-0, W-LEC-0, R-CIP-0 and R-LEC-0) after 28 days of immersion in tap water[42]. This analysis was performed to obtain the chloride content of the mixes due to the existing amount of chlorides that exist in the constituents of the mixes (cementitious material, admixtures, aggregates and water). The results are shown in Table 24. All the values are within the maximum chloride content specified by BS EN 206-1 (2000e) (0.2% by mass of cement).

Table 24 – Chloride content of control plain concrete specimens.

Mix	Chloride content [%]
W-CIP-0	0.007
W-LEC-0	0.013
R-CIP-0	0.010
R-LEC-0	0.016

LEC mixes have higher amount of chlorides than the CIP mixes. When comparing W-CIP with W-LEC mixes, and also R-CIP with R-LEC mixes, it is known that all other constituents were the same, apart from the cement type. Hence, the higher values of chloride content of LEC mixes are probably due to the existing amount of chlorides in the cementitious material. Further investigations should be undertaken on the characterisation of LEC.

RCC mixes have higher chloride content compared to wet mixes. The most significant difference between the mixes, apart from the mix proportion, is the type of aggregate used. Crushed basalt aggregates seem to have more chlorides than the river dragged sand and gravel used for the wet mixes.

The results obtained for the chloride content test, carried out for wet and RCC mixes, are shown in Figure 133. The results of wet mix are represented by one single specimen while the results of RCC are represented by the average of two specimens. Even though two samples were cast per wet mix, only one was used to determine the chloride content due to time limitation.

[42] Assumed to be chloride-free water.

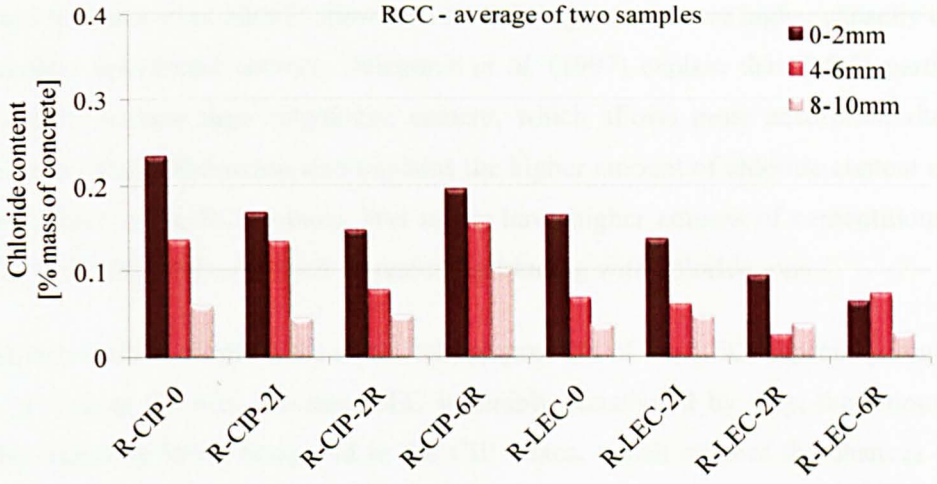

Figure 133 – Chloride content of RCC mixes after 28 days in chloride solution immersion.

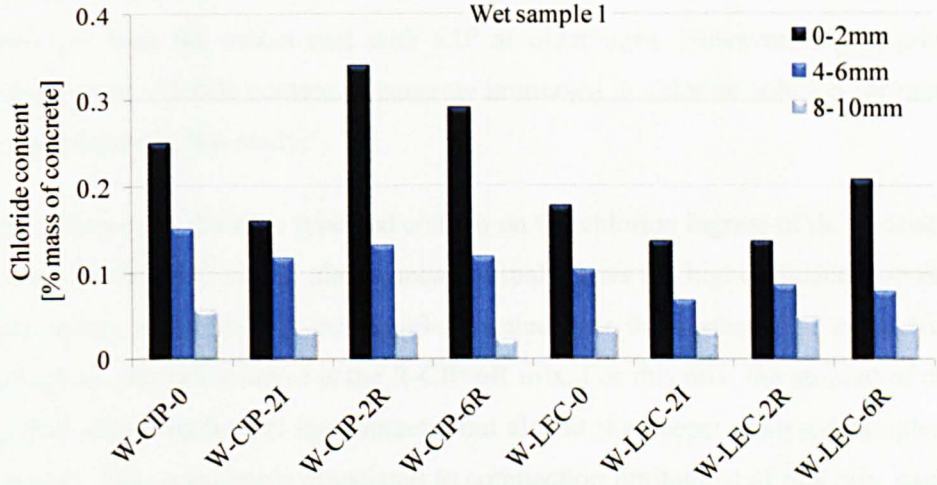

Figure 134 – Chloride content of wet mixes after 28 days in chloride solution immersion.

For the majority of the cases, as it is expected, the chloride content reduces as the depth increases. Very near the surface (0-2 mm), where the concrete was in direct contact with the chloride solution, specimens show the highest concentration of chloride.

Mixes cast with LEC have lower chloride ingress due to diffusion of ions compared to the mixes cast with CIP (valid for both wet and RCC mixes). This can be attributed to the level of refinement of the pore structure of the material caused by the physical characteristics of the cementitious material (e.g. size of the particles and density). It seems that LEC mixes have finer pore structure (even though more porous) than the CIP mixes, which agrees with the results about the resistance coefficient shown in Section 6.2.2.

Another fact that may explain the better behaviour of LEC mixes relies on the rate of hydration of this type of cementitious material, which is lower than the CIP mix and, as a consequence, has lower amount of C-S-H particles at early ages. Studies carried out by Delagrave *et al.*

(1997) and Antiohos *et al.* (2007) show that the C-S-H particles have higher capacity of binding chlorides than unhydrated cement. Delagrave *et al.* (1997) explain that C-S-H particles have higher specific surface than unhydrated cement, which allows more adsorption sites for the chlorides ions. This information also explains the higher amount of chloride content on the wet mixes compared to the RCC mixes. Wet mixes have higher amount of cementitious material compared to the RCC mixes, which increases the binding with chloride ions.

It is also important to mention the chemical composition of the LEC, especially regarding the amount of C_3A in the mix. Because LEC is mainly constituted by slag, the amount of C_3A should be relatively lower compared to the CIP mixes, which reduces the chances of C_3A to bind chloride ions to form chloro-aluminate compounds (Suryavanshi *et al.*, 1995).

Due to further hydration of the LEC at older ages, mixes cast with LEC will probably attain more chlorides than the mixes cast with CIP at older ages. However, this requires further investigation since chloride content of concrete immersed in chloride solution for more than 30 days is not analysed in this study.

About the influence of the fibre type and content on the chloride ingress of the specimens, it can be seen that, for the RCC mixes, plain concrete usually have the highest results compared to the reinforced mixes, especially for the samples located near the surface (0-2 mm). Next mix to have the highest chloride content is the R-CIP-6R mix. For this mix, the amount of chlorides is not only high at the surface of the concrete, but also at the deeper analysed samples (4-6 mm and 8-10 mm). This is probably associated to compaction limitations of this mix, caused by the high amount of recycled fibres, which allow the easy circulation of chlorides throughout the concrete mass.

Mix R-CIP-2I also presents high chloride content at the depth of 4-6 mm, indicating high susceptibility for the chlorides to penetrate into the concrete. At the depth of 8-10 mm, however, the chloride content dropped considerably. This may be attributed to the deposition of chlorides in the concrete pores, which blocks further ingress into the concrete depth. Similar situation seems to occur for the R-LEC mixes. In this case, the accumulation of chlorides seems to occur at the surface of the concrete, blocking the ingress towards the interior of the sample. Mix R-CIP-2R shows the lowest amount of chlorides compared to the other R-CIP mixes.

The results for wet mixes show that plain and 6R mixes have the highest values of chloride content, for both types of cementitious material used (W-CIP-2R also show high values of chloride content). It seems that, for these mixes, the chlorides were deposited in the pores of the concrete located very near the surface of the concrete, which blocked further penetration of

chlorides to the interior of the concrete. All other mixes (W-CIP-2I, W-LEC-2I and W-LEC-2R) show similar behaviour.

6.3.2 Diffusion Coefficient

The diffusion coefficients calculated from the chloride content results are shown in Figure 135 (based on Fick's second Law – Section 3.2.1.3 and 4.4.6.3). The surface chloride content was considered as the amount of chloride at the depth of 0-2 mm. The initial chloride content for each group of mixes W-CIP, W-LEC, R-CIP and R-LEC is based on the values shown in Table 24 (it is assumed that the fibres are chloride-free).

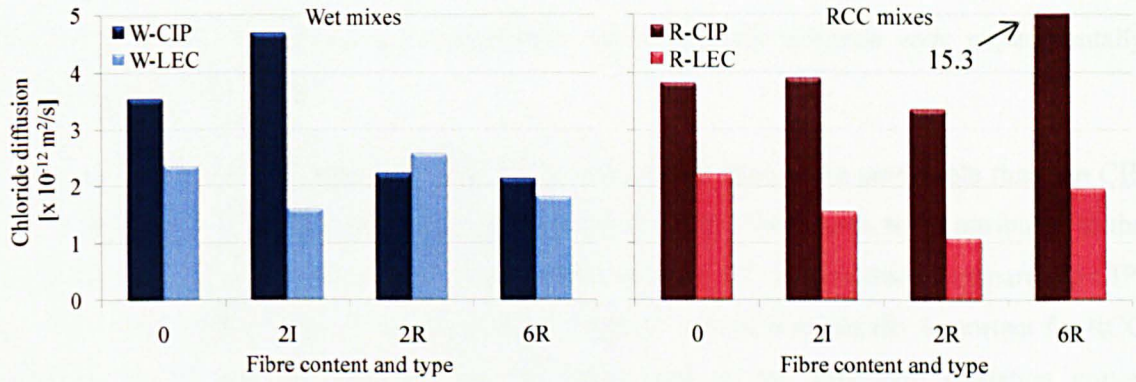

Figure 135 – Diffusion coefficient for wet and RCC mixes.

As for the chloride content, the results for RCC mixes were calculated based on the average of two specimens per mix, while the results for wet mixes represent one specimen per mix. It can be seen that the diffusion coefficient for most of the LEC mixes is lower than the CIP mixes, which is attributed to the fact that the LEC has lower capacity of binding chlorides due to the lower amount of C-S-H.

Plain and 2I W-CIP mixes have the highest diffusion coefficient compared to 2R and 6R from the same group of mixes (W-CIP). The inclusion of recycled fibres in W-CIP mixes seems to reduce the diffusion coefficient of the concrete. The same can be verified when 2R is added to RCC. This may be attributed to the fact that the large number of recycled fibres act as a barrier to the chloride ingress into concrete. The number of industrial fibres is much lower than the amount of recycled fibres and for this reason the barrier-effect is not clear for 2I mixes. The irregular geometry of the recycled fibres may also play a role in blocking the chloride ingress.

The fact that the R-CIP-6R mix has much higher diffusion coefficient than other fibre type and contents is mainly caused by compaction limitations of this mix due to the high amount of recycled fibres, as also concluded from the other transport mechanisms. R-LEC-6R should also

have similar behaviour as R-CIP-6R, however, there seems to be a problem with the chloride content measurements of such mix. This can be also verified in the conductivity graphs shown in Appendix F, where a different behaviour in the conductivity measurements is observed for R-LEC-6R compared to the other mixes.

The results of the chloride content and the diffusion coefficient are later used for the probabilistic chloride ingress analysis, based on the service life prediction of structures subjected to chloride environment, as described in Chapter 10.

6.4 SUMMARY AND CONCLUSIONS

The main mechanisms to transport aggressive agents into the concrete were experimentally investigated in this chapter.

The permeability results show that LEC mixes are considerably more permeable than the CIP mixes, and that this is especially highlighted for RCC mixes. This seems to be attributed to the lower reactivity of LEC mixes, which have smaller amount of C-S-H products compared to CIP; and also to the particle size of the cementitious material, which is especially important for RCC mixes since the cement particles may fit some gaps in the aggregate gradation curve, contributing to a better packing of the concrete constituents.

RCC mixes have higher sorptivity than wet mixes, which seems to be caused by the higher porosity and larger size of RCC pores. The inclusion of fibres does not influence much the sorptivity results.

The temperature used to precondition the specimens for permeability and sorptivity clearly affects the results, as also concluded in the previous chapter. The most appropriate temperature for the preconditioning of specimens seems to be around 80 °C.

Diffusivity results show that LEC mixes have lower diffusion coefficient than the CIP mixes, which is probably due to the lower reactivity and lower C_3A of the cement (which binds less chloride). The addition of recycled fibres seems to create a physical barrier to the ingress of chlorides into concrete, but further investigations should be carried out since this cannot be clearly concluded from the results.

6R RCC mixes have the highest permeability, sorptivity and diffusivity results, which is attributed to compaction limitations of such mixes, as also reported in the previous chapter. This may lead to long-term durability problems. On the other hand, 6R wet mixes usually have the

best results for the transport mechanisms, which is mainly attributed to the lower air content of such mixes.

As a general conclusion, the inclusion of fibres does not seem to play an important role in the transport mechanisms properties of concrete. Exception applies when the inclusion of fibres is associated to compaction limitations (such as for 6R RCC mixes) or other important change in the pore structure of the concrete. The transport mechanisms are mostly affected by the matrix properties (e.g. mix proportion, compaction) than by fibre addition.

The following chapters explain the response of concrete subjected to deterioration processes caused by environmental (chloride ingress and freeze-thaw) and mechanical (fatigue) action. The results of transport mechanisms and some other pore structure-related properties investigated in the previous chapter are then compared to the results obtained from these deterioration processes.

From the results obtained in this chapter, it is expected that RCC specimens will probably be more affected than wet mixes when subjected to deterioration processes. LEC mixes are also more prone to get deteriorated than CIP mixes, except when subjected to chloride ingress. Finally, 6R RCC mixes should have more durability problems than the corresponding mixes with other fibre contents and types.

CHAPTER 7

7. CORROSION RESISTANCE OF SFRC

This chapter deals with the results obtained from the corrosion tests. Specimens were exposed to accelerated corrosion conditions based on wet-dry cycles (Section 4.4.7). The effect of corrosion of fibres on the performance of concrete is evaluated in terms of visual analysis and residual mechanical properties (compressive strength and flexural behaviour).

7.1 VISUAL ANALYSIS

A series of pictures were taken to document the various stages of corrosion: 1) after curing (prior to starting the wet-dry cycles); 2) after 5 months of wet-dry cycles; 3) after 10 months of wet-dry cycles and 4) considering the influence of different solution temperatures used for wet-dry cycles. A scale for the external deterioration is also presented.

7.1.1 Scale for External Level of Corrosion Deterioration

A scale to verify the level of external superficial deterioration was developed. For that, non-corroded specimens are considered as level 0 while the most corroded specimens are considered as level 5. The various levels of the scale are described in Table 25, based on visual observation. Industrially produced fibres usually present the lowest amount of rust on the surface compared to the recycled fibres, and for this reason they occupy the lowest levels of deterioration. Recycled fibres occupy the highest levels of deterioration due to the geometric characteristics of the fibres, which lead to a much higher number of recycled fibres (and more points of corrosion) compared to the same content of industrially produced fibres.

Table 25 – Scale of superficial deterioration due to rust.

Picture	Scale	Description
	0	No deterioration, no signs of rust.
	1	Few and scattered signs of rust, caused by industrially produced fibres located very near the surface of the concrete.
	2	Uniform signs of rust caused by industrially produced fibres located near the surface of the concrete. Rust spreading is clearly visualised.
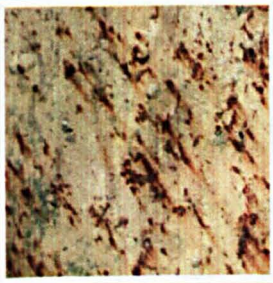	3	Uniform signs of rust caused by recycled fibres located very near the surface of the concrete. Very few signs of rust spreading.
	4	Uniform rusty appearance of the concrete surface, caused by rust spreading and large amount of corroded fibres located near the surface of the concrete.
	5	Accentuated and uniform rusty appearance, caused by rust spreading and large amount of corroded fibres located near the surface of the concrete. Non-corroded parts of the concrete become brownish due to rust spreading.

7.1.2 Prior to Corrosion Simulation

Prior to starting the wet-dry cycles, specimens were removed from the mist room and placed in frames, which could be lifted by an overhead crane to allow the easy movement of specimens in and out of the containers which contained the chloride solution.

Figure 136 shows the external appearance of 6R and 2I RCC specimens after curing. 6R specimens show superficial corrosion (scale 3), while no signs of corrosion are noticed in the 2I specimens. The superficial corrosion noticed in the 6R mixes are due to two factors: 1) high amount of fibres near the surface of concrete, caused by the high fibre content; 2) poor surface finishing in the RCC mixes, which exposes the fibres to the environment. The poor surface finishing is mainly caused by the high amount and irregular shape of recycled fibres, which causes compaction problems and traps voids.

Figure 136 – External appearance of RCC specimens before commencing the wet-dry cycles.

Figure 137 shows 2I and 6R wet mix specimens. It can be observed that the mixes cannot be visually distinguished between them. The specimens do not show any sign of superficial rust, which implies that fibres are protected by a thin layer of cement paste, hence, they are not completely exposed on the concrete surface.

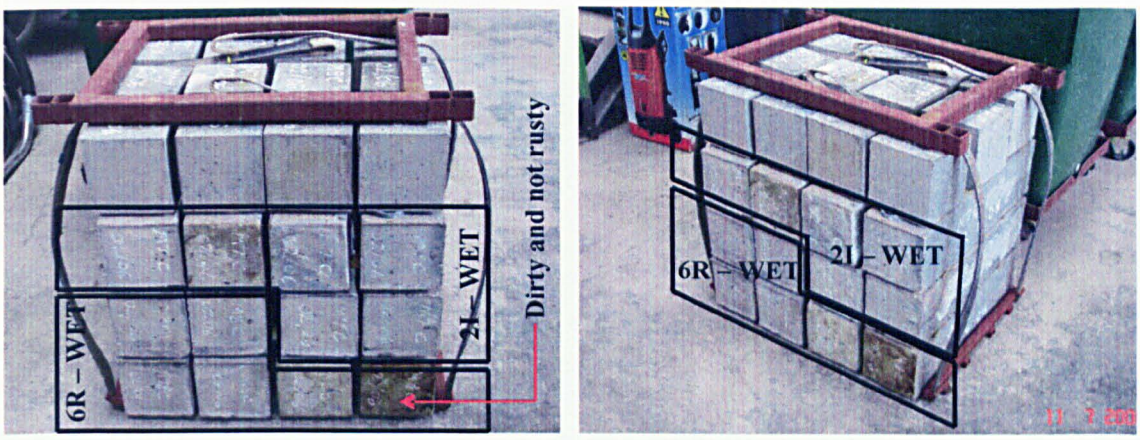

Figure 137 – External appearance of wet mix specimens before wet-dry cycles.

7.1.3 After 5 Months of Corrosion Simulation

The external appearance of specimens exposed to 5 months of wet-dry cycles is shown in Figure 138. RCC specimens reinforced with 6% recycled fibres present the rustiest surface when compared with the other specimens (scale 4). This agrees with the fact that these were the only specimens presenting superficial rust before being exposed to wet-dry cycles. Wet mixes with 6% recycled fibres also present signs of external corrosion, however, to a much lower extent than the 6R RCC specimens.

It can be clearly noted that the fibres located near the surface of 2I RCC specimens, which were coated before the wet-dry cycles with a thin layer of cement paste, became visible due to rust (scale 1). This may be an indication of chloride penetration into the concrete. The 2I wet mixes did not show any signs of corrosion, even for the fibres located near the surface (scale 0).

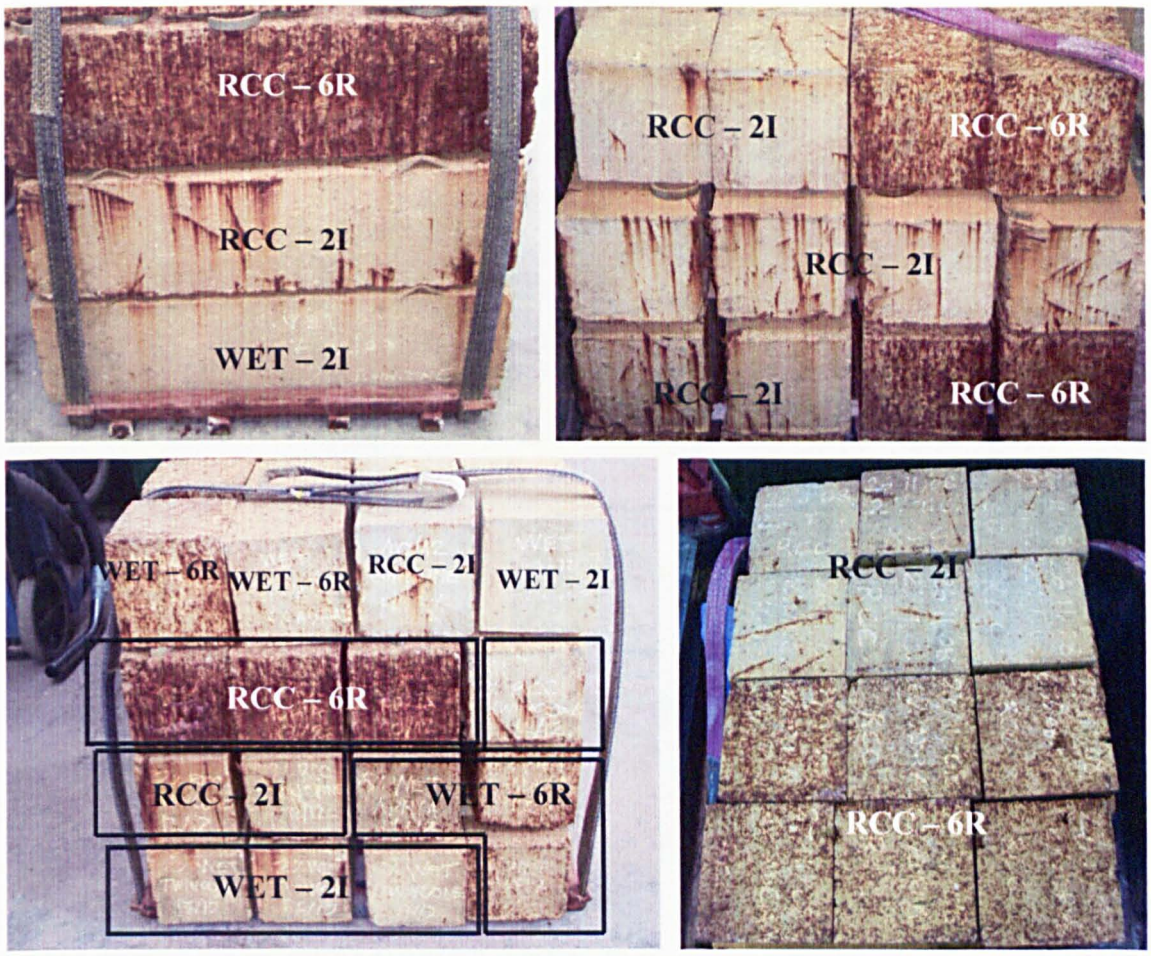

Figure 138 – External appearance of specimens after 5 months of wet-dry cycles.

Figure 139 shows that industrially produced fibres exposed on the concrete surface become very deteriorated, with a large amount of rust and visible loss of cross sectional area (more than 70% reduction). Recycled fibres exposed to the environment also present a very corroded appearance. They also become fragile, since they can be easily broken.

Figure 139 – Corroded fibres exposed to the concrete surface after 5 months of wet-dry cycles.

To determine whether corrosion extends to interior fibres, specimens were crushed after measuring the mechanical properties, and the fractured surfaces were visually examined to identify signs of rust, as shown in Figure 140.

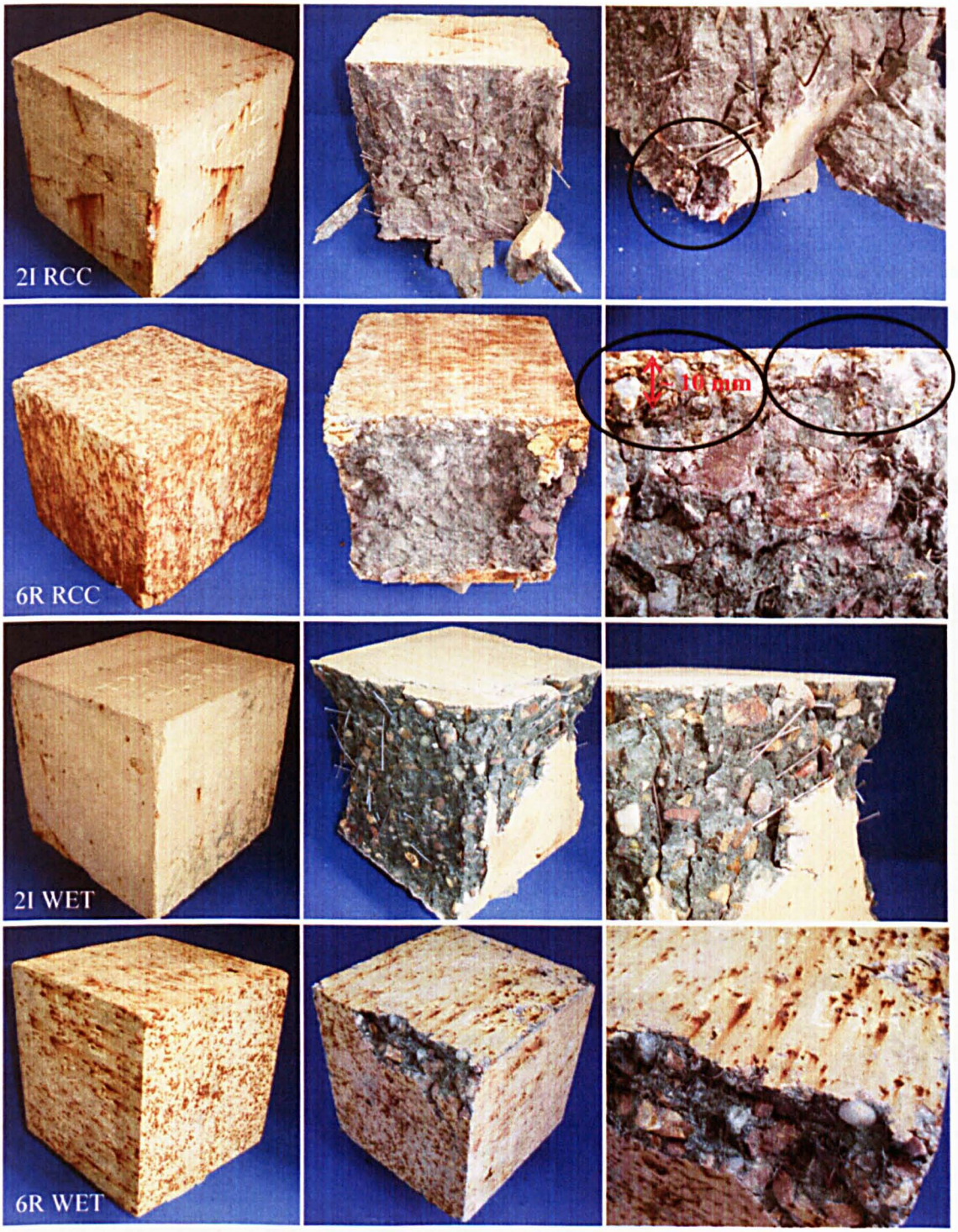

Figure 140 – Internal appearance of specimens after 5 months of wet-dry cycles.

2I RCC specimens do not show any corrosion in the interior of the specimens. Only fibres exposed to surface, or very near the surface, are corroded. 6R RCC specimens have signs of corrosion that extends to approximately 10 mm inside the concrete surface.

Wet mixes (both 2I and 6R) do not show any rust in the interior of the specimens. The corrosion appearance for these mixes can only be seen on the external surface of the specimens, and mainly for the 6R mixes.

7.1.4 After 10 Months of Corrosion Simulation

The external appearance of specimens exposed to 10 months of wet-dry cycles is shown in the figure below. The rusty appearance of 6R (both RCC and wet) specimens was increased compared to the ones observed after 5 months of wet-dry cycles (from scale 3 to 4 for wet mixes and from scale 4 to 5 for RCC mixes). 2I wet mixes can be classified in a scale in-between 0 and 1, while 2I RCC mixes can be classified in-between scales 1 and 2. Therefore, recycled fibres have a more pronounced effect on the appearance of specimens from 5 to 10 months of wet-cry cycles compared to industrially produced fibres.

Figure 141 – External appearance of specimens after 10 months of wet-dry cycles.

Figure 142 shows that fibres located near the concrete surface present a high level of degradation. Industrially produced fibres are completely corroded, with considerable visible loss of cross sectional area.

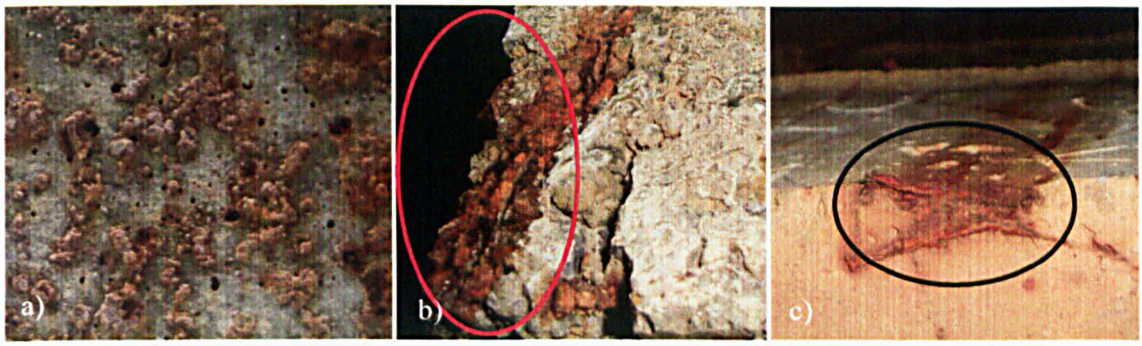

Figure 142 – Corroded fibres exposed to the concrete surface after 10 months of wet-dry cycles.

Recycled fibres do not only present a rusty appearance and fragile behaviour, as noted at 5 months of corrosion simulation, but also have a uniformly-distributed expansive product layer (primarily rust) on the concrete surface. These expansive products probably originate from fibres located near the surface of the concrete (Figure 142a). Since rust volume is larger than the volume of sound steel, it should cause tensile stresses in the concrete. However, these stresses do not lead to cracking because the expansive products find their way out through connected pores before causing tensile failure of the concrete.

As at 5 months, the specimens were analysed internally (after mechanical testing) for signs of corrosion (Figure 143). RCC mixes (2I and 6R), show similar behaviour compared to 5 months. Deterioration did not increase internally when compared to the specimens corroded up to 5 months of wet-dry cycles. It is assumed that the diffusion coefficient is a time-dependent parameter (Tang and Gulikers, 2007), which decreases as age of the concrete increases, thus reducing the rate of chloride ingress. The time influence on diffusion is shown in Appendix H.

2I wet mixes show that fibres located near the surface present few signs of rust, which was not observed at 5 months. However, there is no damage to the integrity and cross sectional area of the fibres. 6R wet mixes show similar behaviour to that observed at 5 months.

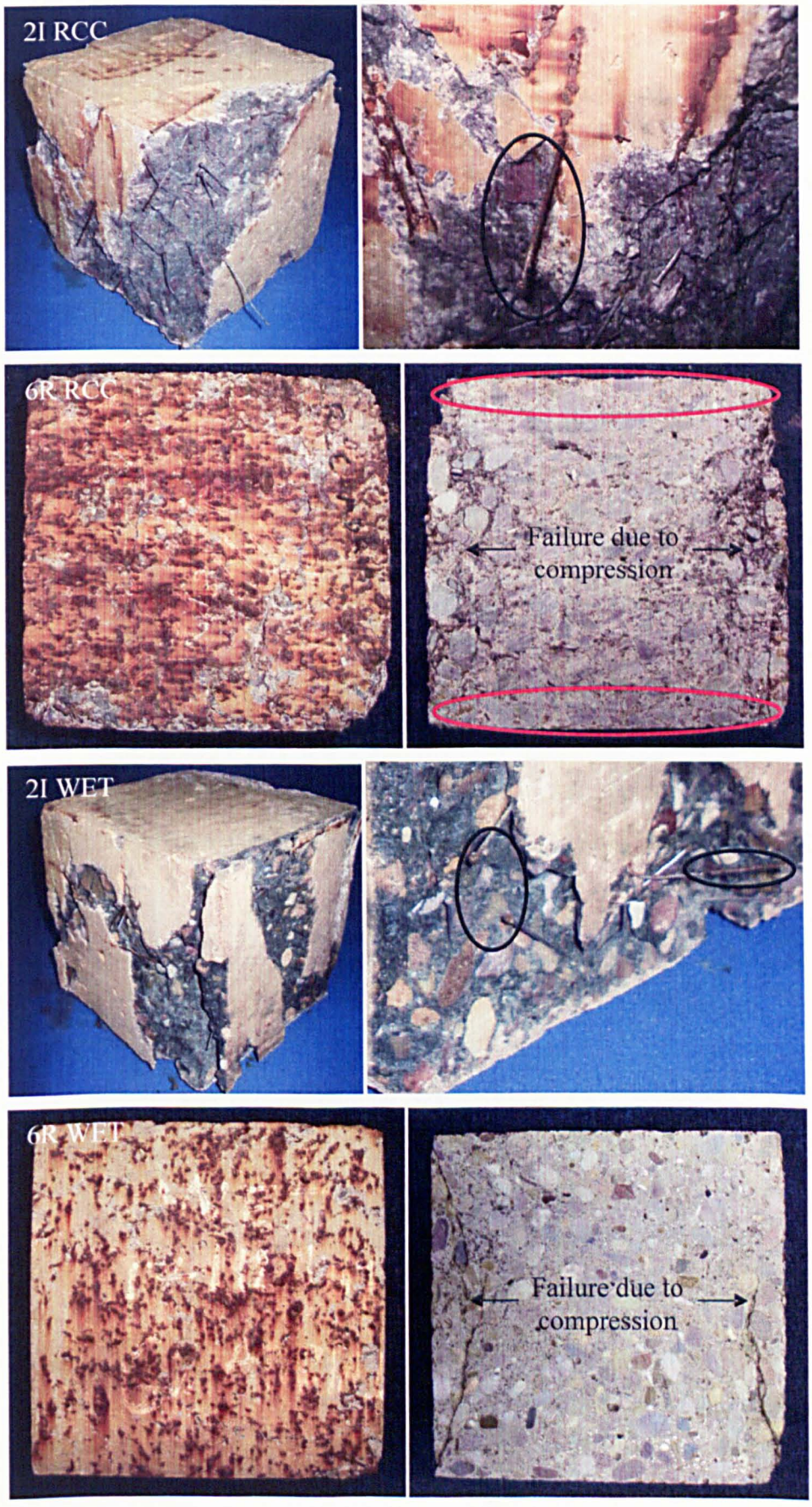

Figure 143 – Internal appearance of specimens after 10 months of wet-dry cycles.

7.1.5 Wet-dry cycles at 20 °C and 40 °C

Figures 144 and 145 show specimens of mix R-CIP-6R exposed to wet-dry cycles at 20 °C and 40 °C, after 5 and 10 months, respectively. At 5 months, specimens exposed to 40 °C show a lower amount of rust (scale 3) on the surface compared to the specimens exposed to 20 °C (scale 4). This may be because the temperature of 40 °C provides a better curing condition, which refines the outer concrete layer of the specimens, keeping fibres protected inside the concrete, even the ones very close to surface and that are only protected by a thin cement paste. After 10 months, however, the rusty appearance is basically the same for both temperatures (in between scale 4-5).

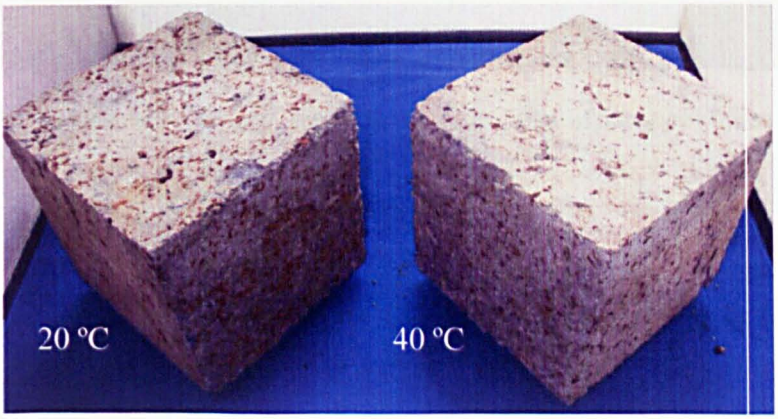

Figure 144 – Specimens exposed to 5 months of wet-dry cycles at 20 °C and 40 °C.

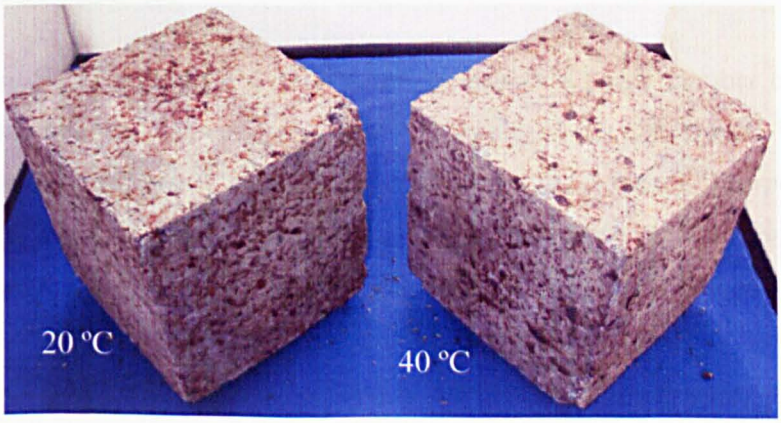

Figure 145 – Specimens exposed to 10 months of wet-dry cycles at 20 °C and 40 °C.

After exposure to 10 months of wet-dry cycles at 40 °C, several points of micro spalling of the surface concrete can be visualised, as shown in Figure 146. This may be due to either of the following two processes: 1) chloride ingress is higher at 40 °C, which produces a higher amount of expansive products inside the concrete, thus leading to micro spalling of concrete; and 2) chloride ingress is similar than at 20 °C, but due to improved curing of concrete at 40 °C, the

pore structure of the concrete becomes more refined (smaller pores) than at 20 °C, which blocks the release of the expansive products to the surface of the concrete, causing micro spalling.

Since the external appearance of the concrete at 40 °C shows less corrosion than at 20 °C, the second hypothesis seems to be more realistic.

Figure 146 – Micro spalling of concrete after 10 months of wet-dry cycles at 40 °C.

7.1.6 Discussion

The effect of wet-dry cycles has a clear aesthetic impact, especially for the mixes with recycled fibres. The high amount of fibres used (three times more the amount used for industrially fibres) and the geometric characteristics (length and diameter) are the main reason for this effect. For a certain amount of fibre content, the number of recycled fibres is much higher than the number of industrially produced fibres.

The compaction procedure used for RCC seems to expose a larger number of fibres on the surface of the concrete than for wet mixes, which leads to a rustier appearance. The compaction method used for RCC, especially with 6% recycled fibres, also seems to incorporate voids into the concrete, which leads to signs of corrosion up to a certain depth (10 mm). However, internal corrosion seems to stabilise after 5 months of wet-dry cycles, which can be attributed to the time-dependent effect of the diffusion coefficient (Tang and Gulikers, 2007), to the improved curing and hydration of the concrete, and also to the fact that the expansive products may be blocking the ingress of chlorides.

21 wet mixes do not show major external corrosion, and just minor traces of internal rust can be observed at 10 months (and only for fibres located very close to the surface). The consequences of wet-dry cycles for the 6R wet mixes can only be seen on the external surface of the concrete.

Wet-dry cycles after 10 months at 40 °C produce several points of micro spalling on the surface of the concrete, which may be due to the improved curing condition at that temperature. This

refines the pore structure of the concrete and blocks the way out of expansive products of corroded fibres located near the surface.

Chloride ingress into concrete is explained in more detail in Chapter 10, where a proposed method to correlate accelerated corrosion tests to real conditions is described. A parametric study on the influence of various variables (type of mix, fibre content and type and cementitious material) on the chloride ingress of concrete is also presented in that chapter.

7.2 MECHANICAL PROPERTIES

7.2.1 Compressive strength

The results of compressive strength after 5 and 10 months of corrosion are shown in Figure 147. The full table of results is shown in Appendix G. It can be seen that there is a considerable increase of strength after corrosion simulation; the main gain is observed after 5 months of wet-dry cycles. This can be attributed to ageing of the concrete compared to the 28 days specimens. The immersion in water during the wet phase of the cycles may also have contributed to the strength increase by providing good curing conditions to the specimens.

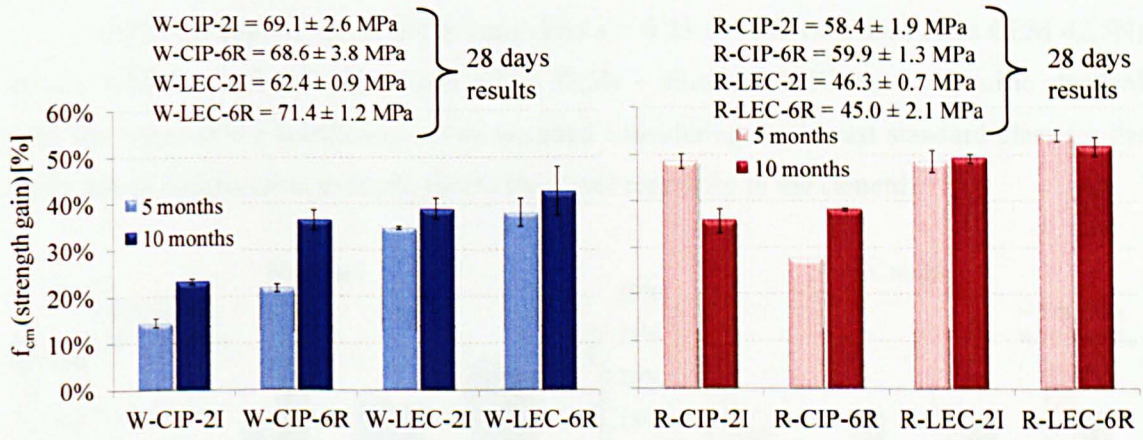

Figure 147 – Compressive strength after corrosion for a) wet and b) RCC mixes.

After 10 months of corrosion simulation, the strength gain is very close to the gain obtained at 5 months of corrosion, indicating that most of the hydration of the cementitious material was completed at 5 months.

It can be observed that the LEC mixes present higher strength gain at 5 and 10 months than the CIP mixes, compared to the 28 days control specimens. This is because LEC, which mainly

comprises of slag, has lower reactivity (around 1.4[43]) than CIP (around 2.4[43]) and is characterised by long-term strength gain. The strength gain for the CIP mixes at 5 months is also considerably high. This can be attributed to the addition of PFA which, even though added in a small amount (only 20%), it is also characterised by lower reactivity (around 0.7[43]).

The fibre type and contents (2I and 6R) do not influence the results for either wet or dry mixes.

To compensate the effect of ageing, the compressive strength of the samples was predicted at the ages of 5 and 10 months after corrosion (plus 28 days of curing), by the BS EN 1992-1-1 (2004b) and CEB-FIP Model Code (1993), following the equation below. This strength is used to normalise the results (by subtracting the effect of ageing) and the gain in strength over what is expected from ageing is shown in Figure 148.

$$f_{cm}(t) = \beta_{cc}(t) f_{cm} \quad (30)$$

Where:

$f_{cm}(t)$ = mean compressive strength at *t* days

f_{cm} = mean compressive strength at 28 days

$\beta_{cc}(t)$ = coefficient depending on the age *t* of concrete $\beta_{cc}(t) = exp\left\{s\left[1 - \left(\frac{28}{t}\right)^{0.5}\right]\right\}$

s = coefficient depending on the cement class s = 0.25 for CIP (standard class CEM 42,5N) and s = 0.38 for LEC (standard class CEM 32,5N – since the LEC has no specific standard class, the value of the coefficient *s* was assumed considering the lowest standard class for the prediction of compressive strength, due to the lower reactivity of the cement).

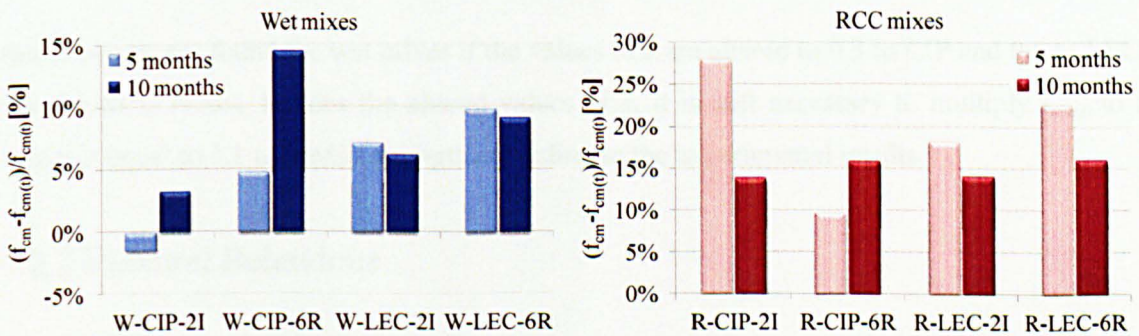

Figure 148 – Comparison between predicted and real compressive strength after exposure to wet-dry cycles.

[43] calculated according to the equation: $reactivity = \frac{CaO+MgO+Al_2O_3}{SiO_2}$ (Lynsdale, 2008).

In all cases (except W-CIP-2I), a higher compressive strength is obtained. The predicted strength gain is lower for wet than for dry mixes. This is probably because the equation to predict strength gain is based on conventional concrete and not RCC.

The above equation is valid for the curing conditions following the recommendations of BS EN 12390-2 (2000c), which does not apply to the conditions experienced during the wet-dry cycles. Theoretically, standard curing should provide better conditions than the wet-dry cycles. Even though the curing conditions of the wet-dry cycles were not as effective as standard curing, the specimens subjected to corrosion still show better behaviour. This can lead to two hypotheses: 1) wet-dry cycles up to 10 months do not affect the compressive strength of SFRC and 2) corrosion may be playing a beneficial role in the compressive strength, as elaborated below.

Granju and Balouch (2005) explain that the second assumption can be true because rust increases friction between the fibre and the matrix, thus leading to gain in strength. However, considering the results obtained from the visual analysis, it is clear that rust can only be observed aesthetically, in the surface of the specimens. Therefore, the strength gain after 5 and 10 months of corrosion simulation is not due to corrosion, but more likely due to ageing and moist condition of the specimens during wet-dry cycles, as also observed by Mangat and Gurusamy (1987c).

It is clear that the predicted strength gain does not match the experimental results. This may be due to two factors: 1) the values of s in Equation 30 are not accurate for LEC and CIP and 2) Equation 30 cannot be applied to RCC and SFRC. Further hydration of cement may improve bond between the fibre and the matrix, thus leading to higher gain in compressive strength than plain concrete.

Better results are found for wet mixes if the values of s are altered to 0.3 to CIP and 0.5 to LEC. For the RCC mixes, besides the altered values of s, it is still necessary to multiply $f_{cm(t)}$ to a constant equal to 1.1 to predict strength according to the experimental results.

7.2.2 Flexural Behaviour

Following the same procedures used to study the flexural behaviour of non-damaged specimens, the flexural behaviour of concretes exposed to wet-dry cycles was investigated experimentally and the results were analysed in terms of flexural strength at the limit of proportionality, ultimate flexural strength, residual flexural strength at CMODs of 0.5 mm, 1.5 mm, 2.5 mm and 3.5 mm, equivalent flexural strength and ratio at a deflection of 3 mm and modulus of elasticity.

The values obtained from the specimens exposed to corrosion are compared to the non-damaged control specimens (cured only for 28 days).

The results of corroded specimens shown in this subsection are represented for the average of three samples. The results obtained for each specimen and the bending-load *versus* mid-span deflection and CMOD curves can be found in Appendix C. The control specimen results are represented by the average of two samples per mix (Section 5.2).

7.2.2.1 Un-cracked specimens subjected to wet-dry cycles at 20 °C

Flexural strength at the limit of proportionality f_{LOP} and ultimate flexural strength f_{ult}

Figure 149a and b shows the results of f_{LOP} based on Che's (2010) approach while Figure 149c and Figure 149d shows f_{ult}. Most of the results for 5 and 10 months of wet-dry cycles are higher than the results of the control specimens (28 days), which again indicates ageing of concrete. As noticed for the compressive strength, specimens exposed to up to 10 months of wet-dry cycles do not present loss in the structural bearing capacity.

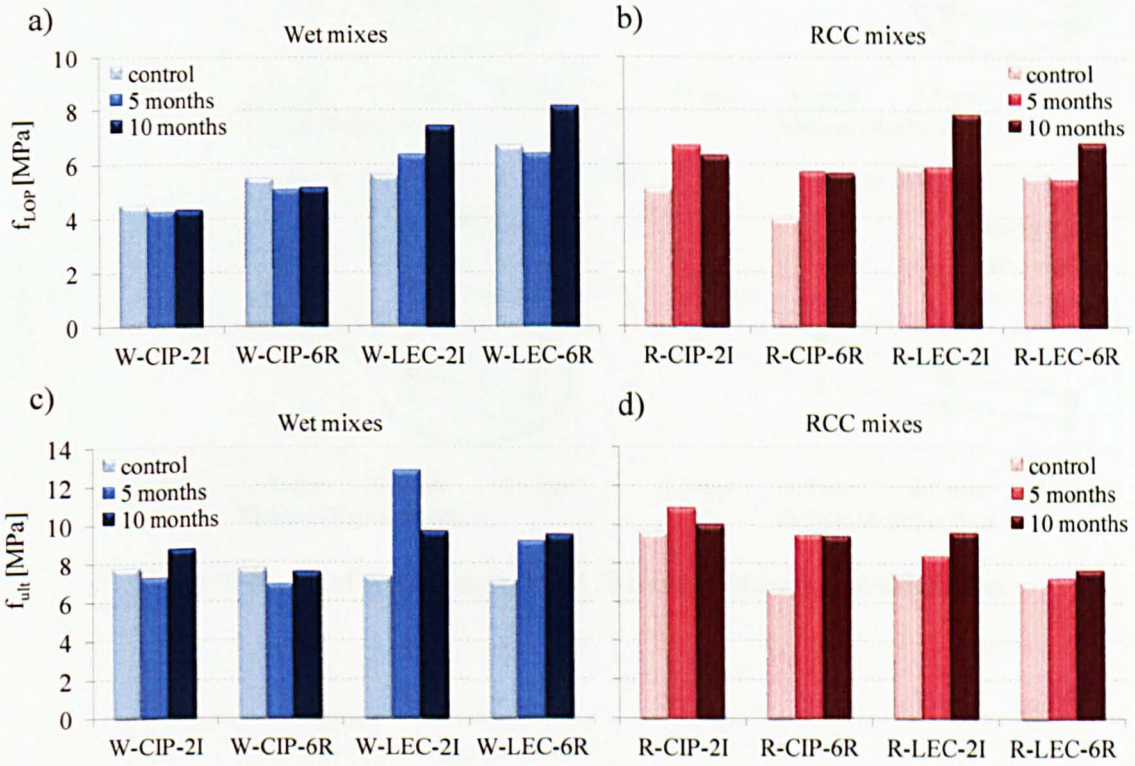

Figure 149 – f_{LOP} and f_{ult} at 5 and 10 months of corrosion simulation.

Wet mixes W-CIP-2I and W-CIP-6R have most of the results of f_{LOP} and f_{ult} for both 5 and 10 months slightly lower than the control specimens. However, this seems to be mainly due to the

variability associated with the casting of the specimens, since the specimens tested at 28 days were not the same as the ones tested at 5 and 10 months of wet-dry cycles.

Residual flexural strength $f_{R,i}$

$f_{R,i}$ results are shown in Figures 150 and 151, for wet and dry mixes, respectively. The values of $f_{R,i}$ are close to the results obtained for the control specimens. However, if small changes in behaviour are taken into account, it can be observed that, for most of the mixes (see highlighted results in the figures below), the values of $f_{R,2.5}$ and $f_{R,3.5}$ of specimens exposed to 10 months of wet-dry cycles tend to reduce in comparison to control specimens. This may be an indication of a slight loss in the energy absorption capacity after concrete has been exposed to 10 months of wet-dry cycles.

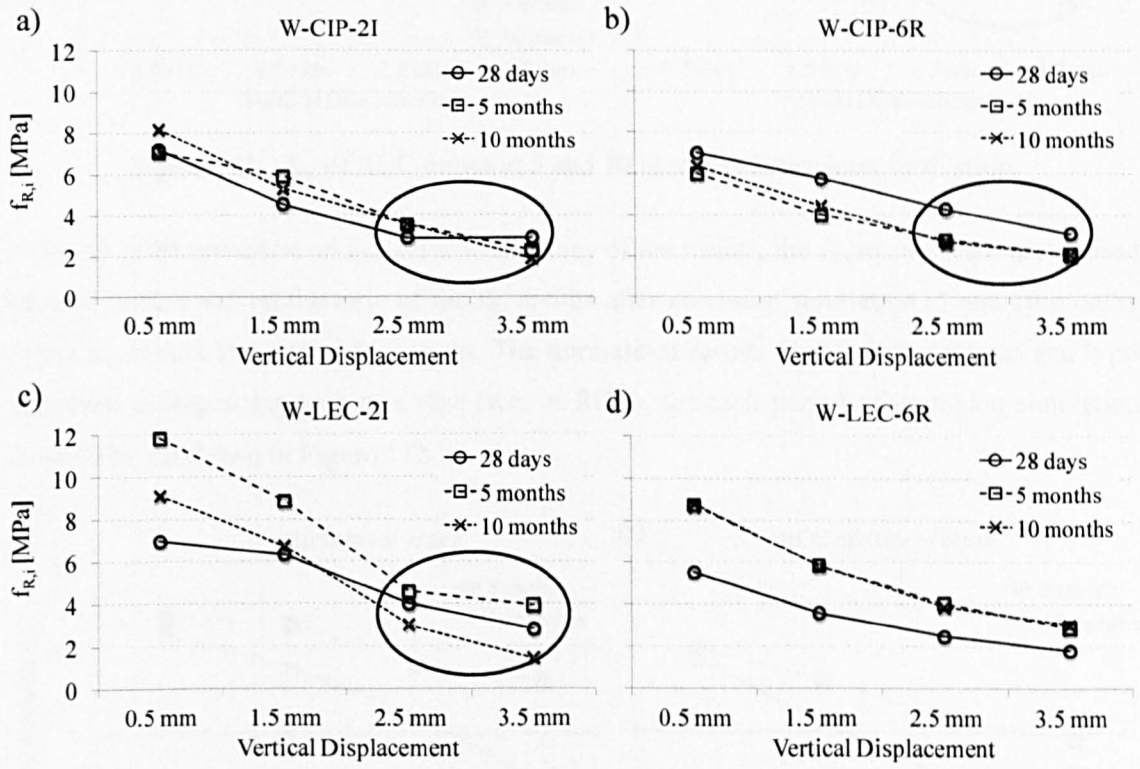

Figure 150 – $f_{R,i}$ of wet mixes at 5 and 10 months of corrosion simulation.

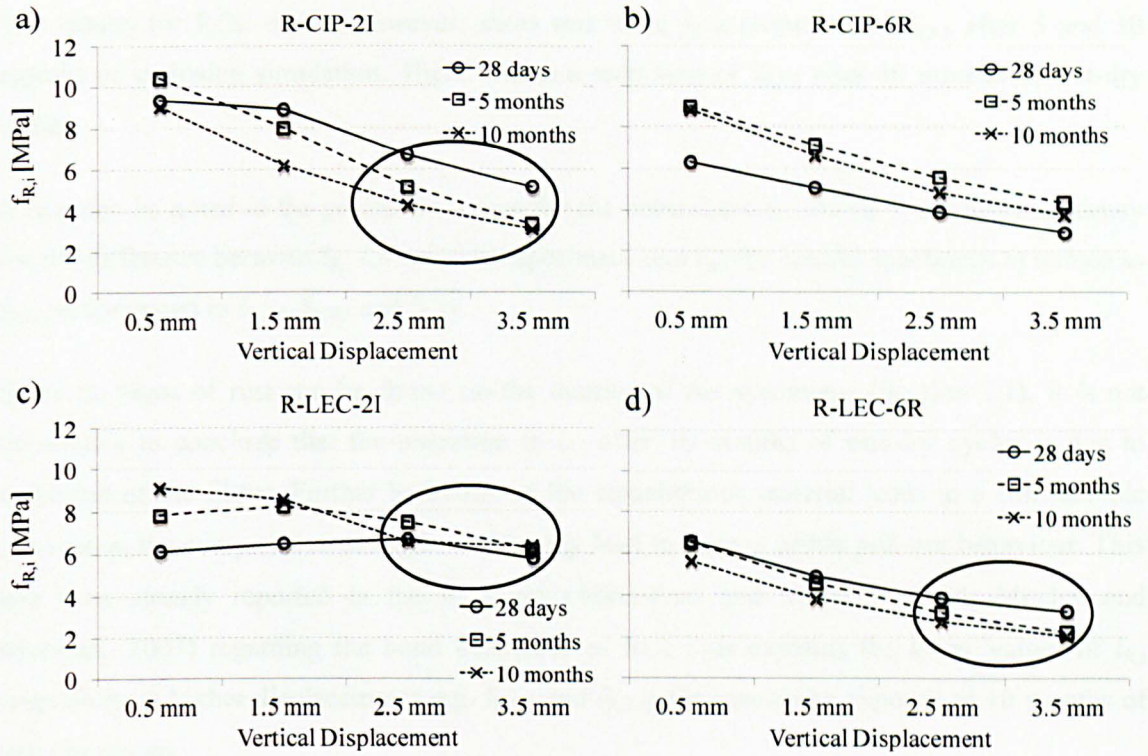

Figure 151 – $f_{R,i}$ of RCC mixes at 5 and 10 months of corrosion simulation.

To verify if the reduction on $f_{R,i}$ is due to accuracy of the results, the $f_{R,i}$ results were normalised, for each mix, based on the ratio of the $f_{R,i}$ results after corrosion simulation (5 and 10 months) by the $f_{R,i}$ results for control specimens. The normalised results for all fibre contents and types were then averaged for each mix type (wet or RCC), for each period of corrosion simulation. The results are shown in Figure 152.

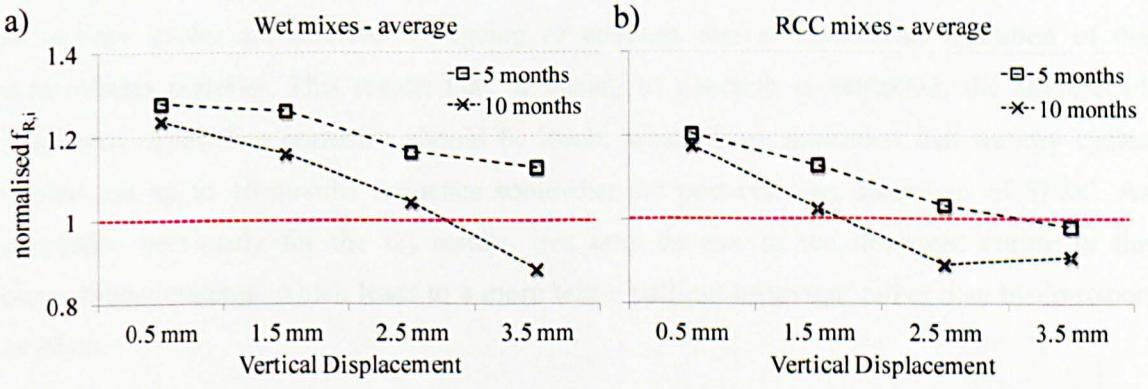

Figure 152 – Averaged normalised $f_{R,i}$ for a) wet and b) RCC mixes.

For wet mixes, most of the results are above 1, meaning that $f_{R,i}$ is not affected by wet-dry cycles, except for $f_{R,3.5}$ after 10 months of corrosion simulation, where a slight reduction (approximately 12%) in $f_{R,3.5}$ occurs compared to the control specimens.

The results for RCC mixes, however, show that there is a reduction of $f_{R,3.5}$ after 5 and 10 months of corrosion simulation. There is also a reduction of $f_{R,2.5}$ after 10 months of wet-dry cycles.

It can also be noted in the graphs that, even for the normalised $f_{R,i}$ above 1, there is a tendency for the difference between $f_{R,i}$ for corroded specimens and $f_{R,i}$ for control specimens to reduce as $f_{R,0.5}$ is compared to $f_{R,1.5}$, $f_{R,2.5}$ and $f_{R,3.5}$.

Since no signs of rust can be found on the interior of the specimens (Section 7.1), it is not reasonable to conclude that the reduction in $f_{R,i}$ after 10 months of wet-dry cycles is due to corrosion of the fibres. Further hydration of the cementitious material leads to a considerable increase in the compressive strength, which may lead to a more brittle pull-out behaviour. This has been already reported in the literature (Alavi-Fard and Marzouk, 2004; Mitchel and Marzouk, 2007) regarding the bond behaviour of RC. This explains the lower values of $f_{R,i}$ (especially at higher displacements e.g. $f_{R,2.5}$ and $f_{R,3.5}$) for specimens exposed to 10 months of wet-dry cycles.

Equivalent flexural strength f_{eq3} and equivalent flexural ratio $R_{e,3}$

The results of f_{eq3} are shown in Figure 153a and b while the results of $R_{e,3}$ are shown in Figure 153c and d. It can be observed that the graphs agree with the $f_{R,i}$ results, indicating that some specimens show reduction in the f_{eq} and $R_{e,3}$ after 10 months of exposure to wet-dry cycles.

It is important to add that, as observed in the compressive strength analysis, specimens exposed to wet-dry cycles are affected by ageing of concrete due to continuous hydration of the cementitious material. This means that, if ageing of concrete is neglected, the strength of specimens exposed to corrosion should be lower, which is an indication that wet-dry cycles carried out up to 10 months influence somewhat the post-cracking behaviour of SFRC. As concluded previously for the $f_{R,i}$ results, this may be due to the improved curing of the cementitious material, which leads to a more brittle pull-out behaviour rather than by corrosion of fibres.

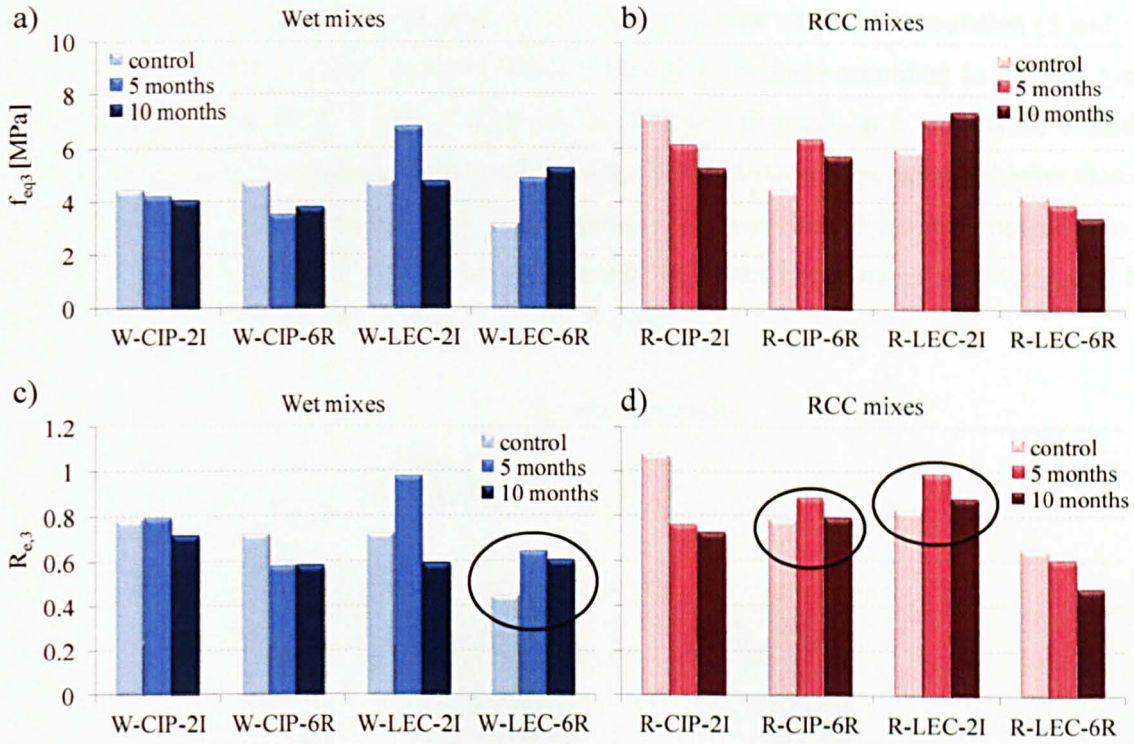

Figure 153 – f_{eq3} and $R_{e,3}$ at 5 and 10 months of corrosion simulation.

Modulus of elasticity E

Figure 154 shows the E results, calculated according to Che's (2010) approach. No clear correlation can be established when comparing E from both exposure periods to the control specimens. A considerably high variability of E for control specimens has already been reported in Section 5.3. Nevertheless, when comparing the 5 months and 10 months results to each other, it is observed that E results for 10 months are in general higher than E for 5 months. This is in line with the results obtained from the f_{LOP} analysis, and is possibly caused by the further hydration of the cementitious material.

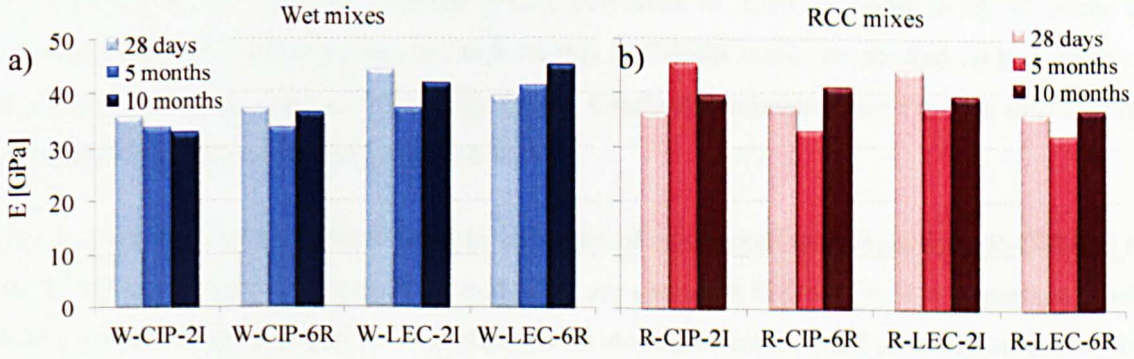

Figure 154 – E at 5 and 10 months of corrosion simulation.

E results were normalised, for each mix, by the ratio of E after corrosion simulation (5 and 10 months) to E of control specimens. The values were then averaged according to the mix type (wet or RCC), as shown in Figure 155. It can be seen that E results at 5 months are slightly lower than the control specimens, and that the results at 10 months are the same or higher than E control and E at 5 months. Since there is an increase in E results at 10 months compared to 5 months, the reduction in E at 5 months compared to control specimens is mainly due to variability in the results, and not due to the loss of bond.

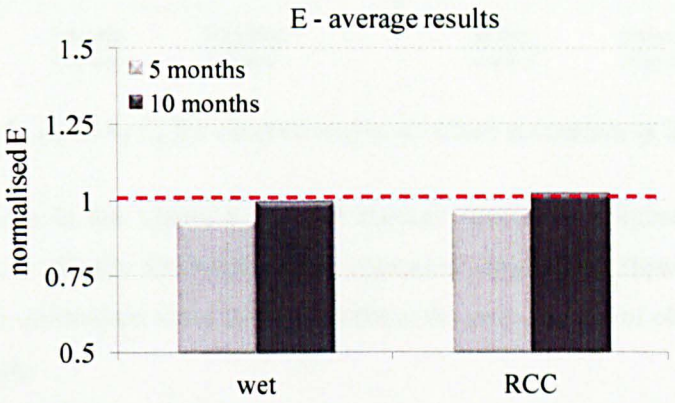

Figure 155 – Averaged normalised E for wet and RCC mixes.

7.2.2.2 Cracked and un-cracked specimens subjected to wet-dry cycles at 20°C and 40°C

Flexural strength at the limit of proportionality f_{LOP} and ultimate flexural strength f_{ult}

Since the procedures to accelerate corrosion in SFRC are not standardised, a higher temperature (40 °C) of the chloride solution was used for the simulation of the corrosive process for one mix (R-CIP-6R). This was performed to verify whether higher temperatures are more efficient in accelerating corrosion than ambient temperatures.

As reported in the literature (Section 3.1.2), corrosion in SFRC is most likely to occur in cracked elements. Therefore, specimens from mix R-CIP-6R were pre-cracked up to a crack of 0.2 mm before being exposed to wet-dry cycles. Cracked specimens were exposed to corrosion simulation at a temperature of 20 °C and 40 °C.

The f_{LOP} and f_{ult} results obtained from the exposure of un-cracked specimens (mix R-CIP-6R) to 40 °C and cracked specimens to 20 °C and 40 °C are shown in Figure 156. It is important to add that, for cracked specimens after 5 months and 10 months of corrosion, f_{LOP} does not refer to the true f_{LOP} of the specimen, but the apparent stress ($f_{LOP,ap}$) at which the initial stiffness is lost, since the specimens were already cracked. The graphs also show the results for un-cracked

specimens at 20 °C for comparison purposes. The results at 28 days include the results of both cracked (during pre-cracking) and un-cracked control specimens.

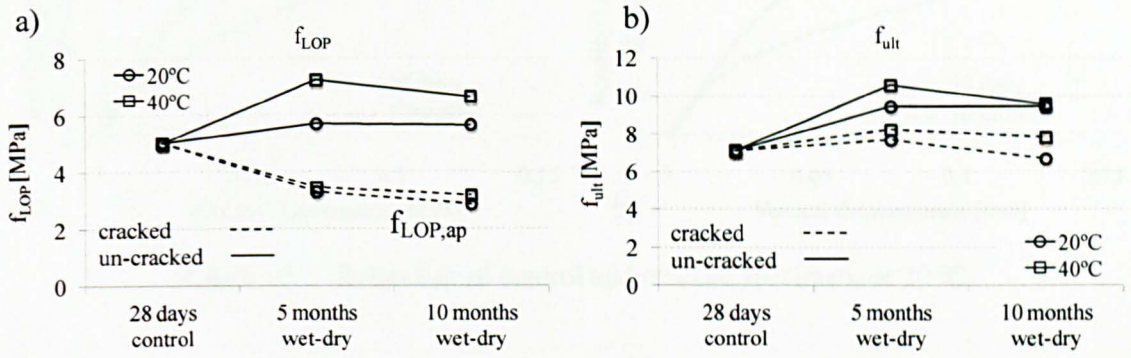

Figure 156 – a) f_{LOP} and b) f_{ult} for cracked and un-cracked specimens at 20 °C and 40 °C.

The considerable drop in the apparent f_{LOP} for cracked specimens (Figure 156a) is expected since specimens were already fractured before corrosion simulation. However, the effects of corrosion need to be understood since the cracks allow the easy ingress of chlorides to the fibres located near the crack.

Un-cracked specimens presented higher f_{LOP} after corrosion simulation than the control specimens, especially at 40 °C. The higher temperature seems to improve curing and accelerate ageing of concrete (Barnett *et al.*, 2006; Hale *et al.*, 2005), and any speeding up of the corrosion process does not lead to flexural strength loss.

Cracked specimens showed similar behaviour for both temperatures used. The results of f_{ult} (Figure 156b) for cracked specimens show a slight increase in strength as expected from ageing, which means that corrosion does not have a major impact on the concrete performance.

The initial behaviour (in terms of $f_{LOP,ap}$) of cracked specimens exposed to corrosion changed considerably when compared to the control specimens. To examine this, the bending load [kN] *versus* vertical displacement [mm] curves were plotted as shown in Figures 157 and 158. The curves of the average of 3 specimens subjected to corrosion are shown in the graphs below.

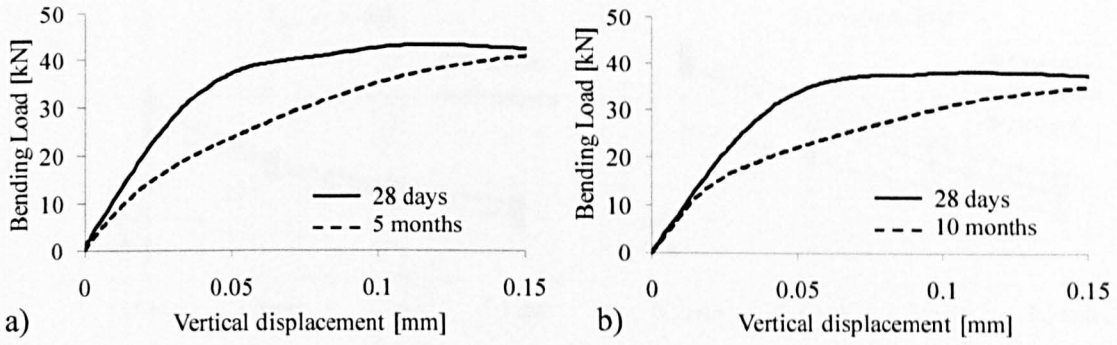

Figure 157 – Behaviour of control and cracked specimens at 20 °C.

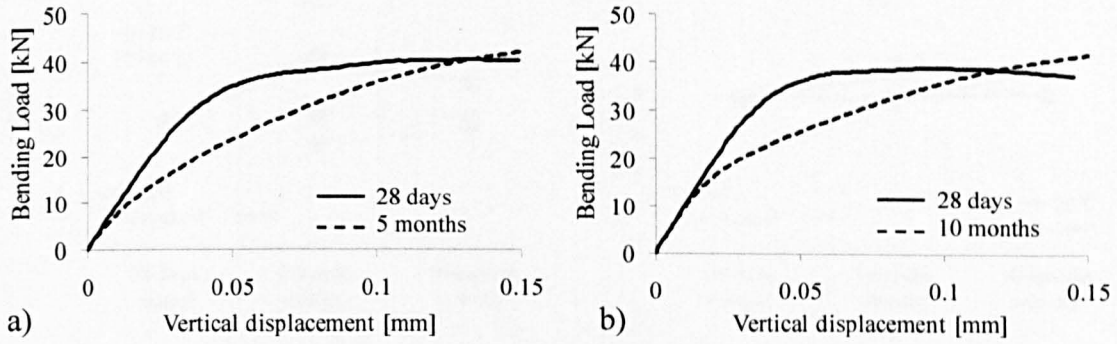

Figure 158 – Behaviour of control and cracked specimens at 40 °C.

It can be seen from the figures that the initial elastic behaviour, especially at 5 months, is affected when re-loading the cracked specimens, indicating some stiffness degradation. This degradation is much less at 10 months which indicates a stiffness increase with time for the cracked specimen. There is also a slight increase in strength at 40 °C (5 and 10 months) which again indicates concrete strength enhancement with ageing and autogeneous healing of the cracks.

More discussion on the curves shown above is made later in this section, together with the discussion on the E results.

Residual flexural strength $f_{R,i}$, equivalent flexural strength f_{eq3} and equivalent flexural ratio $R_{e,3}$

Figure 159 shows the $f_{R,i}$ for the cracked and un-cracked specimens, while Figure 160a shows the f_{eq3} and Figure 160b shows the $R_{e,3}$ values.

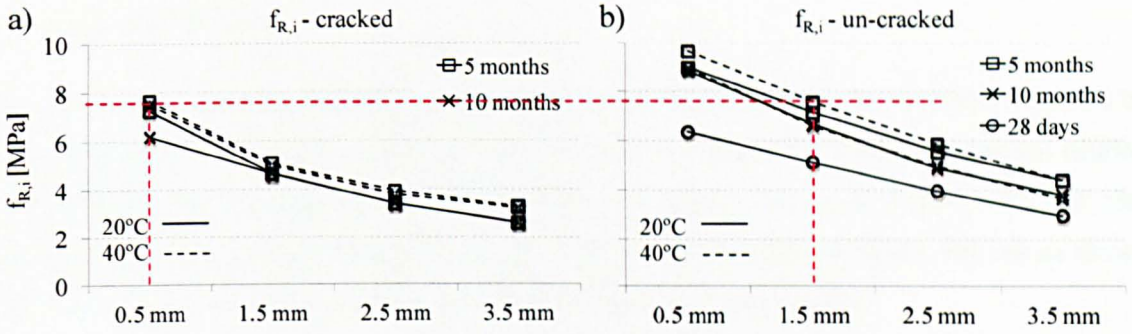

Figure 159 – $f_{R,i}$ for a) cracked and b) un-cracked specimens; at 20 °C and 40 °C.

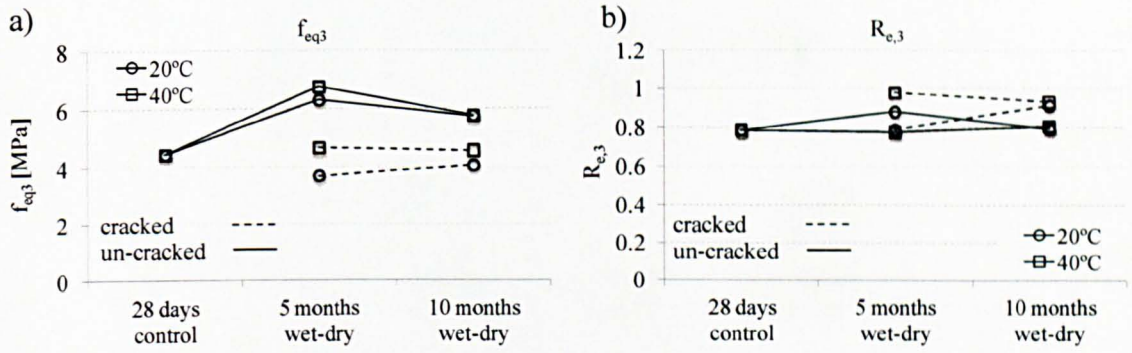

Figure 160 – a) f_{eq3} and b) $R_{e,3}$ for cracked and un-cracked specimens at 20 °C and 40 °C.

The cracked specimens show lower $f_{R,i}$ values than the un-cracked specimens. This is expected since the cracked specimens already have some residual vertical displacement which is not accounted for. However, the residual vertical displacement not accounted for is not expected to be more than 0.1 mm since the specimens were only pre-cracked up to around 0.2 mm CMOD. The shift shown by the dashed lines in Figure 159 is more in the range of 1 mm (for a specific value of $f_{R,i}$). This indicates that some micro damage was done to the specimens in addition to the pre-loading. Since the crack is open, the chlorides could penetrate deeper into the section and corrode the fibres. However, this corrosion does not appear to get worse with time, which might indicate that the cracks or part of the cracks closed due to autogeneous healing of concrete.

The same conclusions can be made for f_{eq3} where the values at 10 months for the cracked specimens are higher than at 5 months.

The $R_{e,3}$ values appear to be similar for the cracked and un-cracked specimens, but this is mostly due to the low values of f_{LOP} obtained for cracked specimens ($R_{e,3}$ is the ratio of f_{eq3} in relation to f_{LOP}).

Modulus of elasticity E

Figure 161 shows that there is a decrease of E for cracked specimens at 5 months followed by an increase at 10 months. E results at 28 days were averaged by E results of cracked (during pre-cracking) and un-cracked control specimens. As already shown in Figures 157 and 158, cracked specimens show stiffness degradation when they are re-loaded, hence, the values shown in the figure below for the cracked specimens should reflect that damage.

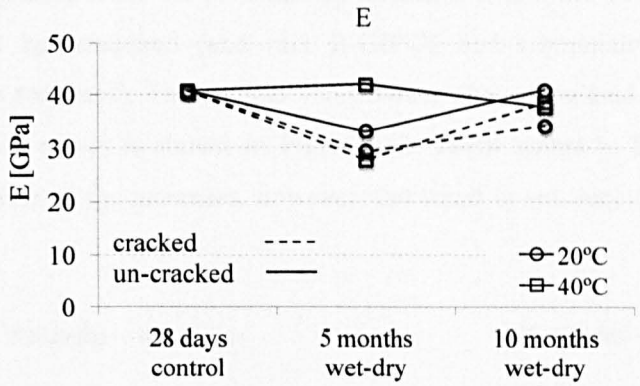

Figure 161 – E for cracked and un-cracked specimens at 20 °C and 40 °C.

However, by examining closely Figures 157 and 158, it can be observed that the initial curve (up to 0.02 mm) of the specimens exposed to 10 months of wet-dry cycles present similar elastic behaviour as when tested at 28 days. This explains the high E results of cracked specimens at 10 months of corrosion, and strongly indicates that autogeneous healing has commenced to restore the continuity of the concrete through the cracks. This also indicates that corrosion degradation stops after cracks are healed.

Autogeneous healing of cracks does not recover the full capacity of the concrete, since the carbonate crystals formed in the cracks are not as strong as the C-S-H products (Torrijos *et al.*, 2010; Edvardsen, 1999). This explains the fact that the bending load versus mid-span displacement curves of cracked specimens deviate earlier from linear elasticity than the un-cracked specimens.

7.3 INFLUENCE OF TRANSPORT MECHANISMS, DENSITY AND POROSITY ON THE CORROSION RESISTANCE

The influence of the transport mechanisms, density and porosity on the performance of concrete when exposed to corrosion simulation is investigated in this section. The properties are correlated to the normalised f_{cm} and f_{LOP} (ratio of strength after 5 and 10 months of wet-dry

cycles – $f_{cm,5m}$, $f_{LOP,10m}$ – to strength at 28 days – $f_{cm,28}$, $f_{LOP,28}$). The results for permeability, sorptivity, porosity and density were obtained from specimens preconditioned at 80 °C.

7.3.1 Compressive Strength

7.3.1.1 Permeability, sorptivity and porosity

RCC results are not plotted since the permeability of mixes R-CIP-6R and R-LEC-6R were too high and could not be measured (and mix R-CIP-2I had compaction problems and the permeability was not recorded). The comparison between the normalised compressive strength to permeability of wet mixes is shown in Figure 162. There seems to be a tendency for the permeability to increase as f_{cm} increases, however, the trend is not very clear due to the small number of data.

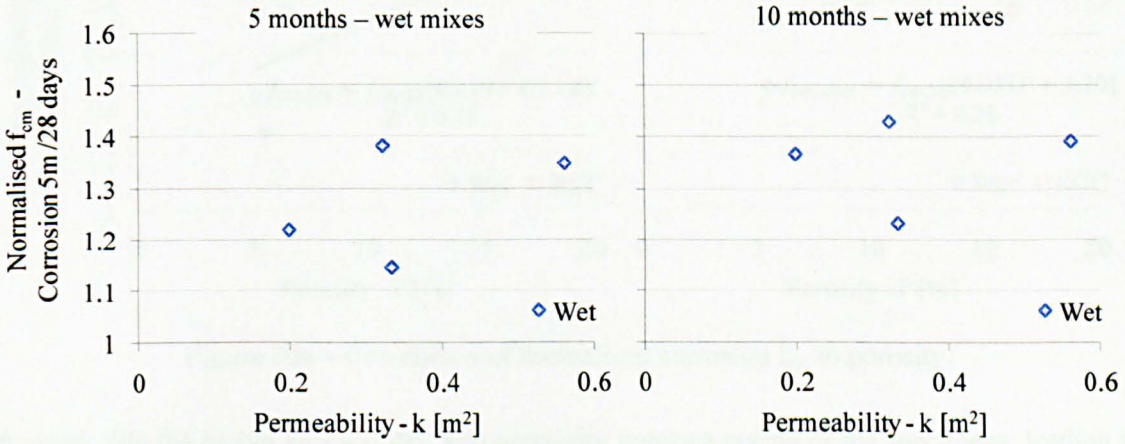

Figure 162 – Correlation of normalised corrosion f_{cm} to permeability.

The comparison between f_{cm} with sorptivity and porosity results show that there is a tendency for the strength to increase as the properties increase. Even though the correlation coefficient for the linear regression analyses shown in both Figures 163 and 164 is low (< 0.55), the same trend was observed for all cases.

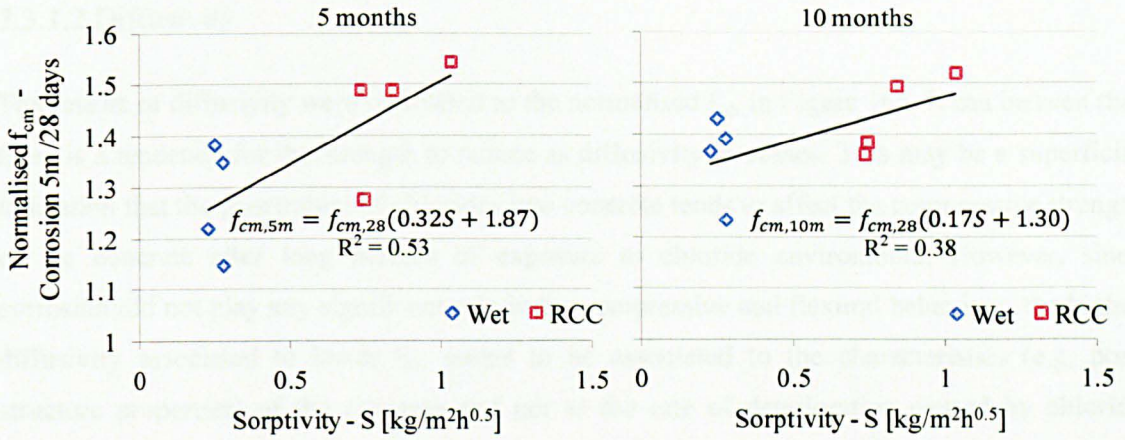

Figure 163 – Correlation of normalised corrosion f_{cm} to sorptivity.

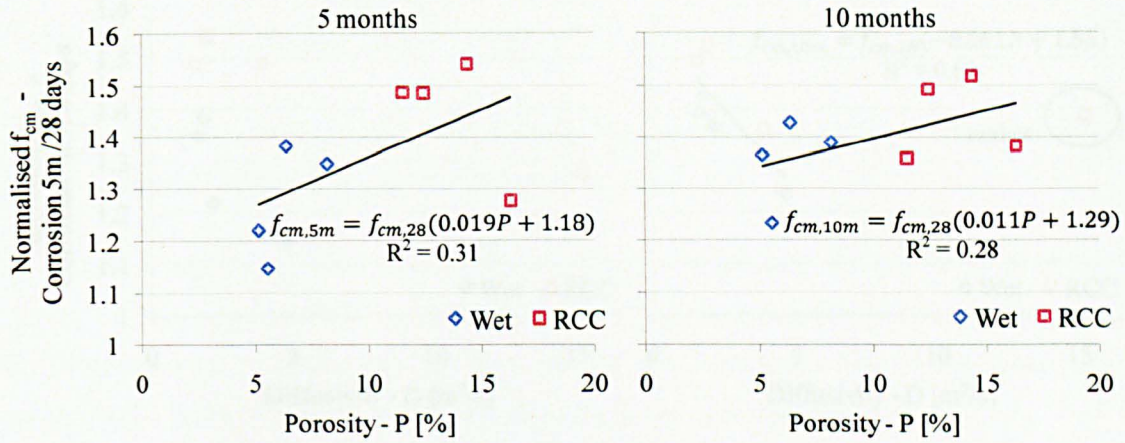

Figure 164 – Correlation of normalised corrosion f_{cm} to porosity.

It seems that the higher permeability and sorptivity improve curing of the specimens, leading to higher strength. It should be noted that the slope of the linear regression decreases at 10 months compared to 5 months of wet-dry cycles. This may be due to the rate of hydration reducing with age, thus reducing the effect of permeability and sorptivity on strength gain. Alternatively, it can be said that the higher rate of hydration due to high permeability, porosity and sorptivity at the early ages of curing and hydration is substantially completed by the 5 months. On the other hand, lower values of permeability, sorptivity and porosity slow down the hydration process and, hence, hydration is still taking place at 10 months.

It is important to add that the values of pore-structure properties were obtained from the control specimens, which means that the time-dependence of these properties is not taken into account.

7.3.1.2 Diffusivity

The results of diffusivity were correlated to the normalised f_{cm} in Figure 165. It can be seen that there is a tendency for the strength to reduce as diffusivity increases. This may be a superficial indication that the penetration of chlorides into concrete tends to affect the compressive strength of the concrete after long periods of exposure to chloride environment. However, since corrosion did not play any significant role in the compressive and flexural behaviour, the higher diffusivity associated to lower f_{cm} seems to be associated to the characteristics (e.g. pore structure properties) of the concrete and not to the rate of deterioration caused by chloride penetration.

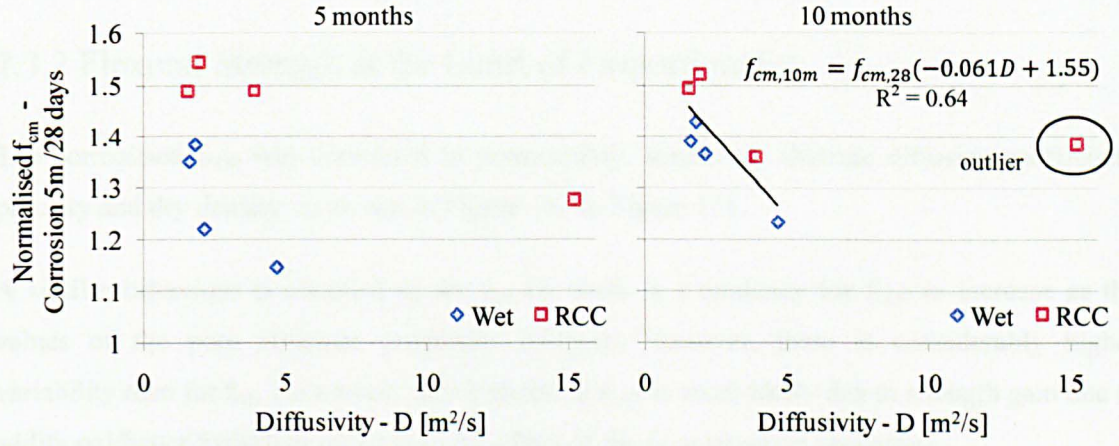

Figure 165 – Correlation of normalised corrosion f_{cm} to diffusivity.

7.3.1.3 Density

The comparison of dry density with normalised f_{cm} is shown in Figure 166. As expected, density increases as the normalised f_{cm} increases. As previously concluded, specimens exposed to wet-dry cycles are affected by curing of the concrete. Curing conditions also contribute to the better hydration of the cementitious material, which refines the pore structure of the concrete and can also increase density. This is in line with the previous conclusion on the effect of permeability, sorptivity and porosity on f_{cm}.

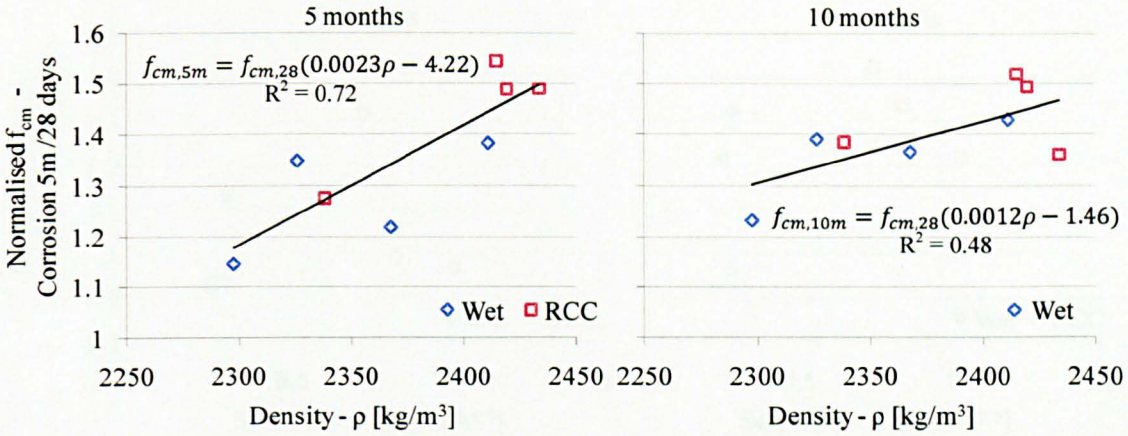

Figure 166 – Correlation of normalised corrosion f_{cm} to dry density.

7.3.2 Flexural Strength at the Limit of Proportionality

The normalised f_{LOP} was correlated to permeability, sorptivity, chloride diffusion coefficient, porosity and dry density, as shown in Figure 167 to Figure 171.

A similar behaviour is obtained as for f_{cm} i.e. there is a tendency for f_{LOP} to increase as the values of the pore structure properties increase. However, there is considerably higher variability than for f_{cm}. As a result, any increase in f_{LOP} is more likely due to strength gain due to additional/better hydration rather than the effect of the pore structure properties.

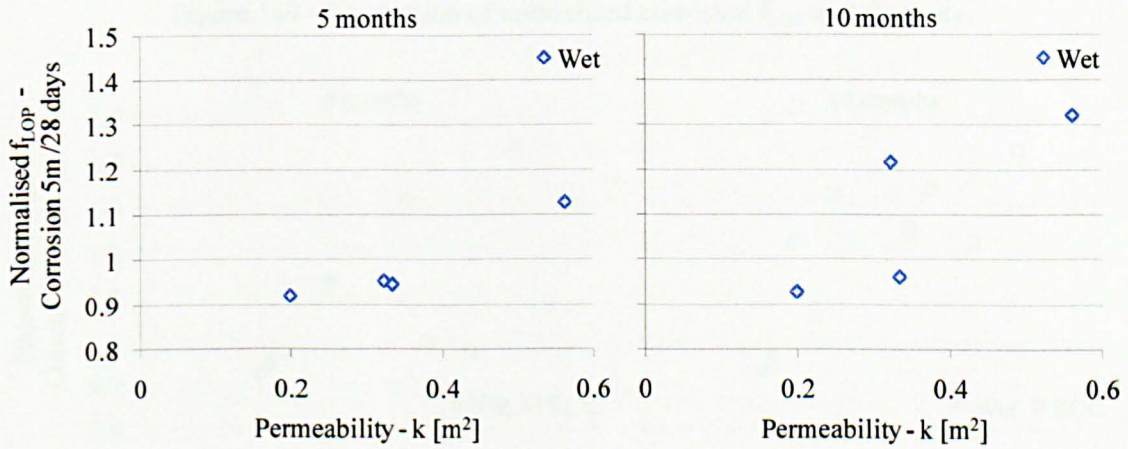

Figure 167 – Correlation of normalised corrosion f_{LOP} to permeability.

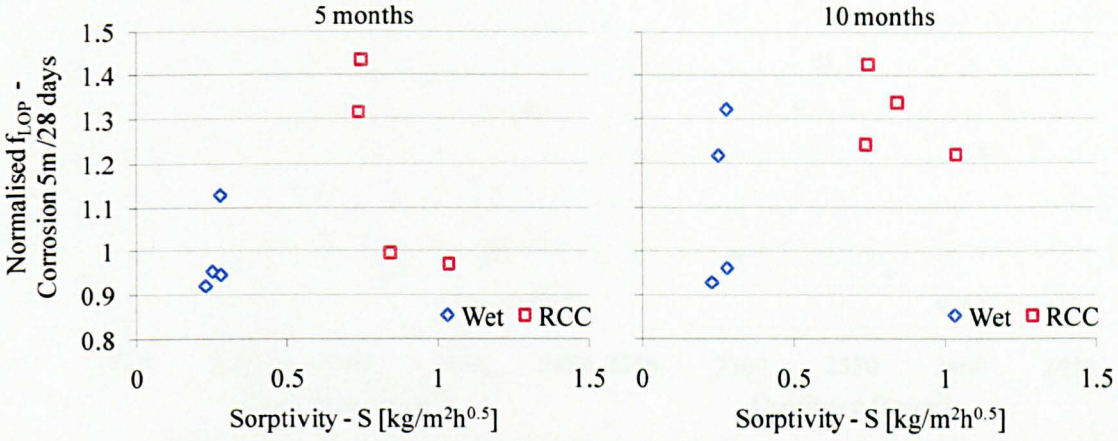

Figure 168 – Correlation of normalised corrosion f_{LOP} to sorptivity.

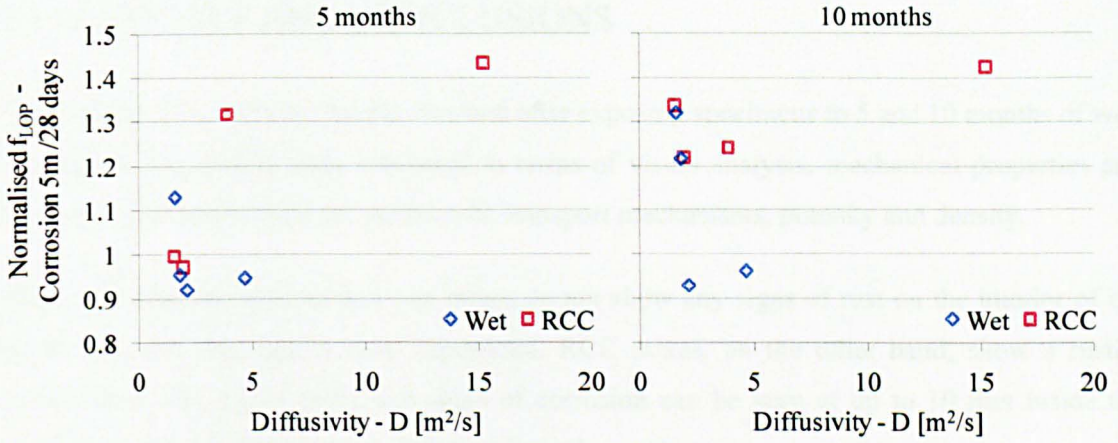

Figure 169 - Correlation of normalised corrosion f_{LOP} to diffusivity.

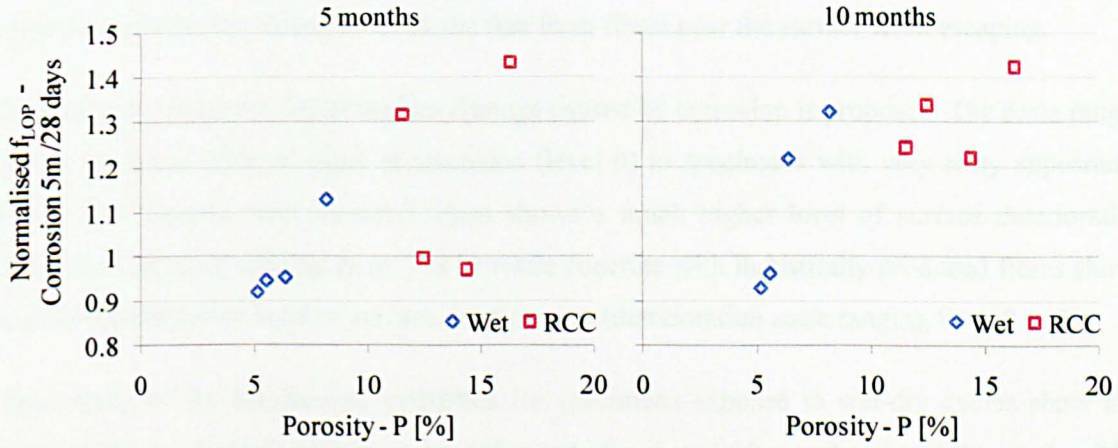

Figure 170 – Correlation of normalised corrosion f_{LOP} to porosity.

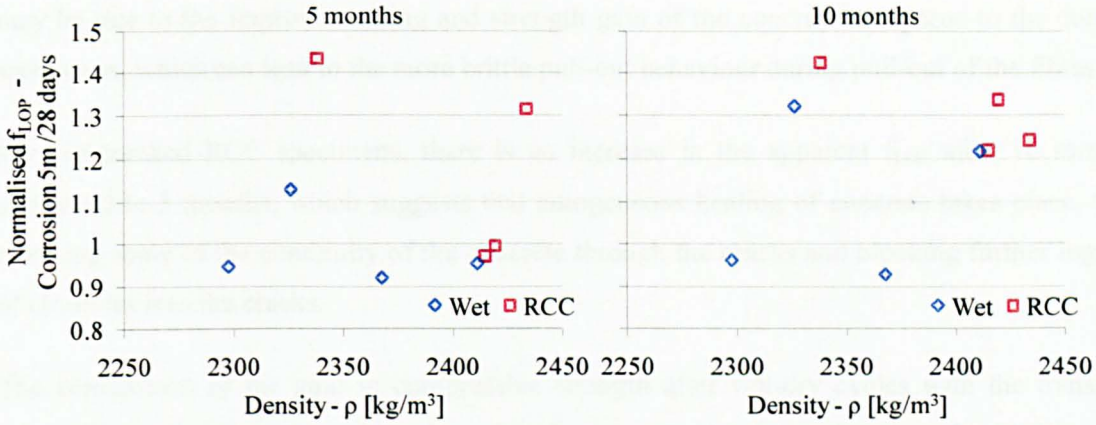

Figure 171 – Correlation of normalised corrosion f_{LOP} to dry density.

7.4 SUMMARY AND CONCLUSIONS

This chapter dealt with the results obtained after exposing specimens to 5 and 10 months of wet-dry cycles. The results were presented in terms of visual analysis, mechanical properties and comparison of mechanical properties with transport mechanisms, porosity and density.

The visual analysis showed that wet mixes do not show any signs of rust on the interior of the specimens, and that rust is only superficial. RCC mixes, on the other hand, show a rustier surface than wet mixes and some signs of corrosion can be seen at up to 10 mm inside the specimens with 6R fibres after 5 months of wet-dry cycles.

However, continuous hydration of the cement appears to refine the pore structure of the concrete and this was found to block the rust from fibres near the surface from escaping.

A scale to measure the visual surface damage caused by corrosion is proposed. The scale ranges from specimens with no signs of corrosion (level 0) to specimens with very rusty appearance (level 5). Concrete with recycled fibres shows a much higher level of surface deterioration (deterioration scale ranging from 3 to 5) while concrete with industrially produced fibres shows a considerable lower level of surface deterioration (deterioration scale ranging from 0 to 2).

The results of the mechanical properties for specimens exposed to wet-dry cycles show that most of the mechanical properties are enhanced after 5 and 10 months of wet-dry cycles. This mainly occurs at 5 months while by 10 months the strength seems to stabilise. This is mainly due to continuous cement hydration. As a consequence, wet-dry cycles up to 10 months do not damage the industrially produced and the recycled SFRC.

Nevertheless, the residual flexural strength results for specimens exposed to wet-dry cycles show that there is some reduction in performance with time of exposure to wet-dry cycles. This

may be due to the improved curing and strength gain of the concrete compared to the control specimens, which can lead to the more brittle pull-out behaviour during pull-out of the fibres.

For pre-cracked RCC specimens, there is an increase in the apparent f_{LOP} after 10 months compared to 5 months, which suggests that autogeneous healing of concrete takes place, thus restoring some of the continuity of the concrete through the cracks and blocking further ingress of chlorides into the cracks.

The comparison of the gain in compressive strength after wet-dry cycles with the transport mechanisms, density and porosity show that there is a tendency for the strength to increase as the pore structure properties (except diffusion) increase. Higher permeability and sorptivity can lead to a higher rate of moisture transport into concrete, which improves curing, and enhances the hydration rate of the cement. The comparison of strength gain with diffusion coefficient shows that there is a tendency for the strength to reduce as diffusion coefficient increases. However, this is mainly due to the characteristics of the concrete (e.g. pore structure) than by damage caused by chloride ingress.

The wet-dry cycles method used to accelerate corrosion in SFRC seems to be effective in making the corrosion process faster than in real situations, by allowing the ingress of chlorides by both immersion and convection (absorption). The penetration of chlorides seems to occur uniformly in all surfaces of the specimens, since the rusty appearance was similar all around the specimens. However, further work should be undertaken to be able to estimate how accelerated the method is compared to specific environmental conditions. Some information on the correlation of wet-dry cycles with less severe conditions can be found in Chapter 10.

As a general conclusion, un-cracked SFRC exposed to chloride-contaminated environment does not show any loss in mechanical performance, and the effects of corrosion are superficial. Nevertheless, it is important to note that accelerated wet-dry cycles were carried out only up to 10 months, and that further investigations should be carried out to verify the effects of corrosion when concrete is exposed to longer periods of chloride exposure.

Another deterioration process investigated in this thesis is due to freeze-thaw damage, which is explained in the following chapter.

CHAPTER 8

8. FREEZE-THAW RESISTANCE OF SFRC

This chapter presents and discusses the experimental results obtained from the accelerated freeze-thaw process. The freeze-thaw investigation was undertaken in terms of visual analysis, loss of mass and loss of compressive and flexural strengths.

8.1 VISUAL ANALYSIS

8.1.1 Wet mixes

Seven cycles

Mixes W-LEC-0 and W-LEC-2I show similar behaviour when exposed to freeze-thaw. After 7 freeze-thaw cycles, both mixes show only few signs of deterioration, represented by isolated points of delamination of concrete. The deterioration of mix W-LEC-6R, however, is mostly characterised by uniform scaling of concrete instead of isolated points of delamination. Figure 172 shows the surface appearance of typical wet mix specimens exposed to 7 freeze-thaw cycles.

Figure 172 – Wet mixes after 7 freeze-thaw cycles.

Fourteen cycles

All wet mixes show uniform scaling of concrete after 14 freeze-thaw cycles, as shown in Figure 173. Scaling of W-LEC-6R exposes some fibres to the surface; and this can be attributed to the large amount of recycled fibres in the mix.

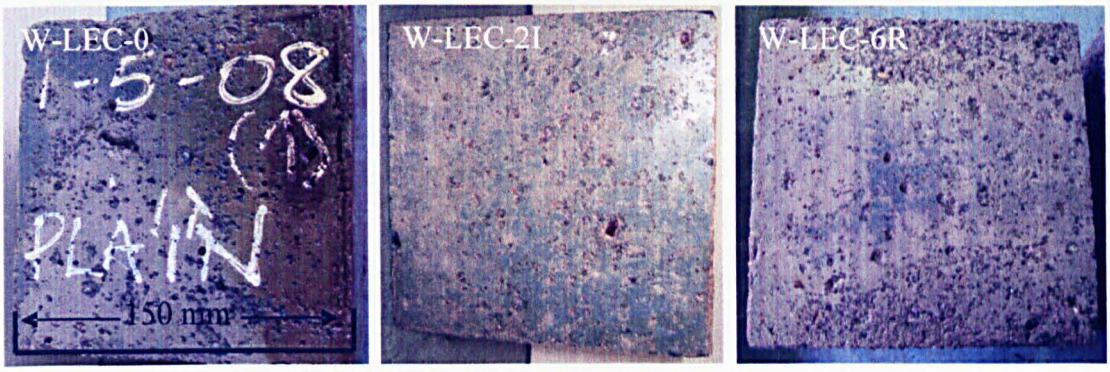

Figure 173 – Wet mixes after 14 freeze-thaw cycles.

Twenty eight cycles

Wet mixes exposed to 28 freeze-thaw cycles present uniform scaling of concrete at a larger degree than at 14 days (Figure 174). Some pop-outs and exposed aggregates can also be observed, as shown in Figure 175. W-LEC-6R mix shows more signs of deterioration than plain and 2I mixes, since the large amount of scaling exposes the aggregates and the fibres near the surface. Recycled fibres are also detached from the concrete. Very few signs of corrosion/rusting of the fibres could be observed.

Figure 174 – Wet mixes after 28 freeze-thaw cycles.

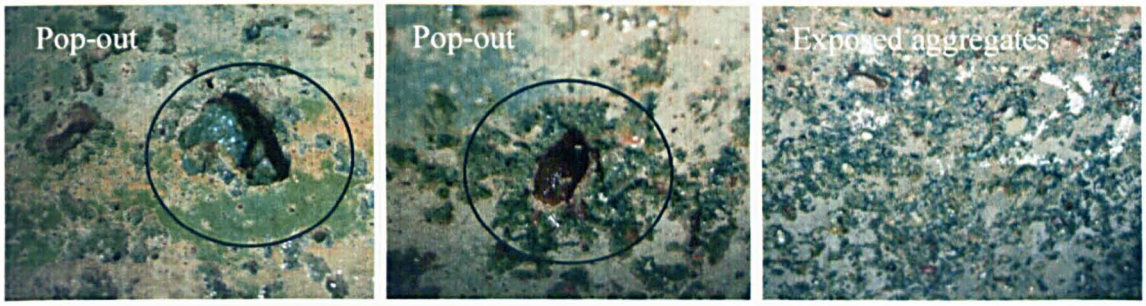

Figure 175 – Pop-outs and exposed aggregates after 28 cycles.

Forty two cycles

The level of deterioration of specimens subjected to 42 freeze-thaw cycles (shown in Figure 176) is visibly higher than that observed for smaller number of cycles. Scaling is uniformly spread around the specimens. Some fibres become visible in the W-LEC-2I mix with some signs of corrosion (Figure 177). The surface of the concrete becomes very rough, even though in most cases it is possible to still see part of the original surface (Figure 177).

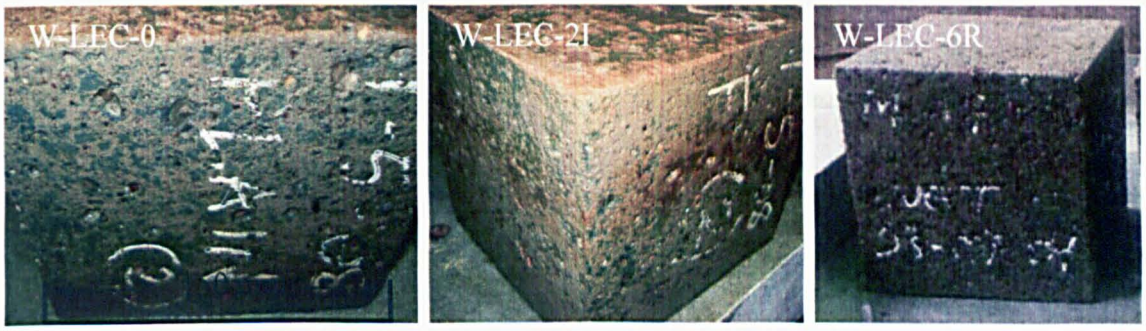

Figure 176 – Wet mixes after 42 freeze-thaw cycles.

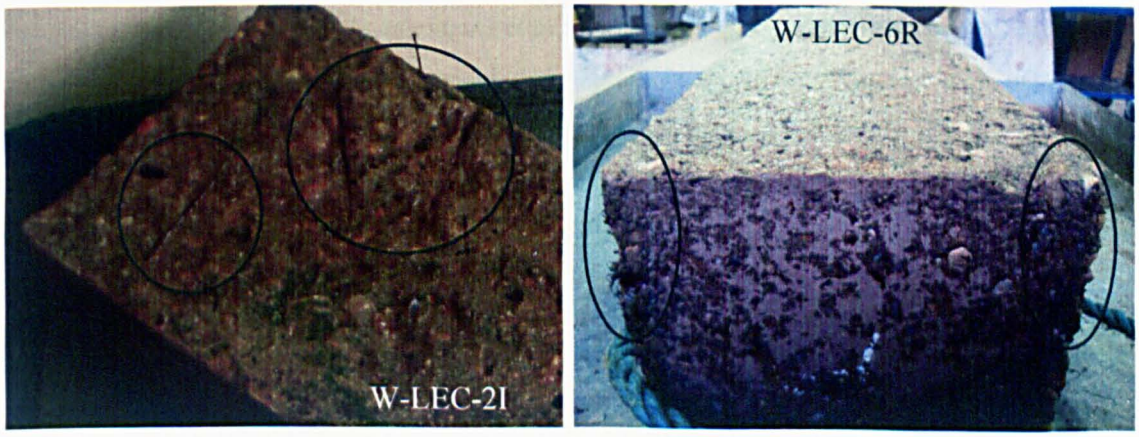

Figure 177 – Fibres exposed to surface after 42 cycles.

Fifty six cycles

After 56 freezing and thawing cycles, the surface of the specimens looks very deteriorated (Figure 178), with visible exposure of aggregates and fibres. In some parts, due to the large amount of scaled material, the original surface has disappeared. W-LEC-6R is the mix that presents most signs of deterioration. Mixes W-LEC-0 and W-LEC-2I show similar behaviour.

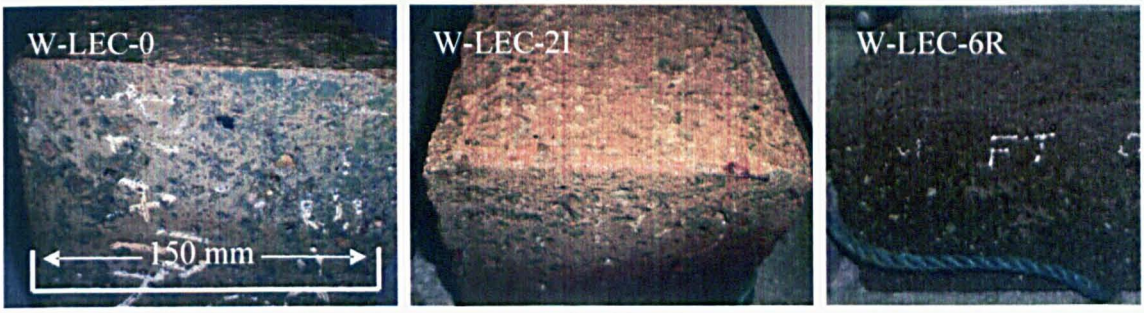

Figure 178 – Wet mixes after 56 freeze-thaw cycles.

Fibres exposed to the surface of the concrete are lightly corroded. They do not show more signs of corrosion because they are always fully-immersed in salt solution, and no contact with oxygen is allowed. However, due to a time-gap after freeze-thaw cycles and prior testing mechanical properties (usually few days), the exposed fibres became superficially rusty, which should have not affected the results.

8.1.2 RCC Mixes

Seven cycles

The appearance of RCC specimens varies completely when compared to wet mixes. Figure 179 shows that RCC specimens show a considerably large amount of deterioration, even after only 7 cycles. The original surface of the specimens is almost unrecognisable, fibres and aggregates become exposed to the surface, and even pop-outs can be noticed (highlighted in the figure below). Plain and 2I mixes show similar behaviour. Fibres exposed to the surface show few signs of rust.

Figure 179 – RCC mixes after 7 freeze-thaw cycles.

Fourteen cycles

RCC specimens exposed to 14 cycles do not show any traces of the original surface (cement paste of the surface has completely scaled), and the surface becomes very rough (Figure 180). Only few signs of rust can be observed in the fibres exposed on the surface of the concrete.

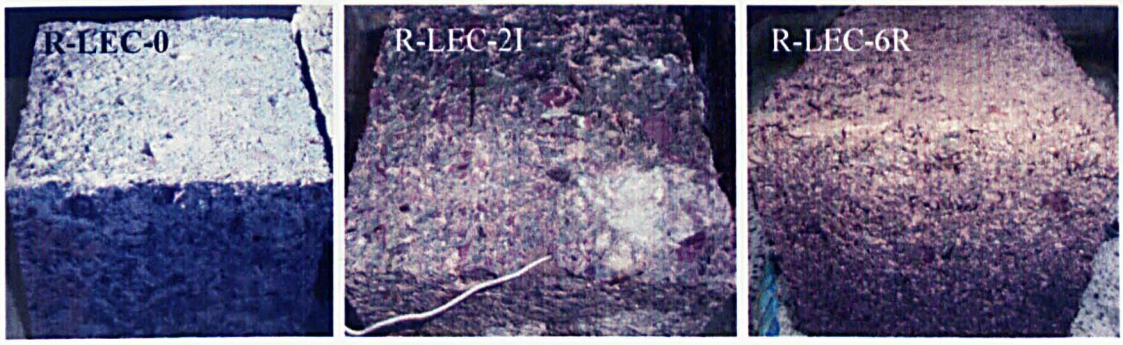

Figure 180 – RCC mixes after 14 freeze-thaw cycles.

Twenty eight cycles

The level of deterioration of RCC specimens after 28 cycles is considerably high (Figure 181), to the point that it starts to reduce the dimensions of the specimens. It can be observed, however, that mix R-LEC-6R presents a flatter surface and that the amount of aggregates exposed to the surface is lower compared to the 2I and plain mixes. This may be due to the large number of recycled fibres compared to the number of industrially produced fibres, which seems to be more efficient in maintaining the integrity of concrete, and reducing scaling.

Figure 181 – RCC mixes after 28 freeze-thaw cycles.

Forty two and fifty six cycles

Same comments as for 28 cycles apply to 42 and 56 cycles; however, the level of deterioration after 42 cycles is visibly higher, as shown in Figure 182. No pictures of specimens exposed to 56 cycles were taken prior to crushing.

Figure 182 – RCC mixes after 42 freeze-thaw cycles.

8.1.3 Discussion on the Visual Analysis

Although wet mixes were designed to resist to severe freeze-thaw exposure (low w/c ratio, considerably high cement content and air-entrainer), superficial deterioration can be seen all around the specimens. The types of freeze-thaw damage observed were scaling and pop-out of concrete, which are the most common types usually observed. Scaling indicates early start of freeze-thaw attack, whilst pop-outs show a more advanced stage of freeze-thaw attack. Advanced scaling and pop-outs can lead to severe deterioration of concrete.

RCC specimens present a considerably higher level of deterioration (scaling and pop-out) compared to wet mixes, which is probably due to the higher porosity and the pore structure characteristics of the material, especially at the boundaries. A considerable amount of pores in the wet mixes is due to air-entraining bubbles, which are beneficial on improving the freeze-

thaw resistance. On the other hand, RCC voids are mainly a result of the compaction technique used for the consolidation of the material. These voids normally do not meet the spacing and size specifications essential to improve the freeze-thaw resistance (Section 3.1.3), which in turn leads to higher rate of deterioration when exposed to freeze-thaw. Figure 183a shows the air-entraining bubbles in wet mix while Figure 183b shows the voids in RCC.

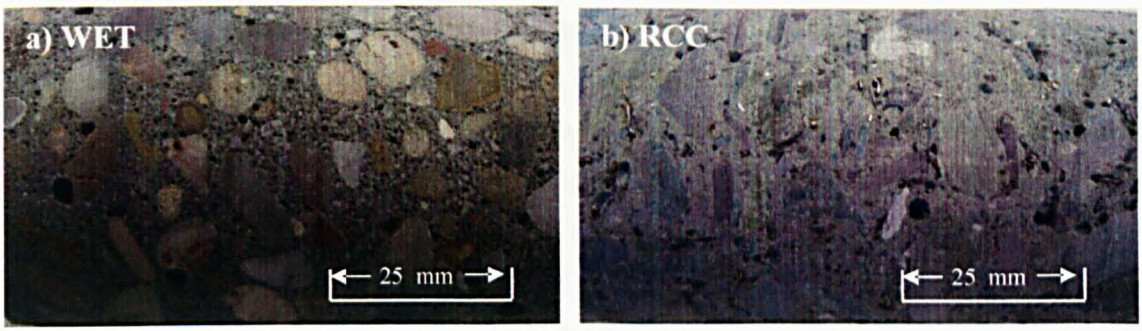

Figure 183 – Pore characteristic of a) wet and b) RCC mix.

The method used to simulate freeze-thaw cycles is quite realistic in terms of the duration of the freezing and thawing periods. However, it can also be considered as an aggressive method since specimens are fully submerged in chloride solution during the 56 cycles of testing, which is an uncommon situation for real structures, especially for pavements. This may explain the deterioration in the wet mixes (which was designed to resist to freeze-thaw attack) and the high level of degradation in the RCC specimens.

During freezing of a fully submerged concrete, water in the concrete pores freezes and expands. In wet mixes, an easy escape outlet for the expanding volume is the space occupied by the air-entraining bubbles (Section 3.1.3). However, because concrete is fully submerged during the thawing phase, the air-entraining bubbles cannot release the water absorbed during the freezing of the concrete, leading to a cumulatively increasing amount of water in the bubbles. This causes the saturation of the bubbles and consequent damage of the concrete due to repetitive freeze-thaw cycles.

The process of freeze-thaw in RCC is different from that in wet mix concrete. This is because the bubbles in RCC are prone to get filled with water even before exposure to freeze-thaw cycles, due to the easy saturation of the concrete. From the first freezing cycle, water in the concrete pores (which are usually coarser than the air-entraining bubbles) tends to expand and, because there are no outlets as in the case of wet concrete, leads to tension in the concrete. Larger pores tend to cause higher tension because of the higher volume of water. This explains the higher level of deterioration in the RCC mixes compared to the wet mixes.

RCC mixes with 6% recycled fibres seem to have better resistance to freeze-thaw cycles than the corresponding plain and 2I mixes. This may be because fibres help resist the tension caused by the expanding forces during freezing. They may also contribute to maintain the integrity of the material by the cracking bridging effect. Because the degradation in wet mixes is low and very superficial (leading to low tensile stresses), fibres are not as important in these mixes.

6R wet mixes show higher deterioration than the other wet mixes. This is mainly caused by the lower amount of air content (Section 5.5.3), associated with the higher density and lower porosity of the mixes (see Figure 184). The low air content is an indication of lower amount of air-entraining bubbles, which reduces the performance of the concrete subjected to freeze-thaw cycles. The air content of W-LEC-6R is below the value required by BS 8500-1 (2006e), which emphasises the need of a specific amount of air content[44] to guarantee a good freeze-thaw resistance.

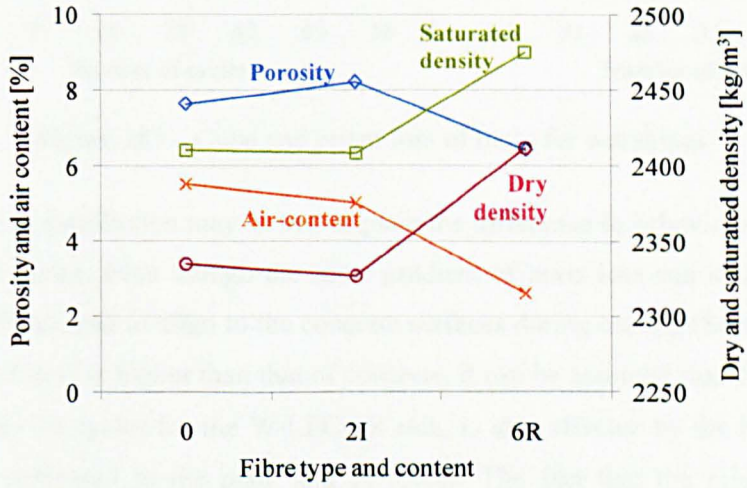

Figure 184 – Comparison among porosity, air content and dry and saturated density results of W-LEC-0, W-LEC-2I and W-LEC-6R mixes.

8.2 LOSS OF MASS

The results of scaled material are analysed for cubes and prisms separately. The loss of mass results of cubes is presented as the percentage of scaled material of the average of three cubes per mix. This is because all three cubes per mix were placed in a single container, which makes impossible to separate the scaled material of each cube. Since prisms were placed in separate containers, each prism (two in total per mix) has its each own percentage of scaled material, but the results are presented for the average of the two.

[44] As discussed in Chapter 4, the same amount of air content was used for all wet mixes to allow comparison among the mixes.

The loss of mass results for cubes and prisms (for wet mixes) are shown in Figure 185. The results show that plain and 2I mixes show very similar behaviour. W-LEC-6R also shows similar behaviour up to 7 and 14 freeze-thaw cycles, however, after 14 days the amount of scaled material is higher than that for plain and 2I mixes (double for cubes). This may be explained again by the fact that W-LEC-6R mix has a lower amount of air content compared to the corresponding plain and 2I mixes (Figure 184). The air-entraining bubbles seem to have been filled up after 14 cycles, thus leading to the higher values of loss of mass after this period.

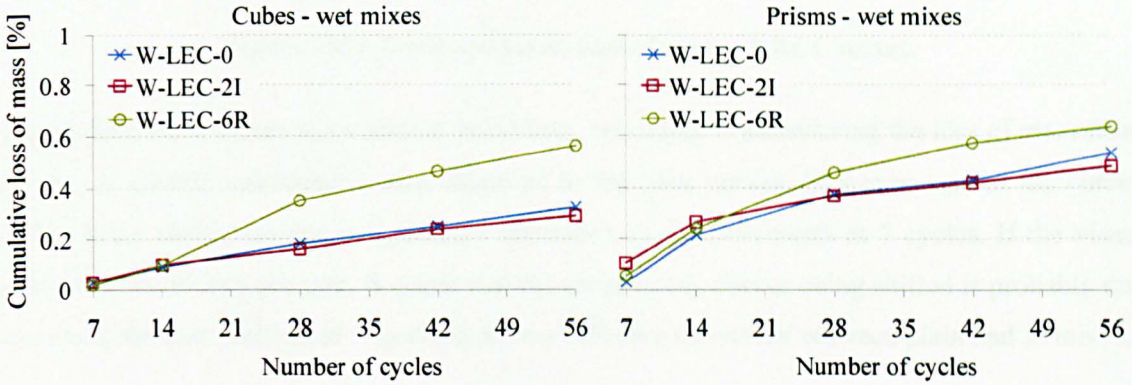

Figure 185 – Cube and prism loss of mass for wet mixes.

Differences in fibre distribution may further explain the difference in behaviour for the W-LEC-6R mix after 14 cycles, even though the same gradient of mass loss can still be observed. If considered that fibres tend to align to the concrete surfaces during casting (Section 2.3.1.3), and that the density of steel is higher than that of concrete, it can be assumed that the increase in the loss of mass, after 28 cycles for the W-LEC-6R mix, is also affected by the higher amount of detached fibres compared to the plain and 2I mixes. The fact that the mixes show similar behaviour up to 14 cycles indicates that up to that moment only the surface concrete paste has scaled, and not the fibres. This analysis is also supported by the visual evidence.

Figure 186 shows that, for the RCC mixes, the R-LEC-6R mix has the best performance compared to plain and 2I mix. It can be seen, especially in the cube results, that the R-LEC-6R curve is initially closer to the other mixes, and that it deviates after 14 days. This seems to be the moment at which fibres start acting in terms of maintaining the integrity of the concrete and resisting to possible tensile stresses originated from freezing of saturated concrete. Before that, the loss of mass seems to be mainly due to scaling of the most outer part of the specimen surface.

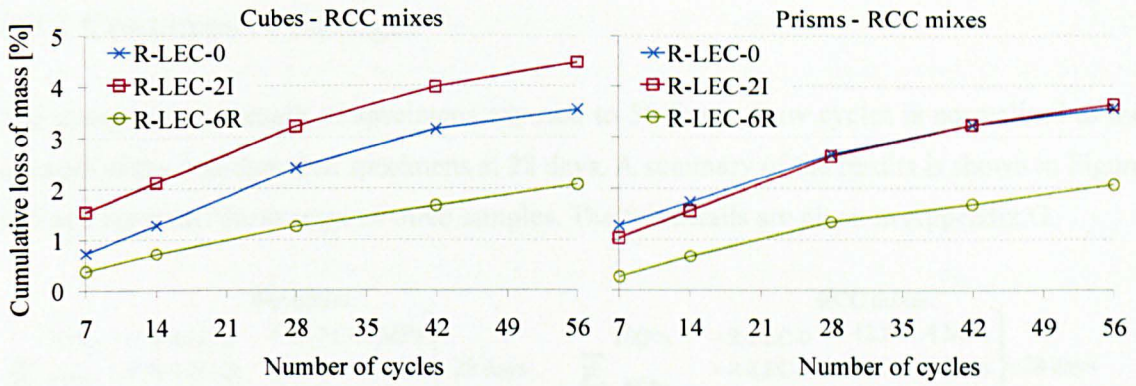

Figure 186 – Cube and prism loss of mass for RCC mixes.

2I and plain RCC mixes show similar behaviour, especially if considering the loss of mass from prisms. A similar behaviour is also observed in the cube curves. However, one of the curves seems to be shifted up due a significant difference of measurements at 7 cycles. If the visual analysis is taken into account, it seems that the cause of the curves being shifted is probably due to a measurement problem at 7 cycles than to a different behaviour between plain and 2I mixes.

As also observed during the visual analysis, the loss of mass of RCC is much higher (approximately 10 times) than taht of wet mixes.

The amount of scaled material seems to stabilise after 42 cycles, following a less accentuated slope of deterioration as the number of cycles increases. This may be due to the fact that concrete located in the outer parts is more susceptible to get deteriorated than concrete in the inner parts due to the boundary conditions that lead to a more porous concrete in those areas. This is especially highlighted for RCC, and also partially explains the larger amount of scaled material for this type of concrete.

The effects of the loss of mass due to scaling in the service life of concrete exposed to freezing and thawing are explained in Chapter 10. A method to predict the service life design for freeze-thaw exposed structures is also described in detail in that chapter.

8.3 MECHANICAL PROPERTIES

The effect of freeze-thaw cycles on the mechanical properties of concrete was evaluated in terms of compressive strength and flexural behaviour, as shown below.

8.3.1 Compressive Strength

The compressive strength of specimens exposed to 56 freeze-thaw cycles is normalised to the strength of the non-damaged specimens at 28 days. A summary of the results is shown in Figure 187 and represent the average of three samples. The full details are given in Appendix G.

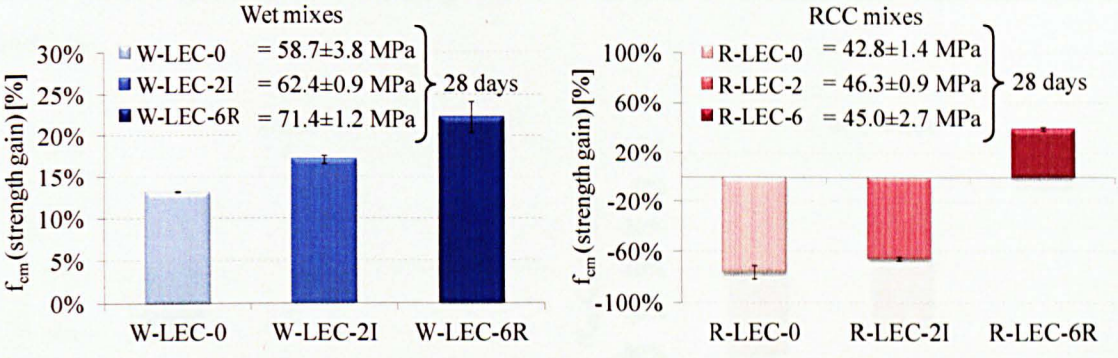

Figure 187 – Compressive strength after 56 freeze-thaw cycles.

Wet mixes exposed to freeze-thaw cycles increase in compressive strength at the end of the exposure period. Usually this increase in the compressive strength is associated to the ageing effect of the concrete. The influence of ageing in the results is discussed later.

Plain and 2I RCC mixes demonstrate a drastic reduction in compressive strength after 56 freeze-thaw cycles (approximately 75% less for plain and 65% less for 2I mix). These mixes were the ones presenting the highest level of deterioration visually and in terms of loss of mass. The drastic reduction of compressive strength indicates that the deterioration caused by freeze-thaw cycles affects not only the external appearance of the concrete, but also the internal structure of the concrete.

Mix R-LEC-6R presents higher compressive strength than the control specimen. It has already been observed in the previous subsections (visual and loss of mass analyses) that RCC reinforced with 6% recycled fibres seem to have improved resistance against freeze-thaw compared to plain and 2I mixes. It seems that the fact that fibres prevent the splitting of concrete during freeze-thaw cycles helps to maintain the internal structure and thus the resistance of concrete to compressive stresses.

The fact that this effect does not occur for the 2I mixes can be explained by the larger number of recycled fibres compared to the number of industrially produced fibres, which makes the 6R mixes more efficient in controlling micro-cracks that develop due to the stresses of water freezing in the pores.

Since the freeze-thaw exposed specimens do not have the same age as the control specimens, the compressive strength of non-damaged specimens after 28 days of curing plus 56 freeze-thaw cycles was predicted following the methods described in Section 7.2.1 (BS EN 1992-1-1, 2004b and CEB-FIP Model Code, 1993). This time-dependent strength is used to normalise the results (by subtracting the effect of ageing) and the gain in strength over what is exceeded from ageing is shown in Figure 188. The same parameters adopted in Section 7.2.1 were used for this analysis.

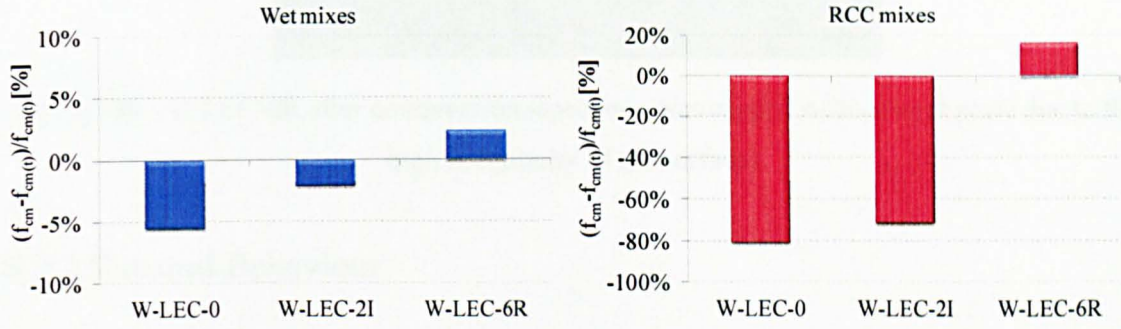

Figure 188 – Comparison between predicted and real compressive strength after freeze-thaw cycles.

It can be seen that the real and predicted results for wet mixes (Figure 188a) are close to each other. However, as discussed in Section 7.2.1, the equation that accounts for ageing is only valid for conventional concrete and commonly used types of cement, which does not apply for LEC mixes. It is also observed in that section that, if the concrete is not deteriorated, experimental values for LEC mixes are considerably higher than the predicted ones, which should also occur for wet mixes, in this case, if the effects of freeze-thaw were not affecting the compressive strength. This suggests that there seems to be a slight reduction in compressive strength for wet mixes due to freeze-thaw. Mix W-LEC-6R has the better behaviour compared to plain and 2I mixes.

The RCC graph (Figure 188b) shows that the difference between the predicted and the freeze-thaw results, for plain and 2I mixes, increased if compared to the difference between the 28 days and the freeze-thaw results. Mix R-LEC-6R, however, presents higher real compressive strength than the predicted one, which is an indication that freeze-thaw cycles do not affect the compressive behaviour of that mix when exposed to freeze-thaw cycles. This is also in line with the results shown in Section 7.2.1. The expansion caused by freezing appears to be mobilising the strength of the recycled fibres and that in turn works as concrete confining stress, which is known to increase compressive strength. The failure mode of the RCC specimens was also more ductile than the failure of the other specimens, as shown in Figure 189.

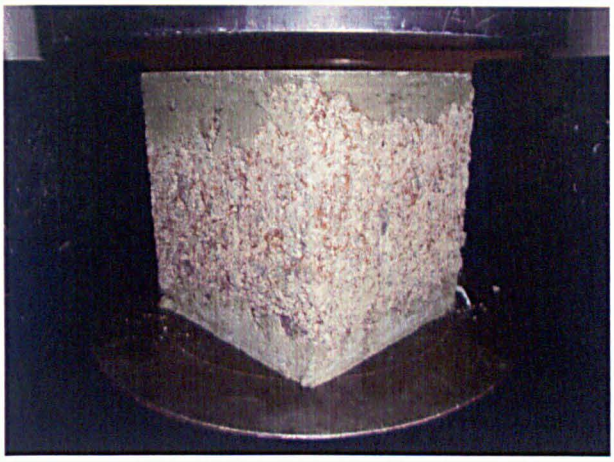

Figure 189 – R-LEC-6R after compression (specimen was capped with cement paste due to the high irregularity of the surface).

8.3.2 Flexural Behaviour

The flexural behaviour of freeze-thaw exposed concrete was studied as for corrosion analysis in terms of: E, f_{LOP}, f_{ult}, $f_{R,i}$, f_{eq3} and $R_{e,3}$. The full table of results and the flexural curves can be found in Appendix C. Two specimens were tested per mix, and for this reason each point in the graphs represents the result of a single specimen. The results obtained from the damaged specimens were compared to the control specimens at 28 days.

8.3.2.1 Modulus of elasticity

Results of E are shown in Figure 190. The results for wet mixes show that there is a slightly increase in the values of E for W-LEC-0 and W-LEC-2I mixes compared to the control specimens. However, it is important to add that, if ageing is taken into account, the values of E for freeze-thaw exposed specimens should be lower than the results shown in the graph, indicating some degradation caused by freeze-thaw. This agrees with the results of compressive strength shown previously.

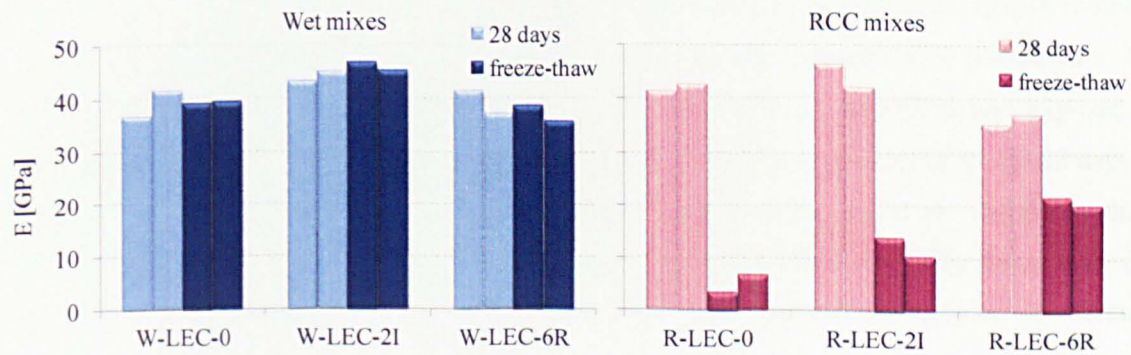

Figure 190 – E after 56 freeze-thaw cycles.

It can also be seen in the W-LEC-6R mix results that there is a small tendency for the values of control specimens to be higher than the values of the freeze-thaw exposed specimens. This is an indication that freeze-thaw cycles lead to matrix micro-cracks and that it affects the elastic behaviour of the material. Figure 191 shows the initial flexural behaviour of the non-damaged compared with the freeze-exposed specimen, which shows an early non-linear behaviour for freeze-thaw exposed specimens.

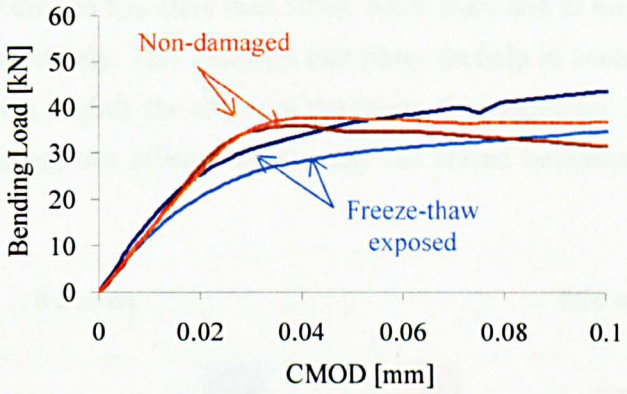

Figure 191 – Initial flexural behaviour for mix W-LEC-6R.

The E results for RCC mixes (Figure 190b) show that there is a massive reduction in the values of E for all mixes, which is especially highlighted for the plain and 2I mixes. The loss of E is extremely severe which indicates that the concrete internally is substantially cracked as many micro-cracks have developed. Except from an expected non-linear initial behaviour as the one observed in previous figure, the low flexural strength of the RCC freeze-thaw exposed specimens gives also an indication of the low values of E. Given the high porosity of RCC specimens, freezing water appears to be cracking the concrete to a considerable depth. The fibres do help in controlling the cracks (since the reduction of E is lower for 2I and 6R) but the concrete is behaving as essentially being cracked.

8.3.2.2 Flexural strength at the limit of proportionality

Figure 192a shows the f_{LOP} results for wet mixes, estimated according to Che's (2010) method. There is a slight increase of f_{LOP} for the plain concrete exposed to freeze-thaw compared to the control specimen, which is probably due to ageing. However, 2I and 6R mixes exposed to freeze-thaw have lower f_{LOP} than the control specimens. There is a tendency of f_{LOP} at 28 days to increase according to the fibre content and type, which does not occur for the freeze-thaw exposed specimens. This indicates that, even though the deterioration caused by freeze-thaw did not alter the compressive strength of concrete, their elastic behaviour seems to be affected,

indicating some internal damage. This was also explained previously for the modulus of elasticity results.

Figure 192b shows that there is a considerable reduction of f_{LOP} for RCC mixes. Plain and 2I specimens present the highest drops of f_{LOP}, which is in accordance with the visual and compressive strength analysis, and also agrees with the modulus of elasticity results. There seems to be an increase in f_{LOP} after exposure to freeze-thaw due to fibre type and content. 6R mix shows the lowest drop in f_{LOP} (less than 50%), while plain and 2I mixes dropped their f_{LOP} by 85% and 65%, respectively. This indicates that fibres do help in controlling the opening of the cracks, thus reducing slightly the effects of the freeze-thaw exposure. However, because the matrix is already cracked, this affects considerably the elastic behaviour of the concrete (in terms of E and f_{LOP}).

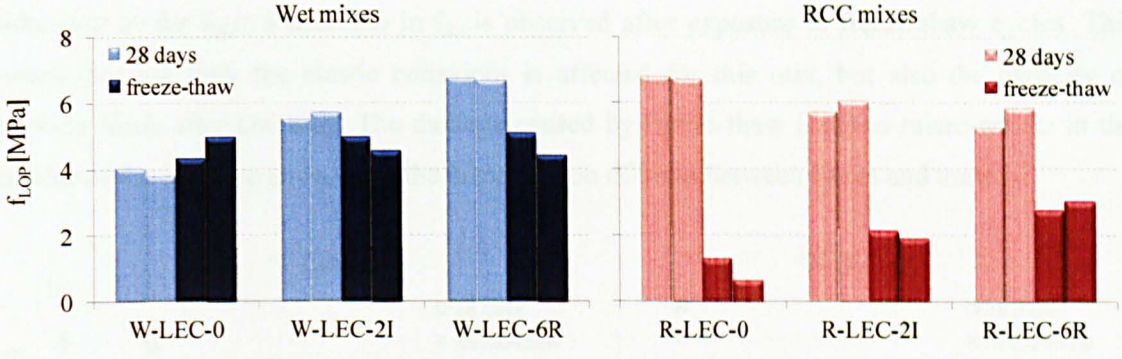

Figure 192 – f_{LOP} after 56 freeze-thaw cycles.

8.3.2.3 Ultimate flexural strength

Figure 193a shows that there seems to be a slight increase of f_{ult} compared to the control specimens in the plain and 6R mixes, and a not so clear effect in the 2I mix. Freeze-thaw degradation does not seem to reduce the peak flexural load capacity of wet mixes.

The results of f_{ult} for RCC mixes are shown in Figure 193b. A similar behaviour as for f_{LOP} can be observed; there is a considerable drop of f_{ult} of freeze-thaw exposed specimens compared to control specimens, and a better resistance according to the amount and type of fibre used (6R mix shows the highest resistance, even though f_{ult} is slightly lower, compared to the control specimens). These results indicate that the freeze-thaw deterioration in RCC do not only affect the elastic behaviour but also the peak load capacity of the concrete.

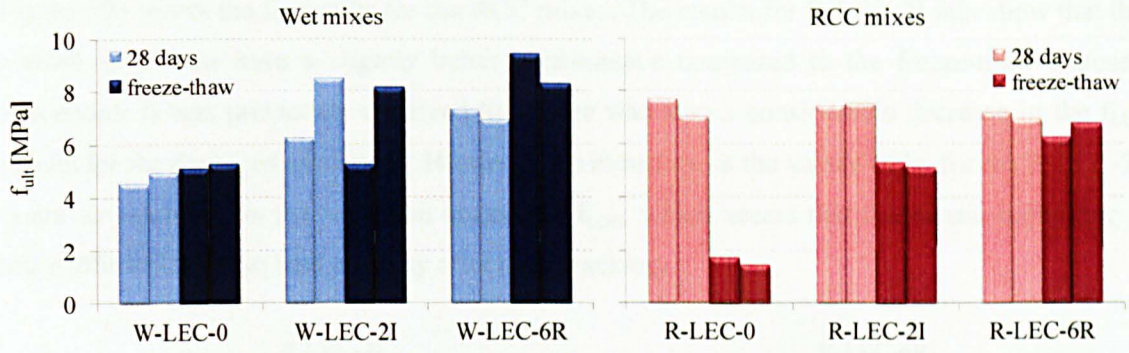

Figure 193 – f_{ult} after 56 freeze-thaw cycles.

8.3.2.4 Residual flexural strength

The $f_{R,i}$ results for wet mixes are shown in Figure 194. W-LEC-2I mix shows a similar behaviour as for f_{LOP}: a decrease in $f_{R,i}$ is observed after exposure to freeze-thaw cycles. This means that not only the elastic behaviour is affected for this mix, but also the capacity of carrying loads after cracking. The damage caused by freeze-thaw leads to micro-cracks in the interior of the concrete and also to the deterioration of bond between fibres and matrix.

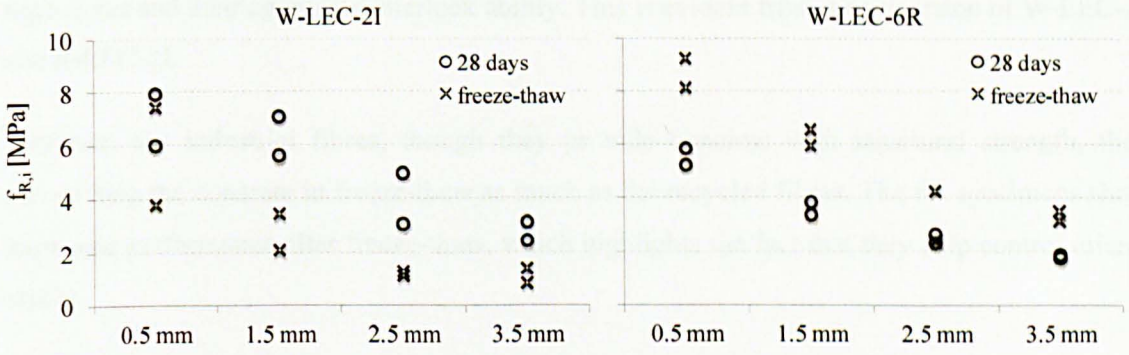

Figure 194 – $f_{R,i}$ after 56 freeze-thaw cycles for wet mixes.

W-LEC-6R mix, on the other hand, presents better performance in terms of $f_{R,i}$ compared to the control specimens. This indicates that only the elastic behaviour is affected by the freeze-thaw cycles for this mix. In this case, it seems that the freeze-thaw damage occurred mainly in the most outer part of the specimens, affecting the matrix of that localised region (with consequences in the elastic behaviour). The freeze-thaw damage did not extend to the interior of the specimens because the fibres resisted the tensile stresses caused by freezing and thawing action and prevented the opening of cracks. As a consequence, bond between fibres and the matrix was not as affected as for the W-LEC-2I mix. In fact, its performance improved with time, and this can only be attributed to concrete ageing.

Figure 195 shows the $f_{R,i}$ results for the RCC mixes. The results for R-LEC-2I mix show that the control specimens have a slightly better performance compared to the freeze-thaw exposed specimens. It was previously observed that there was also a considerable decrease in the f_{LOP} results for the damaged specimens. However, the reduction in the values of $f_{R,i}$ for the R-LEC-2I is not as extensive as the reduction noticed in f_{LOP}, which seems that the elastic behaviour is more affected than the load capacity after post-cracking.

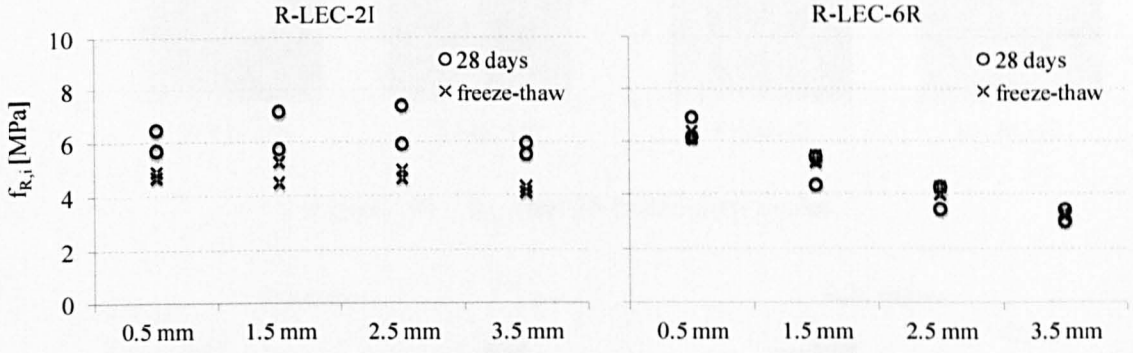

Figure 195 – $f_{R,i}$ after 56 freeze-thaw cycles for RCC mixes.

Part of this enhanced ability to resist loads post-cracking may be attributed to the RCC aggregates and their aggregate interlock ability. This is evident from a comparison of W-LEC-2I and R-LEC-2I.

However, the industrial fibres, though they provide concrete with structural strength, they cannot help the concrete in freeze-thaw as much as the recycled fibres. The 6R specimens show improved performance after freeze-thaw, which highlights the fact that they help control micro-cracks.

8.3.2.5 Equivalent flexural strength and equivalent flexural ratio

The f_{eq3} results are shown in Figure 196. All the mixes show similar behaviour as the ones observed for the $f_{R,i}$ results.

The $R_{e,3}$ results for wet mixes (Figure 197a) show similar behaviour as the results of $f_{R,i}$ and f_{eq3}.

The results for RCC mixes (Figure 197b) show that there is an increase of $R_{e,3}$ for both mixes compared to the control specimens. If the bending load *versus* mid-span deflection curves are taken into account (Appendix C), it can be observed that, even though the elastic behaviour and the load capacity are clearly affected (especially if considering the R-LEC-2I mix), there is a significant capacity of the specimens to maintain the load after cracking. It is important to note, however, that the exceptionally high values of $R_{e,3}$ are mainly influenced by the low f_{LOP} ($R_{e,3}$ is

the relation of f_{eq3} to f_{LOP}). Hence, in this case, the $R_{e,3}$ values higher than 1 are not only an indication of hardening, but an indication of low f_{LOP}.

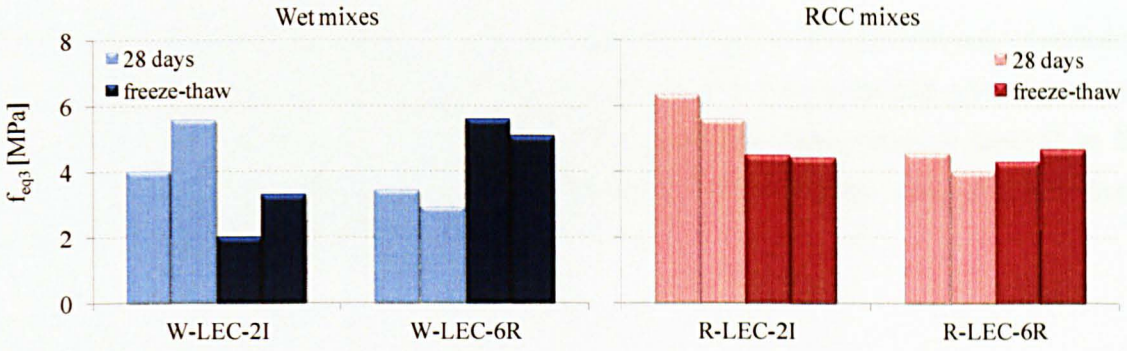

Figure 196 – f_{eq3} after 56 freeze-thaw cycles.

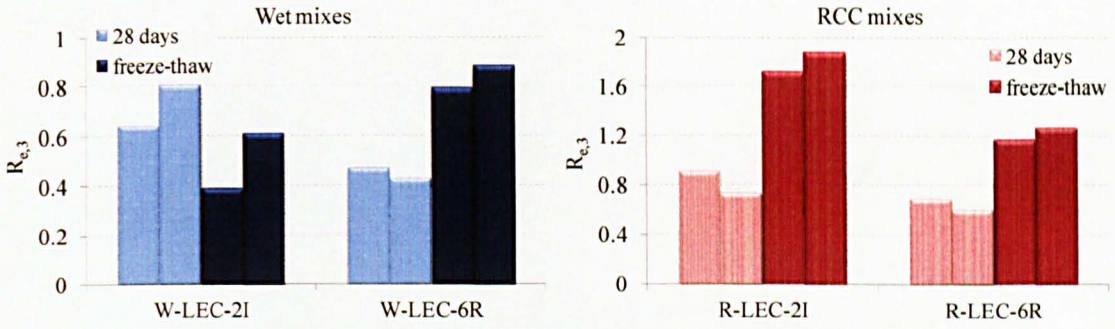

Figure 197 – $R_{e,3}$ after 56 freeze-thaw cycles.

Since the $R_{e,3}$ values are considerably high for the RCC mixes (due to the low f_{LOP}), *pseudo* $R_{e,3}$ values were calculated based on the ratio of f_{eq3} to f_{ult} instead of f_{eq3} to f_{LOP}, as shown in the figure below. The values of *pseudo* $R_{e,3}$ obtained after freeze-thaw simulation are more realistic (smaller) compared to the values shown in the above figure. The values of pseudo $R_{e,3}$ for freeze-thaw exposed specimens are slightly higher than the control specimens. This is mainly because f_{ult} is still lower for damaged specimens than for control specimens.

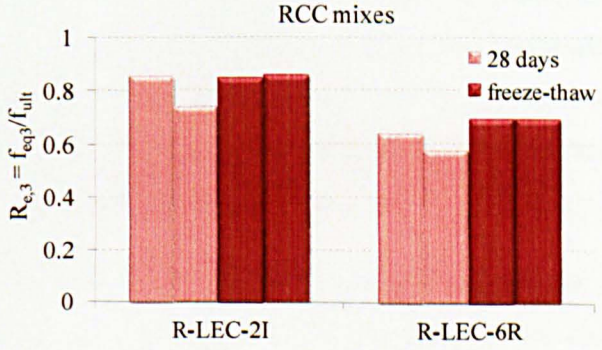

Figure 198 – $R_{e,3} = f_{eq3}/f_{ult}$ for RCC mixes after 56 freeze-thaw cycles.

8.4 INFLUENCE OF TRANSPORT MECHANISMS, POROSITY AND DENSITY ON THE FREEZE-THAW RESISTANCE

The influence of the transport mechanisms, porosity and density on the performance of concrete when exposed to freeze-thaw attack is evaluated in this section. The properties are compared to the residual normalised f_{cm}, f_{LOP} and f_{ult} (ratio of strength after freeze-thaw to strength at 28 days). The results for density, porosity, permeability and sorptivity were obtained from specimens preconditioned at 80 °C.

8.4.1 Density

The comparison of the residual normalised strength (f_{cm}, f_{LOP} and f_{ult}) with dry density is shown in Figure 199.

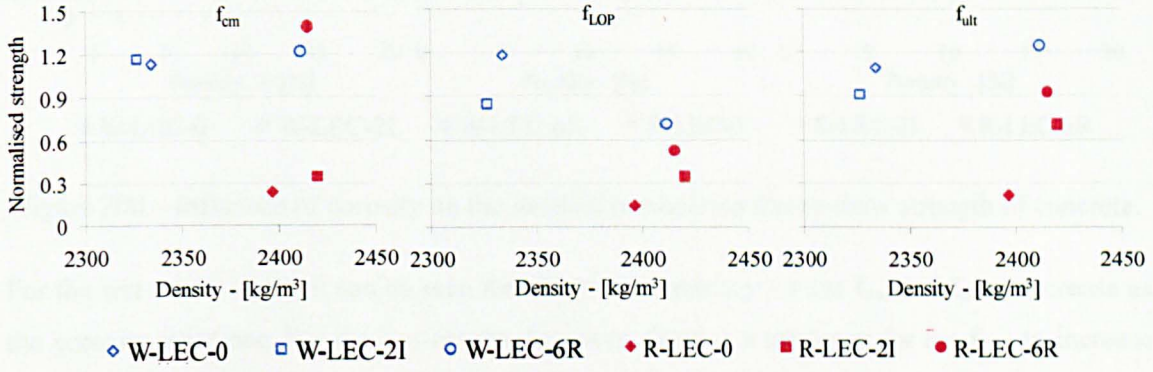

Figure 199 – Influence of density on the residual normalised freeze-thaw strength of concrete.

It can be seen that RCC and wet mixes have different behaviours. For the wet mixes, there is a slight tendency for the normalised f_{cm} and f_{ult} to increase as density increases. The f_{LOP} results for wet mixes, however, show that there is a reduction in the normalised strength as density increases. This tendency is mainly affected by the W-LEC-6R mix, which has higher density and lower strength than the other wet mixes. This mix, as previously discussed, has lower amount of air-entraining bubbles, which leads to freeze-thaw deterioration of the outer parts of the concrete, thus affecting the elastic behaviour. f_{cm} and f_{ult} are not as affected as f_{LOP} because, as already reported, recycled fibres of W-LEC-6R mixes resist the tensile stresses caused by freeze-thaw thus reducing freeze-thaw internal damage.

The RCC results show a certain tendency for the strength to increase as density increases, but the density values are too close to each other to allow for a clear conclusion. This was also observed in Chapter 5. Overall, density by itself does not appear to have a clear influence on the freeze-thaw behaviour.

8.4.2 Porosity

The comparison of porosity with normalised strength is shown in Figure 200. As previously observed in the density results, RCC and wet mixes show two different behaviours: RCC mixes have considerably higher porosity than wet mixes (around double) and lowest strength. Despite the higher amount of pores, it is also important to note that RCC mixes do not have air-entraining bubbles, and that they also have a higher amount of trapped air, which is considerably larger than other types of pores, and leads to a more severe deterioration than for wet mixes.

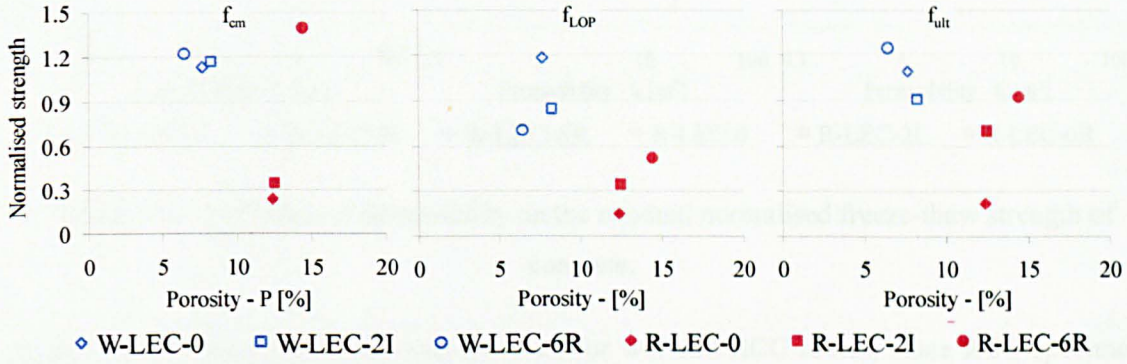

Figure 200 – Influence of porosity on the residual normalised freeze-thaw strength of concrete.

For the wet mixes alone, it can be seen that there is a tendency for the f_{cm} and f_{ult} to decrease as the porosity increases. For the f_{LOP} results, however, there is a tendency for the f_{LOP} to increase as porosity increases. Similar behaviour was observed when density was compared to normalised strength. The trend for f_{LOP} is again mainly influenced by the W-LEC-6R mix, which has lower air-entraining bubbles (low porosity), which is more susceptible to freeze-thaw damage. Overall, though the trends are not so strong, it can be said that porosity does affect freeze-thaw of wet mixes and reducing it should improve performance.

It is clear that the pore structure of RCC mixes plays an important role in the residual strength of the concrete, especially when compared to wet mixes. However, when the RCC results alone are taken into account, it can be seen that there is a tendency for the strength to increase as porosity increases. Therefore, it seems that fibres are also playing an important role in the residual strength. Even though 2I and 6R mixes have higher porosity, they show the highest strength among the RCC mixes results. This agrees with Sun *et al.* (2002), which says that steel fibres contribute in reducing the effects of freeze-thaw damage. Hence, for the RCC mixes it can be concluded that porosity should be reduced to prevent damage, but the recycled steel fibres are very effective in controlling the damage of the concrete.

8.4.3 Permeability

The comparison of permeability with residual normalised strength is shown in Figure 201. Only two results are presented for RCC mixes since no permeability results were obtained from R-LEC-6R mix due to the extremely high permeability of the mix.

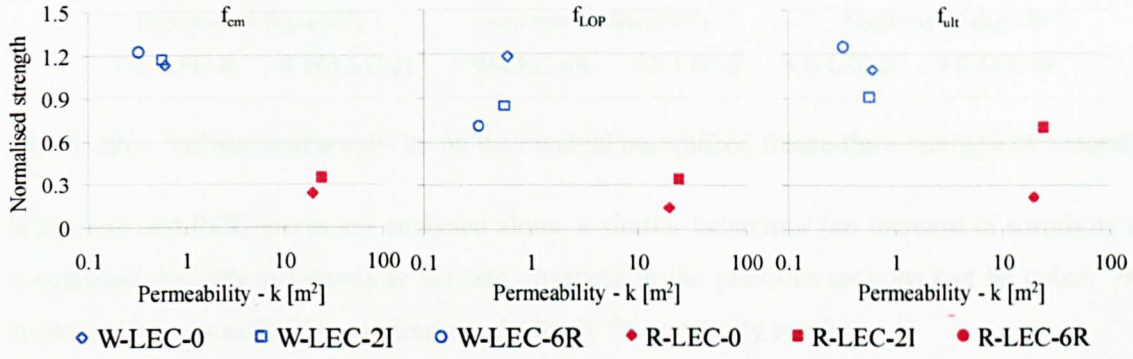

Figure 201 – Influence of permeability on the residual normalised freeze-thaw strength of concrete.

Again, two different behaviours are observed for wet and RCC mixes, since RCC specimens have a much higher permeability and much lower strength than wet mixes. This clearly shows that the freeze-thaw resistance is dependent on the permeability of the mixes.

When the wet mixes are considered alone, it can be seen a very similar behaviour as observed for density and porosity: residual f_{cm} and f_{ult} reduces as permeability increases and residual f_{LOP} increases as permeability increases. Similar conclusions as for porosity apply for permeability results.

The RCC results alone show an increase in all strengths as permeability increases, following similar behaviour as for porosity, which is mainly caused by fibre action rather than by small differences in permeability.

8.4.4 Sorptivity

The sorptivity results are compared to residual normalised strength in Figure 202. It is clear that sorptivity influences the mechanical performance of concrete exposed to freeze-thaw, especially when considering that two different groups were formed: one for RCC with higher sorptivity and lower strength and another for wet mixes with higher strength and lower sorptivity.

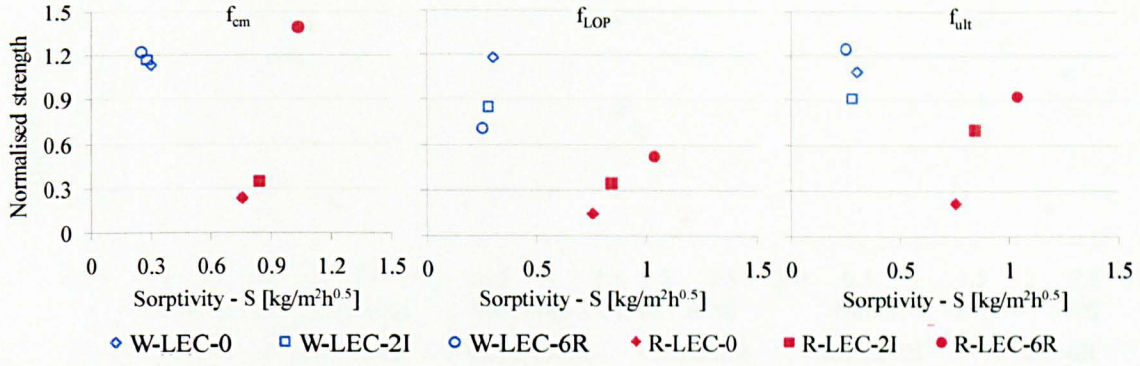

Figure 202 – Influence of sorptivity on the residual normalised freeze-thaw strength of concrete.

When wet and RCC mixes are analysed alone, a similar behaviour (an increase in sorptivity as normalised strength increases) as the one observed in the previous sections can be noted. The same conclusions as for the previous results apply for sorptivity results.

8.4.5 Diffusivity

The diffusivity results are compared to the residual normalised strength in Figure 203. Again, the results aggregate in two different groups: one formed by wet mixes (with the highest values of strength) and another formed by RCC mixes (with the lowest values of strength). However, contrary to what was observed in the previous results, diffusivity does not seem to influence the mechanical resistance of concrete exposed to freeze-thaw cycles, since wet and RCC mixes show results of diffusivity within the same range of values.

The use of chloride solution to immerse specimens for freeze-thaw cycles accelerates the freeze-thaw process by reducing the freezing point of the solution (Sun *et al.*, 2002) and by increasing the osmotic pressure of the concrete, since moisture moves towards zones with higher salt concentration (PCA, 2010c). Therefore, it is not the transport of chloride ions that influences the freeze-thaw behaviour, but the transport of solution into the concrete. The transport of solution, however, is not influenced by diffusivity, but by the sorptivity and permeability of the concrete. This explains the lack of correlation between diffusivity and residual strength.

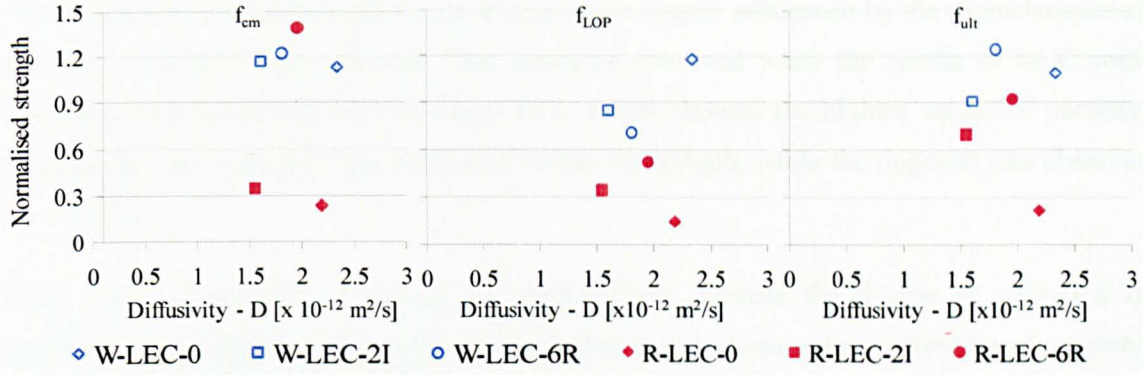

Figure 203 – Influence of diffusivity on the residual normalised freeze-thaw strength of concrete.

8.5 SUMMARY AND CONCLUSIONS

The effects caused by frost-induced damage were investigated by exposing specimens to accelerated cycles of freezing and thawing.

The visual analysis shows that RCC specimens have more signs of freeze-thaw damage than wet mixes, possibly due to the higher porosity, no air-entrained bubbles and higher amount of trapped air (large size of pores) from compaction. Scaling and pop-outs were the types of damage observed during the visual analysis.

The loss of mass results show that RCC specimens have at least 5 times more damage (loss of mass) than the wet mixes, which agrees with the results of the visual analysis. Plain and 2I mixes, for both wet and RCC, have similar freeze-thaw behaviour. RCC specimens with 6% recycled fibres show lower loss of mass compared to other RCC specimens. This is because the high amount of fibres keeps the integrity of the concrete by restraining the stresses caused by freezing of the pore solution. 6R wet mixes have slightly higher loss of mass than the other wet mixes, which is possibly caused by the lower amount of air-entrainment agent.

The compressive strength of wet and 6R RCC mixes increased after accelerated freeze-thaw, while plain and 2I RCC mixes show a considerable reduction in strength. The flexural behaviour shows that the 2I wet mix is affected by freeze-thaw in both elastic and post-cracking behaviour while the 6R wet mix is affected only in the elastic behaviour. RCC mixes are affected in both elastic and post-cracking behaviour, but the damage caused in the flexural behaviour of 6R RCC is much less than the 2I mix. The results from the mechanical properties are in line with the visual and the loss of mass results.

The mechanical freeze-thaw resistance of concrete is clearly influenced by the characteristics of the pore structure of the material. This could be observed when the results of RCC were compared with the results of wet mixes. RCC mixes showed the highest values of porosity, permeability and sorptivity and the lowest values of strength, while the opposite was observed for wet mixes.

High values of porosity, sorptivity and permeability increase the degree of saturation of specimens during freeze-thaw cycles, which lead to higher stresses during freezing of concrete, accelerating the damage and reducing strength. Although the pore structure plays an important role in the freeze-thaw resistance, the addition of fibres also improves the freeze-thaw resistance of the concrete.

As a main conclusion, it is clear that RCC mixes are more affected by accelerated freeze-thaw than wet mixes. The fact that RCC mixes have higher porosity, permeability and sorptivity and also higher size of pores contributes for these results. Therefore, the use of fully-saturated conditions to accelerate freeze-thaw in RCC may not be an adequate method for such mixes. A more appropriate method would be the slab test method proposed by BS DD 12390-9 (2006c). Furthermore, it is evident that the RCC boundaries are extremely porous which clearly influences how the moisture penetrates into the concrete. In practical applications, the RCC will only have one rough surface exposed to moisture and most fibres will actually be oriented along the plane of that surface. This would make the RCC more resistant to moisture penetration and freeze-thaw action. Further investigations should be carried out to examine different methods of accelerating freeze-thaw in RCC as well as the effect of boundaries and fibre orientation. For the latter, an idea is to core specimens from large scale RCC slabs.

The inclusion of 2I fibres, for both wet and RCC, improves slightly the performance of the concrete when subjected to freeze-thaw. On the other hand, the addition of 6R fibres seems to maintain the integrity of the concrete and collaborate to restrain stresses caused by freeze-thaw in a more effective way. It is clear that the number of fibres found in the concrete play an important role in controlling damage produced by the expansion forces of freezing. The higher number of smaller fibres appears to give better results.

The following chapter deals with the last of the deterioration processes studied in this thesis, based on the application of cyclic loads in concrete. As for chloride ingress and freeze-thaw, a probabilistic analysis is also considered when investigating fatigue of concrete.

CHAPTER 9

9. FATIGUE RESISTANCE OF SFRC

This chapter deals with the results obtained from the investigation of the fatigue performance of SFRC. The effect of cyclic loads is evaluated by using two approaches: 1) number of cycles up to failure, based on the stress ratio *versus* number of loading cycles and 2) vertical displacement analysis. Finally, some recommendations for the design of SFRC pavements are discussed.

9.1 CONTROL TESTS – STATIC FLEXURAL AND COMPRESSIVE STRENGTH

Static flexural strength results obtained at 28 days are shown in Section 5.2; these are based on tests carried out at USFD. However, as already reported in Section 4.4.9, the static flexural strength was also obtained at UFRGS, where the specimens were tested against fatigue. The tests carried out at UFRGS were based on the following procedures.

1) Load was applied using the same load configuration shown in Figure 64.
2) Yokes and LVDTs were not used since, for the purpose of calculating the fatigue stresses, only the load was required.
3) Load was applied following the displacement rate of 0.02 mm/min, based on the machine plate displacement.
4) Tests were halted when the peak load was achieved and no post-peak behaviour was recorded.

The graphs of static bending load *versus* machine displacement can be found in Appendix J. The peak loads are shown in Table 26. Two specimens were tested per mix. The age of specimens varied according to the mix, however, they were all tested at least 120 days after casting. The static flexural strength was obtained at UFRGS, for each mix, prior to the dynamic test, to calculate the fatigue loads according to each stress level.

Table 26 – Peak load obtained from static flexural tests carried out at UFRGS and USFD.

Mix	Peak load per specimen – UFRGS [kN]		Average peak load – UFRGS – un-notched [kN]	Age – UFRGS [days]	Average peak load – USFD – 28 days – notched [kN]	Flexural strength gain – reference to 28 days tests at USFD
W-CIP-0	68.3	68.1	68.2	300	23.1	2.05
W-CIP-2R	48.5	52.2	50.4	240	25.7	1.36
W-CIP-6R	81.7	73.5	77.6	240	38.4	1.33
R-CIP-0	61.6	65.8	63.7	180	31.4	1.56
R-CIP-2I	92.5	69.0	80.8	150	53.6	1.12
R-CIP-2R	69.6	65.4	67.5	150	29.7	1.79
R-CIP-6R	79.9	76.8	78.4	120	37.6	1.57

Compressive strength tests were carried out at UFRGS on the same day as the static flexural test (specimens were at least 56 days). The cube compressive strength for the mixes tested against fatigue is shown in Table 27, based on the average of 6 specimens per mix. The compressive strength test was performed for control purposes only, aiming to verify if the target cube strength of 55 MPa (Section 4.2) was achieved.

Table 27 – Compressive strength obtained from tests carried out at UFRGS.

Mix	Compressive strength [MPa]	Standard Deviation [MPa]
W-CIP-0	67.9	5.0
W-CIP-2R	77.0	0.2
W-CIP-6R	76.7	1.9
R-CIP-0	69.7	6.9
R-CIP-2I	74.1	4.2
R-CIP-2R	75.8	3.0
R-CIP-6R	76.8	3.0

All mixes reached the target compressive strength of 55 MPa. It is important to note, however, that the specimens were older than the 28 days required by the BS 8500-1 (2006e) to achieve the target strength of 55 MPa.

It can be observed that mixes with fibre addition show higher compressive strength than the corresponding plain concrete.

9.2 *s – log(N)* CURVES

The flexural fatigue tests were undertaken considering three different stress levels: 0.5, 0.7 and 0.9 (four stress levels for mix R-CIP-6R: 0.5, 0.6, 0.7 and 0.8). The fatigue load for each stress level and for each mix was calculated based on the results shown in Table 26. The applied fatigue loads are presented in Table 28. Ten per cent of the fatigue load was continuously applied to the specimens (the remaining 90% were dynamic loads).

Table 28 – Fatigue loads for each stress level and mix.

Mix	Stress level	Fatigue load [kN]	Mix	Stress level	Fatigue load [kN]
W-CIP-0	0.5	34.1	R-CIP-0	0.5	31.9
	0.7	47.7		0.7	44.6
	0.9	61.4		0.9	57.3
W-CIP-2R	0.5	25.2	R-CIP-2I	0.5	40.4
	0.7	35.3		0.7	56.6
	0.9	45.4		0.9	72.7
W-CIP-6R	0.5	38.8	R-CIP-2R	0.5	33.8
	0.7	54.3		0.7	47.3
	0.9	69.8		0.9	60.8
			R-CIP-6R	0.5	39.2
				0.6	47.0
				0.7	54.9
				0.8	62.7

Specimens were subjected to the fatigue loads shown in the above table until failure or 2 million cycles[45] (whichever came first). The number of cycles *N* until failure was recorded (when specimens failed) or considered as 2 million for the specimens that did not fail. For each mix, the values of log(N) were plotted against the stress level *s*. log(N) was used instead of N to comply with the common procedures usually found in the literature (Ramakrishnan *et al.*, 1989; Singh and Kaushik, 2001 and 2003; Lee and Barr, 2004; Singh *et al.*, 2005a and 2008).

As reported in Section 3.1.1, a considerable variability in the results is expected, mainly because the specimens tested against fatigue were not the same as the ones tested to obtain the flexural strength, and also because of the random distribution of the fibres (for fibre reinforced mixes).

[45] 2 million cycles is assumed as the endurance life for concrete subjected to fatigue (Section 3.1.1).

9.2.1 Wet Mixes

The *s – log(N)* curves obtained from the wet mixes are shown in Figures 204 and 205. The number of cycles until failure for each stress level is shown in Appendix J. Two specimens failed prior to the dynamic tests due to user error in preparing the specimen for the test: one specimen from mix W-CIP-2R at the stress level of 0.5 and one specimen from mix W-CIP-6R at the stress level of 0.7. Two specimens, from all mixes, were used to obtain the static flexural strength. For this reason, only 4 specimens per mix were used at the stress level of 0.9.

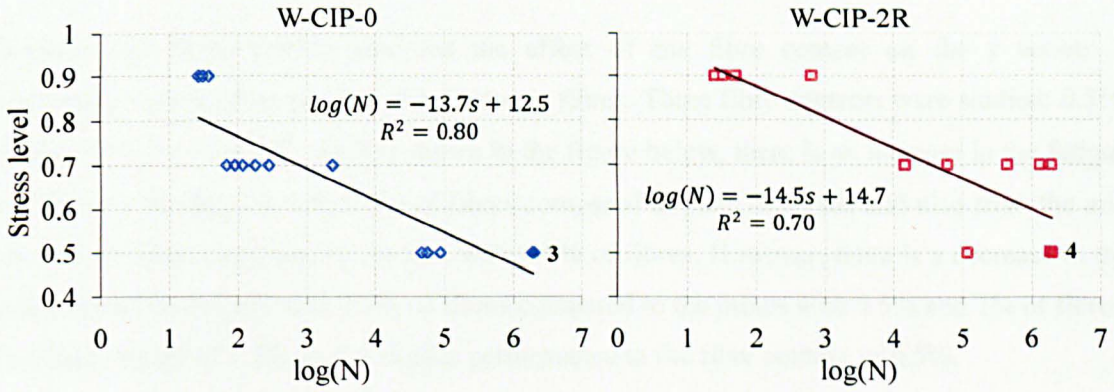

Figure 204 – s *versus* log(N) for a) mix W-CIP-0 and b) mix W-CIP-2R.

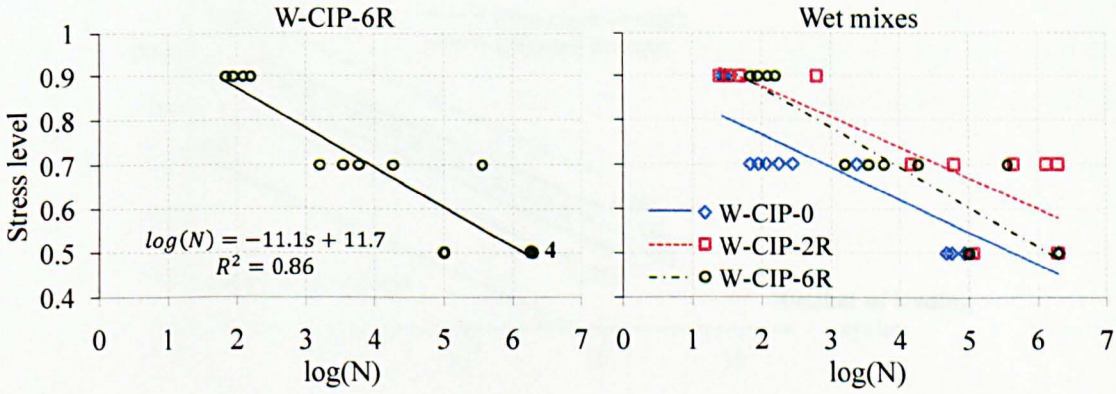

Figure 205 – s *versus* log(N) for a) mix W-CIP-6R and b) comparison of all wet mixes.

W-CIP-0 has the lowest performance (lowest number of cycles until failure) for stress levels ranging from 0.5 to 0.9. This is expected since unreinforced wet mixes do not have a good performance in controlling micro and macro cracks caused by fatigue loads.

The addition of fibres seems to extend the fatigue life of the concrete. However, even though the addition of 6% recycled fibres (W-CIP-6R) presents better performance than the plain concrete, it can be seen that there is a reduction in the fatigue performance compared to the mix with lower amount of fibres (W-LEC-2R). Therefore, it seems that there is an ideal fibre content that

gives the better response in terms of fatigue life. This is in line with results found in the literature, as detailed below.

Singh and Kaushik (2001) studied the fatigue performance of three volume contents of corrugated steel fibres (0.5%, 1% and 1.5%)[46]. They found out that 0.5% and 1% show similar fatigue behaviour while 1.5% shows the lowest fatigue resistance. Lee and Barr (2004) gathered information on the fatigue resistance of SFRC from various authors. They found out that the fibre contents of 0.5% and 1% (by volume) show very similar behaviour between them (not much improvement from 0.5% to 1%).

Johnston and Zemp (1991) analysed the effect of the fibre content on the *s versus N* relationships considering the use of cold-drawn fibres. Three fibre contents were studied: 0.5%, 1% and 1.5% by volume[46]. As it is shown in the figure below, there is an increase in the fatigue performance for the mix with 0.5% of fibres compared to plain concrete, and also from the mix with 1% of fibres compared to the mix with 0.5% of fibres. However, there is a decrease in the performance for the mix with 1.5% of fibres compared to the mixes with 0.5% and 1% of fibres. The fibre content of 1.5% shows similar performance to the fibre content of 0.5%.

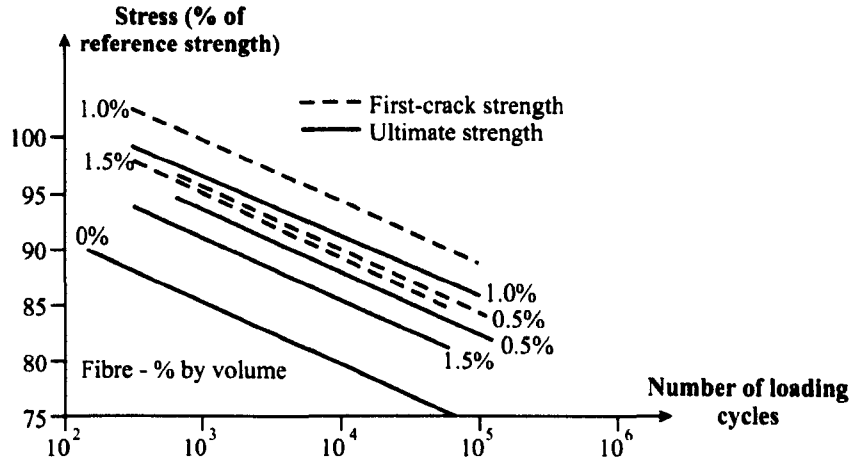

Figure 206 – Effect of fibre content on the s *versus* N relationship [after Johnston and Zemp, 1991].

This does not mean that fibre contents higher than the ideal content cannot be used. The fatigue performance should be considered alongside other properties (mechanical and pore structure-related properties) to provide the most viable, economic and sustainable solution.

[46] Approximately 1.7%, 3.3% and 5% by mass of concrete.

9.2.2 RCC Mixes

The results for the RCC mixes are shown in Figure 207 to Figure 209. One specimen from mix R-CIP-0, which should have been tested at the stress level of 0.7, failed before starting the cyclic tests due to a mistake in preparing the specimen (load applied too fast) for dynamic loads. Mix R-CIP-2I only had 3 specimens tested at the stress levels of 0.5 and 0.9, and four specimens tested at the stress level of 0.7.

Fatigue performance of mix R-CIP-6R was tested at the stress levels of 0.5, 0.6, 0.7 and 0.8. Six specimens were tested at the stress level of 0.5, and since none of these specimens failed (no cracks and no signs of deterioration), five of the non-failed specimens were used to perform the test at the stress level of 0.6 and the remaining non-failed specimen was used to perform the test at the stress level of 0.8 (together with other 4 untested specimens). As a summary, for mix R-CIP-6R, six specimens were tested at the stress levels of 0.5 and 0.7 and five specimens were tested at the stress levels of 0.6 and 0.8. The use of the stress level of 0.8 instead of 0.9 was because the number of cycles reduced drastically when the stress level increased from 0.5 to 0.7, and there was a concern that the mix would not be able to resist to the stress level of 0.9. The number of cycles shown in the graph for the re-tested specimens corresponds only to the higher stress level.

Mixes R-CIP-0 and R-CIP-2R had only 4 specimens tested at the stress level of 0.9, since two specimens from that stress level were used to perform the static flexural strength test. For all other cases, 6 specimens were tested per mix per stress level.

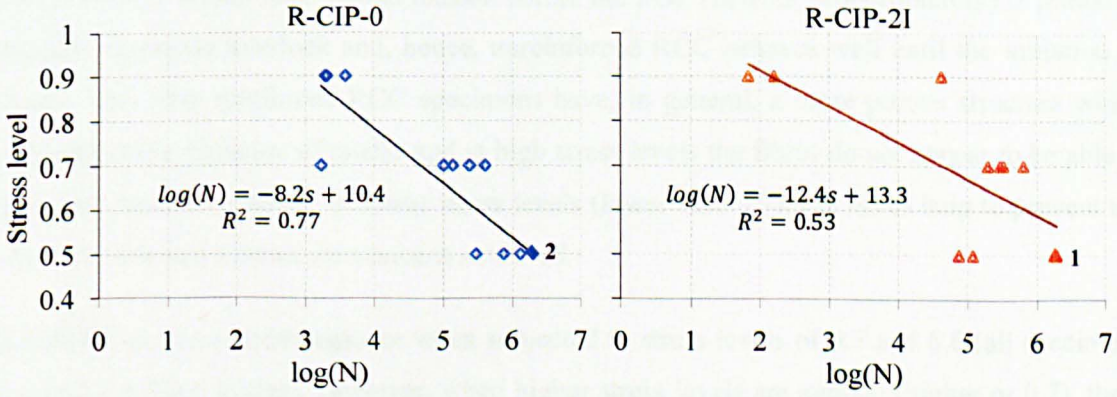

Figure 207 – s *versus* log(N) for a) mix R-CIP-0 and b) mix R-CIP-2I.

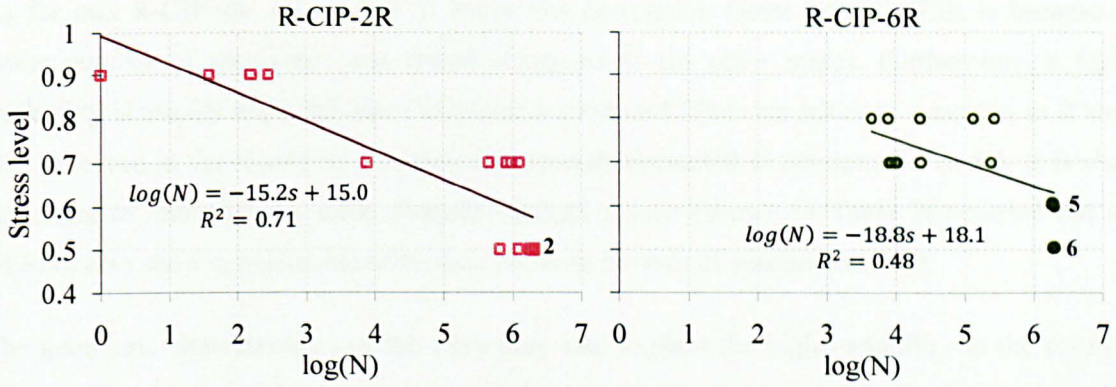

Figure 208 – s *versus* log(N) for a) mix R-CIP-2R and b) mix R-CIP-6R.

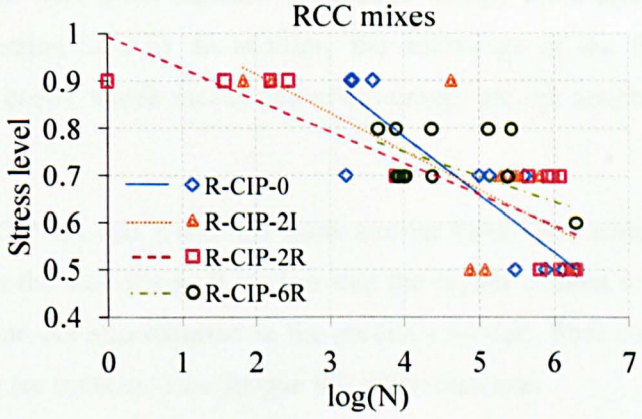

Figure 209 – s *versus* log(N) for comparison of all RCC mixes.

By analysing the graphs above, it can be seen that the plain concrete when subjected to high stress levels (higher than 0.7) shows better performance than the mixes with fibres. This mechanism by which RCC resists tension before the LOP (limit of proportionality) is primarily through aggregate interlock and, hence, unreinforced RCC behaves well until the initiation of cracks. The fibre reinforced RCC specimens have, in general, a more porous structure which encourages the initiation of cracks and at high stress levels the fibres do not appear to be able to arrest the cracks. However, at lower stress levels (lower than 0.7), the fibres help to prevent the crack-growth and a better resistance is achieved.

R-CIP-6R shows a good response when subjected to stress levels of 0.5 and 0.6 (all specimens reached 2 million cycles). However, when higher stress levels are applied (higher or 0.7), there is a change in the behaviour and the fatigue resistance decreases. Recycled fibres, when added at a high content tend to trap more air voids, and when subjected to a high stress level, they seem to lose their bond with concrete. As concluded earlier, they are also not very effective in bridging macro-cracks, which easily appear when concrete is subjected to cyclic high stress levels.

As for mix R-CIP-6R, mix R-CIP-2I has a low correlation factor (=0.53). This is because a lower number of specimens was tested compared to the other mixes. Furthermore, a high variability is usually expected when industrially produced fibres are added to concrete, as it was also observed in the results of mechanical properties presented in Sections 5.1 to 5.3. It is also important to note that the static flexural strength results (shown in Table 26) carried out at UFRGS also show considerable difference between the two 2I specimens tested.

The geometric characteristics of the fibre may also explain the high variability in the results. The longer length and larger diameter of the industrially produced fibres, compared to the recycled fibres, lead to a reduced number of fibres in the mix for the same fibre content. As a consequence, concrete with lower number of fibres is usually more affected by non-uniform fibre-distribution (Section 2.3.1.3). In addition, the anchorage of the fibres is substantially provided by the end cones, which means that micro-cracks are not arrested until they develop into macro-cracks.

Mixes R-CIP-2I, R-CIP-2R and R-CIP-6R show similar behaviour, which is in line with the results obtained from the wet mixes. It is clear that the higher content of fibres in 6R did not improve the behaviour. As also reported in the previous section, fibre content higher than the ideal reduces slightly (or stabilises) the fatigue life of the concrete.

It was observed that the specimens with recycled fibres broke into two halves after failure, as shown in Figure 210 and, thus, had similar failure mode as for plain RCC. It should be noted that the loading machine was applying the specific cyclic load and was programmed to stop when the total displacement exceeded 10 mm. Since only one specimen failed at a time, and the others deformed in general less than 2 mm in total, when the displacement limit was triggered, the weakest specimen was subjected to a deformation of at least 8 mm. Since the recycled fibres are in general short, such a displacement is expected to break the specimen into two. Following inspection of the failed surface, many fibres could be seen sticking out of the concrete, which is an indication that the fibres were pulled out of the matrix.

In the case of the 2I, the specimens did not break into two, but a substantial crack could be seen (see Figure 211). This also confirms that the fibres did not break, but were in the process of being pulled out.

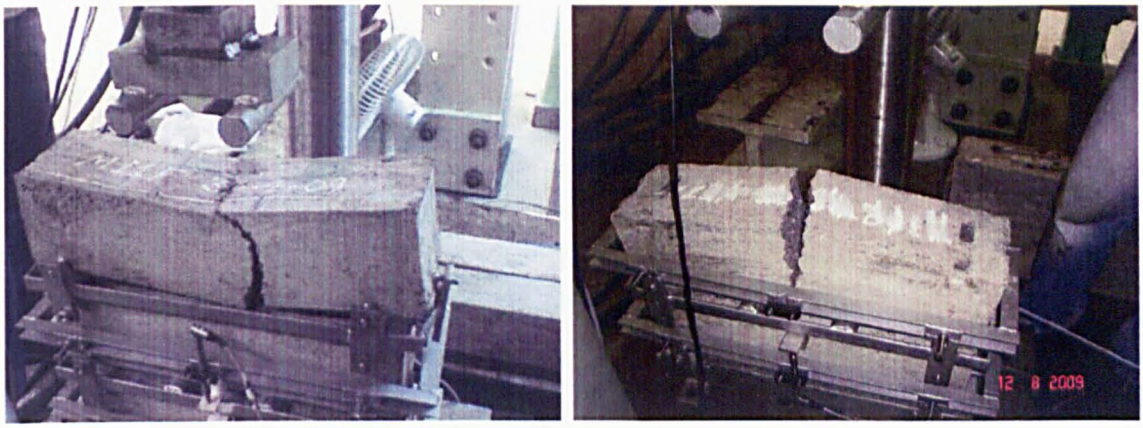

Figure 210 – R-CIP-6R after fatigue failure (stress level of 0.7).

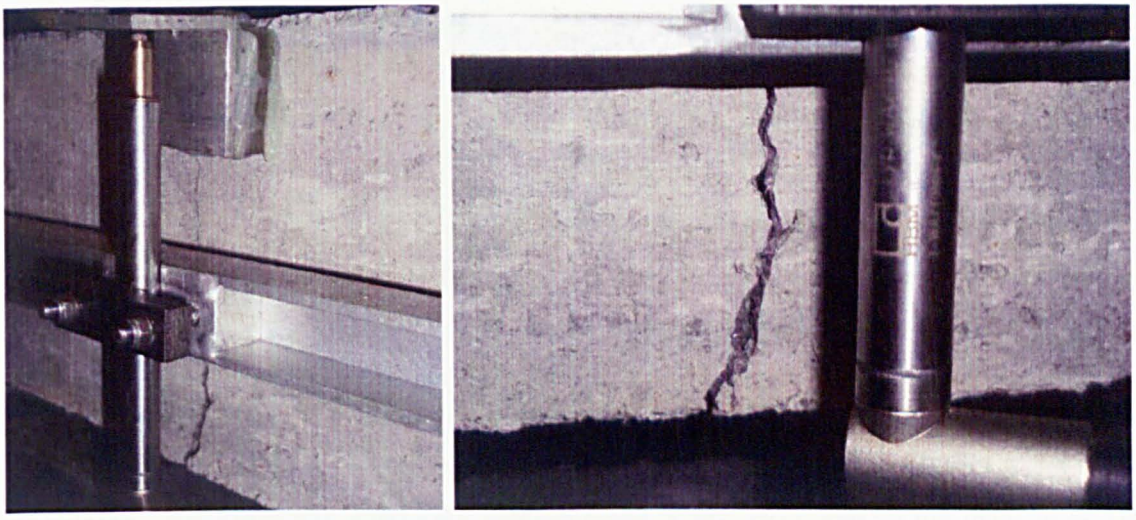

Figure 211 – R-CIP-2I after fatigue failure (stress level of 0.7).

According to Rossi and Parant (2008), the bond between meso-fibres (ranging from 2 to 7 mm in the work carried out by the authors) and the matrix is severely affected when subjected to cyclic loads. Bond deteriorates rapidly for shorter fibres than for longer fibres. This fact may explain the complete loss of bond for recycled fibres after failure. No yielding of the fibres was observed.

9.2.3 Discussion on the RCC and Wet Mixes Results

The results obtained from the wet mixes are compared with the results obtained from the RCC mixes. The equations shown in Figures 204, 205, 207 and 208 were used to calculate the number of cycles at the stress levels of 0.5, 0.7 and 0.9, for each mix. The number of cycles is plotted against the fibre content and type, as shown in Figure 212. Only the plain concrete and the 2R and 6R mixes can be compared directly (2I was only used for the RCC mixes and for this reason cannot be compared with the wet mixes).

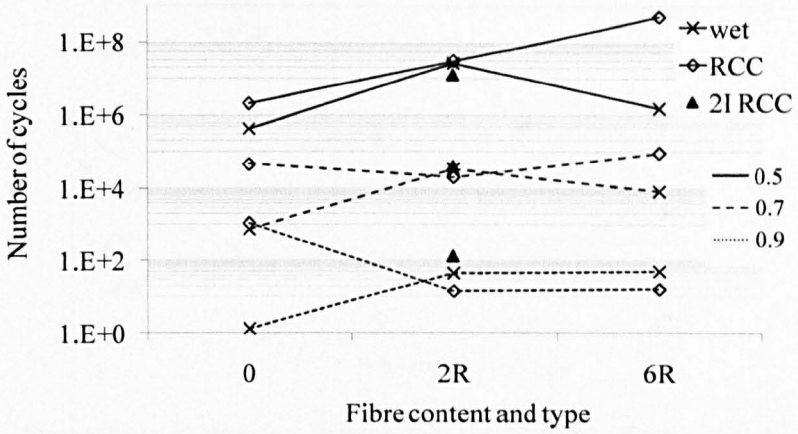

Figure 212 – Comparison between the fatigue life of wet and RCC mixes.

It can be seen that the plain RCC mixes resist higher fatigue loads than the plain wet mixes. This is due to the aggregate interlock effect, which is especially enhanced in the RCC mixes by the use of high quality crushed aggregates and by the high energy applied during compaction. Wet and RCC mixes reinforced with 2% recycled fibres show similar fatigue performance. This is because the cracking control is mostly performed by the fibres and not by aggregate interlock. 6R mixes on average do not enhance the performance beyond that of the 2R mixes. The 2I fibres in general perform better than the 2R fibres, especially at higher stress levels.

Wet mixes show a considerable improvement in the fatigue resistance of the 2R mix compared to the plain mix. The 2R RCC mixes, on the other hand, show similar resistance at the stress level of 0.5 and lower resistance at the stress level of 0.9 compared to the plain mix. The addition of fibres in the RCC mixes seems to slightly contribute to improve the fatigue resistance of the concrete when subjected to the stress level of 0.5. It seems that the addition of fibres tends to negate the effect of aggregate interlock at high stress levels. As mentioned earlier, the addition of fibres in RCC mixes leads to a more porous structure, which increases the amount of initial micro-cracks, thus making crack control more difficult.

The equations shown in Figures 204, 205, 207 and 208 are also used to calculate the endurance limit of the mixes, expressed in terms of maximum stress level at which each mix can be subjected to withstand 2 million cycles. The results are shown in Figure 213. Reinforced RCC mixes and W-CIP-2R present the highest values of stress levels compared to the other mixes. W-CIP-0 has the lowest endurance limit, followed by the W-CIP-6R and, finally, by R-CIP-0. The use of recycled fibres at the content of 2% by mass seems to be a good reinforcement for concrete when subjected to cyclic loads. The recycled fibres appear to perform as well as the industrial fibres at this reinforcement level.

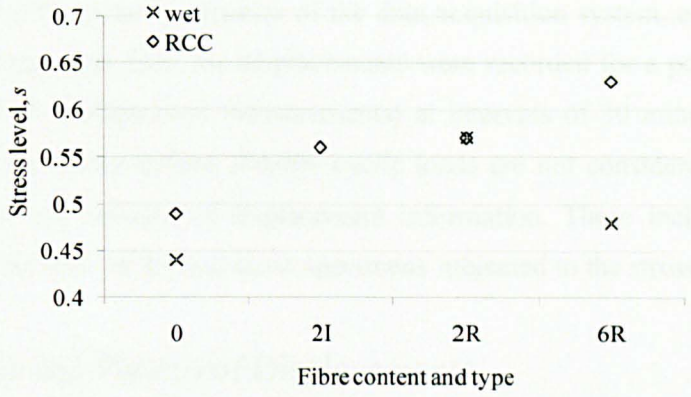

Figure 213 – Endurance limit expressed in terms of stress level.

9.3 VERTICAL DISPLACEMENT ANALYSIS

During fatigue tests, LVDTs were positioned in the mid-span of the prisms to measure the vertical displacement of the specimens during test. Two LVDTs were used per specimen, one on each side. The LVDTs were mounted on to yoke supported at mid-height over each end support.

The LVDTs were connected to a HBM Spider 8® (HBM, 2003) data acquisition system, operated by catman® (HBM, 2010) data acquisition software. The displacement measurements were taken at a frequency of 400 Hz (the frequency of 150Hz was used for specimens R-CIP-6R tested at the stress level of 0.8). This high frequency was used to obtain the points that form the sinusoidal wave pattern of displacements for each cyclic loading. Typical displacement curves are shown in Figure 214 (in general there is an increase in displacement δ as the number of cycles increases).

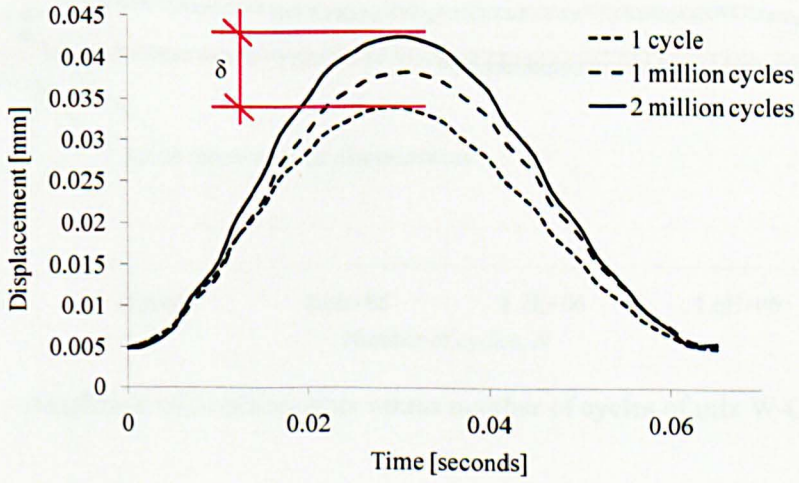

Figure 214 – Typical sinusoidal displacements (mix R-CIP-6R, s = 0.5).

Nevertheless, due to the memory capacity of the data acquisition system, and mainly to avoid getting extremely large data files, the displacements were recorded for a period of 10 seconds (150 cycles and 4000 displacement measurements) at intervals of 30 minutes (27,000 cyclic loads). Specimens that failed before 100,000 cyclic loads are not considered in the following analysis due to the low amount of displacement information. These include the specimens subjected to the stress level of 0.9 and some specimens subjected to the stress level of 0.7.

9.3.1 Amplitude and Pattern of Displacements

The amplitude of the displacements was measured by the average of 150 cycles, at every 27,000 cycles. The only exception is for mix R-CIP-6R subjected to the stress level of 0.8, at which the displacements were measured by the average of 400 cycles, at every 13,500 cycles (or continuously for few specimens). The results obtained are shown in Figure 215 to Figure 228. Different markers in the graphs denote different specimens.

The theoretical static displacements, based on the elastic theory, are also shown in the graphs. The calculation of the static displacements is based on the modulus of elasticity calculated from the control specimens at 28 days. This may lead to some variability in the results since the fatigue specimens were older than the control specimens. It is also important to note that the specimens subjected to high stress levels are loaded beyond their elastic limits. For this reason, the theoretical static displacements shown in the graphs below should be used only as an indication of the static displacement, for comparison purposes with the fatigue displacements.

W-CIP-0

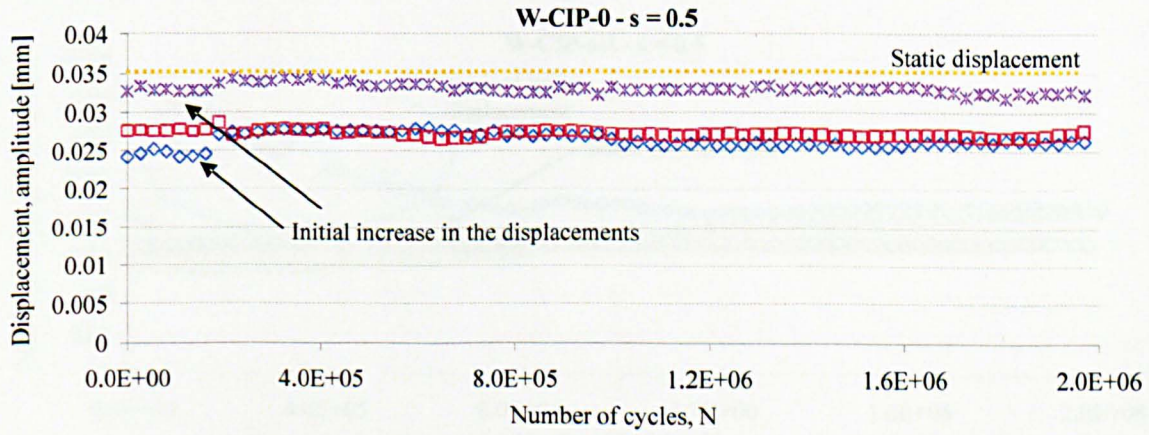

Figure 215 – Amplitude of displacements *versus* number of cycles of mix W-CIP-0, s=0.5.

W-CIP-2R

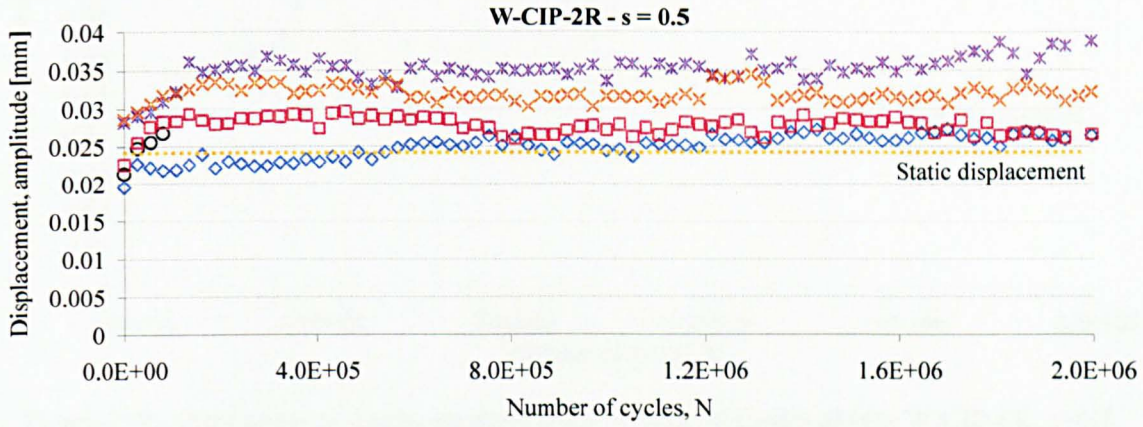

Figure 216 – Amplitude of displacements *versus* number of cycles of mix W-CIP-2R, s=0.5.

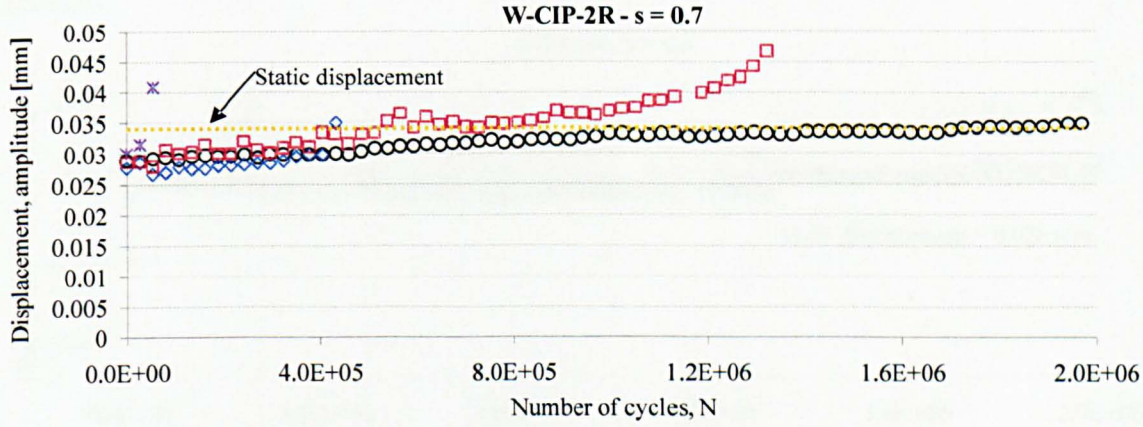

Figure 217 – Amplitude of displacements *versus* number of cycles of mix W-CIP-2R, s=0.7.

W-CIP-6R

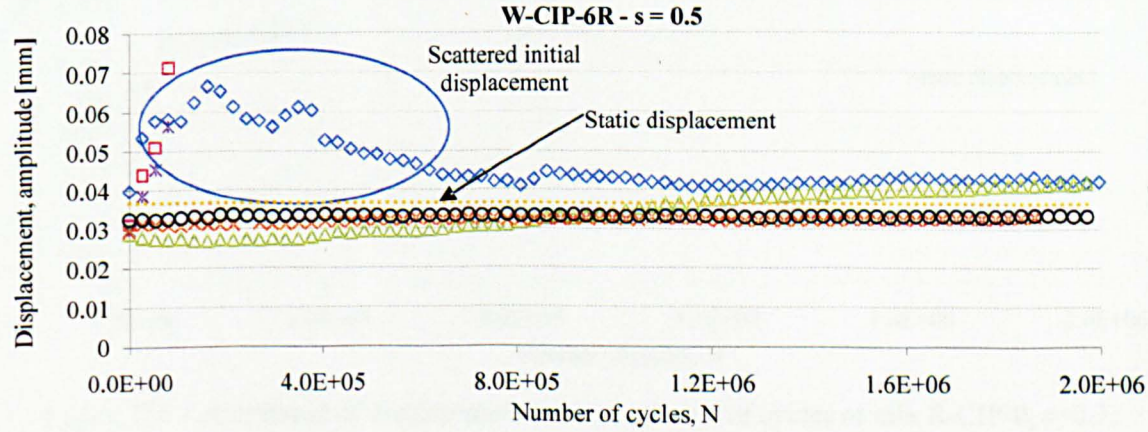

Figure 218 – Amplitude of displacements *versus* number of cycles of mix W-CIP-6R, s=0.5.

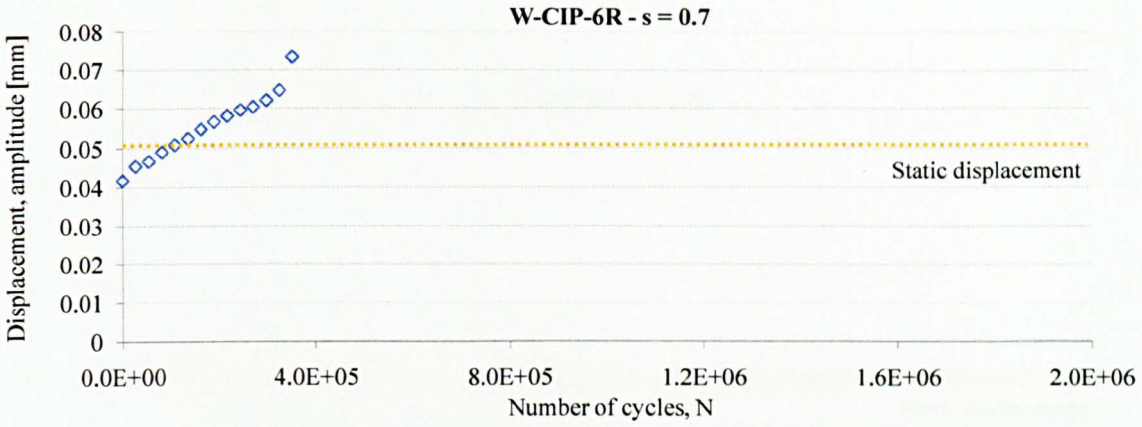

Figure 219 – Amplitude of displacements *versus* number of cycles of mix W-CIP-6R, s=0.7.

R-CIP-0

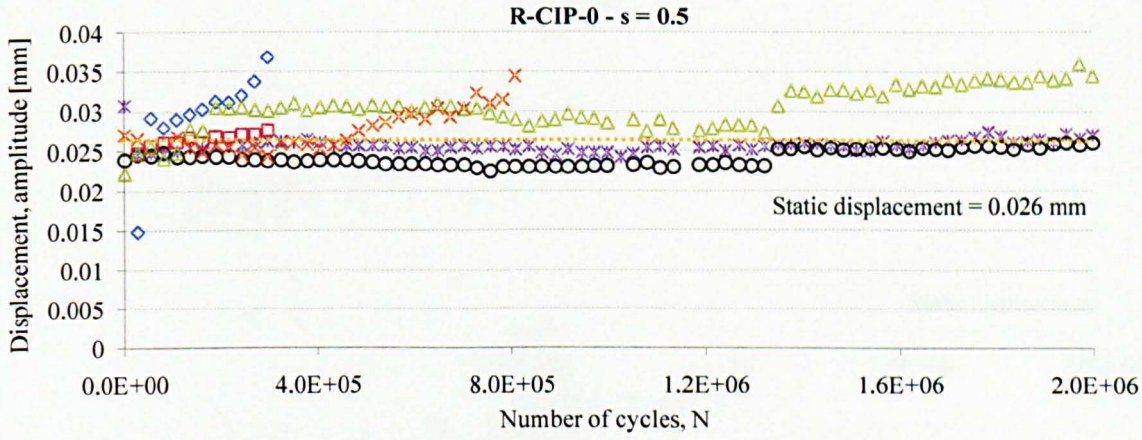

Figure 220 – Amplitude of displacements *versus* number of cycles of mix R-CIP-0, s=0.5.

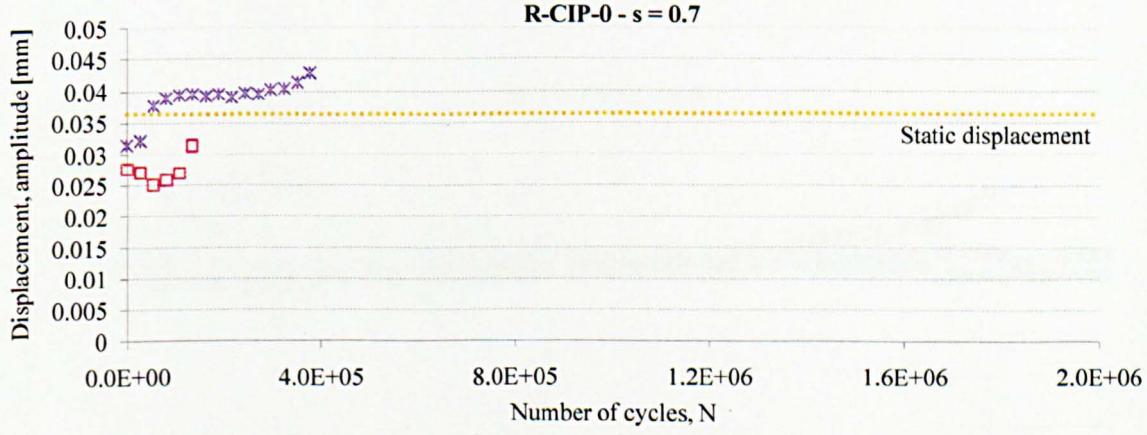

Figure 221 – Amplitude of displacements *versus* number of cycles of mix R-CIP-0, s=0.7.

R-CIP-2I

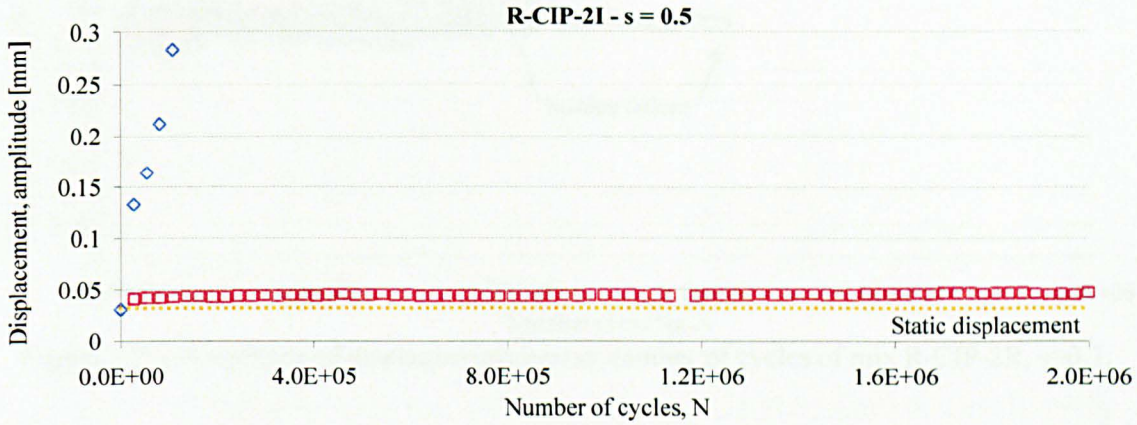

Figure 222 – Amplitude of displacements *versus* number of cycles of mix R-CIP-2I, s=0.5.

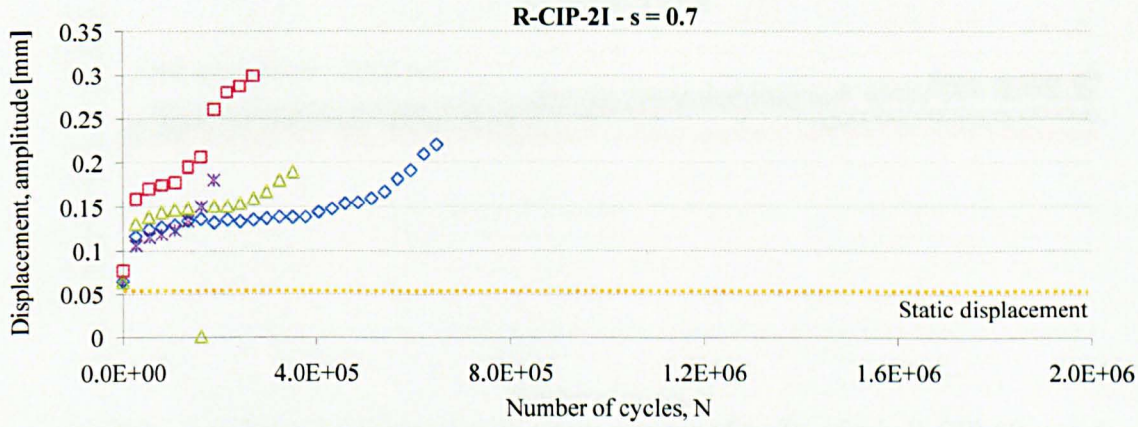

Figure 223 – Amplitude of displacements *versus* number of cycles of mix R-CIP-2I, s=0.7.

R-CIP-2R

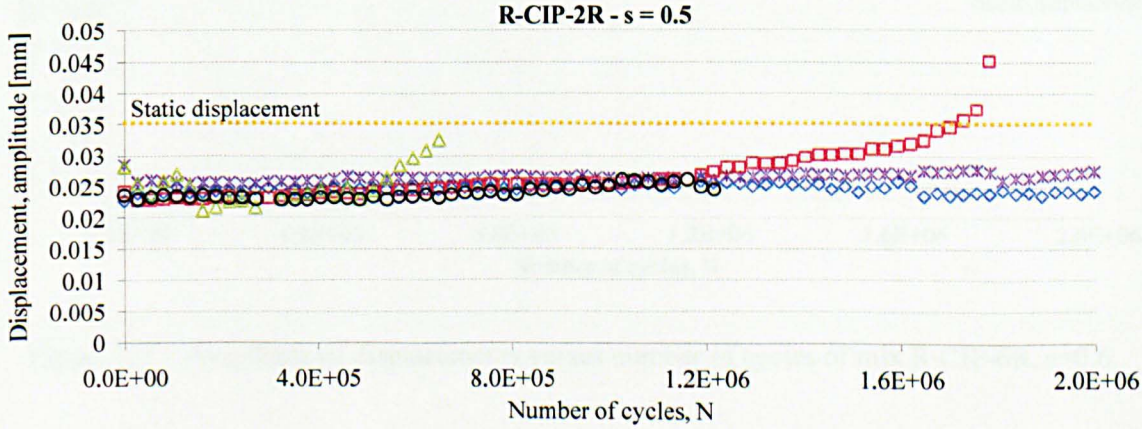

Figure 224 – Amplitude of displacements *versus* number of cycles of mix R-CIP-2R, s=0.5.

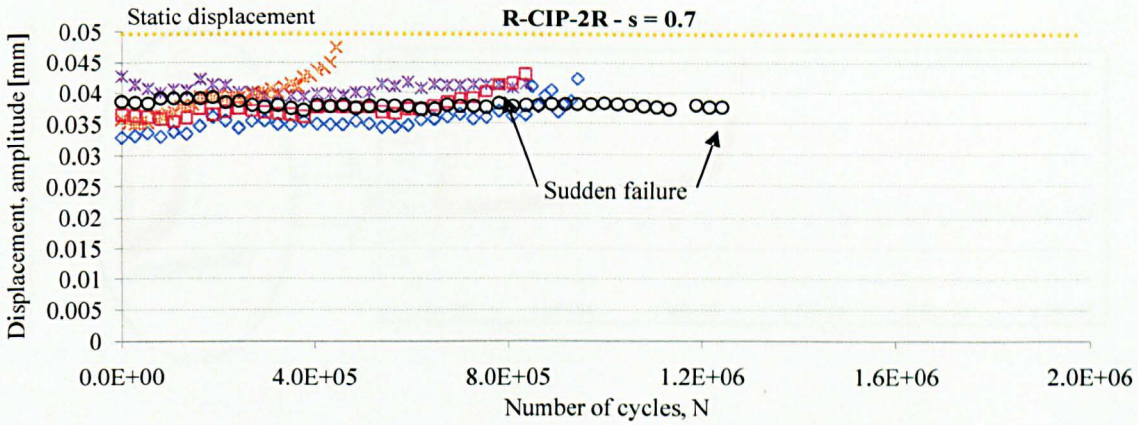

Figure 225 – Amplitude of displacements *versus* number of cycles of mix R-CIP-2R, s=0.7.

R-CIP-6R

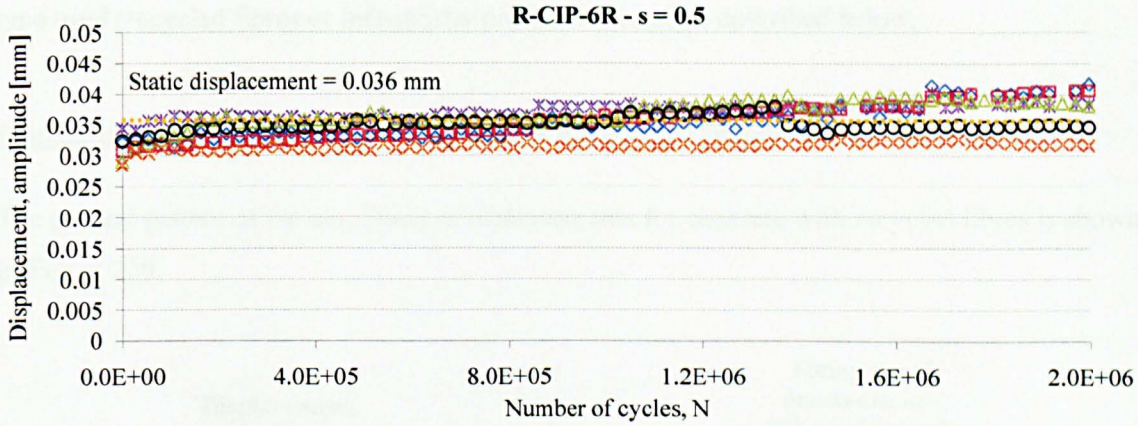

Figure 226 – Amplitude of displacements *versus* number of cycles of mix R-CIP-6R, s=0.5.

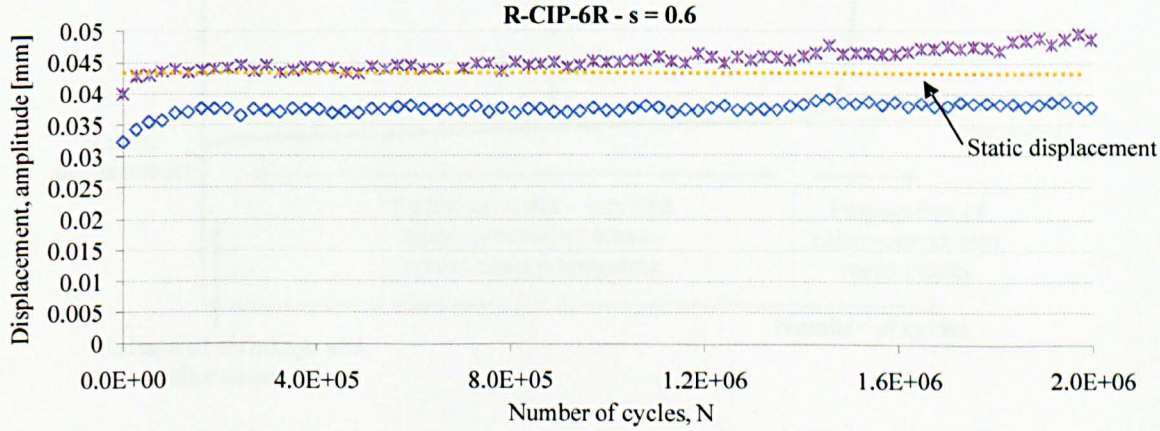

Figure 227 – Amplitude of displacements versus number of cycles of mix R-CIP-6R, s=0.6.

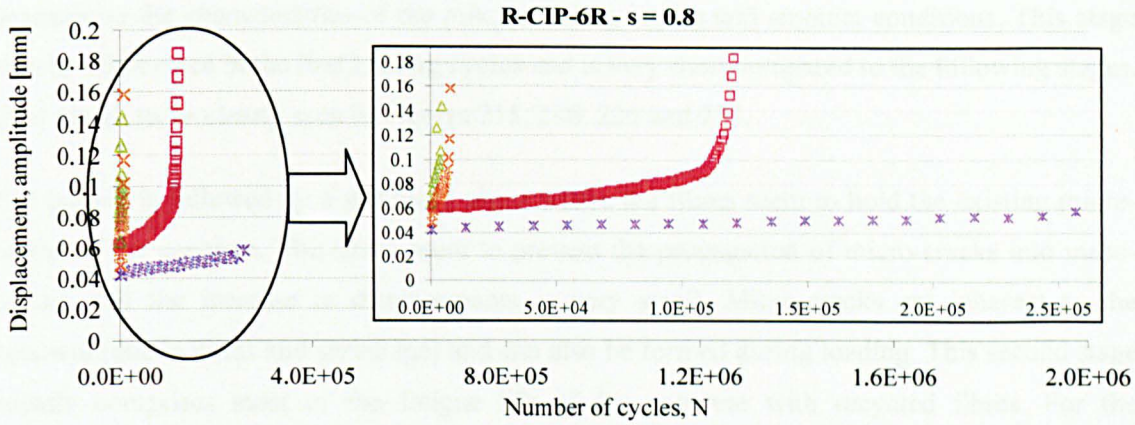

Figure 228 – Amplitude of displacements *versus* number of cycles of mix R-CIP-6R, s=0.8.

Two different patterns of amplitude of displacements can be identified, depending on the fibre type used (recycled fibres or industrially produced fibres) as described below.

Displacement pattern for concrete reinforced with recycled fibres

The general pattern of the amplitude of displacements for concrete with recycled fibres is shown in Figure 229.

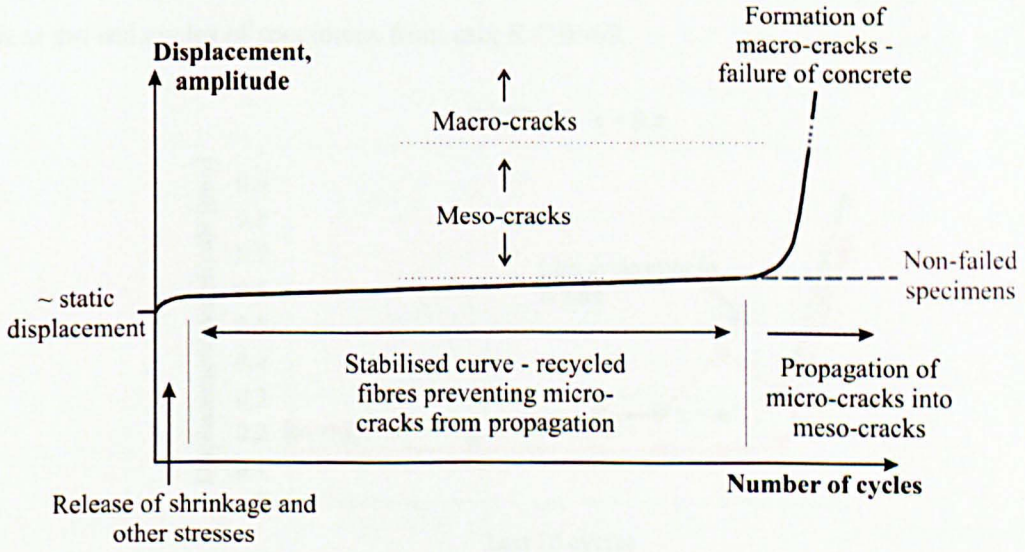

Figure 229 – Sketch of displacements in concrete reinforced with recycled fibres subjected to fatigue.

The pattern of displacements for the concrete reinforced with recycled fibres shows a very small initial increase in displacements, probably due to the release of internal stresses, such as the ones caused by shrinkage and other thermal influences. This initial stage not always occurs, and

depends on the characteristics of the mix, including curing and ambient conditions. This stage usually takes place in the first loading cycles and is very short compared to the following stages. This stage can be clearly seen in Figures 215, 216, 226 and 227.

The pattern is followed by a stabilised phase where the fibres seem to hold the existing micro-cracks of the concrete. The fibres seem to prevent the propagation of micro-cracks into meso-cracks, and the increase in displacements is very small. Micro-cracks are inherent to the concrete (due to voids and shrinkage) and can also be formed during loading. This second stage usually comprises most of the fatigue life of the concrete with recycled fibres. For the specimens that reached 2 million cycles without failing, this phase appears to continue infinitely.

The third stage is dominated by the propagation of micro-cracks into meso-cracks, and the starting point of this stage can be assumed to be the inflexion point at the end of the stabilised curve from the previous stage. After several cycles holding meso-cracks, the mechanical friction between the fibres and the matrix deteriorates due to fatigue, and the meso-cracks quickly propagate into macro-cracks. At this stage, the recycled fibres are not efficient in holding the macro-cracks, and the concrete fails. This last stage is shorter compared to the previous stage, and is represented by a rapid increase in the displacements for a low number of cycles, which takes place until the failure of the concrete. This final stage is exemplified by Figure 230, which looks at the last cycles of specimens from mix R-CIP-6R.

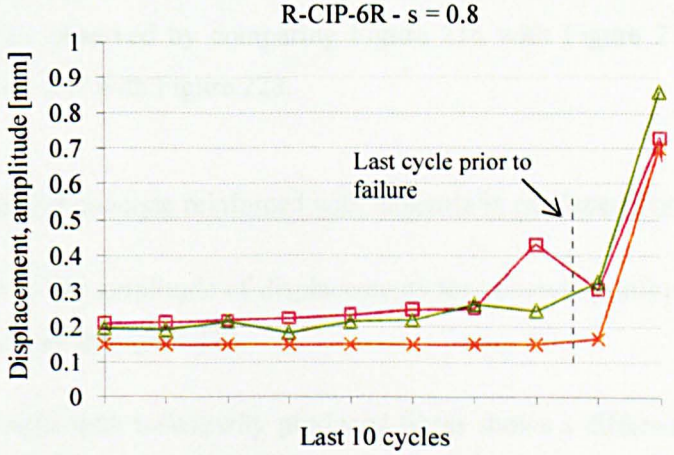

Figure 230 – Last ten cycles before failure (mix R-CIP-6R subjected to the stress level of 0.8).

Since the recycled fibres do not hold the macro-cracks, and also because they are not very effective in restraining the meso-cracks into macro-cracks, a sudden failure occurs. This can be seen in all figures above, where the rapid increase in the displacements was not recorded since it occurs in the period of 27,000 cycles at which no measurements were taken.

It is important to note that the stages of the fatigue life change slightly depending on the fibre content of recycled fibres. The linear rate at which the displacements increase during the second stage for the 2R specimens is usually lower compared to the 6R specimens, as shown in Figure 231. As discussed in the previous sections, this can be attributed mainly to the fact that the 6R specimens trap more voids during casting and, as a result, the 6R mix has a higher amount of initial micro-cracks, thus making it more difficult to prevent their propagation into meso-cracks. Hence, more meso-cracks are formed for 6R specimens during the second stage of the fatigue life.

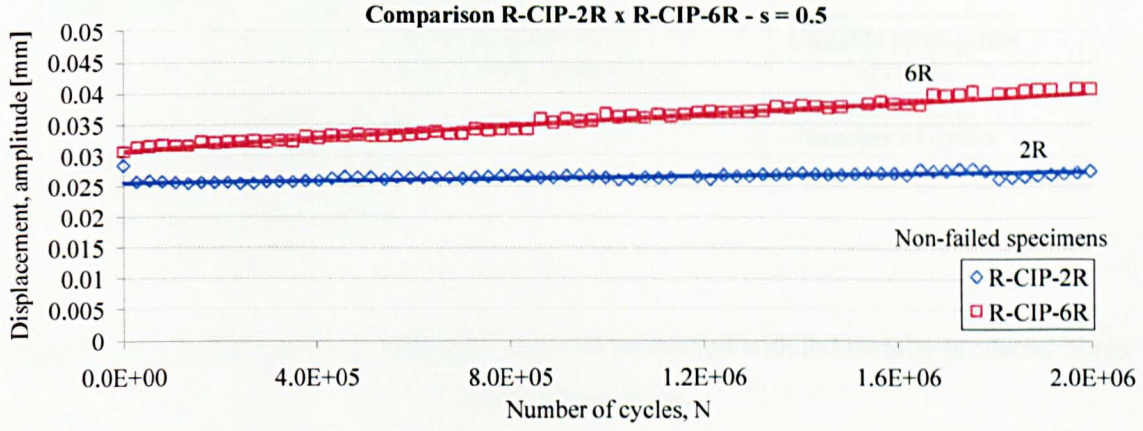

Figure 231 – Comparison between 2R and 6R RCC mixes.

The stress level also appears to influence the rate of increase in displacements during the stabilised stage. The higher the stress level, the higher the rate at which the displacements increase. This can be observed by comparing Figure 216 with Figure 217, Figure 218 with Figure 219 and Figure 227 with Figure 228.

Displacement pattern for concrete reinforced with industrially produced fibres

The general pattern of the amplitude of displacements for concrete reinforced with industrially produced fibres is shown in Figure 232.

The concrete reinforced with industrially produced fibres shows a different behaviour than the concrete with recycled fibres.

The first stage takes place during the first cycles, and it usually lasts for a relatively short period compared to the other stages. Industrially produced fibres are not as effective as the recycled fibres in restraining the propagation of micro-cracks and, as a result, the original micro-cracks of the concrete and those caused by shrinkage and other stresses rapidly turn into meso-cracks and macro-cracks due to cyclic loads.

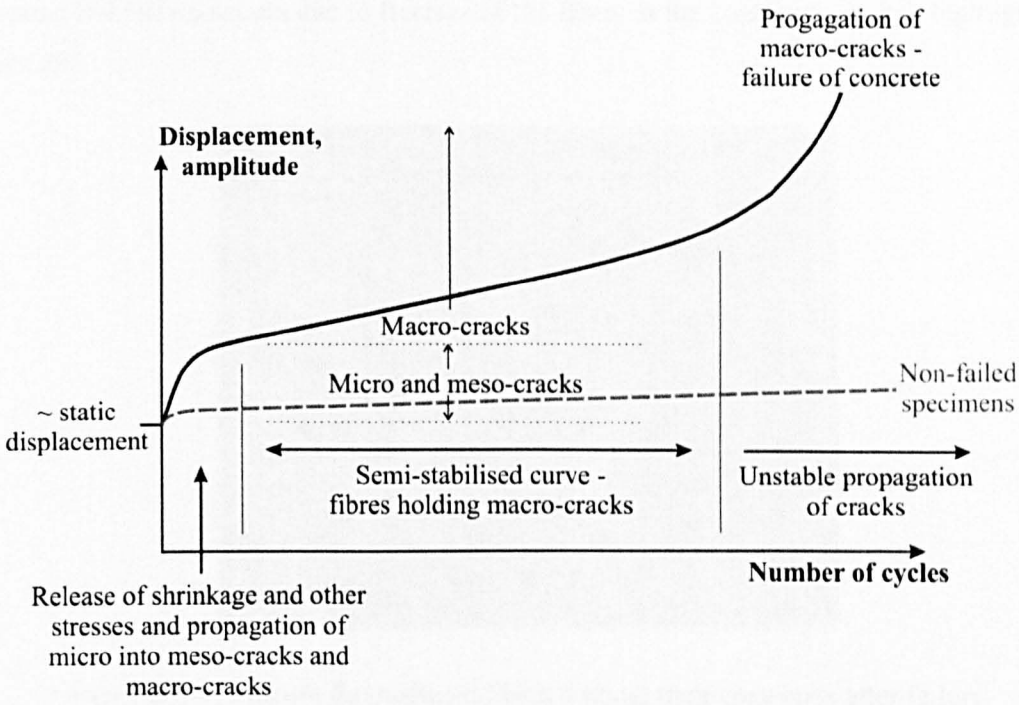

Figure 232 – Sketch of displacements in concrete reinforced with industrially produced fibres subjected to fatigue.

At this first stage, the matrix itself is probably the one responsible for preventing the propagation of micro-cracks instead of the fibres. Hence, for the situations where the specimen reinforced with industrially produced fibres did not fail up to 2 million cycles, this is attributed to the matrix preventing the propagation of micro-cracks into meso-cracks. The same behaviour as for the non-failed concrete with recycled fibres is then expected. It is also important to mention that this behaviour is also expected for plain concrete that resists 2 million cycles.

The second stage is when the fibres start to prevent the propagation of macro-cracks. This stage is not as stabilised as the stage when recycled fibres prevent the propagation of micro-cracks into meso-cracks due to the cracked condition of the concrete (more unstable behaviour). For this reason, this stage is represented by a semi-stabilised curve, where the displacements increase in a linear rate whilst the specimens prevent the unstable propagation of cracks. At the end of the second stage, most of the macro-cracks are already well formed and the fibres are probably fully utilised (are mobilised from end to end). Then a sudden change in the behaviour occurs, represented by an inflexion point at the end of the semi-stabilised curve and the unstable propagation of cracks takes places.

The last stage is when the industrially produced fibres probably start failling. Even though this stage is not as long as the second stage, it is longer compared to the first stage. The industrially produced fibres still hold the cracks together and increase the fatigue life of the cracked

concrete. The failure occurs due to fracture of the fibres at the cone ends, as it is highlighted in Figure 233.

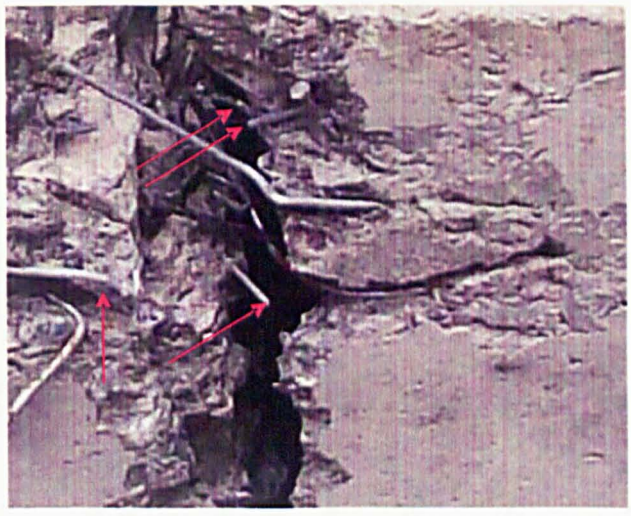

Figure 233 – Industrially produced fibres without their cone ends after failure.

Concrete with industrially produced fibres resists much higher displacements than recycled fibre concrete. This is due to the fact that industrially produced fibres are longer than the recycled fibres, and also because the cones at each end of the fibres improve the mechanical anchorage of the fibres.

To improve the fatigue life of the fibre reinforced concrete, a combination of both recycled and industrially produced fibres would be ideal. At this condition, the recycled fibres would contribute to prevent the propagation of micro-cracks into meso-cracks, both industrially produced and recycled fibres would contribute to preventing the propagation of meso-cracks into macro-cracks, and the industrially produced fibres would hold the macro-cracks together when they appear. As a consequence, the concrete would be able to resist a higher number of cycles at higher stress levels. Similar findings were arrived by Rossi and Parant (2008).

9.3.2 Fracture Toughness

There was an attempt to calculate the fracture toughness as the number of cycles increases. However, a series of factors prevented reliable results from this analysis. This section describes the procedures adopted for the calculation of the fracture toughness as well as the main problems detected during the analysis. Some recommendations are also proposed to understand the influence of the fatigue loads on the fracture toughness of concrete specimens when subjected to cyclic loads.

The fracture toughness of concrete specimens increases as the number of cycles increases (Li and Matsumoto, 1998 and Perdikaris *et al.*, 1986), as shown in Figure 234.

It can be seen in the graph that a considerable increase in the fracture toughness takes place in the last number of cycles, when concrete is close to failure.

To measure the fracture toughness originated by the increase in the number of cycles, the first stage was to create a representative curve of each 150 cycles measured at intervals of 27,000 cycles. The representative curve was obtained by the average of displacements measured for each group of 150 cycles.

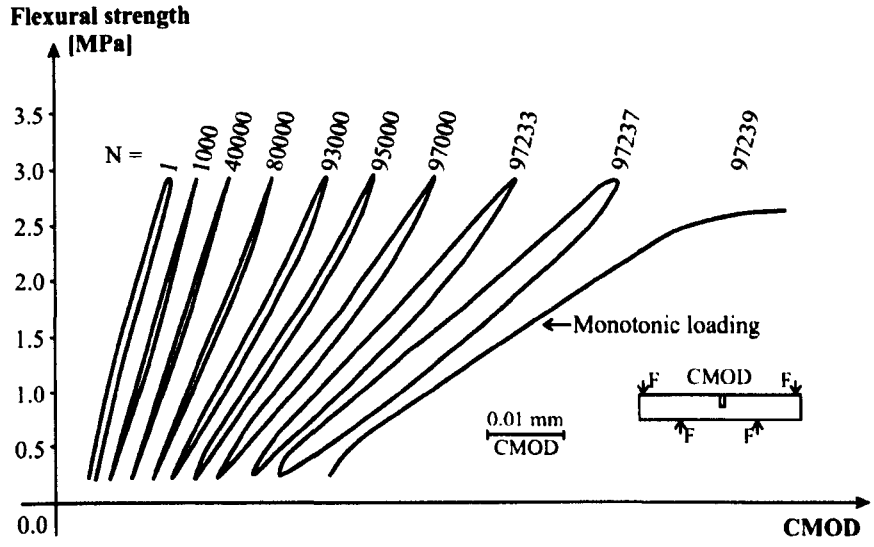

Figure 234 – Increase of fracture toughness as the number of cycles increases (Perdikaris *et al.*, 1986).

Two different data loggers were used during the tests: one from the MTS® controller to record the minimum and maximum load at every 50 cycles and one to record the displacements, as explained in the previous subsection. Since no history of the load measurements were obtained, the loads were calculated based on the sinusoidal wave pattern. The minimum displacement from each group of 150 cycles measured at intervals of 27,000 cycles was synchronised with the minimum load from the load curves calculated based on the sinusoidal wave pattern, as shown in Figure 235a.

The fracture toughness was calculated based on the area formed in-between the ascending and the descending branches of the load *versus* vertical displacement curve, shown in Figure 235b.

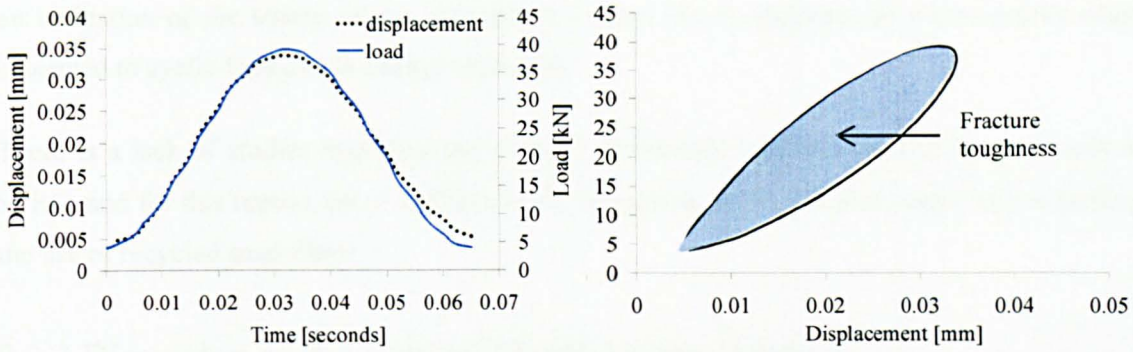

Figure 235 – a) Synchronisation of load and displacement curves and b) fracture toughness calculation (mix R-CIP-6R).

Several problems were observed when dealing with the results, such as negative values of fracture toughness and a considerable variability in the results. This may be attributed to various factors, such as:

1) The difficulty in synchronising the load and displacements curves. A small variation in the synchronisation of the curves leads to large changes in the values of fracture toughness;

2) The noise of the displacement measurements, caused by the vibration of the system and the large frequency (15 Hz) used to apply the cyclic loads. The vibration of the system also causes vibration in the yokes, thus increasing the noise of the measurements. This can be removed by using signal processing techniques;

3) The lack of load history measurements. The use of a load cell connected to the same data logger used for the displacement measurements could provide more reliable data for the analysis. However, it is important to note that inertial effects may also influence the results when dealing with cyclic loads applied at such high frequency;

4) The lack of continuous measurements up to failure, since the main increases in the fracture toughness occur when concrete is close to failure;

5) The displacement measurements were written in the output file based on the order they were recorded by the data logger. Due to the high frequency used, this may account for delays among the transducers measurements. This makes more difficult the synchronisation between the load and the displacement files.

The fracture toughness should give an extra indication of the deterioration caused by cyclic loads, especially in terms of degradation of the elastic behaviour of the material. High values of fracture toughness indicate that the material is beyond the limit of proportionality. It also gives

an indication of the ability of the concrete to control the propagation of macro-cracks when subjected to cyclic load due to energy absorption.

There is a lack of studies regarding the changes in fracture toughness due to fatigue loads in SFRC, and for this reason, more studies should be carried out in this area, especially regarding the use of recycled steel fibres.

9.3.3 Discussion on the Vertical Displacements Analysis

As previously stated, the increase in the displacements in SFRC subjected to flexural fatigue is mainly due to the fibre bridging degradation, caused by loss of bond/friction between the fibres and the matrix. This is also stated by Li and Matsumoto (1998) and by Lee and Barr (2004). However, Balaguru and Shah (1982) and Tan and Saha (2007) attribute the increase in the displacements to the deterioration of the stiffness due to increased cracking; and Whaley and Neville (1973) cited in Balaguru and Shah (1982) and Tan and Saha (2007) attribute to the cyclic creep[47] of the concrete in the compression zone.

The second factor is somehow related to the first factor, since the stiffness deterioration is a consequence of crack bridging degradation. The cyclic creep of the concrete may influence slightly the displacements but, as described previously, the fatigue life is strongly influenced by the capacity of the fibres in preventing the propagation of cracks instead of the characteristics of the plain concrete.

Recycled fibres appear to lose their friction with the matrix suddenly, regardless on the stress level applied. The industrially produced fibres, besides their longer length and larger diameter, have the contribution of the cones at each end of the fibres, which contributes to arresting the propagation of macro-cracks.

The vertical displacement analysis showed that steel fibres contribute for a longer fatigue life of concrete. Recycled steel fibres are mainly effective in the initial and intermediate stages of the fatigue life, by reducing/controlling the propagation of micro and meso-cracks. Industrial fibres, on the other hand, are effective in controlling the propagation of macro-cracks. Therefore, a combination of both recycled and industrially produced fibres can lead to a better fatigue performance of SFRC, by increasing the fatigue life of the concrete. This was also concluded by Rossi and Parant (2008).

[47] According to Whaley and Neville (1973) cited in Balaguru and Shah (1982), variations of stresses from minimum stress level (0.1) to maximum stress level (0.5, 0.7 or 0.9) leads to higher creep strain than if the maximum stress level is constant.

9.4 DESIGN RECOMMENDATIONS FOR FATIGUE OF SFRC PAVEMENTS

Currently, the design of concrete pavements does not take into account the benefits of adding fibres as reinforcement. The TR 34 (The Concrete Society. 2003) accounts for the post-cracking behaviour for the design of industrial floors, however, it does not take into account the fatigue effects. This was presented in Section 2.4.4.10 when the incompatibility of the various design methods of concrete pavements with the use of SFRC was discussed. However, it was found out that the addition of steel fibres does improve the fatigue performance of the concrete through crack control and this should be considered in design of concrete pavements.

This section aims to provide some ideas on how the codes should address the issue of including SFRC in the design guidelines for concrete pavements. A simplified investigation is initially carried out in this section aiming to show by means of a practical example some advantages on the use of recycled fibres to resist fatigue in concrete pavements.

Initially, the stresses in the concrete pavement slabs designed in Section 2.4.4.9 are calculated by using Westergaard (1926) equations. The depths taken into account for the calculations of stresses were those from road sections located near Sheffield (UK) and near Porto Alegre (Brazil), calculated based on the Highways Agency (2006a) and NCHRP (2002) methods. The calculated stresses and the stress ratios (ratio of calculated stresses to the flexural strength of the concrete) are shown in Table 29, based on a standard axle load of 80 kN located in the corner, edge and centre of a concrete pavement slab.

Table 29 – Stresses and stress ratio caused by a 80 kN standard axle in pavement sections.

Road	Method	Stresses			Stress ratio		
		Centre	*Edge*	*Corner*	Centre	Edge	Corner
UK	Highways Agency	1.11	1.47	1.67	0.17	0.23	0.26
	NCHRP	1.54	2.04	2.32	0.24	0.31	0.36
BR	Highways Agency	1.44	1.91	2.18	0.22	0.29	0.34
	NCHRP	1.61	2.14	2.44	0.25	0.33	0.38

The stresses in the corner of the concrete pavement are the highest and, for this reason, they are considered as key damage points for fatigue. The stress ratios calculated are all below the endurance limit shown previously in Figure 213 which, again, clearly confirms that the design codes avoid considering the post-cracking behaviour of concrete.

However, even though the stress ratios are below the endurance limit for both road sections analysed in this thesis, it is important to mention that both road sections are major roads and, hence, the concrete depth is considerably high. For lower volume roads, the concrete depth of pavements is smaller, and, for the same standard axle of 80 kN, the stress ratios are undeniably higher. On the other hand, these lower volume roads will sustain a much lower number of cycles than the major roads, allowing them to be subjected to higher stress ratios than the ones leading to the endurance limit. Since the design methods usually account for fatigue of concrete (since the PCA method, in 1966, fatigue has already been counted as a failure mechanism for concrete pavements – Section 2.4.4), it is not part of this thesis to confront the validity of the codes when dealing with plain concrete, but to propose the inclusion of the benefits of using steel fibres as reinforcement for fatigue.

Assuming, for example, that the SFRC roads shown in Table 29 are forced to resist higher stress ratios by reducing the depth of the concrete slab, then the concrete will crack at a certain point of its service life. This needs to take into account not only the stresses caused by standard axles, but also the number and level of loads that may exceed the standard value of 80 kN, since they may lead to earlier deterioration of the concrete. Since no load spectrum is provided, only the standard axle of 80 kN is considered.

To consider that the concrete cracks at some point, the logical procedure is to apply a slightly higher stress ratio than the one that limits the endurance life of the pavement. Alternatively, the probabilistic analysis (Section 10.4) can be taken into account by considering the stress ratio that causes the concrete to fail after certain number of cycles, for a high probability of failure (to assure concrete cracks).

Assuming that the mix used in the example for both UK and Brazilian sections is the R-CIP-2R mix, which has similar properties as the assumed values of 6.5 MPa and 55MPa used for the flexural and compressive strength of the concrete, respectively, the stress ratio that leads the specimens to sustain 2 million cycles is 0.57 (Figure 213) or, by considering the probabilistic analysis, the stress ratio that leads the specimen to fail before reaching 1 million cycles, for a high p_f of 50%, is 0.6 (Figure 259, Section 10.4). Since slightly higher value than 0.57 should be assumed for the specimen to be considered as cracked before reaching the endurance limit, the stress ratio of 0.6 was assumed in this example, which matches the stress ratio from the probabilistic analysis.

A new depth of concrete pavements can be calculated considering the maximum stress ratio of 0.6, based on the Westergaard (1926) equations (Appendix B). By comparing the new depth

with the depths obtained by using the codes (Section 2.4.4.9), the reduction obtained is shown in Figure 236.

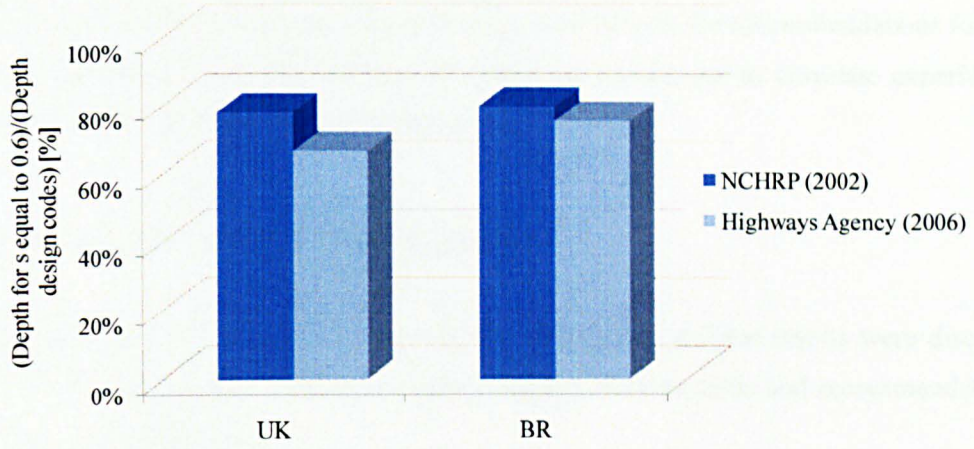

Figure 236 – Comparison of depths calculated by design codes and considering a higher stress level.

If the maximum fatigue performance is taken into account, there is a reduction exceeding 20% for both road sections and codes analysed in this example. However, this calculation does not show the true benefits of using SFRC over plain concrete, since the reduction shown above does not take into account other important effects, such as the environmental loads and other failure mechanisms (due to roughness degradation, for example). It considers the fatigue as the only failure mechanism, and accounts for the fact that the pavement is able to resist cyclic loadings after developing cracks. The above calculation is based on the fact that fibres contribute for increasing the stress ratio to achieve the endurance limit, shown in Section 9.2, and also on the fact that fibres control cracking propagation, shown in Section 9.3.

The fact that the concrete may act in the cracked condition may lead to the assumption that other deterioration processes may initiate through the cracks, caused by the easy penetration of chlorides and other aggressive agents into concrete. However, as reported in Chapter 7, the chloride ingress into concrete seems to halt after a certain period of time due to autogeneous healing of the concrete and rust deposition. The healing of the concrete may also block the penetration of other aggressive agents into concrete. Hence, depending on the opening size of the cracks, no further deterioration is expected.

Another fact that must be taken into account is that, according to Roesler and Barenberg (1998), the fatigue behaviour of concrete beams is different than the behaviour of concrete slabs in real pavements. The author says that slabs are approximately 30% stronger than beams, which leads to an underestimation of the fatigue performance of the concrete when analysing results for

fatigue of concrete beams. Roesler and Barenberg (1998) and Roesler *et al.* (2005) explain that the correlation between the slab and beam results depends on the concrete specimen thickness, slab geometry, load configuration and boundary conditions. This aspect was not evaluated in this thesis, but should be taken into account when dealing with the recommendations for fatigue of SFRC pavements. Further investigation should be carried out to correlate experiments of fatigue beam tests with real concrete pavements.

9.5 SUMMARY AND CONCLUSIONS

Fatigue resistance of SFRC was experimentally investigated and the results were discussed in terms of stress ratio *versus* number of cycles, displacement analysis and recommendations for design of concrete pavements.

The inclusion of recycled fibres in both wet and RCC mixes improved the fatigue performance of the concrete, however, there seems to be an optimum fibre content that gives the best fatigue response. Contents higher than the optimum still improve the fatigue performance compared to plain concrete, but the level of enhancement is lower compared to the optimum fibre content concrete.

The optimum fibre concrete for recycled fibres is found between 2% and 6% by mass of concrete, for both wet and RCC mixes examined. However, further investigations should be carried out since only two fibre contents were examined.

RCC mixes (including plain concrete) have good performance when subjected to higher stress levels, probably because of the effect of aggregate interlock, which contributes to load transfer among cracks.

The investigation on the vertical displacements shows that recycled fibres are more efficient in arresting the propagation of micro-cracks, while industrial fibres are more effective in controlling the propagation of macro-cracks. As a result, concrete with recycled fibres appears to have a more brittle fatigue failure than the ones reinforced with industrially produced fibres.

The use of hybrid fibres (combination of small and larger fibres) should contribute for an improved fatigue behaviour (longer fatigue life) of the concrete, and further investigations should be carried out on the use of both fibre types in concrete.

The measurement of toughness during fatigue cycles may contribute towards a better understanding of the fatigue behaviour of recycled SFRC. However, further investigation should

be carried out to accurately measure the simultaneous displacements and load of specimens subjected to fatigue.

Some recommendations for the design of SFRC pavements subjected to fatigue were suggested based on a simplified practical example. However, further studies are needed to determine the true effect of adding fibres to concrete pavements, and how they affect the outputs of the design guidelines.

As a general conclusion, it can be said that steel fibres act as a reinforcement for concrete subjected to fatigue, thus increasing its service life. Hence, it is important to take into account the post-cracking behaviour of the concrete in the design guidelines, meaning that the pavement is able to resist fatigue loads in the cracked condition.

Accounting for the post-cracking behaviour of recycled SFRC pavements may substantially reduce the thickness of the concrete pavements, thus reducing the cost and the use of natural resources. This, along with the use of recycled steel fibres, contributes for a more sustainable development in road construction.

The following chapter deals with a probabilistic analysis carried out for concrete structures exposed to corrosion, freeze-thaw and fatigue.

CHAPTER 10

10. PROBABILISTIC ANALYSIS

The experimental results on the deterioration processes of SFRC concrete pavements, which were explained in the previous chapters, are important to explain how the recycled SFRC reacts when subjected to the specific degrading conditions. However, it is also important to understand the effects of these results on the design of concrete pavements, especially in terms of how long the structure will be able to maintain its performance. Therefore, this chapter deals with the service life design (SLD) of concrete pavements in terms of chloride ingress and freeze-thaw. A probabilistic fatigue analysis is also carried out.

Initially, some principles of the probabilistic SLD are described, followed by an explanation of the models used to predict the service life of concrete pavements using the concrete mixes investigated in this work. Separate models and results for corrosion and freeze-thaw are presented.

The SLD methods used are based on a probabilistic analysis based on a certain degree of reliability[48] of the structure. The serviceability limit state is used for the predictions of SLD, based on the comfort of the users, mainly in terms of the appearance of the structure.

10.1 SLD METHODS

According to fib bulletin 34 (fib, 2006), the SLD methods should follow either: 1) the use of partial safety factor method; or 2) the use of deemed-to-satisfy method; or 3) be based on the avoidance-of-deterioration method or 4) the general principles for probabilistic analysis;.

The partial safety factor method separates the treatment of uncertainties and variabilities originated from various causes (CEB-FIP, 1993; fib, 2006). The basic variables are, in general, expressed as a ratio to the partial safety factors. When the partial factor method is used, the

[48] Reliability is the ability of a structure to fulfil the basic structural requirements during a certain period of time (usually the working time of the structure), and is usually expressed in probabilistic terms. The degree of reliability depends on the use (importance) and the type of the structure and design variables.

target reliability for not exceeding the requirements of the assumed limit state, during the service life, should not be exceeded. The partial factors should take these requirements into account (fib, 2006).

The deemed to satisfy method is based on rules for dimensioning, material and product selection and execution procedures. These rules should guarantee that the limit state is not exceeded during the service life of the structure, based on certain reliability (fib, 2006).

The method based on the avoidance-of-deterioration is based on the fact that deterioration does not occur if precautionary measures are taken into account (e.g. isolation of the structure against environmental influences) (fib, 2006).

For the purpose of this thesis, the probabilistic analysis is taken into account for the prediction of the SLD. This is due to the high number of variables influencing the processes of chloride ingress and freeze-thaw, which leads to various uncertainties when investigating the processes. It is also encouraged by the continuous use of probabilistic methods to describe the deterioration processes in concrete structures. The general principles for the probabilistic methods are explained in the following subsection.

10.1.1 Probabilistic Methods for SLD

Some of the basic variables[49] may be time-dependent (e.g. deformation, damage caused by corrosion, carbonation, chemical attack, freeze-thaw, etc.) and models can be used to predict the endurance life of structures subjected to deterioration processes.

Mechanical, physical and chemical models are in general used to describe the effects of the environmental influences and actions[50] on the material properties. These models usually include the uncertainties from the essential sources[51]. The probabilistic analysis of SLD takes into account these uncertainties, characterised by probabilistic models, to describe the basic variables.

The basic variables are stochastic processes defined by a number of statistical parameters (e.g. mean, standard deviation, lower and upper bounds, etc).

[49] The basic variables are the actions and environmental influences, geometrical quantities and the materials and products properties of a structure (BS EN 1990, 2002; fib, 2006). They carry the input for the calculation model.
[50] Caused by human influence (e.g. collapse of a vehicle, overloading, etc.)
[51] The essential sources are factors influencing the models of the basic variables.

The models in the probabilistic analysis are usually simplified, which means that the most important factors are taken into account and the less important factors are usually neglected.

10.1.2 Reliability of Structures or Structural Elements

The reliability index β is an indication of how many standard deviations a certain condition exceeds a certain limit state. β can be applied to structural elements and/or structural systems and (for normal probability distributions) is defined as shown in Equation 31.

$$\beta = -\Phi^{-1}(p_f) \tag{31}$$

Where:

p_f = probability of failure

Φ^{-1} = inverse of the Gaussian distribution

The relation between β and p_f is given in Table 30.

Table 30 – Relation between β and p_f.

p_f	10^{-1}	10^{-2}	10^{-3}	10^{-4}	10^{-5}	10^{-6}	10^{-7}
β	1.28	2.32	3.09	3.72	4.27	4.75	5.20

The reliability index takes into account the accepted or assumed statistical variability in action effects and resistances and model uncertainties (BS EN 1990, 2002c).

The structural risk acceptance criterion corresponds to a minimum reliability defined as *target reliability*. The safety of the structure is expressed in terms of the *accepted minimum reliability index* or the *accepted maximum failure probability*.

The target values for structures and/or structural elements with medium consequence for loss of human life and with considerable economic, social or environmental consequences (reliability class RC2 according to BS EN 1990, 2002c) are shown in Table 31. The reliability values for 50 years of working life were used in this work. This was chosen in accordance with the mix proportion design shown in Section 4.2.

For the purpose of this thesis, the SLD of concrete pavements is evaluated in terms of environmental influences, such as the corrosion due to chloride ingress and the freeze-thaw effect. The following subsections explain the methods used for the probabilistic SLD assessment of each influence.

Table 31 – Target reliability index β for class RC2 structures and structural elements (BS EN 1990, 2002c).

Limit state	Target reliability index	
	1 year	50 years
Ultimate	4.7	3.8
Fatigue		1.5 to 3.8[a]
Serviceability (irreversible)	2.9	1.5

[a] depends on the degree of inspectability, reparability and damage tolerance.

10.2 SLD METHOD FOR CHLORIDE CORROSION

Information on the SLD of SFRC is very limited, therefore, the information given in this subsection deals with the models of corrosion deterioration due to chlorides used for conventional RC structures, unless otherwise specified.

When dealing with chloride ingress, the service life of the structure is based on two limit states: 1) the serviceability state based on the depassivation of the reinforcement (also called the initiation period of corrosion) and 2) the ultimate limit state due loss of cross sectional area, loss of bond between concrete and the reinforcement, cracking and spalling of concrete (also called the propagation period). Figure 237 shows the schematic representation of the chloride corrosion limit states.

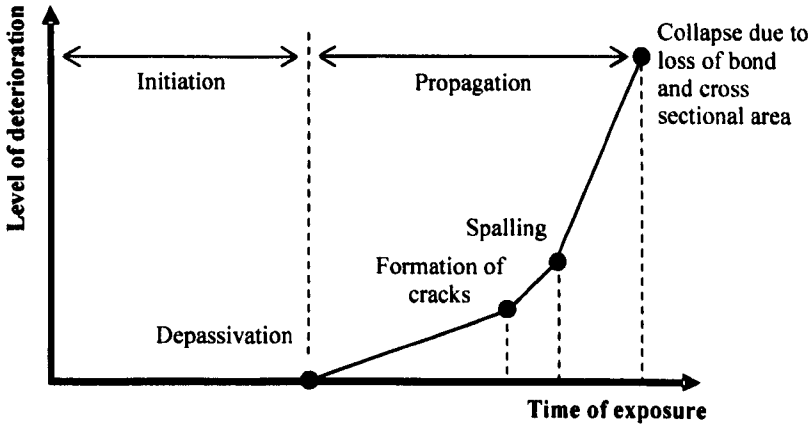

Figure 237 – Limit states of corrosion process in RC structures.

According to Val and Trapper (2008), the propagation phase is usually shorter compared to the initiation period. Hence, the initiation period represents a major parameter controlling the corrosion deterioration of concrete structures.

The results for SFRC in the literature as well as in the ones presented in this thesis show that corrosion affects mainly the surface of the concrete, by giving it a rusty appearance. As a consequence, there is no proper definition for the initiation and the propagation phase of corrosion in SFRC.

A well known probabilistic method used to predict the chloride ingress into concrete structures was developed by during the DuraCrete (1998) project. A software called Life-365 was also developed during the project (Duracrete, 1998). The method considers the Fick's second Law of diffusion as the main parameter influencing the calculations.

10.2.1 Serviceability Limit State for Corrosion

The initiation period of corrosion is based on the ingress of chlorides into concrete, and most of the studies in the area are based on Fick's second law of diffusion (Section 3.2.1.3), especially regarding the use of the analytical solution shown in Equation 12.

As pointed out by Marchand and Samson (2009), there are some limitations in using Fick's second law method to predict the chloride ingress in real structures, such as the fact that the structure needs to be in a fully-saturated condition and that the actual binding capacity of the cementitious materials is not well represented.

For both saturated and non-saturated conditions, the limit state function for depassivation of concrete is shown in Equation 32 (fib, 2006), which assumes that the limit state is exceeded when the chloride content at a certain depth (equal to the concrete cover for RC) is higher than the critical chloride content that causes depassivation of the steel embedded into concrete.

$$p_{dep} = p[C_{crit} - C(x, t_{SL}) < 0] < p_f \quad (32)$$

Where:

p_{dep} = probability that depassivation occurs

C_{crit} = critical chloride content [% by mass of concrete]

$C(x,t_{SL})$ = chloride content at a depth x and a time t_{SL} [% by mass of concrete]

x = concrete cover [mm]

t_{SL} = SLD [years]

p_f = target failure probability to avoid exceedance of limit state

Some works (Alonso and Sanchez, 2009; Markeset, 2009; Glass and Buenfeld, 1997) have been undertaken to obtain the critical chloride content of concrete. However, due to fact that the test cannot be easily performed, and also due to the lack of methodologies on how to perform the test, there is a certain variability and sometimes a conflict among the results.

The fundamentals of chloride ingress in both saturated and non-saturated condition are presented in Appendix H.

10.2.2 Ultimate Limit State for Corrosion

The ULS for corrosion of RC structures is due to the propagation of the process, causing loss of bond between steel and concrete, spalling and subsequent loss of cross sectional area. There are numerous studies for corrosion of RC, but there is a lack of studies on the literature that accounts for the propagation phase of corrosion in SFRC. This is mainly due to the fact that most of the studies on the area (Section 3.1.2) concluded that corrosion is mainly observed in terms of superficial corrosion (depassivation of a thin layer of concrete surface) and not due to loss on the mechanical performance.

The results presented in Chapter 7 shows that there is no loss in the mechanical properties after exposure to 5 and 10 months of wet-dry cycles, for all mix proportions tested. Nevertheless, these results are unique for recycled fibres (no other study on the durability of recycled SFRC can be found on the literature) and further investigation is required to verify whether higher periods of exposure to wet-dry cycles or any other accelerated chloride ingress test leads to loss in the mechanical performance.

10.2.3 Results of Chloride Corrosion Probabilistic SLD

The probabilistic SLD for predicting the chloride ingress in concrete was used for two different studies. The first study correlates the time of accelerated corrosion to real exposure (less severe condition). The second is a parametric study to verify the influence of the various mix proportions on the SLD of a concrete pavement. The analyses were based on the SLS, considering the fully-saturated condition.

10.2.3.1 Proposed Method for the Comparison of Accelerated Tests to Real (Less Severe) Conditions

Fundamentals of the method

The use of wet-dry cycles is a corrosion accelerated test due to the fact that chlorides penetrate into concrete due to the coupled effect of diffusion and convection (non-saturated condition), instead of only diffusion (fully-saturated condition). To compare the damage caused by wet-dry cycles to real conditions, the wet-dry cycles damage needs to be compared with a less severe case of chloride ingress, such as when concrete is fully-submerged in chloride contaminated water.

The time of each cycle of wetting and drying also influences the rate of chloride ingress. According to Val and Trapper (2008), large periods of wetting[52], followed by large periods of drying, increase the amount of total chlorides inside the concrete. The comparison of the experimental results with other periods of wet-dry cycles needs to account for the influence of time-dependent ambient humidity, which is based on chloride ingress in non-saturated condition. As explained previously, the non-saturated condition is not analysed in this study.

The depth of chloride ingress, after a certain period of time, is considered as the SLS in the proposed method. Therefore, in terms of probabilistic analysis, to make sure that the element reached the SLS, a probability of failure of 93% is considered. This follows the opposite idea of the criterion adopted by BS EN 1990 (2002c) which says that a maximum probability of failure of approximately 7% should be consider for the structure not to fail (reliability of 1.5, SLS, SLD of 50 years). In this case, however, a probability of 93% should be an indication that the structure will most probably fail.

Equation 32 is used to calculate the various probabilities of failure for various periods of time, for the known depth of chloride ingress obtained from the accelerated tests, making sure that the results account for probabilities of failure of around 93%. The equation accounts for specific properties of the concrete and also for other parameters that affect the chloride ingress into concrete. Therefore, the probabilities of failure, which are based on certain periods of time, change depending on these properties.

[52] The authors say that periods of wet and dry cycles of 3 months wet followed by 3 months dry leads to more chloride content than concrete subjected to periods of 1 month wet followed by 1 month dry. Following the same idea, periods of 1 month wet followed by 1 month dry leads to more chloride content than periods of 1 day wet followed by 1 day dry.

The main target of the method is to obtain the time needed for the less severe method (e.g. real exposure) to achieve, with 93% of probability, the same depth of chloride ingress as for the accelerated method.

Summary of the method – main procedures

In summary, the following steps/procedures should be used when trying to correlate accelerated corrosive methods to real (less severe) situations.

1) The first step in comparing the use of wet-cycles to fully-saturated conditions (e.g. example of real condition) is to obtain the depth of chloride ingress after a certain period of accelerated corrosion simulation. The depth of chloride penetration can be obtained by breaking the concrete parallel to the chloride ingress gradient, and spraying a solution of silver nitrate on the fractured surfaces of the concrete, as explained in Section 3.2.1.3 (also called as colorimetric or Collepardi's method).

2) The depth of chloride ingress, along with other parameters described in Appendix H, is used to calculate (Equation 32) the probability of failure[53] for various periods of time. The periods of time used should be enough to allow probabilities of failure to vary until at least 93%.

3) The probability of failure is then plotted against the period of time, based on the depth of chloride ingress obtained from the accelerated method (step 1).

4) The depth of chloride ingress (from step 1) should be considered as the SLS for the specified period of corrosion simulation at which the depth was measured.

5) The final step is to find the real period of time equivalent to the probability of failure of 93% for the curve previously plotted. This period of time is the equivalent time for the less severe condition (e.g. fully-saturated) to reach the same level of deterioration (chloride ingress) of the accelerated test.

Examples – parameters used

The mixes subjected to wet-dry cycles (Section 4.3.2.2) are considered as examples for the proposed method. The diffusion coefficient was calculated considering the influence of time (Equation H.2).

[53] Probability of achieving the depth of chloride penetration measured in step 1.

The parameters used to carry out the probabilistic analysis are presented in Table 32 and Table 33, for wet and RCC mixes, respectively. D_{ref} is the reference diffusion coefficient obtained at t_{ref} (based on experiments – Section 6.3). t_{ref} is the time of curing. s is the age factor and it varies according to the cementitious material type (assumed according to fib, 2006). C_s varies according to the mix proportion and is based on experiments (Section 6.3). The value of U/R and the resistance parameter C_{cr} is assumed according to fib (2006). The coefficient of variation of both D_{ref} and x are also assumed according to fib (2006).

Table 32 – Probabilistic parameters used for wet mixes (mean and coefficient of variation).

Parameter		Distribution	R-CIP-2I	R-CIP-6R	R-LEC-2I	R-LEC-6R
Load parameters	D_{ref} [m^2/s]	Lognormal	4.68E10-12 (0.2)	2.13E-12 (0.2)	1.61E-12 (0.2)	1.81E-12 (0.2)
	s	Beta	0.60(0.25)	0.60(0.25)	0.45(0.44)	0.45(0.44)
	t_{ref} [days]	Deterministic	28	28	28	28
	C_s [% by mass cementitious material]	Deterministic	0.89	1.70	0.81	1.21
	U/R [K]	Normal	4800(0.15)	4800(0.15)	4800(0.15)	4800(0.15)
	x [mm]	Normal	(0.2)[a]	(0.2)[a]	(0.2)[a]	(0.2)[a]
Resistant parameter	C_{cr} [% by mass cementitious material]	Beta	0.60(0.25), 0.2/2.0[b]	0.60(0.25), 0.2/2.0[b]	0.60(0.25), 0.2/2.0[b]	0.60(0.25), 0.2/2.0[b]

[a] depths used are shown in Figure 239.
[b] 0.2 is the lower and 2.0 is the upper bound of beta distribution.

Table 33 – Probabilistic parameters used for RCC mixes (mean and coefficient of variation).

Parameter		Distribution	R-CIP-2I	R-CIP-6R	R-LEC-2I	R-LEC-6R
Load parameters	D_{ref} [m^2/s]	Lognormal	3.91E10-12 (0.2)	15.3E-12 (0.2)	1.55E-12 (0.2)	1.96E-12 (0.2)
	s	Beta	0.60(0.25)	0.60(0.25)	0.45(0.44)	0.45(0.44)
	t_{ref} [days]	Deterministic	28	28	28	28
	C_s [% by mass cementitious material]	Deterministic	1.36	1.57	1.10	0.51
	U/R [K]	Normal	4800(0.15)	4800(0.15)	4800(0.15)	4800(0.15)
	w [mm]	Deterministic	-	-	-	0.02[a]
	depth [mm]	Normal	(0.2)b	(0.2)[b]	(0.2)[b]	(0.2)[b]
Resistant parameter	C_{cr} [% by mass cementitious material]	Beta	0.60(0.25), 0.2/2.0[c]	0.60(0.25), 0.2/2.0[c]	0.60(0.25), 0.2/2.0[c]	0.60(0.25), 0.2/2.0[c]

[a] pre-cracked before exposure to wet-dry cycles (based on experiments)
[b] depths used are shown in Figure 240.
[c] 0.2 is the lower and 2.0 is the upper bound of beta distribution.

As shown in the above table, the value of C_s is expressed in terms of *% of cement mass*. To obtain the correlation between *% of concrete mass* shown in Section 6.3 to *% of cement mass*, the mix proportion used for each mix is taken into account and a simple calculation based on the proportions of the materials is then used.

Examples – results and discussion

The probabilistic analyses utilise Monte Carlo simulations with 40,000 samples to calculate the probability of failure according to the various input parameters. The analyses were run in MatLab® version 7.7 (MathWorks, 2010) and the script used for the probabilistic analyses can be found in Appendix I.

To obtain the depth of chloride penetration in the accelerated condition, the visual analysis shown in Section 7.1 provides an idea of these depths, based on signs of rust in the interior of the concrete. For example, it is explained in that section that 6R RCC specimens show traces of rust up to a depth of 10 mm. Other mixes have mainly superficial corrosion, which can be assumed that the depth of chloride ingress should be less or around 5 mm.

However, because the real depth of chloride penetration after wet-dry cycles was not properly measured for each mix, the real comparison of accelerated tests with experiments cannot be clearly quantified in this analysis. Nevertheless, various depths around the values explained in the previous paragraph are assumed, as shown later in Figures 239 and 240, for wet and RCC mixes, respectively. Proper measurements of chloride ingress depth can be performed according to the method described in Section 3.2.1.3. The chloride ingress depth of the accelerated condition is a crucial factor for the full validation of the proposed simplified method.

Mix R-CIP-6R is used in a practical example, which seems to have a chloride ingress depth of around 10 mm after 5 months of wet-dry cycles, according to the visual analysis (signs of rust can be observed at around that depth[54] – Section 7.1). Considering that the same depth should be obtained in the less severe situation (probability of 93%), the corresponding time for fully-saturated condition is 0.7 years (8.4 months) – based on graphical observation shown in Figure 238. If the assumption of the chloride ingress depth for mix R-CIP-6R after wet-dry cycles is true, the accelerated method reduces by 40% the time of the corrosive process compared to a fully-saturated condition.

[54] This value is based on an empirical observation, and it is only assumed as true to allow a practical example of the proposed method.

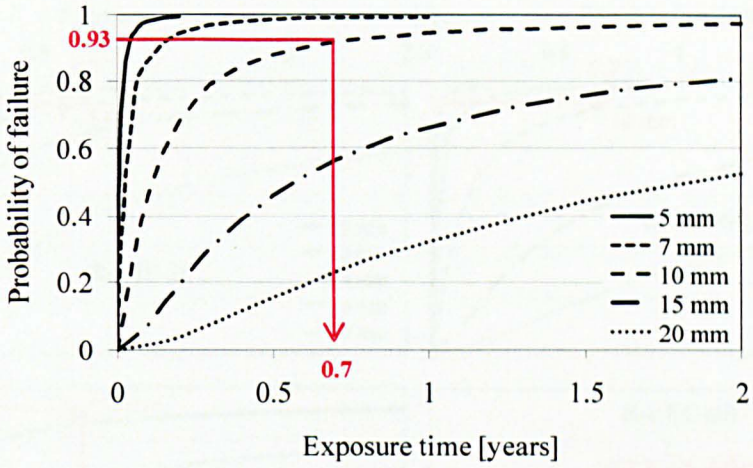

Figure 238 – Example of probabilistic fully-saturated chloride ingress considering various depths of chloride ingress.

If considering that 5 months of wet-dry cycles is equivalent to 8.4 months of fully-saturated condition, the graphs below (Figures 239 and 240) can be used to obtain the depth of chloride ingress for other specimens subjected to the same wet-dry cycles, as highlighted in the figures.

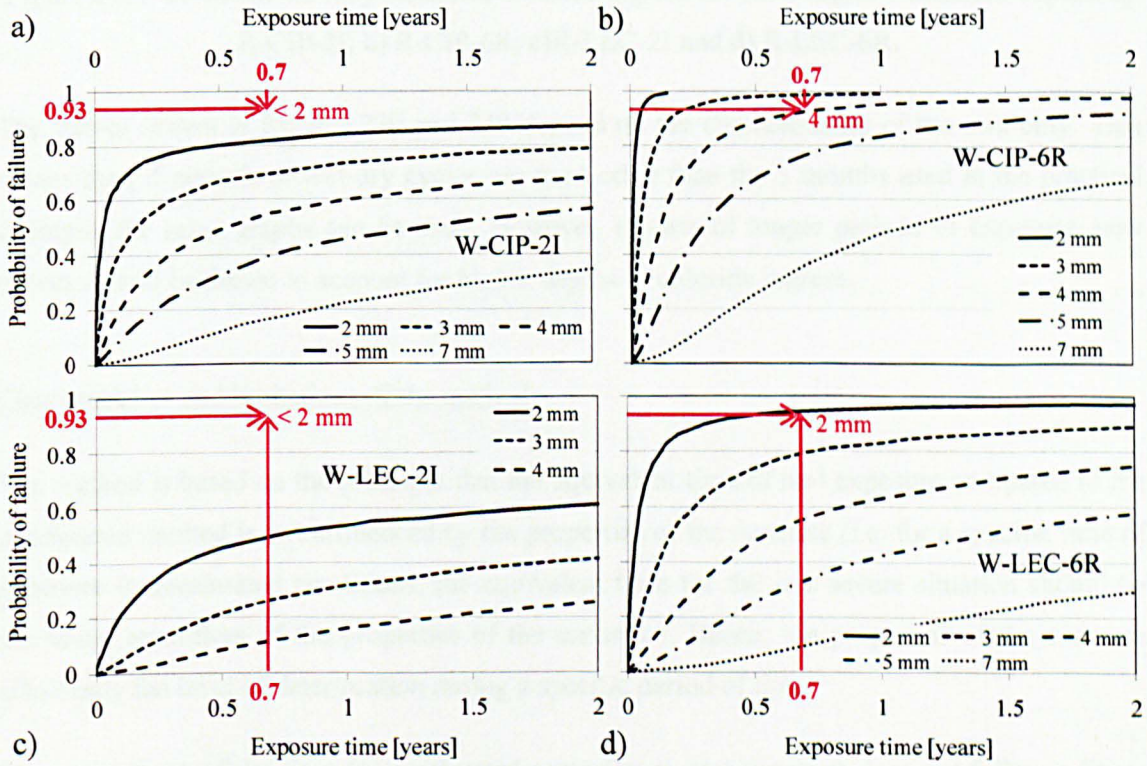

Figure 239 – Probabilistic fully-saturated chloride ingress for wet mixes – different depths. a) W-CIP-2I, b)W-CIP-6R, c)W-LEC-2I and d) W-LEC-6R.

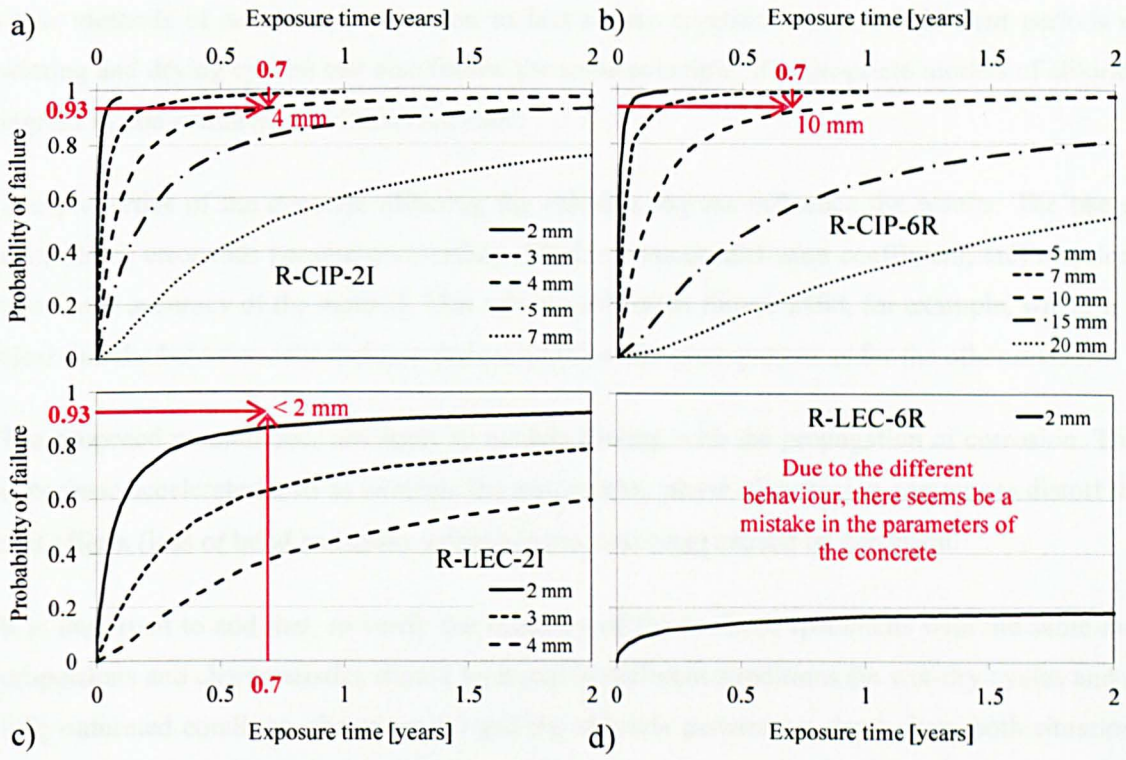

Figure 240 – Probabilistic fully-saturated chloride ingress for RCC mixes – different depths. a) R-CIP-2I, b) R-CIP-6R, c)R-LEC-2I and d) R-LEC-6R.

The curves shown in Figures 239 and 240 depend on the characteristics of the mix only. This means that, if periods of wet-dry cycles are used other than the 5 months used in the practical example, the same graphs can be used. However, in case of longer periods of exposure, new curves should be drawn to account for higher depths of chloride ingress.

Characteristics and limitations of the method

The method is based on the principle that the equivalent time of real exposure compared to the accelerated method is not influenced by the properties of the concrete (i.e. for a specific time of exposure to accelerated conditions, the equivalent time for the less severe situation should be the same, regardless of the properties of the concrete). Hence, the properties of the concrete affect only the level of deterioration during a specific period of time.

The comparison of the time for accelerated corrosion to real exposure does not follow a linear relationship. This is mainly influenced by the nature of the chloride ingress into concrete and also by the influence of the time-dependent properties of the concrete.

The proposed method is based only on the correlation of wet-dry cycles to fully-saturated conditions, considering the chloride ingress only. However, it is expected that a comparison of

other methods of accelerated corrosion to less severe conditions (use of different periods of wetting and drying cycles) can also follow the same principle, if appropriate models of chloride ingress in non-saturated conditions are used.

The properties of the concrete affecting the chloride ingress influence the results. The use of assumed or erroneous parameters (surface chloride content, diffusion coefficient, etc) may lead to a lower accuracy of the method. This can be verified in Figure 240d, for example, where it is clear that the behaviour for that mix does not follow the same pattern as for the other mixes.

The proposed method does not apply to models dealing with the propagation of corrosion. This is because accelerated tests to simulate the propagation phase of corrosion sometimes distort the real effects (loss of bond and cross sectional area, cracking) caused by corrosion.

It is important to add that, to verify the accuracy of the method, specimens with the same mix proportions and characteristics should be tested in different conditions (in wet-dry cycles and in fully-saturated condition, for example) and the chloride penetration depth from both situations should be compared with the values obtained from the proposed correlated simplified method.

10.2.3.2 Parametric study

Another analysis was based on a parametric study to verify the effect of the type of mix, fibre content and type and cementitious material on the chloride ingress of concrete. A service life design of 50 years was considered for the analyses. This SLD is based on concrete fully-submerged in chloride solution. The probability of failure of 7% was used following the recommendations of BS EN 1990 (2002c).

The parameters used for this study are the same as the ones described in Table 32 and Table 33. The parameters of mixes that are not shown in those table are described in Table 34 and Table 35. t_{ref} and C_{cr} are the same as shown in Table 32 and Table 33.

Table 34 – Probabilistic parameters used for wet mixes (mean and coefficient of variation).

Parameter		Distribution	W-CIP-0	W-CIP-2R	W-LEC-0	W-LEC-2R
Load parameters	D_{ref} [m^2/s]	Lognormal	3.53E10-12 (0.2)	2.21E-12 (0.2)	2.34E-12 (0.2)	2.57E-12 (0.2)
	m	Beta	0.60(0.25)	0.60(0.25)	0.45(0.44)	0.45(0.44)
	C_s [% by mass cementitious material]	Deterministic	0.81	1.04	1.98	1.46
	x [mm]	Normal	(0.2)[a]	(0.2)[a]	(0.2)[a]	(0.2)[a]

[a] depths are variable.

Table 35 – Probabilistic parameters used for RCC mixes (mean and coefficient of variation).

Parameter		Distribution	R-CIP-0	R-CIP-2R	R-LEC-0	R-LEC-2R
Load parameters	D_{ref} [m^2/s]	Lognormal	3.83E10-12 (0.2)	3.36E-12 (0.2)	2.19E-12 (0.2)	1.07E-12 (0.2)
	m	Beta	0.60(0.25)	0.60(0.25)	0.45(0.44)	0.45(0.44)
	C_s [% by mass cementitious material]	Deterministic	1.90	1.20	1.32	0.75
	x [mm]	Normal	(0.2)[a]	(0.2)[a]	(0.2)[a]	(0.2)[a]

[a] depths are variable.

Influence of the fibre content and type

The effect of the fibre content and type in the probabilistic SLD is analysed in this section. The type of mix and the cementitious material were kept constant, and only the fibre content and type varied. The curves of the p_f *versus* depth of chloride ingress for the SLD of 50 years are plotted in Figure 241a, b, c and d, for the groups of mixes W-CIP, W-LEC, R-CIP and R-LEC, respectively.

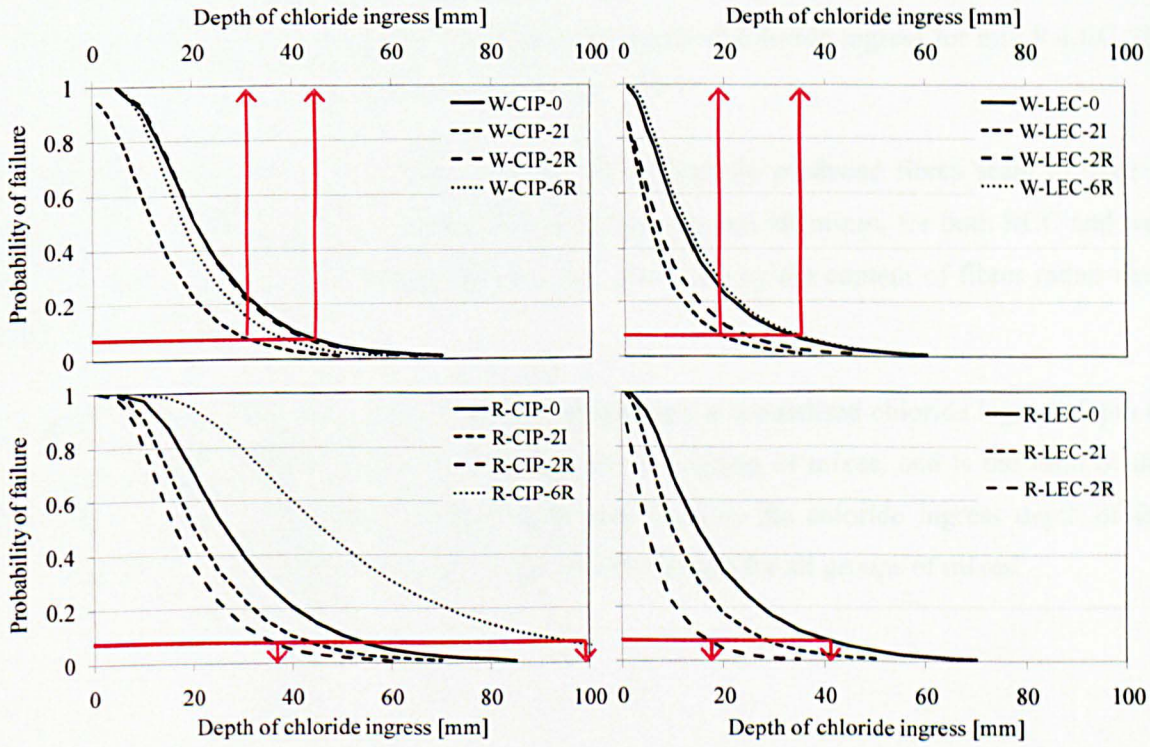

Figure 241 – p_f *versus* depth of chloride penetration for the SLD of 50 years (grouped according to same mix and cementitious material).

It can be seen from the graphs above that the fibre content affects the chloride ingress resistance of the mixes. For the group of W-CIP mixes, 2I mix shows the lowest depth of chloride penetration after 50 years, while plain, 2R and 6R show very similar behaviour among them. The maximum expected depth of chloride penetration (p_f = 7%) after 50 years of SLD should be equal to 31 mm for mix W-CIP-2I against 46 mm for mix W-CIP-0.

A similar behaviour is observed for the group W-LEC. In this case, 2I and 2R mixes have the better performance whilst plain and 6R mixes have the lowest performance. The maximum expected depth of chloride penetration (p_f = 7%) after 50 years of SLD should be equal to 19 mm for mix W-LEC-2I against 34 mm for mix W-LEC-0.

For the R-CIP group of mixes, 2I and 2R mixes show the better performance, followed by the plain concrete. 6R mix, on the other hand, shows the poorest behaviour, following a different pattern than that observed for the other three mixes. The maximum depth of chloride ingress for mix R-LEC-2R is 36 mm whilst for mix R-CIP-6R is 100 mm (p_f = 7%).

In Figure 241d, mix R-LEC-6R is not shown because there seems to be a problem with the parameters of this mix. A similar behaviour in terms of resistance to chloride ingress is observed when comparing to the group of mixes R-CIP: 2R shows the best performance followed by 2I and plain concrete. The maximum depth of chloride ingress for mix R-LEC-2R is 17 mm whilst for plain concrete it is 41 mm (p_f = 7%).

In general, mixes with 2% of either recycled or industrially produced fibres seem to have a higher service life in terms of chloride ingress than plain and 6R mixes, for both RCC and wet mixes. The rate of chloride ingress seems to be influenced by the content of fibres rather than the type of fibres.

Figure 242 shows the influence of the fibre content on the normalised chloride ingress depth at 50 years. The normalised depth is calculated for each group of mixes, and is the ratio of the chloride ingress of the various fibre content and types to the chloride ingress depth of the corresponding plain concrete. The graph includes the results for all groups of mixes.

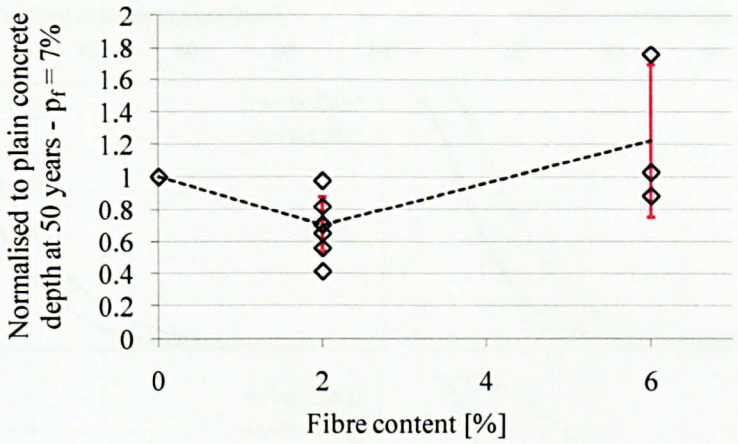

Figure 242 – Influence of fibre content on the depth of chloride ingress.

Despite the large variation observed for the values of the 6R mixes, it is clear that the 2% fibre content gives the lowest depth of chloride ingress compared to the plain and 6R mixes.

Influence of the type of mix

The influence of the type of mix on the SLD of structures is evaluated by comparing the curves of p_f against the depth of chloride penetration, for the SLD of 50 years. Different types of mix (RCC or wet) are compared between them considering that the cementitious material type and fibre content and type are the same. The results presented in Figure 241 are used for this analysis. However, they need to be rearranged to allow the comparison between both types of mix, as shown in Figure 243.

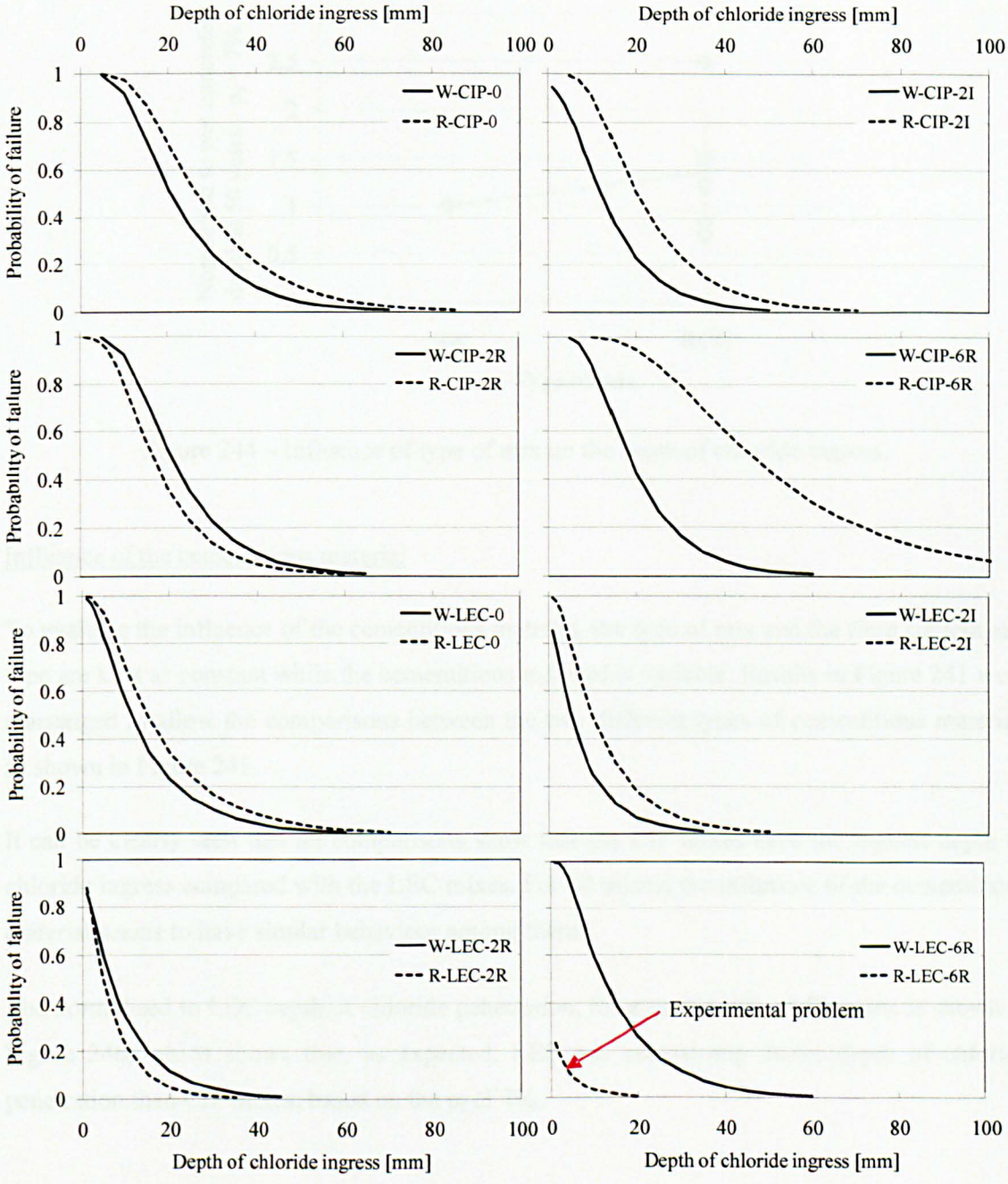

Figure 243 – p_f *versus* depth of chloride penetration for the SLD of 50 years (grouped according to same fibre content and type and cementitious material).

For many graphs above, RCC shows the highest depth of chloride ingress compared with the wet mixes. For the graphs where wet mixes show higher depth values than RCC, it can be seen that both curves are close to each other. The influence of the type of mix on the normalised to wet concrete depth of chloride ingress can be more clearly seen in Figure 244, which indicates the higher resistance of wet mixes to chloride penetration. This is probably due to the lower porosity and refined pore structure of wet mixes.

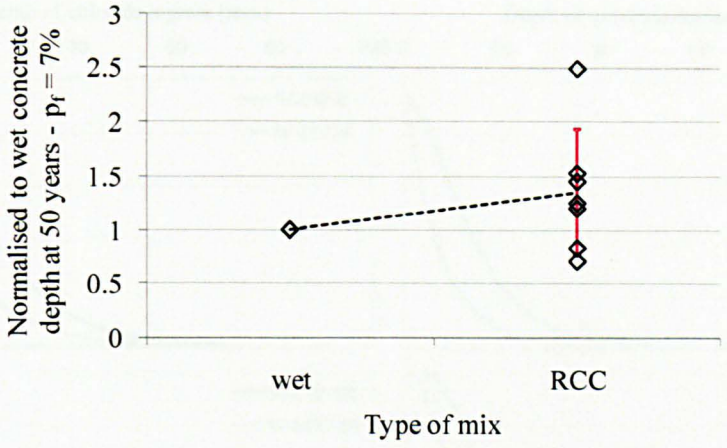

Figure 244 – Influence of type of mix on the depth of chloride ingress.

Influence of the cementitious material

To evaluate the influence of the cementitious material, the type of mix and the fibre content and type are kept as constant while the cementitious material is variable. Results in Figure 241 were rearranged to allow the comparisons between the two different types of cementitious material, as shown in Figure 245.

It can be clearly seen that all comparisons show that the CIP mixes have the highest depth of chloride ingress compared with the LEC mixes. For all mixes, the influence of the cementitious material seems to have similar behaviour among them.

The normalised to LEC depth of chloride penetration, for a service life of 50 years, is shown in Figure 246, which shows that, as expected, LEC has consistently lower depth of chloride penetration than CIP mixes, based on the p_f of 7%.

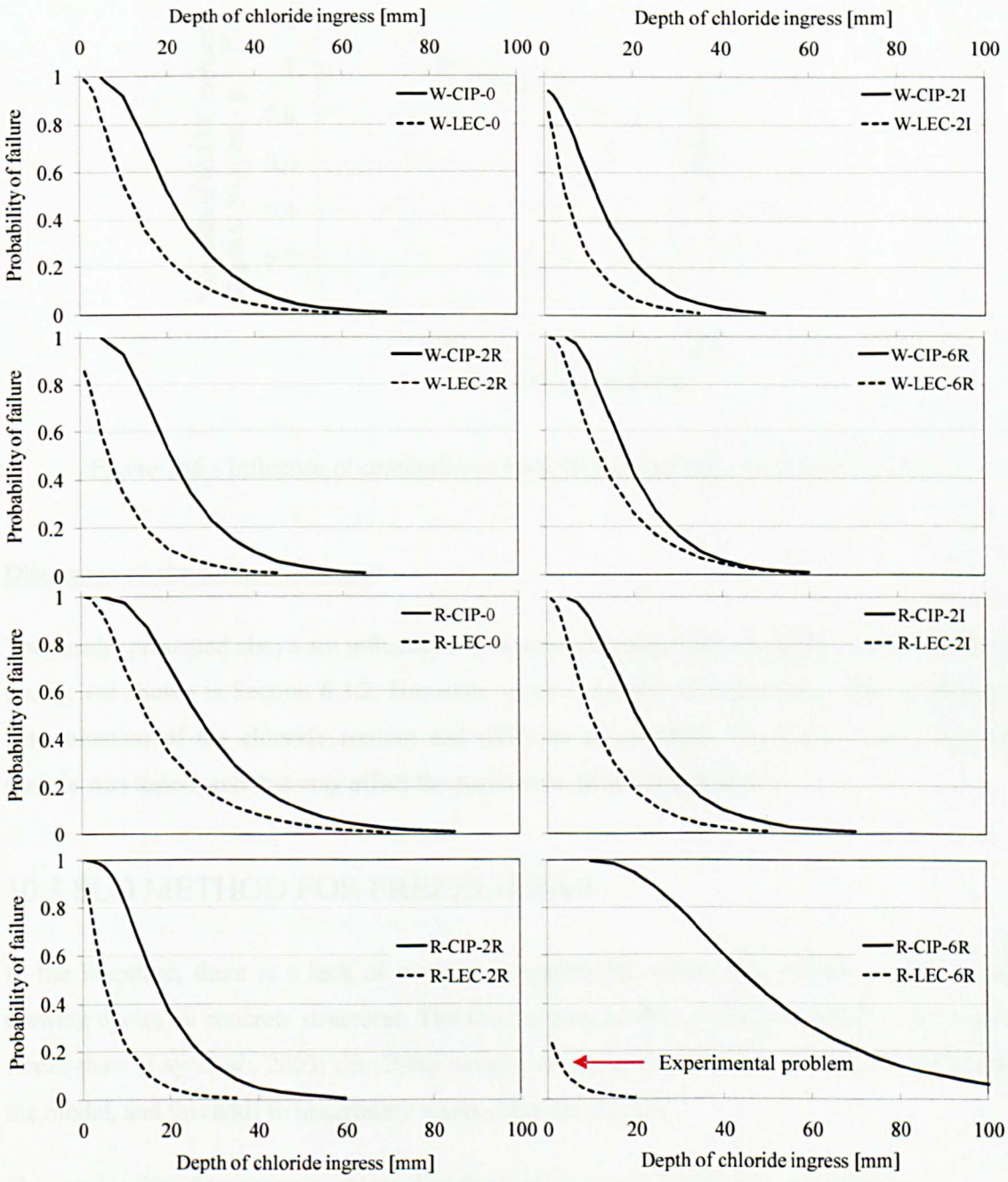

Figure 245 – p_f *versus* depth of chloride penetration for the SLD of 50 years (grouped according to same fibre content and type and type of mix).

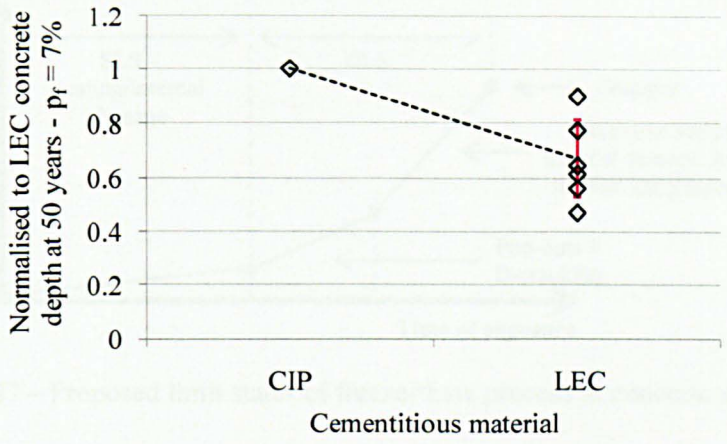

Figure 246 - Influence of cementitious material on the depth of chloride ingress.

Discussion on the parametric study

The results presented above are influenced by a series of parameters, especially by the diffusion coefficient shown is Section 6.3.2. However, some variability is expected in the experimental determination of the chloride content and diffusion of concrete. For many mixes, only one sample was tested, and this may affect the parametric study shown above.

10.3 SLD METHOD FOR FREEZE-THAW

In the literature, there is a lack of models simulating the effects of continuous freezing and thawing cycles on concrete structures. The few existing models on the prediction of SLD due to freeze-thaw (Lay *et al.*, 2003; fib, 2006) usually do not account for the parameters influencing the model, and this adds to uncertainty when using the models.

The service life of a structure subjected to freeze-thaw can be based on two limit states:

1) The serviceability state based on the maximum scaling and/or internal damage the structure can sustain without loss of structural capacity. Maximum acceptable limits for visual appearance and comfort of users.

2) The ultimate limit state caused by excessive scaling and pop-outs, D-crackings, advanced internal damage and loss of structural capacity.

Figure 247 shows a schematic representation of the service life of structures exposed to freeze-thaw.

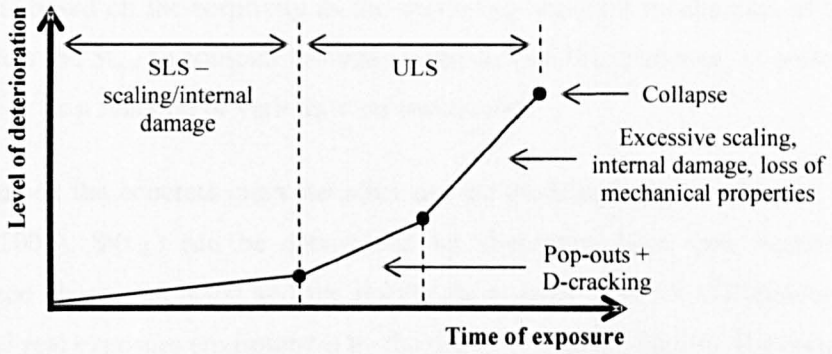

Figure 247 – Proposed limit states of freeze-thaw process in concrete structures.

It can be seen that during the SLS a certain level of deterioration caused by scaling is acceptable. If the concrete is well designed to resist freeze-thaw, the period to reach the SLS is increased and the slope of the rate of deterioration caused by scaling and/or internal damage is reduced or even eliminated.

10.3.1 Serviceability Limit State for Freeze-Thaw

According to fib (2006) and Lay *et al.* (2003), there are basically two SLD methods to predict freeze-thaw SLS in concrete structures based on: 1) induced frost damage and 2) salt-frost induced surface scaling, as described below.

10.3.1.1 Frost induced internal damage

The SLS for frost induced internal damage is given by Equation 33 (fib, 2006), which explains that the limit state is exceeded when the degree of saturation is higher than the critical degree of saturation of the concrete.

$$p_{int.dam.} = p[St_{crit} - St(t_{SL}) < 0] < p_f \quad (33)$$

Where:

$p_{int.dam.}$ = probability that internal damage occurs

St_{crit} = critical degree of saturation at which frost damage starts to occur, dependent on the characteristics of the concrete

$St(t_{SL})$ = saturation at a time t_{SL}

t_{SL} = service life

p_f = target failure probability

Equation 33 is based on the sorptivity as the prevailing transport mechanism of concrete. The model considers the St_{crit} as constant throughout the service life, however, as pointed out by fib (2006), St_{crit} can be a function of various other parameters.

$St(t_{SL})$ depends on the concrete characteristics and the environmental conditions. According to Lay *et al.* (2003), $St(t_{SL})$ can be determined by absorption tests (see Section 3.2.1.2 for commonly used absorption tests) and the results are compensated for differences between the laboratory and real exposure environment by the use of correction factors. However, due to lack of absorption tests in existing structures, an uncertainty aspect needs to be added to the function.

A model proposed by DuraCrete (1998) cited in Lay *et al.* (2003) to predict $St(t_{SL})$ is shown in Equation 34, based on laboratory tests of water absorption.

$$St(t_{SL}) = (St_k + bt_{max}^c)m \quad (34)$$

Where:

St_k = point at which the graph of degree of saturation *versus* square root of time changes slope (from non-saturated to maximum degree of saturation)

b,c = regression parameters obtained from the water absorption test[55]

t_{max} = longest wetting period of the structure during t_{SL}

m = uncertainty model (according to Lay *et al.*, 2003 no uncertainty model is available so far)

t_{max} is dependent on the micro-climate at the concrete surface. According to fib (2006), factors that influence t_{max} are how the concrete is exposed to rain or splash and the frequency and duration of the conditions for drying. Provisional values of t_{max} according to Fagerlund (2004) cited in fib (2006) are: 1) t_{SL} for submerged surface; 2) 4 months for horizontal surfaces which are wet during winter and 3) one week for vertical surfaces exposed to rain and dryness periods.

10.3.1.2 Salt-frost induced surface scaling

The SLS for salt-frost induced surface scaling is based on two principles: 1) the temperature of the concrete and 2) the amount of scaling. The methods are described below.

[55] fib (2006) says that b and c are the slope of degree of saturation *versus* time in logarithmic scale, after S_k, in a long-term water absorption test. However, some further clarification is needed since it is not explained which parameter refers to the slope of the long-term water absorption test, and how the other parameter can be obtained.

Model based on the temperature of the concrete

Equation 35 is used to describe the limit state of salt-frost induced surface scaling based on the temperature of the concrete. The equation shows that the limit state is exceeded when the concrete temperature exceeds the scaling resistance temperature (fib, 2006).

$$p_{scaT} = p[T_R - T(t_{SL}) < 0] < p_f \quad (35)$$

Where:

p_{scaT} = probability that temperature is higher than resistance scaling temperature

T_R = resistance scaling temperature

$T(t_{SL})$ = concrete temperature at a time t_{SL}

t_{SL} = service life

p_f = target failure probability

According to fib (2006), T_R should be determined in the laboratory for a specific type of concrete. For that, specimens should be tested at three freezing temperatures to verify the critical freezing temperature for scaling to occur. The critical amount of scaling should be defined prior to the test. T_R is a time-dependent parameter and is influenced by the characteristics of the concrete.

The concrete temperature can be calculated according to Equation 36 (fib, 2006).

$$T(t_{SL}) = T_{air} + \frac{\alpha_r}{\alpha_r + \alpha_c}(T_{sky} - T_{air}) \quad (36)$$

Where:

T_{air} = temperature of the air [K]

T_{sky} = corresponding sky temperature

= $[1.2(T_{air} - 273) - 14] + 273$ [K], for horizontal surfaces and clear sky;

= $[1.1(T_{air} - 273) - 5] + 273$ [K], for vertical surfaces and clear sky;

= T_{air} [K], for cloudy sky.

α_r = surface heat conductance due to radiation = $4 \times \varepsilon \times \sigma \times \frac{(T_{sky} - T_{air})^3}{2}$ [J/sm^{2}K]

ε = concrete emissivity = 0.9

σ = Stefan-Bolzmann number = 5.67E-8 J/sm^{2}K^4

α_c = surface heat conductance due to convection = $6 + 4u$ [J/sm^{2}K], for wind speed u lower than 5 m/s

T_{air} is usually expressed as a probabilistic distribution of real extreme temperatures of the location of the structure.

The main advantage of this model is that the effect of the temperature is considered in the analysis. However, there is a need to determine experimentally T_R, and no methodology is provided to perform the tests. The critical amount of scaling is considered indirectly when determining T_R (as explained in Equation 35), which adds to uncertainty of the model.

Model based on the amount of scaling

Equation 37 explains the salt-frost induced surface scaling model based on the amount of scaled material, based on the principle that the structure fails when the amount of scaled material exceeds the critical amount of scaled material (Lay *et al.*, 2003).

$$p_{scaS} = p[S_{cr} - S(t_{SL}) < 0] < p_f \quad (37)$$

Where:

P_{scaS} = probability that scaling higher than a limit occurs

S_{cr} = critical limit for scaling

$S(t_{SL})$ = scaled material at a time t_{SL}

t_{SL} = service life

p_f = target failure probability

The model considers that $S(t_{SL})$ can be obtained by correlating accelerated tests with in-situ measurements of scaled material. The correlation is obtained by multiplying the accelerated $S(t_{SL})$, which is associated to a number of freeze-thaw cycles, with a model uncertainty factor.

According to Lay *et al.* (2003), the model uncertainty factor can be described as the equivalent number of accelerated cycles at which the in-situ structure is subjected. The variation in the minimum temperature of the real condition is the main parameter of the model, shown in Equation 38.

$$N_C = \sum_{i=1}^{N} \frac{T_i^2}{T_{ref}^2} \quad (38)$$

Where:

N_c = equivalent number of accelerated cycles

N = number of freeze-thaw cycles in real conditions where the water content in the surface layer of the concrete is high enough to damage the concrete

T_i = lowest temperature in each cycle

T_{ref} = lowest temperature of accelerated tests

There is no explanation if N is related to annual number of cycles or the number of cycles in the entire service life. When dealing with service life prediction, the most appropriate would to be to assume the total expected number of freeze-thaw cycles during the entire service life.

The advantage of this model is that it considers the amount of scaling as the limit state of the structure, and not by indirect measurement as for the previous method. However, even though the temperatures of the cycles are taken into account in the model uncertainty to correlate experimental results with in-situ measurements, there is no information on the lowest temperatures responsible for causing damage to concrete.

Another disadvantage of the method is that the correlation from accelerated freeze-thaw cycles to in-situ structures takes into account only the temperature. It does not consider, for example, the fact that in some accelerated freeze-thaw tests specimens are fully-saturated during freezing and thawing.

10.3.2 Ultimate Limit State for Freeze-Thaw

The existing models for SLD of concrete exposed to freeze-thaw are very limited and very few studies can be found in the area (Lay *et al.*, 2003; fib, 2006; Fagerlund, 2004 cited in Lay *et al.*, 2003). Moreover, these studies are only based on the SLS due to internal damage and scaling and no information can be found on the SLD of concrete exposed to freeze-thaw that accounts for the ULS.

Further investigation is required to account for the ULS in the SLD methods for concrete structures subjected to freeze-thaw. This is especially valid for SFRC, where the number of studies is even more limited than for RC. As reported in Chapter 8, the addition of fibres, especially the recycled fibres, seems to influence the freeze-thaw performance of concrete in terms of scaling and mechanical performance and, as a consequence, should influence the SLD.

10.3.3 Results of Freeze-thaw Probabilistic SLD

The results of the freeze-thaw SLD are initially based on a proposed probabilistic method used to predict the SLD (in terms of SLS) of concrete exposed to freeze-thaw. The probabilistic proposed method is then used to predict the service life design of the mixes subjected to accelerated tests in this study. A sensitivity analysis is also carried out to verify the influence of various assumed parameters in the proposed method of SLD for freeze-thaw exposed structures.

10.3.3.1 Proposed Probabilistic Method to predict SLD of Concrete Exposed to Freeze-Thaw

Fundamentals and main procedures of the method

Due to the lack of examples of practical applications for the models described in the previous section, there is an attempt in this thesis to propose a freeze-thaw SLD method based on a practical example.

The method combines some of the information described in the previous section, especially regarding the salt-frost induced surface scaling. This is because the experimental results obtained from the freeze-thaw accelerated tests used immersion of specimens in chloride solution.

Data of weather stations based on extreme temperatures should be used to obtain the number of freezing cycles at which a concrete structure is subjected to during the period of one year. The number of freezing cycles is the number of times, in one year, at which the real temperature of concrete drops below the critical lowest temperature at which scaling (damage) occurs. The concrete temperature is calculated according to fib (2006), using Equation 36.

To account for the effect of ageing of concrete (as proposed by fib, 2006), the critical temperature needs to be multiplied by an ageing factor. No studies appear in the literature on the ageing frost resistance, hence, the influence of ageing on T_R is taken into account by adopting the BS EN 1992-1-1 (2004b) equation for predicting the ageing effect on compressive strength of concrete, described in Equation 39. However, it is important to add that this expression is used due to the lack of more appropriate equations to predict the effect of ageing on T_R. Therefore, further investigation is needed to verify whether or not the equation below is valid for the purpose that it is used in this work.

$$\beta_{cc}(t) = exp\left\{s\left[1 - \left(\frac{28}{t}\right)^{0.5}\right]\right\} \quad (39)$$

Where:

s = coefficient depending on the cementitious material

t = time of exposure

The ageing effect on T_R is finally described by Equation 40.

$$T_R(t) = T_R\beta_{cc}(t) \quad (40)$$

To account for the effect of accelerated tests[56], the equivalent number of cycles, N_c, in real situations (compared to the accelerated condition) is calculated based on Equation 38 (Lay *et al.*, 2003).

The fact that not all freezing cycles in real conditions occur when concrete is wet is taken into account by correlating the equivalent number of cycles, N_c, with the number of wet days in the period where freezing occurs, N_{wd}, which is obtained from meteorological stations close to the area where the structure is located. The equivalent number of cycles is then called the effective number of wet cycles, N_{wfc}, which is obtained by multiplying N_c by a constant depending on the number of wet days. Assuming that freezing cycles occur only in half a year (mainly in winter, end of autumn and beginning of spring), N_{wfc} can be described based on the probability that both events (wet and freezing cycles) occur at the same time, which is given by Equation 41.

$$N_{wfc} = \left(\frac{N_c \times N_{wd}}{\frac{365}{2}}\right) \quad (41)$$

Where:

N_{wd} = number of wet days during the period where freezing cycles occur.

The effective number of wet cycles at which a structure is subjected gives an indication of the freeze-thaw damage (amount of scaling). The correlation of number of cycles to scaling, for the purpose of this study, is based on the loss of mass results of the accelerated freeze-thaw tests, shown in Section 8.2. Since the freeze-thaw resistance depends on the characteristics of the concrete, each concrete mix needs to have its own correlation of scaled material and number of cycles.

[56] Accelerated freeze-thaw tests usually increase the damage of the concrete, for a certain number of cycles compared to in-situ structures, due to fact that more severe conditions are used (e.g. lower temperatures, fully-saturated condition).

The amount of scaling is then calculated, per year, based on regressions obtained from experimental data, considering the effective number of wet cycles. The effective number of wet cycles in one year is then cumulatively added to subsequent years, since damage caused by freeze-thaw depends on the cumulative number of freezing cycles.

The method also accounts for another level of aggressiveness of the accelerated freeze-thaw tests (not only based on the lowest temperature), caused by the constant full immersion of specimens in chloride solution. This is accounted by multiplying the amount of scaling by a model uncertainty factor.

The amount of scaling, after a certain period of time, is finally compared to the critical amount of scaling allowed at the SLS. The output result is the probability of failure (probability that the amount of scaling is higher than the critical amount of scaling) after a certain period of exposure to freezing and thawing cycles (usually defined as the expected service life of the material).

Practical example of the method

A practical example based on the proposed method of SLD for frost-exposed concrete is described in this subsection, with explanation of the parameters used for the probabilistic SLD.

The resistance temperature T_R of the concrete was assumed as proposed by Cai and Liu (1998), which says that most effects of freeze-thaw in concrete occurs when the concrete temperature ranges from 0 °C (273 K) to -5 °C (268 K). Due to lack of acceptable distributions, T_R was assumed as a beta distribution with mean -2.5 °C (270.5 K), and lower and upper bounds of -5 °C (268 K) and 0 °C (273 K), respectively. Beta distributions are commonly used to generate random numbers where the distribution is limited by lower and upper bounds. According to fib (2006), T_R can be calculated in laboratory conditions for each mix proportion. Nevertheless, further investigations should be carried out to develop procedures to perform the test.

The same ageing coefficient, *s*, used for chloride ingress (Section 10.2.3.1) is used in this analysis. The ageing coefficient is described as a beta distribution with mean 0.6, standard deviation of 0.15 and lower and upper bounds equal to 0 and 1, respectively, according to fib (2006).

The temperature of the concrete is calculated by considering the radiation and convection influence, as showed previously in Equation 36. The air temperature T_{air} is based on real data of the lowest daily temperatures of the city of Sheffield, UK, based on meteorological data from 2006 to 2009 (Sheffield Weather, 2011), as shown in Figure 248. The lowest temperatures comprise the period of half a year, from end of autumn to beginning of spring, when there is

chance for the temperatures to go below zero. T_{air} is assumed as a normal distribution with mean 2.9 °C (275.9 K) and standard deviation of 3.2 °C (3.2 K).

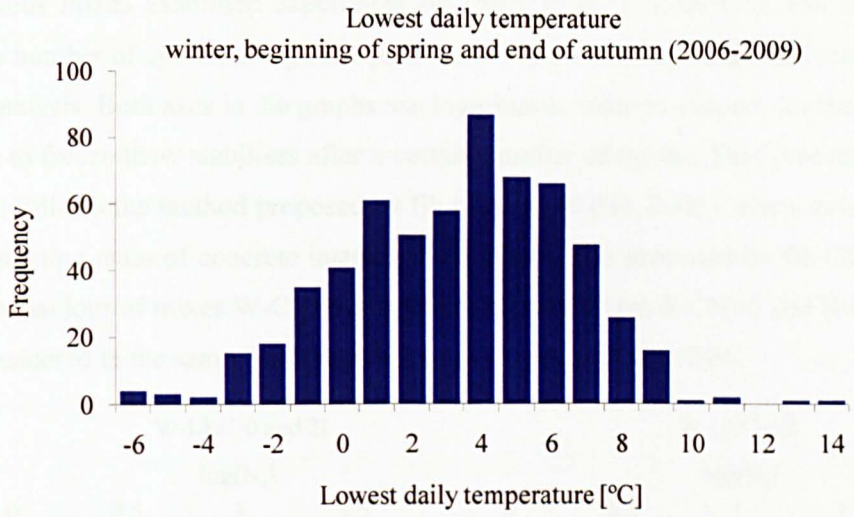

Figure 248 – T_{air} for Shefield, UK.

The wind speed was assumed as a deterministic value equal to 4.12 m/s, based on data for Sheffield, UK (MetOffice, 2010).

The Monte Carlo framework is used to calculate the number of cycles reaching temperatures below T_R. For that, 36500 simulation cycles are used[57], and the simulation cycles with concrete temperature lower than the resistance temperature are used to calculate the equivalent number of accelerated cycles N_c, according to Equation 38. T_{ref} in Equation 38 is the lowest temperature of the accelerated tests: -15 °C (258 K).

The value of N_c is then divided by 100 to obtain the equivalent number of cycles in 365 (36500 simulations divided by 100)[57] days.

For the purpose of this study, the number of wet days N_{wd} is obtained by the average of the number of wet days per year from 1971 to 2000, in a weather station located in Sheffield, UK (MetOffice, 2010). According to MetOffice (2010), the number of wet days in winter is approximately 45 days while in summer it drops to 35 days.

Assuming that the number of wet days in spring and autumn is the average of the number of wet days in summer and winter (= 40 days), N_{wd} in Sheffield, UK can be assumed as 85 days (45 days in winter and 40 days in the end of autumn and beginning of spring). N_{wd} can be assumed as a distribution function, however, due to the lack of data for the standard deviation from the

[57] The number of simulations may vary. In this case, 36500 simulations were used to make it easy to correlate the number of simulations to the total number of days in a year by dividing 36500 by 100.

weather station data, it is assumed as a deterministic value in this example. N_{wfc} is calculated following Equation 41.

For the various mixes examined experimentally (Section 8.2), scaling, *S*, can be calculated based on the number of cycles, using the equations in Figure 249 which are derived using linear regression analysis. Both axes in the graphs use logarithmic scale to account for the fact that the damage due to freeze-thaw stabilises after a certain number of cycles. This procedure to assess deterioration follows the method proposed by fib bulletin 40 (fib, 2007). The *y* axis is shown in terms of remaining mass of concrete instead of mass loss, also proposed by fib (2007). Due to the similar behaviour of mixes W-CIP-0 and W-CIP-2I and mixes R-CIP-0 and R-CIP-2I, each pair was considered in the same linear regression, as shown in Figure 249.

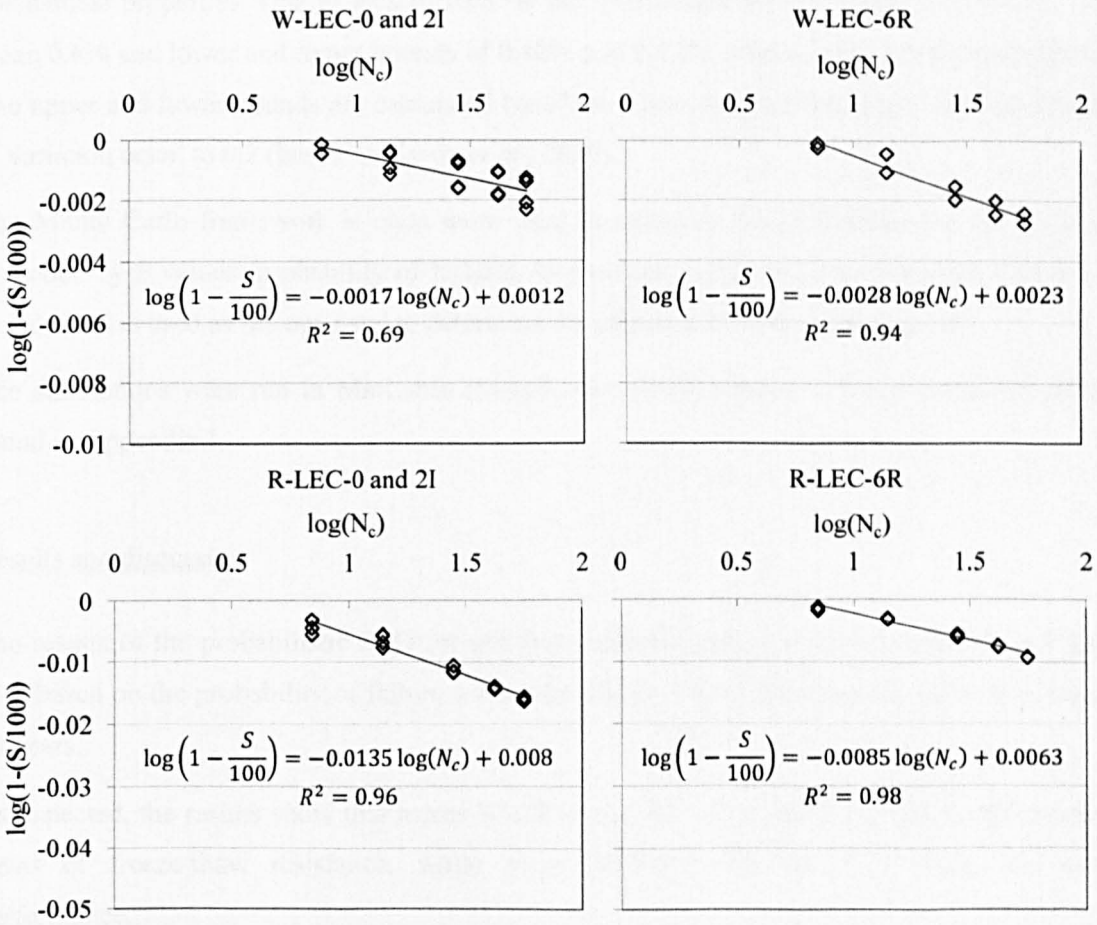

Figure 249 – Correlation of N_c to scaling S.

The results of S also need to be multiplied by a model uncertainty factor to account for the level of aggressiveness of the accelerated tests, due to the fact that specimens are fully-submerged in the chloride solution for the entire period of the test. This environment, as already mentioned in Section 3.1.3, contributes to a higher level of freeze-thaw deterioration of the specimens. Due to lack of data on model uncertainty factor, this is assumed to have a lognormal distribution with mean 0.8 and coefficient of variation of 0.2 (this coefficient of variation is commonly used

when dealing with probabilistic analysis, also used in Kwon *et al.*, 2009). The value of model uncertainty factor can be determined experimentally by comparing the level of deterioration of specimens subjected to freezing and thawing cycles in fully-submerged conditions and in partially-saturated conditions (DD EN 12390-9, 2006c provides three alternative methods of accelerated freeze-thaw tests).

The values of S are then compared with the maximum allowed scaling, S_{cr}, for the structure not to exceed a SLS. There are no values of S_{cr} in the literature and, as a consequence, the values of S_{cr} were obtained based on the visual analysis carried out in this thesis (Section 8.1). The visual analysis shows that up to 0.6% of loss of mass, the surface (finishing level) of the specimens can still be seen (no serious surface deterioration) and there is no significant loss in the mechanical properties. Due to lack of data on the distribution for S_{cr}, a beta distribution with mean 0.6% and lower and upper bounds of 0.48% and 0.72%, respectively, are assumed for S_{cr}. The upper and lower bounds are calculated based on ± one standard deviation, for a coefficient of variation equal to 0.2 (based on Kwon *et al.*, 2009).

The Monte Carlo framework is once more used to calculate the probability for the S_{cr} to be exceeded by S values (probability of failure), in a certain period of time. The same number of simulations is used as the one used to determine the effective number of wet cycles.

The simulations were run in MatLab® (MathWorks, 2010) version 7.7 and the script can be found in Appendix I.

Results and discussion

The results of the probabilistic SLD for salt-frost induced surface scaling are shown in Figure 250, based on the probability of failure *versus* the service life of the structure, up to the limit of 50 years.

As expected, the results show that mixes W-CIP-0 and W-CIP-2I have the best performance in terms of freeze-thaw resistance, while mixes R-CIP-0 and R-CIP-2I show the worst performance.

If the maximum p_f according to BS EN 1990 (2002c) is taken into account (p_f = 7%, reliability index = 1.5), the expected service life of the mixes analysed for freeze-thaw is: 41 years for mixes W-LEC-0 and W-LEC-21; 25 years for mix W-LEC-6R; 8 years for mixes R-CIP-0 and R-CIP-2I and 11 years for mix R-CIP-6R. None of the mixes would be able to endure the target service life of 50 years without exceeding the SLS assumed for the model.

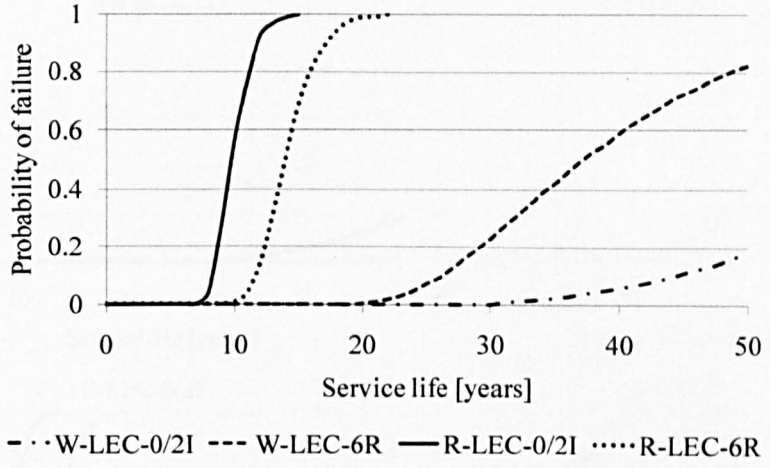

Figure 250 – Probabilistic SLD for concrete structures subjected to freeze-thaw.

However, it is important to add that the results above are dependent on many parameters that were assumed for the analysis, and that many of them play an important role in the model results, such as the loss of mass results from the accelerated tests. A sensitivity study was carried out to verify the influence of these parameters in the output result of the freeze-thaw SLD, as shown below.

10.3.3.2 Sensitivity Analysis

The parameters analysed are resistance temperature, critical scaling and model uncertainty, as shown below.

Influence of resistance temperature

The influence of using different resistance temperatures on the proposed method to simulate SLD of frost-exposed concrete is shown in Figure 251. Three T_R beta distributions are used based on the decrease of increments of 1 °C from the mean, maximum and minimum temperatures. The distributions analysed, in terms of [mean, minimum and maximum T_R] are: 1) [-2.5 °C (270.5 K), -5 °C (268 K), 0 °C (273 K)]; 2) [-3.5 °C (269.5 K), -6 °C (267 K), -1 °C (272 K)]; 3) [-4.5 °C (268.5 K), -7 °C (266 K), -2 °C (271 K)].

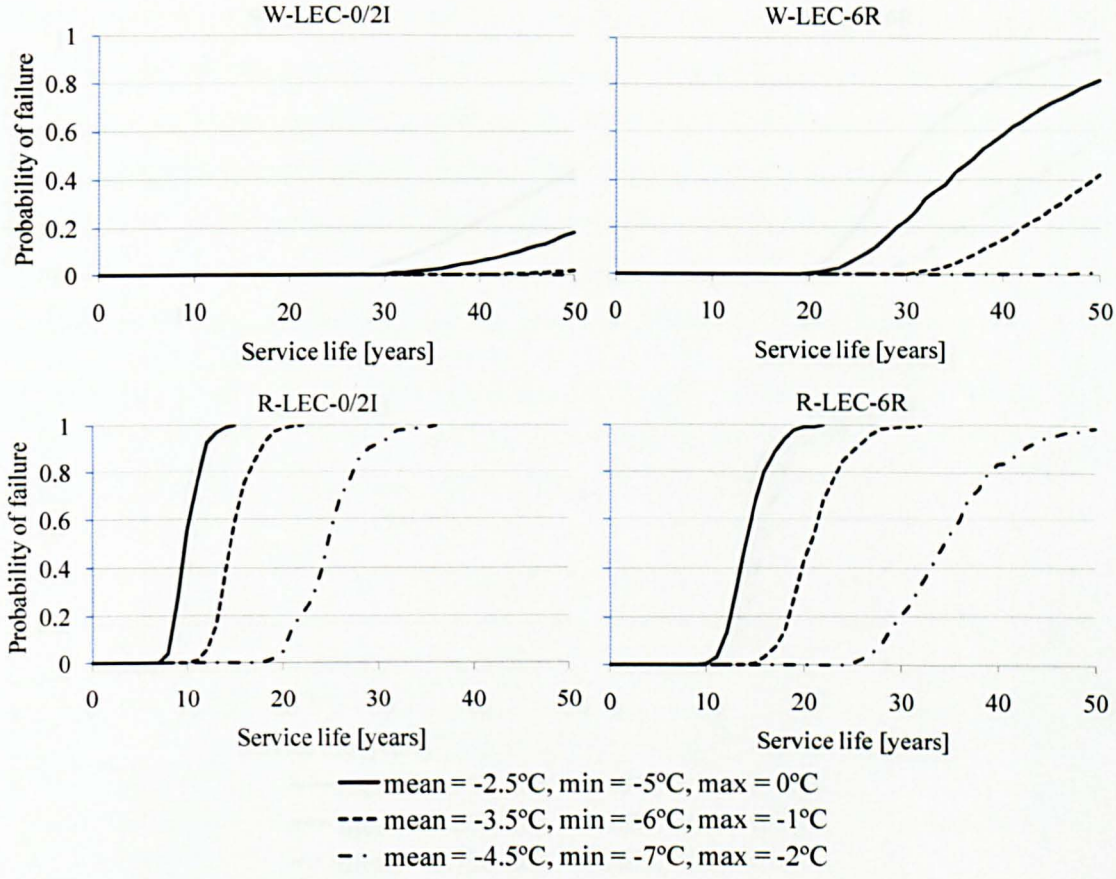

Figure 251 – Influence of resistance temperature on SLD of frost exposed concrete.

The resistance temperature plays an important role on the freeze-thaw SLD, since small changes of 1-2 °C affects considerably the results. Figure 251c and d show that a decrease of 2 °C in the mean T_R more than doubles the service life of the structure.

The influence of T_R on the freeze-thaw SLD depends on the characteristics of the mixes.

The fact that T_R considerably influences the results agrees with the fact that there is a need to determine the true resistance temperature of the concrete when dealing with freeze-thaw SLD methods.

Influence of critical scaling

The influence of the critical scaling on the SLD of frost-exposed concrete is shown in Figure 252. Three different beta distributions of S_{cr} are considered in the comparison, by varying in ± 0.1 the mean value. The distributions used, in terms of [mean, minimum and maximum S_{cr}] are: 1) [0.5%, 0.4%, 0.6%]: 2) [0.6%, 0.48%, 0.72%]; 3) [0.7%, 0.56%, 0.84%]. The upper and lower bounds were calculated based on ± one standard deviation, for the coefficient of variation equal to 0.2.

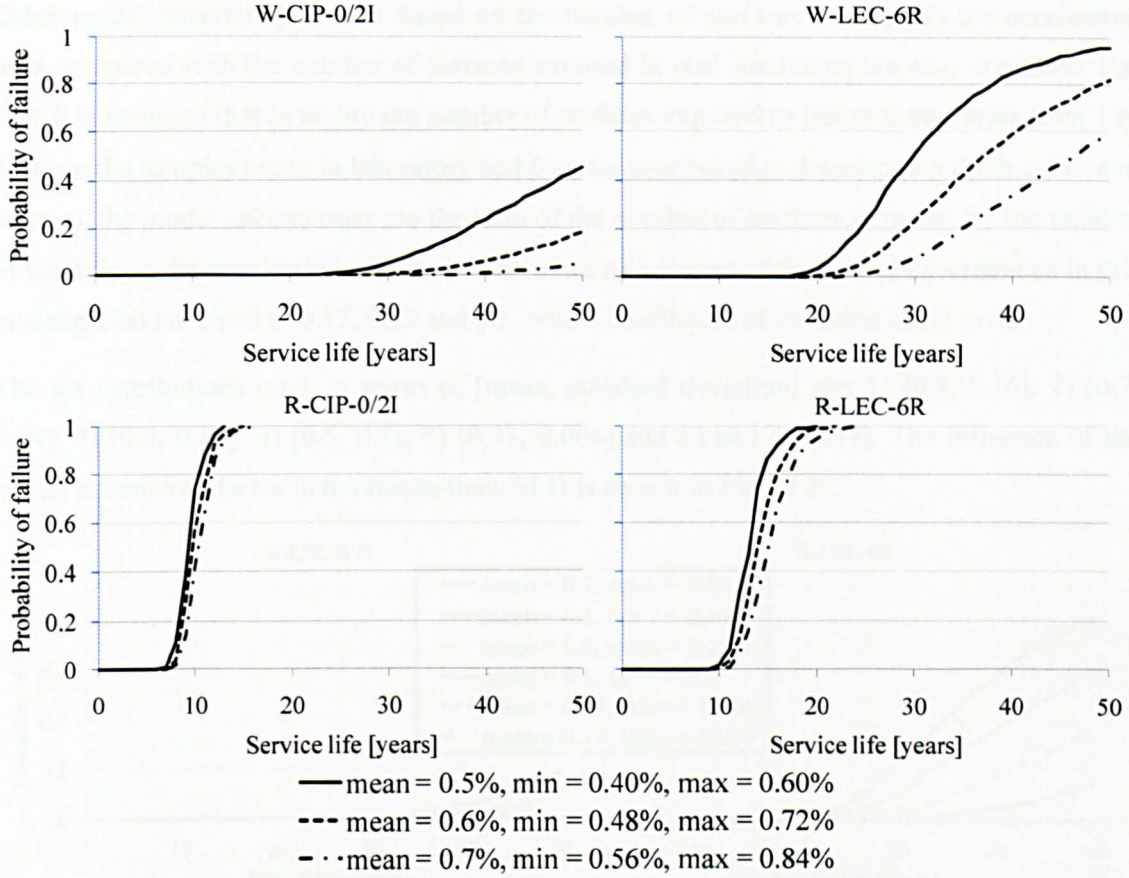

Figure 252 – Influence of critical scaling on SLD of frost exposed concrete.

The critical scaling also affects the endurance life in the proposed SLD method. The effects of using a different value of S_{cr} on the freeze-thaw SLD depends on the characteristics of the mix.

Variations of ± 0.1% in the values of S_{cr} affect more the results for wet mixes than for RCC mixes. This is because RCC mixes have a much more accentuated level of scaling than wet mixes. RCC mixes are probably more influenced by changes in S_{cr} if a higher standard deviation is used or if higher values of S_{cr} are assumed.

As pointed out on the discussion of the limitations and characteristics of the method, there is a lack of data on the critical value of scaling and more work should be carried out to calibrate the proposed SLD method.

Influence of model uncertainty factor

The influence of the model uncertainty factor is analysed by decreasing the mean model uncertainty by increments of 0.1. The log-normal distributions have the coefficient of variation equal to 0.2.

Other model uncertainty factors based on the number of surfaces exposed in the accelerated tests compared with the number of surfaces exposed in real conditions are also examined. For that, it is assumed that in reality the number of surfaces exposed to freeze-thaw varies from 1 to 3. Since the samples tested in laboratory had 6 surfaces exposed to deterioration (both cubes and prisms), the model uncertainties are the ratio of the number of surfaces in reality by the number of surfaces in the accelerated condition. Therefore new means of the model uncertainties in this investigation are equal to 0.17, 0.33 and 0.5, with a coefficient of variation equal to 0.2.

The six distributions used, in terms of [mean, standard deviation] are: 1) [0.8, 0.16]: 2) [0.7, 0.14]; 3) [0.6, 0.12]; 4) [0.5, 0.1]; 5) [0.33, 0.066] and 6) [0.17, 0.034]. The influence of the model uncertainty factor in the freeze-thaw SLD is shown in Figure 253.

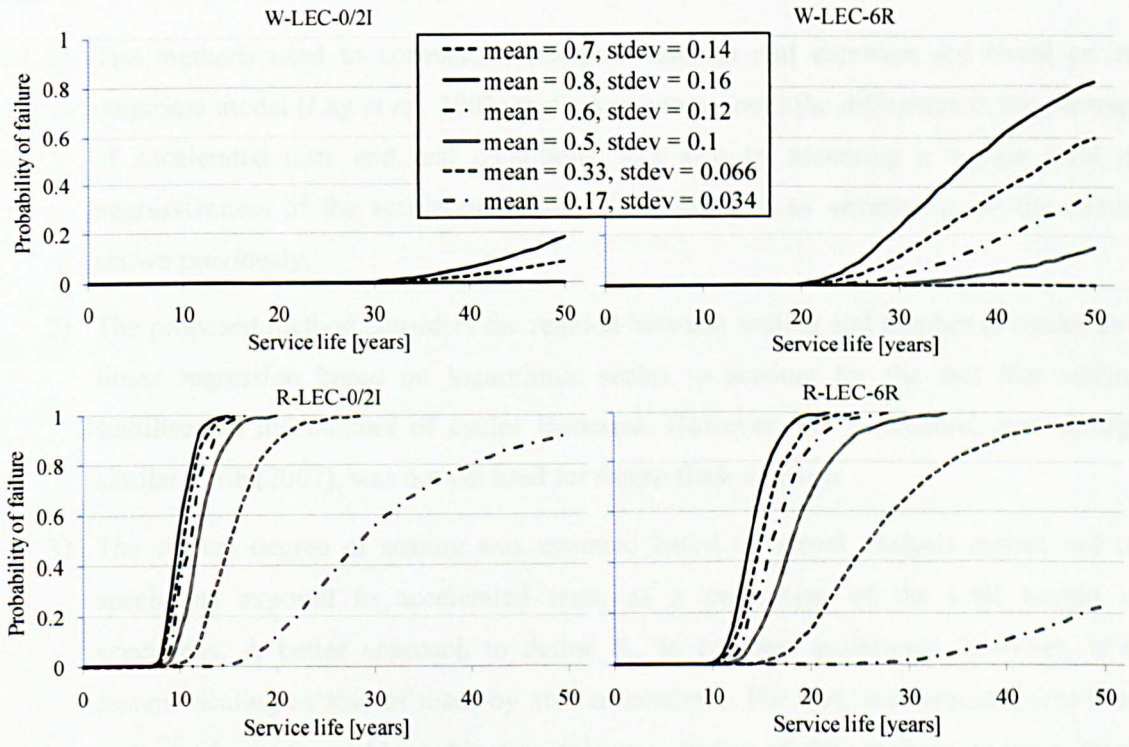

Figure 253 – Influence of model uncertainty on SLD of frost exposed concrete.

The model uncertainty factor affects considerably the endurance life of both RCC and wet mixes. If the model uncertainty is based on the number of surfaces exposed to freeze-thaw, and considering that pavements have usually only one main surface prone to freeze-thaw deterioration, it can be seen that the RCC mixes show a much better behaviour than when using higher values of model uncertainty factor. It is also important to note that pavements with RCC mixes are most probably sealed with an asphalt layer (due to lower rolling resistance than asphalt and other concrete pavements), which means that the contact of the pavement with water is most probably eliminated, unless the pavement is placed directly on the subgrade (without base and subbase layers).

More information on the correlation of accelerated tests and real exposure should be undertaken to allow good predictions of freeze-thaw SLD.

10.3.3.3 Characteristics and limitations of the method

The proposed method to predict SLD of concrete structures exposed to freeze-thaw seems to convergence well and to give results that are within acceptable limits. However, it can be seen that, even though the concretes used in the example were actually designed to have a good freeze-thaw resistance over the service life of 50 years, none of them are durable enough to endure this period of time without exceeding the scaling SLS.

This can be attributed to the following factors:

1) The methods used to correlate accelerated tests to real exposure are based on an empirical model (Lay *et al.*, 2003) that takes into account the difference in temperature of accelerated tests and real conditions, and also by assuming a certain level of aggressiveness of the accelerated tests, which leads to an uncertainty on the results shown previously.

2) The proposed method considers the relation between scaling and number of cycles as a linear regression based on logarithmic scales to account for the fact that scaling stabilises as the number of cycles increases. However, this procedure, even though similar to fib (2007), was not yet used for freeze-thaw damage.

3) The critical degree of scaling was assumed based on visual analysis carried out on specimens exposed to accelerated tests, as a percentage of the total weight of specimens. A better approach to define S_{cr} in concrete pavements, however, is to assume scaling as loss of mass by area of concrete. For that, accelerated freeze-thaw tests can be performed by subjecting only one surface of the specimen to frost attack. As an example, the accelerated freeze-thaw plate test method suggested by DD EN 12390-9 (BS, 2006c) may be used.

4) The resistance temperature of the concrete was assumed from information in the literature (Cai and Liu, 1998). However, each mix proportion has its own freeze-thaw resistance temperature (the finer the pore structure, the lower is the resistance temperature)[58]. A methodology to determine the resistance freeze-thaw temperature of specimens should be developed.

The method takes into account the SLS due to scaling only. To account for the effects of internal damage, some of the information shown in Section 10.3.1.1 can be followed.

[58] Finer capillaries freeze at lower temperature than larger pores.

10.4 FATIGUE PROBABILISTIC ANALYSIS

Due to the high variability usually encountered when analysing the fatigue behaviour of plain and SFRC in terms of $s - log(N)$ curves, this analysis focuses on the probabilistic reliability analysis, aiming to provide more information on how to correlate the stress levels and the number of cycles obtained from Section 9.2 to a certain probability of failure.

The analysis presented in this section can be used in practice, for design purposes, to predict the fatigue resistance of the mixes investigated in this thesis for a specific probability of failure.

10.4.1 Graphical Method – Procedures

The graphical method proposed by McCall (1958) and slightly modified by Singh *et al.* (2005a and 2008) was used to obtain the family of $s - log(N) - p_f$ curves (where p_f is the probability of failure) for each mix.

The specimens tested at each stress level are first ranked according to the crescent number of cycles N_i, as shown in Table 36 (mix R-CIP-0 at stress level of 0.5). The mean and the standard deviation of the log(N_i) values are also calculated. The mean was subtracted from the value of log(N_i), for each specimen, and then divided by the standard deviation $\left(\frac{|\log(N_i)-\mu|}{\sigma}\right)$.

Table 36 – Ranking of specimens for probabilistic analysis (mix R-CIP-0 at stress level of 0.5).

i	N_i	$Log_{10}(N_i)$	Mean μ and standard deviation σ of log(N_i)	$\frac{\lvert\log(N_i)-\mu\rvert}{\sigma}$	Remark
1	295400	5.47		1.18	discarded
2	296050	5.47		1.18	discarded
3	756903	5.88	$\mu = 5.92$	0.11	OK
4	1305150	6.12	$\sigma = 0.38$	0.50	OK
5	2000000	6.30		0.99	OK
6	2000000	6.30		0.99	OK

This procedure is performed because the number of specimens for all stress levels should be the same. Since usually only 4 specimens were tested at the stress level of 0.9, all other stress levels should conform to this number of specimens. The procedure shown in table below was performed to reduce from 6 to 4 the number of specimens at the stress level of 0.5.

The specimens showing the highest values of $\frac{|\log(N_i)-\mu|}{\sigma}$ were discarded from the probabilistic analysis. This procedure follows the Chauvenet's criterion of rejection, which considers as

outliers the values that deviate significantly from the mean. Considering the example described in the table above, it can be seen that the specimens 1 and 2 were not taken into account in the probabilistic analysis.

The next step for the graphical representation of the family of $s - log(N) - p_f$ curves comprises the calculation of the p_f for each rank of specimens. The p_f is calculated by dividing the rank of specimens i by $(n+1)$, where n is total number of specimens tested per stress level. According to Singh *et al.* (2005a), the ratio m/(n+1) can be considered as the best estimate of probability of failure for fatigue analysis.

Table 37 shows the probability of failure for each rank (mix R-CIP-0). The rank is divided by $(n+1)$ instead of n to prevent the specimen with the highest fatigue resistant from having a probability of failure equal to *1* (Singh *et al.*, 2005a and 2008).

Table 37 – Number of cycles and probability of failure (mix R-CIP-0).

i	Stress level			$p_f = \frac{i}{(n+1)}$
	0.5	0.7	0.9	
1	756903	36850	1915	0.2
2	1305150	99175	1975	0.4
3	2000000	136072	2056	0.6
4	2000000	402839	3791	0.8

The family of $log(N) - p_f$ curves is the first to be obtained (one curve per stress level), followed by the $s - log(N)$ (one curve per p_f). The $s - p_f$ family of curves (one curve per each chosen number of cycles: 4000, 10,000, 100,000, 500,000 and 1 million) is then obtained by graphical interpolation, based on the linear approximation curves plotted on the $s - log(N)$ graph. The detailed explanation of the steps for the graphical calculation is shown in Appendix J.

10.4.2 Mathematical Method – Procedures

The probability of failure can also be calculated by a mathematical model. According to McCall (1958), the function that describes the $s - log(N) - p_f$ relationship is shown in Equation 42. The equation is based on the general form of the $s - log(N)$ curves and by relationships used by other authors (refer to the McCall, 1958 for the list of authors).

$$p_f = 1 - 10^{-a(s)^b(logN)^c} \quad (42)$$

Where:

p_f = probability of failure

s = stress level

N = number of cycles

a, b, c = experimental constants

The values of a, b and c were obtained based on the fatigue life data obtained from the experiments, for each mix. The constants shown in Table 38 were obtained following the procedures described in McCall (1958) and Singh *et al.* (2005a and 2008). More information about the numerical method used to obtain the constants can be found in Appendix J.

Table 38 – Experimental constants based on the fatigue life data.

Mix	Experimental constants		
	a	b	c
W-CIP-0	4.45E-1	13.65	5.15
W-CIP-2R	2.00E-3	16.07	7.90
W-CIP-6R	2.69E-4	24.75	12.86
R-CIP-0	1.01E-12	22.16	22.30
R-CIP-2I	5.10E-3	4.49	3.96
R-CIP-2R	1.27E-1	6.95	2.71
R-CIP-6R	1.52E-7	16.30	12.91

10.4.3 Results – Graphical and Mathematical Methods

The $s - log(N) - p_f$ family of curves for each mix, from both graphical and mathematical methods, is shown in Figure 254 to Figure 260. The $log(N) - p_f$ curves are presented in the graph in the bottom left, the $s - log(N)$ curves are shown in the upper right graph and, finally, the $s - p_f$ curves are shown in the upper left graph of the figures below.

10.4.3.1 Wet mixes

W-CIP-0

The results presented for mix W-CIP-0 (Figure 254) show that the mathematical model does not fit very well the results from the graphical interpolation method, especially when taking into account the s–p_f family of curves. This is mainly due to the reduced number of specimens used

for the graphical interpolation method, which led to a low correlation to many of the linear regressions used for the *s–log(N)* family of curves.

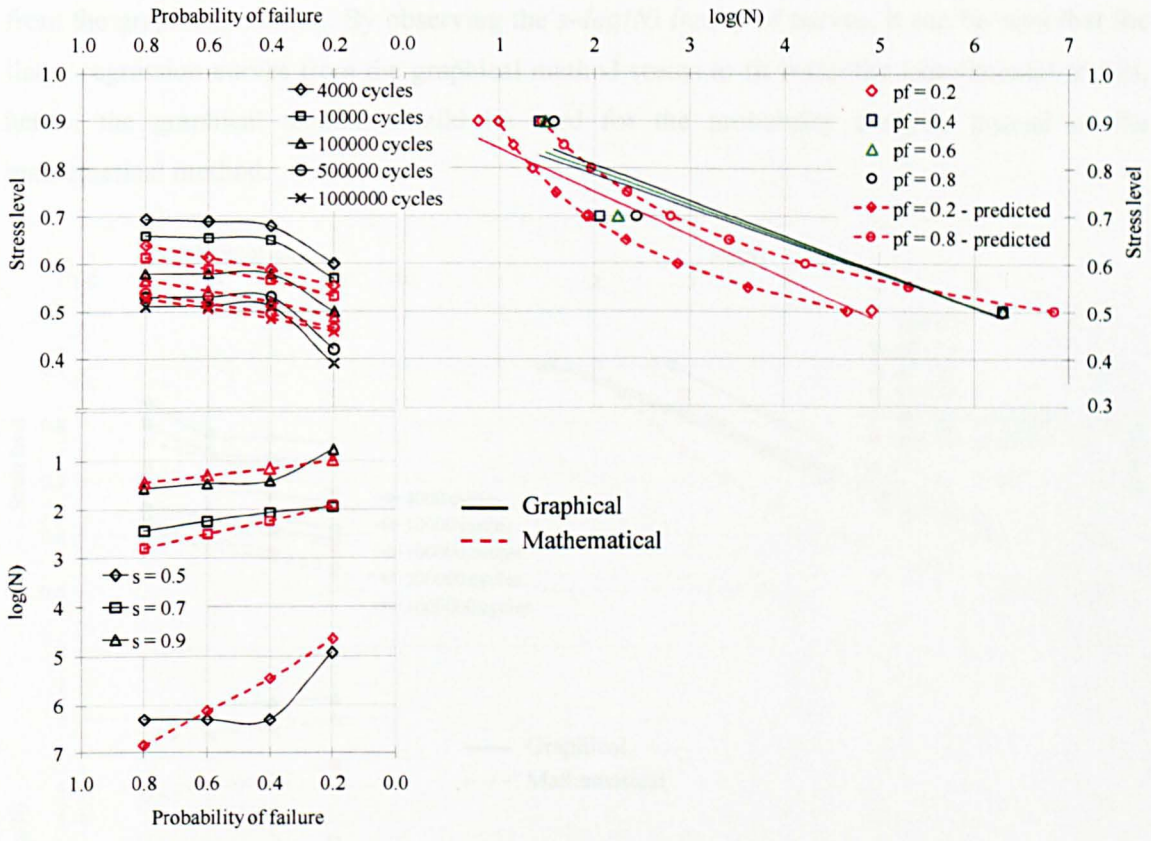

Figure 254 – Probabilistic analysis for mix W-CIP-0.

However, it can be seen that the non-linear curves of the mathematical method seems to fit better the *s–log(N)* results, which means that, for this particular case, the mathematical model predicts the fatigue life of concrete more accurately than the graphical method.

By analysing the s-pf family of curves, and taking into account the mathematical model (which gives the best fit for the experimental results), it can be observed that there is a probability of failure of 80% when specimens are subjected to 1 million cycles at the stress level of 0.53. The probability reduces to 20% when the stress level drops to 0.46. It can also be verified that the mix has very low resistance to high stress levels. There is a probability of 80% for the specimens subjected to the stress level of about 0.64 to fail before reaching 4000 cycles.

A change in the stress level from approximately 0.50 to 0.60 changes drastically the fatigue behaviour of the mix (reference to a probability of failure equal to 50%). This means that at the stress level of 0.5 the specimens should resist up to 1 million cycles, and at the stress level of 0.6 the specimens should resist only up to 4000 cycles.

W-CIP-2R

The results of the mathematical method for mix W-CIP-2R (Figure 255) do not fit the results from the graphical method. By observing the *s–log(N)* family of curves, it can be seen that the linear regression curves from the graphical method seems to fit better the experimental results, hence, the graphical method should be used for the probability analysis instead of the mathematical method.

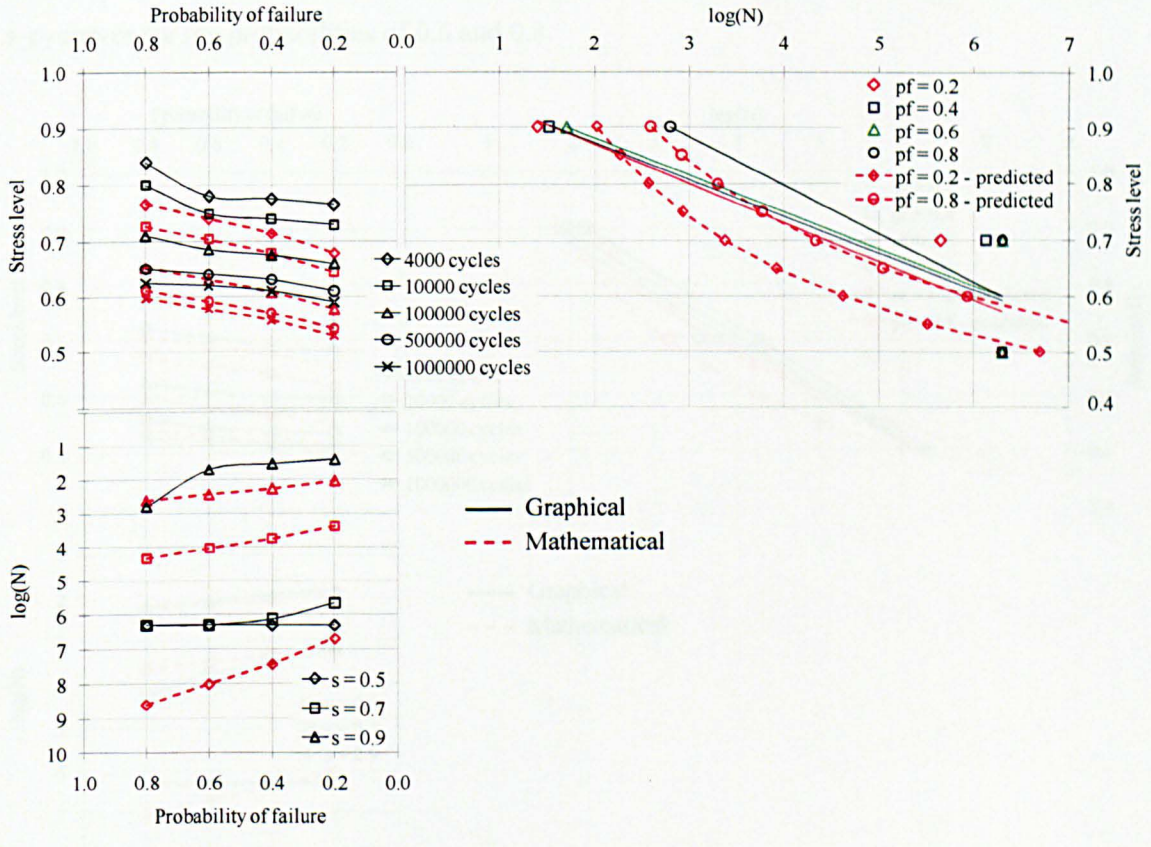

Figure 255 – Probabilistic analysis for mix W-CIP-2R.

Mix W-CIP-2R has better performance than mix W-CIP-0 when subjected to high as well as low stress levels. The mix should achieve one million cycles at the stress level of 0.6, with a probability of failure of 20%. The mix should resist up to 4000 cycles with a stress of 0.84, with a probability of failure of 80%.

The fatigue performance of the mix changes considerably if the stress level changes from 0.62 to 0.78 (with reference to a probability of failure equal to 50%). This interval is higher than the same interval for mix W-CIP-0, which means that a small change in the stress level for 2R mix does not affect the fatigue performance as much as for plain wet mix.

W-CIP-6R

Figure 256 shows that, for mix W-CIP-6R, the results of the mathematical method fit some of the graphical method results. If the *s–log(N)* family of curves are taken into account, it can be observed that some of the results are best fitted by the mathematical method (for p_f of 0.2) while some are best fitted by the linear regression curves from the graphical method (for p_f of 0.8). As a result, the best way to describe the probabilistic behaviour of mix W-CIP-6R is by using the mathematical $s–p_f$ curves for the probabilities of failure of 0.2 and 0.4 and to use the graphical $s–p_f$ curves for the probabilities of 0.6 and 0.8.

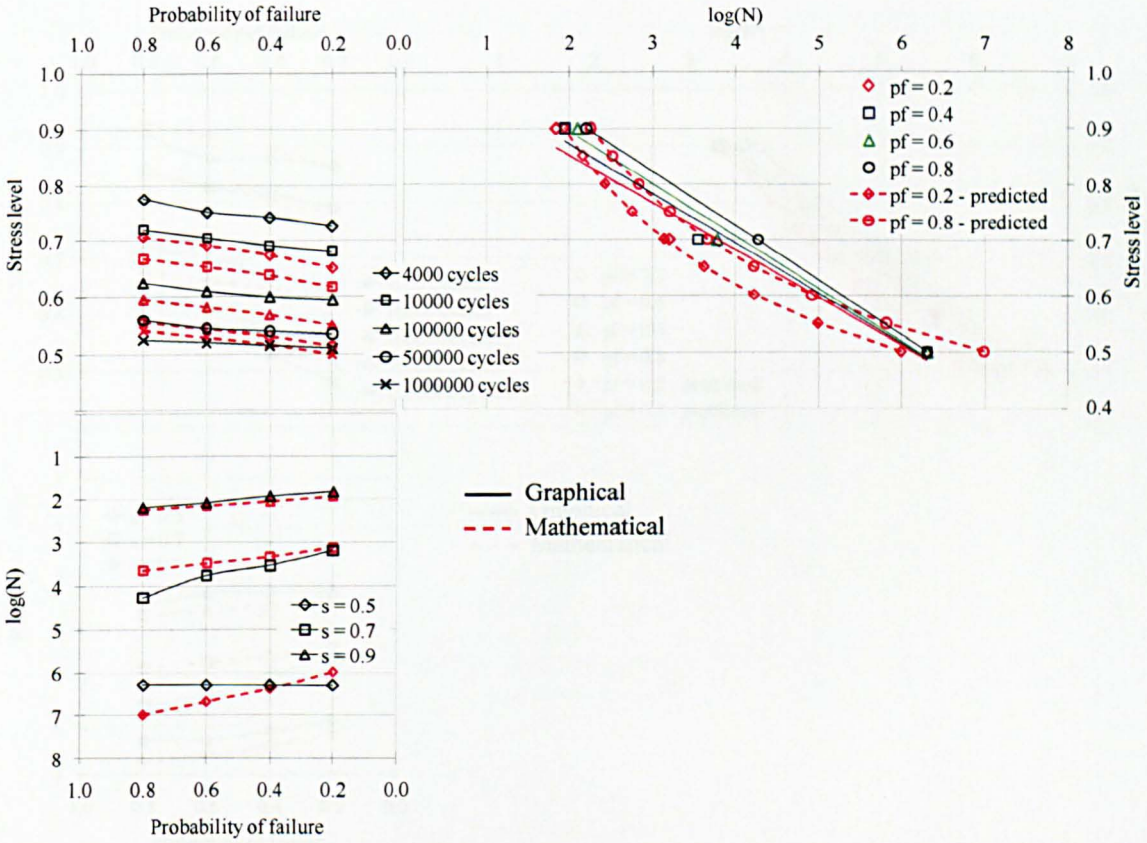

Figure 256 – Probabilistic analysis for mix W-CIP-6R.

The 6R wet mix has better fatigue resistance than the W-CIP-0 and lower resistance than W-CIP-2R mix. W-CIP-6R is expected to last up to one million cycles at the stress level of about 0.50, with a probability of failure of 20%. The mix should last up to 4000 cycles at the stress level of 0.77, with a probability of failure equal to 80%.

The W-CIP-6R mix seems to have a more homogeneous fatigue performance compared to plain and 2R wet mixes, which means that a higher change in the stress level (from 0.52 to 0.72, p_f = 50%) is necessary to change the number of cycles from 4000 to 1 million for a certain p_f.

10.4.3.2 RCC mixes

R-CIP-0

The mathematical method seems to fit reasonably well the results from the graphical method of mix R-CIP-0, as shown in Figure 257. This is because both graphical and mathematical *s–log(N)* family of curves are close to each other, and fit some of the experimental results. However, the linear regressions of the graphical method appear to fit slightly better the experimental results and, hence, seem to be more appropriate.

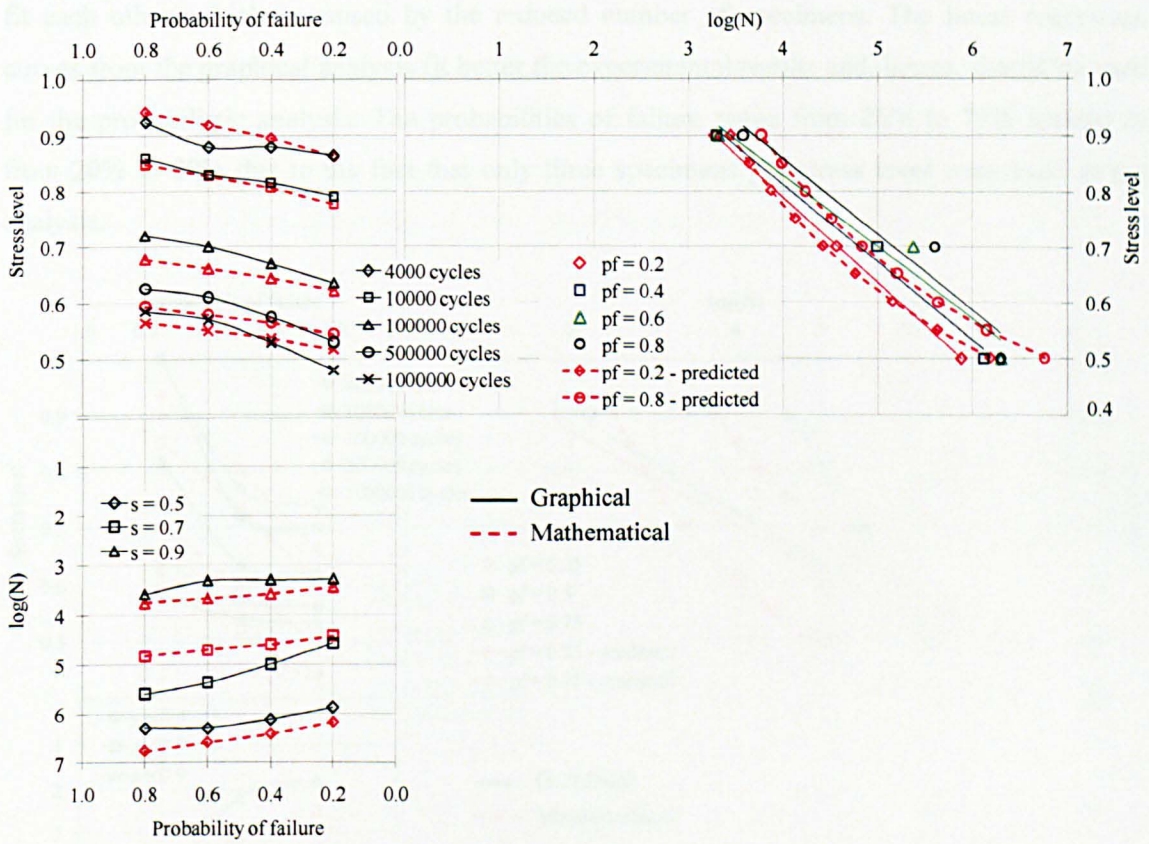

Figure 257 – Probabilistic analysis for mix R-CIP-0.

The mix appears to have good resistance when subjected to high stress levels. In the worst case scenario, the mix seems to resist up to 4000 cycles at the significant stress level of 0.93, for a p_f of 80%..

The mix can sustain up to one million cycles at the stress level of 0.48 with a probability of failure of 20%.

The mix seems to have a more uniform behaviour compared to the wet mixes, which means that small changes in the stress level do not cause considerable changes in the fatigue performance.

For the number of resisting cycles to vary from 4000 to one million, there should be a change in the stress level from 0.88 to 0.55 (reference to a probability of failure equal to 50%).

As previously reported in Section 5.7, the good behaviour of the RCC mix may be due to the aggregate interlock effect.

R-CIP-2I

The mathematical curves do not fit well the results from the graphical method for mix R-CIP-2I. As it can be seem in Figure 258, this is because both methods show *s–log(N)* curves that do not fit each other, which is caused by the reduced number of specimens. The linear regression curves from the graphical analysis fit better the experimental results and, hence, should be used for the probabilistic analysis. The probabilities of failure range from 25% to 75% instead of from 20% to 80% due to the fact that only three specimens per stress level were used in the analysis.

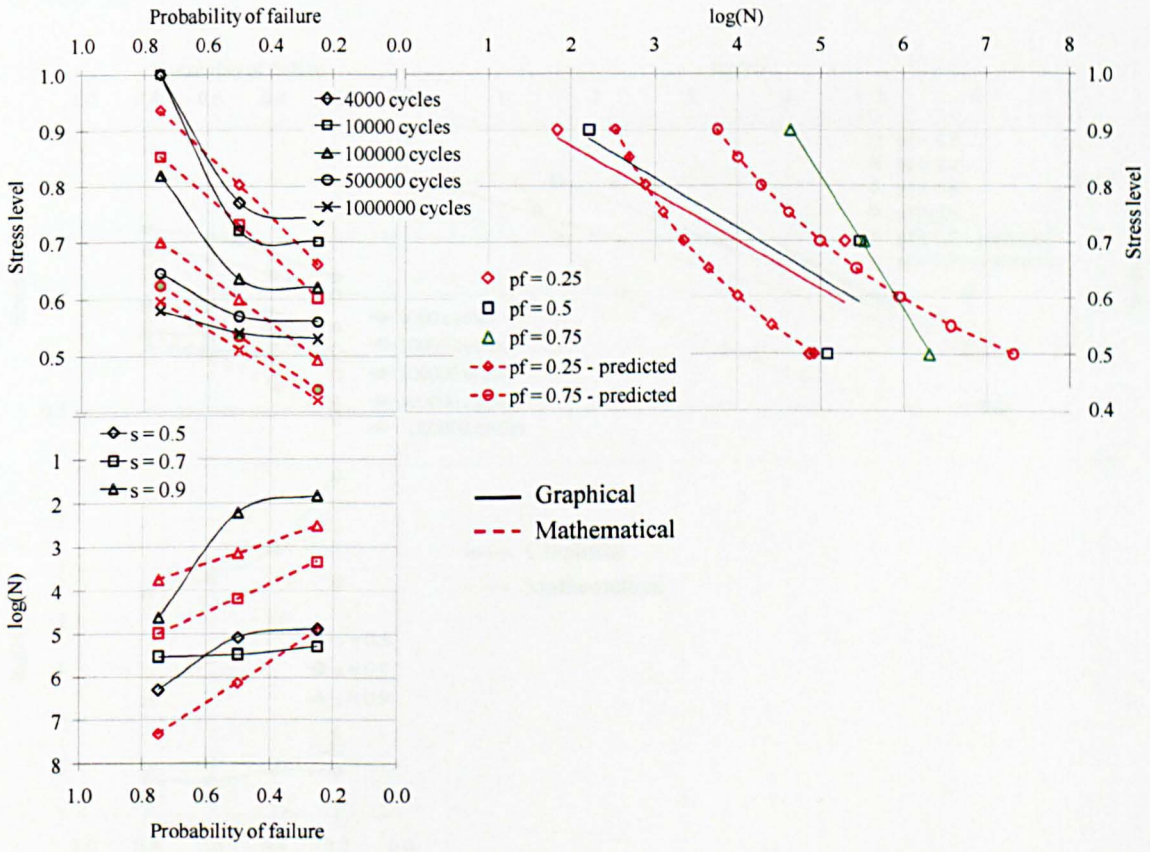

Figure 258 – Probabilistic analysis for mix R-CIP-2I.

The mix seems to have a good fatigue performance when subjected to both high and low stress levels. It appears that the mix performs slightly better than the corresponding plain mix when

subjected to low stress levels, since the mix should resist up to one million cycles when subjected to a stress level of 0.53 (p_f of 25%).

For a p_f of 75%, the mix should resist 4000 cycles subjected to loads close to the peak static ones. However, it is important to note that, due to the reduced number of specimens, and also due to the high variability encountered in the fatigue and static results for this mix, the analysis of the probability of failure for this mix is equally influenced by the variability in the results, and any results from this analysis should be used with care.

R-CIP-2R

As observed from most of the previous mixes analysed, the mathematical curves also do not fit well the results from the graphical method for mix R-CIP-2R, shown in Figure 259. The *s–log(N)* linear regression curves from the graphical method seem to fit better the experimental results than the mathematical curves and, for this reason, the graphical method should be followed for this mix.

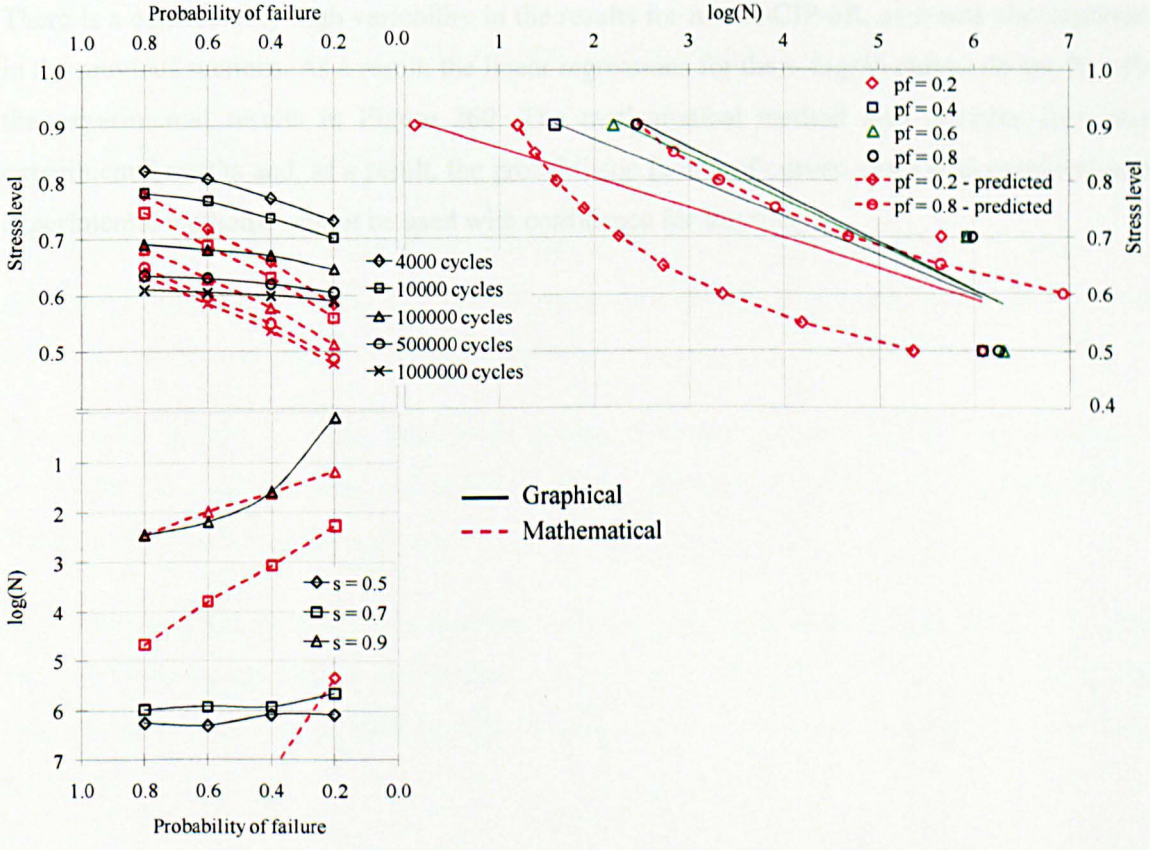

Figure 259 – Probabilistic analysis for mix R-CIP-2R.

The $s–p_f$ curves of mix R-CIP-2R have similarities with the $s–p_f$ curves of Figure 255. Both mixes have the same fibre content and type, even though they are different in terms of mix (wet and RCC).

Mix R-CIP-2R shows better fatigue performance at low stresses than at higher stresses. The mix seems to resist up to one million cycles subjected to a stress level of 0.6, with a p_f of 20%. In the worst case scenario, the mix can resist up to 4000 cycles subjected to a stress level of 0.82 (with 80% p_f).

As also observed for mix W-CIP-2R, the fatigue performance of the mix changes drastically if the stress level changes from 0.6 to 0.78 (with reference to a p_f equal to 50%). This effect may be associated with the bond between the recycled fibres and the matrix. There seems to be a moment at which recycled fibres suddenly lose their bond with the matrix when subjected to cyclic loads.

R-CIP-6R

There is a considerably high variability in the results for mix R-CIP-6R, as it was also reported in the previous sections. As a result, the linear regressions for the *s–log(N)* curves do not fit well the experimental results in Figure 260. The mathematical method also deviates from the experimental results and, as a result, the probabilistic family of curves, from both graphical and experimental methods, cannot be used with confidence for this mix.

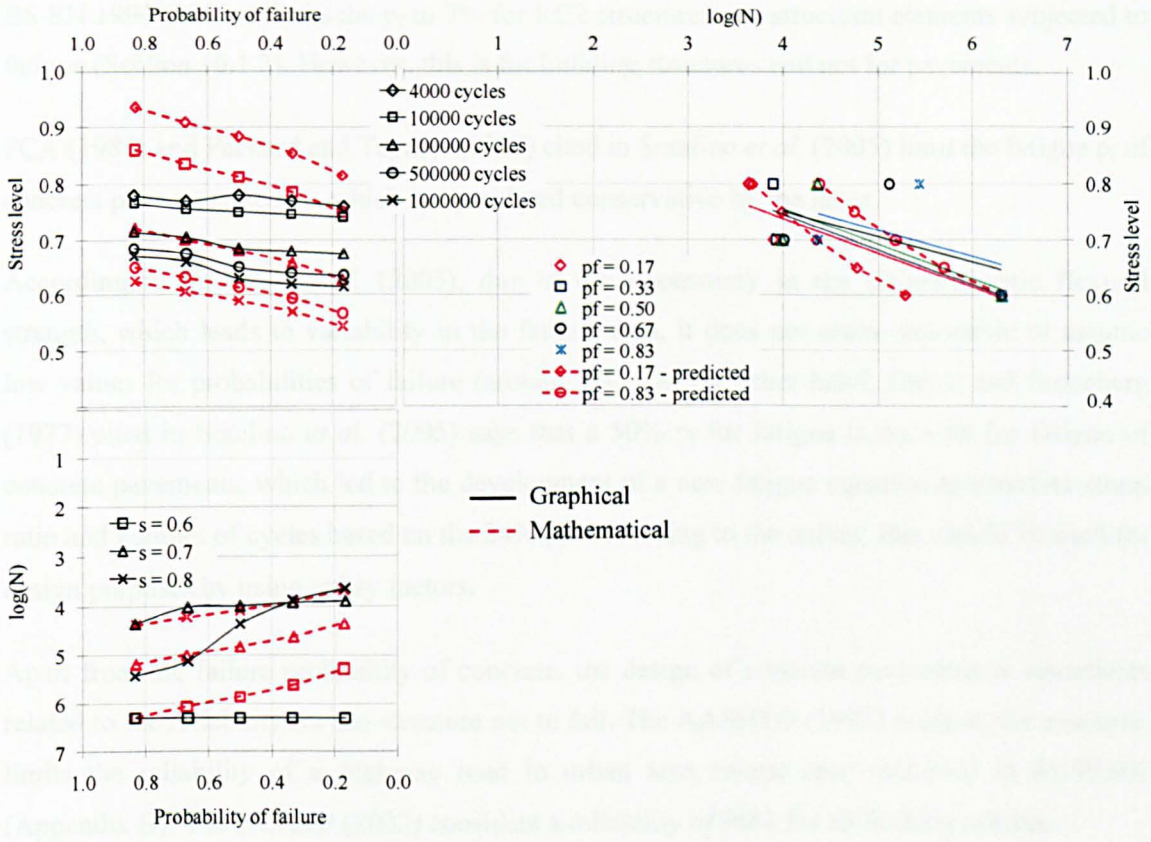

Figure 260 – Probabilistic analysis for mix R-CIP-6R.

10.4.4 Discussion on the Probabilistic Analysis

The applicability of the probabilistic analysis in design methods of concrete pavements is subjected to the understanding of the limit probability of failure[59] that can be acceptably used when dealing with fatigue of concrete pavements.

The number of studies on the limit p_f for fatigue is limited and they usually contradict each other. For the example cases, as described below, failure is determined by the initiation of cracking of the unreinforced concrete.

Oh (1986) and Shi *et al.* (1993) developed a probabilistic analysis for the fatigue of plain concrete based on the Weibull distribution, and assumed values of probability of failure ranging from 1% to 10% and 5% to 50%, respectively. However, they did not recommend a specific p_f for design.

Many authors derived fatigue equations, based on the probability of failure of 50% (Darter & Barenberg, 1997 cited in Sotelino, 2005; Roesler and Barenberg, 1998; Zhang *et al.*, 1996).

[59] Maximum probability of failure that assumes the structures will probably not fail (Section 10.1.2).

BS EN 1990 (2002c) limits the p_f to 7% for RC2 structures and structural elements subjected to fatigue (Section 10.1.2). However, this is for building structures and not for pavements.

PCA (1984) and Packard and Tayabji (1985) cited in Sotelino *et al.* (2005) limit the fatigue p_f of concrete pavements to 5%, which is considered conservative by the latter.

According to Sotelino *et al.* (2005), due to the uncertainty in the ultimate static flexural strength, which leads to variability in the fatigue data, it does not seem reasonable to assume low values for probabilities of failure (around 5%). On the other hand, Darter and Sorenberg (1977) cited in Sotelino *et al.* (2005) says that a 50% p_f for fatigue is not safe for fatigue of concrete pavements, which led to the development of a new fatigue equation to correlate stress ratio and number of cycles based on the 24% p_f. According to the author, this should be used for design purposes by using safety factors.

Apart from the failure probability of concrete, the design of concrete pavements is sometimes related to the reliability for the structure not to fail. The AASHTO (1993) method, for example, limits the reliability of a highway road in urban area (worst case scenario) in 85-99.9% (Appendix B). The NCHRP (2002) considers a reliability of 90% for all faulting criteria.

Yoder (1969) cited in Basma and Al-Balbissi (1989) proposed a method based on the least-cost to calculate the reliability of a concrete pavement, which considers that the optimum design value (e.g. thickness of the pavement) depends on the cost ratio *CR*, the variability of the subgrade *CV* and the traffic conditions. The method proposed by Yoder (1969) was modified by Basma and Al-Balbissi (1989) and is shown in Figure 261.

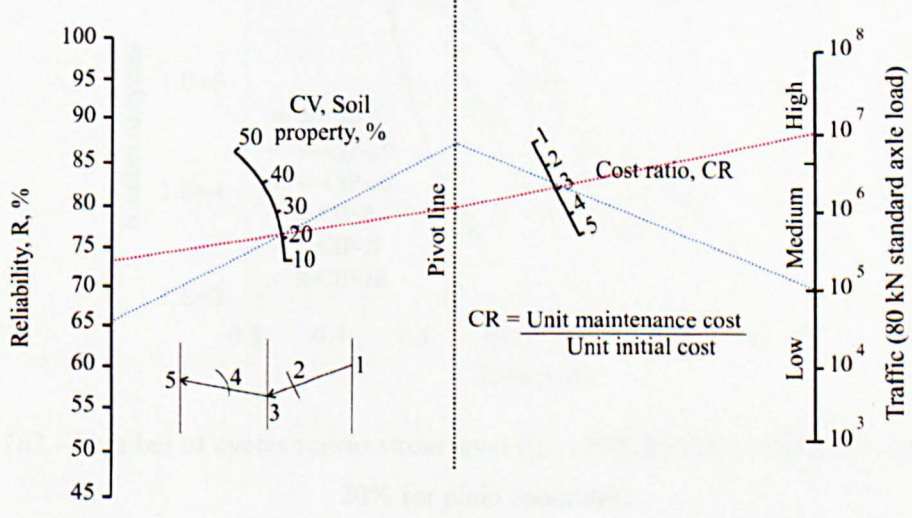

Figure 261 – Reliability for the least-cost design [after Basma and Al-Balbissi, 1989].

The above graph shows that different values of p_f can be assumed when dealing with different design parameters. This can be seen when CV and CR are constant, and two different traffic conditions are assumed.

The reliability of a concrete pavement is not only related to the fatigue performance of the structure, but also to the variability in the materials and to the variability of the mechanical and environmental loads. The above figure shows that the reliability of a pavement may easily vary from 50 to 95%, at which only part of it is due to fatigue reliability.

It appears reasonable to assume a p_f for fatigue of unreinforced concrete roads around 10-20%. Values of p_f lower than 10% may lead to conservative fatigue designs, whilst values above 20% may lead to reduced safety of the structure due to the uncertainty associated with fatigue data. This agrees with most of the works cited above. Nevertheless, higher values of p_f may be assumed when dealing with SFRC due to the fact that fibres improve the performance of concrete.

For the purpose of this thesis, the maximum probability of failure assumed for SFRC was 25% whilst for plain concrete the value drops to 20%. Focusing on this assumption, a comparison was made among the mixes in terms of stress ratio *versus* number of cycles, for specific number of cycles (4000, 10,000, 100,000, 500,000 and 1 million), as shown in Figure 262. The results account for either the graphical or the mathematical method, according to the discussions carried out previously for each mix. Due to the variability encountered for mix R-CIP-6R, this is not included in the graph below.

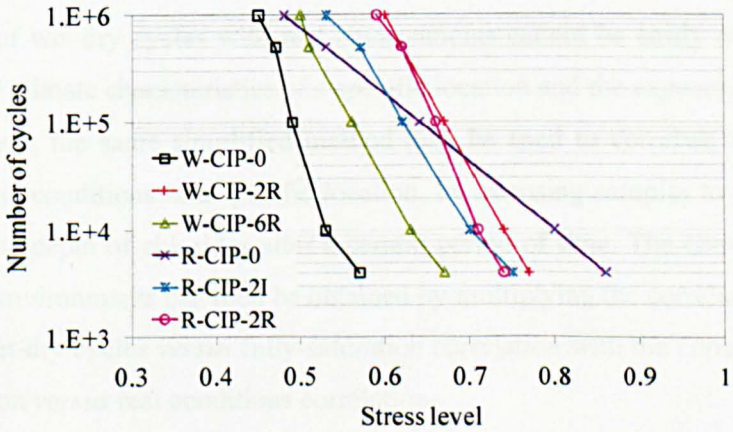

Figure 262 – Number of cycles *versus* stress level (p_f = 25% for fibre reinforced mixes and p_f = 20% for plain concrete).

It can be clearly seen that mix W-CIP-0 needs to be subjected to the lowest stress level to achieve the same number of cycles as the other mixes, followed by the W-CIP-6R and R-CIP-2I.

Mixes W-CIP-2R and R-CIP-2R show very similar behaviour and they can be subjected to higher stress levels than the other mixes when the number of cycles is higher than 100,000. Both 2R mixes show the best performance in terms of resisting 1 million cycles at a higher stress level than the other mixes.

Mix R-CIP-0 seems to resist well to low number of cycles (4000 and 10,000) at higher stress levels than the other mixes, which is due to the effect of the aggregate interlock.

10.5 SUMMARY AND DISCUSSION

This chapter explained the probabilistic approach used to predict the SLD of SFRC structures subjected to chloride ingress and freeze-thaw attack. Specific methodologies for both deterioration processes were used. This chapter also explained the results from the probabilistic approach to analyse fatigue data.

Chloride ingress SLD findings

A simplified methodology was proposed to correlate wet-dry cycles with the fully-saturated condition. Basically, the method considers the comparison of the depth of chlorides measured during wet-dry cycles after a certain period of time, with the predicted depth of chloride ingress based on the analytical solution using Fick's second law. The method is exemplified by a practical example. However, due to a lack of accurate measurement of the depth of chloride ingress during wet-dry cycles, the example cannot be considered as a true correlation between wet-dry cycles and the fully-saturated condition.

The correlation of wet-dry cycles with real environments cannot be easily obtained since it is dependent on the climate characteristics of a specific location and the exposure conditions of the structure. However, the same simplified method may be used to correlate the fully-saturated condition with the conditions at a specific location, by exposing samples to the real condition and measuring the depth of chlorides after a certain period of time. The correlation of wet-dry cycles with real environments can then be obtained by multiplying the correlation factor (Figure 238) from the wet-dry cycles *versus* fully-saturation correlation with the correlation factor from the fully-saturation *versus* real conditions correlation.

A comparison was carried out to verify the influence of various variables of the research on the chloride ingress of the concrete. For that, the analytical solution using Fick's second law was used to predict the service life of structures subjected to the fully-saturated condition. The main outputs are the following: 1) the RCC mixes have reduced endurance life than the wet mixes, which is mainly due to the higher amount of trapped air of RCC mixes and also to the boundary conditions of such mixes, leading to a more porous concrete in the outer parts; 2) the addition of

2% fibre content shows better performance than plain and 6R; 3) LEC leads to longer service life than CIP, especially due to the binding capacity of the mixes. These findings are based on the chloride content and diffusion analysis shown in Section 6.3. However, it is important to note that there may be some variability in these analyses, which may affect the comparison in terms of SLD.

Freeze-thaw SLD findings

The freeze-thaw SLD procedures were based on a combination of both temperature and loss of mass models in terms of scaled material. This thesis proposes a methodology for calculating the endurance life of structures subjected to freeze-thaw by a simplified and direct method. It includes weather data from where the structure is located, which means that it can be applied in any place where climate data is available. The method was exemplified by a practical application of the method, based on the mixes tested experimentally in this thesis.

By means of a sensitivity analysis, it was found that the resistant temperature, the critical scaling and model uncertainty factor influence considerably the results, and that they are dependent on the characteristics of the mix. There is a need to understand better these parameters to allow accurate calculations of SLD for structures exposed to freeze-thaw, which includes the correlation of accelerated methods with environmental exposures or to perform more realistic acceleration techniques of freeze-thaw.

The freeze-thaw procedures used in this chapter were based on specific mixes tested in laboratory. However, the method may be improved by considering the influence of the various properties and characteristics of the mixes (e.g. porosity, density, compressive strength, w/c ratio, cement content, etc) on the freeze-thaw SLD.

Fatigue probabilistic analysis findings

The fatigue probabilistic analysis can be used in design procedures to predict a certain number of cycles that a structure will be able to resist for a certain stress level and probability of failure.

The results presented in this chapter are based on the graphical and mathematical model to predict the correlation between families of s-N-p_f curves. However, a higher number of specimens is necessary to give more accurate results.